

Myonuclear dynamics in muscle plasticity and the transcriptional regulation of resistance training induced hypertrophy.

Mark Robert Viggars

**Thesis submitted in partial fulfilment of the requirements of
Liverpool John Moores University for the degree of DOCTOR OF
PHILOSOPHY**

September 2021

Student:

Mark Viggars (BSc Hons, MPhil, AFHEA),
Research Institute for Sport and Exercise Sciences (RISES),
Liverpool John Moores University,
Liverpool,
L3 3AF,
United Kingdom

Director of Studies:

Jonathan Jarvis BSc PhD DIC ARCS FHEA
Professor of Sport and Exercise Science
Research Institute for Sport & Exercise Sciences (RISES),
Liverpool John Moores University,
Liverpool,
L3 3AF
United Kingdom

Declaration

I Mark Viggars declare that all work presented here in this thesis was written by me and is my own. No portion of the work referred to in this thesis has been submitted in support of an application for another degree or qualification at Liverpool John Moores University, any other university or other institute of learning.

Contents

Acknowledgements	10
Publications	11
Abbreviations and Acronyms	12
List of Figures	20
List of Tables	24
Abstract	25
Chapter 1: Introduction	26
1.1 Skeletal Muscle Structure and Function	27
1.2 Relationship Between Muscle Activity and Myosin Heavy Chain Isoform Expression	32
1.3 Relationship Between Muscle Activity & Mitochondria	39
1.4 Unloading and Muscle Atrophy & The Ubiquitin Proteasome Pathway	45
1.5 Loading and Muscle Hypertrophy	49
1.6 Models of Hypertrophy	59
1.7 Hyperplasia, Muscle Fibre Splitting & Changes in Fiber Length Following Mechanical Loading & Functional Overload	63
1.8 Skeletal Muscle During Development	67
1.9 Satellite Cells & Adult Myogenesis	70
1.10 Thesis Aims & Objectives	74
Chapter 2: Materials and Methodology	76
<i>Cell Culture</i>	
2.1 In-vitro Cell Culture	77
2.2 C2C12 & Human Primary Myoblast/Myotube Cell Culture	77
2.3 Routine Culture of C2C12 Myoblast and Myotubes in Monolayer	77

2.4 Routine Culture of Human Skeletal Muscle Derived Myoblasts and Myotubes in Monolayer	78
2.5 Immunofluorescent labelling of cells	78
2.6 Fluorescent microscopy of cells	80

In-vivo Electrical Stimulation Experiments

2.7 Electrical Stimulation of The Tibialis Anterior Muscle Via Implantable Pulse Generators to Produce Loaded & Unloaded Contractions in Rodents	80
2.8 Ethics & Animals Used	81
2.9 Miniature Implantable Stimulators for Rats	84
2.10 Implant Procedure	84
2.11 Electrode Configuration	85
2.12 Stimulation Protocols	85
2.13 Deuterium delivery for dynamic proteomic profiling	86
2.14 Terminal Procedure and Tissue Preparation for Regional Investigations	86

In-vivo Nerve Block Experiments

2.15 Background	88
2.16 Nerve Blockade of The Common Peroneal Nerve (CPN) Using A Nerve Cuff to Produce Atrophy in The Tibialis Anterior Muscle in Rats	88
2.17 Implant Contents & Implant Procedure	89
2.18 Nerve Block Protocol	89
2.19 Terminal Procedure and Tissue Preparation	90

In-vivo Functional Overload Experiments

2.20 Mechanical Overload of The Plantaris Via Synergist Ablation in Wild-Type and LMNA+/ Δ K32 Mice	90
2.21 Background to Lamin A Mutations & Surgical Procedure	90

2.22 Procedure and Tissue Preparation	92
---	----

Single Fiber Preparation and Analysis

2.23 Background to human biopsy sample access and eccentric damaging protocol induced by electrical stimulation.....	93
2.24 Single Muscle Fibre Analysis	94
2.25 Preparation and Extraction.....	94
2.26 Immunostaining	94
2.27 Fluorescent microscopy imaging and analysis of single muscle fibers.....	94

Histology and Immunohistochemistry

2.28 Histological Analysis of Frozen Cryosections of Muscle Tissue	95
2.29 Tissue Sectioning	95
2.30 Hematoxylin and Eosin Stain for Fibre Morphology & Damage Assessment	96
2.31 Nicotinamide Adenine Dinucleotide (NADH) Staining for Assessment of Muscle Mitochondrial Content	97
2.32 Adenosine triphosphate-ase (ATPase) Staining for Assessment of Muscle Myosin Heavy Chain Content	97
2.33 Immunohistochemistry.....	98
2.34 Fluorescent microscopy and tile scanning	98
2.35 Myovision 2.0 Development and Analysis.....	98

RT-qPCR Analyses

2.36 Tissue Homogenisation and RNA Extraction (TRIzol Method)	103
2.37 RNA Concentration & Purity Analysis for RT-qPCR.....	104
2.38 RNA Sample Dilution	104
2.39 Design of Primers for Polymerase Chain Reaction (PCR).....	104

2.40 QiAgility Automated Sample Preparation for RT-qPCR	105
2.41 Rotor Gene-Q Real Time Cycler for RT-qPCR	105
2.42 Quantification of Relative Gene Expression using RT-qPCR Using the $2^{-\Delta\Delta Ct}$ Method for Fold Change Calculations	107

Next-Generation RNA Sequencing

2.43 mRNA Library Preparation	108
2.44 Pre-alignment QA/QC	110
2.45 Read Trimming	112
2.46 STAR Alignment 4.4.1d to <i>Rattus Norvegicus</i> , Rnor_6.0 genome assembly	113
2.47 Post-alignment QA/QC	114
2.48 Quantification to Ensembl transcriptome annotation model <i>Rattus Norvegicus</i> , Rnor_6.0	117
2.49 Normalisation Background and DESeq2 median of ratios	120
2.50 Differential Gene Expression Analysis	121
2.51 Principal Component Analysis	121
2.52 KEGG Pathway Analysis	121
2.53 Self-Organising Map (SOM) Analysis	122
2.54 Venn Diagram Analysis	122
2.55 Comparative Transcriptome Analysis	122

Chapter 3: Computational Analysis of Skeletal Muscle Immunohistochemistry to Assess Myonuclear Turnover with Changes in Activity, Loading & Unloading of Rodent Hindlimb Muscles	123
3.1 Abstract	124
3.2 Introduction	124

3.3 Methods.....	127
3.4 Results.....	136
3.5 Discussion.....	154
3.6 Conclusion.....	161
3.7 Future technical considerations/observations from assessing changes in muscle mass and fiber type characteristics in response to spillover training	162
Chapter 4: A pilot investigation into the long-term effects of long-term resistance training, long term detraining following detraining and long-term recovery from severe disuse atrophy	168
4.1 Abstract.....	169
4.2 Introduction	170
4.3 Methods.....	172
4.4 Results.....	175
4.5 Discussion.....	192
4.6 Conclusion.....	195
Chapter 5: Timecourse transcriptome analysis of programmed resistance exercise in rats.	197
.....	
5.1 Abstract.....	198
5.2 Introduction	200
5.3 Methods.....	202
5.4 Results.....	207
5.5 Discussion.....	256
5.6 Conclusion.....	265
Chapter 6: Investigating Pericentriolar Material-1 (PCM1) as a marker for skeletal muscle myonuclei: A cross-species and models approach.....	267

6.1 Abstract.....	268
6.2 Introduction	269
6.3 Methods.....	272
6.4 Results.....	278
6.5 Discussion.....	292
6.6 Conclusion.....	296
Thesis Conclusion	298
References	300
Appendices	338

Acknowledgements

I would like to express a special thanks and gratitude for all of those who have made it possible to complete my PhD journey, something I never thought I would achieve. Firstly, I would like to express a special thanks to my DoS and mentor, Professor Jonathan Jarvis, without which I would not have the love for skeletal muscle biology that I have today. Jonathan has been a fountain of knowledge throughout my PhD for things both inside and outside of my research area. Our thoughtful conversations and your willingness to give me freedom with research projects has allowed me to develop my independence and understanding of the 'bigger picture'. I hope to continue to profit from your mentorship as I progress in my career. I would like to say a special thanks to co-supervisor Professor Claire Stewart, who I started my research journey with during my undergraduate programme. You have always had time for everyone and anyone and have an unbelievable work ethic of which I am envious. Your ability to play devil's advocate has developed my scientific rigor and has always pushed me to produce the best quality science that I can. To Dr. Daniel Owens, I would like to thank him for his invaluable experience and friendship both inside and outside the lab, your contributions have accelerated my development towards being a thoughtful, independent scientist. I must thank Dr. Hazel Sutherland for your friendship, passing on your immense practical expertise and organisation without which none of my work would have been possible. I also give my thanks to Steve Broadfoot and the rest of the LSSU staff for their time, dedication and flexibility when performing animal interventions. I would like to thank Dr. Yuan Wen from the University of Kentucky for his expertise and willingness to openly collaborate, without which a large part of my analyses would not have been possible. I also give thanks to fellow post-graduate researchers (Dr. Steffen Eickhoff, Dr. Dan Sadler, Dr. Alex Brown, Dr. Daniel Turner and Andy Nolan) who assisted in my development through thoughtful discussion both inside and outside the lab, and virtually during the confinement of a worldwide pandemic. I also give thanks to my amazing friends in and outside of cricket, for giving me much needed relief outside of work. Finally, and most importantly, I would like to thank my family (John, Linda & Michael) and my best friend and girlfriend Ruby, for their endless and selfless support throughout my education and life. I wouldn't be where I am now without your love, kindness, and encouragement through the challenges I've experienced in recent years.

Publications (By Date)

- Seaborne, R.A., **Viggars, M.** and Sharples, A.P., (2019). How Long Does Muscle Memory Last? The Role of Epigenetics. *Journal Of Applied Physiology*, 127(6), 1819-1819.
- Owens, D.J., Messéant, J., Moog, S., **Viggars, M.**, Ferry, A., Mamchaoui, K., Lacène, E., Roméro, N., Brull, A., Bonne, G. and Butler-Browne, G., (2021). Lamin-related congenital muscular dystrophy alters mechanical signaling and skeletal muscle growth. *International journal of molecular sciences*, 22(1), p.306.
- Hughes, D.C., Turner, D.C., Baehr, L.M., Seaborne, R.A., **Viggars, M.**, Jarvis, J.C., Gorski, P.P., Stewart, C.E., Owens, D.J., Bodine, S.C. and Sharples, A.P., (2021). Knockdown of the E3 Ubiquitin ligase UBR5 and its role in skeletal muscle anabolism. *American Journal of Physiology-Cell Physiology*, 320(1), pp.C45-C56.
- Turner, D.C., Gorski, P.P., Seaborne, R.A., **Viggars, M.**, Murphy, M., Jarvis, J.C., Martin, N.R., Stewart, C.E. and Sharples, A.P., (2021). Mechanical loading of bioengineered skeletal muscle in vitro recapitulates gene expression signatures of resistance exercise in vivo. *Journal of Cellular Physiology*.
- **Viggars, M.**, Wen, Y., Peterson, C., and Jarvis, J.C., (2022). Critical assessment of automated cross-sectional analysis of trained, severely atrophied and recovering whole rat skeletal muscle using MyoVision 2.0. *Journal of Applied Physiology*.
- **Viggars, M.**, Owens, D.J., Stewart, C.E., Coirault, C., Mackey, A.L., and Jarvis, J.C., (2022). PCM1 labelling reveals myonuclear and nuclear dynamics in skeletal muscle across species. Under Review.

Abbreviations & Acronyms

Abra	Actin Binding Rho Activating Protein
ACSM	American College of Sports Medicine
Actn2	Actinin Alpha 2
Actn3	Actinin Alpha 3
Actr	Activinin Receptor
Akt	Protein kinase B
Alk	Activinin Receptor-like kinase
Amd1	Adenosylmethionine Decarboxylase 1
AMP	Adenosine monophosphate
Ampd1	Adenosine monophosphate deaminase 1
AMPK	Adenosine monophosphate kinase
Angpt12	Angiopoietin-like 2
Ankrd1	Ankyrin Repeat Domain 1
Ankrd2	Ankyrin Repeat Domain 2
Anxa2	Annexin A2
Apoe	Apolipoprotein E
Arfgap3	ADP Ribosylation Factor GTPase Activating Protein 3
Arfp2	Adenosine monophosphate ribosylation Factor Interacting Protein 2
Arntl1	Aryl Hydrocarbon Receptor Nuclear Translocator Like 1
Arrdc3	Arrestin Domain Containing 3
Asb5	Ankyrin Repeat And SOCS Box Containing 5
Atf3	Activating Transcription Factor 3
ATP	Adenosine 5'-triphosphate
Bcat2	Branched-chain-amino-acid aminotransferase
Bcl2l11	Bcl-2-like protein 11/BIM
Bgn	Biglycan
Bmal1	Brain and Muscle Arntl Like Factor 1
BMP	Bone Morphogenetic Protein
bp	base-pairs
BSA	Bovine Serum Albumin
Btg2	BTG Anti-Proliferation Factor 2
C1QB	Complement C1q B Chain
Calm2	Calmodulin 2
Camk	Calmodulin-dependent kinase
CD14	Cluster of differentiation 14
CD4	Cluster of differentiation 4
CD68	Cluster of differentiation 68
CI	Confidence Interval
Ckap4	Cytoskeleton Associated Protein 4
CLFS	Chronic Low Frequency Stimulation
CLOCK	Circadian Locomotor Output Cycles Kaput
Cnn2	Calponin 2
Col1a1	Collagen Type I Alpha 1 Chain

Col18a1	Collagen Type XVIII Alpha 1 Chain
Col3a1	Collagen Type III Alpha 1 Chain
Col4a1	Collagen Type IV Alpha 1 Chain
Col4a2	Collagen Type IV Alpha 2 Chain
Col5a2	Collagen Type V Alpha 2 Chain
Col6a1	Collagen Type VI Alpha 1 Chain
Col6a2	Collagen Type VI Alpha 2 Chain
Coro1c	Coronin 1c
Cotl1	Coactosin Like F-Actin Binding Protein 1
Cox	Cyclooxygenase
Cox6a1	Cytochrome C Oxidase Subunit 6A1
Cox7a1	Cytochrome C Oxidase Subunit 7A1
Cox7a2l	Cytochrome C Oxidase Subunit 7A2l
CPM	Counts per million
CPN	Common Peroneal Nerve
Creb	cAMP-response element binding protein
Cryab	Crystallin Alpha B
CSA	Cross-Sectional Area
Csfr1	Colony Stimulating Factor 1 Receptor
Csrnp1	Cysteine And Serine Rich Nuclear Protein 1
Csrp3	CYSTEINE-RICH PROTEIN 3/ MLP/ Muscle LIM Protein
Cry1	Cryptochrome Circadian Regulator 1
cT	cycle Threshold
CV	Coefficient of Variation
Cyb	Cytochrome B
Dach2	Dachshund Family Transcription Factor 2
DAP	Death Associated Protein
DAPI	4',6-diamidino-2-phenylindole
Dbp	D-Box Binding PAR BZIP Transcription Factor
Dbt	Dihydrolipoamide Branched Chain Transacylase E2
Ddit3	DNA Damage Inducible Transcript 3
DEG	Differentially Expressed Genes
DEPTOR	DEP Domain Containing MTOR Interacting Protein
Dgkz	Diacylglycerol Kinase Zeta
Dhrs4	Dehydrogenase/Reductase 4
Dhrs7c	Dehydrogenase/Reductase 7C
DM	Differentiation Media
DMEM	Dulbecco's Modified Eagle Medium
Dnaja4	DnaJ Heat Shock Protein Family (Hsp40) Member A4
Dnajb1	DnaJ Heat Shock Protein Family (Hsp40) Member B1
dNTP	Deoxynucleotide triphosphate
DPX	Di-N-Butyl phthalate in xylene
dsDNA	Double Stranded Deoxyribonucleic Acid
DSHB	Developmental Studies Hybridoma Bank
Ecm1	Extracellular Matrix Protein 1

EDL	Extensor digitorum longus
Efna1	Ephrin A1
Egr1	Early Growth Response 1
Ehd4	Eps15 Homology Domain Containing 4
eiF3F	Eukaryotic Translation Initiation Factor 3 Subunit F
eiF4E	Eukaryotic Translation Initiation Factor 4 Subunit E
Eif4e3	Eukaryotic Translation Initiation Factor 4 Subunit E3
Elk1	ETS domain like protein-1
Em	Emission
Emp1	Epithelial Membrane Protein 1
Enah	ENAH Actin Regulator
ERK	Extracellular-signal-regulated kinase/ MAPK1
Ex	Excitation
Fabp5	Fatty Acid Binding Protein 5
Fam78a	Family With Sequence Similarity 78 Member A
FAP	Fibroblast Proliferation Antagonist
FAK	Focal Adhesion Kinase/ PTK2 Protein-tyrosine kinase 2
FBXO32	F-box only protein 32, also known as MAfbx and Atrogin-1
Fhl1	Four And A Half LIM Domains 1
Flnc	Filamin C
FO	Functional Overload
Fos	Fos Proto-Oncogene, AP-1 Transcription Factor Subunit
Foxo	Class O of forkhead box transcription factors FOXO
GAST	Gastrocnemius
GDF-8	Growth Differentiation Factor 8 (Myostatin)
Gfpt2	Glutamine-Fructose-6-Phosphate Transaminase 2
Glmp	Glycosylated Lysosomal Membrane Protein
GM	Growth Media
Gpmmb	Glycoprotein Nmb
Gpx1	Glutathione Peroxidase 1
Gramd1b	GRAM Domain Containing 1B
GSA	Gene Set Analysis
Gsn	Gelsolin
Gstm7	Glutathione S-transferase
H&E	Hematoxylin and Eosin
Habp4	Hyaluronan Binding Protein 4
Hbegf	Heparin-binding EGF-like growth factor
HDAC	Histone Deacetylase
Hect	Homologous to the E6-AP Carboxyl Terminus
hiFBS	Heat-Inactivated Fetal Bovine Serum
HIIT	High intensity interval training
Hjv	Hemojuvelin
Hk2	Hexokinase2
Hmox1	Heme Oxygenase 1
Hras	Harvey rat sarcoma viral oncogene homolog, Proto-Oncogene, GTPase

Hsc70	Heat Shock cognate 71 kDa protein
Hsp1ab	Heat Shock 70kDa protein 1B
Hsp40	Heat Shock Protein 40
Hspb6	Heat Shock Protein Family B (Small) Member 6
Hspb7	Heat Shock Protein Family B (Small) Member 7
IB	Immunobuffer
Id4	Inhibitor Of DNA Binding 4, HLH Protein
Ier5	Immediate-early response 5
IGF1	Insulin Growth Factor 1
IPG	Implantable Pulse Generator
Ifrd1	Interferon Related Developmental Regulator 1
Irs2	Insulin Receptor Substrate 2
Itga5	Integrin Subunit Alpha 5
Jun	Jun Proto-Oncogene, AP-1 Transcription Factor Subunit
Junb	Jun Proto-Oncogene, AP-1 Transcription Factor Subunit b
Kank2	KN Motif And Ankyrin Repeat Domains 2
kb	kilobases
KEGG	Kyoto Encyclopedia of Genes and Genomes
Klf5	Kruppel Like Factor 5
Klhl40	Kelch Like Family Member 40
Ky	Kyphoscoliosis Peptidase
LARP1	La-related protein 1
Lgals3	Galectin3
Lipg	Lipase G
LKB1	Serine/threonine kinase 11
LMNA	Gene encoding nuclear envelope lamins A and C
LMNA-CMD	Lamin A Congenital Muscular Dystrophy
Lmod1	Leiomodin 1
Lox	Lysyl Oxidase
Loxl1	Lysyl Oxidase Like 1
Lrrc30	Leucine Rich Repeat Containing 30
LSM	Low Serum Media
Lum	Lumican
Mafbx	Muscle Atrophy F-box gene. Also known as FBXO32 and Atrogin-1
Maff	MAF BZIP Transcription Factor F
Map1a	Microtubule Associated Protein 1A
MAPK	Mitogen Activated Protein Kinase
Masp1	MBL Associated Serine Protease 1
MCAM	Melanoma Cell Adhesion Molecule
Me1	Malic Enzyme 1
MEF2	Myocyte enhancer factor 2
Mfap4	Microfibril Associated Protein 4
mg	Milligram
Mgp	Matrix Gla Protein
MyHC	Myosin Heavy Chain

Midn	Midnolin
Mitr	MEF2-interacting transcription repressor (HDAC9)
MLC	Myosin Light Chain
mLST8	MTOR Associated Protein, LST8 Homolog
Mmp9	Matrix metalloproteinase 9
MO25	Mouse binding protein 25/calcium binding protein 39
MoTrPAC	Molecular Transducers of Physical Activity Consortium
MSIN1	mammalian stress activated protein kinase interacting protein 1
Msn	Moesin
mtDNA	Mitochondrial deoxyribonucleic acid
MTJ	Myotendinous Junction
mTOR	Mechanistic/mammalian target of rapamycin
mTORC1	Mechanistic/mammalian target of rapamycin complex 1
MURF1	Muscle RING-finger protein-1, also known as Trim63
Mustn1	Musculoskeletal, Embryonic Nuclear Protein 1
Myc	Myelocytomatosis Proto-Oncogene, BHLH Transcription Factor
Myh	Myosin Heavy Chain
Mylk2	Myosin Light Chain Kinase 2
NADH	Nicotinamide adenine dinucleotide
NAFLD	Non-alcoholic fatty liver disease
NFAT	Nuclear factor of activated T-cells
NG-RNA-Seq	Next Generation Ribonucleic Acid Sequencing
NMJ	Neuromuscular Junction
Nr4a1	Nuclear Receptor Subfamily 4 Group A Member 1
Nr4a3	Nuclear Receptor Subfamily 4 Group A Member 3
NRF	Nuclear Respiratory Factor
nt	Neural tube
Nupr1	Nuclear Protein 1, Transcriptional Regulator
N-WASP	Neural Wiskott-Aldrich syndrome protein
OCT	Optimal Cutting Temperature
Olfml3	Olfactomedin Like 3
Otud1	OTU Deubiquitinase 1
P4htm	(Prolyl 4-Hydroxylase, Transmembrane
p70s6k	Ribosomal protein S6 kinase beta 1
PA	Phosphatidic acid
Pax7	Paired box protein 7
PBS	Phosphate Buffer Saline
PCA	Principal Component Analysis
PCM1	Pericentriolar Material-1
PCR	Polymerase Chain Reaction
PDK1	Pyruvate Dehydrogenase Kinase 1
PDK4	Pyruvate Dehydrogenase Kinase 4
Per1/2	Period 1/2
PGC-1α	Peroxisome proliferator-activated receptor-gamma coactivator alpha
Phkg1	Phosphorylase Kinase Catalytic Subunit Gamma 1

Phlda1	Pleckstrin Homology Like Domain Family A Member 1
Pi3k	Phosphoinositide 3-kinase
PIC	Pre-initiation complex
PIP2/3	Prolactin Induced Protein
Pkb	Protein kinase B (Akt)
PLD	Phospholipase D
PLN	Plantaris
Pmp22	Peripheral Myelin Protein 22
Pnrc1	Proline Rich Nuclear Receptor Coactivator 1
Pol	Polymerase
Ppie	Peptidylprolyl Isomerase E
Ppp1r27	Protein Phosphatase 1 Regulatory Subunit 27
Ppp1r36	Protein Phosphatase 1 Regulatory Subunit 36
PRAS40	Proline-rich AKT1 substrate 1
Pvalb	Parvalbumin
Pygm	Glycogen Phosphorylase Muscle Associated
QA/QC	Quality assurance/ quality control
R3hdm2	R3H Domain Containing 2
Rab7b	RAB7B, Member RAS Oncogene Family
Raptor	Regulatory associated protein of mTOR
Rbm3	RNA Binding Motif Protein 3
Rcan1	Regulator Of Calcineurin 1
Reep1	Receptor expression-enhancing protein 1
Rheb	Ras Homolog, MTORC1 Binding
Rhoc	Ras Homolog Family Member C
Rictor	Rapamycin-insensitive companion of mTOR
RIN	RNA Integrity Number
RNA	Ribonucleic Acid
Rnf115	Ring Finger Protein 115
Ror	RAR-related orphan receptor alpha
Rplp0	Ribosomal Protein Lateral Stalk Subunit P0
Rplp2	Ribosomal Protein Lateral Stalk Subunit P2
Rps2	Ribosomal Protein S2
Rps6	Ribosomal Protein S6
Rrad	Ras Related Glycolysis Inhibitor And Calcium Channel Regulator
RT1-T24-4	RT1 class I, locus T24, gene 4
Rtn4	Reticulon 4
RT-qPCR	Real Time Quantitative Polymerase Chain Reaction
Sar1b	Secretion Associated Ras Related GTPase 1B
SC	Satellite Cell
Scd2	Stearoyl-CoA desaturase-2
SD	Standard Deviation
Sel1l3	SEL1L Family Member 3
Serpine1	Serpin Family E Member 1
Sfrp4	Secreted Frizzled Related Protein 4

Sh3gl1	SH3 Domain Containing GRB2 Like 1, Endophilin A2
Slc20a1	Solute Carrier Family 20 Member 1
Slc9a2	Solute Carrier Family 9 Member A2
Slfn2	Schlafen 2
SMAD	'Small worm' mothers against decapentaplegic homolog
Snai3	Snail Family Transcriptional Repressor 3
snRNA-seq	Single nuclei ribonucleic acid sequencing
SOL	Soleus
SOM	Self-organising mapping
Sorbs3	Sorbin And SH3 Domain Containing 3
Sp1	Specificity protein 1
Sparc	Secreted Protein Acidic and Cysteine Rich
Srbd1	S1 RNA Binding Domain 1
ssRNA	Single strand ribonucleic acid
STK11	Serine/Threonine Kinase 11 (LKB1)
STRAD	STE20-related kinase adapter protein alpha
TA	Tibialis Anterior
Tab2	TGF-Beta Activated Kinase 1 (MAP3K7) Binding Protein 2
Taf9	TATA-Box Binding Protein Associated Factor 9
Tcap	Titin-cap (Telethonin)
Tcea3	Transcription Elongation Factor A3
TFAM	Transcription Factor A, Mitochondrial
TGFβ	Transforming growth factor beta
Thbs1	Thrombospondin 1
Thy1	Thy-1 Cell Surface Antigen (CD90)
TIF-1B	Transcription intermediary factor 1-beta (TRIM28)
Timm10	Translocase Of Inner Mitochondrial Membrane 10
Tinagl1	Tubulointerstitial Nephritis Antigen Like 1
Tm	Temperature Melt
Tmem140	Transmembrane Protein 140
Tmem233	Transmembrane Protein 233
TMM	Trimmed mean of M values
Tnf	Tumor necrosis factor
Tnfrsf12a	TNF Receptor Superfamily Member 12A
Trim63	Tripartite Motif Containing 63. Also known as MURF1.
Tsc1/2	Tuberous Sclerosis 1/2
Tsp	Thrombospondin 1
TTX	Tetrodotoxin
Tuba1c	Tubulin Alpha 1c
Tuba4b	Tubulin Alpha 4b
Tuba8	Tubulin Alpha 8
Tubb4b	Tubulin Beta 4B Class IVb
Tyrobp	Transmembrane Immune Signaling Adaptor
Uap1l1	UDP-N-Acetylglucosamine Pyrophosphorylase 1 Like 1
Ubc1	Ubiquitin Conjugating Enzyme 1

UBF	Upstream Binding Transcription Factor
UBR5	E3 ubiquitin-protein ligase UBR5
UCP3	Uncoupling Protein 3
ULK1	Unc-51 Like Autophagy Activating Kinase 1
Usp2	Ubiquitin carboxyl-terminal hydrolase 2
Vat1	Vesicle Amine Transport 1
Vegfa	Vascular Endothelial Growth Factor Alpha
Vopp1	<i>VOPP1</i> WW Domain Binding Protein
Vps34	ATG14L-containing vacuolar protein sorting 34
WT	Wildtype
Xirp1	Xin Actin Binding Repeat Containing 1
Zfand2a	Zinc Finger AN1-Type Containing 2A
Zfp622	Zinc finger protein 622

List of Figures

Figure 1.1: The skeletal muscle sarcomere and sliding filament theory	28
Figure 1.2: Cross-bridge cycle force generation hypothesis.....	30
Figure 1.3: Graphical representation of Rattus Norvegicus Myosin Heavy Chain isoforms and their general contraction velocity.....	33
Figure 1.4: IGF1/mTOR/p70s6k signalling pathway regulating muscle mass.....	53
Figure 1.5: Activin A/Myostatin/TGF β signalling pathway regulating muscle mass	57
Figure 1.6: Skeletal myogenesis from the embryo to the adult	69
Figure 2.1: Schematic representation IPG and electrode placements	80
Figure 2.2: Implantable Pulse Generators (IPG)	84
Figure 2.3: Preparation of muscle slices	87
Figure 2.4: TTX Osmotic Pump Placement and Nerve Cuff Placement	88
Figure 2.5: Cryostat Set Up and Sectioning	96
Figure 2.6: Regional Differences in Fiber Size Following Regeneration	99
Figure 2.7: RNA-seq pre-alignment average Phred quality score (base quality) as a percentage of total reads and base quality score per position across all samples	112
Figure 2.8: RNA-seq visualisation of total reads per sample and percentage trimmed reads based on Phred quality score for each sample.....	112
Figure 2.9: RNA-seq coverage and Alignment Summary	116
Figure 2.10: RNA-seq quantification report	119
Figure 3.1: Schematic representation of electrical stimulation experimental time courses studied and timepoints of euthanasia	127
Figure 3.2: Schematic representation of TTX experimental time courses studied and timepoints of euthanasia	129
Figure 3.3: Morphology and phenotype of 64 tibialis anterior muscles from control rats ..	138

Figure 3.4: Response to 7 days continuous low frequency stimulation (20Hz)	141
Figure 3.5: Timecourse response to loaded & unloaded resistance training	146
Figure 3.6: Timecourse response to TTX-induced atrophy and recovery.....	148
Figure 3.7: Correlations between adaptive responses to electrical stimulation induced resistance training. Correlations between adaptive responses to TTX-induced atrophy and subsequent recovery.	153
Figure 3.8: Timecourse of spillover resistance training, muscle mass responses in the EDL, soleus, plantaris and gastrocnemius	163
Figure 3.9: Myosin heavy chain expression at the proximal, mid-belly and distal part of the tibialis anterior via RT-qPCR	166
Figure 4.1: Experimental timecourse for long term training, detraining and recovery pilot experiments	172
Figure 4.2: Long term TTX-recovery nerve health	173
Figure 4.3: Long term, training, detraining and recovery from TTX changes in muscle mass	175
Figure 4.4: Long term training and detraining changes in fiber CSA, myonuclei per fiber-cross-section and myonuclear domain size	177
Figure 4.5: Long term training and detraining changes in fiber type composition and fiber type specific fiber areas	180
Figure 4.6: Long term training and detraining changes in fiber type specific myonuclear content and domain sizes	183
Figure 4.7: Long term recovery from TTX-induced atrophy changes in fiber CSA, myonuclei per fiber-cross-section and myonuclear domain sizes	185
Figure 4.8: Long term recovery from TTX-induced atrophy changes in fiber type composition and fiber type specific fiber areas	188

Figure 4.9: Long term recovery from TTX-induced atrophy changes in fiber type specific myonuclear content and domain sizes	191
Figure 5.1: Resistance training timecourse transcriptional analysis study design, muscle mass, body mass, fiber area, mitochondrial content, fiber-type specific analysis, mitochondrial encoded gene expression, adult myosin heavy chain gene expression	207
Figure 5.2: Principal component analysis, gene set analysis timecourse hierarchical cluster analysis and self-organising map profiling	216
Figure 5.3: Electively chosen genes regulating mass and identified genes that show a more accurate representation of the hypertrophic response	222
Figure 5.4: Venn Diagram Analysis reveals 'Early Responses, 'Always Responsive' and 'Adapted Response' genes and pathways	226
Figure 5.5: Ribosomal response to a timecourse of spillover resistance training and GeneMANIA network analysis reveal Myc as a central regulator	231
Figure 5.6: The timecourse response of the 'Proteasome' pathway	233
Figure 5.7: The timecourse response of the 'Protein processing in endoplasmic reticulum' pathway	234
Figure 5.8: The timecourse response of the 'mTOR signalling' pathway	236
Figure 5.9: The timecourse response of the 'Oxidative Phosphorylation' pathway	237
Figure 5.10: Venn Diagram analysis of differentially expressed genes following synergist ablation, voluntary mouse weightlifting, spillover training and 2 human resistance training meta-analyses containing the acute and chronic responses	242
Figure 5.11: A timecourse transcriptional assessment into the contralateral effects of unilateral training and SOM profiling	251
Figure 5.12: Transcriptional assessment reveals circadian disruption in unexercised muscles	255
Figure 6.1: PCM1 localisation in C2C12 myoblast/myotube cultures	279

Figure 6.2: PCM1 localisation in human muscle-derived primary myoblasts/myotubes shows a very similar progression to the C2C12 cultures	280
Figure 6.3: PCM1 localisation and Pax7+ counts on single rat fibers post training	281
Figure 6.4: PCM1 localisation in human transverse cross-sections and single fibers	283
Figure 6.5: Number of Pax7, PCM1+ satellite cells following a timecourse of recovery from severe eccentric damage in humans	284
Figure 6.6: PCM1 localisation on transverse muscle cross-sections and co-localisation with CD68 macrophages	285
Figure 6.7: PCM1 localisation on necrotic human muscle fibers	286
Figure 6.8: PCM1 localisation 30 days post eccentric damage in human fibers	287
Figure 6.9: PCM1 localisation on single fibers in WT and LMNA ^{+/ΔK32} mouse fibers before and following functional overload	289
Figure 6.10: Morphology of WT and LMNA ^{+/ΔK32} mouse plantaris muscle on transverse cross-sections before and following functional overload.	291

List of Tables

Table 2.1: Antibodies & Fluorescent Conjugates for immunofluorescent labelling of cells, single muscle fibers and transverse cross-sections	79
Table 2.2: Rat Usage	81
Table 2.3: Mouse Usage (Experiments performed in Owens et al. (2021))	91
Table 2.4: Primer Sequences designed and used	105
Table 2.5: Pre-alignment QA/QC	111
Table 2.6: Individual Sample Read Trimming Summary	113
Table 2.7: STAR Alignment 4.4.1d Rattus Norvegicus Rnor 6.0 Run Settings.	114
Table 2.8: Summary report of post alignment QA/QC.	115
Table 2.9: Summary report of post alignment count quantification report.	118

Thesis Abstract

Skeletal muscle is highly responsive to changes in mechanical load or activity and can adjust its morphological, metabolic, and contractile properties accordingly. The remodeling of these characteristics is controlled by the reprogramming of the transcriptional output of the myonuclei along the length of the muscle fiber. To meet the transcriptional demands of growth and increased activity, myonuclei can be added to the existing cytoplasm through the fusion of satellite cells, to support synthetic activity. This project utilises improved methodologies including automated, high-throughput immunohistochemical analysis and bulk RNA-sequencing of skeletal muscle. With these techniques, we define the temporal patterns of myonuclear dynamics and how they correspond to fiber-type specific adaptations in response to loading, unloading, reloading and changes in activity and how the acute transcriptional response is altered, dependent on the training status of the muscle. To induce these modalities of activity or inactivity, we utilised *in-vivo* models from our lab including, (1) programmed exercise delivered through miniature implanted pulse generators (IPGs) to induce muscle hypertrophy or metabolic adaptation and (2) disuse by means of tetrodotoxin-induced nerve silencing to induce muscle atrophy. We report that the genes that most closely track with changes in muscle mass are controlled centrally by the basic-helix-loop-helix transcription factor Myc, that functions to bind to E-box containing DNA sequences. In addition, we identify 10 other genes that appear as important regulators across species and modalities of exercise that warrant further investigation. Lastly, we investigate a promising marker for specifically identifying myonuclei, pericentriolar material-1 (PCM1), which would allow for deconvolution of mRNA signals from bulk skeletal muscle mRNA analysis, allowing for identification of myogenic and non-myogenic transcriptional changes. In summary, our aim is to provide key mechanistic insights into myonuclear dynamics and how adaptation of skeletal muscle is regulated at the transcriptional level.

Chapter 1: Introduction

1.1 Skeletal Muscle Structure and Function

Muscle appears in the mammalian body in two distinct forms; smooth muscle found in vessels which contracts slowly, and striated muscle found in cardiac and skeletal muscle. Skeletal muscle in most cases is voluntarily controlled, except for those muscles involved in breathing (primarily the diaphragm), which are instead ordinarily controlled by the autonomic nervous system. Skeletal muscle is capable of contraction within a limited range, therefore, to produce gross bodily movements, multiple muscles work together as lever systems to move the skeleton.

Skeletal muscle is mainly made up of many individual multinucleated cells known as muscle fibres or myofibres amongst other cells that support the structure and function of skeletal muscle such as satellite cells (SC), fibroadipogenic cells (FAPS), macrophages, vascular endothelial cells and pericytes. Skeletal muscle fibres consist of ~20% protein (contractile, regulatory, cytoskeletal) and ~1-10% fat and the remaining ~75% water content. Also known as myofibers, they vary considerably in length (mm-cm) dependent on function but vary less so in width (10-70 μ m) across mammalian species due to a ceiling effect where it is metabolically advantageous to limit diffusion distances of oxygen delivered via capillaries to the muscle mitochondria and the successive diffusion of produced ATP to cellular ATPases.

Skeletal muscles are encased in fascia called the epimysium and can be further broken down into interconnected fascicles sheathed by the perimysium, Rowe (1981). Myofibres within these bundles are themselves encased in loose, areolar connective tissue called the endomysium which also contains capillaries and nerves, Sakamoto (1996). An individual myofibre is composed of many myofibrils, which are cylindrical structures of around 1 μ m in diameter. These myofibrils are mainly composed of thick (myosin) and thin (actin) filaments which overlap each other during physiological lengths. These filaments are attached in series along the length of the myofibril and make up the functional contractile apparatus of muscle and give it the characteristic striated appearance.

The contractile apparatus of striated muscle consists of thick (Myosin) filaments and thin (Actin) filaments. Actin contains active or binding sites for myosin heads to attach. Myosin is a heterohexamer with a molecular weight of 520 kDa and consists of two myosin heavy chains. All myosins contain two domains, the first an amino-terminal motor/head domain and

the second a carboxy-terminal tail domain which together associate to form an α -helical coiled-coil rod or 'myosin tail' Schiaffino and Reggiani, (1994). The amino portions of the myosin heavy chains (MyHC) are separated to form two extended, globular domains known as myosin heads. At the head-tail junction each MyHC associates with two myosin light chains (MLC), one of which belongs to the MLC1 family and one to the regulatory MLC2 family also known as the regulatory P-light chain. In vertebrates, the light chains do not bind Ca^{2+} and are therefore do not modulate the activity of the ATPase head directly but instead structurally support contractile activity during the phosphorylation of the S1 fragment.

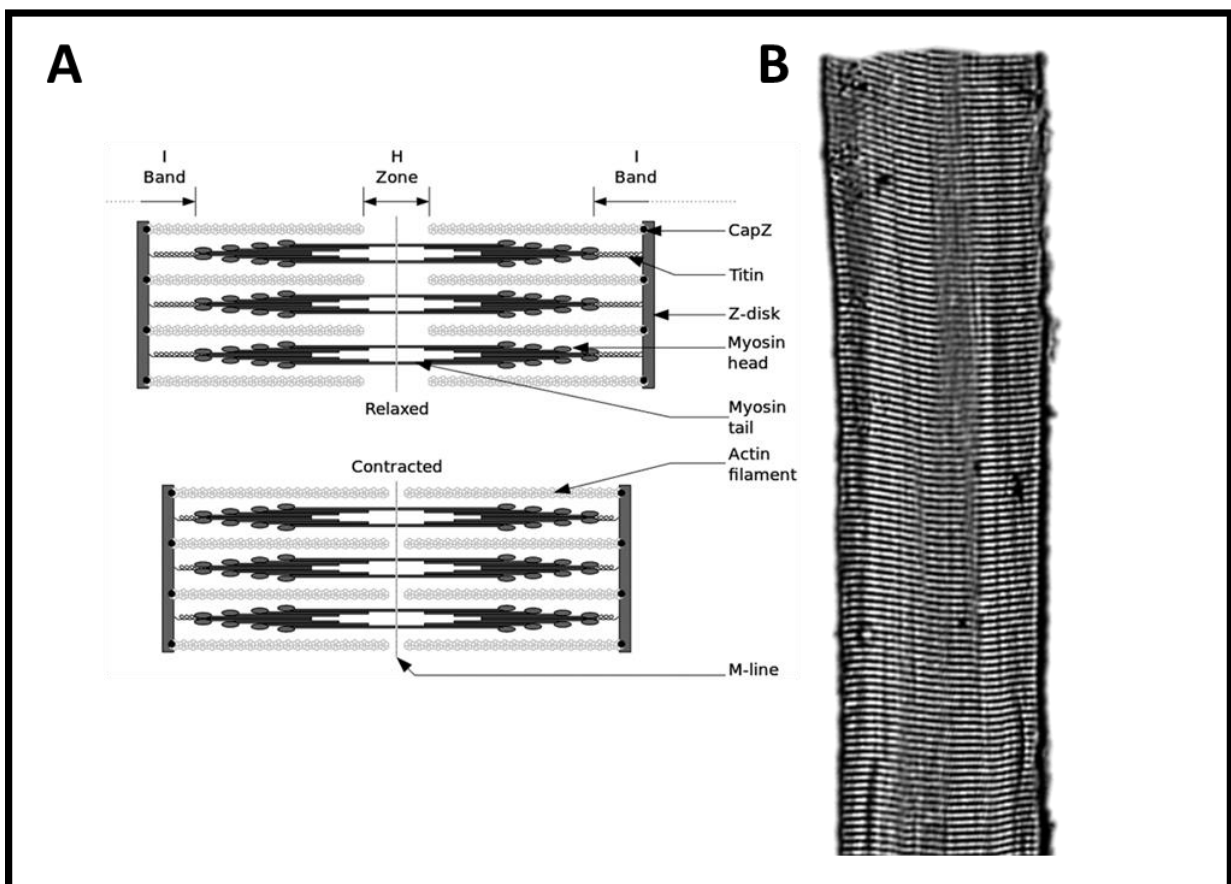


Figure 1.1: The skeletal muscle sarcomere and sliding filament theory.

The sarcomere consists of thick myosin filaments and thin actin filaments. Myosin heads interact with actin filaments through molecular cross-bridges causing actin filaments to slide towards each other shortening the I band (distance between thin actin filaments) and H zone (contains only thick myosin filaments). The Z-disks defines the boundaries of an individual sarcomere of which the centre is labelled as the M-line. Titin is a long elastic protein- the largest known (containing ~27,000 to ~35,000 amino acids depending on the splice variant),

that functions as a molecular spring, connecting the Z-disk to the M-line. The arrangement of myosin and actin proteins gives skeletal muscle its striated appearance which is visible under polarised transmitted light as dark and light bands (thick and thin filaments).

Activity of skeletal muscle is controlled through one or more motor nerves which consists of large, myelinated axons, delivering electrical impulses from the brain or spinal cord to the muscle itself. These efferent nerves, often termed α -efferent or α -motor axons possess conduction velocities of 30.1 ± 2.8 m/s in 100-150-g and 55.0 ± 6.9 m/s in 450-500-g rats Stanley, (1981).

Nerves follow the connective tissue of skeletal muscle, branching through the epimysium, perimysium before entering the endomysial tissue surrounding individual myofibers. Upon reaching the muscle tissue itself, the terminal branch of an α -motor axon forms into a specialised synapse (pre-synaptic structure usually visualised with synaptophysin/neurofilament) to increase sarcolemmal permeability and conductance, known as the neuromuscular junction Deschenes et al., (2011), R Deschenes, (2011). The axon terminal forms into multiple short branches extending elliptically around the fiber into a pretzel like shape known as the motor end plate. When an action potential reaches the motor end plate, acetylcholine is released via exocytosis from synaptic vesicles into the synaptic cleft (synapse) that separates the nerve ending and the myofiber sarcolemma. The acetylcholine in the synaptic cleft is then bound to nicotinic acetylcholine receptors on the sarcolemma which contain 5 subunits ($\alpha 1$, $\beta 1$, δ , and ϵ subunits in a 2:1:1:1 ratio) surrounding a central pore. When acetylcholine binds to this complex, permeability and therefore conductance increases in the postsynaptic membrane (often visualised with α -bungarotoxin) causing a new action potential in the muscle fibre membrane. propagated along the length of the sarcolemma and into its interior along t-tubules, depolarising the inner portion of the muscle fiber. The depolarisation activates dihydropyridine receptors, also known as L-type voltage-dependent calcium channels in the t-tubule membranes. These activated voltage-gated calcium channels physically interact with the calcium-release channels (also known as ryanodine receptors), which are in turn activated themselves allowing for release of calcium from the sarcoplasmic reticulum.

The calcium ions released from the sarcoplasmic reticulum bind to troponin molecules, causing the tropomyosin molecule to shift and expose the myosin binding site on the actin filament. Myosin heads can then attach to actin forming an actin-myosin crossbridge. The myosin head then flexes causing the actin filament to slide past the myosin filament, resulting in shortening and force generation from the sarcomere often referred to as 'cross-bridge cycling' and the 'power stroke'. As sarcomeres are joined end to end at the Z-disc via α actinin molecules across the length of the myofibre, a larger force can be produced resulting in the overall muscle to shorten, to produce the desired muscle action Ashley et al., (2007b), Ashley et al., (2007a). ATPases hydrolyse ATP causing detachment of the myosin head from the actin molecule allowing for repeated reattachment at a further binding site. Upon cessation of nervous stimulation and calcium ion active transport, tropomyosin again blocks the actin filament binding site resulting in muscle to passively lengthen to a resting state. Whilst all mammalian cells can produce forces, the unique structure of the sarcomere and their actin-myosin interactions allow these cells to produce much greater forces than non-muscle cells. In humans, dependent on fiber type, it is estimated that muscle fibers can generate forces of $\sim 540 \mu\text{N}$ Krivickas et al., (2011), with each myosin head contributing $\sim 6\text{pN}$ Piazzesi et al., (2007).

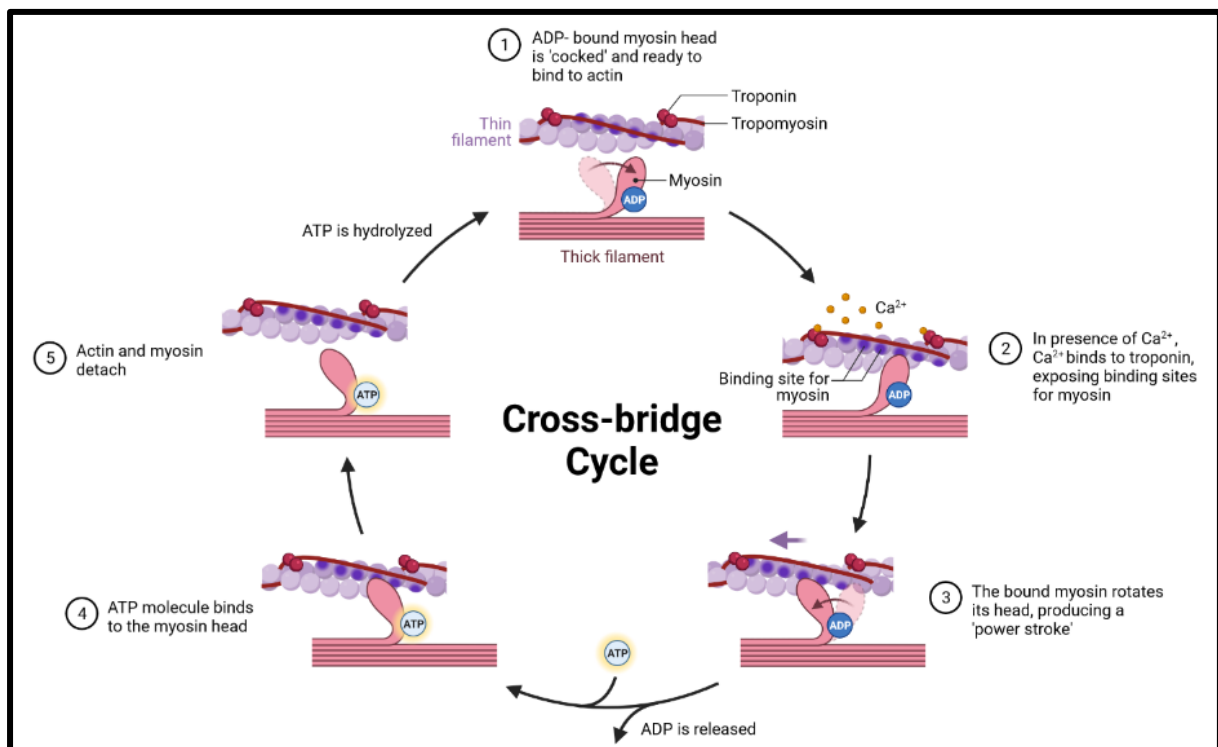


Figure 1.2: Cross-bridge cycle force generation hypothesis.

The force produced by skeletal muscle is transmitted through the myotendinous junction into dense connective tissue known as tendon which consist of millions of collagen fibrils that constitute thousands of collagen fibers that make up the entire tendon. Traditionally it was thought that force produced by sarcomeres was transmitted to bone via tendon longitudinally through the myotendinous junction only, but more recently the idea of forces transmitting laterally across costameres has been supported through tenotomy of individual and multiple distal heads of the EDL muscle (a dorsiflexor muscle that connects to the digits of toes 2, 3, 4 and 5). When performing tenotomy on each of these heads individually, force production did not reduce which would be the case if all force was transmitted longitudinally, but instead remained the same dependant on the number and individual tendons tenotomised, providing evidence of lateral force transmission to neighbouring intact distal insertions Huijing et al., (1998). Additionally, Westman et al., (2019) elegantly performed in-situ and in-silico measurements on the pennate latissimus dorsi muscle in the rat to determine how the site of volumetric muscle injury affects force transmission through the myotendinous junction. Their results illustrated that the site of injury can impair or increase lateral force production dependant on the amount of end-to-end (tendon to tendon) myofibres damaged. The amount of end-to-end myofibres damaged was negatively correlated to force production which then resulted in more lateral force transmission. Historically, the arrangement of sarcomeres was proposed to be in an end-to-end formation in series, along the length of a muscle fiber into tubular like myofibrils with separate parallel myofibrils. More recently, Willingham et al., (2020) demonstrated through focused ion beam-scanning electron microscopy that striated muscles in fact form a continuous myofibrillar matrix, with sarcomeres frequently branching out into adjacent sarcomeres to produce a continuous mesh. This phenomenon is most prevalent in postnatal development and is also higher in slow-twitch fibers in comparison to fast-twitch and may suggest that lateral force transmission is produced by the continuous sarcomeric matrix, generating force as a singular network rather than many individual parallel myofibrils.

Muscle contraction can be further classified into three types in relation to the action it is performing. A dynamic concentric muscle action (often referred to as isotonic) results in shortening of the muscle during contraction as the muscle action brings the origin and insertion of the muscle closer together. A static or isometric contraction is characterised by

the production of force in the absence of movement, when the resistance balances the force generated by the muscle. A dynamic eccentric contraction results in lengthening of the muscle as the origin and insertion move further apart from each other when the external force is higher than the force generated by the muscle.

1.2 Relationship Between Muscle Activity and Myosin Heavy Chain Isoform Expression

The complement of MyHC isoforms determines the structural and functional capabilities of the muscle fiber as this is the subunit in which the enzymatic and motor function is produced. Both MyHC's and MLC's exist in various isoforms which appear in different distributions in various muscle fibre types but are generally highly conserved between species Salmons and Sreter, (1976). In the Wistar Rat (*Rattus Norvegicus*), the primary animal studied throughout this thesis, there are several MHC isoforms present which help to constitute the unique properties of different muscle actions. These genes are located on two of the 21 pairs of chromosomes in *Rattus Norvegicus*, chromosomes 10 and 15. The 'fast' myosin heavy chain genes are all found on chromosome 10. Myh3 (embryonic) and Myh8 (neonatal) are predominantly found during muscle development but are also expressed following regeneration and formation of new muscle fibers in adulthood following injury or damaging exercise. Upon maturity and innervation, these myosins are replaced with Myh2 (MyHCIIA), Myh1 (MyHCIIIX) and Myh4 (MyHCIIIB), termed 'type II' or 'fast-twitch' muscle fibers Brooke and Kaiser, (1970), Schiaffino and Reggiani, (1996), Schiaffino et al., (1989).

Myh13 is also found in specialised skeletal muscles such as the laryngeal and extraocular muscles which have differential developmental programmes than the above described limb muscles that developmentally originate from myotomes whereas the extraocular muscles originate from the paraxial portion of the head mesoderm Chal and Pourquié, (2017). Due to the extreme specialisations of these muscles they are often referred to as a superfast myosin Briggs and Schachat, (2002) The Myh7 gene, more commonly referred to as 'type I' or 'slow twitch' is found instead on chromosome 15 along with Myh6 (MyHC- α) which forms the alpha heavy chain subunit of cardiac myosin, found primarily in atrial tissue Holm et al., (2011).

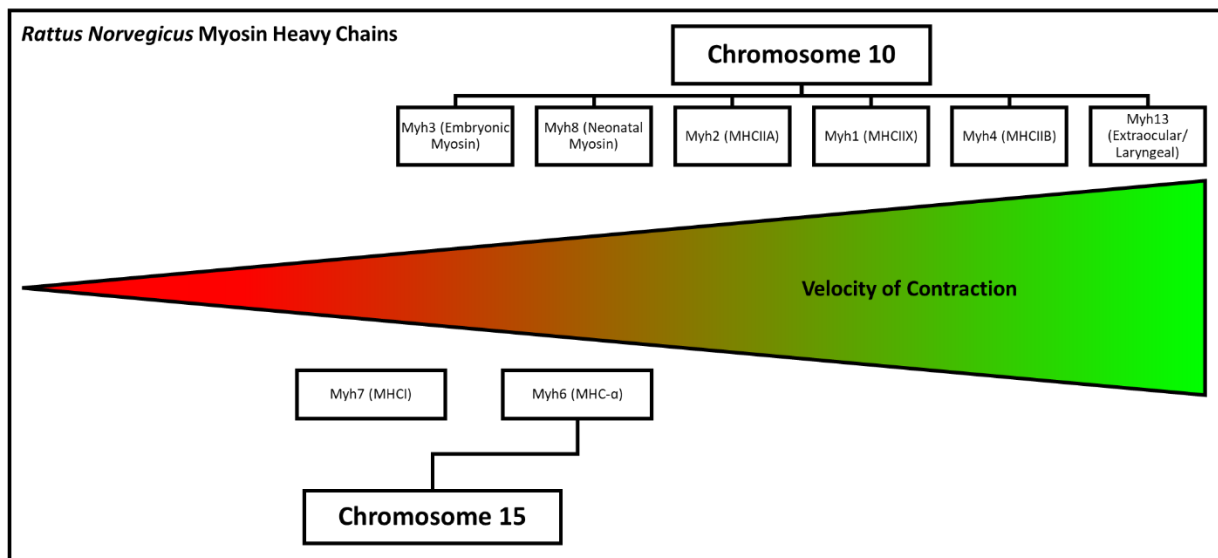


Figure 1.3: Graphical representation of *Rattus Norvegicus* Myosin Heavy Chain isoforms and their general contraction velocity.

Type I muscle fibers primarily produce ATP through aerobic metabolism and are often referred to as oxidative muscle fibres. The myosin head has a relatively low ATPase enzyme activity and thus the cross-bridge cycling rates are also low. As a result, the speed of contraction is slow but is sustainable over long periods of activity. Type I fibers are highly abundant in both mitochondria, the ATP producing centres and myoglobin, an iron-containing protein which aids in shuttling oxygen from the vascular system to the mitochondria to maintain energy production for muscle contraction. Myoglobin also gives oxidative muscle its characteristic red appearance, in contrast to its fast counterpart which contains less myoglobin and therefore has a white appearance. This is further supported by the greater number of capillaries surrounding type I fibres to provide a constant supply of oxygen and removal of by-products of energy metabolism, which may act to inhibit muscle contraction inside the muscle fiber. Type I fibers are activated under low thresholds for firing, with impulses from the motor neurone at a rate of 10-20Hz and have low conduction velocities.

Type II muscle fibers as discussed briefly above can be separated into three sub-categories, each of which has its own ATPase enzyme activity. Type IIA fibers use both aerobic and anaerobic metabolic pathways to generate ATP and have a greater ATPase activity than Type I fibers. Type IIA and IIB fibers have greater speeds of contraction but are more reliant on

anaerobic pathways of energy production and are less resistant to fatigue. This increasing susceptibility to fatigue along the spectrum of IIA to IIX to IIB fibers is due to a decreasing number of resident mitochondria and capillary content surrounding the fiber categories. ATPase activity shows an inverse relationship with mitochondrial content; IIB fibers have the highest ATPase activity and thus the highest speed of contraction. These fibers are innervated by axons with larger diameters than Type I fibers which require higher thresholds for activation. The unique combinations of ATPase activity and mitochondrial content across fiber types also influences their force-velocity relationship characteristics. Power generation is not only dependant on the overlap of thick myosin and thin actin filaments, but also the velocity at which the muscle lengthens or shortens. Generally, as velocity of muscle shortening increases, the force produced by the muscle decreases until it reaches a velocity at which force can no longer be sustained, known as the maximum velocity of unloaded shortening (V_{max}). In contrast, when additive force or external load is placed upon a muscle, the velocity of shortening decreases. In Type II muscle fibers, ATP production through anaerobic metabolism occurs at a high rate, allowing for a faster cross-bridge cycling rate. Conversely, in Type I fibers, cross-bridge cycling rates are low and therefore the rate of ATP hydrolysis for energy production is also low meaning that V_{max} is substantially lower in Type I muscle fibers. This relationship between force and velocity shows that the high forces cannot be exerted in very rapid movements and the highest velocities are achieved during unloaded contractions. Changes in activity and loading have shown that muscle fiber phenotype can be altered through shifting of MyHC isoform expression and thus the force-velocity curve can also be shifted to meet their functional demands.

Muscle fibers were originally thought to contain only one myosin isoform until the discovery of hybrid fibre types which express more than one MyHC isoform and which are proposed to show greater ability to transform their phenotype in response to changes in activity and loading Termin et al., (1989b), Termin et al., (1989a). These combinations of MyHCs within one myofiber allow for greater diversity in ATPase activity and therefore muscle function. Whilst changes in MyHC protein levels have been extensively studied following electrical stimulation by our group Sutherland et al., (1998), Jarvis et al., (1996b), Salmons and Sreter, (1976), less is known about the transcriptional control of MyHC genes that precedes adaptations at the protein level. Studies that have measured mRNA of MyHCs Bodine and

Pierotti, (1996), Jänkälä et al., (1997) in models of denervation or immobilization which produce a slow to fast transformation, have shown that acute changes in MyHC gene expression do correspond to changes in MyHC at the protein level at later timepoints. Traditionally, these studies measure gene transcript levels from isolated mRNA from a muscle homogenate which may contain several fiber types. This provides information on changes in MyHC expression at the transcriptional level which may indicate gradual changes in protein abundance and muscle functionality but provides minimal information about how this is regulated between the multinucleated syncytium of the myofiber, whose transcriptional activity is controlled by hundreds of myonuclei spread across the length of the sarcolemma. In healthy myofibers, myonuclei are dispersed equally along the sarcolemma Bruusgaard et al., (2006), apart from at specialised regions such as the myotendinous junction (MTJ) where myonuclei appear centralised Jakobsen et al., (2018), or the neuromuscular junction (NMJ) where myonuclei appear in a cluster adjacent to the underneath of the synapse Hastings et al., (2020), Roman and Gomes, (2018). Myonuclei often appear in the centre of muscle fibers in several disease states including myopathies such as centronuclear myopathy and muscular dystrophy which are characterised by persistent degeneration, regeneration, and muscle atrophy Roman and Gomes, (2018), Owens et al., (2021)

More recently, advancements in technologies to visualise localisation of specific gene transcript localisation in fixed tissues through fluorescent in-situ hybridization targeting ribonucleic acid molecules (RNA-FISH), often referred to as RNA Scope™ in the literature due to the commercial development of the technique has allowed us to gain an understanding into transcriptional control of MyHC in muscle fibers Kann and Krauss, (2019). Development of transcriptomic screening technologies has recently brought rise to single cell sequencing, as well as single-nucleus RNA-sequencing (snRNA-seq) which has recently been applied to myonuclei as well as other cell types resident in skeletal muscle tissue across development, denervation, regeneration and disease Dos Santos et al., (2020), Kim et al., (2020), Petraný et al., (2020a). Previous work has established that myonuclei localised to the NMJ exhibit functional specialist transcriptional programmes to form and maintain the synaptic junction, such as for the production of acetylcholinesterase and acetylcholine receptors Sanes and Lichtman, (2001), Hippenmeyer et al., (2007), Burden et al., (2018), Li et al., (2018b), Li et al., (2018a)

Specific co-ordinated transcriptomic programmes in myonuclei near the MTJ are also known to produce specific tissue junction proteins such as Collagen XXII Jakobsen et al., (2021a), Jakobsen et al., (2021b), Koch et al., (2004), Dos Santos et al., (2020). Regionalised specialisation of specific transcripts and their protein translation rather than protein transport would perhaps also be less energetically costly to the cell. Whilst the transcriptomic profile of these small sub-populations that account for ~6% of myonuclei Dos Santos et al., (2020) is generally understood, less is known about the large remainder of myonuclei within the myofiber, referred to as body myonuclei and how they control MyHC expression. Heterogeneity in nuclear protein import has previously been reported Cutler et al., (2018), as well as stochastic gene expression along the myofiber, otherwise described as transcriptional bursting Newlands et al., (1998), which could potentially cause heterogenous gene expression at a given gene locus between myonuclei across the myofiber. Recent drosophila studies have shown that these mRNA pulses allow nuclei to adjust their position along the myofiber, as well as their size and synthetic activity Windner et al., (2019).

Through snRNA-seq and RNA-FISH, Dos Santos et al., (2020) and Petraný et al., (2020b) have shown that the majority of myonuclei in healthy, but unexercised EDL express only one MyHC isoform in the mouse and that on rare occasions (~5%) myonuclei would simultaneously co-express Myh7 and Myh2 (MyHCI/IIA) or Myh1 and Myh4 (IIX/IIB MyHC) or Myh1 and Myh2 (IIA/IIX MyHC). The expression of multiple fast MyHCs was reported to occur both mono-allelically and bi-allelically and that occasionally two fast MyHCs were transcribed concurrently on the same locus. In the soleus, co-expression of two MyHC's was more common than in the EDL (~45%), with Myh1 and Myh2 (IIA/IIX) co-expression occurring in ~25% of myonuclei. As discussed previously slow twitch myofibers contain more mitochondria than fast twitch myofibers and thus rely on different metabolic pathways for ATP production. snRNA-seq also confirmed that the myonuclei that expressed specific fast MyHC genes also co-transcribed specific metabolic genes related to glucose uptake, glycolysis, TCA cycle enzymes such as Pfkfb3, Tbc1d1, Aldolase A and Idh2 illustrating that MyHC isoform and metabolic gene expression is highly co-ordinated Dos Santos et al., (2020). When studying co-ordination of MyHC expression across all myonuclei within single myofibers of the EDL it was found that MyHC expression was highly co-ordinated, although in

contrast the soleus showed many uncoordinated myofibers that expressed multiple MyHC isoforms across the length of the myofiber. The MyHC mRNAs were also shown to remain near the myonuclei that produced them, demonstrating that diffusion of MyHC mRNAs was confined to their local domain Dos Santos et al., (2020).

Transgenic models and the use of transfection of promoter-reporter constructs have uncovered that MyHC transcript expression is controlled by transcription factors such as myocyte enhancing factor 2 (MEF2) and nuclear factor of activated T-cells (NFAT) Chin et al., (1998), Wu et al., (2000), Baldwin et al., (1972), Spangenburg and Booth, (2003). The activity of these transcription factors is modulated by signalling pathways influenced by the Ca^{2+} flux induced by the motor activity of the muscle, as well as O_2 levels, hormones, and nutrient availability. Slow motoneuron firing commonly seen in endurance exercise leads to sustained low-level elevation of calcium concentrations within the myofiber which are able to activate calcineurin and Ca^{2+} /calmodulin-dependant protein kinases (CaMK), whilst fast motoneuron firing leads to brief high concentrations within the myofiber that do not activate calcineurin Rao et al., (1997), Naya et al., (2000). The activation of calcineurin and CaMK increase the activity of MEF2 and NFAT which subsequently increases Myh7 gene expression and can induce a shift to a slower phenotype Sakakibara et al., (2016), Sakakibara et al., (2014), Sharlo et al., (2019). Together with increases in Myh7 gene expression, increases in muscle activity and CaMK signalling activate transcription factors PGC1a and PPAR β which in turn modulate the increase in myofiber mitochondrial content and proteins involved in oxidative metabolism which will aid the requirement for the typically more continuous requirement for ATP of slower MyHCs. Specific skeletal muscle knockout of PGC1a has no effect on muscle fiber type in the mouse but does reduce oxidative capacity Rowe et al., (2013), whilst skeletal muscle specific deletion of PPAR β contrastingly leads to an increased number of fast fibers with reduced oxidative capacity Schuler et al., (2006). Conversely, less is known about the regulation of fast type MyHC genes which are controlled by histone deacetylases (HDACs), Sox6, Linc-Myh, MyoD, Six1 homeoprotein and Eya1 co-factor Grifone et al., (2004), Hagiwara et al., (2007), Potthoff et al., (2007), An et al., (2011), Quiat et al., (2011), Sakakibara et al., (2014), Sakakibara et al., (2016). Perhaps most strikingly, in adult skeletal muscle, Six1 homeoprotein accumulates in the myonuclei of adult fast-type muscles to a greater extent than in adult slow-type muscles in mice, an enrichment that happens during perinatal growth.

The wild-type mouse soleus muscle comprises of 45% MyHCIIA myofibers and 55% MyHCI myofibers at 12 weeks of age, but under skeletal muscle specific, inducible Six1 knockout the fast specialisation in the soleus is completely lost and the soleus muscle shifts to consist of 100% MyHCI myofibers with no detection of MyHCIIA by qPCR. This completely slow phenotype of the Six1 knockout mouse was found to be concomitant with the removal of the expression of several genes encoding glycolytic enzymes and fast-type intracellular calcium homeostasis, as well as the lack of Sox6, a key repressor of slow sarcomeric genes Grifone et al., (2004), Sakakibara et al., (2016). Work on the VL muscles in drosophila has also revealed that nuclear scaling, arrangement, and transcriptional activity is also tightly controlled by motoneuron activity Windner et al., (2019).

With calcineurin activity clearly a main contributor to control of transcription factors and MyHC isoform expression, the removal of motoneuron activity via denervation severely affects the co-ordination of MyHC expression. Following one week of denervation in both the EDL and soleus, snRNA-seq and RNA-FISH reveal that the highly organised co-ordination of MyHC gene expression is lost, as shown through an increase in hybrid fibres and myonuclei co-expressing MyHC isoforms and a shift to a slow phenotype in the EDL (Control: 80% Myh4, ~10% Myh4+Myh1, ~10% Myh1 vs. Denervation ~40% Myh4, ~25% Myh4+Myh1, ~5% Myh1, ~25% Myh1+Myh2, ~2% Myh2, ~8% Myh4+Myh1+Myh2). Conversely, whilst co-ordination is still lost following one week of denervation in the soleus, the muscle instead shifts to a faster phenotype (Control: ~10% Myh1, ~45% Myh1+Myh2, ~5% Myh2, ~40% Myh- vs. ~5% Myh1, ~40% Myh1+Myh2, ~20% Myh2, ~40% Myh-), showing again that there is an absolute requirement for motoneuron input to control MyHC gene expression, but that the co-ordination of MyHC expression through calcineurin signalling may play a larger role in specific muscles Dos Santos et al., (2020). The slow to fast transformation of predominately fast muscles and fast to slow transformations of predominately slow muscles is well reported in a number of models that involve partial or fully transected models of denervation which can be reversed, and atrophy partially prevented with the use of functional electrical stimulation Salmons and Sreter, (1976), Gorza et al., (1988), Ashley et al., (2007a).

1.3 Relationship Between Muscle Activity & Mitochondria

John Holloszy's seminal work Holloszy, (1967) was the first to show that exercise can bring about transformation of muscle phenotype through an increase in mitochondrial biogenesis or mitochondrial mass, which allows for greater glucose usage and ATP production. The original study showed that progressive endurance exercise training in rats significantly improved exercise time to exhaustion (186 mins for trained vs 29 mins for untrained) and that this was concomitant with striking changes in the colour of the trained gastrocnemius muscles, which were a darker red colour than their pink, untrained counterparts. The apparent changes in muscle colour were attributed to doubling of cytochromes (proteins containing a haem molecule) and myoglobin content present in muscle Pattengale and Holloszy, (1967). Furthermore, the activity of mitochondrial respiratory chain enzymes, capacity to oxidize pyruvate and total mitochondrial protein were all increased following the training period Holloszy, (1967). Increases in mitochondrial biogenesis (size and number) in rodents and human skeletal muscle have been shown multiple times following exercise training Gollnick et al., (1972), Gollnick et al., (1973) and is known to occur in all fiber types Baldwin et al., (1972).

Mitochondria are double membrane bound organelles that are the principal source of chemical energy/ATP production in all cells. The system of membranes and intermembrane spaces are of great significance to their function. The outer membrane contains many integral proteins, known as porins which are voltage-dependant anion channels which allow for small molecules <5 KDa to diffuse freely across the membrane. The outer membrane is also smooth and often attached to other organelles such as microtubules. Conversely, the inner mitochondrial membrane is ion impermeable and is continually folded to form tubular invaginations known as cristae, to provide a large surface area. Mitochondria range from 0.5-10µM in diameter and their size, shape, and locality relative to the basement membrane vary depending on the energy requirements of the tissue Vafai and Mootha, (2012) and in skeletal muscle, the training status of the individual Holloszy, (2011). Mitochondria are also unique in the respect that they contain their own mitochondrial DNA (mtDNA), which contains 37 genes that code for 2 rRNA, 22 tRNA and 13 proteins which are essential for mitochondrial

maintenance and performance as they encode the protein components of the respiratory chain responsible for ATP production which will be introduced and explored within the thesis Hock and Kralli, (2009).

Mitochondrial volume increases significantly after just 1.5 weeks of continuous chronic electrical stimulation in rabbits Eisenberg and Salmons, (1981). This elevated volume remained for 2-7 weeks of continuous activity before declining. It was suggested by the authors that this initial large increase in mitochondria acted as a super compensatory mechanism as the phenotype and content of myosin heavy chain isoforms shifts from that of a predominately fast muscle to predominately expressing slow myosin heavy chain protein Eisenberg and Salmons, (1981). Both continuous and intermittent electrical stimulation have been shown to cause increases in mitochondrial biogenesis and mitochondrial enzyme activity through the assessment of succinate dehydrogenase, citrate synthase and nicotinamide adenine dinucleotide phosphate-tetrazolium reductase, which are generally higher in slow myofibers and in exercised myofibers independent of fiber type Takahashi and Hood, (1993). Whilst the time course of mitochondrial enzyme changes is well documented following continuous and intermittent electrical stimulation, the transcriptional regulation of important mitochondrial transcription factors and mitochondrial respiratory complexes is less understood. Whilst Fisher, (2010) investigated the time and activity dependence of transcriptional changes to continuously stimulated rat skeletal muscle, even less is known about the transcriptional regulation of mitochondria following 'resistance like' exercise induced by electrical stimulation. The study of transcriptional regulation of mitochondria is made even more complicated as their remodelling and biogenesis requires the expression of genes found in both mtDNA and the DNA found within the cell's nucleus/nuclei.

The first discovery of a mitochondrial transcription factor was that of nuclear respiratory factor 1 (NRF1), NRF2 and specificity protein 1 (SP1) Evans and Scarpulla, (1989), Evans and Scarpulla, (1990), Virbasius and Scarpulla, (1994), Virbasius et al., (1993), which together regulate transcription of the cytochrome c gene amongst other proteins involved in the electron transport chain. These genes also regulate mitochondrial transcription factor A (TFAM), a nuclear-encoded transcription factor which translocates to mitochondria to regulate the transcription and replication of mtDNA Virbasius and Scarpulla, (1994), Scarpulla, (2008), Zaid et al., (1999). As a result, both NRF1 and TFAM are often used as transcriptional

indicators of mitochondrial biogenesis. Mitochondrial uncoupling protein 3 (UCP3) is also implicated in mitochondrial biogenesis, primarily in skeletal muscle, and more importantly in fast than in slow twitch fibers Zaid et al., (1999). The role of UCP3 is believed to be to create proton leaks across the inner mitochondrial membrane, therefore uncoupling oxidative phosphorylation, resulting in production of heat without ATP production. Additionally, during energy metabolism when fatty acid supplies to mitochondria exceed maximal oxidation capacity, UCP3 enables the export of fatty acids to protect against lipid-induced oxidative stress. As fast twitch muscle fibers contain less mitochondria, the increased expression of UCP3 may protect against excessive reactive oxygen species build up. This is primarily supported through the muscles of mice lacking UCP3 showing evidence of oxidative damage and increased reactive oxygen species production Vidal-Puig et al., (2000).

Furthermore, Puigserver et al., (1998) were the first group to report the importance of peroxisome proliferator-activated receptor gamma coactivator-1 α otherwise known as PPAR- γ coactivator-1 α (PGC-1 α) which was found whilst studying how cold temperatures cause the induction of thermogenesis in brown adipose tissue. Spiegelman and colleagues found that PGC-1 α protein bound to PPAR- γ , which subsequently activated transcription of UCP1, amongst other key mitochondrial genes such as cytochrome c oxidase subunit II (COXII) Wu et al., (1999). PGC-1 α was highly expressed following cold exposure in brown adipose tissue and was described as thermogenic coactivator Puigserver et al., (1998). Further work revealed that PGC-1 α was key in the regulation of transcription factors that regulated mitochondrial encoding genes and was thus a key driver of mitochondrial biogenesis, and was later found to interact with other transcription factors relating to myosin heavy chain isoform expression and the expression of specific metabolic enzymes Baar et al., (2002), Puigserver, (2005). Overexpression of PGC-1 α in myotubes in culture Wu et al., (1999), cardiac muscle Lehman et al., (2000) and mouse skeletal muscle Wende et al., (2007) results in robust increases in mitochondria. Additionally, PGC-1 α deficient mice have a lower mitochondrial number and decreased expression of mitochondrial genes Leone et al., (2005).

As well as increasing mitochondrial biogenesis, overexpressing PGC-1 α also causes an increase in GLUT4 expression (a key insulin-regulated glucose transporter found in higher abundances in type 1 oxidative fibers Kong et al., (1994)), by binding to GLUT4 transcription factors at their NH2 terminal domain, thereby activating them which allows for chromatin

remodelling and RNA processing via its COOH terminal domain Monsalve et al., (2000), Michael et al., (2001), Wende et al., (2007). Prolonged over expression even leads to a fast-to slow conversion of myosin heavy chain isoforms, concomitant with expression of slow specific proteins such as myoglobin, resulting in a darker, more red coloured muscle; much like the transformation that occurs following chronic low frequency electrical stimulation Lin et al., (2005), Lin et al., (2002).

As previously outlined, as well as chronic endurance training, there are a multitude of studies that demonstrate that just one bout of exercise or electrically stimulated muscle contractions results in increases in PGC-1 α transcription Baar et al., (2002), Fisher, (2010), Goto et al., (2000), Norrbom et al., (2004), Pilegaard et al., (2003), Russell et al., (2005), Short et al., (2003), Terada et al., (2002) and resultant PGC-1 α protein expression Baar et al., (2002), Russell et al., (2003), Russell et al., (2005), Terada et al., (2005). Whilst it is often considered that the acute increase in transcription of PGC-1 α is necessary to upregulate mitochondrial biogenesis and GLUT4 expression, time course studies post exercise have revealed that mitochondrial proteins with both very short and long $t_{1/2}$, such as citrate synthase and cytochrome c were increased at both the mRNA and protein level long before an increase in PGC-1 α protein expression, when studied immediately post 6 hours of swimming in rats Wright et al., (2007). At this timepoint, there was an increase in binding of NRF1 and NRF2 to both cytochrome c and COXIV protein and translocation of PGC-1 α protein from the cytoplasm into the nucleus. This suggests that the acute stage of mitochondrial biogenesis is regulated by PGC-1 α mRNA, which is most abundant at approximately 1 hour post exercise Fisher, (2010), Kuang et al., (2020), whereas the latter stages are regulated by increases in PGC-1 α protein Wright et al., (2007), which peaks around 18-24 hours post exercise dependant on species and exercise stimuli and slowly returns to basal levels due to its short $t_{1/2}$ Wright et al., (2007), Kuang et al., (2020). PGC-1 α protein itself is activated following p38 mitogen activated kinase (MAPK) which phosphorylates and, in the process, removes the repressor protein, p160 myb Akimoto et al., (2008), Akimoto et al., (2004), Fan et al., (2004), Knutti et al., (2001), allowing for translocation from the cytoplasm into the nucleus. Once in the nucleus PGC-1 α can bind to and activate transcription factors for mitochondrial proteins such as TFAM and PGC-1 α itself. Exercise is well known to induce activation of the MAPK and extracellular signal regulated kinase (ERK) pathway through changes in intracellular calcium

levels, hormonal and mechanically activated phosphorylation events Fan et al., (2004), Knutti et al., (2001), Puigserver et al., (2001). In-vitro myotube overexpression of MAPK 6 and 3 which activate p38 MAPK, also increases PGC-1 α promoter activity directly Fan et al., (2004), Knutti et al., (2001). This also occurs indirectly through p38 MAPK phosphorylation and subsequent activation of the ATF-2 protein, a cyclic AMP response element binding protein (CREB) family member that can also bind to and activate the PGC-1 α promoter region (Akimoto *et al.* 2008). This is supported by work in mouse skeletal muscle in which they added a luciferase reporter molecule to the PGC-1 α protein to display its rapid activation following contraction Akimoto et al., (2004), which was subsequently lost when MEF-2 and CREB proteins were deliberately mutated to prevent the ATF-2 and MEF-2 transcription factors from binding to the recognition sites on the PGC-1 α promoter region, thus inhibiting its transcription.

PGC-1 α is also regulated through adenosine monophosphate (AMP)-activated protein kinase (AMPK) Suwa et al., (2006). AMPK protein is a serine-threonine kinase which contains α , β and γ subunits. Throughout the exercise and metabolism literature it is considered the 'key cellular energy sensor' Carling and Hardie, (1989), Winder and Hardie, (1999), and is highly conserved in all eukaryotes. AMPK signalling is regulated by responses to the AMP to ATP ratio in periods of energy deprivation or exercise. Changes result in signalling cascades to conserve ATP levels by inhibiting anabolic pathways that require ATP such as protein synthesis, fatty acid synthesis and gluconeogenesis whilst stimulating catabolic processes that generate ATP such as fatty acid oxidation Dreyer et al., (2006). Increases in AMP activates AMPK signalling through multiple ways including the direct binding of AMP to AMPK, resulting in decreased protein phosphatase binding and increased substrate activity with kinase complexes serine threonine kinase 11 (STK11) also known as liver kinase B1 (LKB1), STE20-related kinase adapter protein alpha (STRAD), mouse binding protein 25/calcium binding protein 39 (MO25) Hawley et al., (2003). Increases in AMP also lead to allosteric activation of the LKB1 tumour suppressor, STRAD α/β and MO25 α/β . AMPK signalling cascades can also be generated through AMP triggered conformational changes in the γ subunit of AMPK, exposing a threonine 172 binding site allowing for subsequent phosphorylation and activation of AMPK Hawley et al., (1996). Following the induction of exercise where there is an initial fall in cellular energy levels (ATP), AMPK phosphorylates acetyl-CoA carboxylase, blocking its activity and

thus preventing conversion of acetyl-CoA to malonyl-CoA. The lack of malonyl-CoA results in increased carnitine palmitoyltransferase-1 activity, a key enzyme in the active transport of fatty acids into the mitochondria for oxidation and ATP production during exercise Saha et al., (2000). AMPK can also phosphorylate glycogen synthase, again blocking its activity and consequently turning on another catabolic process, the breakdown of glycogen Carling and Hardie, (1989), Nielsen and Wojtaszewski, (2004).

Chronic continuous electrical stimulation of skeletal muscle is a potent stimulus to activate AMPK signalling, whereas previous evidence has shown that a resistance-like pattern of high-frequency stimulation, with rest periods between each set does not activate AMPK signalling cascades to the same extent, potentially due to recovery of ATP during the rest periods Atherton et al., (2005). Whilst AMPK activation is considered to induce catabolic signalling cascades, it poses the question as to how contractile activity from resistance exercise results in increases in protein synthesis and hypertrophy after prolonged periods of training, if AMPK signalling inhibits any anabolic pathways. However, Dreyer et al., (2006) displayed that both during, immediately after and 1-hour post-acute resistance exercise in humans caused an elevation in AMPK α 2 activity due to the high demands of ATP. Using stable isotope techniques to calculate fractional synthesis rates, they found that during exercise, muscle fractional synthetic rate was significantly decreased, along with reduced phosphorylation of the eukaryotic translation initiation factor 4E (eIF4E)-binding protein 1 (4E-BP1), but was significantly increased both 1 and 2 hours post exercise. The increases in fractional synthetic rates were corroborated by an increase in abundance and phosphorylation activity of protein kinase B/Akt (PKB), mTOR and S6K1 with a reduction in eEF2 phosphorylation, all of which increases protein synthesis through controlling translational rate and efficiency of proteins. Furthermore, PGC-1 α has also been implicated in the acute response to resistance training induced hypertrophy. Whilst it is most commonly known to regulate the expression of mitochondrial and oxidative phosphorylation encoding proteins, more recent work has demonstrated that alternative promoter usage and splicing of PGC-1 α , PGC-1 α 4 results in induction of the IGF1 growth pathway whilst downregulating myostatin Ruas et al., (2012). Overexpression both in-vitro and in-vivo resulted in robust hypertrophy and provided protection of muscle mass wasting in response to cancer cachexia Ruas et al., (2012).

1.4 Unloading, Muscle Atrophy and The Ubiquitin Proteasome Pathway

The plasticity of skeletal muscle can be attributed to co-ordinated changes in protein synthesis and protein degradation which allow muscles to hypertrophy following increases in mechanical load and atrophy during mechanical unloading and catabolic periods where energy availability is low. Skeletal muscle atrophy is a common feature of disuse caused by physical inactivity or forced bed rest, as well as in ageing where it is termed sarcopenia. During this atrophy, protein degradation rates exceed synthetic rates which reduces muscle fiber diameter, as well as its sarcomeric and cytoplasmic contents in the absence of degeneration, necrosis, or loss of muscle fibers themselves.

Proteolytic pathways involved in muscle protein degradation mainly involve the ubiquitin-proteasome pathway. The ubiquitin proteasome and associated ubiquitin enzymes have been well characterised in the progression of muscle atrophy across multiple models Sandri et al., (2004), Bodine and Baehr, (2014). Ubiquitin is highly conserved amongst all living organisms and is a small 76-residue protein Hershko and Ciechanover, (1998). Ubiquitin itself functions as a post-translational lysine modification on proteins which subsequently affects their stability, localisation, or ability to perform a function at another target protein Hershko and Ciechanover, (1998), Sun and Chen, (2004).

The co-ordination of the enzymes E1, E2 and E3, often called ubiquitin ligases facilitate the binding of the c-terminal glycine of the ubiquitin protein to the ϵ -amino group of the lysine on the target protein which will then be deemed ubiquitinated. Ubiquitin and ubiquitin-like proteins are activated by an E1 ligase. Upon activation, the ubiquitin is transferred to the active-site cysteine of an E2 ligase. An E2 ligase thioester then interacts with an E3 ubiquitin ligase which allows transfer of ubiquitin from the E2 ligase to a lysine residue of a substrate. Proteins with one ubiquitin protein (monoubiquitinated) can either dissociate from the E3 ligase or can acquire further ubiquitin modifications on the ubiquitin protein itself which has a total of seven lysines, resulting in polyubiquitination Eldridge and O'brien, (2010). Most studied is the ubiquitination of lysine 48 (K48-linked polyubiquitination which functions to target the substrate protein to the 26S proteasome system for degradation into short oligopeptides, releasing free ubiquitins Sandri et al., (2004), Eddins et al., (2011).

Specific substrate recognition and targeting of ubiquitin to a particular protein's lysine is controlled by an E3 ligase, of which there reportedly over 600 Deshaies and Joazeiro, (2009). The two main classes of E3 ubiquitin ligases are RING E3's and HECT domain containing E3's (Homologous to the E6-AP Carboxyl Terminus). In skeletal muscle atrophy, the main E3 ligases implicated are Trim63, also known as MuRF1 and Fbxo32, also known as MAFbx or Atrogin-1 Bodine et al., (2001b), Sandri et al., (2004), Clarke et al., (2007), Eddins et al., (2011), Bodine and Baehr, (2014). In-vitro studies in muscle cells first showed that Trim63 was essential for degradation of MyHCs and MLCs and showed that there was a physical interaction between the Trim63 and the MyHC substrate through co-immunoprecipitation. When skeletal muscle myotubes in-vitro are treated with dexamethasone (a cachectic glucocorticoid), the normal response is atrophic and concomitant with a loss in MyHC protein, but with siRNA-mediated depletion of Trim63 the loss of MyHC is blocked Clarke et al., (2007), Fisher, (2012). This was further replicated in-vivo by Clarke et al., (2007) who found that Trim63 knockout mice spared MyHC proteins in response to dexamethasone in comparison to WT mice. Other work has shown that Trim63 is an important regulator of protein synthesis through the degradation of particular substrates such as the eukaryotic translation initiation factor 3 subunit F (EIF3f), which is a regulatory subunit important in the IGF/mTOR/p70s6K pathway that when upregulated leads to an increase in protein synthesis and muscle hypertrophy Bodine et al., (2001a), Rommel et al., (2001).

Transcription factors are proteins that can both initiate and control the rate of transcription of a particular gene or sub-set of genes. Myogenin and Foxo are transcription factors that have been implicated in skeletal muscle atrophy. Myogenin whilst involved in muscle development and adult myogenesis, has also been identified as a potent regulator of Fbxo32 and Trim63 when transcriptionally upregulated through the indirect action of histone deacetylases (HDACs). HDACs as their name suggests can remove acetyl groups from lysine's on proteins such as histones and can be classified into five classes dependent on their sequence identity and domain organisation (I, IIa, IIb, III and IV) and have been implicated in skeletal muscle atrophy. Histones are proteins that function to package DNA into structural units called nucleosomes and determine how tightly packed DNA winds. Acetylation of histones decreases their affinity with DNA, resulting in conformational changes that increase the accessibility of chromatin to transcription factors. Assessment of genome-wide chromatin

accessibility is becoming a powerful tool in understanding the molecular biology of skeletal muscle adaptation and transcriptional regulation Dos Santos et al., (2020), with the current most popular technique being 'ATAC-seq', known as Assay for Transposase-Accessible Chromatin using sequencing. Histone deacetylation is the removal of the acetyl group from the histone, often performed by one of the family of HDAC's, reversing the conformational change of the chromatin landscape and therefore on most occasions reducing transcriptional activity through inhibiting transcription factor binding to its target substrate Baar, (2010). The role of myogenin in muscle atrophy specifically involves Hdac4 and Hdac5 which both belong to class IIa HDAC's Luo et al., (2019a). Hdac4 and Hdac5 repress dachshund homolog 2 (Dach2) and MEF2-interacting transcription repressor (Mitr) which are both negative regulators of myogenin. Therefore, when Hdac4 and Hdac5 are active, myogenin expression increases, which promotes expression of Fbxo32 and Trim63. Deletion of myogenin from adult mice reduces expression of MuRF1 and atrogin-1 during neurogenic atrophy and can preserve muscle mass Belova et al., (2020), Moresi et al., (2010). Furthermore, deletion of Hdac4 and Hdac5 prevents myogenin upregulation and therefore also preserves muscle mass following denervation Moresi et al., (2010). Forced expression of myogenin in Hdac4/Hdac5 deplete mice after denervation-induced atrophy restores the usual muscle atrophy response showing that myogenin is essential for neurogenic muscle atrophy. Conversely, when myogenin is overexpressed in WT mice, its expression is not sufficient to induce muscle atrophy, showing that neurogenic muscle atrophy follows a specific pathway for muscle wasting Moresi et al., (2010).

Despite their names, HDACs not only modify the acetyl molecules on histones but can also deacetylate cytosolic proteins and non-histone nuclear proteins. Class II HDACs (HDACs 4, 5, 6, 7, 9 and 10) are able to translocate in and out of the nucleus dependent on their phosphorylation state Belova et al., (2020), Moresi et al., (2010) to achieve both histone and cytosolic deacetylation. Recently, Luo et al., (2019a) displayed that following denervation-induced atrophy, HDAC4 was able to deacetylate MyHCs, peroxisome proliferator-activated receptor gamma co-activator 1-alpha (PGC-1 α), and heat shock cognate 71 kDa protein (Hsc70) which leads to both loss of contractile proteins and mitochondria. The use of specific class IIa or HDAC4 inhibitors were sufficient in rescuing MyHC, PGC-1 α and Hsc70 at the

protein level therefore preventing muscle atrophy and maintaining mitochondrial biogenesis Luo et al., (2019a).

Forkhead Box Class O (Foxo) transcription factors were first characterised in the *Drosophila* and are characterised by a shared 100 amino acid DNA-binding motif, termed the 'forkhead domain' Tzivion et al., (2011). Whilst there are several Foxo genes conserved across basic and complex eukaryotes, Foxo1, Foxo3 and Foxo4 are all expressed in skeletal muscle and have been implicated in skeletal muscle atrophy Sandri et al., (2004). Mechanistic studies involving dexamethasone treatment of muscle cells in-vitro to produce atrophy have shown that Fbxo32 and Trim63 are upregulated at the transcriptional level. Co-treatment of dexamethasone with IGF-1 prevented this upregulation of Fbxo32 and Trim63 through downstream IGF-1 signalling. IGF-1 binds to its receptor phosphatidylinositol 3-kinase (PI3K) which in turn phosphorylates protein kinase B (Akt). When phosphorylated Akt, can phosphorylate Foxo transcription factors which then associate with 14-3-3 sequestered proteins within the cytoplasm and remain inactive. During conditions of atrophy, IGF1 remains inactive, meaning that PI3K cannot phosphorylate Akt. As a consequence of Akt inactivity, Foxo remains unphosphorylated causing it to dissociate with 14-3-3 proteins, allowing it to translocate to the nucleus where it can activate transcription of Trim63 and Fbxo32 Sandri et al., (2004). In-vivo, transgenic over-expression of Foxo1 results in severe muscle atrophy and muscle function Kamei et al., (2003). Atrophy has also been inhibited (~40%) in-vivo during hindlimb suspension, through electroporation and expression of a dominant-negative Foxo3a protein in rat which contains only the DNA binding domain, which lacks full functionality Senf et al., (2010).

Contrastingly, whilst the ubiquitin-proteasome pathway is at the centre of muscle atrophy, it has also recently been deemed important in the adaptive process of hypertrophy. Recent work by our group has identified the HECT domain E3 ligase ubiquitin protein ligase E3 component n-recogin 5 (UBR5, also termed EDD1) to be significantly altered at the DNA methylation and mRNA level in human skeletal muscle following mechanical loading Seaborne et al., (2018a), Seaborne et al., (2018b). Following 7 weeks of resistance exercise, UBR5 mRNA expression increased whilst DNA methylation decreased (hypomethylation). These increases in gene expression and hypomethylation were augmented following 7 weeks of further resistance exercise after a period of detraining. These changes were highly correlated with

changes in skeletal muscle mass, suggesting that UBR5, whilst a HECT domain E3 ligase is involved in hypertrophy as opposed to the atrophy associated E3 ligases MuRF-1 and MAFbx. These changes have been confirmed in a number of mechanical loading models including acute loading in bioengineered myofibers, synergist ablation, 'Spillover' stimulation and also during recovery of muscle mass following TTX induced atrophy and hindlimb suspension without changes in MuRF-1 and MAFbx expression Seaborne et al., (2019a). Mechanical loading in human myotubes in-vitro which had siRNA silencing of UBR5, was able to recover UBR5 expression suggesting that its expression is downstream of a mechanical sensor. When UBR5 was silenced in mouse tibialis anterior via miR-based RNAi and electroporation, skeletal muscle fiber size was significantly reduced after 30 days along with total RNA production, global protein synthesis and ERK1/2 phosphorylation suggesting that UBR5 acts as a positive modulator of muscle mass Hughes et al., (2020), Turner et al., (2019), and warrants further investigation.

1.5 Loading and Muscle Hypertrophy

Resistance exercise training provides both a mechanical and metabolic stress within skeletal muscle to stimulate hypertrophy and increase force generating capacities van Ingen and Kirby, (2021), Wackerhage et al., (2019). The increase in skeletal muscle fiber cross-sectional area is the result of accretion of myofibrillar contractile proteins and other organelles that are densely packed within the cytosol. Decades of research have revealed that mechanical overload-induced hypertrophy occurs because of prolonged net increases in protein synthesis, to increase the amount of myofibrillar protein present in muscle fibers Glass, (2005), Bodine et al., (2001b), Chaillou et al., (2015), Chaillou et al., (2013). This is orchestrated through the reprogramming of the muscle transcriptome to positively regulate cell growth and translational capacity, whilst suppressing negative regulators of cell growth Schiaffino et al., (2020). These signals themselves come from within the muscle fiber 'myonuclei', interstitial cells such as satellite cells as well as from distal organs Sartori et al., (2021). The anabolic process is reported to be centrally controlled by the insulin-like growth factor (IGF1)/ protein kinase B (Akt)/ mechanistic target of rapamycin complex-1 (mTORC1) signalling pathway and its upstream regulators and downstream effectors Baar and Esser, (1999a), Sartori et al., (2021), Ogasawara et al., (2017), Ogasawara et al., (2016), Hornberger, (2011), You et al., (2019). However, it is important to note that these mechanisms are not 'on

and off switches', with synthesis and degradation occurring simultaneously. In fact, the synthesis of individual proteins may undergo temporal patterns and shifts Hesketh et al., (2016), Hesketh et al., (2020b), that simultaneously occur alongside activation of the autophagy-lysosome system and ubiquitin proteasome degradation system Grumati et al., (2011), Cui et al., (2020). An example of this is that amino acids released by the lysosome/proteasome following protein degradation themselves can directly stimulate mTOR Liu and Sabatini, (2020) and therefore may increase protein synthesis. This can be explained by the need to synthesise and degrade proteins constantly to maintain protein quality, so that the process of growth or atrophy is a modulation of ongoing processes that are also influenced by nutritional supply.

Insulin (synthesised in the pancreas) and IGF1 (predominately synthesised in the liver under the action of growth hormone produced in the pituitary gland) act as anabolic factors that stimulate muscle growth through binding to the insulin receptor and IGF1 receptor, subsequently activating a cascade of phosphorylation events that both positively and negatively regulate the activity and translocation of proteins, enzymes and transcription factors Schiaffino et al., (2020). Muscle specific overexpression of IGF1 is well known for producing increases in muscle mass and strength and alleviating age-related loss of muscle mass Musarò et al., (2001). The IGF1 gene which contains six exons is highly conserved across species and can be transcribed into heterogeneous mRNA transcripts and subsequently translated into different IGF-1 polypeptides through the combination of multiple transcription initiation sites and alternative splicing. The biological action of each isoform and their ability to bind to cell membrane receptors is mediated through different N-terminal signal peptides (Class 1 or 2) or through the removal of their carboxy-terminal E-peptides (Ea, Eb, commonly known as mechano-growth factor MGF, Ec) Philippou et al., (2014), Matheny Jr et al., (2010). Of these isoforms, IGF-1Ea seems to be the most potent at increasing muscle mass independent of age in mice Ascenzi et al., (2019).

The action of IGF1 and insulin itself are most well-known for activating the mitogen-activated protein kinase/extracellular signal regulated kinase (MAPK/ERK) and Phosphoinositide 3-kinases (PI3K-Akt-mTOR) pathways that are ubiquitously responsible for regulating cell growth and death in mammalian cells. Interestingly, a number of these pathway components have been selectively overexpressed in skeletal muscle via electroporation and transfection

with plasmids Bodine et al., (2001b), Pallafacchina et al., (2002). Protein kinase B/Akt overexpression has been found to both prevent atrophy during disuse and produce robust hypertrophy without mechanical overload Bodine et al., (2001b), Pallafacchina et al., (2002). Similar results have been reported using muscle-specific transgenic mice which increased skeletal muscle mass and strength without satellite cell activation and fusion Blaauw et al., (2009). The proposed central hub of the latter pathway, mTOR, a 289 kDa serine/threonine kinase Sabers et al., (1995) is responsible for integrating multiple signals such as cytokines, nutrients, energy availability and communicating to the translational machinery via p70s6k, a mitogen-activated Serine/Threonine protein kinase, which subsequently induces the components required for protein synthesis, ribosomal protein s6 (Rps6) and factor 4E binding protein 1 (4EBP1), the latter of which negatively regulates the ribosomal eukaryotic translation initiator factor 4E Liu and Sabatini, (2020). As well as positively regulating synthetic components, mTOR can also inhibit protein breakdown by blocking autophagy via phosphorylation-dependent inhibition of Unc-51 like autophagy activating kinase (ULK1) Call et al., (2017), Fuqua et al., (2020). Under mTOR inhibition or amino acid withdrawal, ULK1 phosphorylates Beclin-1 which promotes the activity of the autophagy related proteins. Specifically, the ATG14L-containing vacuolar protein sorting 34 (Vps34) complex for autophagy induction Russell et al., (2013). mTOR itself can interact with several proteins to form different protein complexes, mTORC1 and mTORC2 Hara et al., (2002), Loewith et al., (2002). The rapamycin sensitive TORC1 complex contains the regulatory associated protein of mTOR (RAPTOR) Hara et al., (2002), Kim et al., (2002), Kim et al., (2003), mTOR associated protein LST8 homolog (mLST8/G β L) Kim et al., (2003), Dishevelled, Egl-10 and Pleckstrin (DEP) domain containing mTOR-interacting protein (DEPTOR) Peterson et al., (2009) and proline rich Akt substrate of 40 kDa (PRAS40) Sancak et al., (2007), Vander Haar et al., (2007) and has been linked to promoting protein synthesis and preventing muscle atrophy Bodine et al., (2001b), Rommel et al., (2001), Solsona et al., (2021).

There is also a rapamycin-insensitive TORC2 complex which contains the protein, RAPTOR Independent Companion Of mTOR Complex 2 (Rictor) Loewith et al., (2002), mLST8/G β L, DEPTOR and mammalian stress activated protein kinase interacting protein 1 (mSIN1) Chen et al., (2018). Here, we concentrate on mTORC1 activity as mTORC2 has less of an anabolic effect and mediates glucose and lipid homeostasis Liu and Sabatini, (2020). Furthermore,

Rictor knockout in mice do not show an adverse muscle phenotype whereas Raptor/mTOR knockout mice (mTORC1 complex) show reduced muscle size and growth due to a large reduction in fast fiber area Bentzinger et al., (2008), Risson et al., (2009). Interestingly, slow fibers do not seem to be affected during post-natal growth in these mTORC1 deficient mice. mTORC1 deficient mice also develop a progressive muscular atrophy/dystrophy phenotype.

Inhibition of mTORC1 through pharmacological treatment with rapamycin (sirolimus) treatment prevents muscle growth following anabolic stimuli Pallafacchina et al., (2002). Pioneering work from the Hornberger lab and others has shown that inducible knockdown of Raptor specifically in skeletal muscle does inhibit hypertrophy but does not affect protein synthesis following synergist ablation induced mechanical overload as measured through puromycin incorporation You et al., (2019). Other genetic ablation studies in rodents have resulted of Raptor or other mTORC1 components have led to decreased mRNA translation or a serious myopathic phenotype. Furthermore, conditional deletion of mTOR with transfection of catalytically inactive mTOR resulted in reduced muscle growth rate after just 1 week of age Bentzinger et al., (2008). In both of these models, muscles still grow but to a lesser extent and develop myopathic phenotypes that are prone to muscle degeneration suggesting that mTOR may be involved in not only growth but other pro-survival pathways Schiaffino et al., (2020). Additionally, despite inhibition of the mTORC1 complex in these models, autophagy is not hyperactivated but is conversely hindered which results in the degenerative/myopathic phenotype observed in these animals Castets et al., (2013), Zhang et al., (2019). Further evidence supporting this phenomenon comes from transgenic mice with hyperactivation of mTORC1, caused by inhibition of TSC Complex Subunit 1 (TSC1) Castets et al., (2013), who have reduced autophagy activity and thus develop a myopathic phenotype.

Skeletal muscle hypertrophy induced through mechanical load is also controlled through mTORC1 activity, as first suggested by the Esser lab Baar and Esser, (1999b). High resistance eccentric contractions through activation of the sciatic nerve resulted in phosphorylation of the mTOR target 70kDa ribosomal S6 kinase (p70s6k) six hours after the resistance training bout, which further showed a near perfect correlation after 6 weeks with increases in muscle size. The Esser lab have also shown that early activation of mTORC1 signalling occurs independently of the PI3K/Akt signalling through mitogen activated protein kinase (MAPK) and extracellular signal-related kinase (ERK), which occurs through phosphorylation of TSC2

instead of PI3K and Akt Miyazaki et al., (2011). ERK1/2 pathways also help control muscle homeostasis and growth through the inhibition of TSC1/TSC2 activity and promotion of key transcription factors, Myelocytomatosis Proto-Oncogene, BHLH Transcription Factor (Myc), Jun Proto-Oncogene, AP-1 Transcription Factor Subunit (Jun), Fos Proto-Oncogene, AP-1 Transcription Factor Subunit (Fos) and ETS domain like protein-1 (Elk1) Davis, (1993), Guan, (1994).

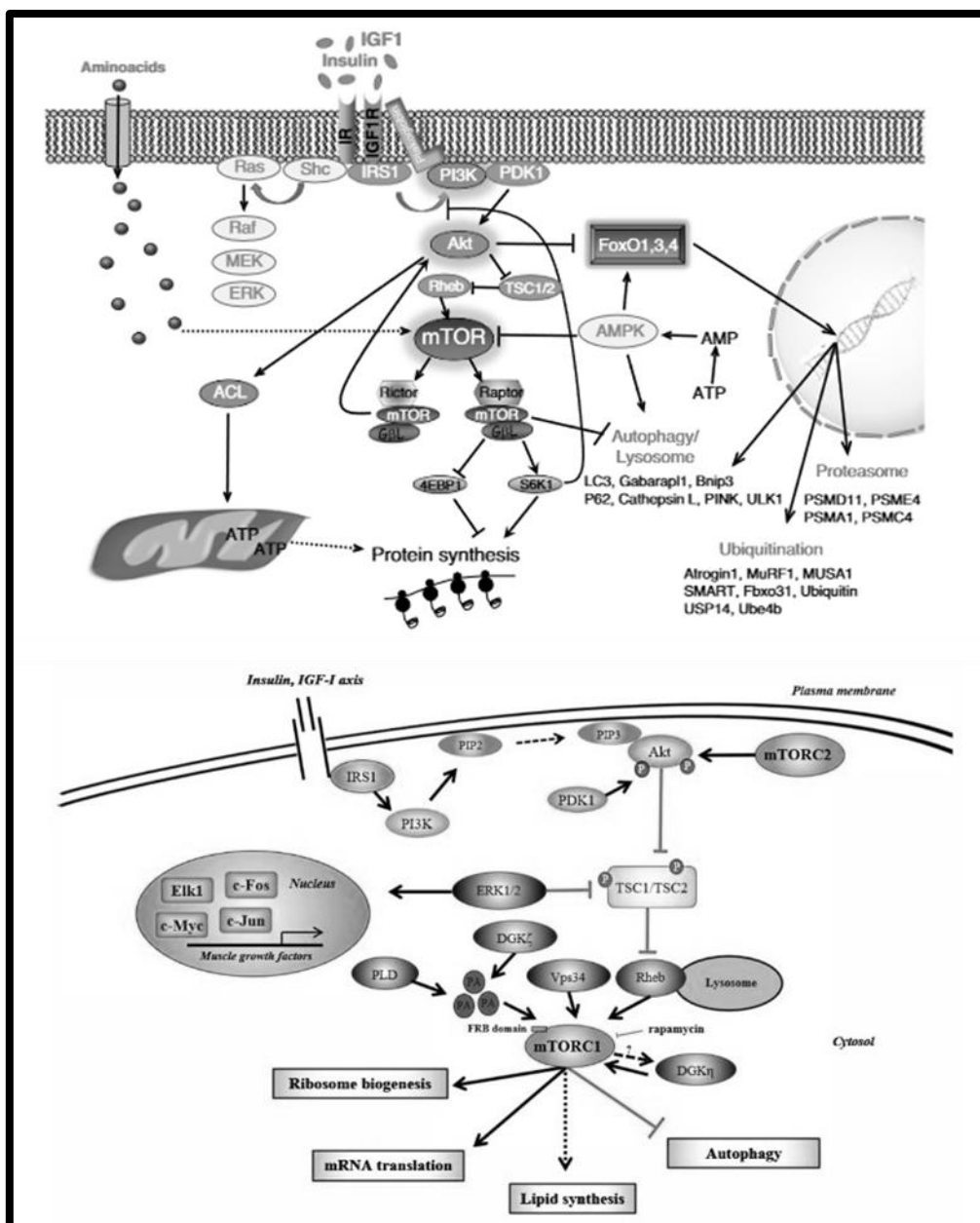


Figure 1.4: Both insulin and IGF1 bind to specific receptors on the plasma membrane of muscle cells, namely the insulin receptor and IGF1 receptor. Binding results in activation of a cascade of protein phosphorylation activity, resulting in promotion of protein synthetic machinery whilst inhibiting protein breakdown through autophagy and the ubiquitin proteasome system. In brief, once activated, IRS1 stimulates production of phosphatidylinositol-3,4,5 triphosphates (PIP3, 4, 5) at the plasma membrane through the recruitment of PI3K. PI3k can then phosphorylate phosphatidylinositol diphosphate (PIP2), which then generates phosphatidylinositol triphosphate (PIP3) which can activate kinase phosphoinositide-dependant kinase-1 (PDK1) Solsona et al., (2021). PDK1 can then phosphorylate AKT, thus activating it and promoting the inactivation of tuberous sclerosis complex 1/2 (TSC1/2). mTOR can then be activated through the Ras homolog enriched in brain GTPase (Rheb) Araki et al., (1994), Myers et al., (1994), KADOWAKI et al., (1996), Sarah Eckstein et al., (2017), Garami et al., (2003), Tomasoni and Mondino, (2011), Toker and Dibble, (2018), Alessi et al., (1997), Stokoe et al., (1997), Castro et al., (2003), Inoki et al., (2003). This can also occur through mTORC2 complex activity, whereby mTORC2 phosphorylates Akt on Serine-473 allowing for PDK1 binding and phosphorylation on the threonine site 308 Sarbassov et al., (2005). Ultimately Akt positively regulates the mTORC1 complex for protein synthesis whilst inhibiting FoxO1-3 protein signalling for protein breakdown. Interestingly, there are several feedback loops involving mTORC1 including mTORC1 blocking of IRS1 via S6K1, consequently inhibiting AKT activity. AMPK, which is upregulated during endurance exercise/energy stress is also known to block mTORC1 activity and activate FoxO systems and autophagy. As well as mechanical stimuli, mTOR can also be activated directly through branch chain amino acids that promote mTOR to the lysosomal surface where mTOR is activated by Rheb GTPase. Recent evidence also suggests that mTOR can be directly stimulated through diacylglycerol kinase zeta (DGK η) and phosphatidic acid (PA) Mobley et al., (2015), Joy et al., (2014), You et al., (2018), You et al., (2014), Goodman and Hornberger, (2014), Hornberger et al., (2006), Hornberger, (2011), Jacobs et al., (2014). Phospholipase D (PLD) synthesises PA and DGK η which can bind directly to mTOR, activating it through its FKBP rapamycin binding domain. Taken with permissions from Sartori et al., (2021), Solsona et al., (2021). Under Creative Commons Attribution 4.0 International License.

Myostatin regulation of skeletal muscle growth

Myostatin (often referred to as growth differentiation factor 8 (GDF-8), a member of the transforming growth factor β (TGF β) superfamily is one of the most studied ligands involved in inhibiting muscle growth. Knockdown of myostatin in WT mice results in extreme muscular hypertrophy McPherron et al., (1997), and stronger, more muscular muscles in *mdx/myostatin* knockdown mice in comparison to *mdx* knockdown mice, as well as reduced fibrosis and negative fibro-adipogenic remodelling Wagner et al., (2002). This function seems to be observed across species, including cattle (often referred to as 'double-muscled') Grobet et al., (1997), Grobet et al., (1998), Kambadur et al., (1997). Naturally occurring loss of function mutations in the myostatin gene in humans also result in robust hypertrophy without abnormalities in cardiac structure or function Schuelke et al., (2004), independent of increased levels of testosterone or IGF1 Schuelke et al., (2004). Conversely, persistent systemic overexpression of myostatin leads to progressive muscle wasting Zimmers et al., (2002). Interestingly, myostatin also appears to inhibit the activity and fusion of satellite cells which may add to negative regulation of muscle mass McCroskery et al., (2003). Treatment for Duchenne muscular dystrophy through myostatin inhibition therapy has gained large attention in recent decades but has since failed to translate from pre-clinical investigations Rybalka et al., (2020).

The activin A/Myostatin/TGF β signalling proteins bind to activin type IIA/B receptors and TGF β receptors associated with the plasma membrane to recruitment and activation of the activin receptor-like kinases (ALK), ALK4, ALK5 and ALK7 to induce phosphorylation of 'Small worm' mothers against decapentaplegic homolog (SMAD) proteins SMAD2 and SMAD3, to promote heterotrimeric protein complex formation with SMAD4 Sartori et al., (2021), which has recently been identified as a central regulator of the transcriptomic exercise response through meta-analysis of multiple transcriptomic exercise data sets Amar et al., (2021). Although, genetic ablation of SMAD4 in muscles of mice did not produce hypertrophy but resulted in muscle atrophy and decreased strength Sartori et al., (2013). Once these SMAD protein complexes are formed, the complex can translocate into the nucleus where they act as transcription factors. Inhibiting SMAD2/3 is sufficient to promote muscle growth Sartori et al., (2009), Winbanks et al., (2012), linking these transcription factors to targets positively regulating protein synthesis or decreasing ubiquitination and protein degradation. mTOR signalling is a prime candidate for this crosstalk, with experiments in mice showing that

rapamycin treatment or knockdown of mTOR revert the hypertrophic effects of follistatin blockade of myostatin Winbanks et al., (2012).

Bone morphogenetic proteins (BMPs) and growth differentiation factors (GDFs) which are also controlled through extracellular cytokines such as noggin or follistatin, also converge on this pathway Sartori et al., (2013), Traore et al., (2019). BMP/GDF ligands preferentially bind to type II cell surface receptors on the plasma membrane including BMP type II receptor (BMPRII), activin receptor IIA and IIB (ActRIIA/B), but can also bind to type I receptors such as ALK2 (ACVR1), ALK3 (BMPRIA) and ALK6 (BMPRII) Salazar et al., (2016), Brazil et al., (2015). Again, these ligand-receptor complexes promote the phosphorylation of SMAD1/SMAD5/SMAD8, allowing for trimerization with SMAD4, allowing for translocation into the nucleus and altering transcription. Modulation of this pathway is also controlled downstream of its receptors within the cytosol by SMAD6 and SMAD7 which prevent receptor mediated activity of SMAD1-SMAD5-SMAD8 and SMAD2-SMAD3 protein complexes with SMAD4 Winbanks et al., (2013). Evidence suggesting that both BMP signalling and activin/myostatin pathways control epistasis (the action of one gene upon another) within skeletal muscle is evident through the overexpression of noggin, a cytokine that acts antagonistically to BMP, which can remove the hypertrophic phenotype observed in myostatin knockout mice. Furthermore, hypertrophy induced through follistatin administration both blocks myostatin/activin signalling and stimulates SMAD1, SMAD5 and SMAD8 activation Sartori et al., (2021), Davey et al., (2016), Winbanks et al., (2013), resulting in decreased levels of activity/phosphorylation of SMAD2 and SMAD3, allowing for SMAD4 to interact with phosphorylated SMAD1-SMAD5-SMAD8 protein complexes to increase growth or prevent muscle wasting Sartori et al., (2009), Sartori et al., (2021), Sartori et al., (2013).

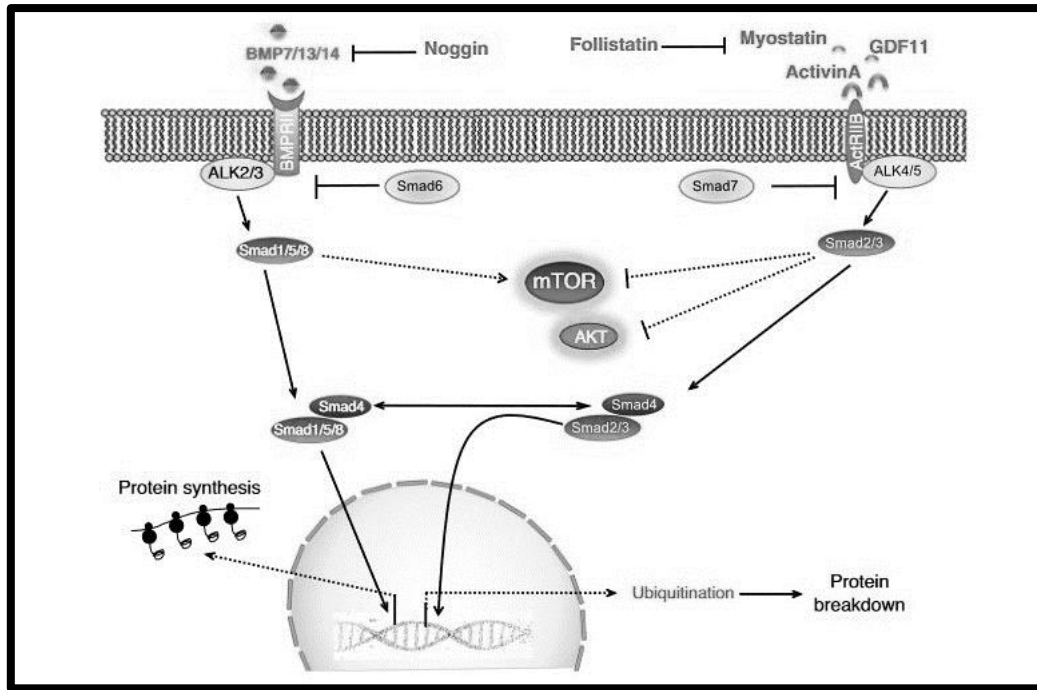


Figure 1.5: Activin A/Myostatin/TGF β signalling proteins regulate muscle mass through binding to cell surface receptors which induces phosphorylation of and SMAD4 protein complexes capable of translocating to the nucleus. SMAD1-SMAD5-SMAD8-SMAD4 protein complexes positively regulate transcription with the function of increasing protein synthesis and opposingly SMAD2-SMAD3-SMAD4 protein complexes promote protein degradation. Dashed lines indicate pathway interactions that have not yet been fully defined. Taken with permissions from Sartori et al., (2021). Under Creative Commons Attribution 4.0 International License.

Ribosomal Biogenesis & Translational Control

Muscle hypertrophy and protein synthesis is not only reliant on the transcription of positively regulating genes and the activity of their protein products but also on the abundance and translational capacity and of the ribosomes themselves Wen et al., (2016), Figueiredo et al., (2021), Figueiredo and McCarthy, (2019). Ribosomes assemble amino acid sequences according to the delivered mRNA to create polypeptide chains. The process of ribosomal biogenesis starts with ribosomal RNA (rRNA) transcription by RNA polymerase I (Pol I) as a 47S pre-rRNA. This mRNA transcript is then cleaved into 28S, 18S and 5.8S and assembled with ribonuclear proteins to make large and small subunits Aubert et al., (2018). DNA polymerase I therefore acts as a primary regulatory mechanism of ribosomal biogenesis,

forming a pre-initiation complex (PIC) with activity of the transcription initiation factor IB (TIF-1B) and the upstream binding factor (UBF) Voit and Grummt, (2001), Moss and Stefanovsky, (1995), Geiss et al., (1997). This rRNA pool makes up approximately 80% of the total RNA pool Lodish and Zipursky, (2001). mTOR regulates ribosomal biogenesis including through mTORC1 activation of TIF-1A for pre-ribosomal RNA synthesis through the activity of Pol I Michels et al., (2010), Shor et al., (2010). mTOR can also phosphorylate the MAF1 homolog, inhibiting its function as a repressor of RNA polymerase III transcription, leading to transfer of RNA synthesis Michels et al., (2010), Shor et al., (2010). Additionally, mTOR interaction with La-related protein 1 (LARP1), regulates production of ribosomal proteins as well as initiation and elongation factors Solsona et al., (2021), Berman et al., (2021), Schiaffino et al., (2013), Schiaffino et al., (2020), Fonseca et al., (2015). mTORC1 also regulates the transcription factor c-Myc during chronic resistance training Ogasawara et al., (2017), Ogasawara et al., (2016), Mori et al., (2020), an oncogene that acts as a transcription factor to coordinate protein synthesis through upregulation of numerous genes related to processing rRNA and ribosomal proteins themselves. C-Myc also regulates genes associated with the initiation of mRNA translation and nuclear export of ribosomal subunits Van Riggelen et al., (2010). These genes include UBF, TIF-1A, TIF-1B, DNA polymerase I, II and III Van Riggelen et al., (2010), Campbell and White, (2014), Brook et al., (2019), Jin and Zhou, (2016), Grandori et al., (2005).

During hypertrophy, protein synthesis rates increase but it is still disputed as to whether ribosomal density (translational capacity) or efficiency (rate of translation of mRNA) are the main limiting factors that could be inhibiting maximal levels of protein synthesis. Exercise-induced hypertrophy increases both total RNA and rRNA content Stec et al., (2016), Mobley et al., (2018), Figueiredo et al., (2021), Figueiredo et al., (2016), Figueiredo and McCarthy, (2019), Figueiredo et al., (2015), von Walden et al., (2012). Studies in humans and mice have revealed that ribosomal DNA (rDNA) copy number is positively correlated with ribosomal biogenesis in response to an acute bout of resistance exercise and that the acute bout also alters rDNA methylation patterns in enhancer and intergenic regions associated with c-Myc binding von Walden et al., (2020), Figueiredo et al., (2021). This may be indicative of the ribosomal biogenesis response being predictive of the chronic hypertrophy response following resistance training. Blocking ribosomal production in-vitro also negatively affects

hypertrophy of myotubes Stec et al., (2016), providing further evidence that ribosomal number and activity are key drivers of the hypertrophic process Wen et al., (2016).

Mechanotransduction through the myonucleus

As well as mechanosensitive biochemical signalling events occurring following resistance exercise, there is evidence emerging suggesting that the nucleus/myonucleus itself can act as a mechanosensitive element, translating mechanical forces in cellular cascades that promote muscle growth through nuclear envelope stretching, modification of nuclear envelope proteins, histone modifications and chromatin accessibility, transcription factor localisation and subsequent gene expression Wagh et al., (2021), van Ingen and Kirby, (2021), Kirby and Lammerding, (2018), Lomakin et al., (2020), Venturini et al., (2020), Enyedi and Niethammer, (2016), Aureille et al., (2019), Stephens et al., (2019a), Stephens et al., (2019b), Guilluy et al., (2014), Guilluy and Burridge, (2015), Le et al., (2016), Nava et al., (2020), Elosegui-Artola et al., (2017), Cosgrove et al., (2021). Despite some evidence linking nuclear envelope proteins mutations to reduced muscle function, ability to hypertrophy and severe laminopathies/myopathies/dystrophies Owens et al., (2021), Owens et al., (2020a), Puckelwartz et al., (2010), Zhou et al., (2017), Piekarowicz et al., (2019), Bonne et al., (1999), it remains to be elucidated how these mechanical signals are integrated with the biochemical signals that are much better documented in muscle growth due to difficulties in decoupling the biochemical cellular responses from that of the mechanosensitive response Guilluy and Burridge, (2015), Guilluy et al., (2014), van Ingen and Kirby, (2021)

1.6 Models of Hypertrophy

Understanding the mechanisms behind the plasticity of muscle mass in response to loading requires models of mechanical loading that replicate resistance training like stimuli in humans. Tools to manipulate mice genetically or pharmacologically, or rats through electroporation and transfection, have allowed the field to start to understand how the gain or loss of a gene/or part of a gene affects the functional significance *in-vivo*. Combining an appropriate model of resistance training with these genetic tools will enable a greater understanding of load-induced hypertrophy and allow the design of interventions/therapeutics to increase and maintain muscle mass and quality. Many models have been used to mechanically load/overload muscle to produce hypertrophy but are often not transferrable

to human muscle hypertrophy, due to the rapid rate and magnitude of muscle growth which can exceed increases of 40% in a matter of weeks Murach et al., (2020a).

The most commonly used method of mechanical overload induced hypertrophy is synergist or synergistic ablation which involves the removal of a large muscle or multiple muscles to produce compensatory growth in a smaller muscle that performs the same function during weight bearing or ambulatory activity. This model whilst adopted by many, could be considered the least translatable to human resistance exercise and has a number of pitfalls that include invasiveness of surgery, extensive damage in the initial static overload phase, degeneration and regeneration, muscle fiber splitting, rate and magnitude of growth, systemic and local profiles of inflammation and metabolism Murach et al., (2020a). This method of overload is also non-reversible and occurs continuously so has limited translatability. It also remains to be answered whether this method of hypertrophy is induced by stretch, tension or both so mechanistic studies are often hindered (discussed in greater detail in section 1.7 '*Hyperplasia, Muscle Fibre Splitting & Fiber Length*'). As well as its effects on muscle, synergist ablation also produces extensive and rapid new tendon growth Gumucio et al., (2014).

Progressive weighted wheel running has shown promise in producing hypertrophy in rats (15-25% dependent on fiber type after 8 weeks), Ishihara et al., (1998). In this model, weight is progressively added to a wheel to provide resistance whilst running and therefore provides both a high-load and high-volume stimulus, similar to resistive cycle training or concurrent training in humans which causes an improvement in both power and fatigue resistance Murach and Bagley, (2016), Murach et al., (2016), Fry et al., (2014a), Fry et al., (2014b). Results therefore cannot necessarily be extrapolated to resistance training per se. Rodents and especially mice are innately driven to run long periods throughout the night, so do not require operant conditioning to perform exercise, therefore allowing for minimal invasiveness and the ability to measure workload. Whilst workload is measurable, it is not yet controllable with reports that female mice will run between 10-12km per night with males slightly less and aged mice around half of the volume Murach et al., (2020b), Englund et al., (2020), Dungan et al., (2019). Ideally, an automatic lock to control or limit volume could prove useful for reducing training volume, with a greater resistance applied for a shorter period. However this is dependent on the willingness of the individual to exercise at a range of intensities: several

labs have reported a reduction in compliance when resistance is too high Call et al., (2010), Ishihara et al., (1998), Konhilas et al., (2005), Roemers et al., (2018), Soffe et al., (2016). Additionally, monitoring of training load can only be performed successfully on single-housed mice which challenges recommended husbandry. However, progressive weighted wheel running is arguably the most minimally invasive approach and allows for the study of training, de-training, and re-training Dungan et al., (2019), which is highly translatable to humans and their natural training tendencies, as well as disuse through injury and bed rest.

In terms of muscle hypertrophy, it is still a matter of debate whether unloaded wheel running can produce hypertrophy Allen et al., (2001), Brooks et al., (2018), Li et al., (2006), although evidence for hypertrophy across muscle groups and in a fiber-type specific manner is strong in PoWeR, also known as progressive weighted wheel running Dungan et al., (2019). Specifically, the plantaris, soleus and gastrocnemius both grow between 15-30% in wet mass and individual fiber cross-sectional area Dungan et al., (2019), Murach et al., (2019c). It must also be noted that because of high volume of training, muscles show a glycolytic to oxidative fiber type shift which may also complicate extrapolation of load mediated adaptations whilst other metabolic changes are occurring.

Graber et al. (2019) used a similar custom progressive wheel running approach but instead fitted mice with alterable weighted vests to improve muscle power output in both adult and aged mice. Aged mice showed a positive but impaired hypertrophic response in comparison to their younger counterparts. One benefit of this approach is that exercise is administered in multiple, short ~1-minute sets to failure and is therefore controllable in terms of load and frequency. Whilst the model requires specialised equipment, it may be adopted by other groups in the future.

Other running models include high-intensity incline treadmill running protocols, recently developed by two independent labs Goh et al., (2019), Seldeen et al., (2018), Seldeen et al., (2019), inducing hypertrophy in both the dorsi and plantar flexors of the lower hindlimb. Again, these models are progressive, increasing both speed and gradient of the treadmill across a period of 8-16 weeks, with 3 sessions per week. Whilst exercise volume, frequency and intensity can be monitored, the model requires some level of operant conditioning by means of an electric shock grid to achieve the higher running intensities. Like other concurrent

models, weeks of training results in a shift to an endurance phenotype in conjunction with hypertrophy.

A multitude of other models have also been described which require operant conditioning in the form of starvation and the need to seek food or avoid nociceptive stimulation to initiate movement Klitgaard, (1988), Wirth et al., (2003). Often intensive periods and handling is required prior to experimental training for the animals to perform the task as the researcher intends. These models include weighted squat exercises Cholewa et al., (2014), Ho et al., (1980), Klitgaard, (1988), Lowe and Alway, (2002), Tamaki et al., (1992), Cui et al., (2020) and various ladder climbing protocols with weights added to tails to provide additional load Duncan et al., (1998), Hornberger Jr and Farrar, (2004), Yarasheski et al., (1990). The magnitude of hypertrophy across these models varies greatly and research is often contradictory, with some groups finding hypertrophy in certain muscle groups but others reporting no changes, which questions the efficacy and complete reproducibility of load and technique in such models. Other concerns include the study of extremely small muscles such as the flexor hallucis longus in which the hypertrophy may not be completely transferable to larger muscle groups, with larger motor functions, Hornberger Jr and Farrar, (2004). Furthermore, models that require food restriction as a motivating factor to initiate exercise may produce different signalling cascades and hypertrophic responses das Neves et al., (2018). More recently, Cui et al., (2020) developed a novel weightlifting cage design for mice, whereby individually housed mice perform a squat-like exercise whilst wearing a metal neck collar in order to push against a weight-loaded (150% bodyweight) lever plate in order to access food. Voluntary weightlifting had several beneficial effects on transcriptional output, contractile adaptations, and metabolic adaptations specifically through the mTOR signaling pathway whilst concurrently regulating autophagy in the gastrocnemius which increased its mass by 14% after 8 weeks of training. Again, this model falls short in replicating human resistance exercise by being a high repetition model to generate hypertrophy, eliciting on average 419 ± 82 lifts in 12 hours of the active dark cycle.

High-frequency electrical stimulation using electrodes connected to an external stimulator has been employed for a number of decades to induce muscle hypertrophy with both internally applied load (produced by co-contraction of the plantarflexors and dorsiflexors Baar and Esser, (1999a), and with an external weight to apply load to the contracting muscle

Eftestøl et al., (2016), Wong and Booth, (1988). The main advantage of this model is the ability to have complete control over extensive training parameters which include load, sets, repetitions, rest, and time of day, much like resistance training in humans. However, this approach requires some level of expertise and can be labour intensive in the respect that animals need to be anaesthetised for every session, legs shaven and electrodes inserted through the skin near the common peroneal or tibial nerve. Alternatively, this can be done transcutaneously but offers less specificity in targeting a particular muscle group and often leads to stimulation of untargeted muscles. The issue of repeated anaesthesia and precision of electrode placement can be avoided through the use of programmed exercise of the dorsi/plantarflexors in free living rodents delivered by implantable pulse generators as published by our group Schmoll et al., (2018) and explored throughout this thesis. Direct nerve does not replicate the gradual activation of motor units as performed in voluntary resistance exercise, but can easily be arranged to eliminate the variability of recruitment in voluntary exercise. Whilst highly controllable, the invasiveness of surgery and the appropriate recovery must be considered when planning experiments. However, we believe this current model is the best rodent model available that replicates the standard sets and repetitions method of human weightlifting.

1.7 Hyperplasia, Muscle Fibre Splitting & Changes in Fiber Length Following Mechanical Loading & Functional Overload

The use of supraphysiological loading models to produce muscle hypertrophy in rodents often show discrepancies between increases in wet muscle mass and increases in individual muscle fiber cross-sectional area Gollnick et al., (1981), Taylor and Wilkinson, (1986), Timson et al., (1985). Whilst skeletal muscle hypertrophy is generally considered as the growth of individual muscle fibers, extreme loading or volume of training can induce the appearance of newly formed muscle fibers or 'hyperplasia'. The appearance of new skeletal muscle fibers detected in histological sections can be attributed to the formation of new muscle fibers (hyperplasia) formed by the fusion of multiple satellite cells, the longitudinal branching or splitting of existing muscle fibers, or as an artefact as a result of changes in pennation angle and inconsistencies in histological sampling of the muscle mid-belly Murach et al., (2019c). The

change in total number of muscle fibers per cross-section in animal models has often been neglected due to the required to make a reliable estimate.

Such extreme models of hypertrophy such as the avian stretch-enlargement of the accessory muscles, performed by permanently adding a weight to the birds wings can induce rapid hypertrophy of between ~110% and ~320% after 12 days and 4 weeks respectively, concomitant with drastic increases in muscle fiber number per cross-section (~82%) and histological evidence of degeneration and regeneration Antonio and Gonyea, (1993), Antonio and Gonyea, (1994). As well as the addition of de-novo fibers through the proliferation and fusion of satellite cells, stretch-enlargement in birds also induces longitudinal branching or fragmentation of muscle fibers often referred to as 'fiber splitting'. Similar work has found the same extent of growth and fiber splitting Alway et al., (1989), Kennedy et al., (1988), McCormick and Schultz, (1992), Winchester and Gonyea, (1992). Similar models of persistent functional overload of a muscle have been used in mammals but produce less severe phenotypes, such as the synergist ablation model.

As described earlier, synergist ablation functional overload has been extensively used in rodents to study skeletal muscle hypertrophy and the role of satellite cells in hypertrophy due to the simplicity of the surgical approach Kirby et al., (2016b), Kirby et al., (2016a), McCarthy et al., (2011). The surgery involves the removal of a primary-mover muscle in the hindlimb of the rodent and can be performed unilaterally or bilaterally. The removal of function of the primary mover muscle, can be achieved either through the literal removal of the muscle or tenotomy of the tendon which is then sutured into the muscle belly so that the shortening of the muscle cannot produce force at the joint. The removal of this muscle causes compensation to occur in the smaller synergistic muscles through normal ambulatory cage behaviour and therefore hypertrophy. Whilst this can be done following slightly different methods, the most common form of surgery involves the removal of the gastrocnemius and soleus to overload the plantaris muscles (Peterson Lab) or the removal of the tibialis anterior to overload the extensor digitorum longus (Gundersen Lab). Exact methods to produce more relevant amounts of hypertrophy without degeneration and regeneration have been argued due to the effects on blood supply and hypoxia which may exacerbate a degenerative response which accompanies hypertrophy Egner et al., (2017), McCarthy et al., (2017).

Typically, synergist ablation overload following partial removal of the gastrocnemius/soleus complex results in robust, doubling of muscle mass within 1-2 weeks and an increase in muscle fiber cross-sectional area by 35% over a longer period Murach et al., (2019c). Again, this model of hypertrophy substantially exceeds the rate of growth observed in humans and in the early adaptation to constant overload is characterised by degeneration and regeneration for up to 2 weeks post-surgery, as well as expression of developmental myosin, central myonuclei and small calibre fibers. Even at this early stage of hypertrophy, the number of muscle fibers per muscle cross-section is elevated. As well as de-novo muscle fibers, it has been postulated that changes in pennation angle which occur during the hypertrophic process may explain the increases in muscle fiber per cross-section Jorgenson and Hornberger, (2019), Murach et al., (2019c).

Previous studies have reported plantaris pennation angle changes from 14° to 16°. If pennation angle is altered but histology is taken from the same muscle position perpendicular to the long axis of the muscle, it may artefactually produce the appearance of more muscle fibers Murach et al., (2019c). As the adaptive hypertrophic process between muscle groups and muscles with more severe or multiple pennation angles is so different, this level of artefact may differ significantly.

Whilst numerous animal models such as stretch-enlargement in the avian flight muscles and synergist ablation in cats and rodents has shown to induce fiber branching or splitting Antonio and Gonyea, (1993), Antonio and Gonyea, (1994), Ho et al., (1980), Roy and Edgerton, (1995), the mechanisms and exact stimulus resulting in this are yet to be elucidated. There are a number of hypotheses put forward by Murach et al., (2019c), as to how an increase in muscle fibers per cross-sectional area can occur independent of addition of de-novo muscle fibers or changes in pennation angle.

Defective regeneration is one proposed phenomenon which gains evidence from the consistent appearance of central myonuclei present before the 'split' of the muscle fiber. The constant overload during the regeneration-degeneration process causes sarcolemmal damage whilst the basal lamina remains intact Mackey and Kjaer, (2017a). The muscle fiber is then degraded, and satellite cells are activated to initiate regeneration. As myonuclei are mispositioned in the center of the muscle fiber rather than the periphery during the regeneration of the basal lamina, the basal lamina becomes branched which is followed by

regeneration of the sarcolemma into a branched muscle fiber Murach et al., (2019c). However, data from synergist ablation performed in Pax7-DTA mice, in which tamoxifen treatment activates diphtheria toxin A specifically in satellite cells resulting in ~90% depletion still show the appearance of split muscle fibers and increased muscle fiber number on cross-sections. Robust hypertrophy still occurs after ~2 weeks of overload despite the muscle not being able to regenerate effectively Murach et al., (2019c), McCarthy et al., (2011).

A second hypothesis involves the grafting of a myocyte onto an existing fiber to produce a branched appearance. As the sarcolemma is damaged in the hypertrophic process, satellite cells activate, fuse, and form a myotube which then grafts onto the existing muscle fiber during the renewal of the basal lamina and sarcolemma resulting in a branched muscle fiber Murach et al., (2019c). An alternative view is that the muscle fibers split themselves through an unknown mechanism when they become too large to efficiently transport oxygen (oxygen diffusion capacity) to the deepest parts of its cytoplasm, and upon reaching this point the fiber splits either partially or fully to function most efficiently. Evidence for this final hypothesis was presented by Dungan et al., (2019) who showed that after 8 weeks of weighted resisted running in mice muscle fibers significantly increased in size. However, after 12 weeks the loss of largest muscle fibers was concurrent with an increase in muscle fibers per fiber cross-section, despite the same increases in muscle mass.

Whilst there is limited evidence of this phenomena occurring in healthy, untrained human skeletal muscle and following prolonged resistance exercise, the appearance of split or branching of myofibers or myotubes is highly prevalent in steroid users. Whilst some evidence suggests that these are a consequence of the extreme loading and volume bodybuilding steroid users often perform in comparison to non-steroid resistance trained individuals Murach et al., (2019c), treatment of mouse myotubes with selective androgen receptor modulators or testosterone in-vitro results in consistent branching of myotubes as opposed to single elongated structure without any load or applied tension (Owens *et al.* Unpublished observations).

Jorgenson and Hornberger (2019) also put forward the claim that increases in fiber length following mechanical load-induced growth are also important factors resulting in increases in muscle fibers per cross-section. As changes in pennation angle typically occur over longer periods (~months), compared to changes in fiber length (~weeks) this may be a more

important measure. Roy and Edgerton (1995), reported a 13% increase in muscle fiber length following a two weeks of synergist ablation overload, which occurred alongside a doubling in muscle weight. Jorgenson and Hornberger (2019) report that with just a small increase of 13% in fiber length without muscle fiber hypertrophy or fiber splitting would lead to a 52% increase in both whole muscle cross-sectional area and the number of muscle fibers per fiber cross-section when measured at the mid-belly. See Figure 1 & 2 of Jorgenson and Hornberger, (2019) for calculations. To date, very few studies measure fiber length due to the difficulty in performing measurements meaning that its role in overload induced hypertrophy is yet to be understood and is likely significantly undervalued at present in the field.

1.8 Skeletal Muscle During Development

Formation of skeletal muscle in the vertebrate embryo involves highly regulated molecular mechanisms and expression of myogenic regulatory factors that drive limb muscle formation and growth. As the embryo develops, mesodermal cells leave the primitive streak, also known as the blastopore and migrate both anteriorly and laterally to the lateral and dorsal positions, adjacent to the notochord and neural tube. From the mesoderm, different paths of cell differentiation lead to the paraxial, intermediate, and lateral plate mesoderm's form Chal and Pourquié, (2017). Whilst the heart and various other vital reproductive and digestive organs arise from the intermediate and lateral plate mesoderm's, skeletal muscles of the limbs as well as their associated bones, ligaments, tendons, and cartilage form from somites. In contrast, skeletal muscles of the head and neck are derived from the anterior paraxial mesoderm itself Chal and Pourquié, (2017).

Deriving from the paraxial mesoderm, somites are formed after extensive proliferation of pre-somitic progenitor cells and differentiation into anterior presomitic dermomyotomal progenitors. After formation, somites become compartmentalised along the dorsoventral axis into the dermomyotome which gives rise to skeletal muscle, brown fat and dermal tissue of the back and the ventral mesenchymal sclerotome which gives rise to the axial skeleton and tendons Chal and Pourquié, (2017). The dermomyotome can then be further classified as the central dermomyotome, dorsomedial lip and ventrolateral lip. From the dermomyotome, myotomes are formed beneath the four lips of the dermomyotome dorsally and the sclerotome ventrally Ordahl and Le Douarin, (1992), Ordahl, (1993). This formation of

myotomes is then driven by cell delamination from the ventrolateral lip which gives rise to skeletal muscle progenitors, commonly known as myoblasts which characteristically express the paired box transcription factor, Pax3 and tyrosine receptor, c-Met. Developmental studies in mice which genetically ablated these genes have shown that their removal prevents delamination of cells from the ventrolateral lip and consequently, no limb muscles are formed Bladt et al., (1995), Tajbakhsh et al., (1997). Migrating skeletal muscle progenitors are directed towards myogenic lineage by the expression of basic helix-loop-helix transcription factors, Myf5 and MyoD Bober et al., (1994). Commitment and terminal differentiation of myoblasts into post-mitotic myocytes is regulated by myogenic regulatory factors, myogenin and MRF4 Buckingham et al., (2003), Hasty et al., (1993), Nabeshima et al., (1993), Venuti et al., (1995).

Myogenesis and the fusion of myocytes during development occurs in two distinct phases classified as an early embryonic/primary phase (E10.5 to E12.5 in mice) and a later fetal/secondary phase (E14.5-17.5 in mice) Biressi et al., (2007), Stockdale, (1992). The first fusion that occurs of primary myofibers forms the early myotomes and limb muscles. These primary myofibers provide a scaffold for adult muscles to be built as outlined in Figure 1.6, taken from Chal and Pourquié, (2017). These primary myofibers express Myh7 and myosin light chain 1 (My11) Kelly et al., (1997). During the second stage of myogenesis, a subset of Pax3+ progenitors begin to express Pax7 whilst downregulating Pax3. These Pax7+ cells when activated can either fuse together themselves to produce de-novo fetal myofibers or fuse to existing primary myofibers to aid in muscle growth. However, growth of muscle fibers is primarily attributed to the fusion of Pax7+ progenitors into the myofiber to add new myonuclei, whilst proliferation of Pax7+ progenitors is maintained to continually produce a pool of new progenitor cells. At this stage of secondary myogenesis where the muscle becomes fully innervated and the basal lamina forms around fibers, some fibers will start to express fast myosin heavy chain isoforms Kelly et al., (1997), Fougousse et al., (2002), Keller et al., (1992), Messina et al., (2010), Van Horn and Crow, (1989). A subset of Pax7+ cells remain dormant in the cell cycle and form a pool of adult muscle stem cells, known as satellite cells, to aid in adult skeletal myogenesis and repair following damage and exercise-induced damage. This pool of adult stem cells was initially discovered by Alexander Mauro and given its name for its unique satellite positioning located between the sarcolemma and the basal

lamina Mauro, (1961). Satellite cells are small, densely packed cells with very little cytoplasm. During the fetal and perinatal growth periods where increases in muscle mass are at the most rapid, the pool of satellite cell progenitors actively divide and constitute 30% of the mononucleated cells in the mouse Allbrook et al., (1971), Hellmuth and Allbrook, (1971). Shortly after birth, the number of resident satellite cells is severely reduced to only a few percent of mononucleated cells in adult muscle and even less of the total nuclei Allbrook et al., (1971), Cardasis and Cooper, (1975), Schmalbruch and Hellhammer, (1977).

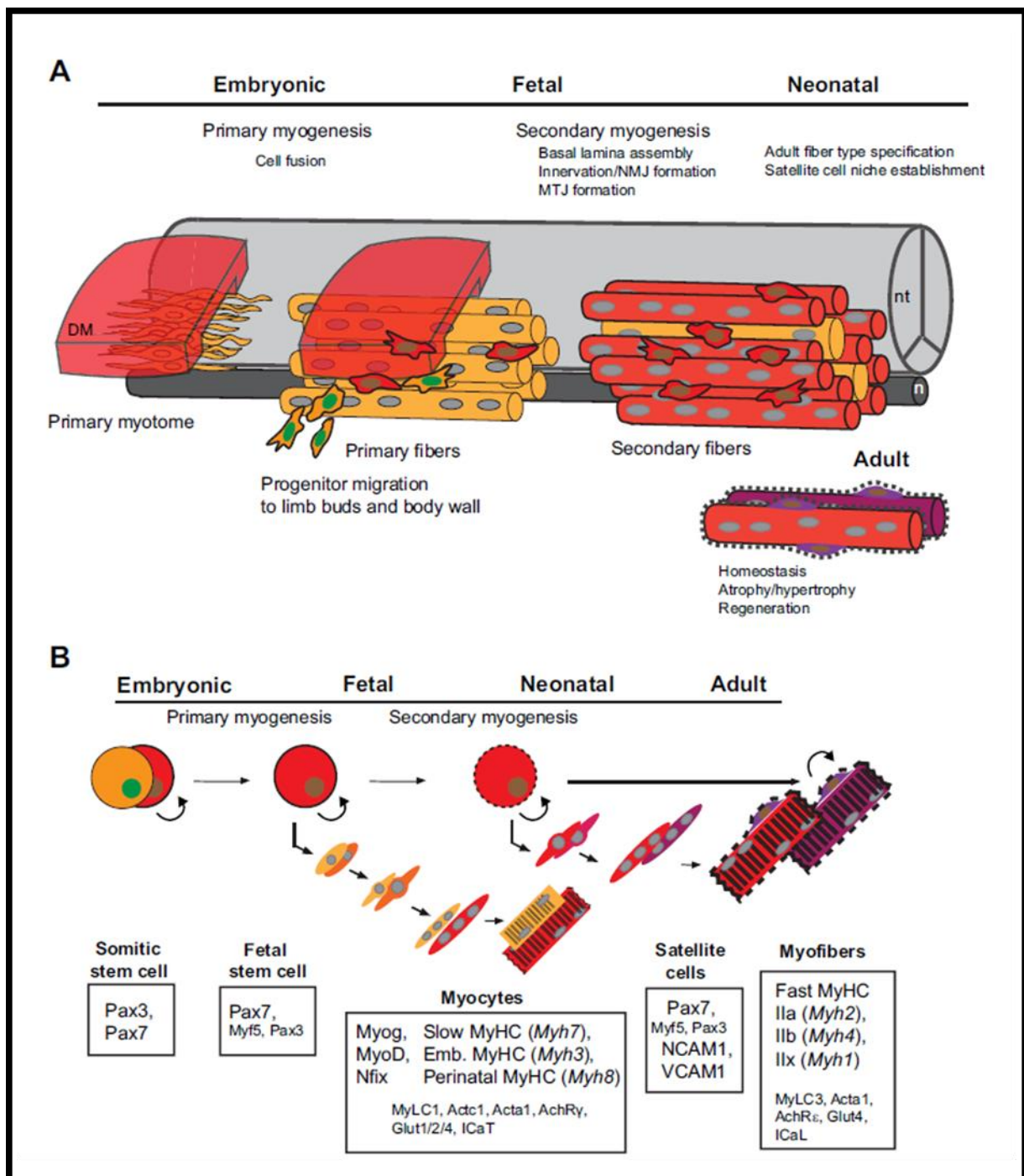


Figure 1.6: Skeletal myogenesis From the embryo to the adult taken with permission from Chal and Pourquié, (2017), reproduced through permissions from Copyright Clearance Center. (A) In the early stages, the myotome (yellow) is composed of primary myocytes which align along the anteroposterior axis of the dermomyotome and traverse each somite adjacent to the neural tube (nt) and notochord (n). During primary myogenesis, Pax3+ progenitor cells (yellow cytoplasm with green nuclei) delaminate from the dorsal section of the dermomyotome and contribute to the fusion and formation of primary myofibers (yellow). Whilst most fuse, some Pax3+ progenitors migrate to the ventral lip to occupy the body wall and limb buds, also known as the hypaxial domain. Secondary myogenesis consists of a shift from Pax3+ progenitors to a population of Pax7+ progenitors (red cytoplasm with brown nuclei) that fuse and contribute to secondary fiber formation whilst utilizing the primary myofibers as a scaffold to grow the fetal skeletal muscles. As well as contributing to growth and fusion of new myofibers, some satellite cell precursors (purple cytoplasm with brown nuclei) re-localise to underneath the basal lamina (dotted line) of the existing myofibers to provide a pool of regenerative cells for adult myogenesis. During this fetal period, innervation occurs with the formation of a neuromuscular junction and muscles are attached to bones through the formation of a tendon and myotendinous unit. In the neonate, myofibers begin to express their adult myosin heavy chain isoforms and satellite cell niches are formed ready for adult myogenesis in response to injury or exercise. (B) During muscle development, differentiation of somitic progenitors occurs toward skeletal muscles and adult satellite cells. Whilst differentiation takes place prior to fetal myogenesis, a pool of progenitor cell is maintained which in adult skeletal muscle, appear in a unique niche between the basal lamina and the sarcolemma of the muscle fiber. For each stage of muscle development, associated protein markers for mononucleated cells and multinucleated myofibers are presented and colour coded as above in relation to their lineage.

1.9 Satellite Cells & Adult Myogenesis

Despite constituting such a small fraction of the total mononucleated cells in skeletal muscle, recombination-based technologies have uncovered that satellite cells (Pax7+) are essential for muscle regeneration in adulthood Lepper et al., (2011), McCarthy et al., (2011), Murphy et al., (2011), Sambasivan et al., (2011), despite evidence of other Pax7- muscle resident stem cells being able to follow a myogenic lineage Relaix and Zammit, (2012). Various methods to induce muscle regeneration including toxins and venoms have been well established and

applied in the field such as cardiotoxin, barium chloride and notexin as well as other non-chemical models such as freezing, crushing, burning and volumetric removal of muscle. Whilst these models have great reproducibility in causing necrosis and degeneration and subsequent regeneration of skeletal muscle tissue, they are best suited for the study of pathological muscular conditions and enhancing muscle regeneration. The harshness of these models means that satellite cell behaviour and communication cannot be directly translated to the important role of satellite cells in response to mechanical loading and subsequent hypertrophy, which field is growing extensively. For example, most notably during regeneration satellite cells are known to divide through symmetric division, whereas their division during growth and homeostatic aging in the absence of regeneration occurs through asymmetric division Tierney et al., (2018), Morgan and Partridge, (2020).

As earlier described, the primary adult muscle stem cell population is resident beneath the basal lamina which surrounds the muscle fiber and is commonly identified through the expression of the paired box protein Pax7 Seale et al., (2000), Seale and Rudnicki, (2000). As well as fusing to produce new muscle fibers, during post-natal development and adulthood, these cells can fuse to growing fibers and contribute new myonuclei to the multinucleated syncytia White et al., (2010). When Pax7+ satellite cells are depleted through genetic ablation in pre-pubertal mice, muscle fibers are significantly smaller by adulthood Bachman et al., (2018) and fail to hypertrophy in response to mechanical overload by synergist ablation Egner et al., (2016), Egner et al., (2017), Murach et al., (2017), McCarthy et al., (2017). However, when genetically ablated during adulthood (>4 months), muscle can however sustain a short-term period of hypertrophy (~2 weeks) in the absence of satellite cells Fry et al., (2014a), Fry et al., (2017), Kirby et al., (2016b), Kirby et al., (2016a), McCarthy et al., (2011), although over a longer period of mechanical overload (~8 weeks), hypertrophy is attenuated Englund et al., (2020), Fry et al., (2014a), Fry et al., (2017). Some evidence suggests that myonuclear accretion is a determinant of exercise-induced remodeling and that myonuclei are added prior to the initiation of growth itself Bruusgaard et al., (2010), Goh et al., (2019) and that their addition is dependent on the amount of load applied during training and is not limited to resistance training but also endurance exercise to aid with transcriptional output. D'Hulst et al., (2020), Masschelein et al., (2020), Eftestøl et al., (2016). In terms of hypertrophy, satellite cells are only required beyond a set threshold of myofiber growth in order to govern

a larger area of cytoplasm, often referred to as the myonuclear domain Conceicao et al., (2018), Petrella et al., (2006), Petrella et al., (2008), or the maximal area in which a myonucleus can transcriptionally control. Other evidence suggests that these adaptations may be also dependent on species, age, muscle, exercise modality, and may be fiber type specific Conceicao et al., (2018), Damas et al., (2018a), Fry et al., (2014a), Fry et al., (2014b), Gundersen, (2016), Karlsen et al., (2015), Karlsen et al., (2019), Kirby et al., (2016a), Mackey et al., (2014), Moro et al., (2020), Murach et al., (2018a), Murach et al., (2018b), Snijders et al., (2014), Snijders et al., (2016), Snijders et al., (2019), Snijders et al., (2020a), Snijders et al., (2020b), Winje et al., (2018), Psilander et al., (2019), Bass et al., (2021).

Aside from the role of satellite cells in myonuclear addition to support muscle fiber hypertrophy or exercise induced remodeling, recent evidence has linked satellite cells and other resident mononucleated cells such as fibroblasts and stromal/capillary nuclei to additional supportive roles. There is mounting evidence that satellite cells support hypertrophy and muscle remodeling through crosstalk between other mononucleated cells such as fibroblasts to control extracellular matrix formation and collagen orientation/deposition during hypertrophy, at least in part by microRNA delivery which regulate transcription in resident muscle fibroblasts via extracellular vesicles early during continuous mechanical loading to support long term growth Fry et al., (2014a), Fry et al., (2017), Mackey and Kjaer, (2017a), Mackey et al., (2017), Murphy et al., (2011). These experiments have included co-culture of different cell types in-vitro as well as in-vivo transgenic experiments allowing for the tracking of crosstalk molecules. Satellite cell macrophage crosstalk has also been highlighted during adaptation to mechanical overload Mackey and Kjaer, (2017a), Mackey et al., (2017), Patsalos et al., (2017), as well as the communication between satellite cells and the vascular niche to maintain satellite cell Verma et al., (2018). The first data to illustrate satellite cell to myofiber crosstalk through extracellular vesicle delivery of microRNA's indicate that satellite cell communication is pivotal for long term hypertrophy through microRNA repression of matrix metalloproteinase 9 (Mmp9) Murach et al., (2018b). Further experiments showed that a robust long-term hypertrophic response was still possible, even when blocking myonuclear accretion through the satellite cell specific genetic deletion of Neural Wiskott-Aldrich Syndrome protein (N-WASP), an essential protein in actin polymerization and myoblast fusion Murach et al., (2020c), Yablonka-Reuveni and Lepper,

(2020). Targeting the satellite cell secreted factors that control the transcription within the myonuclei and myofiber warrant further interest in the pursuit of therapeutics to preserve or increase muscle mass and quality.

1.10 Thesis Aims & Objectives

The overarching aim of the present thesis was to build on, improve and exploit non-supraphysiological models in the rat to study the effects of loading, changes in activity and unloading on skeletal muscle. Once established, we could investigate the timecourse of changes to muscle mass, fiber cross-sectional area, mitochondrial content, myonuclear content and the changes to the transcriptome during these periods. Therefore, a series of experiments were conducted to achieve these aims:

- 1 In the first experimental chapter we aimed to improve an existing automated image analysis program to objectively quantify immunofluorescent microscopy images for muscle fiber shape, size, fiber type and myonuclear content in a timelier manner. The efficacy of our rodent models could then be appropriately assessed to establish the timecourse of adaptations in response to loading, unloading and changes in muscle activity. We identified numerous load and activity dependant changes in fibre type and size. We also identified that myonuclear accretion and loss was both load and activity dependant.
- 2 In Chapter 4, after identifying the timecourse of changes in fiber size, fiber type and myonuclear content in response to relatively short periods of loading, unloading and changes in activity (less than ~1 month), we aimed to assess whether longer intervention (~25% of a rat's lifespan) would have further effects to muscle phenotype. This was accomplished by training, detraining, and allowing severely atrophied muscle to recover for long periods to establish the likely lasting effects of our models. This pilot data provided evidence that added myonuclei are not always permanent and that their permanence may be related to the mechanism underpinning their original fusion.
- 3 Following the success of our resistance training-induced hypertrophy timecourse experiments, we aimed to characterise the acute transcriptional response through NG-RNA-Sequencing and bioinformatic analyses to a single daily resistance training session in exercise naive rats, and rats that had undergone training for 2, 10, 20 or 30 days. This would allow us to determine different gene regulatory networks that are always responsive to resistance exercise and those that are involved in the early and adapted

response to exercise. Additionally, we made a critical comparison between our carefully controlled timecourse and previously published transcriptomic arrays/NG-RNA-Seq datasets from rodent supra-physiological models of resistance exercise and meta-analyses from human resistance exercise to identify areas of correspondence and difference.

- 4 Finally, as our RNA-sequencing method relied on bulk extraction of mRNAs from skeletal muscle tissue the resultant signals likely contain gene signatures and patterns belonging to cell types other than muscle fibers such as endothelial cells, satellite cells and macrophage populations. While cell deconvolution computational analysis aims to estimate the proportions of different RNA signals to specific cell types, the efficacy of such techniques is not established in adult skeletal muscle tissue. Therefore, we aimed to independently validate a recently published marker, that was claimed to specifically label myonuclei in different species, Pericentriolar Material-1 (PCM1). If we could confirm that this was the case, future work in our lab could extract pre-mRNA and DNA from the 'myonuclei' specifically to determine myogenic and non-myogenic changes with resistance training. This was accomplished by assessing PCM1 immunolabelling on single muscle fibers and histological samples from exercised rat, WT and LMNA Δ K32 mutated mice before and after functional overload, and human biopsies before and after an extensive damaging protocol. Our analysis showed that PCM1 was not specific to myonuclei and was also found in nearby satellite cells, interstitial cells, and macrophages.

Chapter 2: Materials & Methods

Note: All the methods used in experimental chapters are collected here for reference. However, relevant methods are also included in each results chapter.

Cell Culture

2.1 *In-vitro* Cell Culture

The study of immature muscles through myotube formation, growth, repair and loss is an old field, with the first work cited in the 1830s to 1860s, long before the discovery of adult muscle stem cells Mauro, (1961). Briefly, as early as 1839 Schwann, (1839), the concept of muscle cell fusion was proposed and the idea that muscle could regenerate itself. This knowledge continued to expand, with scientists providing the first evidence of *in vitro* myotube formation early in the 20th century Lewis and Lewis, (1917). The concept that mature myonuclei found within muscle fibers are incapable of replication was first reported in the late 1950s Lash et al., (1957), suggesting that skeletal muscle fibres, are terminally differentiated and are also incapable of replication Scharner and Zammit, (2011). For this thesis, C2C12 myoblasts originally obtained through serial passage of myoblasts cultured from the thigh muscle of a 2-month-old C3H mice after a crush injury Yaffe and Saxel, (1977) were used for protein localisation experiments.

2.2 C2C12 & Human Primary Myoblast/Myotube Cell Culture

Both rodent and human primary myoblasts were studied *in-vitro* for the change in localisation of PCM1 in mononucleated cells and as they terminally differentiate and fuse into multinucleated myotubes.

2.3 Routine Culture of C2C12 Myoblast and Myotubes in Monolayer

C2C12 murine skeletal myoblasts Yaffe and Saxel, (1977), Blau et al., (1985), purchased from ATCC[®], (Virginia, United States), were incubated on gelatin (0.2%) coated plastic cover slips placed into 12 well-plates in a humidified 5% CO₂ atmosphere at 37°C in 1ml growth medium (GM) containing DMEM, 10 % foetal bovine serum, 10% newborn calf serum, 1% l-glutamine (2mM final) and 1% penicillin–streptomycin solution. Upon reaching confluence, cells were either fixed with 0.5% PBS/BSA containing 2% paraformaldehyde or, to produce

multinucleated myotubes, myoblasts were differentiated by washing with PBS and transferring to low serum media (LSM; DMEM with 2% horse serum, 1% l-glutamine and 1% penicillin–streptomycin). C2C12 cells spontaneously differentiate under these conditions without the addition of additional growth factors Blau et al., (1985). Media was topped up every 2 days. Following 2 and 7 days in LSM, cultures were washed and fixed with 0.5% PBS/BSA containing 2% paraformaldehyde for 1 hour. The fixative solution was then removed and washed with immunobuffer (IB): PBS (10mM phosphate pH 7.4, 150mM NaCl), 50mM glycine (Merck 1.02401_1000), 0.25% BSA, 0.03% saponin (Sigma 100g S-7900), 0.05% sodium azide.

2.4 Routine Culture of Human Skeletal Muscle Derived Myoblasts and Myotubes in Monolayer

Human muscle derived cells from a healthy, young male were donated by the Sharples lab, (originally obtained under ethical approval granted by NHS West Midlands Black Country, UK, Research Ethics Committee (NREC approval no. 16/WM/0103) and cultured in monolayer onto gelatin (0.2%) coated plastic six-well plates in 2ml of human GM containing Ham's F10 nutrient mix supplemented with 10% hi-NCS, 10% hi-FBS, 100U mL⁻¹ penicillin, 100µg mL⁻¹ streptomycin, 2.5µg mL⁻¹ amphotericin B and 5mM L-glutamine until confluent. GM was then removed, and cells washed 3 times in PBS before transference to 2ml of DM containing Ham's F10 nutrient mix supplemented with 2% hiFBS, 100 U mL⁻¹ penicillin, 100µg mL⁻¹ streptomycin, 2.5µg mL⁻¹ amphotericin B and 5 mM L-glutamine). Following 3 days and 7 days in LSM, myoblast/multinucleated myofibres were washed and fixed as above.

2.5 Immunofluorescent labelling of cells

Following fixation as described above, immunobuffer (IB) was added to 12 well plates (C2C12s) or 6 well plates (Human). Primary antibodies were diluted as per table 2.1 in IB + plus 0.2% Triton-X100 (Sigma-Aldrich) overnight and then washed 3 x 10 minutes in IB. Secondary antibodies were diluted as per Table 2.1 in IB for 2 hours, followed by 3 x 10 minutes in IB. Following incubation with primary and secondary antibodies to immunolabel C2C12 cells, the plastic coverslips were removed, blotted dry and placed on glass slides in mounting medium (Vectashield® Antifade Mounting Medium with DAPI (1.5µg/ml),

Burlingame, CA, USA)) before cell imaging. Human cells were imaged directly in the 6 well plate in which they were cultured following the addition of DAPI.

Table 2.1: Antibodies & Fluorescent Conjugates for immunofluorescent labelling of cells, single muscle fibers and transverse cross-sections.

Primary Ab	Secondary Ab	Reference
Pax7 DSHB Supernatant 1:100	Goat Anti-Mouse IgG H&L (Alexa Fluor® 488 (ab150113) or (AlexaFluor 594) preadsorbed (ab150120)	Mackey and Kjaer, (2017a)
Anti-PCM1 HPA023370 Sigma Aldrich (Merck) 1:1000	Goat Anti-Rabbit IgG H&L (Alexa Fluor® 594) preadsorbed (ab150088) or (Alexa Fluor® 488 (ab150077) or Alexa Fluor® donkey anti-rabbit 568, (ab175693)	Winje et al., (2018)
MANDYS8(8H11) DSHB Supernatant 1:100 Morris, G.E. (DSHB Hybridoma Product)	Goat anti-mouse IgG H&L (AlexaFluor® 594) preadsorbed ab150120	Mackey and Kjaer, (2017a)
Anti-Collagen IV AB769 Merck Millipore, Darmstadt, Germany. 1:500	Alexa Fluor® donkey anti-goat 680, (A-21084)	Mackey and Kjaer, (2017a)
Anti-CD68 (MO718) Dako, Denmark. 1:500	Alexa Fluor® donkey anti-mouse 488, (ab150109)	Mackey and Kjaer, (2017a)
Phalloidin-FITC (Sigma, P5282) or Alexa Fluor® 568 Phalloidin (ThermoFisher Scientific, A12380) 1:500		/
Dystrophin Polyclonal Antibody. Catalog #PA5-32388. (Thermofisher Scientific)	Goat anti-Rabbit IgG (H+L) Cross-Adsorbed Secondary Antibody, Alexa Fluor 633.	Winje et al., (2018)
BA-D5 (anti type I myosin) DSHB Supernatant. Schiaffino, S. (DSHB Hybridoma Product)	Goat anti-Mouse IgG2b Cross-Adsorbed Secondary Antibody, Alexa Fluor 488.	See MyoVision chapter
SC-71 (anti type IIA myosin) DSHB Supernatant. Schiaffino, S. (DSHB Hybridoma Product)	Goat anti-Mouse IgG1 Cross-Adsorbed Secondary Antibody.	See MyoVision chapter
6H1 (anti type IIX myosin) DSHB Supernatant. Lucas, C. (DSHB Hybridoma Product)	Goat anti-Mouse IgM Cross-Adsorbed Secondary Antibody.	See MyoVision chapter
BF-F3 (anti type IIB myosin) DSHB Supernatant. Schiaffino, S. (DSHB Hybridoma Product)	Goat anti-Mouse IgM Cross-Adsorbed Secondary Antibody.	See MyoVision chapter

**All antibodies used in this thesis have well established protocols and confirmed antigen specificity across mouse, rats, and humans. References are provided above for protocols.*

2.6 Fluorescent microscopy of cells

Myoblasts/myotubes were imaged under 20x magnification using a widefield fluorescent microscope (Leica DMB 6000, Wetzlar, Germany) to determine PCM1 presence and localisation. An A4 filter was used to image DAPI (EX: 340-380, EM: 450-490), L5 filter to image FITC and Alexa Fluor® 488 (EX: 460-500, EM: 512-542) and an RHO filter to image Alexa Fluor® 568 and 594 (EX: 541-551, EM: 565-605). Images were taken with a monochrome DFC365 FX camera (Leica, Wetzlar, Germany) and fluorescent channels overlayed to determine PCM1 and localisation.

In-vivo Electrical Stimulation Experiments

2.7 Electrical Stimulation of The Tibialis Anterior Muscle Via Implantable Pulse Generators to Produce Loaded & Unloaded Contractions in Rodents

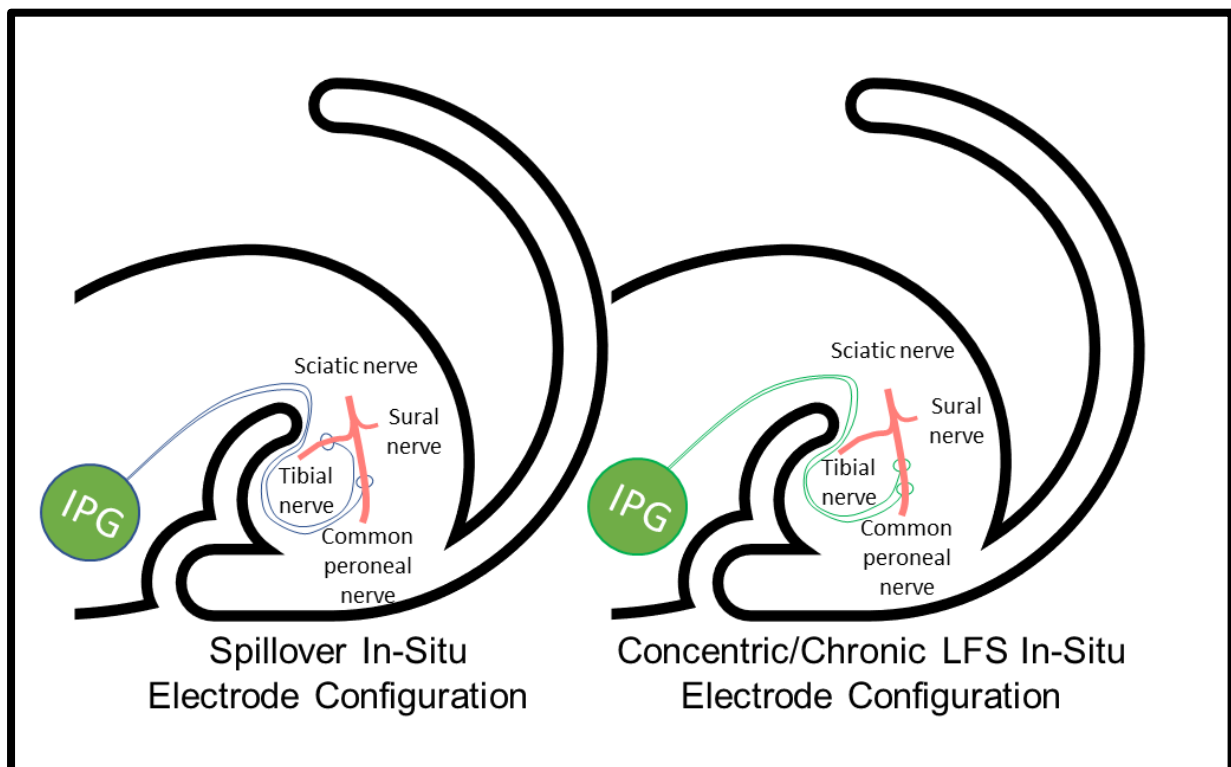


Figure 2.1 Schematic representation IPG and electrode placements. For electrical stimulation experiments, an implantable pulse generator (IPG) was placed within the abdomen with electrodes leading subcutaneously to the left hindlimb with two possible electrode

placements. Either with the anode placed under the tibial nerve with the cathode under the common peroneal nerve (CPN) to produce Spillover (loaded) resistance training or by placing both electrodes under the CPN to elicit concentric (unloaded) resistance exercise or continuous low frequency stimulation (CLFS) mimicking endurance training.

2.8 Ethics & Animals Used

Animal experiments were conducted under the provisions of the Animals (Scientific Procedures) Act 1986 and approved by the British Home Office (PPL 40/3280). Male Wistar rats were group-housed with 2-3 per cage maintaining an alternating 12 h light 12 h dark cycle. Welfare of experimental rats was monitored daily by dedicated animal welfare staff and by the research team.

Table 2.2 Rat Usage

Rat No.	Animal Weight (g)	Treatment	Control TA Weight (mg)	Experimental TA Weight (mg)	% Change in TA Weight
1673	404	14 Days Atrophy	740	372	-50
1674	373		694	368	-47
1675	445		686	347	-49
1676	394		729	364	-50
1677	434		819	365	-55
1678	393		772	366	-53
279	360		687	549	-20
280	381		743	697	-6
281	362		805	681	-15
1680	409		7 Days Atrophy	737	513
1681	392	772		575	-26
1688	411	810		529	-35
1689	422	847		547	-35
1742	438	754		580	-23
1744	428	889		664	-28
276	344	744		731	-2
277	355	779		748	-4
278	339	689		655	-5
161	301	574		444	-23
168	335	619	412	-33	
1745	460	3 Days Atrophy	870	805	-8
1746	485		888	830	-7
1747	401		781	723	-7

1750	449		792	701	-12
1751	457		836	798	-5
1752	460		851	813	-5
1764	412		748	476	-36
1768	421	14 Days Atrophy+ 7 Days Recovery	771	634	-18
1769	384		808	639	-21
1770	392		802	645	-20
1772	419		759	481	-37
1773	413		767	648	-16
285	502	14 Days Atrophy+ 120 Days Recovery	990	1002	1
286	456		811	841	4
287	527		927	925	0
1758	413	20 Hz Stimulation 7 Days	712	589	-17
1759	425		658	578	-12
1760	416		771	652	-15
1761	387		711	604	-15
1762	367		704	679	-4
1763	391		664	582	-12
1721	291	TTX Sham 7 Days	857	861	1
1722	473		946	956	1
1723	458		887	850	-4
1724	477		875	879	1
1725	466		890	919	3
1753	548		902	897	-1
188	540	2 Days 'Spillover'	839	859	2
189	523		992	1024	3
193	382		645	681	6
229	519		846	863	2
190	394		657	726	11
191	370		654	714	9
192	390		667	723	8
257	460		789	800	1
258	544		885	916	3
259	479		870	965	11
145	400	10 Days 'Spillover'	752	915	22
146	340		622	654	5
147	397		740	898	21
148	400		791	901	14
G18	411		994	1077	8
215	381		809	906	12
216	382		686	815	19
217	421		849	941	11
218	356		685	756	10
260	509		935	1047	12
261	493		949	1122	18

262	489		988	1073	9
272	512		797	904	13
149	466	20 Days 'Spillover'	885	1005	19
150	442		844	978	16
151	405		740	886	20
152	366		685	847	24
221	416		847	738	-13
222	442		959	1103	15
223	400		793	876	11
224	394		847	960	13
263	539		957	1089	14
264	563		901	1002	11
265	677		1103	1317	19
157	503		944	1136	20
158	425		879	965	10
159	605	Taken for Micro-CT			
160	492	990	1110	12	
153	494	1010	1187	18	
154	432	888	955	8	
155	598	1042	1262	21	
156	424	775	979	26	
226	487	920	1043	13	
227	448	827	954	15	
228	421	842	972	15	
268	553	973	1243	28	
267	630	1000	1161	16	
275	632	1084	1297	20	
269	601	Continuous 120 Days 'Spillover'	935	986	5
270	600		1123	1299	16
271	643	30 Days 'Spillover' with 120 Days Detraining	1043	1131	8
273	777		1039	1152	11
274	618		963	1117	16
169	337	Sham Surgery with 4 Day Recovery	581	546	-6
170	323		593	554	-7
171	361		688	648	-6
172	372		608	571	-6
219	456	Sham Surgery with 3- weeks Recovery	961	933	-3
220	396		776	721	-7
213	373		695	672	-3
214	352		640	659	3

2.9 Miniature Implantable Stimulators for Rats

For loaded and unloaded contraction experiments, radiofrequency controlled IPGs MiniVStim 12B, (Competence Team for Implanted Devices, Center for Medical Physics and Biomedical Engineering, Medical University Vienna, Austria) were used which could be switched on, off, and sessions programmed via a bluetooth tablet. The stimulator is able to deliver monophasic (charge balanced), rectangular waveforms (Max. stimulation current: 2mA, Max. Output Voltage: 3V, Max. pulse width: 1ms, Volume: 1.5cm (diameter) x 0.7; 1.2cm³). Stimulators were encapsulated in a coating of biocompatible silicone rubber (3140 RTV Coating, Non-Corrosive Flowable Silicone Rubber, Dow Corning®, Michigan USA) with Dacron™ mesh extending from the silicone rubber to facilitate suturing in-vivo. Electrodes (Cooner Sales Company, Chatsworth, California, U.S.A.), were PVC-insulated and made from multi-stranded stainless steel. The ends were uninsulated and contained loops which could be sutured to the underlying muscle close to the nerve of interest.

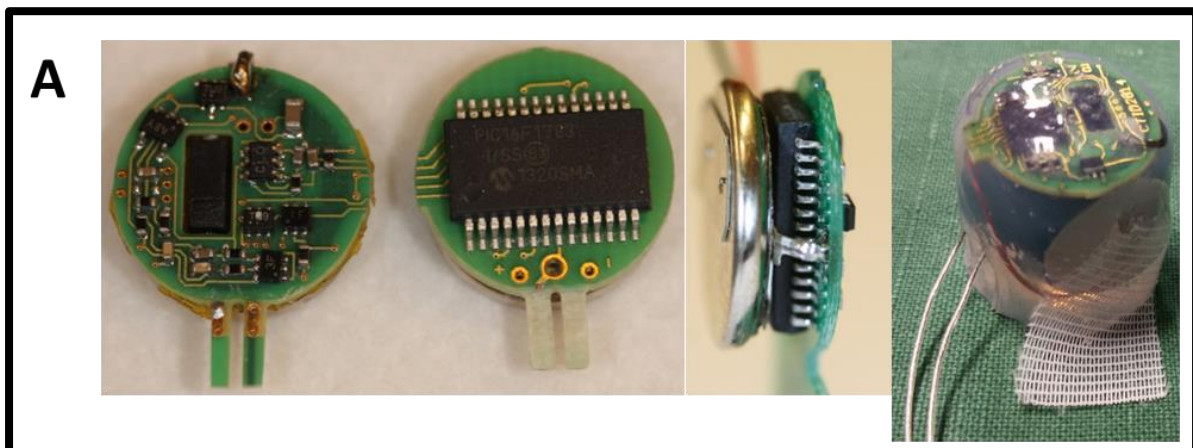


Figure 2.2: Left to Right. Printed circuit board (front/back). Printed circuit boards soldered to cell battery. Printed circuit board and battery are encapsulated in biocompatible silicone with electrodes protruding. Polyester mesh extends from inside the silicone allowing for suturing in-vivo to keep the implant in place in the abdominal cavity.

2.10 Implant Procedure

Animals were anaesthetised during implant procedures by inhalation of a gaseous mixture of isoflurane in oxygen at approximately 3% for induction and 1-2% for maintenance. Once anaesthetised, a subcutaneous injection of Enrofloxacin (5mg/kg⁻¹ body mass (Baytril®) and

an intramuscular injection of Buprenorphine ($0.05\text{mg}/\text{kg}^{-1}$ body mass) (Temgesic, Indivior, Slough, UK) into the right quadriceps was administered with strict asepsis maintained throughout the procedure. Silicone encapsulated radio frequency controlled implanted pulse generators (IPGs) (MiniVStim 12B, Competence Team for Implanted Devices, Center for Medical Physics and Biomedical Engineering, Medical University Vienna, Austria) were used to deliver impulses. The devices were implanted into the abdominal cavity accessed by a lateral incision through the skin and peritoneum, between the rib cage and pelvis on the left side of the animal. A polyester mesh attached to the IPG was incorporated into the suture line closing the peritoneum, securing the device against the abdominal wall. Two PVC-insulated stainless-steel electrode leads (Cooner Sales Company, Chatsworth, California, U.S.A.) with terminal conductive loops, were fed through the peritoneal incision and tunnelled under the skin to the lateral side of the upper left hind-limb. A second incision was made through the skin and biceps femoris muscle to give access to the CPN under which the cathode was placed (to stimulate the dorsiflexors).

2.11 Electrode Configuration

The anode was either placed alongside the cathode to stimulate the CPN alone and thus to produce unresisted (concentric) contractions or placed in the muscular tissue deep to the tibial nerve about 5mm distal to its bifurcation from the sciatic nerve to allow Spillover stimulation Schmoll et al., (2018), to produce additional partial activation of the plantarflexors to resist the contraction of the dorsiflexors. Electrodes were passed underneath the nerves of interest using a 21-gauge needle and sutured in close proximity without being in physical contact to the nerve. All incisions were closed in layers and 3-7 days were allowed for recovery from surgery before the start of the training protocol.

2.12 Stimulation Protocols

As previously reported (Schmoll et al., 2018), SpillOver stimulation consisted of one daily training session which consisted of a pattern to accommodate the animal ($F = 4\text{Hz}$, $\text{PhW} = 258\ \mu\text{s}$, $I = 1\ \text{mA}$) for 10 seconds. This was followed by 5 sets of strong tetanic contractions, with 10 contractions per set of 2 s stimulation at 100Hz followed by 2 s rest, with a further 2.5 minutes between sets. The stimulation was conducted in the left hind-limb only, providing

the right hind-limb as an unstimulated contralateral control. Anesthesia administration was not necessary during the period of training as the stimulation was tolerated very well by all animals (regular observations during daily training across the time course revealed no adverse effects in behaviour). This was also performed using the 'concentric' electrode placements to produce unresisted contractions. This stimulation pattern was performed for periods between 2 and 120 days without adverse effects.

Additionally, chronic low-frequency stimulation (CLFS) was performed using the 'concentric' electrode placements. This model has been well characterised on the dorsiflexors in previous work from our lab Jarvis et al., (1996a), Fisher et al., (2017), Jarvis and Salmons, (1991), Jarvis, (1993), Lexell et al., (1993). Briefly, ankle dorsiflexors were continuously stimulated (24 h per day), at 20Hz for 7 days. This pattern has previously been shown to induce a transformation from the control fast phenotype towards a slower phenotype in the TA.

2.13 Deuterium delivery for dynamic proteomic profiling

Whilst the results from dynamic proteomic profiling are not reported or discussed in this thesis, most of our experiments involved the incorporation of stable isotope tracers in order to measure the abundance and rates of synthesis and degradation of individual proteins for other collaborators. Briefly, when reported in the experimental chapters deuterium oxide ($2\text{H}_2\text{O}$; Sigma-Aldrich, St. Louis, MO) administration was initiated by an intraperitoneal loading injection of $10 \mu\text{l/g}$ 99% $2\text{H}_2\text{O}$ -saline, and then, maintained by administration of 5% (v/v) $2\text{H}_2\text{O}$ in the drinking water available to the rats, as described previously Hesketh et al., (2016), Hesketh et al., (2020b).

2.14 Terminal Procedure and Tissue Preparation for Regional Investigations

Upon completion of the animals training period, animals were humanely killed using rising concentrations of carbon dioxide, confirmed by cervical dislocation. The resting length of the TA and EDL were measured in-situ from insertion to origin using digital calipers. TA, EDL, PLN, SOL and GAST muscles from both lower limbs were harvested, excess connective tissue removed and immediately weighed. The TA and EDL were then pinned to cork cutting boards at resting length and were cut transversely using a specially made cutter which comprised 13

razor blades separated by 2mm thick plastic perspex pieces which were held together tightly with two screws that ran through pre-drilled holes in the perspex. This produced 13-15 2mm thick muscle sections (Figure 2.3). The individual sections were then individually blotted dry, individually weighed, and then imaged proximally to distally next to their associated contralateral control section, alongside a graticule using a dual 12MP wide-angle camera (Apple Inc., California, United States).

Muscle slices designated for histology were frozen and fixed onto cork discs in OCT (Tissue-Tek® O.C.T. Compound, Sakura® Finetek, USA), using isopentane, pre-cooled in liquid nitrogen. Designated slices for RNA/Protein samples were placed into Eppendorf tubes and frozen straight in liquid nitrogen and later transferred to a -80°C freezer.

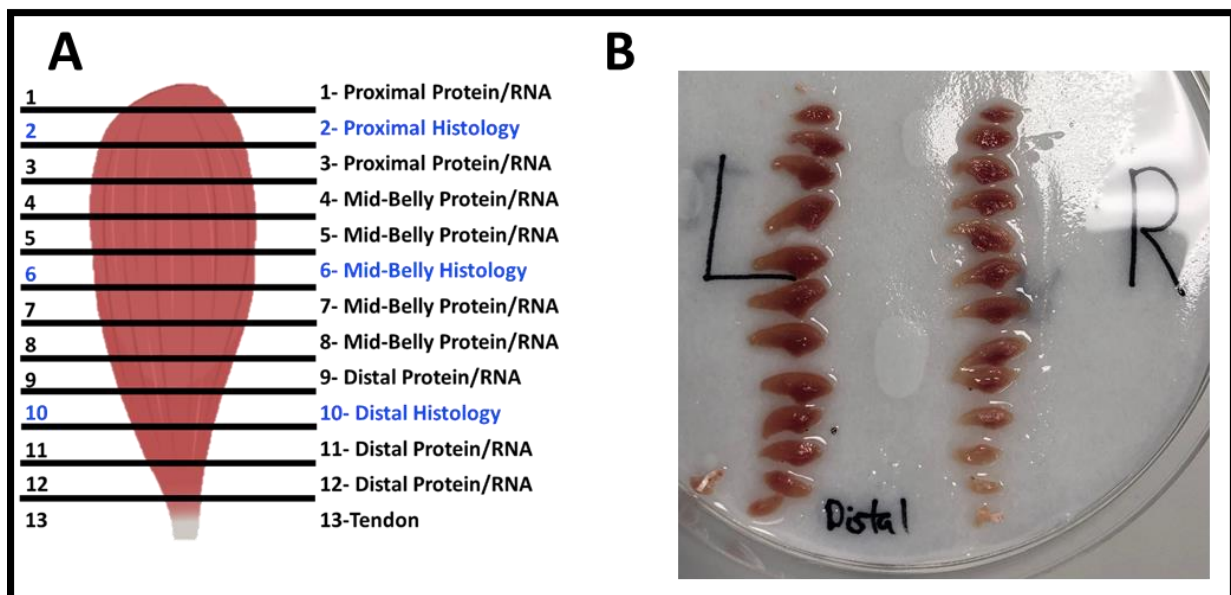


Figure 2.3 (A): Preparation of muscle slices following cutting with designation to biochemical/histological analysis and muscle region. Figure 2. (B): Example of muscle slices post cutting. Stimulated vs unstimulated muscles (20 Days) laid out from proximal (top) to distal (bottom). Note larger slice cross-sectional area vs contralateral control and increase in redness (marker of oxidative capacity). (For all conditions, see appendix 1).

***In-vivo* Nerve Block Experiments**

2.15 Background

Classically, cessation of nerve activity is achieved by complete or partial nerve transection or by hind-limb suspension to reduce motor activity. We employ tetrodotoxin (TTX), a potent neurotoxin that blocks voltage-gated sodium channels and therefore action potentials. Our group has previously demonstrated that its application to the common peroneal nerve results in atrophy without damage to the nerve and muscle Fisher, (2010), Fisher, (2012), Fisher et al., (2017). Its name derives from *Tetraodontiformes*, an order that includes pufferfish, porcupinefish, ocean sunfish, and triggerfish.

2.16 Nerve Blockade of The Common Peroneal Nerve (CPN) Using A Nerve Cuff to Produce Atrophy in The Tibialis Anterior Muscle in Rats

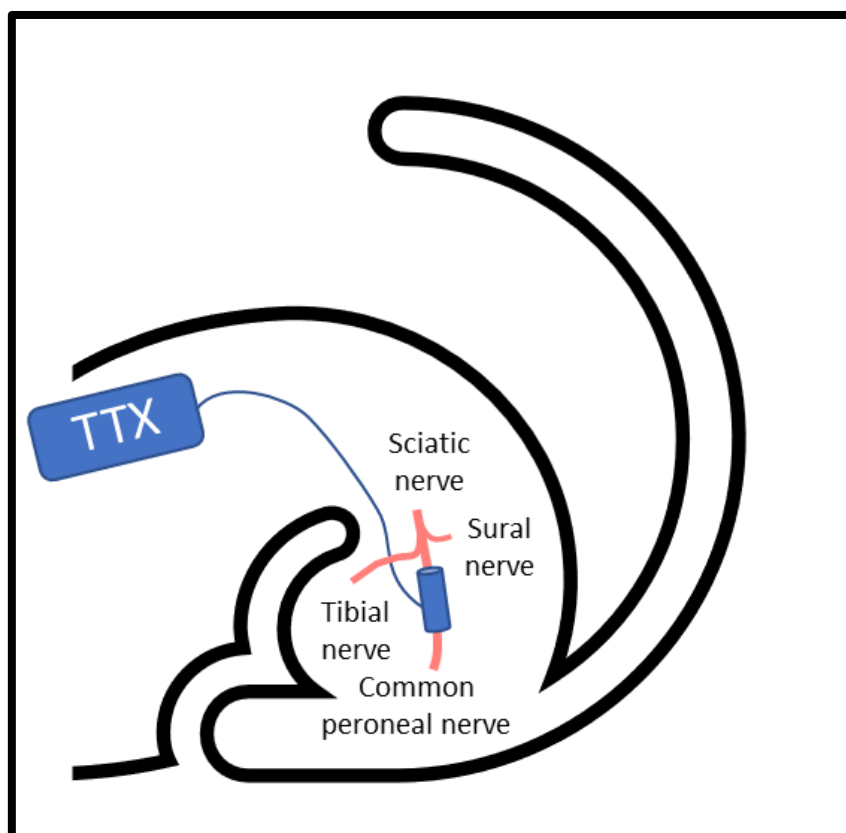


Figure 2.4: An overview of the in-situ placement of the osmotic pump loaded with a pre-determined volume of tetrodotoxin (TTX), placed in the scapula region with silicone tubing leading to the left hind-limb and the silicone cuff that encircled the common peroneal nerve (CPN) to selectively block the ankle dorsiflexors, while maintaining normal plantarflexion.

2.17 Implant Contents & Implant Procedure

Animals were anaesthetised as previously described for the implantable stimulator surgeries. A miniosmotic pump (Mini Osmotic Pump 2002; Alzet, Cupertino, CA, USA) implanted subcutaneously in the scapular region. Silicone tubing was tunnelled under the skin to the site of the CPN. A second incision was made laterally through the skin, just proximal to the knee joint and bicep femoris muscle (posterior compartment of the thigh) in order to give access to the CPN responsible for action of the dorsiflexors. A silicone cuff extending from the silicone tubing was placed around the nerve. All incisions were closed in layers. The miniosmotic pump (Mini Osmotic Pump 2002; Alzet, Cupertino, CA, USA) was placed between the scapulae and delivered TTX, a sodium channel blocker that prevents generation and propagation of action potentials at the CPN of the left hind-limb. The osmotic pump successfully delivered 0.5µl/h TTX (350mg/ml in sterile 0.9% saline), and thus by continuously blocked ankle dorsiflexion, whilst maintaining normal voluntary plantarflexion via the tibial nerve. Disuse of the dorsiflexors by this means produces progressive atrophy Fisher et al., (2017). The welfare and mobility of the rats was checked daily by animal welfare staff. There was little disturbance to mobility, but sometimes 'foot drop' was observed, a gait abnormality characterised by dropping of the forefoot due to the inhibition of dorsiflexion.

2.18 Nerve Block Protocol

Osmotic pumps were appropriately loaded to silence the common peroneal nerve for set periods of 3, 7 and 14 days to induce atrophy by means of disuse. Further experimental groups underwent 14 days of nerve silencing followed by subsequent recovery periods of 7, and 120 days of recovery. The primary researcher checked for return of motor activity through means of observation.

2.19 Terminal Procedure and Tissue Preparation

As previously described, upon completion of the animals' atrophy or atrophy with recovery period, animals were humanely killed using rising concentrations of carbon dioxide, confirmed by cervical dislocation. TA, EDL, PLN, SOL and GAST muscles from both lower limbs were harvested, excess connective tissue removed and immediately weighed. A section was then removed from the mid-belly for histology and frozen and fixed onto cork discs in OCT (Tissue-Tek® O.C.T. Compound, Sakura® Finetek, USA), using isopentane, pre-cooled in liquid nitrogen. The remainder of the muscle was placed into an Eppendorf and frozen straight in liquid nitrogen and later transferred to a -80°C.

***In-vivo* Functional Overload Experiments**

2.20 Mechanical Overload of The Plantaris Via Synergist Ablation in Wild-Type and LMNA+/ Δ K32 Mice

Mechanical overload by means of synergist ablation was performed on the plantaris of both hind-limbs by tenotomy of the soleus and gastrocnemius muscles in the Coirault Lab at INSERM. More details on mechanical overload induced hypertrophy can be found in Chapter 1.6. We would like to thank Dr. Daniel Owens and his supervisor Dr. Catherine Coirault for the use of these tissues for investigating PCM1 localisation in a model of hypertrophy in healthy and mice with hypertrophic/regenerative defects Owens et al., (2021).

2.21 Background to Lamin A Mutations & Surgical Procedure

All animal experiments were performed in accordance with the European Guidelines for the Care and Use of Laboratory Animals and were approved by the institutional ethics committee (APAFIS#2627-2015110616046978, 9 May 2016 at INSERM). Lmna+/ Δ K32 and WT C57Bl/6_129/6J littermates were 3 months old at the beginning of the experiments. All mice used were male. Lmna+/ Δ K32 mice in a C57Bl/6_129/SvJ genetic background were generated by homologous recombination as described previously Bertrand et al., (2014). The heterozygous Lmna+/ Δ K32 mouse was chosen over homozygous mice as it is the same

mutation seen in LMNA-CMD patients. Data from these tissues has been previously reported Owens et al., (2020b).

Mice underwent either a sham operation or functional overload (FO) of the plantaris muscles, induced through the tenotomy of soleus and gastrocnemius muscles, in both hind limbs Serrano et al., (2008). The cut distal tendons were folded proximally and sutured to the proximal musculotendinous region leaving the plantaris intact with strict asepsis maintained throughout. Animals recovered within 1-2 hours following the end of the procedure and were then monitored daily following surgery for signs of discomfort and infection. For pain management, Buprenorphine was administered prior to and following surgery (Vetergesic© 0.3 mg/ml, SC: 0.10 mg/kg).

Table 2.3 Mouse Usage (Experiments performed by Dr. Daniel Owens at INSERM Owens et al., (2021))

Mice from Paris (INSERM)		
455	WT Control 1 Week	Histology
536		Histology
534		Histology
535		Histology
599		Single Fibre
603		Single Fibre
594		Single Fibre
523		WT Control 4 Weeks
524	Histology	
461	WT Overload 1 Week	Histology
462		Histology
450		Histology
448		Histology
598		Single Fibre
602		Single Fibre
591		Single Fibre
542		WT Overload 4 Week
546	Histology	
515	Histology	
459	Heterozygous LMNA+/ Δ K32 Control 1 Week	Histology
520		Histology
533		Histology
458		Histology
625		Single Fibre
627		Single Fibre

633		Single Fibre	
634		Single Fibre	
528	Heterozygous LMNA+/ Δ K32 Control 4 Week	Histology	
526		Histology	
521		Histology	
525		Histology	
640		Single Fibre	
642	Heterozygous LMNA+/ Δ K32 Overload 1 Week	Single Fibre	
650		Single Fibre	
655		Single Fibre	
25		Single Fibre	
26		Single Fibre	
453		Histology	
454		Histology	
457		Histology	
456		Histology	
514		Heterozygous LMNA+/ Δ K32 Overload 4 Week	Histology
543			Histology
541	Histology		
545	Histology		
547	Histology		
540	Histology		

2.22 Procedure and Tissue Preparation

After 1 week or 4 weeks of functional overload by synergist ablation or sham surgery, animals were humanely killed by cervical dislocation, plantaris muscles were dissected, and visible fat and connective tissue removed. Isolated plantaris muscles were snap frozen in isopentane pre-cooled by liquid nitrogen for histological analysis or fixed in 4% paraformaldehyde at room temperature for one hour for analysis of single muscle fibres. After fixation, plantaris muscles were placed on ice and sucrose solution was added in increasing molarity from 0.5mM, 1mM, 1.5mM and then frozen at -80°C in 2mM sucrose. When ready to isolate, sucrose frozen fibres were placed on ice and sequentially changed into decreasing molarity sucrose into immunobuffer (IB): PBS (10mM phosphate pH 7.4, 150mM NaCl), 50mM glycine (Merk 1.02401_1000), 0.25% BSA, 0.03% saponin (Sigma 100g S-7900), 0.05% sodium azide.

Single Fiber Preparation and Analysis

2.23 Background to human biopsy sample access and eccentric damaging protocol induced by electrical stimulation

We would like to thank Dr. Abigail Mackey from the University of Copenhagen for use of biopsy material from previous experiments in her lab Mackey and Kjaer, (2017b) during an exchange visit by Mark Viggars to the Institute of Sports Medicine, University of Copenhagen.

The Regional Scientific Ethical Committees of Copenhagen in Denmark approved this study (Ref: HD-2008-074) and all procedures conformed to the Declaration of Helsinki. Young, healthy males ($n=2$), age; 20.5 ± 0.5 years, height; 1.78 ± 0.02 cm, body mass; 76.5 ± 1.5 kg) gave informed consent on inclusion and underwent a muscle injury protocol which consisted of 200 forced lengthening contractions with the use of electrical stimulation to activate the target muscle during each contraction, as described in detail Mackey et al., (2016). The protocol was performed on the vastus lateralis muscles of one leg, leaving the other as an internal control. The muscle biopsies analysed in this study are a subset of samples from previous studies selected from participants in whom extensive muscle damage was observed Mackey et al., (2016), Mackey and Kjaer, (2017a).

Muscle biopsies were collected from the vastus lateralis muscle immediately before the damaging exercise from both legs and 2, 7 and 30 days from the damaged leg thereafter. Biopsies were taken under local anaesthetic (1% lidocaine: Amgros I/S, Copenhagen, Denmark), using the percutaneous needle biopsy technique of Bergström Bergström, (1975), with 5–6-mm-diameter biopsy needles and manual suction.

On extraction, biopsies were prepared for both histology and single fibre analysis. Parts of the biopsy suited for histology were aligned in parallel, embedded in Tissue-Tek (Sakura Finetek Europe, Zoeterwoude, The Netherlands), frozen in isopentane pre-cooled by liquid nitrogen and stored at -80°C until analysis. If the biopsy contained long intact bundles of fibres, those were prepared for single fibre analysis Bergström, (1975). Fibre bundles were pinned to maintain fibre length and covered in Krebs-Henseleit bicarbonate buffer (containing 0.1% procaine) for 2 minutes, followed by Zamboni fixative (2% formaldehyde, 0.15% picric acid) for 30 min. Fibres were then transferred into fresh Zamboni fixative and placed in the fridge

for approximately 4 hours. Zamboni fixative was then replaced with 50% glycerol in PBS and moved to -20°C on the following day until extraction, staining and observation.

2.24 Single Muscle Fibre Analysis

Single muscle fiber preparation, immunolabelling and analysis was performed on samples from rat, mouse and human biopsies. The following sections introduce the method learnt whilst in the Mackey lab and then applied to all tissue types.

2.25 Preparation and Extraction

Rat and human biopsies were placed into a petri dish containing IB prior to single fibre extraction. Single fibres were mechanically teased from fibre bundles from all species with the aid of a stereomicroscope. For mouse muscles frozen in ascending grades of sucrose, when ready to isolate, sucrose frozen fibres were placed on ice and sequentially changed into decreasing molarity sucrose into IB. Due to the reduced size and sensitivity to handling of WT and LMNA^{+/ Δ K32} mouse fibres both with and without overload, they were instead extracted in small bundles of fibres to avoid breaking.

2.26 Immunostaining

Primary antibodies were diluted as per table 2.1 in IB + plus 0.2% Triton-X100 (Sigma-Aldrich) overnight and then washed 3 x 10 minutes in IB. Secondary antibodies were diluted as per table 2.1 in IB for 2 hours, followed by 3 x 10 minutes in IB. Following incubation with primary and secondary antibodies, single fibres were mounted in DAPI (Vectashield® Antifade Mounting Medium with DAPI (1.5µg/ml), Burlingame, CA, USA) onto glass slides and cover slips added and stored at -20°C until imaging.

2.27 Fluorescent microscopy imaging and analysis of single muscle fibers

Myofibres were imaged under 20x magnification and 30µm Z-stacks produced with 3µm steps using a widefield fluorescent microscope (Leica DMB 6000, Wetzlar, Germany) to determine PCM1 presence and localisation. An A4 filter was used to image DAPI (EX: 340-380, EM: 450-490), L5 filter to image FITC and Alexa Fluor® 488 (EX: 460-500, EM: 512-542) and an RHO

filter to image Alexa Fluor® 568 and 594 (EX: 541-551, EM: 565-605). Images were taken with a monochrome DFC365 FX camera (Leica, Wetzlar, Germany) and fluorescent channels overlaid to determine PCM1 and Pax7 localisation. The percentage of Pax7+ cells that also displayed PCM1 positivity were studied on single myofibres across all models.

Histology and Immunohistochemistry

2.28 Histological Analysis of Frozen Cryosections of Muscle Tissue

Histological analysis is widely used across muscle physiology for assessment of muscle fiber morphology, damage, connective tissue content amongst other pathological assessments. Muscle samples taken from rodents or biopsy material from humans can be laid out perpendicular to the surface they are attached to for transverse sectioning or in parallel for longitudinal sectioning. The most common method as previously discussed is snap freezing in isopentane, pre-cooled in liquid nitrogen prior to being stored at -80°C. Freezing muscle tissue in this manner, allows tissue to be preserved quickly without damaging muscle morphology, whilst also preventing the actions of proteases that may degrade proteins of interest.

2.29 Tissue Sectioning

When ready for sectioning, muscles were moved from -80°C and left to equilibrate at -20°C in a cryostat (OTF5000, Bright Instruments Ltd, Luton, United Kingdom) prior to sectioning. Histological analysis is often performed at a tissue thickness of 4-15µm in the literature. Throughout this thesis, sectioning is performed at 10µm. Histological sections with a thickness of 10µm were cut from either the mid-belly or for regional studies, from the proximal, mid-belly and distal end together with stimulated and unstimulated muscle cross-sections collected on the same Thermo Scientific™ SuperFrost Plus™ Adhesion slides (Thermo Fisher Scientific Inc, Waltham, USA). Having multiple sections along the long axis of the tibialis anterior muscle allows for identification of regional damage caused by surgery or by the stimulation itself. Slides were stored at -80°C until further use.

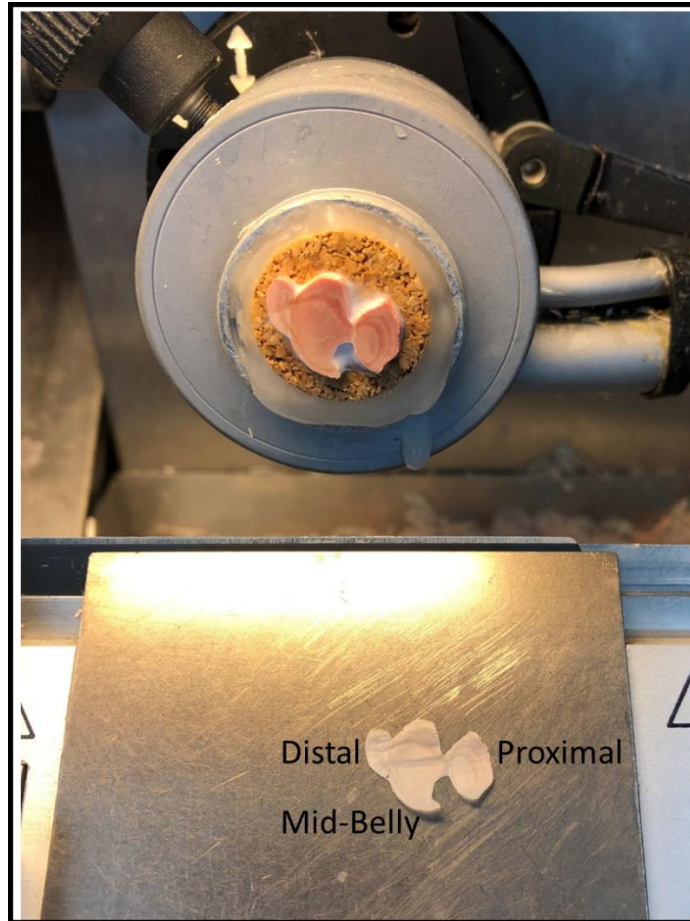


Figure 2.5: Cryostat set up with example of proximal, mid-belly and distal muscle slices prior to collection.

2.30 Hematoxylin and Eosin Stain for fiber morphology & damage assessment

Hematoxylin and eosin (H&E) staining was used to assess the general morphology of muscle fibers and to investigate signs of muscle damage, necrosis, fibrosis, denervation, and regeneration following stimulation and TTX nerve block.

Eosin stains muscle fibers to appear pink (binding non-specifically to proteins) and hematoxylin nuclei to appear blue. Before staining, sections were removed from the -80°C freezer and left for 30 minutes to adjust to room temperature. Sections were then dipped in tap water to rehydrate. Sections were then placed in Hematoxylin solution for 3 minutes before washing in warm, running tap water for 3 minutes. To remove excess hematoxylin, sections were dipped in 1% hydrochloric acid for 10 seconds. The sections were then placed

in eosin for 2 minutes before being dipped in running tap water for 10 seconds. The sections were then dehydrated through ascending grades of alcohol (50%, 70%, 90% and 100%), cleared in xylene twice and finally mounted in Di-N-Butyl phthalate in xylene (DPX).

2.31 Nicotinamide Adenine Dinucleotide (NADH) Staining for Assessment of Muscle Mitochondrial Content

NADH tetrazolium reductase staining was performed to assess mitochondrial content (NADH dehydrogenase activity), using tetrazolium salt as an electron acceptor for the site of dehydrogenase enzyme. 1mg of NADH was added to a 5ml tetrazolium solution (0.2M Tris Buffer, pH 7.4, 1mg/ml of Nitroblue tetrazolium). The solution was pipetted onto thawed sections and incubated for 30 minutes at RT. Sections were then dehydrated through ascending grades of alcohol to xylene as above and mounted in DPX.

2.32 Adenosine triphosphate-ase (ATPase) Staining for Assessment of Muscle Myosin Heavy Chain Content

Skeletal muscle can be histochemically separated into its MyHC sub-classifications (MyHC I, IIA and IIX/IIB) using the calcium dependant ATPase reaction Tunell and Hart, (1977). Cryosections were preincubated at 25°C for 7.5 minutes in a 0.1M glycine-3.7% aqueous formaldehyde-1% CaCl₂ solution at pH 7.25, followed by 3x5 minute washes in distilled water. Sections were then incubated at 37°C in ATPase medium at pH 9.4 for 50 minutes Ashley et al., (2007b), Ashley et al., (2007a). All reagents were made fresh, and pH checked before use.

Glycine and formaldehyde work in a synergistic manner to distinguish between fibre types 2A and 2X. The enzyme ATPase, present in muscle fibres at different activities, removes the phosphate group from ATP and forms calcium phosphate which is insoluble in alkaline conditions. This is then rendered visible by substitution of cobalt for calcium and of sulphide for phosphate. Type IIX/IIB fibres are stained intermediately, type IIA fibres dark and type I fibres pale. Unfortunately, this technique does not allow for differentiation between IIX and IIB fibers due to similar levels of ATPase. Therefore, for quantitative analysis antigen specific immunolabelling was performed with antibodies specific to the four adult myosin heavy chain isoforms.

2.33 Immunohistochemistry

Pre-cut 10µm sections were removed from -80°C storage and thawed to room temperature, before being circled in a hydrophobic pen to keep IB containing antibodies on the tissue sections. Primary antibodies were diluted as per table 2.1 in IB + plus 0.2% Triton-X100 (Sigma-Aldrich) overnight and then washed 3 x 10 minutes in IB. Secondary antibodies were diluted as per table 2.1 in IB for 2 hours or overnight for ease, followed by 3 x 10 minutes in IB. Following incubation with primary and secondary antibodies, single fibres were mounted in DAPI (Vectashield® Antifade Mounting Medium with DAPI (1.5µg/ml), Burlingame, CA, USA) onto glass slides and cover slips added and stored at -20°C until imaging.

2.34 Fluorescent microscopy and tile scanning

Muscle cross-sections were imaged under 20x magnification using a widefield fluorescent microscope (Leica DMB 6000, Wetzlar, Germany). For whole muscle cross-sections multiple images were taken and stitched together using the tilescan feature in Leica Application Suite X (Leica Microsystems GmbH, Wetzlar, Germany). Extracted .tif files were converted to .PNG files for MyoVision 2.0 Analysis.

2.35 MyoVision 2.0 Development and Analysis

As already discussed, key challenges in understanding the turnover of myonuclei following changes in activity and load within the muscle can be attributed to the processing and interpretation of immunohistochemical muscle cross-sections. Historically, rodent muscle hypertrophy and myonuclear domain studies have only analysed a select number of myofibres from certain fields of view due to the inability to manually quantify skeletal muscle fibre size and their associated myonuclei per fibre cross-section. More recent work has shown that this type of analysis is not sufficient to be representative of the entire muscle average CSA. Desgeorges et al., (2019) showed that there was a large potential for fibre cross-sectional area measurement error in 30-day post cardiotoxin injured mouse tibialis anterior muscle, ranging from -26.8% to + 55.7% in random fields of view compared to analysis of the entire muscle cross-section (Figure 2.6).

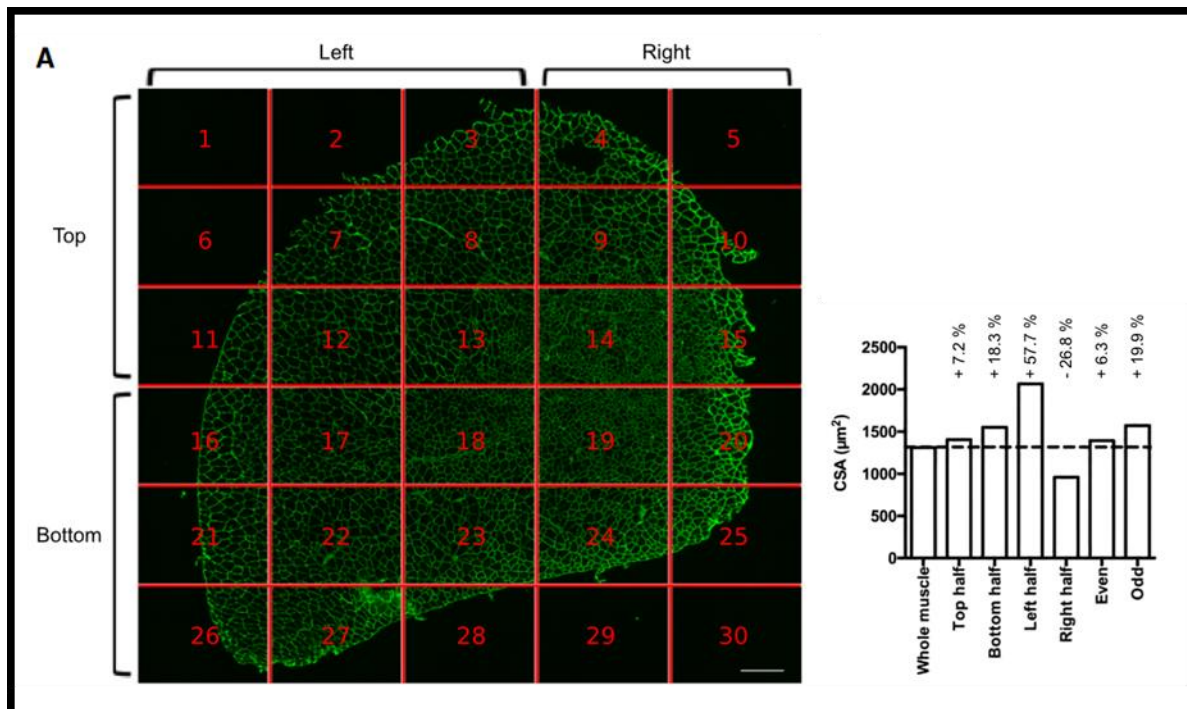


Figure 2.6: Immuno-labelled laminin in the tibialis anterior muscle, 30-days post cardiotoxin injury reveals the heterogeneity of muscle fibre size across a whole muscle cross-section which would produce large bias dependant on chosen images. Fibres on the periphery appear considerably larger in comparison to the centre of the muscle that is still regenerating. Taken with permission from Figure 3 of Desgeorges et al. (2019, Creative Commons Attribution 4.0 International License).

This is partially due to regeneration post cardiotoxin injury being a centripetal process, whereby fibres in the periphery recover quicker than those in the centre, most likely due to the larger vascularisation in these regions. We also report the same centripetal regeneration in Chapter _ in WT & LMNA+/ Δ K32 mice 7 days post synergist ablation of the plantaris. Heterogeneity of muscle fibre size is also present in the tibialis anterior of the rat, where the small proportion of smaller type I fibres appear only in the proximal-deep region and to some extent at the mid-belly but are completely absent in the distal and superficial regions of the muscle. Changes in fibre pennation angle are also likely to cause changes in fiber cross-sectional area measurements, if minimum feret diameter is not used to correct for the area, as more pennate/longitudinal fibres in a transverse section would likely present larger areas. Jorgenson and Hornberger, (2019) report that changes in fibre number (fibre splitting), fibre length and simultaneous changes in pennation angle following chronic mechanical overload via synergist ablation may change the number of fibres in an anatomical muscle cross-section

when histology is taken at the mid-belly and may subsequently affect fibre area measurements. The multitude of these factors combined during muscle adaptation to loading may explain some differences between the amount of hypertrophy of myofibres reported using the same or similar models of overload between different research groups when measured through histology.

Factors such as changes in pennation angle are also likely to affect manual identification of the number of myonuclei per fibre cross-section, even if effort is taken to study the histology of muscles at the same anatomical region. This is made more challenging as myonuclei appear near both satellite cells and interstitial nuclei. The myonucleus can be demarcated from others in proximity by labelling cryosections with laminin or dystrophin, showing their subsarcolemmal positioning. Most interstitial nuclei and myonuclei tend to partially overlap these boundaries making manual identification prone to false-positive and false-negatives. This process is extremely time-consuming and can only be performed on a small proportion of the skeletal muscle cross-section. Researchers are left with the dilemma of performing myonuclear analyses on a few full isolated single myofibres which is considerably more accurate than cross-sectional analysis or studying a snapshot of the muscle in a single whole transverse cross-section, which may be more representative of the whole muscle as myonuclei are reported to be evenly distributed across the myofibre in healthy skeletal myofibres.

In more recent years automated, computational analyses of whole anatomical cross-sections of skeletal muscle has been made possible with fluorescent labelling and computational segmentation and measurements of muscle fibre cross-sections. Wen et al., (2018b) published a publicly available software Myovision v1.0, allowing for automated detection of fibre-type specific cross-sectional area using immuno-histochemical labelled dystrophin or laminin frozen muscle cross-sections, with an accuracy of >94% when compared with manual measurements. That is, myonuclear counting accuracy is estimated to be $94.9 \pm 1.7\%$ relative to manual counts. Whilst Myovision v1.0 (<https://www.uky.edu/chs/muscle/myovision>), (<https://www.myoanalytics.com/index.html>), has been heavily used by the muscle community with over 60 citations and works considerably well with mouse muscle cross-sections and human skeletal muscle biopsies which may contain several hundred fibres, larger muscle cross-sections require more extreme computing power. Due to the size of our muscle

of interest, the rat tibialis anterior which has a cross-section of ($\sim 1\text{-}2\text{cm}^2$, containing ~ 3000 to $12,000$ fibres depending on the region of cross section), gaining representative data of muscle fibre size changes and myonuclei per fibre is particularly challenging and open to regional bias. Until now, objective analysis of a large data set of large whole muscle cross-sections have not been possible.

Due to the issues with MyoVision v1.0 and other software struggling to cope with such large images, a collaboration was made with the primary author Dr. Yuan Wen in order to have pre-public access to MyoVision v2.0 which we were able to pilot test on our own samples in Chapters 4 and 5. This following data analyses would not have been possible without the input from Dr. Yuan Wen and Dr. Charlotte Peterson from the Center of Muscle Biology, University of Kentucky. The following myonuclear domain assessment workflow has been described in detail Wen et al., (2018b) and has been compared in depth with other publicly available, peer-reviewed automatic techniques to measure muscle fibre CSA Bergmeister et al., (2016), Smith and Barton, (2014). Briefly, MyoVision v1.0 would take muscle cryosections fluorescently labelled with DAPI to visualise all nuclei and an antibody against the protein dystrophin/laminin, to delineate the subsarcolemmal positioning of myonuclei and the myofibre border. The myofiber border (dystrophin/laminin) channel is first filtered and enhanced for line and edge structures using standard median filter and multiscale frangi enhancement. The enhanced image is then segregated into membrane and cytoplasmic regions using K-means Binarization (Euclidian Distance K-Means clustering) and the edge detection flipped with the background. Each cytoplasmic region is then sub-classified into seed regions belonging to multiple connected cells, a single cell or interstitial space using the shape descriptors 'Area', 'Solidity', 'Extent', 'Convexity', 'Eccentricity'. At this stage interstitial/extracellular regions are removed. Seed regions more likely to be connected cells were then identified and selected for watershed separation. The watershed separated fibres and single cells were then combined to produce finalised seed regions which were adjusted using spline-evolution until convergence. Contour evolution was performed using the Chan Vese – Vector Field Convolution. The completed fibre outlined in yellow is then used as a mask overlay for nuclei localisation. Myonuclei were then defined as nuclei with their centroid or more than 50% of their area inside the sarcolemma. Data can then be exported for further analyses.

MyoVision v2.0 introduced major upgrades to the original MyoVision software, but the fundamental workflow including fiber detection, fiber type classification, and myonuclear counting remained essentially the same as described previously Wen et al., (2018b). For fiber detection, the software uses the single channel intensity image of dystrophin labelling as an input as well as the pixel scale ($\mu\text{m}/\text{pixel}$) to allow for calculation of mean fiber cross-sectional area in units of square micrometres. Following fiber detection, a single channel intensity image of immuno-labelled myosin heavy chain or nuclei can be provided to the software to classify fiber type or quantify myonuclei number. For each myofiber cytoplasmic region excluding the periphery, the mean myosin heavy chain immunofluorescence intensity can be quantified on a scale of 0 to 1, with 1 being maximum signal for the section. Only fibers with mean myosin heavy chain intensity greater than 0.5 were classified as true for that particular fiber type. When analysing multiple fiber types, the image corresponding to each fiber type was analysed independently. Thus, a fiber classified as “negative” would represent false for all fiber types included in the analysis whereas a “hybrid” classification would indicate co-expression of at least two different myosin heavy chain isoforms within the same fiber. The criteria for myonuclear classification remain the same as in the previous version; specifically, a nuclear region with its centroid inside the fiber dystrophin border and at least 50% of its total area within the fiber cytoplasm is counted as a myonucleus.

A major upgrade to the software is the implementation of neural networks in fiber detection and fiber type classification steps. Multiple steps in the previous MyoVision algorithm have been replaced with U-net models Ronneberger et al., (2015), which demonstrated superior performance in the segmentation of grayscale intensity based images of cells. The models were trained using annotated images of 256 by 256 pixels. Briefly, images of whole cross-sections were labelled as true for foreground (i.e., fiber boundary) and false for background (i.e., non-specific signals or staining artefacts). These images along with their ground truth label were separated into 256x256 pixel regions. The same image and ground truth label were then reduced by two-fold in size sequentially, and 256x256 pixel regions were extracted from the smaller images in a similar fashion as the original image. Reducing the image size allows for the model to learn at different image resolutions and different magnifications. Images representing 1x, 0.5x, and 0.25x along with their ground truth labels were used to train the weights of a U-net model for up to 100 epochs at 300 steps per epoch using Keras (v2.2.4)

and Tensorflow (v1.13.1). Models were similarly trained for each step in the algorithm to replace the corresponding steps in the previous version of the software (Supplementary Figure 2). Of note, the previous software included the active contour algorithm by default, which expands the fiber contour as close to the inner edge of the dystrophin border as possible to allow for myonuclear counting. This step had been relocated to the nuclear counting analysis exclusively due to its resource intensiveness and the fact that general fiber detection does not require such stringent delineation of the inner edge of the sarcolemma. This modification led to slightly smaller fiber cross-sectional area values (~5%) compared to the previous version of the software. This modification was favorable not only from a computational resource perspective, but also resulted in values more in line with various other approaches in the literature that do not include any myonuclear analysis. The software will be made freely available to the research community and additional documentation for the current version can be found on www.myoanalytics.com/myovision2.

In addition, users now have control over circularity, solidity and eccentricity parameters for identifying fibers for analysis of different muscle phenotypes and extreme atrophic conditions. Other functionalities introduced in this upgrade include robust detection of whole cross-sections, batch processing of images for large projects, export of representative images from the software, exporting images from Olympus microscopes, adjusting images to control for background noise, and output of multiple shape descriptors for each fiber.

RT-qPCR Analyses

2.36 Tissue Homogenisation and RNA Extraction (TRIzol Method)

Frozen muscle samples (approx. 300mg) were added to 2ml MagNA Lyser Green Bead screw-capped tubes, prefilled with 1.4-mm (diameter) ceramic beads (PN:03358941001, Roche, Germany) and 1ml of Trizol (Thermo Fisher Scientific Inc, Waltham, USA). Samples were homogenised using a MagNA Lyser (Roche Diagnostics, Germany) for 40 secs at 6 m/s before being placed back on ice. This was repeated 5 times to ensure complete disruption of the muscle sample. RNA was extracted using the standard Tri-Reagent procedure with chloroform/isopropanol for phase separation and precipitation of RNA, with further washing

with 75% ethanol. RNA pellets were resuspended in 51µl of DEPC-treated water (Thermo Fisher Scientific Inc, Waltham, USA).

2.37 RNA Concentration Analysis & RNA Purity Analysis for RT-qPCR

For each sample, 1µl of the RNA containing DEPC-treated water was suspended and measured in the Nanodrop 2000 spectrophotometer™ (Thermo Fisher Scientific Inc, Waltham, USA) for RNA quality and quantity. As the absorbance of proteins, RNA and DNA is well known this can be used to assess the contents of each sample. Briefly, once the sample is positioned, surface tension is used to hold samples in place between two optical fibers and ultraviolet (UV) light is passed through the sample. The resultant ratio of absorbance maximum at 260nm to 280nm (protein) was used to determine the purity of the sample in relation to a potential protein contamination. A ratio of 2.0 was indicative of high RNA purity or 'RNA quality'.

2.38 RNA Sample Dilution

Once all samples were assessed for RNA quantity, they were diluted in DEPC-treated water (Thermo Fisher Scientific Inc, Waltham, USA) to normalise concentrations between samples. RNA Samples were then retested to confirm concentration similarity between samples.

2.39 Design of Primers for Polymerase Chain Reaction (PCR)

Forward and reverse primers were designed to amplify genes of interest following strict guidelines as follows; Primer Length: 18-24bp, Temperature Melt (T_m): 57-62°C to ensure optimal annealing temperatures, GC Content (%): ~50% GC Content, 3 or more GC bases were avoided in the last 5 bases at the 3' end of the primer, Amplicon Length: Less than 300bp, General Considerations: Primers should span an exon-intron boundary where possible. Primers were all self-designed using reference mRNA sequences for *Rattus norvegicus*, which were accessed through <https://www.ncbi.nlm.nih.gov/>. mRNA sequences were then transferred to PrimerBlast, a National Center for Biotechnology Information resource <https://www.ncbi.nlm.nih.gov/tools/primer-blast/> to check for possible multiple isoforms (multiple transcript variants) of genes or genes not of interest. In these cases, multiple isoform sequences were analysed using Clustal Omega (<https://www.ebi.ac.uk/Tools/msa/clustalo/>)

a multiple sequence alignment tool to find a section of mRNA that is present in all isoforms of the gene of interest. Primers were synthesised by Sigma Aldrich (Merck). All stock (desalted) primers were suspended in TE buffer (pH 8.0, Ambion®, Invitrogen, California, USA) to a concentration of 100 µM.

Table 2.4: Primer Sequences designed and used:

Target Gene	Entrez Gene ID		Primer Sequence (5'-3')	Reference Seq. Number	Product Length (bp)
Rat_18S rRNA	24723	F:	TTGACGGAAGGGCACCACCAG	X01117	131
Rat_18S rRNA		R:	GCACCACCACCCACGGAATCG		
Rat_MyHCI	29557	F:	CTACCCAACCCTAAGGATG	NM_017240	75
Rat_MyHCI		R:	TTGTGTTTCTGCCTAAGGTGC		
Rat_MyHCIIa	691644	F:	CCTCAGGCTTCAAGATTTGGTGG	L13606	265
Rat_MyHCIIa		R:	TTGTGCCTCTCTTCGGTCATTC		
Rat_MyHCIIb	360543	F:	TACAAGAGACAAGCAGAGGAGG	NM_019325	152
Rat_MyHCIIb		R:	TGAACCTCTCGGCTCTTCACC		
Rat_MyHCIIx	287408	F:	TTACCAAACCTGAGGAAGACCGC	NM_001135158.1	279
Rat_MyHCIIx		R:	GTCACCTTTCCTGCTTTGGATCG		

2.40 QiAgility Automated Sample Preparation for RT-qPCR

For improved throughput and accuracy, all PCR reactions and samples were automatically pipetted using the QiAgility Automated Sample System (Qiagen, UK) into a Rotor Disc-100 plate (Qiagen, Crawley, UK) and sealed using heat-sealing film and Rotor-Disc Heat Sealer (Qiagen, Crawley, UK). Reactions were performed using the QuantiFast™ SYBR® Green RT-PCR one-step kit. Each reaction tube was set up as follows; 9.5 µl experimental sample (5.26 ng/µl totalling 50 ng per reaction), 0.15 µl of both forward and reverse primer of the gene of interest (100 µM), 0.2 µl of QuantiFast RT Mix (Qiagen, Manchester, UK) and 10 µl of QuantiFast SYBR Green RT-PCR Master Mix (Qiagen, Manchester, UK).

2.41 Rotor Gene-Q Real Time Cycler for RT-qPCR

Rotor discs were transferred and locked into the PCR thermal cycler (Rotor-Gene 3000Q, Qiagen, UK). Reverse transcription was initiated with a hold at 50 °C for 10 minutes (cDNA

synthesis), followed by a 5-minute hold at 95 °C (transcriptase inactivation and initial denaturation), before 40 PCR cycles of; 95 °C for 10 sec (denaturation) followed by 60 °C for 30 secs (annealing and extension).

The following outlines the reaction that occurs during RT-qPCR. Following isolation of mRNA from muscle tissue, the single stranded RNA (ssRNA) must be reverse transcribed forming complimentary DNA (cDNA) before the target sequence is amplified for quantitative measurement. For the reverse transcription (RT) process to occur, oligonucleotides (dNTPs) are added to ssRNA using the enzyme reverse transcriptase which synthesizes cDNA from the 3' to 5' end of the mRNA molecule. The 3' and 5' indicate the carbon numbers in the DNA sugars backbone also known as 3' prime or 5' prime. The 5' carbon has a phosphate group attached and the 3' carbon a hydroxyl (-OH) group which gives the directionality of the DNA molecule. Once synthesized, DNA is amplified through 3 steps which constitute 1 cycle of a PCR reaction which is repeated for 30-40 cycles to produce over 1 billion copies of the target sequence. Firstly, double stranded DNA (dsDNA) is denatured through exposure to high temperatures (95°C) which separates the DNA into two strands exposing the 3' end of the DNA. The temperature is then lowered to allow for annealing of primers to enable binding of short sequence (18-30bp) primers to the DNA strands. Lastly, RNA polymerase binds to primers and synthesizes the complementary strand using free deoxyribonucleotide triphosphate (dNTPs). With each PCR cycle, a fluorescent dye or probe (in our case 2x Power SYBR™ Green PCR Master Mix, (Thermo Fisher Scientific Inc, Waltham, USA) binds to each dsDNA molecule after primers anneal to the 3' end. The amount of light excited and emitted from the fluorescent molecule can provide 'real-time' measurement of DNA amplification as the amount of light measured by the fluorometer within the PCR thermocycler instrument is directly proportional to the amount of targeted DNA produced. This can be quantified according to the number of cycles required to exceed the fluorescence cycle threshold (C_T), defined as the point at which the fluorescent signal reaches an intensity above those of background signals (which changes dependant on the initial abundance of dsDNA. Thus, the lower the C_T value, the higher the expression levels as the fluorescence are being detected at an earlier point. Additionally, C_T values of the target gene must be compared to a housekeeper or reference gene. In our investigation we used 18SrRNA as a stable housekeeper for electrical stimulation experiments as evidenced in previous work from the lab Fisher, (2010). The

expression of this gene should remain consistent across all experimental conditions, to determine absolute or relative quantities of the target gene of interest's expression.

Melt curve analysis was also performed of the product formed during RT-qPCR using each primer set. The melt curve is a plot of the total fluorescence recorded as a function of temperature. $-d(RFU)/dT$ is the rate of change of fluorescence in the PCR reaction and a significant change in fluorescence accompanies the melting of the double-stranded PCR products. Therefore, it was confirmed that each primer set showed a single peak. Multiple peaks would indicate lack of primer specificity, potentially forming several peaks that would represent different products of the reaction.

2.42 Quantification of Relative Gene Expression using RT-qPCR Using the $2^{-\Delta\Delta Ct}$ Method for Fold Change Calculations

Sample efficiencies were routinely checked to ensure doubling efficiency of product per cycle. An efficiency value of 2 represents a 2-fold increase (100% which is derived from dividing the efficiency value by 2 and multiplying by 100) of amplicon with each PCR cycle. To obtain the raw CT values for each sample, a threshold line was self-adjusted on the amplification curve according to where an exponential rise in fluorescence occurred. The CT values from duplicate or triplicate assays were used to quantify relative gene expression using the comparative Delta Delta CT ($\Delta\Delta CT$) equation Schmittgen and Livak, (2008) against a reference gene (18SrRNA) and a control sample from the contralateral limb/contralateral muscle region.

Delta Delta CT ($\Delta\Delta CT$) Equation:

- 1) $\Delta CT = CT(\text{Target Gene}) - CT(\text{Target Gene-Housekeeper})$
- 2) $\Delta\Delta CT = \Delta CT(\text{Target Sample}) - \Delta CT(\text{Control Sample/Contralateral Control Region})$
- 3) $2^{-\Delta\Delta CT}$ (normalised expression ratio)

Where appropriate $\Delta\Delta CT$ was log₂ transformed for illustrative purposes.

In addition to this ΔCT values were studied in treated and untreated limbs to measure whether rates of transcription were higher in different regions of the tibialis anterior.

Next-Generation RNA Sequencing

The transcriptomic profile of a cell is a key determinant in its function and its ability to adapt to external challenges. Next generation sequencing of the RNA frozen within a cell at a particular point in time gives an incredible amount of detail into the RNA landscape. RNA-sequencing does not require species or transcript specific probes like microarrays. This non-targeted approach allows for determination of new genes, previously unknown to a set stimulus as well as novel gene transcripts, transcript variants (alleles), gene fusions, single nucleotide variations within a gene and small insertions and deletions within a gene. The interest in employing such techniques in exercise physiology and specifically a timecourse of adaptation to resistance training is increasing as scientists seek to map the effects of exercise type, duration and training status on multiple tissues and different clinical populations.

2.43 mRNA Library Preparation

Frozen muscle samples (approx. 300mg) were added to 2ml MagNA Lyser Green Bead screw-capped tubes, prefilled with 1.4-mm (diameter) ceramic beads (PN:03358941001, Roche, Germany) and 1ml of Trizol (Thermo Fisher Scientific Inc, Waltham, USA). Samples were homogenised using a MagNA Lyser (Roche Diagnostics, Germany) for 40 secs at 6 m/s before being placed back on ice. This was repeated 5 times to ensure complete disruption of the muscle sample. RNA was extracted using the standard Tri-Reagent procedure with chloroform/isopropanol for phase separation and precipitation of RNA, with further washing with 75% ethanol. RNA pellets were resuspended in 51µl of DEPC-treated water (Thermo Fisher Scientific Inc, Waltham, USA).

For next generation RNA sequencing, samples were analysed, and next-generation libraries generated at the Genome Centre, Blizard Institute, Barts and the London School of Medicine and Dentistry, Queen Mary University of London (See Appendix 2). Full lab protocols and processing is available in supplementary information. Briefly, RNA quality and quantity was assessed using a chip-based, capillary electrophoresis microfluidics-based platform, Agilent 2100 Bioanalyzer 250320 ES (Agilent Technologies, Santa Clara, CA, USA). RNA integrity number (RIN) scores >7 is deemed high quality for subsequent fragmentation. RIN scores were 8.5 ± 0.3 , $n= 24$.

High quality mRNA libraries were prepared using NEBNext® Ultra™ II Directional RNA Library Prep with Sample Purification Beads kit, #E7765S (New England Biolabs, MA, USA) as per manufacturers guidelines. 100ng of RNA was used for mRNA isolation. NEBNext Magnetic Oligo d(T) beads were covalently coupled to the poly(A) region of mRNA molecules in a sealed PCR plate placed in a thermal cycler at 65°C for 5 minutes to denature RNA and facilitate binding of the mRNA poly-A tail to the magnetic beads. Purified mRNA was then fragmented, primed and first strand cDNA synthesis performed using First Strand Enzyme Master mix by combining NEBNext Strand Specificity Reagent and NEBNext First Strand Synthesis Enzyme Mix in a thermal cycler (25°C for 10 mins, 42°C for 50 mins, 70°C for 15 mins, 4°C Hold). Second strand cDNA Synthesis was then performed using Second Strand Master mix (containing nuclease free water, NEBNext Second Strand Synthesis Buffer, NEBNext Second Strand Synthesis Enzyme Mix) in a thermal cycler at 16°C for 1 hour. Double stranded cDNA was then purified using 1.8X AMPure XP Beads (Beckman Coulter, IN, USA). Purified cDNA was added to End prep master mix (NEBNext Ultra II End Prep Reaction Buffer and NEBNext II End Prep Enzyme Mix) and placed in a thermal cycler for (20°C for 30 minutes, 65°C for 30 minutes followed by 4°C Hold).

Adaptor ligation was then performed using NEBNext Adaptor in adaptor diluted buffer, freshly mixed with ligation master mix containing (NEBNext Ligation Enhancer and NEBNext Ultra II Ligation master Mix) with a thermal cycler at 20°C for 15 minutes. USER Enzyme was then added to the solution and subjected to 37°C in the thermal cycler for a further 15 minutes. Purification of the ligation reaction was then performed using AMPure XP beads to enrich libraries for sequences between 300-450bp long and the resultant DNA target eluted in 0.1X TE buffer.

PCR library enrichment was performed by adding NEBNext Q5 Hot Start Hifi PCR Master Mix to the eluted DNA target with NEBNext Multiplex Oligos for Illumina (96 Index Primers). Samples were ran in a thermal cycler for the following amplification programme (98°C for 30 seconds, 98°C 10 seconds, 65°C 75 seconds with x13 cycles followed by 65°C for 5 mins, and 4°C Hold). The subsequent PCR product was purified using Agencourt AMPure XP beads and later resuspended in 0.1X TE Buffer. The resultant libraries were quantified (stock concentrations measured), performed using the Qubit HS dsDNA kit on 1000bp ScreenTape. Briefly, Qubit DNA standards were made up based on manufacturers guidelines

(ThermoFisher Scientific, UK) with pre-prepared calf thymus DNA to Qubit working solution and ran on the Qubit 2.0 Fluorometer ThermoFisher Scientific, UK). 1 μ l of experimental sample was added to 199 μ l of the Qubit working solution and stock concentrations calculated. Quality control was performed using the Agilent 4200 TapeStation system (CA, USA) as previously described. Postscript analysis was performed to confirm high quality mRNA libraries with a peak around 300-450bp and low PCR duplicate rate <10% and libraries with molarities 4-5nM.

Prior to Illumina loading, libraries were denatured by combining an equal volume of library and 0.2N NaOH in a 1.5ml LoBind microcentrifuge tube. After vortexing and briefly centrifuging, the tubes were kept at room temperature for 5 minutes. 200mM Tris-HCl was then added to the same volume as the library volume to neutralise the NaOH (Example standard starting molarities are available in the supplementary NGS workflow). Samples were vortexed and centrifuged briefly, before HT1 buffer was added with 1.2 μ l of 20pM PhiX to bring the total volume to 1.3ml. Samples were then vortexed and centrifuged briefly before being placed on ice prior to loading into the sequencing cartridge. Sequencing cartridges were prepared by inverting the thawed cartridge 10 times to mix reagents. The total volume of denatured library was then added to sequencing cartridges and then sequenced on an Illumina NextSeq. The NextSeq sequences libraries on a single flow cell with 4 lanes, allowing for paired-end sequencing.

2.44 Pre-alignment QA/QC

Raw FastQ files were imported to Partek Flow Software (Partek Incorporated, Missouri, USA) for pipeline processing. Firstly, samples were assessed for pre-alignment QA/QC on all reads for a measure of total reads, read length, average read quality, % N and % GC content (Table 2.5). Phred score a measure of read quality refers to the probability of an incorrect base call. For example, a Phred quality score of 10 has a 1 in 10 probability of an incorrect base call (90% accuracy). A Phred score of 30 has a 1 in 1000 probability of an incorrect base call (99.9% accuracy). A Phred score of 40 has a 1 in 10,000 probability of an incorrect base call (99.99% accuracy).

Table 2.5: Pre-alignment QA/QC.

Sample name	Condition	Timepoint	Total reads	Read length	Avg. read quality	% N	% GC
257L	2 Days	2 Days	13339864	37	34.327	0.028087	50.5728
257R	Control	2 Days	12709717	37	34.3258	0.02826	50.4687
258L	2 Days	2 Days	12620387	37	34.3502	0.02882	50.584
258R	Control	2 Days	12171400	37	34.2213	0.028391	50.0114
259L	2 Days	2 Days	12738062	37	34.3336	0.028056	50.2158
259R	Control	2 Days	13275818	37	34.3837	0.02846	50.218
260L	10 Days	10 Days	12352118	37	34.363	0.027688	50.3693
260R	Control	10 Days	14173615	37	34.4009	0.028352	49.5336
261L	10 Days	10 Days	12325676	37	34.3397	0.028024	50.9436
261R	Control	10 Days	12606773	37	34.3789	0.028018	50.3545
262L	10 Days	10 Days	12615800	37	34.3734	0.028431	50.4567
262R	Control	10 Days	12568659	37	34.3381	0.028243	50.615
263L	20 Days	20 Days	11697225	37	34.3802	0.027987	49.8634
263R	Control	20 Days	12584383	37	34.3875	0.027797	50.4781
264L	20 Days	20 Days	12825013	37	34.349	0.028171	50.8898
264R	Control	20 Days	12373301	37	34.3542	0.028091	50.4678
265L	20 Days	20 Days	12095193	37	34.3716	0.028022	49.0895
265R	Control	20 Days	11627649	37	34.3634	0.028472	49.7111
267L	30 Days	30 Days	11777034	37	34.3802	0.028578	49.3673
267R	Control	30 Days	11249306	37	34.3769	0.028272	49.0829
268L	30 Days	30 Days	12453530	37	34.4059	0.028976	48.6869
268R	Control	30 Days	8284797	37	34.3935	0.028995	49.4586
275L	30 Days	30 Days	11767146	37	34.4014	0.028399	48.4951
275R	Control	30 Days	12886417	37	34.1814	0.028883	50.4885

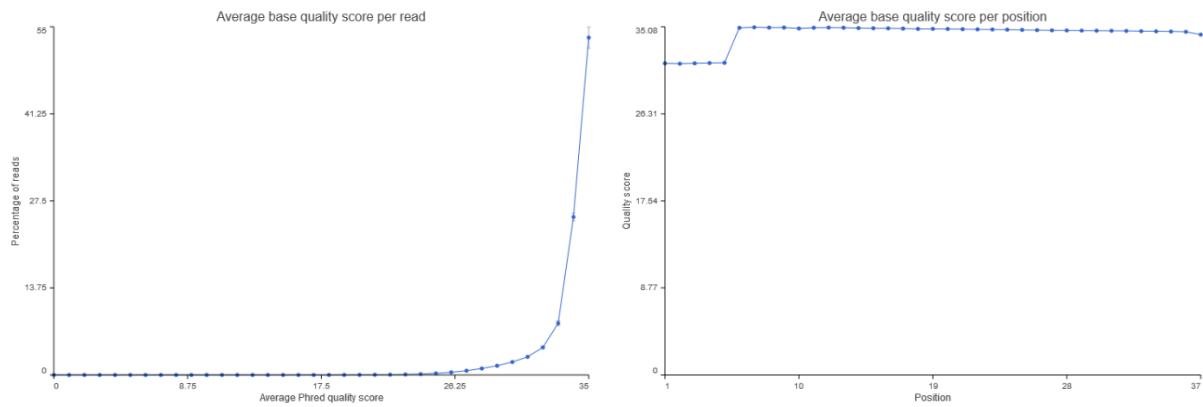


Figure 2.7: Pre-alignment average Phred quality score (base quality) as a percentage of total reads and base quality score per position across all samples.

2.45 Read Trimming

Poor quality reads were trimmed from the 5' or 3' end (or both) for the first base at or above the specified Phred quality score (20). All bases previous to this position were trimmed (from the left if the 5' end, or from the right if the 3' end). The results of which can be seen in Table 2 and Figure 2.

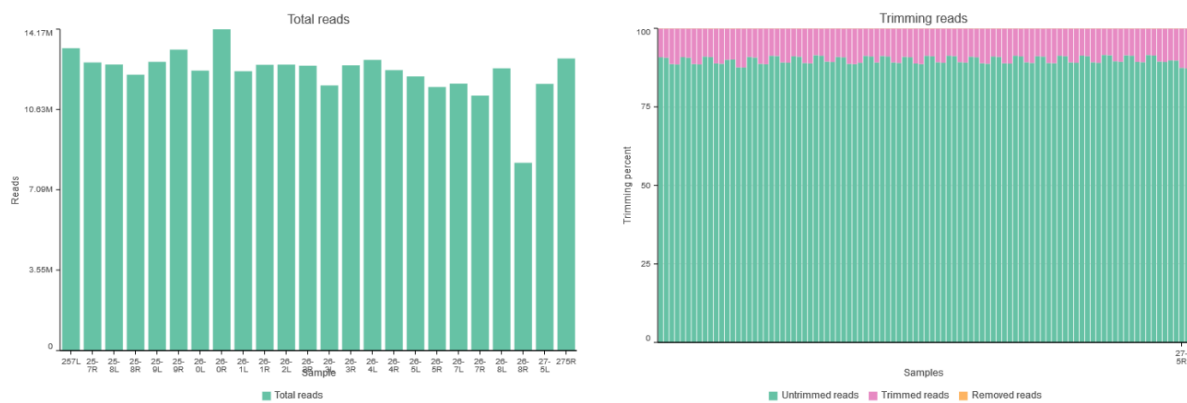


Figure 2.8: Visualisation of total reads per sample and percentage trimmed reads based on Phred quality score for each sample.

Table 2.6: Individual Sample Read Trimming Summary

Sample Name	Condition	Total reads	Reads trimmed	% Reads trimmed	Reads removed	% Reads removed	Average bases trimmed	Pre-trim quality	Post-trim quality
257L	2 Days	13339864	1370715	10.27	9335.00	0.07	1.39	34.42	34.45
257R	Control	12709717	1304157	10.26	8668.00	0.07	1.39	34.43	34.47
258L	2 Days	12620387	1270129	10.06	9892.00	0.08	1.41	34.45	34.48
258R	Control	12171400	1353128	11.11	9248.00	0.08	1.41	34.47	34.50
259L	2 Days	12738062	1300114	10.20	8630.00	0.07	1.40	34.43	34.46
259R	Control	13275818	1296118	9.76	8683.00	0.07	1.39	34.46	34.49
260L	10 Days	12352118	1229402	9.95	8634.00	0.07	1.39	34.47	34.50
260R	Control	14173615	1354809	9.56	9769.00	0.07	1.40	34.48	34.51
261L	10 Days	12325676	1254383	10.17	9132.00	0.07	1.40	34.44	34.48
261R	Control	12606773	1236796	9.81	8802.00	0.07	1.39	34.46	34.49
262L	10 Days	12615800	1239866	9.82	9035.00	0.07	1.40	34.45	34.49
262R	Control	12568659	1274757	10.14	8444.00	0.07	1.39	34.43	34.47
263L	20 Days	11697225	1142693	9.77	8092.00	0.07	1.40	34.47	34.50
263R	Control	12584383	1224584	9.73	8813.00	0.07	1.39	34.43	34.46
264L	20 Days	12825013	1292271	10.07	9166.00	0.07	1.41	34.44	34.48
264R	Control	12373301	1240101	10.02	8699.00	0.07	1.39	34.44	34.47
265L	20 Days	12095193	1184235	9.79	8645.00	0.07	1.40	34.46	34.49
265R	Control	11627649	1153815	9.92	7958.00	0.07	1.39	34.46	34.49
267L	30 Days	11777034	1150210	9.76	8321.00	0.07	1.39	34.48	34.51
267R	Control	11249306	1097891	9.76	7876.00	0.07	1.39	34.48	34.51
268L	30 Days	12453530	1179151	9.46	8791.00	0.07	1.39	34.51	34.54
268R	Control	8284797	796284	9.61	5658.00	0.07	1.39	34.48	34.51
275L	30 Days	11767146	1120154	9.52	8797.00	0.07	1.39	34.49	34.52
275R	Control	12886417	1465551	11.37	8751.00	0.07	1.41	34.46	34.49

2.46 STAR Alignment 4.4.1d to *Rattus Norvegicus*, Rnor_6.0 genome assembly

Trimmed reads were then aligned using STAR alignment 4.4.1d to the *Rattus Norvegicus*, Rnor_6.0 genome assembly. Alignment was performed under the following default settings (Table 2.7).

Table 2.7: STAR Alignment 4.4.1d Rattus Norvegicus Rnor 6.0 Run Settings.

Input parameters			
Option	Value		
Generate unaligned reads	TRUE	Non-canonical gap open penalty	-8
Name, sequence, and quality lengths	NotEqual	GC/AG gap open penalty	-4
Max junctions	1000000	AT/AC gap open penalty	-8
Type of filtering	Normal	Extra score	-0.25
Multimap score range	1	Deletion open penalty	-2
Max read mapping	10	Deletion extension penalty per base	-2
Max mismatches	10	Insertion open penalty	-2
Mismatch mapped ratio	0.3	Insertion extension penalty per base	-2
Mismatch read ratio	1	Max score reduction	1
Min score	0	Search start point	50
Normalized min score	0.66	Normalized search start point	1
Min matched bases	0	Max seed length	/
Normalized min matched bases	0.66	Max mapping for stitching	10000
Filter alignment using their motifs	None	Max seeds per read	1000
Collapsed splice junctions reads	All	Max seeds per window	50
Max junction gap	50000 100	Max one seed loci per window	10
Non-canonical motifs	TRUE	Min intron size	21
Min overhang length for splice junctions	30	Max intron size	/
Min unique map read count per junction	3	Max gap between two mates	/
Min total read count per junction	3	Min spliced alignment overhang	5
Min distance to other junctions' donor/acceptor	10	Min annotated spliced alignment overhang	3
GT/AG motif	TRUE	Spliced mate min read length	0
Min overhang length for splice junctions	12	Normalized spliced mate min read length	0.66
Min unique map read count per junction	1	Max windows per read	10000
Min total read count per junction	1	Max transcripts per window	100
Min distance to other junctions' donor/acceptor	0	Max hits	10000
GC/AG motif	TRUE	Read ends alignment type	Local
Min overhang length for splice junctions	12	Soft-clip past reference end	Yes
Min unique map read count per junction	1	Max loci anchors	50
Min total read count per junction	1	Bin size for windows/clustering	16
Min distance to other junctions' donor/acceptor	5	Max bins between two anchors	9
AT/AC motif	TRUE	Left and right flanking region size	4
Min overhang length for splice junctions	12	Chimeric alignment	(Default: f
Min unique map read count per junction	1	Two pass mapping	None
Min total read count per junction	1	Cufflinks-like strand field flag	intronMot
Min distance to other junctions' donor/acceptor	10	SAM attributes	All
Extra alignment score	2	Add to quality score	0
Gap open penalty	0	WASP filtering	(Default: f

2.47 Post alignment QA/QC

Post alignment QA/QC was performed to evaluate total reads, total alignments, % reads aligned, unique singleton, unique paired, coverage, average coverage depth, average length, average quality and % GC content. Visual interpretation of Table 2.8 can be observed in Figure 2.9.

Table 2.8: Summary report of post alignment QA/QC.

Sample name	Condition	Total reads	Total alignments	Aligned %	Total unaligned	Unaligned %	Total unique paired	Unique paired
257L	2 Days	13330529	30286996	95.52418	596651	4.475824	11430210	85.74461
257R	Control	12701049	28606780	95.35683	589731	4.643168	10910599	85.90313
258L	2 Days	12610495	28579924	95.6423	549528	4.357704	10844983	85.99966
258R	Control	12162152	27307672	95.0777	598658	4.922303	10379018	85.33866
259L	2 Days	12729432	28805410	95.69359	548182	4.306414	10941354	85.9532
259R	Control	13267135	29954146	95.65814	576041	4.341864	11394159	85.88259
260L	10 Days	12343484	28081926	95.7429	525475	4.257104	10572263	85.65056
260R	Control	14163846	32050110	95.42367	648184	4.576328	12111205	85.50788
261L	10 Days	12316544	27789646	95.56359	546413	4.436415	10605042	86.10404
261R	Control	12597971	28463894	95.53101	563002	4.468989	10826377	85.93747
262L	10 Days	12606765	28744230	95.60127	554537	4.398726	10765051	85.39107
262R	Control	12560215	28437158	95.39089	578914	4.609109	10759598	85.66412
263L	20 Days	11689133	26603164	95.5582	519208	4.441801	9950869	85.12923
263R	Control	12575570	28366578	95.57274	556753	4.427259	10803077	85.90527
264L	20 Days	12815847	29037654	95.45002	583118	4.549976	10943538	85.39067
264R	Control	12364602	27790636	95.47944	558949	4.520558	10620394	85.89354
265L	20 Days	12086548	27536168	95.74502	514280	4.254978	10283763	85.08437
265R	Control	11619691	26283424	95.65087	505356	4.349135	9956739	85.6885
267L	30 Days	11768713	27063034	95.79198	495230	4.208022	9951739	84.56098
267R	Control	11241430	25785266	95.74593	478218	4.254067	9507772	84.57796
268L	30 Days	12444739	28656438	95.8038	522206	4.196199	10516271	84.50375
268R	Control	8279139	18869516	95.6202	362610	4.379803	7058024	85.2507
275L	30 Days	11758349	27160308	95.80234	493576	4.197664	9900528	84.19998
275R	Control	12877666	28989846	95.03996	638737	4.960037	10977624	85.24545
Sample name	Condition	Total non-unique paired	Non-unique paired	Coverage	Avg. coverage depth	Avg. length	Avg. quality	%GC
257L	2 Days	1303668	9.779567	1.91875	20.6765	36.9376	34.449	50.5457
257R	Control	1200719	9.453699	1.94552	19.2625	36.9376	34.4482	50.423
258L	2 Days	1215984	9.642635	1.95429	19.1705	36.9384	34.4706	50.5666
258R	Control	1184476	9.739033	1.83393	19.5135	36.9329	34.3646	49.9462
259L	2 Days	1239896	9.740387	1.86542	20.2443	36.9377	34.4539	50.1602
259R	Control	1296935	9.775547	1.91395	20.5061	36.9408	34.4976	50.1258
260L	10 Days	1245746	10.09234	1.98522	18.537	36.9393	34.4775	50.3433
260R	Control	1404457	9.915788	1.92428	21.8391	36.9419	34.517	49.4851
261L	10 Days	1165089	9.459545	1.81922	20.0124	36.9379	34.4608	50.8928
261R	Control	1208592	9.593545	1.86878	19.9446	36.9405	34.4914	50.2793
262L	10 Days	1287177	10.21021	2.05426	18.3302	36.9402	34.4919	50.4311
262R	Control	1221703	9.726768	1.92698	19.3236	36.9382	34.4582	50.5646
263L	20 Days	1219056	10.42897	1.66184	20.9806	36.9406	34.4952	49.8165
263R	Control	1215740	9.667474	1.8662	19.9063	36.9405	34.4986	50.3883
264L	20 Days	1289191	10.05935	1.87133	20.3336	36.9387	34.4743	50.8401
264R	Control	1185259	9.585905	1.93969	18.7671	36.9391	34.473	50.3898
265L	20 Days	1288505	10.66065	2.05431	17.5787	36.9405	34.4918	49.0353
265R	Control	1157596	9.962365	1.79364	19.197	36.9397	34.4781	49.6391
267L	30 Days	1321744	11.231	1.80399	19.6754	36.9405	34.4927	49.3159
267R	Control	1255440	11.16797	1.59051	21.2578	36.9406	34.4911	48.9605
268L	30 Days	1406262	11.30005	1.69774	22.1471	36.9423	34.5162	48.615
268R	Control	858505	10.3695	1.51204	16.3572	36.9415	34.5081	49.3748
275L	30 Days	1364245	11.60235	1.72901	20.6063	36.9423	34.515	48.4586
275R	Control	1261305	9.794516	1.8674	20.3271	36.9308	34.3295	50.4094

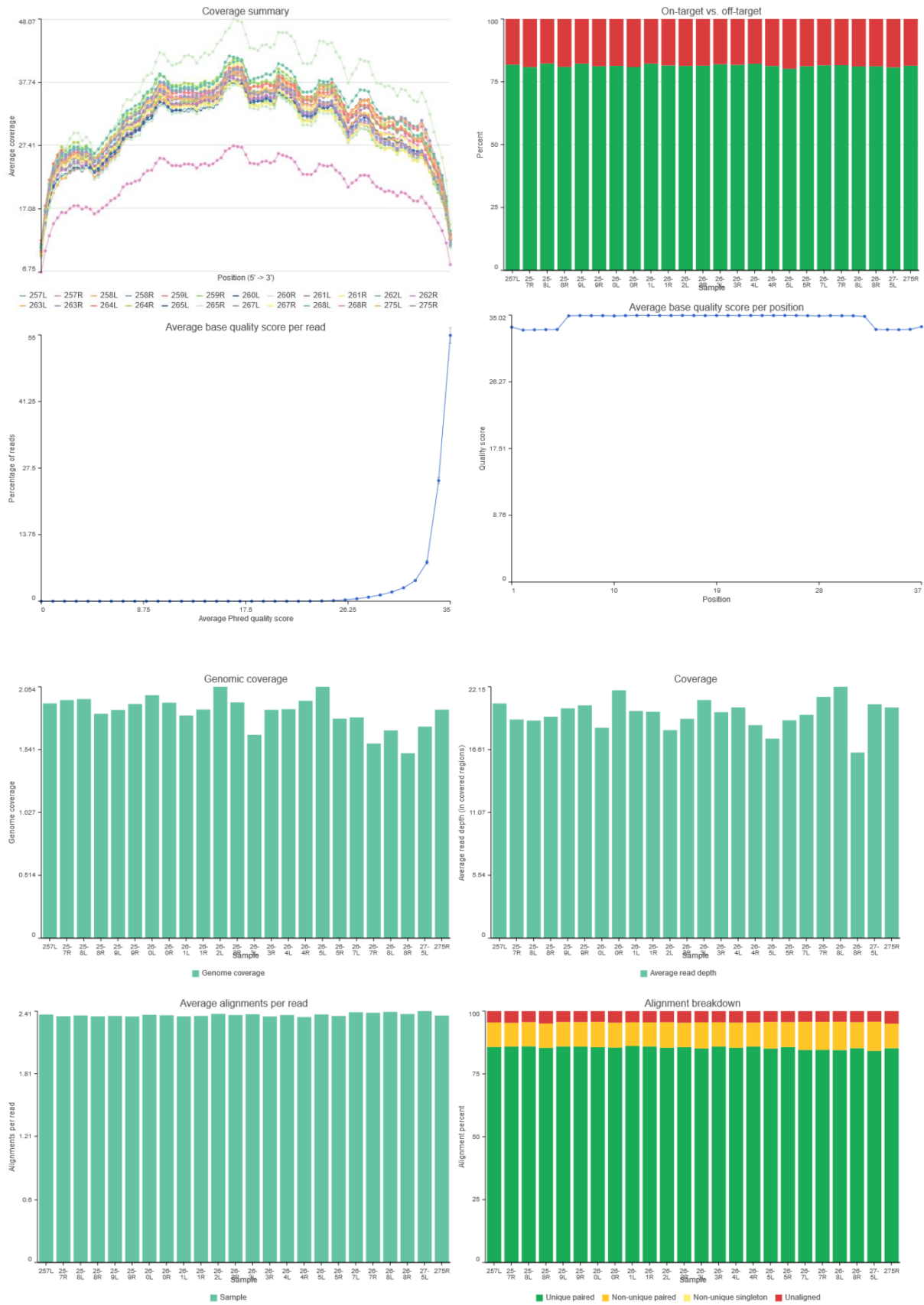


Figure 2.9: Reading left to right, top to bottom. (a) Summary report of read coverage, describing the average number of reads that align to, or "cover," known reference bases in

each library sequenced. (b) Percent of on target (green) vs off target (red) reads for individual samples. (c) Post-alignment average Phred quality score (base quality) as a percentage of total reads. (d) Average post-alignment average base quality score per position. (e) Genomic coverage in each individual sample. Coverage in sequencing refers to the number of unique reads that include a given nucleotide in the reconstructed sequence of which are samples show high coverage. (f) Average read depth for each sample. The mean mapped read depth is the sum of the mapped read depths at each reference base position, divided by the number of known bases in the reference sequence. The mean read depth metric indicates how many reads, on average, are likely to be aligned at a given reference base position. A mean read depth of 20 is considered above adequate for murine genomes. (g) Average alignments per read for each individual sample. (h) Breakdown of the aligned reads and unaligned reads.

2.48 Quantification to Ensembl transcriptome annotation model *Rattus Norvegicus*, Rnor_6.0.

Aligned reads were then quantified to the Ensembl transcriptome annotation model associated with *Rattus Norvegicus* Rnor 6.0. A quantification report was also produced to illustrate the characteristics of the aligned reads/gene counts and their coverage (Table 2.9, Figure 2.10).

Table 2.9: Summary report of post alignment count quantification report.

Sample name	Condition	Timepoint	Total reads	Fully within an exon	Partly within an exon	Fully within an intron	Fully intergenic	Incompatible paired-end	Compatible junctions	Total junctions
257L	2 Days	2 Days	12733878	71.90%	1.35%	2.76%	8.38%	15.61%	1029414	1257430
257R	Control	2 Days	12111318	70.99%	1.41%	2.79%	9.11%	15.69%	980027	1206604
258L	2 Days	2 Days	12060967	73.16%	1.30%	2.76%	7.78%	15.00%	926264	1118339
258R	Control	2 Days	11563494	72.01%	1.36%	2.76%	8.63%	15.24%	864677	1057372
259L	2 Days	2 Days	12181250	73.20%	1.29%	2.73%	7.76%	15.01%	930773	1126262
259R	Control	2 Days	12691094	71.91%	1.35%	2.61%	8.73%	15.41%	1000008	1225524
260L	10 Days	10 Days	11818009	71.66%	1.33%	3.00%	8.89%	15.13%	938141	1138576
260R	Control	10 Days	13515662	72.24%	1.30%	2.79%	8.71%	14.97%	1053644	1286758
261L	10 Days	10 Days	11770131	72.43%	1.37%	2.63%	8.27%	15.30%	937474	1136763
261R	Control	10 Days	12034969	71.67%	1.36%	2.65%	8.73%	15.59%	980454	1199701
262L	10 Days	10 Days	12052228	71.63%	1.33%	3.06%	8.63%	15.36%	949347	1156025
262R	Control	10 Days	11981301	71.35%	1.36%	2.70%	8.91%	15.68%	981010	1202947
263L	20 Days	20 Days	11169925	73.54%	1.22%	2.36%	8.07%	14.81%	835720	1016107
263R	Control	20 Days	12018817	71.93%	1.31%	2.46%	8.84%	15.46%	983229	1203917
264L	20 Days	20 Days	12232729	72.96%	1.32%	2.50%	7.91%	15.32%	917297	1118151
264R	Control	20 Days	11805653	71.40%	1.37%	2.78%	8.89%	15.57%	945686	1161783
265L	20 Days	20 Days	11572268	71.97%	1.26%	3.42%	8.70%	14.66%	822068	1000631
265R	Control	20 Days	11114335	71.94%	1.30%	2.69%	8.70%	15.37%	873359	1068995
267L	30 Days	30 Days	11273483	73.84%	1.19%	2.50%	7.60%	14.87%	797795	971467
267R	Control	30 Days	10763212	74.26%	1.13%	2.06%	7.75%	14.81%	769815	944322
268L	30 Days	30 Days	11922533	74.33%	1.12%	2.43%	7.77%	14.34%	799108	974876
268R	Control	30 Days	7916529	72.69%	1.24%	2.46%	8.64%	14.97%	612004	748363
275L	30 Days	30 Days	11264773	73.76%	1.13%	2.53%	7.98%	14.61%	770192	942058
275R	Control	30 Days	12238929	71.68%	1.35%	2.55%	8.87%	15.55%	985440	1208533
Average	N/A	N/A	11741979	72.41%	1.30%	2.67%	8.43%	15.19%	903456.1	1102979

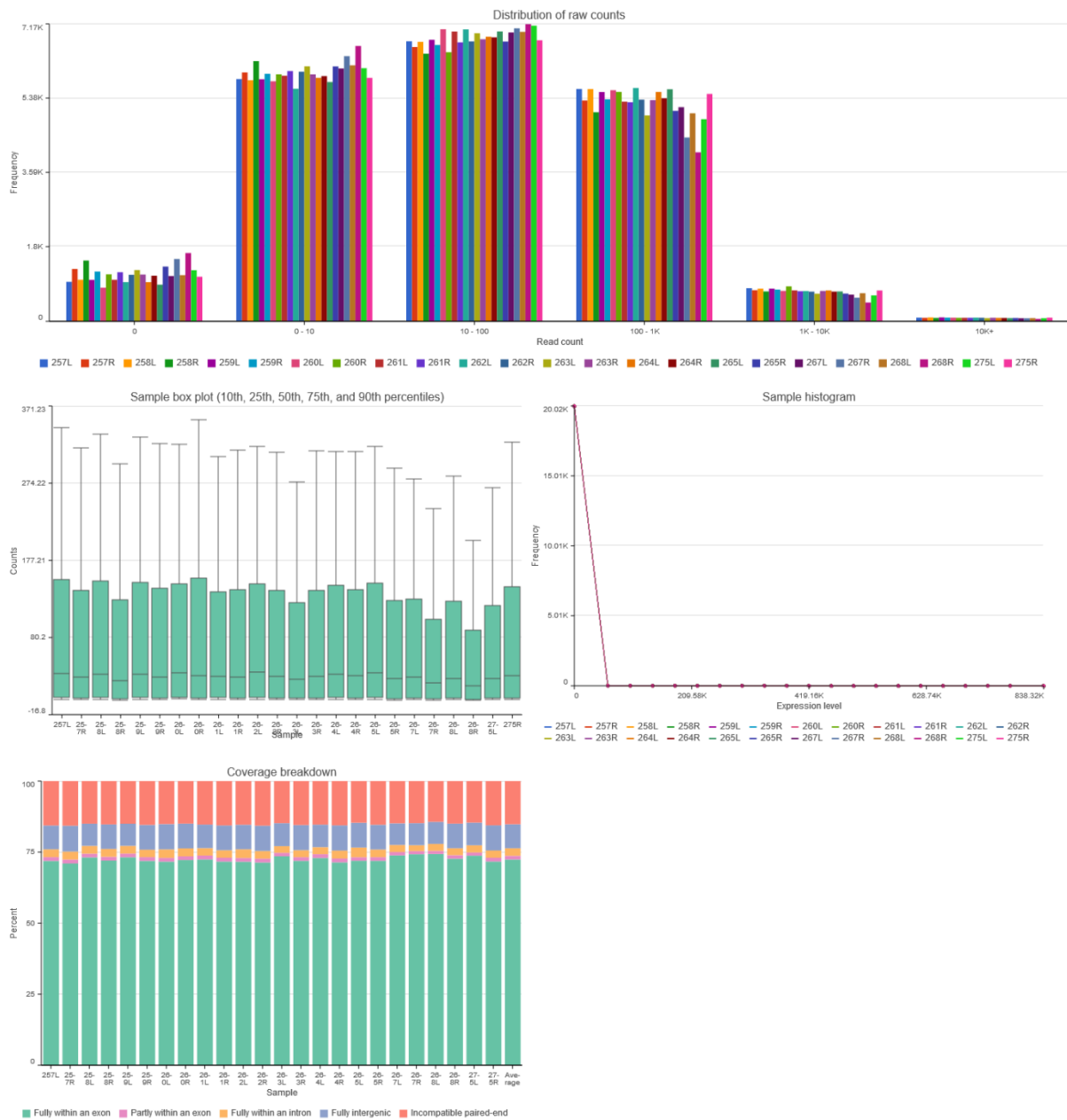


Figure 2.10: Quantification Report. (a) Frequency distribution of read counts per gene identified shows a normal distribution. (b) Box plots indicating the average count per gene for each individual sample. (c) Number of genes plotted against their mean expression level (counts associated with the gene). (d) Coverage breakdown of all reads per sample as a percentage fully within an exon, partly within an exon, fully within an intron, fully intergenic and incompatible paired ends.

2.49 Normalisation Background and DESeq2 median of ratios

Following alignment and quantitation to an annotation model, gene set analysis can nearly be performed. Prior to differential gene/transcript expression analysis and unsupervised clustering analyses, it is necessary to normalise raw counts/reads to make accurate comparisons between samples and between groups. The counts of mapped reads from the sequencing are both proportional to the expression of the RNA, as well as other factors such as sequencing depth, gene length and RNA composition. Normalisation can be performed in a number of ways to remove the effects of the additional factors listed above, so that changes in counts directly correspond to changes in the mRNA of interest and not as a result of other variables.

Sequencing depth (often referred to as read depth) describes the number of reads associated with a given nucleotide in a particular sequence of a gene. For example, in a biological replicate, if the total read time of sequencing is different, the subsequent total reads between samples will be different and therefore will need to be normalised to avoid samples with more reads conveying higher abundance of genes.

Gene length normalisation is important for comparing expression between different genes within the same biological sample. For example, if gene A is double the length of gene B, it is likely that gene A would have more overall reads mapped to it, which doesn't mean that the gene is in fact more abundant

RNA composition refers to normalising reads based on large changes in a few highly differentially expressed genes between samples and is essential for differential expression analysis. For example, in the transcriptome of a fast twitch skeletal muscle, 10% of all reads may be mapped to the fast myosin genes. If between conditions there is a complete transcriptional switch off of fast myosins there would be 10% more availability in total reads, allowing for more of the overall reads to be mapped to lower abundance genes. An increase in counts in this instance would be as a result of increased read availability rather than an actual increase in abundance of a gene/transcript.

Counts per million (CPM) is the total amount of counts scaled by the total number of reads and therefore accounts for sequencing depth but neglects the consideration of gene length

and RNA composition and can therefore only be used for gene count comparisons between replicates of the same group rather than between groups. Transcripts per kilobase million (TPM) refers to the counts per length of the gene transcript (kb), per million reads mapped so therefore accounts for both sequencing depth and gene length. Similarly, to TPM, RPKM/FPKM (reads/fragments per kilobase of exon per million reads/fragments mapped) considers sequencing depth and gene length but does not consider RNA composition of the samples. There are currently two methods that consider RNA composition in the count normalisation protocol including DESeq2's median of ratios (Anders & Huber, 2010) which uses counts divided by specific size factors determined by the median ratio of gene/transcript counts, as a relative proportion of the geometric mean per gene. Furthermore, EdgeR's trimmed mean of M values (TMM), also considers gene length by normalising by using a weighted trimmed mean of the log expression ratios between samples (Robinson & Oshlack, 2010), enabling normalisation by all factors (gene length, sequencing depth and RNA composition).

2.50 Differential Gene Expression Analysis

For our analyses we used Partek Flow's own implementation of DESeq2 median of ratios algorithm from R to normalise our read counts. Principal Component Analysis was performed on samples assigned to groups, control limbs ($n=12$), 2, 10, 20 and 30 ($n=3$ per group) days of spillover stimulation based on 24 principal components from data that was not log transformed. Gene set analysis was performed using Partek Flow Software (Partek Incorporated, Missouri, USA) and to identify differentially expressed genes between the control group and the 2, 10, 20, 30 days of training timepoints from the 20,027 gene transcripts identified.

2.51 Principal Component Analysis

Partek Flow Software (Partek Incorporated, Missouri, USA) was used to perform a principal component analysis on a default number of 24 principal components.

2.52 KEGG Pathway Analysis

Partek Flow Software (Partek Incorporated, Missouri, USA) was used to perform KEGG pathway analysis on selected filtered lists of genes.

2.53 Self-Organising Map (SOM) Analysis

In order to plot/visualise temporal changes in gene expression across the time-course studied, we implemented Self Organising Map (SOM) profiling of the change in mean gene expression within each condition using Partek Genomics Suite V.7.0 (Partek Inc. Missouri, USA).

2.54 Venn Diagram Analysis

Venn Diagram Analysis was performed using Partek® Flow® and using the VIB/UGent Venn online tool, <http://bioinformatics.psb.ugent.be/webtools/Venn/>.

2.55 Comparative Transcriptome Analysis

In order to identify common genes that are differentially expressed in response to resistance exercise, we accessed and selected genes based on their order of significance from the following publicly available studies datasets Chaillou et al., (2013), Chaillou et al., (2015), Cui et al., (2020), Pillon et al., (2020), Turner et al., (2019).

**Chapter 3: Computational Analysis of Skeletal Muscle
Immunohistochemistry to Assess Myonuclear Turnover with
Changes in Activity, Loading & Unloading of Rodent Hindlimb
Muscles.**

3.1 Abstract:

The number of myonuclei within a muscle fiber is an important factor in muscle growth, but its regulation during muscle adaptation is not well understood. We aimed to elucidate the timecourse of myonuclear dynamics during endurance training, loaded/unloaded resistance training, and nerve silencing-induced atrophy with subsequent recovery. Thus, we modulated tibialis anterior muscle activity in free-living rats with implantable pulse generators delivering electrical stimulation and with implantable osmotic pumps delivering tetrodotoxin (TTX) to silence the motor nerve without transection. We used the updated, automated software MyoVision to measure fiber type-specific responses on whole tibialis anterior cross-sections (each ~8000 fibers). Seven days of continuous low frequency stimulation (CLFS) reduced muscle mass (-12%), increased slower myosin isoforms and reduced IIX/IIB (-32%) and substantially increased myonuclei especially in IIX/IIB fibers (55.5%). High load resistance training (Spillover), produced greater hypertrophy (~16%) in muscle mass and fiber cross-sectional area (CSA) than low load resistance training (concentric) (~6%) and was associated with myonuclear addition in a fiber type-independent manner (35-46%). TTX-induced nerve silencing resulted in progressive loss in muscle mass, fiber CSA, and myonuclei per fiber cross-section peaking after 14 days (-50.7%, -53.7%, -40.7%, respectively). Myonuclear loss occurred in a fiber type-independent manner, but subsequent recovery during voluntary habitual activity suggested that type IIX/IIB fibers contained more new myonuclei during recovery from severe atrophy. This study demonstrates the power and accuracy provided by the updated MyoVision software and introduces new models for studying myonuclear dynamics in response to training, detraining, retraining, repeated disuse, and recovery.

3.2 Introduction:

Skeletal muscle is highly responsive to changes in mechanical forces, with added load being a key regulator of muscle hypertrophy, and muscle unloading being a trigger for muscle atrophy Schiaffino et al., (2013). There are several potential adaptive mechanisms that may allow trained muscle to recover faster than untrained muscle from periods of catabolism including epigenetic modifications Sharples et al., (2016), Seaborne et al., (2018a) and/or miRNA levels and myonuclear shape Murach et al., (2020b). Myonuclear number itself has also been suggested as a potentially stable indicator of previous episodes of hypertrophy Gundersen,

(2016). Myonuclei can alter their transcriptional activity in response to mechanical cues, such as those caused by exercise, as well as to internal factors such as proximity to other myonuclei Joplin et al., (1987), Cramer et al., (2020), Kirby et al., (2016b), Windner et al., (2019). Increase in synthetic activity following exercise probably reflects a shift in mRNA expression to reprogram cellular phenotype in response to the demands imposed on the muscle fiber, as well as increasing rRNA expression to increase translational efficiency and capacity Goldspink et al., (1995), Joplin et al., (1987), Nader et al., (2005).

To support transcriptional demands during muscle remodelling, it may be necessary to increase the number of myonuclei per unit cell volume. Since muscle fibers are post-mitotic, this is achieved through muscle stem cells (satellite cells), which can proliferate and then fuse to myofibers adding new myonuclei. The presence of satellite cells is not completely obligatory for short term load-induced hypertrophy McCarthy et al., (2011), or androgen-induced hypertrophy Englund et al., (2019b); however, in adult skeletal muscle Murach et al., (2017), their depletion alters the myonuclear transcriptome and blunts adaptation to exercise, proprioception and exercise capacity Goh et al., (2019), Englund et al., (2020), Englund et al., (2021). Satellite cells also play an important role in muscle homeostasis by communicating with endothelial and fibroadipogenic progenitor cells in skeletal muscle, as well as with the myonuclei themselves Verma et al., (2018), Madaro et al., (2019), Murach et al., (2020c), Murach et al., (2021). However, whether all nuclei or newly added myonuclei are permanent and able to act as a cellular memory Gundersen, (2016), or whether they can be lost through caspase dependent and caspase-independent (Endonuclease G) mechanisms is yet to be fully confirmed Dupont-Versteegden et al., (2006).

Training followed by subsequent 'detraining' has revealed that different individual muscles show a variety of responses. Six months of detraining, after 2 months of progressive weighted wheel running (PoWeR) revealed that the fiber type shifts, fiber hypertrophy and increases in myonuclear number caused by training were reversed after detraining in the gastrocnemius and plantaris Dungan et al., (2019), Murach et al., (2020b). By contrast, the soleus muscle did not lose PoWeR adaptations following detraining; however, type I fibers showed higher myonuclear content with no increase in fiber size. Clearly, the loss or addition of myonuclei following training and detraining is a complicated phenomenon with findings suggesting that there are large differences between responses according to models used, species, age, muscle

group and muscle fiber type Snijders et al., (2020a). How muscle disuse compares with detraining and whether recovery from disuse atrophy is comparable to training-induced hypertrophy in terms of myonuclear dynamics are currently unknown. The requirement for new myonuclei and whether those nuclei are retained may be controlled by a combination of motor activity, oxidative capacity and tonic stretch.

Currently, the most direct and accurate methods to assess myonuclei number are myonuclear counts in single extracted myofibers, or intravital imaging of the small number of myonuclei visible in superficial fibers Bruusgaard and Gundersen, (2008), Stewart et al., (2009), Hastings et al., (2020), Cramer et al., (2020), Hansson et al., (2020). However, these methods are labor intensive and may not represent the population of myonuclei within a muscle that may have thousands to tens of thousands of fibers with complex architectural properties, different resting/working lengths and differing activation patterns. Thus, assessing entire whole muscle cross-sections via immunohistochemical labelling as we have done here remains the most accessible and unbiased approach if performed by automatic, high throughput image analysis.

In this investigation, we combined the improved capabilities of MyoVision automated histological analysis software to characterize adaptive changes in myonuclei number per fiber on whole cross-sections of tibialis anterior, each containing between 6000 and 10,000 fibers, in 3 adaptive conditions: 1) A time course of programmed daily resistance exercise (high load, Spillover) vs. (unloaded contractions (concentric) to induce hypertrophy, 2) continuous low frequency stimulation (CLFS) to induce an endurance-trained phenotype and 3) disuse atrophy by means of reversible nerve silencing with subsequent recovery Fisher et al., (2017), Schmoll et al., (2018). We hypothesized that following our exercise training protocols, as all muscle fibers are activated synchronously, the extent of growth and myonuclear accretion may reflect the total activity time/loading similarly in all fiber types. Furthermore, as our atrophy model prevents propagation of action potentials in all muscle fibers, myonuclei may be lost in a fiber type-independent manner, but the recovery by habitual voluntary activity might produce myonuclear accretion according to the normal graded recruitment of muscle fibers.

3.3 Methods:

Disclaimer

The computational methods used in this chapter, specifically MyoVision 2.0 automated image analysis software was developed by Dr. Yuan Wen at the University of Kentucky. My own contributions to the development of the new version of the software included extensive pilot testing as an independent laboratory on the samples generated in this thesis, the data of which is provided in this chapter and Viggars et al., (2022).

Experimental Design

The animal experiments were conducted under the provisions of the Animals (Scientific Procedures) Act 1986 and approved by the British Home Office (PPL 40/3280). Male Wistar rats were group-housed with 2-3 per cage maintaining an alternating 12 h light 12 h dark cycle. The mean weight of animals used was 418 ± 57 g, with a mean age of 18 ± 2 weeks when euthanised.

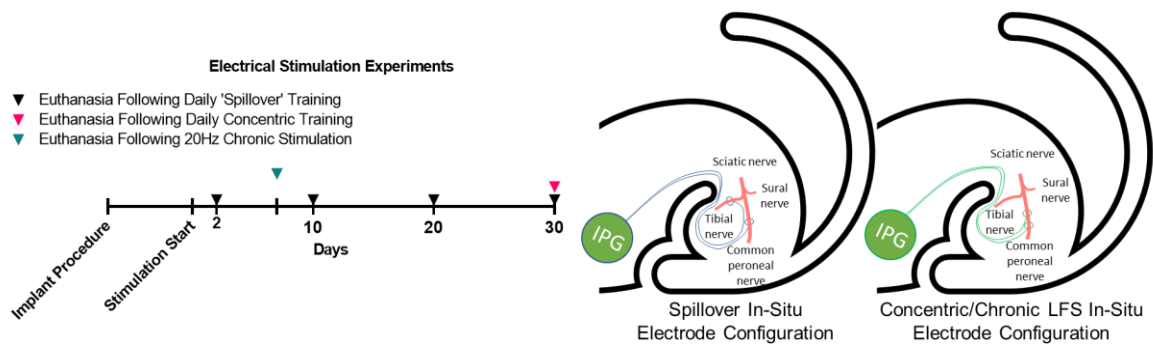


Figure 3.1: Schematic representation of electrical stimulation experimental time courses studied and timepoints of euthanasia. For electrical stimulation experiments, an implantable pulse generator (IPG) was placed within the abdomen with electrodes leading subcutaneously to the left hindlimb with two possible electrode placements. Either with the anode placed under the tibial nerve with the cathode under the common peroneal nerve (CPN) to produce Spillover (loaded) resistance training or by placing both electrodes under the CPN to elicit concentric (unloaded) resistance exercise or continuous low frequency stimulation (CLFS) mimicking endurance training.

Resistance Training Protocols & Pattern

Animals received 1 session per day of high (Spillover) or low load (concentric) resistance training in the left hind-limb via stimulation from an implanted pulse generator (IPG) as previously described Schmoll et al., (2018), for 2, 10, 20 or 30 days or underwent sham surgery. Briefly, for high load (Spillover) exercise to elicit slight stretch under load, the dorsiflexor muscles, tibialis anterior (TA) and extensor digitorum longus (EDL), received supramaximal activation via a cathode placed underneath the common peroneal nerve (CPN), while the anode was positioned underneath the tibial nerve and the stimulation current was adjusted by remote programming, to recruit enough of the gastrocnemius, plantaris and soleus (plantarflexor muscles) to provide resistance against the contraction of the dorsiflexors. In an additional group, animals received 1 session per day of unresisted (concentric) contractions of the dorsiflexors for 30 days by placing both electrodes under the CPN during implantation so there was no activation of the plantarflexor muscles, and the dorsiflexors contracted against a low load.

Daily training was delivered automatically by the IPG and consisted of an initial 10 seconds of preparatory stimulation at a low frequency ($F = 4\text{Hz}$, phase width $=258\ \mu\text{s}$, current $=$ approximately 1 mA), followed by 5 sets of 10 tetanic contractions at 100 Hz. Each contraction lasted for 2s with 2s rest between contractions and 2.5 minutes of rest between sets. The stimulation was delivered only in the left hind-limb, so muscles of the right hind-limb act as unstimulated contralateral controls. Stimulation with these settings and the amplitude chosen to balance dorsiflexion and plantarflexion described above was well-tolerated by all animals without further anaesthesia or sedation. Regular observations during daily training across the time course revealed no adverse behavioural signs.

Continuous Low Frequency Stimulation (CLFS)

As previously described Jarvis and Salmons, (1991), Fisher et al., (2017), the ankle dorsiflexors of the left hind-limb were continuously stimulated (24 h per day), at 20Hz for 7 days. This pattern has previously been shown to induce a transformation from the control fast phenotype towards a slower phenotype in the TA Jarvis, (1993).

Electrical Stimulation Surgical Procedure

Animals were anaesthetised during implant procedures by inhalation of a gaseous mixture of isoflurane in oxygen at approximately 3% for induction and 1-2% for maintenance. Once

anaesthetised, a subcutaneous injection of Enrofloxacin ($5\text{mg}/\text{kg}^{-1}$ body mass (Baytril®) and an intramuscular injection of Buprenorphine ($0.05\text{mg}/\text{kg}^{-1}$ body mass) (Temgesic, Indivior, Slough, UK) into the right quadriceps was administered with strict asepsis maintained throughout the procedure. Silicone encapsulated radio frequency controlled implanted pulse generators (IPGs) (MiniVStim 12B, Competence Team for Implanted Devices, Center for Medical Physics and Biomedical Engineering, Medical University Vienna, Austria) were used to deliver impulses. The devices were implanted into the abdominal cavity accessed by a lateral incision through the skin and peritoneum, between the rib cage and pelvis on the left side of the animal. A polyester mesh attached to the IPG was incorporated into the suture line closing the peritoneum, securing the device against the abdominal wall. Two PVC-insulated stainless-steel electrode leads (Cooner Sales Company, Chatsworth, California, U.S.A.) with terminal conductive loops, were fed through the peritoneal incision and tunnelled under the skin to the lateral side of the upper left hind-limb. A second incision was made through the skin and biceps femoris muscle to give access to the CPN under which the cathode was placed (to stimulate the dorsiflexors). The anode was either placed alongside the cathode to stimulate the CPN alone and thus to produce unresisted (concentric) contractions or placed in the muscular tissue deep to the tibial nerve about 5mm distal to its bifurcation from the sciatic nerve to allow Spillover stimulation to produce additional partial activation of the plantarflexors to resist the contraction of the dorsiflexors. All incisions were closed in layers and 3-7 days were allowed for recovery from surgery before the start of the training protocol.

Nerve Silencing-Induced Disuse by Tetrodotoxin & Recovery Protocols

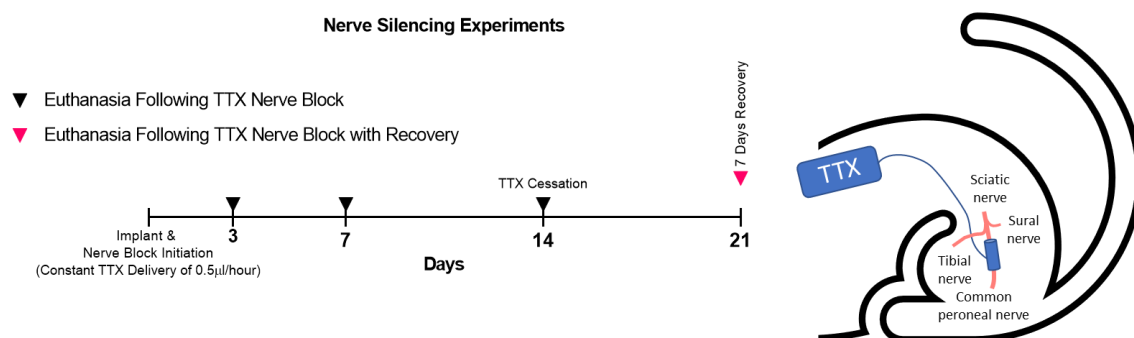


Figure 3.2: An overview of the in-situ placement of the osmotic pump loaded with a pre-determined volume of tetrodotoxin (TTX), placed in the scapula region with silicone tubing

leading to the left hind-limb and the silicone cuff that encircled the common peroneal nerve (CPN) to selectively block the ankle dorsiflexors, while maintaining normal plantarflexion.

The CPN, the motor nerve responsible for contraction of the TA and EDL, was silenced for pre-set periods of 3 days, 7 days, or 14 days. Atrophy of the dorsiflexors was produced without signs of fiber necrosis or denervation assessed by H&E staining. A separate group was used to assess recovery after 14 days of tetrodotoxin (TTX) treatment. Osmotic pumps were appropriately loaded so that the TTX infusion was exhausted after 14 days, and nerve activity could resume during 7 days of muscle recovery via habitual physical activity. Pumps were weighed before implantation and again after explant to confirm that the expected volume of TTX had been delivered over the time course of the experiment. Muscle mass data from these groups has previously been reported Fisher et al., (2017).

Tetrodotoxin Administration Surgical Procedure

Animals were anaesthetised as previously described for the implantable stimulator surgeries. A miniosmotic pump (Mini Osmotic Pump 2002; Alzet, Cupertino, CA, USA) was implanted subcutaneously in the scapular region. Silicone tubing was tunnelled under the skin to the site of the CPN. A second incision was made laterally through the skin, just proximal to the knee joint and bicep femoris muscle (posterior compartment of the thigh) in order to give access to the CPN responsible for action of the dorsiflexors. A silicone cuff extending from the silicone tubing was placed around the nerve. All incisions were closed in layers. The miniosmotic pump (Mini Osmotic Pump 2002; Alzet, Cupertino, CA, USA) delivered TTX, a sodium channel blocker that prevents generation and propagation of action potentials at the CPN of the left hind-limb. The osmotic pump successfully delivered 0.5 μ l/h TTX (350mg/ml in sterile 0.9% saline), by continuously blocking ankle dorsiflexion, whilst maintaining normal voluntary plantarflexion via the tibial nerve. Disuse of the dorsiflexors by this means produces progressive atrophy Fisher et al., (2017). The welfare and mobility of the rats was checked daily by animal welfare staff. There was little disturbance to mobility, but sometimes 'foot drop' was observed, a gait abnormality characterised by dropping of the forefoot due to the inhibition of dorsiflexion.

Rat muscle sampling and preservation

Animals were humanely sacrificed using rising concentrations of carbon dioxide, followed by cervical dislocation. TA muscles from both hind limbs were immediately harvested, cleaned of excess connective tissue and weighed. The mid-belly of the TA was cut out, placed on cork for transverse sectioning and frozen in melting isopentane above liquid nitrogen for later immunohistochemical analysis.

Immunohistochemistry

Muscle samples were sectioned at 10µm using an OTF5000 Cryostat (Bright Instruments, UK) onto Thermo Scientific™ SuperFrost Plus™ Adhesion slides (Thermo Fisher Scientific Inc, Waltham, USA). Muscle cross-sections were labelled with primary antibodies against dystrophin (MANDYS8-8H11 or a polyclonal dystrophin antibody) to demarcate the inside of the sarcolemma for all the experimental samples. Fiber type analysis was performed on TA muscles within the 30 days Spillover resistance training, 30 days concentric resistance training, 7 days 20Hz CLFS, 14 days atrophy and 14 days atrophy with 7 days recovery groups, through labelling of dystrophin, as well as BA-D5 (anti myosin type I) and SC-71 (anti myosin type IIA) hybridoma supernatants, diluted in immunobuffer (IB) overnight and then washed 3 x 10 minutes in IB. Unstained muscle fibers were later measured as IIX/IIB fibers. Appropriate secondary antibodies with specific Ig fragments were diluted in IB for 2 hours, followed by 3 x 10 minutes in IB. IB consists of 50mM glycine (Merk 1.02401_1000), 0.25% BSA, 0.03% saponin (Sigma 100g S-7900), and 0.05% sodium azide in phosphate buffered saline (PBS, 10mM phosphate pH 7.4, 150mM NaCl).

For all cross-sections, following incubation with primary and secondary antibodies (Table 2.1), nuclei were labelled with DAPI (D1306, Thermofisher Scientific) at a concentration of 30nM diluted in PBS for 30 minutes, prior to 3 x 5-minute washes in PBS. Coverslips were then mounted onto cross-sections with VECTASHIELD® Antifade Mounting Medium (Vector Laboratories, UK). Hematoxylin and Eosin (H&E) staining was also performed on serial or 'near serial' sections within ~10-60µm, to check for evidence of damage, de/regeneration, and fiber loss by independent researchers.

While SDS-Page is generally considered as a gold standard 'semi-quantitative' measure of myosin heavy chain content, performing reproducible blots can be labour-intensive. Immunohistochemistry is now more widely used in the field due to it being relatively

inexpensive, reproducible, and accurate determination of fiber type. Antibodies generated by Dr. Schiaffino's lab in Padova (BA-D5-type I-MIgG2b, SC-71-IIA-type IIA-MIgG1, BF-F3-type IIB-MIgM), and Dr. Hoh's lab in Sydney (6H1-type IIX-MIgM), are almost always used by the muscle community after they were deposited to the Developmental Studies Hybridoma Bank (DSHB) for extremely cheap redistribution and have been shown to react across a wide range of species (Bovine, Canine, Fish, Goat, Guinea Pig, Horse, Human, Lamb, Llama, Mouse, Porcine, Rabbit, Rat, Zebrafish) due to the conservation of the native myosin heavy chain protein. Of note the SC-71 antibody is specific to IIA in rodents, whereas it recognises IIA and IIX in humans and canines. Due to the wide use of these monoclonal antibodies by our collaborators at the University of Kentucky, we did not need to perform optimisation of antibody concentration on unfixed rat tissue. See the following from collaborators and other labs that have utilised the same antibody cocktails, Burke et al., (2021), Eftestøl et al., (2016), Hettinger et al., (2021), Lucas et al., (2000), Mortreux et al., (2021), Murach et al., (2019b), Murach et al., (2020b), Roberts et al., (2020), Schiaffino, (2018), Viggars et al., (2022), Wen et al., (2018a).

Imaging

Once labelled, whole muscle cross-sections were imaged using a widefield fluorescent microscope (Leica DMB 6000, Wetzlar, Germany) with a 10x objective. Multiple images were automatically stitched together using the tilescan feature in the Leica Application Suite.

MyoVision 2.0 Analysis:

MyoVision 2.0 introduced major upgrades to the original MyoVision software, but the fundamental workflow including fiber detection, fiber type classification, and myonuclear counting remained essentially the same as described previously Wen et al., (2018b). For fiber detection, the software uses the single channel intensity image of dystrophin labelling as an input as well as the pixel scale ($\mu\text{m}/\text{pixel}$) to allow for calculation of mean fiber cross-sectional area in units of square micrometres. Following fiber detection, a single channel intensity image of immuno-labelled myosin heavy chain or nuclei can be provided to the software to classify fiber type or quantify myonuclei number. For each myofiber cytoplasmic region excluding the periphery, the mean myosin heavy chain immunofluorescence intensity was quantified on a scale of 0 to 1, with 1 being maximum signal for the section. Only fibers with

mean myosin heavy chain intensity greater than 0.5 were classified as true for that fiber type being measured. When analysing multiple fiber types, the image corresponding to each fiber type was analysed independently. Thus, a fiber classified as “negative” would represent false for all fiber types included in the analysis whereas a “hybrid” classification would indicate co-expression of at least two different myosin heavy chain isoforms within the same fiber. The criteria for myonuclear classification remain the same as in the previous version; specifically, a nuclear region with its centroid inside the fiber dystrophin border and at least 50% of its total area within the fiber cytoplasm is counted as a myonucleus.

A major upgrade to the software is the implementation of neural networks in fiber detection and fiber type classification steps. As summarized in Appendix 3, multiple steps in the previous MyoVision algorithm have been replaced with U-net models Ronneberger et al., (2015), which demonstrated superior performance in the segmentation of grayscale intensity based images of cells. The models were trained using annotated images of 256 by 256 pixels. Briefly, images of whole cross-sections were labelled as true for foreground (i.e., fiber boundary) and false for background (i.e., non-specific signals or staining artefacts). These images along with their ground truth label were separated into 256x256 pixel regions. The same image and ground truth label were then reduced by two-fold in size sequentially, and 256x256 pixel regions were extracted from the smaller images in a similar fashion as the original image. Reducing the image size allows for the model to learn at different image resolutions and different magnifications. Images representing 1x, 0.5x, and 0.25x along with their ground truth labels were used to train the weights of a U-net model for up to 100 epochs at 300 steps per epoch using Keras (v2.2.4) and Tensorflow (v1.13.1). Models were similarly trained for each step in the algorithm to replace the corresponding steps in the previous version of the software (Appendix 3). Of note, the previous software included the active contour algorithm by default, which expands the fiber contour as close to the inner edge of the dystrophin border as possible to allow for myonuclear counting. This step had been relocated to the nuclear counting analysis exclusively due to its resource intensiveness and the fact that general fiber detection does not require such stringent delineation of the inner edge of the sarcolemma. This modification led to slightly smaller fiber cross-sectional area values (~5%) compared to the previous version of the software. This modification was favorable not only from a computational resource perspective, but also resulted in values

more in line with various other approaches in the literature that do not include any myonuclear analysis. The software will be made freely available to the research community and additional documentation for the current version can be found on www.myoanalytics.com/myovision2.

In addition, users now have control over circularity, solidity and eccentricity parameters for identifying fibers (Appendix 4), for analysis of different muscle phenotypes and extreme atrophic conditions. Other functionalities introduced in this upgrade include robust detection of whole cross-sections, batch processing of images for large projects, export of representative images from the software, exporting images from Olympus microscopes, adjusting images to control for background noise, and output of multiple shape descriptors for each fiber.

A total of 166 complete cross-sections of rat TA were generated by tile scanning and reconstructing to generate single image files for each muscle. These were analyzed in the process of beta testing of the new software taking an average of 29.80 ± 4.87 minutes per cross-section for detection and analysis of fiber CSA, three fiber types and myonuclear number on a PC Specialist laptop, equipped with an Intel® Core™ i7-6700K CPU 4.00GHz processor and 64GB of RAM.

Further information on the use of MyoVision 2.0 software can be found in appendices 3-6.

Manual Quantification versus Myovision 2.0 for assessing severely atrophied muscle fibers

Hematoxylin and Eosin (H&E) stained cross-sections were used for manual quantification of fiber number, which was performed on 5 self-selected fields of view containing (~450-600) muscle fibers with the most severe atrophy after 14 days of TTX treatment. Using the multi-point tool in Image-Pro Plus 5.1 software (Media Cybernetics, MD, USA), fiber number was counted and then compared with analysis by Myovision of the serial immunohistochemically labelled field of view, identified by means of landmarks such as blood vessels or distinctive connective tissues.

Statistics

Data are presented as the % change between the left experimental hind-limb and right internal contralateral control hind-limb for overall muscle mass (mg/kg bodyweight), fiber

CSA, myonuclei per fiber cross-section and myonuclear domain across all experimental models, that is, the absolute difference (positive or negative) expressed as a percentage of the control value. The resultant percentage changes were then compared via one-way ANOVA, followed by Tukey's post-hoc analysis to confirm differences between groups. For fiber type-specific analysis, absolute values of fiber number, fiber type proportion, fiber CSA, myonuclei per fiber cross-section and myonuclear domain were compared between groups using one-way ANOVA's, followed by Tukey's post-hoc analysis to confirm differences between groups. Simple linear regression was also performed on % changes between muscle mass, fiber CSA, myonuclei per fiber cross-section and myonuclear domain size. For the recovery group from TTX, co-efficient of variation was performed on values produced by expressing the 14 days TTX with 7-day recovery muscle values, as a percentage change from the mean 14-day TTX treatment values to show the extent of myonuclear addition as a % increase, rather than a % decrease from baseline. Significance was set at $P < 0.05$ for all statistical analyses, performed in GraphPad Prism 9.0 software. All data are presented as mean \pm standard deviation (SD).

Furthermore, in order for one-way ANOVAs to be performed on percentage change data, it was confirmed that there were no significant differences between any of the control limb measurements which may bias or influence the data. Viggars et al., (2022) reported that there were no significant differences in body weight (Table 1) between any of the control groups. Further analysis revealed no significant differences between any of the groups when the raw TA muscle weight of the contralateral control limb was compared via a one-way ANOVA with Tukey's multiple comparisons test, to generate an adjusted P value. For this reason, we continued with presenting statistical analysis on the percentage changes between the left and right limbs for muscle mass and CSA. Despite there being no significant differences between groups, we note that there was a trend towards significance between 3- and 7-days atrophy in the contralateral muscle weights ($P = 0.0932$) with a mean difference of 0.0515 grams. In the spillover resistance training dataset, there was a trend for a significant difference between the sham contralateral muscle weights and 30 days spillover training contralateral muscle weights, ($P = 0.0636$), with a mean difference of 0.1205 grams between these muscle groups. As the variance in the individual data points is shared within the figures for fiber type specific

measurements, we do not believe this will affect the interpretation of the findings. These differences can be visualised in Appendix 7.

3.4 Results:

Tibialis anterior (TA) fiber type, number, size and myonuclear characteristics in control hind-limbs

We first sought to assess the fiber type composition, fiber cross-sectional area (CSA) and myonuclear-related characteristics of the rat TA muscle in 32 untreated control hind-limbs across all our experimental conditions. Despite the TA being a predominately fast-twitch muscle, we pay particular attention to the slower, more oxidative myosin isoform-containing muscle fibers as they still make up about 25% of all muscle fibers at the mid-belly. Our data (Figure 3.3A) confirms previous measurements of fiber type percentages in rat TA with IIX/IIB fibers ($75.7 \pm 8.4\%$) representing a significantly higher population than all other measured fiber types ($P < 0.00001$). While IIA fibers represented a significantly lower proportion of the TA muscle ($21.29 \pm 7.1\%$), they represented a significantly higher proportion than type I/IIA hybrids ($3.09 \pm 2.4\%$, $P = < 0.0001$) or pure type I fibers ($2.04 \pm 1.1\%$, $P = < 0.0001$), respectively. There was no significant difference between the proportion of type I and type I/IIA hybrid fibers, $P = 0.859$. As well as being the predominant fiber types in the TA, type IIX/IIB fibers also possess significantly higher mean fiber CSA ($2380 \pm 327 \mu\text{m}^2$) than all other fiber types measured (Figure 3.3B), $P < 0.00001$. Type IIA mean fiber CSA ($1399 \pm 212 \mu\text{m}^2$), was significantly larger than both type I/IIA hybrid fiber CSA ($1158 \pm 208 \mu\text{m}^2$, $P = 0.0010$) and type I fiber CSA ($1180 \pm 229 \mu\text{m}^2$, $P = 0.0053$). Furthermore, there was no significant difference between type I/IIA hybrids and type I fiber CSA. Interestingly, there was no significant difference between any of the fiber types for the number of myonuclei per fiber cross-section (Figure 3.3C), with type I, I/IIA hybrids, IIA, and IIX/IIBs containing 0.96 ± 0.2 , 1.01 ± 0.22 , 1.09 ± 0.22 , 1.03 ± 0.23 myonuclei per cross-section, respectively. As a result, myonuclear domain size was significantly larger in type IIX/IIB fibers ($2564 \pm 1742 \mu\text{m}^2$) than all other fiber types measured, $P < 0.0001$ (Figure 3.3D). There was no significant difference between type I ($1417 \pm 620 \mu\text{m}^2$), type I/IIA hybrids ($1483 \pm 727 \mu\text{m}^2$) and type IIA ($1362 \pm 544 \mu\text{m}^2$) myonuclear domain sizes. The mean total fiber number detected across all control TAs ($n=32$) was $8060 \pm$

1078 per TA (Figure 3.3E). Despite a large sample size, co-efficient of variation (CV) was still 13.38% for total fiber number, demonstrating the need for an internal contralateral control measurement. The CV of the difference in fiber number between left and right hind-limbs is only 5.04% from 63 pairs of TAs in this study. Total fiber number was not significantly different between any group or between the left experimental TA and right internal contralateral control TA after any treatment ($P > 0.05$) (Figure 3.3E). Some variation was present between left and right hind-limbs in the same animal which we believe is a combination of natural fiber number variation between contralateral limbs.

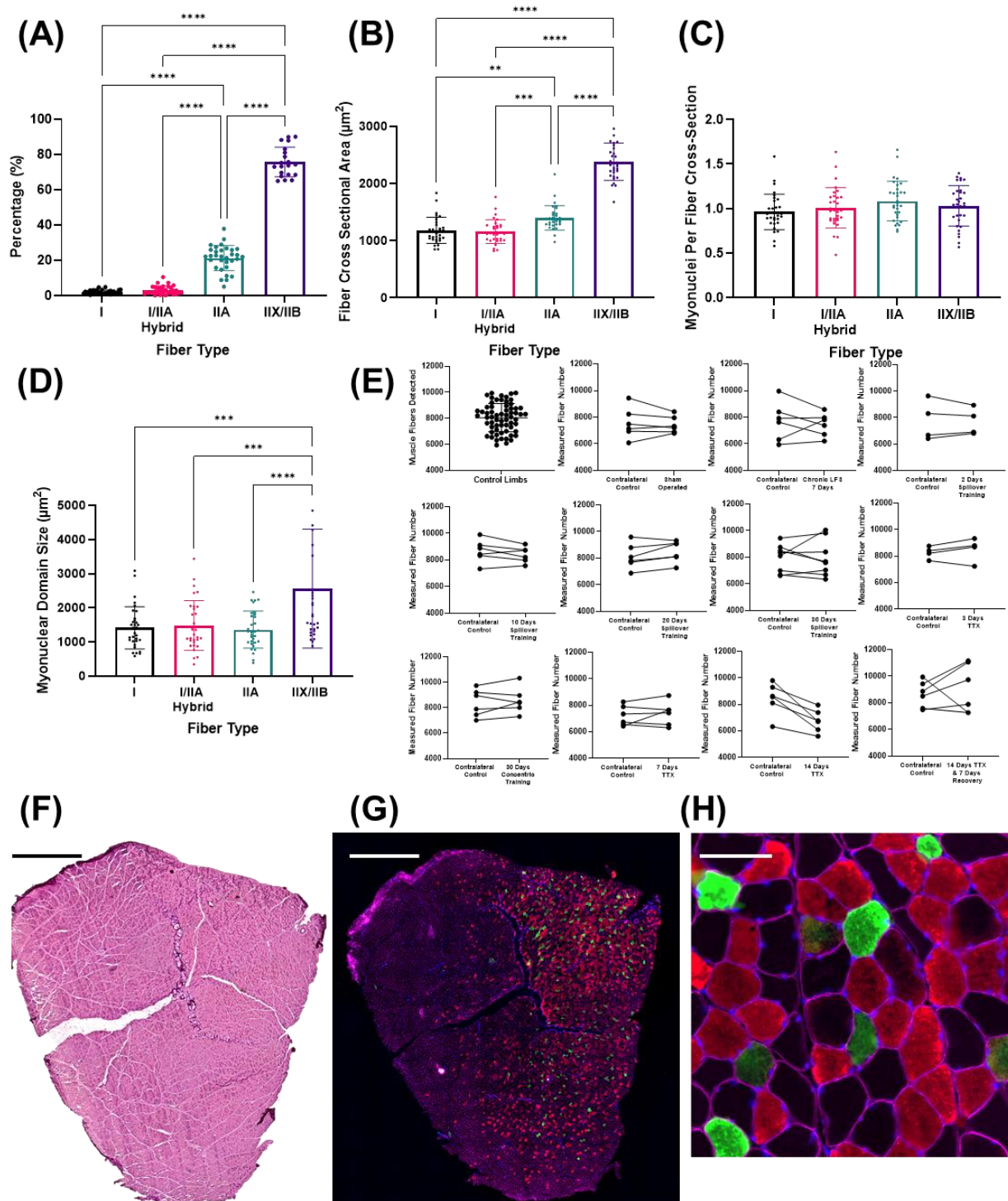


Figure 3.3: Control tibialis anterior (TA) muscles. (A) Fiber type distribution, (B) Muscle fiber cross-sectional area, (C) Myonuclei per fiber cross-section, (D) Myonuclear domain size. $n = 32$. (E) Muscle fibers detected per mid-belly transverse cross-section. $n = 64$. (F) Muscle fibers detected between experimental condition groups and their contralateral control limb. $*P \leq 0.05$. $**P \leq 0.01$. $***P \leq 0.001$. $****P \leq 0.0001$. Mean \pm Standard Deviation. (G) Example

Hematoxylin and eosin staining of TA mid-belly cross-section following 14 days of TTX treatment for assessment of damage, degeneration and denervation. (H) Serial immunofluorescence section of G, depicting the deep oxidative portion toward the top right of the transverse section (More green and red fibers). (Magenta = Dystrophin, Blue = Nuclei, Green = Type 1, Red = Type IIA, Black Fibers = Type IIX/IIB). Scale bar = 2000 μ m. (I) Higher magnification of muscle fiber staining from deep oxidative portion. Scale bar = 40 μ m.

Continuous low frequency stimulation (CLFS) of the TA induced a reduction in fiber CSA, an increase in myonuclear content and changes in myosin heavy chain isoform composition.

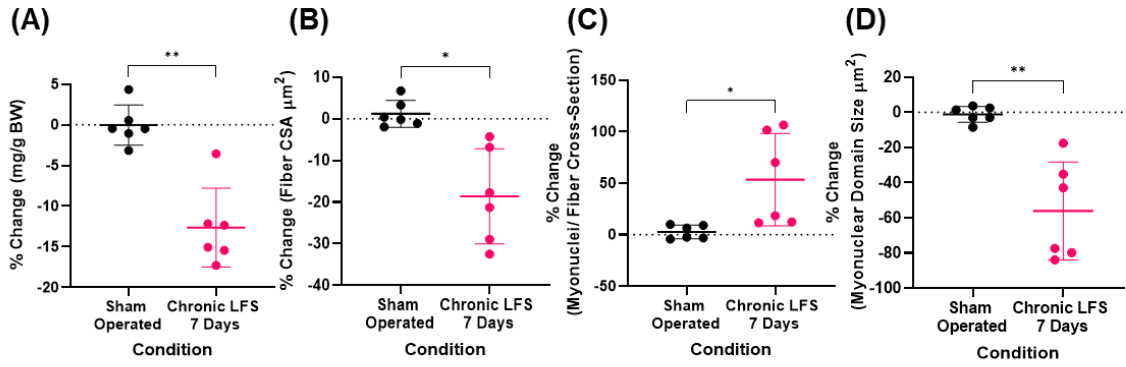
To check that surgical intervention alone did not alter muscle mass, fiber CSA or myonuclear characteristics, sham IPGs and electrodes were implanted in the left hind-limb, and animals given 7 days to recover before euthanasia and muscle assessment. There were no significant differences in any characteristics studied between the operated and contralateral control TA in this sham group (Figure 3.4A-D). By contrast, 7 days of 24 hour per day 20Hz stimulation caused a significant decrease in muscle mass ($-12.6 \pm 4.86\%$, $P = 0.0026$) (Figure 3.4A) in comparison to the unoperated control TA, concomitant with a similar decrease in muscle fiber CSA ($-18.59 \pm 11.41\%$, $P = 0.024$), Figure 3.4B). Despite the loss in mass and fiber CSA, there was a highly variable yet significant increase in myonuclei per fiber ($53.44 \pm 44.87\%$, $P = 0.0328$, Figure 3.4C) when assessed across the entire muscle cross-section, resulting in a significantly lower myonuclear domain size ($-56.08 \pm 27.87\%$, $P = 0.0097$, Figure 3.4D).

When assessing fiber type-specific changes, there was a shift in fiber type proportion (Figure 3.4E-H) with a significant reduction in IIX/IIB fibers from $80.5 \pm 8.4\%$ to $62 \pm 11.3\%$, $P = 0.0003$ after 7 days of CLFS. The percentage of type I ($2.09 \pm 1.6\%$ vs. $4.95 \pm 2.95\%$, $P = 0.99$) and IIA fibers ($15.65 \pm 6.75\%$ vs. $15.53 \pm 2.9\%$, $P = 0.99$) did not alter significantly between control and CLFS limbs respectively, although there was a substantial increase in Type I/IIA hybrids following CLFS ($1.78 \pm 1.8\%$ to $17.52 \pm 8.2\%$, $P = 0.0032$) suggesting that IIX/IIB fibers had shifted to IIA and existing IIA fibers had shifted to a type I/IIA hybrid phenotype. Interestingly, there were no significant differences in fiber CSA (Type I Control, $1357 \pm 225\mu\text{m}^2$ vs. Type I CLFS, $1252 \pm 100\mu\text{m}^2$, $P = 0.99$. Type I/IIA hybrid control $1201 \pm 370\mu\text{m}^2$ vs. Type I/IIA Hybrid CLFS $1061 \pm 160\mu\text{m}^2$, $P = 0.97$. Type IIA Control $1370 \pm 141\mu\text{m}^2$ vs. Type IIA CLFS $1316 \pm 157\mu\text{m}^2$, $P = 0.99$. Type IIX/IIB control $2253 \pm 371\mu\text{m}^2$ vs. Type IIX/IIB CLFS $1954 \pm 312\mu\text{m}^2$, P

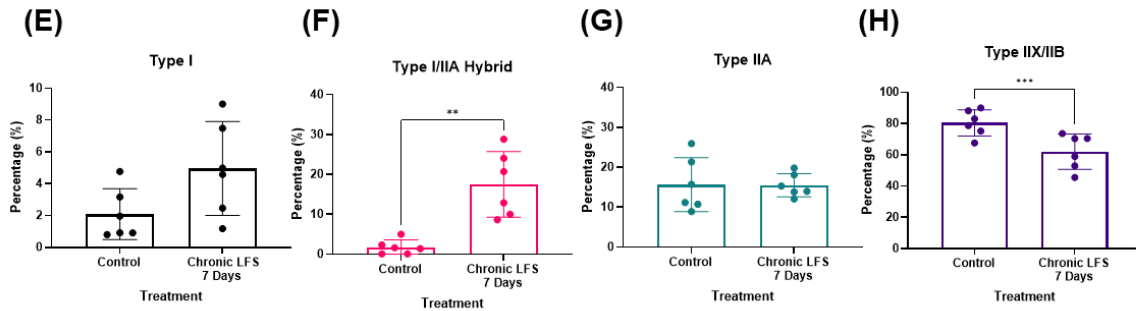
= 0.45 (Figure 3.4I-L), despite the overall significant decrease in muscle fiber CSA ($-18.59 \pm 11.41\%$, $P = 0.024$). Therefore, the transformation of IIX/IIB to IIA myosin isoforms is probably the combined effect of insignificant decreases in fiber size, as well as a shift in fiber type proportion (Figure 3.4E-H).

To further elucidate the significant increase in myonuclei per fiber across the entire muscle cross-section following CLFS, we analysed myonuclei per fiber cross-section for each fiber type. While there were trends suggesting addition of myonuclei in Type I (0.88 ± 0.15 vs. 1.06 ± 0.16 , $P = 0.83$, Figure 3.4M), Type I/IIA hybrid (0.94 ± 0.06 vs. 1.1 ± 0.16 , $P = 0.85$, Figure 3.4O), and Type IIA (0.94 ± 0.19 vs. 1.26 ± 0.23 , $P = 0.14$, Figure 3.4N) fibers, the increase only reached significance in IIX/IIB fibers (0.85 ± 0.23 vs. 1.32 ± 0.31 , $P = 0.0044$, Figure 3.4M-P). This was further reflected in the sizes of the myonuclear domain, with no significant differences between control and CLFS in Type I ($1825 \pm 441\mu\text{m}^2$ vs. $1177 \pm 294\mu\text{m}^2$, $P = 0.95$, Figure 3.4Q), Type I/IIA hybrid ($1603 \pm 948\mu\text{m}^2$ vs. $932 \pm 262\mu\text{m}^2$, $P = 0.94$, Figure 3.4R), and Type IIA ($1634 \pm 468\mu\text{m}^2$ vs. $893 \pm 304\mu\text{m}^2$, $P = 0.90$, Figure 3.4S) fibers, but a significantly lower in IIX/IIB myonuclear domain size ($3990 \pm 2554\mu\text{m}^2$ vs. $1232 \pm 394 \mu\text{m}^2$, $P = 0.0007$, Figure 3.4T).

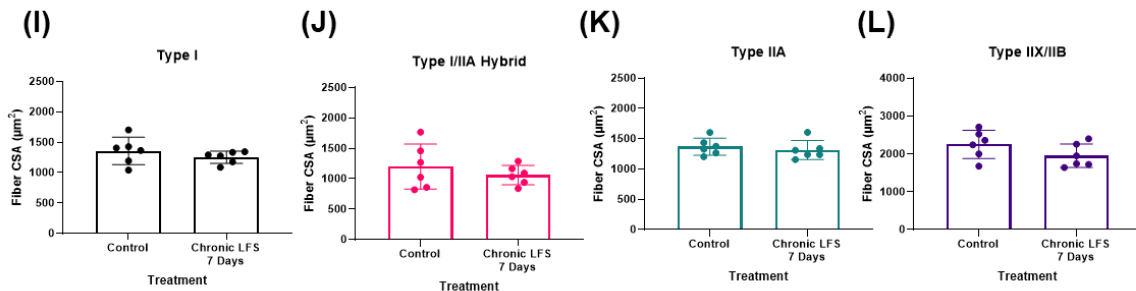
Response to 7 days continuous, low frequency stimulation (20Hz)



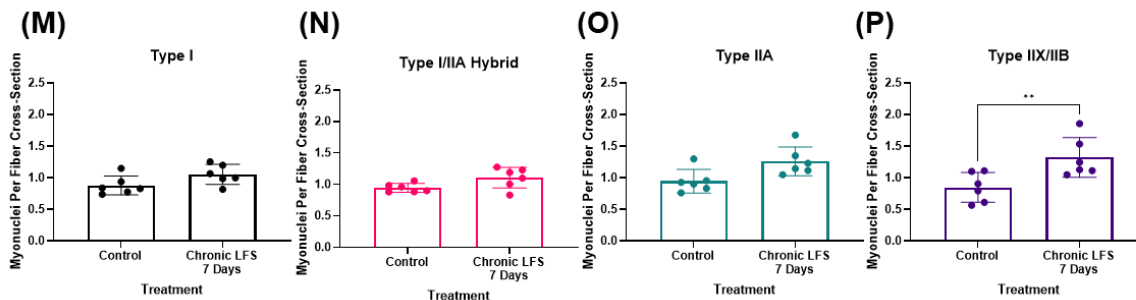
Fiber Type Percentages



Fiber Area



Myonuclei Per Fiber Cross-section



Myonuclear Domain Size

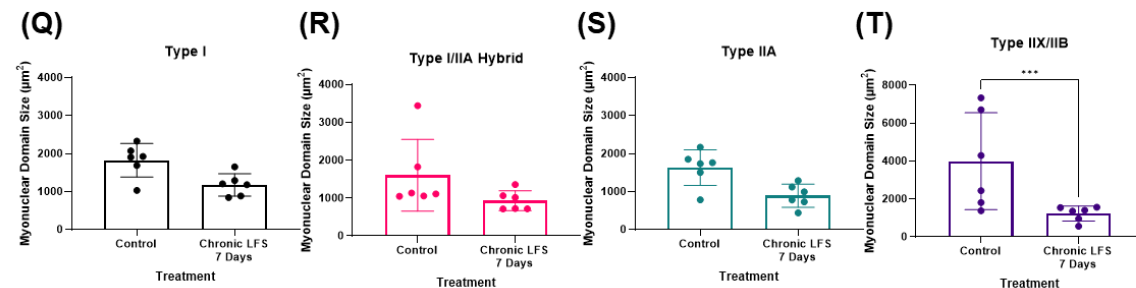


Figure 3.4: (A) Percentage change in muscle mass between the left experimental tibialis anterior (TA) and right contralateral control TA, following 7 days of continuous 24-hour low-frequency stimulation (CLFS) and 7 days post sham surgery. (B-D) Fiber CSA, myonuclei per fiber cross-section and myonuclear domain size assessed across all muscle fibers, expressed as percentage change between left experimental TA and right contralateral control TA. (E-H) Fiber type proportions in control, 30 days Spillover training and 30 days concentric training. (I-L) Fiber type-specific fiber CSA. (M-P) Fiber type specific myonuclei per fiber cross-section measurements. (Q-T) Fiber type specific myonuclear domain sizes. * $P \leq 0.05$. ** $P \leq 0.01$.

*** $P \leq 0.001$. **** $P \leq 0.0001$. Mean \pm Standard Deviation.

Spillover resistance training produces a greater hypertrophic and myonuclear response than concentric resistance training.

Spillover resistance training (loaded contractions) produced a $3.3 \pm 1.6\%$ change in muscle mass after just 2 days of stimulation ($P = 0.1$) and reached statistical significance after 10 days ($13.6 \pm 5.8\%$, $P = < 0.0001$), 20 days ($16.7 \pm 4.4\%$, $P = < 0.0001$) and 30 days ($15.9 \pm 5.6\%$, $P = < 0.0001$), in comparison to both sham surgery ($P < 0.001$) and their contralateral internal controls ($P < 0.001$) (Figure 3.5A). There were no significant differences between 10, 20 and 30 days of Spillover stimulation, illustrating that muscle mass had plateaued between 10 and 20 days and thus, further daily training did not increase muscle mass. Thirty days of training with the identical daily activation but no active resistance from the plantar flexors produced a significant increase in muscle mass ($6.2 \pm 4.5\%$, $P = 0.05$), but was significantly lower than with 10, 20 or 30 days of Spillover stimulation ($P = 0.0493$, $P = 0.0036$ and $P = 0.0037$, Figure 3.5A). Analysing overall changes in muscle fiber CSA revealed a delayed increase compared to muscle mass (Figure 3.5B), with a trend suggesting an increase in fiber CSA after 20 days vs the sham control group ($7.61 \pm 1.58\%$, $P = 0.316$), which reached significance after 30 days vs the sham control group ($17.55 \pm 8.56\%$, $P = < 0.0001$). Concentric resistance training did not cause a significant increase in fiber CSA vs the sham control group ($5.19 \pm 2.23\%$, $P = 0.78$), meaning that 30 days Spillover training showed significantly higher increases in CSA than 30 days of concentric training ($P = 0.0019$). Part of the early increases in mass may be due to muscle swelling, and the lack of a plateau in the CSA data suggests that fiber hypertrophy is ongoing even after 30 days of Spillover training. Similarly, myonuclei per fiber cross-section

did not increase after 2 ($-8.8 \pm 14.5\%$, $P=0.97$), or 10 days ($1.42 \pm 10.9\%$, $P = 0.99$) and showed a trend for increase after 20 days ($35.29 \pm 21.18\%$, $P = 0.1948$, Figure 3.5C). Myonuclear accretion eventually reached significance after 30 days of Spillover training ($54.59 \pm 42.64\%$, $P = 0.0041$), which was significantly higher than the 30-day concentric training group ($11.89 \pm 10.06\%$, $P = 0.0255$, Figure 3.5C). The concentric training group was not significantly different from the sham control group ($P = 0.983$). Furthermore, there were no significant differences from the sham operated group in myonuclear domain size after 2 days ($11.53 \pm 10.55\%$, $P = 0.7548$), 10 days ($0.96 \pm 15.83\%$, $P = 0.9998$), 20 days ($-19.04 \pm 11.2\%$, $P = 0.3012$), or 30 days of Spillover training ($-21.15 \pm 2.42\%$, $P = 0.14$), nor with 30 days of concentric training (-5.33 ± 10.22 , $P = 0.966$) vs. the control group ($-1.16 \pm 4.54\%$, Figure 3.5D). However, due to a slight increase in myonuclear domain size after 2 days of Spillover, there was a significant reduction in the percentage change between the 2-day Spillover training group and both the 20-day ($P = 0.0306$) and 30-day ($P = 0.0111$) Spillover training groups.

After identifying significant increases in both muscle mass, fiber CSA and myonuclei per fiber cross-section after 30 days of Spillover training, but no significant changes in anything but muscle mass after 30 days of concentric training, we sought to identify any potential fiber type-specific adaptations at 30 days. Type I fibers showed no significant shifts in overall proportion between the control group ($2.54 \pm 1.05\%$) and both 30 days of Spillover training ($6.57 \pm 4.96\%$, $P = 0.94$), and 30 days of concentric training ($5.01 \pm 2.36\%$, $P = 0.99$), (Figure 3.5E). Similarly, there were no significant differences between the control ($2.79 \pm 1.5\%$), 30-day Spillover ($5.16 \pm 2.99\%$), or 30-day concentric groups ($5.86 \pm 1.52\%$) for type I/IIA hybrid fiber proportions ($P > 0.9$), (Figure 3.5F), and between control ($21.02 \pm 6.98\%$), 30-day Spillover ($17.81 \pm 8.39\%$) or 30-day concentric ($25.29 \pm 3.04\%$) groups for type IIA fiber proportions ($P > 0.51$), (Figure 3.5G). There were no significant differences in fiber proportion in type IIX/IIB fibers between the control ($73.64 \pm 7.87\%$) and 30 days Spillover group ($70.47 \pm 13.98\%$, $P = 0.995$), (Figure 3.5H). As there were no clear alterations in fiber type proportions, we investigated fiber type-specific CSA to determine the cause of the increase in muscle mass and average fiber CSA. 30 days of Spillover training produced a significant increase in type I fiber CSA above the control group ($1507 \pm 261\mu\text{m}^2$ vs. $1105 \pm 241\mu\text{m}^2$, $P = 0.0031$), whereas 30 days of concentric training was not significantly different between the control and 30-day Spillover training group. ($1273 \pm 73.9\mu\text{m}^2$, $P > 0.907$), (Figure 3.5I). While fiber CSA seemed to

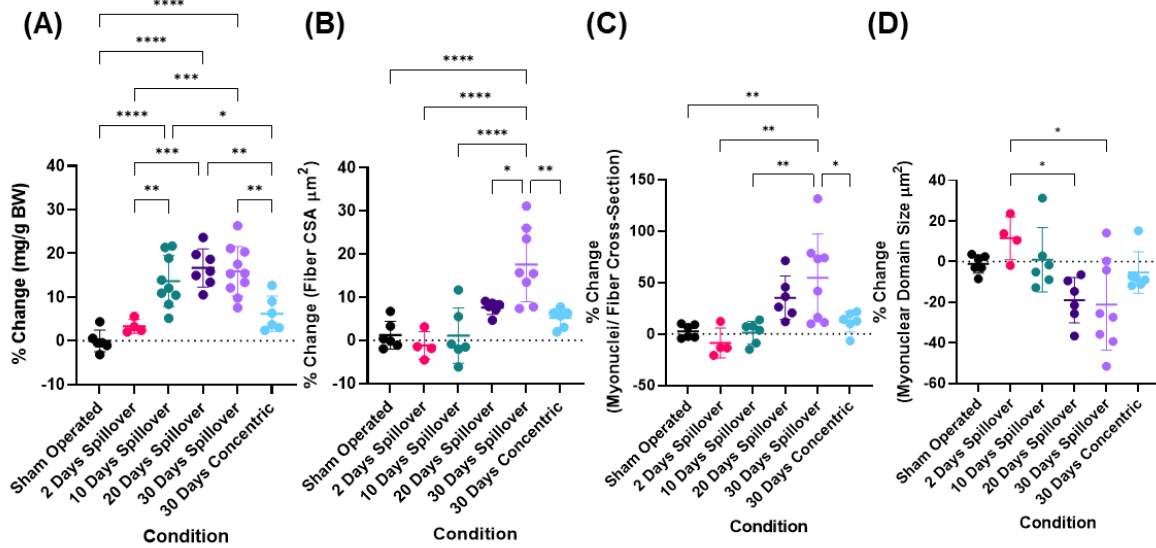
be observably higher in some animals, large variation in the training groups revealed no significant differences between Type I/IIA hybrid fibers between control ($1149 \pm 188\mu\text{m}^2$) and both 30 days of Spillover ($1359 \pm 307\mu\text{m}^2$, $P = 0.558$), or 30 days of concentric training ($1302 \pm 95\mu\text{m}^2$, $P = 0.9474$, Figure 3.5J). Although modest trends appeared, no significant differences were detected in Type IIA fibers between control fiber CSA ($1392 \pm 154\mu\text{m}^2$), and both 30 days of Spillover ($1650 \pm 265\mu\text{m}^2$, $P = 0.236$), or 30 days of concentric training ($1522 \pm 135\mu\text{m}^2$, $P = 0.984$), (Figure 3.5K). By contrast, a robust increase in Type IIX/IIB fiber CSA was observed between the control and 30 days of Spillover training (2481 ± 222 vs. $2969 \pm 268\mu\text{m}^2$, $P < 0.0001$), which was not observed after 30 days of concentric training ($2673 \pm 176\mu\text{m}^2$, $P = 0.795$, Figure 3.5L).

Myonuclei per fiber cross-section was significantly higher across all fiber types studied after 30 days of Spillover training vs control: Type I (1.43 ± 0.26 vs. 1.023 ± 0.16 , $P = 0.0078$, Figure 3.5M); Type I/IIA hybrids (1.28 ± 0.35 vs. 0.93 ± 0.14 , $P = 0.023$ Figure 3.5N); Type IIA (1.5 ± 0.31 vs. 1.047 ± 0.17 , $P = 0.0015$, Figure 3.5O); and Type IIX/IIB (1.448 ± 0.36 vs. 1.062 ± 0.24 , $P = 0.0161$, Figure 3.5P). By contrast, with unloaded training (concentric) we only observed modest trends suggesting that myonuclei were added after 30 days but none reached significance (Type I, 1.23 ± 0.16 , $P = 0.823$. Type I/IIA Hybrids, 1.28 ± 0.18 , $P = 0.11$. Type IIA, 1.31 ± 0.22 , $P = 0.46$. Type IIX/IIB, 1.39 ± 0.21 , $P = 0.18$), (Figure 3.5M-P). Despite this, there were no significant differences between myonuclei per fiber after 30 days Spillover and 30 days concentric training (Type I, $P = 0.89$. Type I/IIA Hybrids, $P = 0.98$ Type IIA, $P = 0.93$. Type IIX/IIB, $P = 0.98$) (Figure 3.5M-P). Furthermore, there were no significant differences in myonuclear domain size across any of the fiber types investigated between the control and both loaded (Spillover) and unloaded (concentric) 30-day training groups (Figure 3.5Q-T), so on average myonuclei were added in proportion to the increase in fiber CSA.

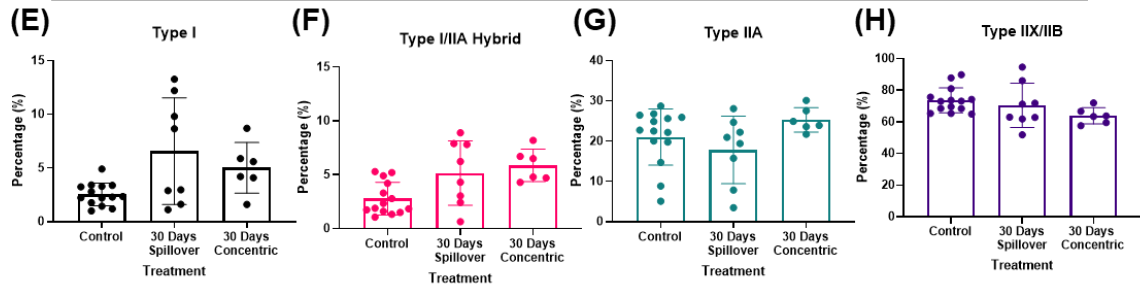
Using simple linear regression analysis to assess the relationships between measured variables across our timecourse of resistance training, we found significant positive correlations between percent changes in muscle mass and percent changes in fiber CSA ($R^2 = 0.2324$, $P = < 0.007$) and myonuclei per fiber cross-section ($R^2 = 0.1568$, $P = 0.0303$, Figure 3.7A-B). The co-efficient of variation between percent changes in muscle mass and percent change in myonuclear domain size was not significant, ($R^2 = 0.08682$, $P = 0.114$, Figure 3.7C).

Percent change in fiber CSA had a significant positive correlation with percent change in myonuclei per fiber cross-section ($R^2 = 0.3826$, $P = 0.0003$) and had a positive trend toward significance with the percent change in myonuclear domain size ($R^2 = 0.1214$, $P = 0.0592$, Figure 3.7D-E). As expected, the co-efficient of variation for percent change in myonuclear domain size and percent change in myonuclei per fiber cross-section reached significance ($R^2 = 0.8137$, $P = <0.0001$, Figure 3.7F).

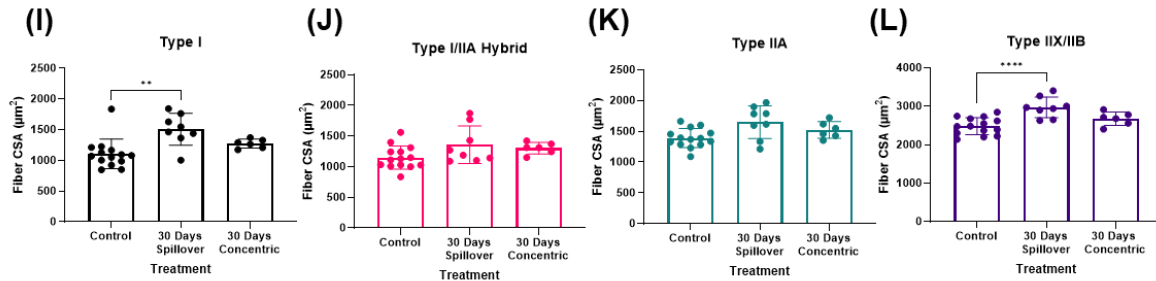
Time course response to loaded & unloaded resistance training



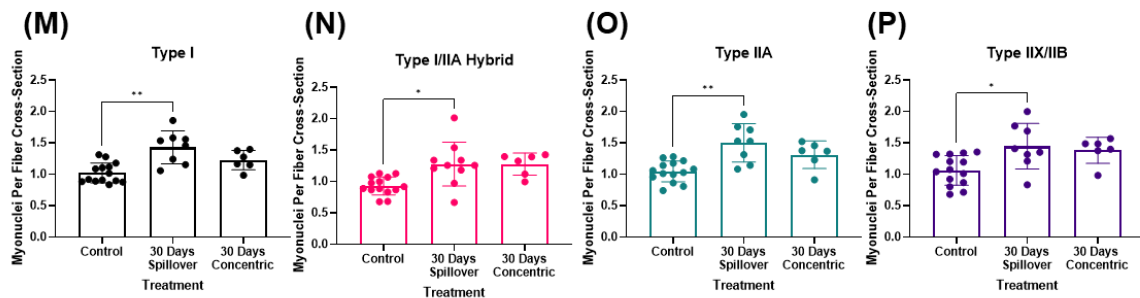
Fiber type percentages following 30 days of loaded and unloaded resistance training



Fiber area following 30 days of loaded and unloaded resistance training



Myonuclei per fiber cross-section following 30 days of loaded and unloaded resistance training



Myonuclear domain size following 30 days of loaded and unloaded resistance training

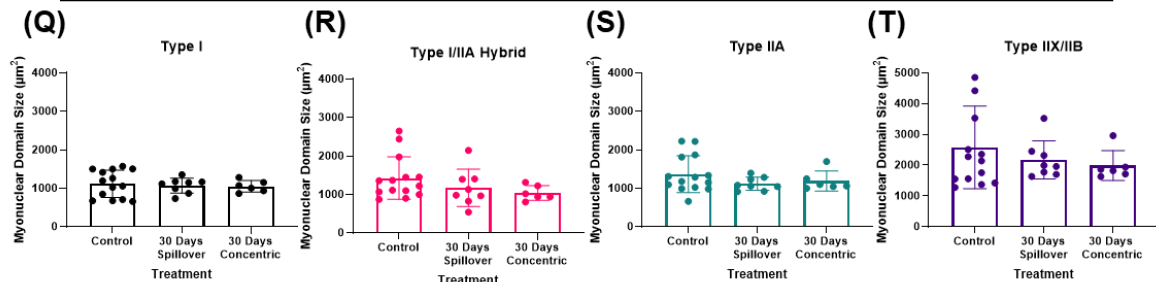
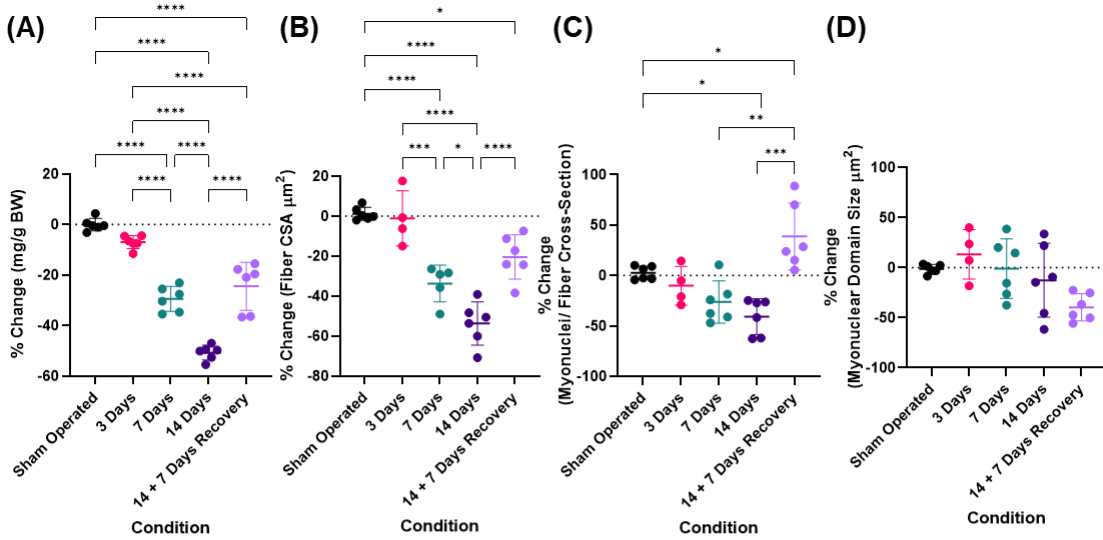


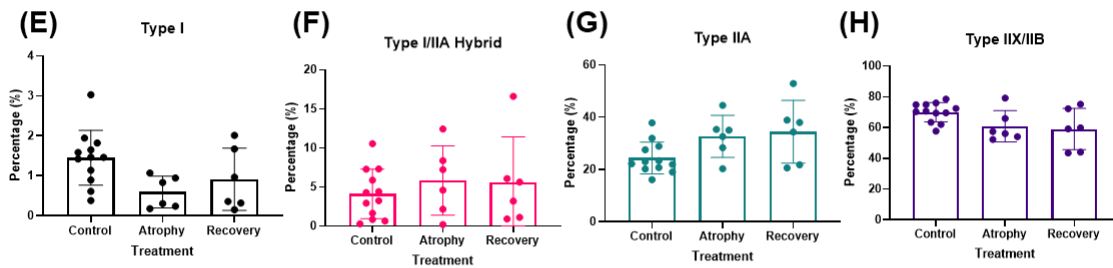
Figure 3.5: (A) Percentage change in muscle mass between the left experimental tibialis anterior (TA) and right contralateral control TA, over a time course of Spillover training and following concentric training. (B-D) Fiber CSA, myonuclei per fiber cross-section and myonuclear domain size assessed across all muscle fibers, expressed as percentage change between left experimental TA and right contralateral control TA. (E-H) Fiber type proportions in control, 30 days Spillover training and 30 days concentric training. (I-L) Fiber type specific fiber CSA. (M-P) Fiber type specific myonuclei per fiber cross-section measurements. (Q-T) Fiber type-specific myonuclear domain sizes. * $P \leq 0.05$. ** $P \leq 0.01$. *** $P \leq 0.001$. **** $P \leq 0.0001$. Mean \pm Standard Deviation.

TTX-induced skeletal muscle disuse atrophy causes a loss of myonuclei, and subsequent recovery of muscle mass is associated with substantial myonuclear addition.

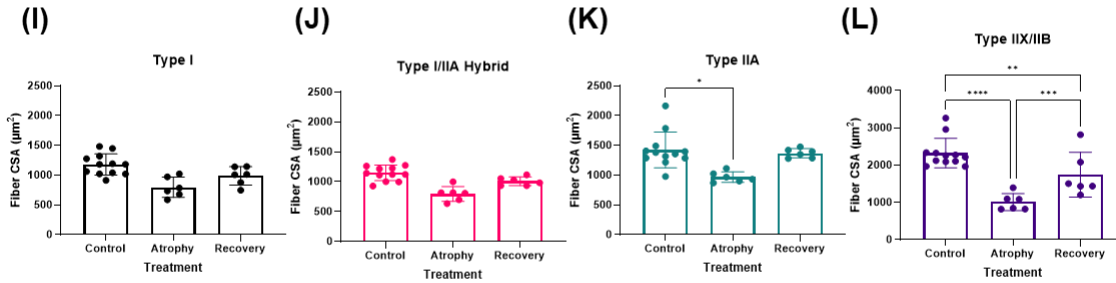
Time course response to TTX-induced atrophy and recovery



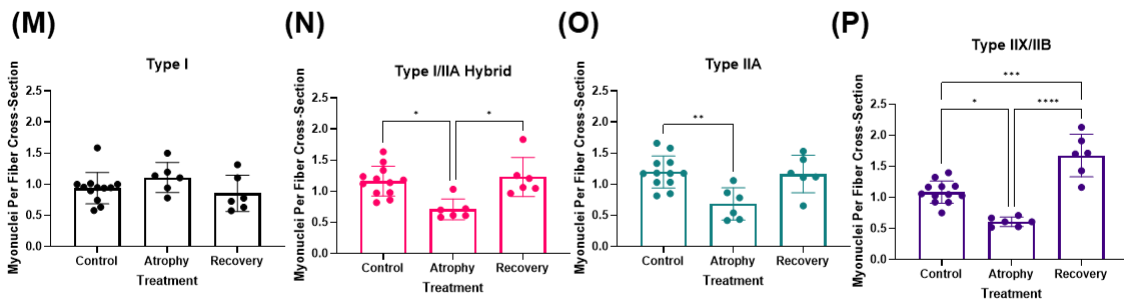
Fiber type percentages in disuse atrophy and recovery



Fiber area in disuse atrophy and recovery



Myonuclei per fiber cross-section in disuse atrophy and recovery



Myonuclear domain size in disuse atrophy and recovery

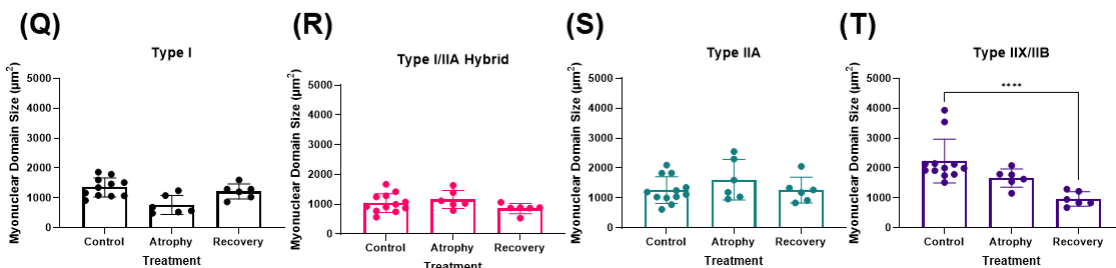


Figure 4.6: (A) Percentage change in muscle mass between the left experimental tibialis anterior (TA) and right contralateral control TA, over a time course of tetrodotoxin (TTX)-induced nerve silencing atrophy and subsequent recovery through habitual activity. (B-D) Fiber CSA, myonuclei per fiber cross-section and myonuclear domain size assessed across all muscle fibers, expressed as percentage change between left experimental TA and right contralateral control TA. (E-H) Fiber type proportions in control, following 14 days atrophy and following 14 days of atrophy with 7 days of subsequent recovery. (I-L) Fiber type-specific fiber CSA. (M-P) Fiber type-specific myonuclei per fiber cross-section measurements. (Q-T) Fiber type-specific myonuclear domain sizes. * $P \leq 0.05$. ** $P \leq 0.01$. *** $P \leq 0.001$. **** $P \leq 0.0001$. Mean \pm Standard Deviation.

As previously reported Fisher et al., (2017), exposure to TTX produced a progressive loss in TA muscle mass of $-6.98 \pm 2.5\%$ at 3 days, $-29.4 \pm 5\%$ at 7 days and $-50.7 \pm 2.9\%$ after 14 days. The changes were significant at all time points vs. the sham operated group, -0.03 ± 2.5 ($P < 0.0001$), (Figure 3.6A). After 14 days of TTX exposure, followed by 7 days of recovery by habitual activity, muscle mass significantly recovered by 51.7% vs. 14 days of TTX exposure ($P < 0.001$). Seven days of recovery did not completely restore muscle mass, as muscle mass was still significantly lower than the sham group ($P < 0.001$), although muscle mass was not significantly different to the 7 days of TTX administration group ($P = 0.56$), which suggests that the rate of loss over 7 days is similar to the rate of recovery. We made a completely new immunohistochemical analysis for this paper, cutting new sections from the same frozen muscles for analysis of whole muscle cross-sections with the updated MyoVision software. A trend was observed, suggesting a loss in detected fibers after 14 days atrophy of $-19.5 \pm 7.8\%$, ($P=0.052$). However, when fiber number was manually counted on Hematoxylin and eosin (H&E) stained tissue sections from 14-day TTX treatment, looking specifically at the most severely atrophied fibers, there was good agreement with the automatic detection in the most challenging fields of view, ($87.7 \pm 4.3\%$), where $\sim 13\%$ of the fibers had become too small or squashed to be successfully identified by MyoVision as a muscle fiber as opposed to interstitial tissue. With MyoVision 2.0, we added a feature for users to change the myofiber identification parameters in relation to circularity, solidity and eccentricity to allow for adjustment to muscle phenotypes where cross-sectioned fibers become less round (more pennate architecture and may be not identified based on default parameters. However, for

our analyses we kept the default parameters the same for consistency across experimental groups (0.6 circularity, 0.85 solidity, 0.95 eccentricity).

H&E staining showed no evidence of fiber loss, splitting or newly formed fibers in any of our multiple endpoints as previously reported Fisher et al., (2017), Schmoll et al., (2018). Muscle fiber CSA progressively declined vs. the sham operated group, reaching significance at 7 days ($-33.7 \pm 9.2\%$, $P < 0.0001$) and further declining at 14 days ($-53.7 \pm 10.8\%$, $P < 0.0001$). After cessation of TTX delivery and 7 days recovery, muscle fiber CSA was still significantly lower than the sham operated group ($P = 0.012$), despite significantly increasing ($-20.4 \pm 11.1\%$) vs. the 14-day atrophy timepoint. Much like muscle mass, fiber CSA losses were not significantly different to the 7 days atrophy timepoint ($P = 0.293$), suggesting CSA recovered at the same rate as CSA loss (Figure 3.6B).

Measurements of myonuclei per fiber cross-sectional area revealed a trend suggesting myonuclei were being progressively lost after only 7 days of atrophy ($-26.2 \pm 21\%$, $P = 0.45$), later reaching significance after 14 days of atrophy ($-40.72 \pm 21\%$, $P = 0.0489$). From the substantial loss of myonuclei per fiber cross-section observed after 14 days of atrophy ($-40.72 \pm 21\%$), 7 days of recovery allowed for myonuclei per fiber cross-section to significantly increase by $38.67 \pm 33.08\%$ vs. their internal contralateral controls ($P = 0.049$). This suggests that myonuclei are added in substantial numbers above baseline values in order to aid in the regrowth of muscle following atrophy, (Figure 3.6C). Myonuclear domain size % changes did not differ significantly between any of the time points, (Figure 3.6D). There was high variability between animals, although a trend was observed for a decreased myonuclear domain size in the 14-day atrophy with 7-day recovery groups ($P = 0.12$).

To identify whether the changes in myonuclear content varied between fiber types, we conducted further analyses on the 14-day atrophy group and 14-day atrophy with 7 days recovery group. Analysis of fiber type proportions at both timepoints revealed no significant differences in overall fiber type percentage, though a trend was observed for an increase in type IIA fibers after 14 days of atrophy ($32.72 \pm 8.07\%$, $P = 0.357$) and 14 days of atrophy with 7 days recovery ($34 \pm 12.04\%$, $P = 0.118$) vs. the control limbs ($24.43 \pm 6.12\%$), (Figure 3.6E-H). This was concomitant with trends suggesting a reduction in type IIX/IIB fibers after 14 days

atrophy ($60.86 \pm 10.14\%$, $P = 0.2153$), and following subsequent recovery ($59.04 \pm 13.44\%$, $P = 0.0575$) versus the control group ($70.01 \pm 6.19\%$) (Figure 3.6H).

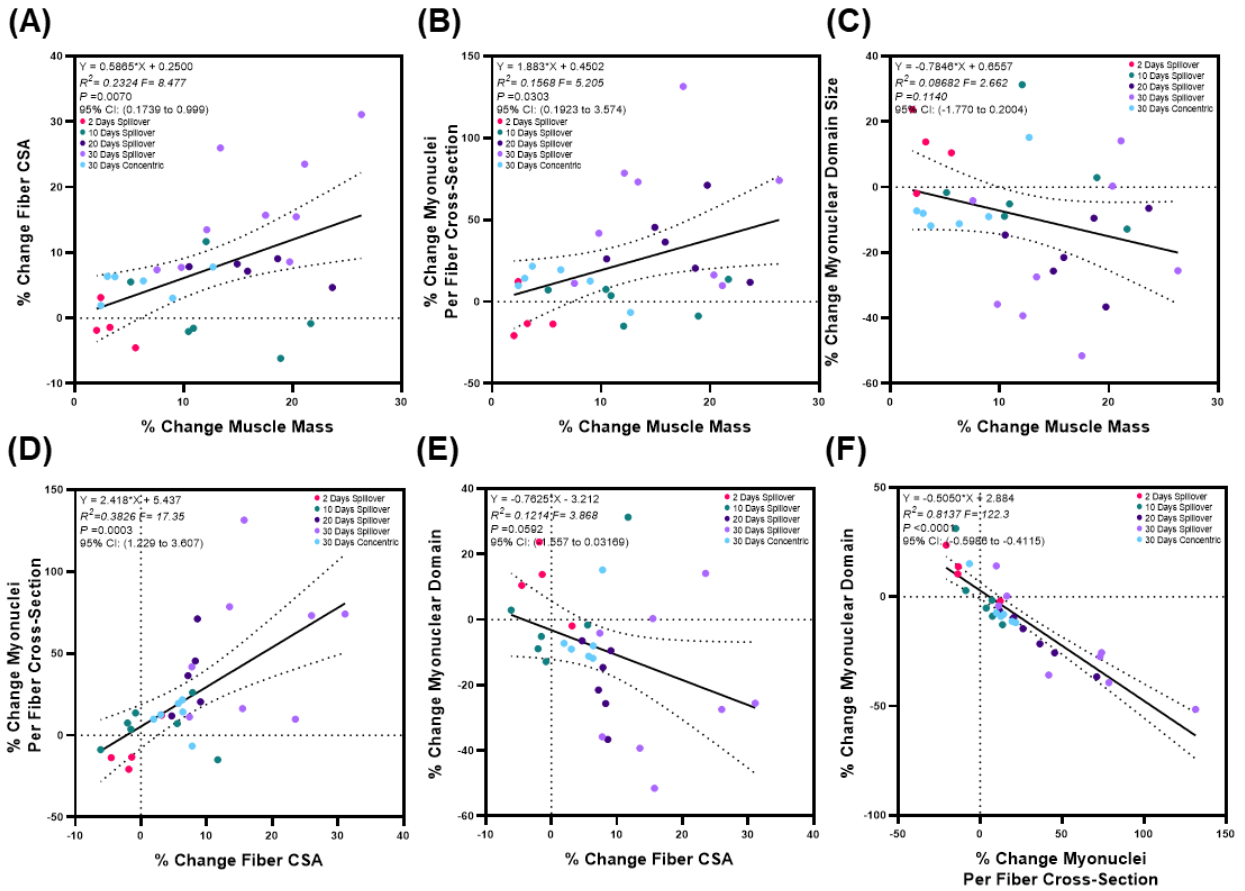
With no clear shifts in fiber type, we assessed fiber CSA to determine whether atrophy was similar across fiber types. The shape of the bar charts looks similar for each fiber type, but significant differences were only noted in type IIA and IIX/B fibers. In comparison to the control type I fibers ($1179 \pm 178\mu\text{m}^2$), 14 days of TTX treatment did not cause a significant decrease in fiber CSA ($796 \pm 170\mu\text{m}^2$, $P = 0.14$), nor a significant change in the recovery group ($988 \pm 155\mu\text{m}^2$), from either the control ($P = 0.94$), or atrophied muscles ($P = 0.98$, Figure 3.6I). Similarly, type I/IIA hybrids ($1148 \pm 130\mu\text{m}^2$) showed no significant decline following atrophy ($796 \pm 125\mu\text{m}^2$, $P = 0.24$), or recovery from atrophy ($1009 \pm 72\mu\text{m}^2$, $P = 0.957$, Figure 3.6J). However, there was a significant decrease in type IIA fiber CSA after 14 days ($1423 \pm 298\mu\text{m}^2$ vs. $968 \pm 89\mu\text{m}^2$, $P = 0.035$), which had recovered back to the mean control CSA after recovery ($1368 \pm 77\mu\text{m}^2$, $P = 0.99$, Figure 3.6K). By contrast, while type IIX/IIB fiber CSA was reduced by 56.6% in the atrophy group ($2325 \pm 394\mu\text{m}^2$ vs. $1010 \pm 228\mu\text{m}^2$, $P < 0.0001$), fiber CSA was not able to recover completely to the level of the control muscle after 7 days of recovery ($1746 \pm 601\mu\text{m}^2$, $P = 0.0016$), although this was significantly higher than the 14 days of atrophy timepoint ($P = < 0.0001$, Figure 3.6L).

Assessment of myonuclei per fiber cross-section in type I fibers revealed no differences between the control TA (0.93 ± 0.25) and the 14-day atrophy group (1.11 ± 0.24 , $P = 0.96$), or the 14-day atrophy with 7 days of recovery group (0.86 ± 0.29 , $P = 0.99$), (Figure 3.6M). Myonuclei per fiber cross-section in type I/IIA hybrid fibers revealed a significant reduction in myonuclei (1.16 ± 0.24 vs. 0.71 ± 0.17 , $P = 0.0219$), but recovered back to control levels after just 7 days (1.23 ± 0.31 , $P = 0.99$), and was significantly higher than the 14-day atrophy timepoint ($P = 0.0239$) for this fiber type (Figure 3.6N). A similar trend was observed in type IIA fibers which lost myonuclei after 14 days of atrophy (1.2 ± 0.26 vs. 0.68 ± 0.26 , $P = 0.0046$), but recovered after 7 days (1.16 ± 0.3 , $P = 0.05$) to the extent that there was no significant difference from the control group ($P = 0.99$), (Figure 3.6O). While myonuclei number in the type IIX/IIB fiber was significantly reduced after the atrophy period compared to the control group (1.09 ± 0.18 vs. 0.61 ± 0.08 , $P = 0.01$), myonuclei number per fiber cross-section significantly increased in the recovery group (1.68 ± 0.34), both above the 14 days atrophy

group ($P = <0.0001$) and surprisingly further beyond the control group ($P = 0.0005$), (Figure 3.6P). We then assessed whether the myonuclear domain size was therefore altered following substantial atrophy and found no significant differences in type I ($P >0.3$), type I/IIA hybrid ($P >0.98$), or type IIA ($P >0.90$) fibers, between the control, atrophy and atrophy with recovery groups, (Figure 3.6Q-S). However, a trend was detected in type IIX/IIB fibers, suggesting a decrease in domain size between the control and 14-day atrophy group ($2232 \pm 731\mu\text{m}^2$ vs. $1664 \pm 310\mu\text{m}^2$, $P = 0.285$). A significantly lower myonuclear domain size was detected between the control TAs and the 14-day atrophy with 7-day recovery group ($970 \pm 241\mu\text{m}^2$, $P <0.0001$), (Figure 3.6T).

Linear regression analysis revealed a significant positive correlation between percent change in muscle mass and percent change in fiber CSA ($R^2 = 0.8589$, $P = <0.0001$), percent change in myonuclei per fiber cross-section ($R^2 = 0.8589$, $P = <0.0001$) and percent change in myonuclear domain size ($R^2 = 0.4550$, $P = 0.0008$, Figure 3.7G-I). There were also significant positive correlations between percent change in fiber CSA and both percent change in myonuclei per fiber cross-section ($R^2 = 0.8079$, $P = <0.0001$) and percent change in myonuclear domain size ($R^2 = 0.5439$, $P = 0.0001$, 3.7J-K). The co-efficient of variation between the percent change in myonuclei per fiber cross-section and percent change in myonuclear domain size was also significant ($R^2 = 0.2468$, $P = 0.022$, Figure 3.7L).

Correlations between adaptive responses to electrical stimulation-induced resistance training



Correlations between adaptive responses to TTX induced atrophy and subsequent recovery

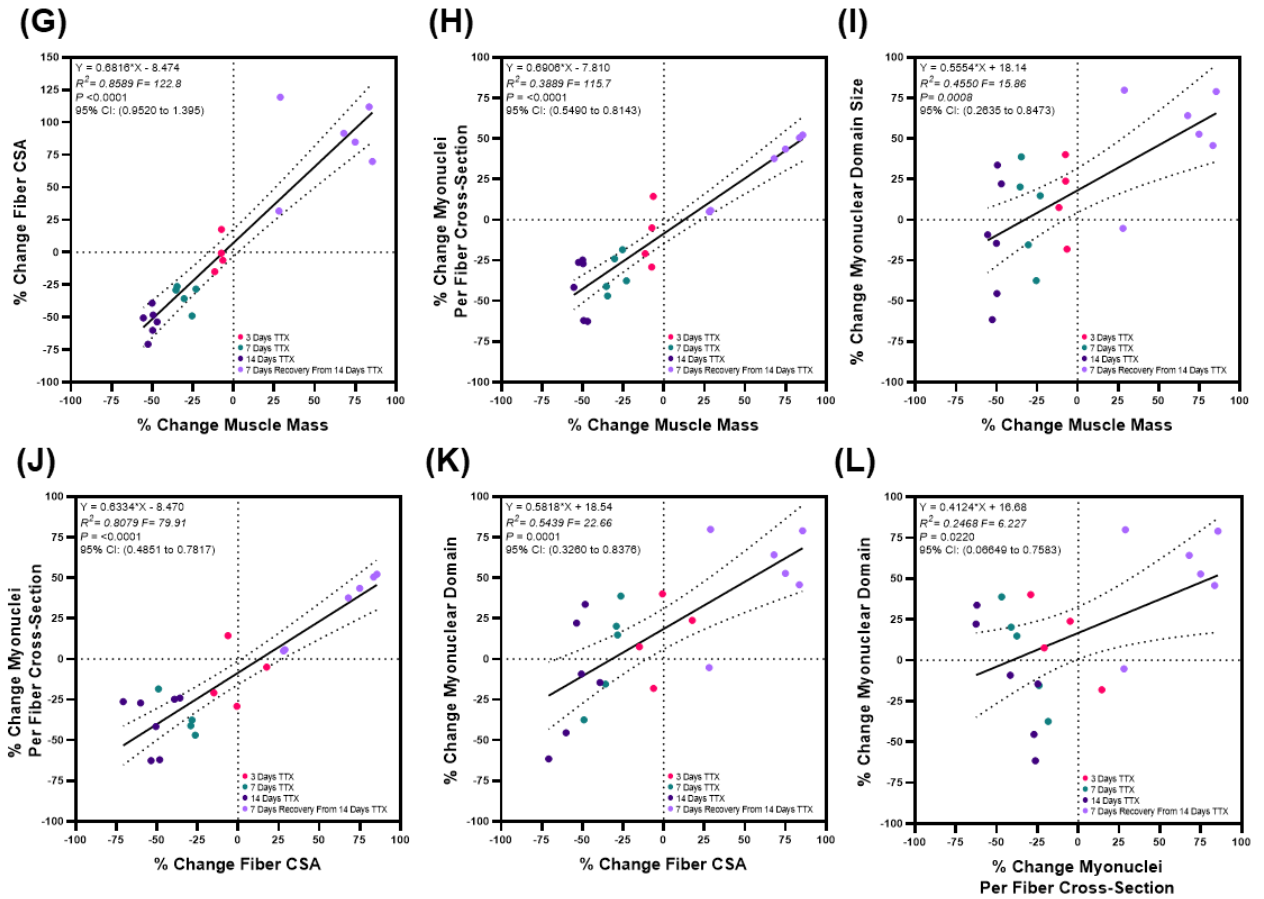


Figure 3.7: (A-F) Correlations between percentage changes in muscle mass, muscle fiber CSA, myonuclei per fiber cross-section and myonuclear domain size following a time course of loaded and unloaded resistance training. (G-L) Correlations between percentage changes in muscle mass, muscle fiber CSA, myonuclei per fiber cross-section and myonuclear domain size following a time course of TTX-induced atrophy. The subsequent 7-day recovery following 14 days of TTX induced atrophy is expressed as the difference between the mean 14 days TTX value versus the individual 7-day recovery values.

3.5 Discussion:

In both developing and adult mammalian skeletal muscle, myonuclei number, often referred to as DNA content, varies with muscle fiber size although this relationship is not completely linear, nor is it fully understood in all contexts of muscle plasticity Cramer et al., (2020), Karlsen et al., (2015), Snijders et al., (2020a). Using high-content microscopy, we studied the relationships between fiber size and myonuclear content in response to various programmed exercise protocols in free living rats and following disuse atrophy and subsequent recovery. Quantification of high-content images has traditionally been slow due to the requirement for well-trained human analysts. The semi-automatic program, SMASH, was the first to be made freely available to the muscle research community and improved analysis time considerably Smith and Barton, (2014). We developed MyoVision as the first unbiased, fully automatic software that is freely available to the muscle research community, and since then, there has been significant interest in such analytical packages for muscle cross-sections Mayeuf-Louchart et al., (2018), Encarnacion-Rivera et al., (2020), Lau et al., (2018), Waisman et al., (2021), Kastenschmidt et al., (2019), Sertel et al., (2011). Despite the overall interest, MyoVision remains one of only two freely available software that includes myonuclear quantification and the only one for which this function is validated. A major limitation of MyoVision was its computational inefficiency that precluded analysis of large cross-sections, such as the rat TA, taken at high magnification. Additionally, MyoVision analysis was sensitive to background noise, which increased the requirement on microscope image quality. In order to address these shortcomings, we have updated MyoVision and optimized the software to allow for rapid and unsupervised quantification of hundreds of thousands of individual myofibers and millions of nuclei on histological cross-sections

(www.myoanalytics.com/myovision2). Using this improved software, we critically assessed myofiber morphometry, including myonuclear content and myonuclear domain, in exercise trained, severely atrophied, and recovering whole rat skeletal muscle.

Continuous low frequency (20Hz) stimulation (CLFS) for 7 days caused a significant reduction in both mean muscle mass ($-12.6 \pm 4.9\%$, $P = 0.0026$) and mean fiber CSA ($-18.6 \pm 11.4\%$, $P = 0.024$). These reductions occurred without histological evidence of damage and were consistent with a shift in myosin heavy chain fiber content from predominately glycolytic to smaller, more oxidative fibers (type IIX/IIB fibers fell from 81% to 62%) and are therefore deemed as functional adaptations rather than degenerative. There were no changes in fiber CSA for any fiber type (Figure 3.4I-L). This suggests that the larger IIX/IIB fibers that shifted myosin heavy chain content also reduced their fiber area which may be an adaptation to reduce the diffusion distance to allow increased respiratory gas exchange associated with a shift to oxidative metabolism Brown et al., (1976), Egginton and Hudlicka, (1999), Hudlicka et al., (1977), Hudlicka et al., (1982), Hudlická et al., (1988).

Myonuclear addition is generally considered to be a feature of resistance exercise-induced hypertrophy, as a mechanism to support both repair of damaged muscle fibers unaccustomed to exercise Mackey and Kjaer, (2017a), Murach et al., (2020b) and to support transcription across a larger area of cytoplasm Karlsen et al., (2015), Karlsen et al., (2020), Snijders et al., (2020b). However, we found significant increases in myonuclei per fiber cross-section especially in type IIX/IIB glycolytic fibers in response to CLFS. As mean fiber area did not change, IIX/IIB myofiber cytoplasm was hypernucleated per fiber cross-section and thus had a significant reduction in myonuclear domain size (-69% , $P = 0.0007$), which was closer to its oxidative counterparts at control level. Again, rather than a damage response, we propose that this myonuclear accretion is probably an adaptation to support additional protein synthetic demands in response to stimulation, as they initially have a significantly larger myonuclear domain size. Whilst we cannot completely exclude the potential that early damage had occurred; we presume that there would be some histological remnants. CLFS has revealed barely any evidence of degeneration or damage with similar activation in rabbit tibialis anterior muscle Lexell et al., (1993), Sutherland et al., (1998); and none in rat Jarvis et al., (1996b).

We then studied the use of high frequency stimulation with (Spillover) and without (concentric) synchronous resistance from the antagonistic muscle group. As higher frequency stimulation (similar to higher load resistance exercise) is often associated with more damage and myonuclear accretion to support regeneration and hypertrophy, we sought to test how these parameters changed during a time-course of loaded (Spillover) and unloaded (concentric) resistance exercise and whether there would be a variation between fiber types in hypertrophy and myonuclear accretion. Our model avoids the complication of variable recruitment among fiber types during the exercise intervention. Muscle mass was substantially greater after just 10 days of Spillover stimulation (Figure 3.5A) and plateaued between 20 and 30 days of daily training. Most interestingly, fiber CSA only increased significantly after 30 days in line with a significant increase in myonuclei per fiber, both of which were trending to increase after 20 days of Spillover stimulation (Figure 3.5B-C), which probably reflects the time course including early muscle swelling and, muscle fiber hypertrophy during adaptation. Recent unpublished findings from our group also reveal an increase in Pax7+ satellite cell activity through the change in localization of PCM1 on single muscle fibers after just 10 days of Spillover training, however this does not seem to result in fusion until at least 20 days of training. Damas and colleagues Damas et al., (2018a) observed that early satellite cell activity and proliferation in humans following resistance exercise does not correlate with increases in myonuclear number in the early stages of hypertrophy, suggesting a role for satellite cells in signalling and repair before a later involvement in fusion to aid in transcriptional requirements. These differential requirements during exercise have also been recently shown using conditional knockdown of Myomaker in satellite cells, preventing fusion of satellite cells to existing muscle fibers Goh et al., (2019). Knockout at the initiation of high intensity interval training (HIIT) produced intolerance to exercise and a fibrotic phenotype, whereas knockout after 4 weeks of exercise maintained exercise volume but blunted the hypertrophic effect showing the nuanced distinction between altering the functionality of satellite cells versus removing them altogether. Furthermore, complete ablation of the Pax7+ cell pool seems to allow for some hypertrophic adaptation without fibrosis, although there is evidence to suggest that the blunting of hypertrophy varies in extent between muscles Englund et al., (2020), Englund et al., (2021), Murach et al., (2021).

Thirty days of Spillover training caused significantly larger increases in muscle mass, fiber CSA and myonuclear accretion than 30 days of concentric training. Several independent models of resistance training and concurrent exercise in rodents have found a similar strong positive relationship between load and myonuclear accretion. Eftestøl and colleagues used a non-surgical model to exercise rat dorsiflexor muscles using transcutaneous electrical stimulation with external load added through the use of a resisting footplate Eftestøl et al., (2016). They reported that higher load was associated with greater fiber hypertrophy and greater myonuclear accretion but did not assess fiber type specific effects. They also reported fiber type shifts in the EDL from IIB to IIX independent of load. Whilst we found no significant evidence of fiber type shift across the TA, the similarity in the models suggests that there may have been a shift from IIB to IIB/IIX hybrids, and increased number of pure IIX fibers, which we did not identify specifically in our analyses. Interestingly, concurrent training using a voluntary high load resistance wheel, produced myonuclear accretion in a load dependent manner in the plantarflexor muscles of mice, although the addition of myonuclei occurred similarly across all fiber types Masschelein et al., (2020). In contrast, progressive weighted wheel running (PoWeR) in mice results in both fiber type-specific and fiber type-independent adaptations that differ based on the muscle studied Murach et al., (2020b). This probably reflects differences in activation and load during voluntary exercise, as well as early damage-related fusion of satellite cells which has previously been reported after unaccustomed exercise Smith et al., (2001), Cramer et al., (2007), Mackey and Kjaer, (2017a). Concurrent training in humans also produces greater increases in myonuclei per fiber, ribosomal biogenesis, and capillary content than resistance training alone which may be a result of increased total motor activity Lundberg et al., (2020). It has previously been argued that slower fibers are more susceptible to exercise-induced damage but this can often be explained by their greater activation in voluntary movement, being recruited to a larger extent than fast oxidative and fast glycolytic fibers Vijayan et al., (1998), Vijayan et al., (2001). As our models of stimulation recruit all motor units at once rather than in a progressive manner with voluntary exercise, the total volume of activation can be excluded as a factor for differences between fiber type in terms of exercise induced myonuclear accretion. Interestingly, after 30 days of Spillover training, fiber area increased significantly in type I fibers by a mean of 36% (Figure 3.5I) and by a mean of only 19% in type IIX/IIB fibers (Figure 3.5L). Whilst this increase is somewhat larger in the slow muscle fibers, the relatively small

proportion of type I fibers (<6%) and large proportion of IIX/IIB fibers result in IIX/IIB contributing more to whole muscle fiber hypertrophy. However, this is an interesting observation of the potential functional significance of hypertrophy of small populations of slow fibers in a predominantly fast twitch muscle during hypertrophy. Furthermore, myonuclear accretion seemingly occurred to the same extent across all fiber types (Figure 3.5M-P), suggesting that the accretion of myonuclei is strongly associated with load and activity in this instance.

Myonuclear loss or maintenance during muscle disuse is of particular interest, since the signals related to exercise and load are reduced. Previously, the relationship between muscle loss during disuse in rodents has been performed using supra-physiological models. Denervation by complete transection of the sciatic nerve Ashley et al., (2007a), Ashley et al., (2007b), Bruusgaard and Gundersen, (2008) may be more representative of a peripheral nerve injury than disuse-induced atrophy or unloading/detraining. Another popular method is hind-limb unloading which can consistently and rapidly induce muscle atrophy Dupont-Versteegden et al., (2006), Jackson et al., (2012), Seaborne et al., (2019a), although this model does not control for motor activity, which may even be increased in some instances, whilst load is reduced Michel and Gardiner, (1990), Pierotti et al., (1990). The use of TTX to study muscle atrophy has been less widely adopted Cormery et al., (2000), Salter et al., (2003), Bruusgaard and Gundersen, (2008), Fisher et al., (2017). However, TTX nerve treatment causes muscle atrophy through prevention of generation or propagation of action potentials at the nerve, without axonal damage so disuse can be followed by a period of recovery. Trophic factors dependent on axon integrity may continue to have influence on their associated muscle fibers, while substantial sarcoplasm is lost within the muscle fibers Martinov and Njå, (2005), Reid et al., (2003), Fisher et al., (2017).

As we have previously reported Fisher et al., (2017), onset of TTX treatment causes a progressive loss in muscle mass, reaching significance after 7 days and further declining at 14 days (Figure 3.6A-B). We show here with data from a new analysis that the loss of mass was strongly associated with decreased fiber CSA (Figure 3.6G), mainly attributed to significant loss of CSA in type IIA and IIX/IIB fibers (Figure 3.6L). No significant shifts in fiber type occurred, although there appeared to be a trend suggesting a shift of slow fibers to fast oxidative glycolytic and fast glycolytic to fast oxidative glycolytic (Figure 3.6E-H). Similar

changes have been reported in the soleus and medial gastrocnemius Cormery et al., (2000). A similar experiment in rats with TTX treatment of the entire sciatic nerve for 2 weeks found that type IIA muscle fibers appeared to atrophy less ($29 \pm 10\%$) than type IIB fibers ($43 \pm 7\%$) in the TA Salter et al., (2003). Sciatic nerve block also prevents activity of the plantarflexors; it was observed that the lateral gastrocnemius IIB and IIA fibers showed less atrophy (23-26%) than the resident type I fibers (44%), but in the soleus, both fast and slow fibers atrophied to the same extent (39% versus 43%). Differences in the rates and total extent of muscle atrophy have been reported between different muscles and different fiber types which may be related to oxidative capacity, protein synthetic/degradation rates and the angle at which the limb is immobilized Baehr et al., (2016), Baehr et al., (2017), Salter et al., (2003). Immobilizing a muscle at shorter lengths has been shown to induce more atrophy than muscles immobilized at resting or a greater than resting length, suggesting that passive tension and stretch influence muscle atrophy, as well as lack of active contraction. It has been suggested that the nuclei themselves may be able to sense tension within the muscle and that this signal acts to stabilize resident myonuclei in some muscle groups or models Salter et al., (2003).

Intriguingly, type I fibers did not atrophy significantly, although the mean was reduced, and they maintained their myonuclei. In type I/IA hybrid fibers, myonuclei were lost without a reduction in fiber CSA. The severity of fiber CSA atrophy increased along the continuum to the fastest fibers so that the CSA of type IIA fibers reduced by 47% after 14 days of TTX treatment and IIX/IIB fibers by 56%. This occurred with a reduction in myonuclei per fiber cross-section in both IIA and IIX/IIB fibers (43%). As fiber CSA loss and myonuclear loss occurred simultaneously in IIA and IIX/IIB fibers, myonuclear domain sizes remained unchanged in all fiber types following 14 days of nerve silencing. Only one study to our knowledge has measured myonuclei number in response to TTX treatment, although this was performed in mice. Intravital imaging showed no decrease in myonuclei with intravital imaging after 3 weeks in the EDL muscle, but considerable turnover in the nuclei of cells between the muscle fibers Bruusgaard and Gundersen, (2008). This may be a species difference (mouse/rat) or because the EDL crosses two joints (ankle and knee) and therefore has a higher level of passive tension, enough to prevent loss of myonuclei.

Filling the osmotic pumps with a pre-determined amount of TTX allows for motor activity to return after 14 days of nerve silencing, so that muscle can 'regrow' following severe atrophy.

After 14 days of TTX exposure followed by 7 days of cessation in the recovery group, muscle mass significantly recovered by 51.7% versus 14 days of TTX exposure ($P < 0.001$). Seven days of recovery did not completely restore muscle mass, as muscle mass was still significantly lower than control ($P < 0.001$) and total muscle mass was similar to the values at 7 days of TTX administration, which suggests that rates of loss over 7 days are in line with rates of recovery. At the fiber type level, after 7 days of recovery type I and type I/IIA hybrid fibers were unchanged from control and atrophy conditions, although the loss of myonuclei in type I/IIA hybrids had recovered back to control levels. Subsequent recovery back to baseline fiber CSA in type IIA fibers occurred after just 7 days of recovery and was coupled with myonuclei per fiber cross-section measurements in line with control levels. This recovery was not matched in the less oxidative type IIX/IIB fibers which had only partially recovered their CSA from 14 days of nerve silencing ($P = 0.003$) and were still significantly lower than control levels ($P = 0.0016$). Remarkably, myonuclei per fiber cross-section was higher in comparison to both the atrophied muscle ($P = <0.0001$) and the control muscle ($P = 0.0005$), suggesting that myonuclear populations did not only recover back to the point of baseline, but were also added past homeostatic levels in order to support the substantial recovery of muscle mass and fiber CSA from severe atrophy, somewhat like resistance exercise induced myonuclear accretion. This resulted in type IIX/IIB fibers to be hypernucleated, with a smaller myonuclear domain size in comparison to control type IIX/IIB fibers. We also observed this characteristic in our 7 days of CLFS model, further supporting that due to type IIX/IIB fibers having larger myonuclear domains than their slower, more oxidative counterparts, they may be more dependent on myonuclear accretion to support the transcriptional demands of extreme activity or periods of regrowth. Jackson and colleagues Jackson et al., (2012) reported that recovery from hind-limb suspension was not blunted by satellite cell depletion in adult mice, and therefore myonuclei are not required for regrowth following atrophy. However, they reported no loss of myonuclei during the 14 days of unloading suggesting that the resident myonuclei population were able to meet transcriptional demands of the hypertrophy by habitual activity. The amount of fiber atrophy was also substantially less (~25% loss), versus (~54% loss) in our study. Perhaps myonuclei are only lost past a threshold of myonuclear domain size as evidenced by significant myonuclear loss only at 14 days when myofiber atrophy was most severe. It is of significant interest as to whether type IIX/IIB fibers retain the extra myonuclei added during the recovery from TTX-induced atrophy and or whether

they are lost as muscle returns to basal mass and therefore act as ‘temporary’ myonuclei to support the rapid growth and also how this would affect subsequent periods of unloading.

3.6 Conclusion:

Future Considerations:

The use of IPGs allows for programming and control over both endurance and resistance exercise with considerations for training duration, contraction modality, repetitions, sets, rest and the timing of exercise within the circadian cycle. IPGs can be easily programmed to switch on or off allowing for periods of detraining and subsequent retraining with minimal intervention or use of supraphysiological methods. Analogously, the careful planning and loading of osmotic pumps to deliver TTX to a motor nerve allows for periods of disuse induced atrophy and subsequent recovery. The replacement of the osmotic pump or use of programmable infusion pumps would also allow for continuous cycling of nerve block and recovery to simulate repeated bed rest in humans. Again, these methods require minimal intervention post-surgical implantation. We also suggest that the TA and other dorsiflexors may be more susceptible than plantarflexors to detrain both metabolically and at the myonuclear level due to the lack of habitual load and activity placed on dorsiflexors.

Further functionalities to the automated image analysis program, MyoVision, are continually being added to www.myoanalytics.com/myovision2, including guidance on supported image file types and minimum recommended computer requirements.

We propose that the number of myonuclei is not fixed, reflects the biosynthetic requirements of the muscle fiber, and does not necessarily correlate with fiber size. The myonuclear domain appears highly flexible and adaptations may differ by fiber type. High load resistance training causes increased size associated with higher myonuclear content, whereas low-load continuous stimulation causes increased myonuclei but reduced size. TTX results in atrophy and myonuclear loss, but both can be restored with recovery. Overall, our models of high load short duration and low load continuous stimulation, and recovery after disuse all resulted in substantial increases in myonuclei without histological signs of muscle damage as assessed by histology.

3.7 Further technical considerations/observations from assessing changes in mass and fiber type characteristics in response to spillover training:

Further to the investigations discussed above, we also extracted the other 'classically studied' muscles in the lower limb of the rat including the second largest dorsiflexor (EDL), and three ankle plantarflexors, the soleus, plantaris and gastrocnemius. As the tibialis anterior shows the greatest growth response Schmolle et al., (2018), we chose to study this muscle in greatest detail throughout this thesis.

Spillover resistance training produces hypertrophy in the EDL but not gastrocnemius, plantaris or soleus muscles.

Here we present data from our timecourse of spillover training in muscles other than the tibialis anterior, *Figure 3.8*. In brief, sham surgery did not alter muscle mass to a large extent in the EDL ($-3.8 \pm 3.2\%$). Following 2 days of training, trained EDL muscles did not differ from EDL muscles whose limb had undergone sham surgery ($0.328 \pm 1.5\%$, $P = 0.49$). However, there was a consistent significant increase in muscle mass after 10 ($6.68 \pm 6.04\%$, $P < 0.0001$), 20 ($4.79 \pm 3.35\%$, $P = 0.002$) and 30 ($6.78 \pm 3.85\%$, $P < 0.0001$) days of spillover training versus sham surgery. Why the EDL responds less than the tibialis anterior muscle, despite being fully activated is out of the scope of this thesis, but we put forward the suggestion that the reduced hypertrophy may be as a result of different architectural properties of the EDL and the fact that it crosses both the ankle and knee joint, so the degree of stretch may be different.

In the gastrocnemius, sham surgery also did not alter muscle mass ($0.38 \pm 3.17\%$). However, following 2 days of spillover training there was a significant decrease in muscle mass ($-9.29 \pm 4.1\%$, $P = 0.0053$) versus sham surgery. However, this loss in muscle mass seems to recover by 10 days of training where there appears to be a small, hypertrophic effect of training, despite the variance being high between individuals. Trends occurred suggesting an increase in gastrocnemius muscle mass after 10 ($5.33 \pm 3.6\%$, $P = 0.07$), 20 ($4.79 \pm 3.36\%$, $P = 0.27$) and 30 ($5.27 \pm 3.66\%$, $P = 0.07$) days of spillover training. The plantaris did not differ significantly after 2 ($-2.6 \pm 7.1\%$), 10 ($1.17 \pm 3.6\%$), 20 ($0.76 \pm 4.1\%$) and 30 ($-1.11 \pm 5.55\%$) days of spillover training versus sham surgery ($-0.74 \pm 7.1\%$), $P > 0.67$. Similarly, the soleus did not significantly differ from the sham surgery condition ($-0.2 \pm 7.4\%$, $P > 0.45$), after 2 ($-6 \pm 5.6\%$), 10 ($0.08 \pm$

8.15%), 20 ($1.3 \pm 6.4\%$) and 30 days ($2.5 \pm 7.2\%$) of spillover training. The large variance in changes in mass between the plantarflexor muscles is unfortunately out of the scope of this thesis, but we suggest that the recruitment may differ more in the plantarflexors as they are only partially activated. We suggest that cage activity may provide more information on whether changes in plantarflexor mass are associated with changes in habitual loading through the anti-gravity plantarflexors. We also predict that as the gastrocnemius is more complex (the medial and lateral heads insert behind the knee so it can be difficult to maintain consistency during dissection), the differences in muscle harvesting may result in variance between left and right limbs which we try best to negate during dissection.

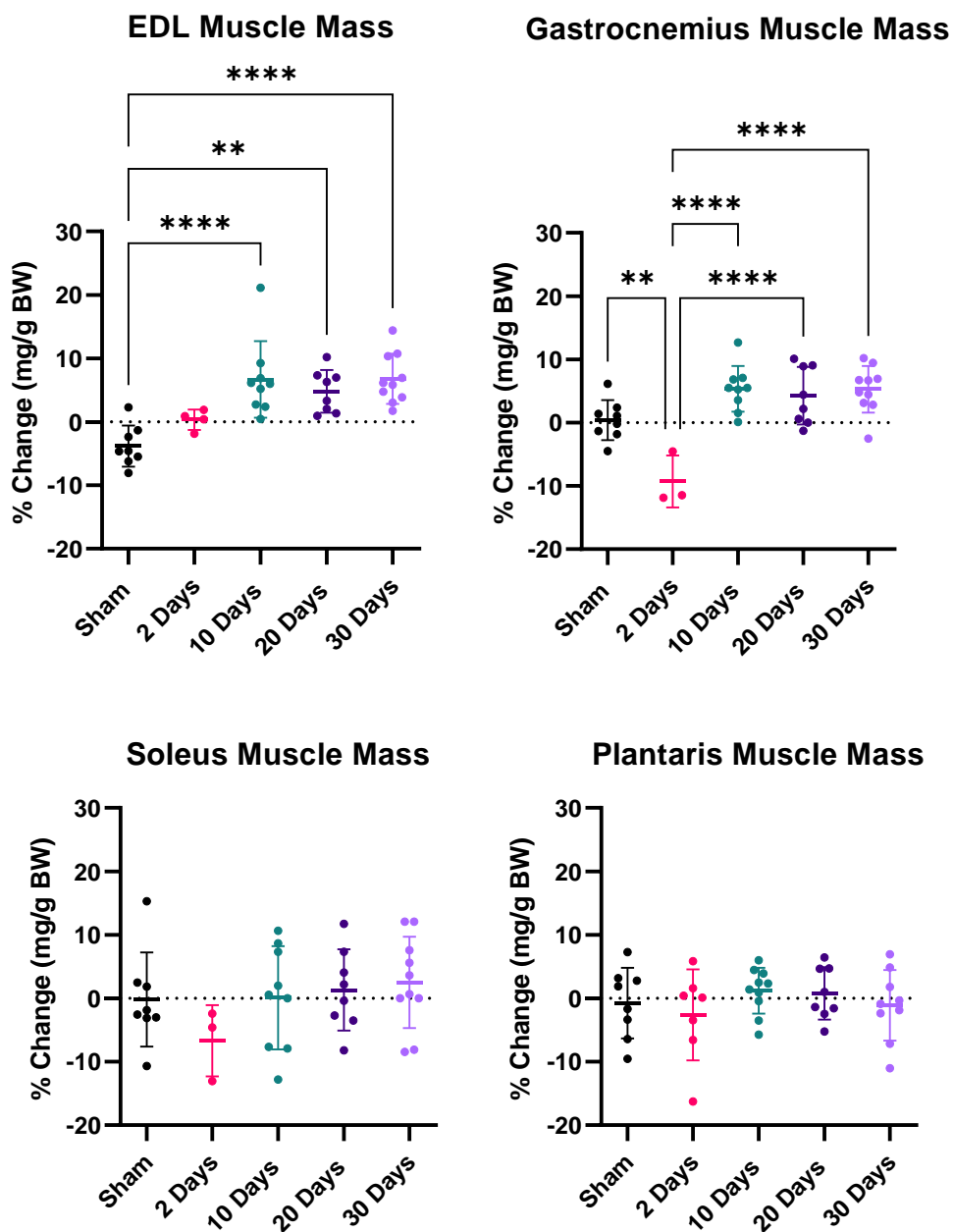


Figure 3.8: Percent changes in muscle mass (mg/g/body weight) across the timecourse of spillover training in extensor digitus longus, gastrocnemius, plantaris and soleus. * $P \leq 0.05$. ** $P \leq 0.01$. *** $P \leq 0.001$. **** $P \leq 0.0001$. Mean \pm Standard Deviation.

Qualitative observations of changes in tibialis anterior muscle shape following spillover training.

We note that the above observations of changes in fiber type are based on fiber size assessed at the mid-belly of the tibialis anterior. However, we note that upon muscle slicing to prepare the muscle (as seen in Figure 2.3 and 2.29) after 10, 20 and 30 days of spillover training we observed changes in muscle shape most obviously at the distal end of the tibialis anterior, where the muscle is thinner and joins the distal tendon. Pre-covid, our plan was to analyse whole muscles of trained tibialis anterior to assess changes in regional morphology and fiber pennation through iodine-enhanced micro computerized tomography as previously described in collaborative experiments between the Jarvis lab and University of Liverpool in skeletal muscle, cardiac muscle and bone Aslanidi et al., (2012), Jeffery et al., (2011), Ni et al., (2013), Vickerton et al., (2013), Vickerton et al., (2014). As we measured each individual slice, we note that variably, that changes in muscle mass from the proximal to distal insertion were more prominent between contralateral distal sections, suggesting more remodelling at the distal end of the muscle where there are less muscle fibers and therefore more force/strain transmitted. These adaptations can be depicted through the muscle slice images and histograms presented in Appendix 1.

As suggested previously, different training modalities (concentric vs. eccentric) may cause different architectural adaptations in muscle. Different muscle groups and muscle regions also often show differing molecular responses due to differing levels of stretch and activation, for example different phosphorylation states of key integrins and cytoskeletal proteins involved in transmitting signals to growth pathways Franchi et al., (2018), Zabaleta-Korta et al., (2020), Mandić et al., (2020), Lundberg et al., (2019), Fayh et al., (2020). Unfortunately, studying regional molecular signalling and adaptations was out of the scope of this thesis.

Changes in myosin heavy chain gene expression across the length of the tibialis anterior as assessed through RT-qPCR.

Following extensive immunostaining/ATPase of transverse cross-sections throughout this PhD project, we note the observation that in the tibialis anterior there were significantly

fewer and sometimes no slow, more oxidative fibers at the distal end of the muscle. However, at the mid-belly there were considerable oxidative fibers which increased in number as the muscle was cut transversely toward the proximal origin of the muscle. However, we could not follow this up in detail due to time constraints lost through the COVID-19 pandemic.

Despite this, here we present pilot data from RT-qPCR experiments on 16 control TA muscles to investigate whether isolating mRNA from different muscle regions would agree with our observations that myosin heavy chain content differs across the length of the muscle. If differences were found, it would suggest that due to the differing metabolic properties found in slow vs fast muscle fibers, that the resultant transcription in response to exercise may differ considerably. It would therefore be imperative to ensure that contralateral comparisons were made on the same muscle region or on homogenous samples taken from the proximal, mid-belly and distal regions together.

Relative to the proximal region, MyHCI mRNA levels did not significantly differ with the mid-belly ($0.32 \pm 0.27 \text{ Log}^2 \text{ FC}$, $P=0.77$). There was considerably lower MyHCI mRNA in the distal region ($-2.67 \pm 0.49 \text{ Log}^2 \text{ FC}$) relative to both the proximal and mid-belly region ($P < 0.0001$). Similarly, there were no differences in MyHC IIA expression between the proximal and mid-belly regions ($-0.23 \pm 0.27 \text{ Log}^2 \text{ FC}$, $P=0.89$). Again, the distal region contained significantly less MyHCIIA mRNA relative to the proximal region ($-2.45 \pm 0.49 \text{ Log}^2 \text{ FC}$, $P < 0.0001$) and the mid-belly ($P < 0.0001$). When studying the mRNA transcript levels from the faster MyHCIIX fibers, there was significantly higher levels of MyHCIIX mRNA in the mid-belly relative to the proximal region ($0.45 \pm 0.2 \text{ Log}^2 \text{ FC}$, $P=0.047$). Towards the distal end, significantly more MyHCIIX mRNA was measured relative to the proximal region ($0.78 \pm 0.43 \text{ Log}^2 \text{ FC}$, $P=0.05$) and reached significance between the mid-belly and distal end ($P=0.001$). These changes were more prominent when studying MyHCIIB mRNA levels. The mid-belly of the TA contained significantly higher levels of MyHCIIB mRNA ($0.8 \pm 0.91 \text{ Log}^2 \text{ FC}$, $P=0.0089$), relative to the proximal region. The distal end showed significantly higher amounts of MyHCIIB mRNA ($1.93 \pm 0.83 \text{ Log}^2 \text{ FC}$, $P < 0.0001$) than the proximal end and was significantly higher than the mid-belly region ($P=0.0072$).

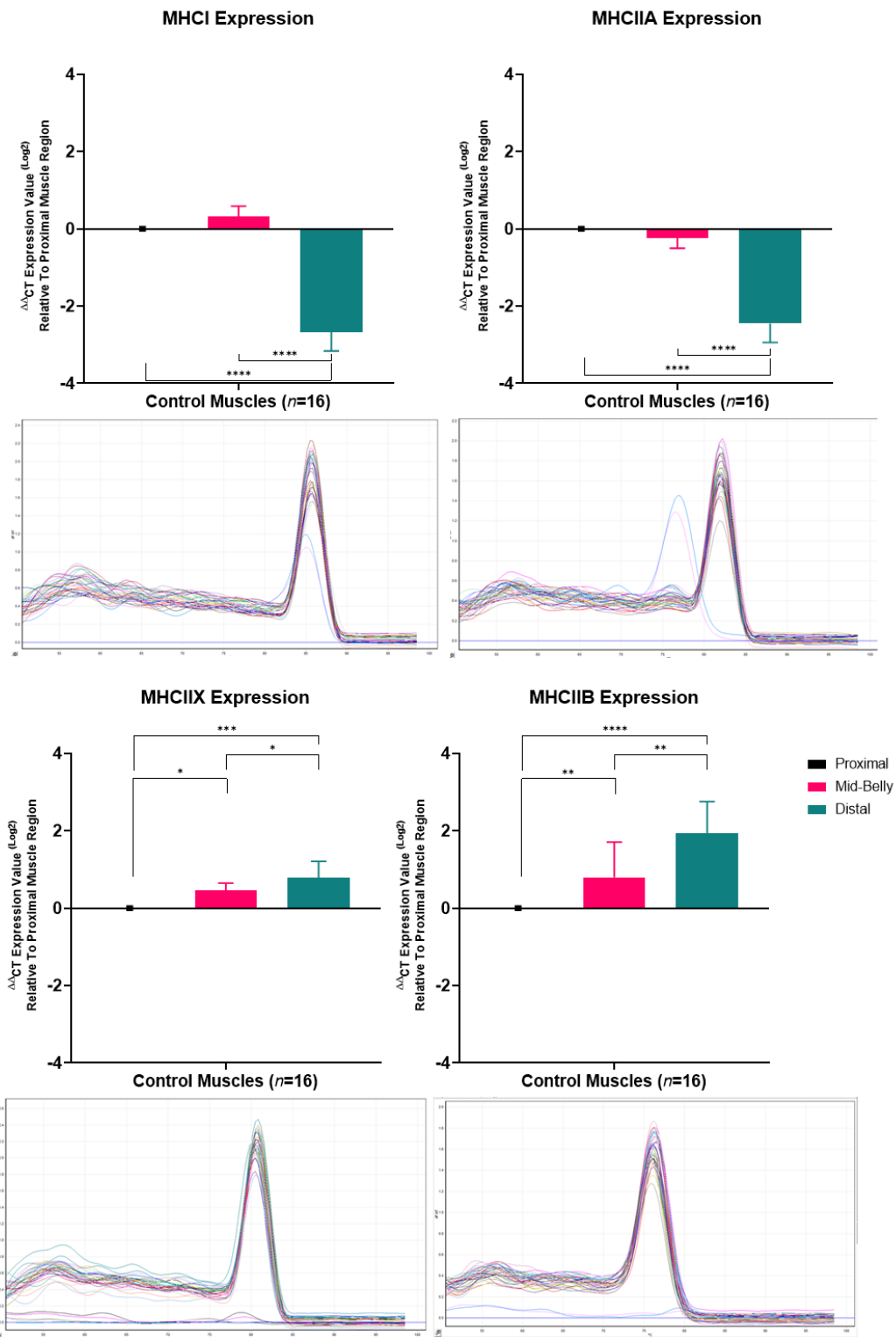


Figure 3.9: RT-qPCR data showing $\Delta\Delta CT$ mRNA expression values \log^2 transformed fold changes relative to the proximal muscle region reveal that the proximal end of the TA muscle contains considerably more slower MyHC mRNA which decreases toward the distal end, where there is considerably more fast MyHC mRNA. We note that mean, raw CT values were lowest for MyHCII B (18 ± 3 cycles) and increased progressively for MyHCII X (21 ± 3 cycles), MyHCII A

*(23 ± 5 cycles) and MyHCI (25 ± 7 cycles) which coincides with the immunofluorescent fiber type measurements observed in Figure 3.3. Melt curves are also provided for each primer set illustrating the formation of one PCR product. *P ≤ 0.05. **P ≤ 0.01. ***P ≤ 0.001. ****P ≤ 0.0001. Mean ± Standard Deviation assessed through ANOVA analysis with Tukey's- post hoc analysis on individual contralateral fold changes.*

We also note that following these findings we ensured that in Chapter 6, that tibialis anterior muscle was appropriately homogenised with muscle sections taken equally from the proximal, mid-belly and distal regions prior to next-generation RNA-sequencing. Future research should consider investigating whether the molecular/transcriptional response to exercise differs across the length of the muscle and in different fiber types as some studies have started to do through proteomics Eggers et al., (2021), Deshmukh et al., (2021), Hesketh et al., (2020a).

Chapter 4: A pilot investigation into the long-term effects of long-term resistance training, long term detraining following detraining and long-term recovery from severe disuse atrophy

4.1 Abstract:

Research from the previous chapter and amongst the exercise training field have noted that increases in muscle fiber size often coincide with increases in myonuclei. The Gundersen lab have for many years presented data suggesting that myonuclei are permanent, and not subject to apoptosis and therefore the number of myonuclei in a muscle fiber reflects the previous training history of that individual. However, much of this data has been derived from supra-physiological induction of hypertrophy through synergist ablation or testosterone and muscle loss produced through nerve transection Gundersen et al., (2018). Nevertheless, this has gathered worldwide media attention with potential implications for exercise prescription at a young age and potential ramifications for anabolic steroid users who may retain an advantage after a period of anabolic steroid use through myonuclei themselves and epigenetic adaptations Gundersen, (2016), Gundersen et al., (2018), Fisher et al., (2017), Seaborne et al., (2018b), Seaborne et al., (2019c). With the development of our new physiological and reversible models of resistance exercise-induced hypertrophy and nerve-silencing-induced atrophy we planned to study the long-term effects that training, detraining and long-term recovery from severe atrophy had on muscle mass, fiber size, fiber-type specific adaptations and myonuclei. However, only a pilot experiment could be performed due to the COVID-19 pandemic and length of the proposed experiments that are detailed in the methods section of this chapter. Despite low numbers of animals in each group, data was relatively tightly pooled giving good promise for future investigations. Our data suggests that long periods of detraining do not allow muscle mass to return to normal in the TA, despite measures of overall and fiber-type specific fiber area returning to baseline. Interestingly, the substantial shift from IIB to IIX fibers following training only partially reverts to baseline following detraining. Myonuclei gained during the hypertrophic process had also seemingly been lost as myonuclei per fiber cross-section measurements returned to basal levels. Contrastingly, in our TTX-induced atrophy model with long term recovery, muscle mass returned to baseline, as did measures of fiber area and fiber type composition. However, our data suggested that the myonuclei added during the early recovery phase potentially remained even after long term recovery, meaning the tibialis anterior was still potentially hypernucleated and requires further replicates. In conclusion, our two models of myonuclear addition may involve different mechanisms or may harbour differential genetic/epigenetic

adaptations that mean that myonuclear density is maintained or reverts to that of a control muscle which warrants further investigation.

4.2 Introduction:

In this chapter, we outline and present pilot data as a continuation of the work completed in Chapter 4. Whilst there is a wealth of literature on the timecourse of muscle growth/loss in humans and rodents and associated changes in myonuclear content Chaillou et al., (2015), Chaillou et al., (2013), Loenneke et al., (2017), Seynnes et al., (2007), Narici et al., (1989), Häkkinen et al., (2001), DeFreitas et al., (2011), Psilander et al., (2019), Stock et al., (2017), Damas et al., (2018b), there is less of a focus on how quickly muscle loses its size and metabolic adaptations when training ceases, or whether they retain biochemical adaptations Mujika and Padilla, (2001), Ivey et al., (2000), Häkkinen et al., (1985), Psilander et al., (2019), Snijders et al., (2020a), Beiter et al., (2020), Murach et al., (2019a), Wen et al., (2021), Murach et al., (2020b), Dungan et al., (2019), Brownson et al., (1992), Bruusgaard et al., (2010).

As well as the number of myonuclei themselves potentially contributing to faster adaptation during anabolic periods, there is growing interest in how exercise training alters the epigenome of muscle nuclei. Specifically, how and why DNA/histone methylation changes that occur may allow genes to be switched on easier (hypomethylation) or are harder to transcribe (hypermethylation) that subsequently benefit the muscle by slowing wasting and increasing the rate at which muscle can adapt to training or recovery from catabolic periods Figueiredo et al., (2021), Fisher et al., (2017), Seaborne et al., (2019b), Seaborne et al., (2018b), Seaborne et al., (2019c), Sharples et al., (2016), Turner et al., (2019), Wen et al., (2021).

We aim to start elucidating the long-term effects of spillover resistance training, long term detraining after a period of resistance training and finally, long term-recovery following 14 days of TTX-induced atrophy on the tibialis anterior. A wistar rat has a life expectancy of around 18-22 months. Four months, or 120 days therefore reflects around 18-22% of the rat's lifespan Alvarado et al., (2014), so was selected as a good timepoint to study the effects of chronic resistance exercise on the tibialis anterior muscle, whether the muscle retained any of the beneficial characteristics of a previous resistance exercise programme after detraining

and lastly, whether there were any lasting repercussions of severe atrophy induced by 2 weeks TTX nerve silencing.

We also extend our current knowledge of fiber type specific adaptations to 30 days spillover resistance training, 14 days TTX-induced atrophy and 14 days TTX-induced atrophy with 7 days recovery by assaying for type I, IIA, IIX, IIB fibers, as opposed to our previous method that assayed for type I, IIA and combined IIX/IIB fibers.

For the 3 pilot experiments we hypothesised the following:

- 120 days of daily spillover stimulation would become less of a hypertrophic stimulus and more of an endurance like stimulus and would therefore induce a fast-to-slow transformation of the myosin heavy chain isoforms as previously seen with long-term chronic low frequency stimulation Sutherland et al., (1998). We also hypothesised that the hypertrophy seen after 30 days of training may have reduced as a result of an overtraining response.
- 30 days of daily spillover stimulation followed by 120 days of detraining (no stimulation) would result in the tibialis anterior returning to a phenotype close to its untrained contralateral control due to the removal of changes in activity and load.
- 14 days of TTX-induced atrophy followed by 120 days recovery would allow for the muscle to completely recover back to contralateral control levels.

4.3 Methods:

Surgeries for spillover stimulation and TTX-induced nerve silencing were performed as outlined in the Chapter 2 and 5 and muscles harvested as previously described for histological and immunohistochemical assessment.

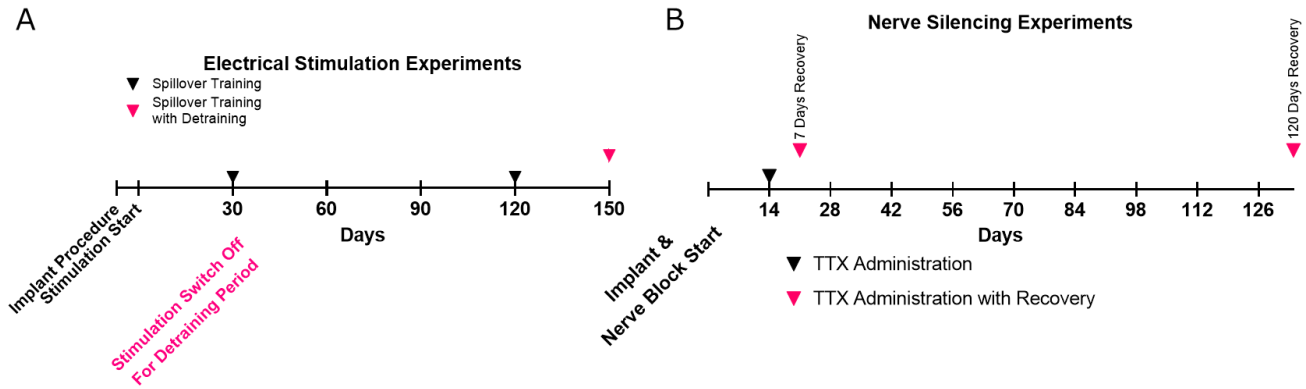


Figure 4.1: Experimental timecourse for electrical stimulation (A) (30- and 120-days training) and detraining experiments (30 days training with 120 days detraining). Animals in the 30-day group were used previously in Chapter 4. (B) Timecourse for nerve silencing (14 days) and experiments with subsequent recovery from nerve silencing (7 days and 120 days). Animals in the 14 days TTX treatment and 14 days TTX treatment with subsequent recovery were used previously in Chapter 5.

For the 120 days Spillover group ($n=2$), muscle stimulation was checked, and implants reset every ~ 2 weeks to ensure successful stimulation. On the day prior to harvesting, implants were switched off after the training session. On the day of harvest, stimulators were switched back on for an acute spillover training session and harvested 1 hour post the end of the training bout, for future assessment of the transcriptional response to exercise. Wistar rats in the 30 days spillover training with 120 days detraining group ($n=3$), had stimulators switched off after the animals 30th training session and switched on again for an acute training bout after 120 days of no training. Muscles were harvested 1 hour post the end of the training bout, for future assessment of the transcriptional response to exercise. Out of the 5 stimulators used in these two pilot experiments, 4 were successfully switched on the day of harvest demonstrating the ability to use stimulators for long periods of training and detraining

in future. During dissection and muscle harvesting, it was noted that both the implant device and electrodes were still securely placed as they were during surgery. Both the tibial and common peroneal nerve as well as surrounding tissues were also noted to be looking healthy despite long term implantation.

Wistar rats in the long-term recovery from TTX group ($n=3$) were observed daily for foot drop during the 14 days of treatment, confirming silencing of the common peroneal nerve and was not present in the days shortly following TTX cessation. During muscle harvesting and dissection, it was noted that the nerve cuff was still secured around the common peroneal nerve and both the nerve and surrounding tissue was healthy. We also confirmed that the osmotic pump was still securely attached the silicone tubing running to the nerve cuff, as seen in Figure 4.2.

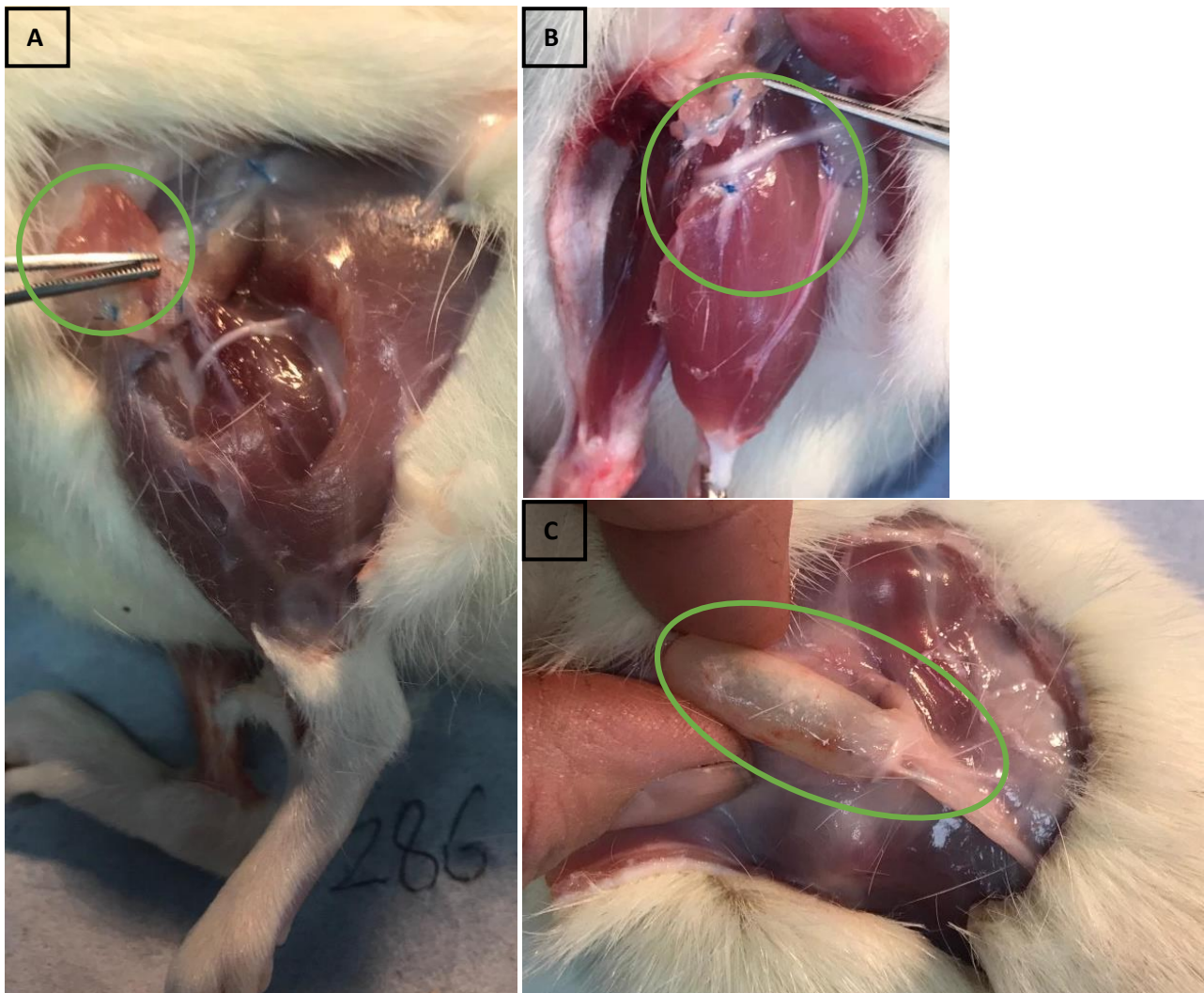


Figure 4.2: (A) illustrates the TTX cuff after being cut away from the common peroneal nerve to reveal the healthy nerve after being in place for 134 days. (B) illustrates the common

peroneal nerve further distally to the tibialis anterior showing a healthy white colour. (C) illustrates the osmotic pump still attached to the silicone tubing that runs subcutaneously to the nerve cuff.

Following histological preparation and sectioning, serial 10 μ m cross-sections from the mid-belly of the tibialis anterior were labelled with two different antibody mixtures to assess all 4 fiber types. Solution 1 consisted of antibodies against dystrophin, type IIB myosin (BF-F3) and type IIA myosin (SC-71) in IB. Solution 2 consisted of antibodies against dystrophin, type IIX myosin (6H1) and type I myosin (BA-D5) in IB and were all later counterstained with DAPI for myonuclear identification. Full cross-sections were imaged as previously described and ran through Myovision 2.0 as previously described. Full details on primary and secondary antibodies used are available in table 2.1.

Statistical analyses were performed on the resultant muscle masses, fiber type percentages, overall mean fiber CSA, fiber type specific mean CSA, overall mean myonuclei per fiber cross-section, fiber type specific mean myonuclei per fiber cross-section, overall mean myonuclear domain size, fiber type specific mean myonuclear domain size by between group one-way ANOVA's, followed by Tukey's post-hoc analysis to confirm differences between groups. Controls from all stimulation/detraining experiments were pooled into one group, as were the controls from all TTX/recovery experiments.

4.4 Results:

Muscle mass, overall CSA, myonuclei per fiber cross-section and myonuclear domain sizes following long term training and detraining.

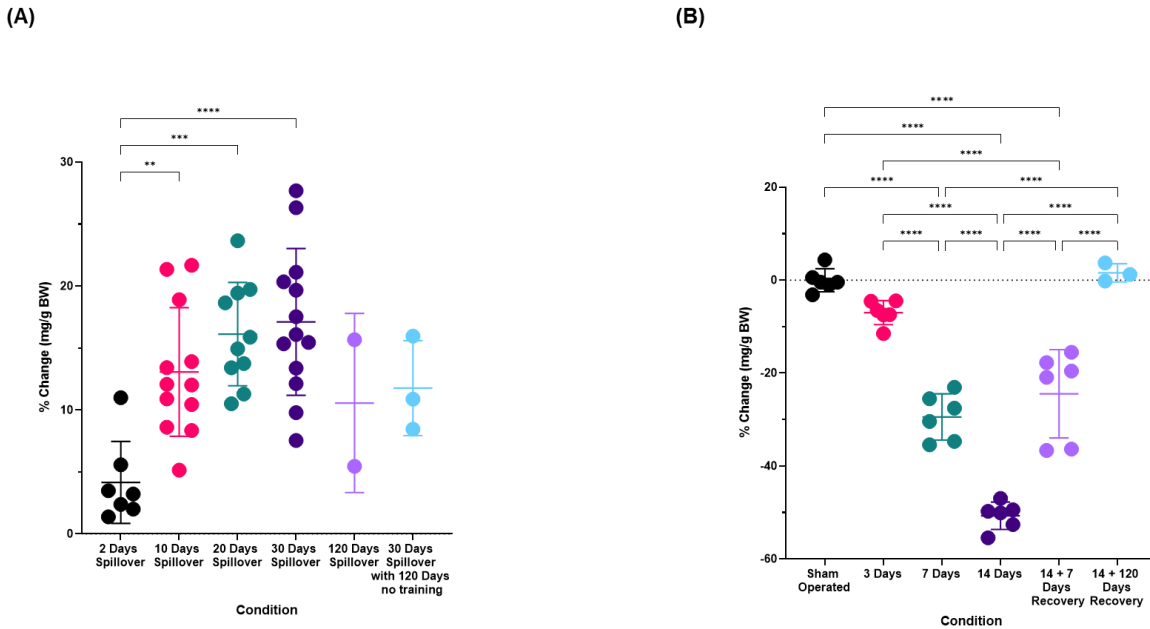


Figure 4.3: Changes in tibialis anterior muscle mass as percentage change from the right unoperated limb and left experimental limb in mg/g bodyweight. (A) Timecourse of Spillover resistance training from 2 to 120 days followed by 120 days detraining. (B) Timecourse of TTX-induced nerve silencing induced atrophy from 3 to 14 days with subsequent 7- and 120-days recovery by habitual cage activity. * $P \leq 0.05$. ** $P \leq 0.01$. *** $P \leq 0.001$. **** $P \leq 0.0001$. Mean \pm Standard Deviation.

Age and body mass data on the animals used for 30 days spillover training, 14 days TTX treatment and 14 days TTX treatment with 7 days recovery are available in Chapter 4. Male wistar rats ($n=2$) in the 120 days of daily spillover training group had a mean body mass of 529.5 ± 3.5 g and were 20 weeks of age when implanted. When harvested, the mean body mass was 600.8 ± 0.6 g and animals were 39 weeks of age. As outlined in chapter __, spillover training produces a hypertrophic effect seen through measures of muscle mass and fiber CSA that plateaus between 10 and 30 days of daily training. 120 days of spillover training caused a significant increase in muscle mass versus sham control ($10.56 \pm 7.29\%$, $P = 0.004$), which did not significantly differ versus 10, 20 and 30 days of training respectively ($13.6 \pm 5.8\%$, $16.7 \pm 4.4\%$, $15.9 \pm 5.6\%$). Male wistar rats ($n=3$) in the 30 days spillover training with 120 days

detraining had a mean body mass of $563 \pm 66.5\text{g}$ and were 20 weeks of age when implanted. When harvested, the mean body mass was 679 ± 69.9 and animals were 43 weeks of age. Interestingly, despite 120 days of no training after 30 days spillover training, muscle mass was still significantly higher than the sham operated control ($11.76 \pm 3.83\%$) and was not significantly different to the 10, 20, 30 and 120 days of training groups ($P > 0.05$).

In a fresh analysis on new whole cross-sections, there was a significant increase in the overall average fiber CSA between control ($1907 \pm 115\mu\text{m}^2$), 30 days of spillover training ($2147 \pm 68.3\mu\text{m}^2$, $P = 0.004$) and 120 days spillover training ($2533 \pm 184.6\mu\text{m}^2$, $P = 0.001$) but was not significantly different to the 30 days training with 120 days detraining group ($1956 \pm 55.8\mu\text{m}^2$, $P > 0.05$) showing that the muscle had not returned to control levels (Figure 4.3A). 120 days of training was also significantly higher than the 30-day training group ($P = 0.03$). Myonuclei per fiber cross-section was significantly higher in the 30 days spillover training group (1.16 ± 0.06 , vs. 1.59 ± 0.14 , $P < 0.0001$), but there was no additive affect after 120 days (1.66 ± 0.03 , $P = 0.45$). Interestingly myonuclei number was significantly lower after 120 days of detraining (1.19 ± 0.09 , $P = 0.001$) when compared with 30 and 120 days of spillover training and did not differ with the control group, suggesting that the myonuclei added during hypertrophy are not permanent (Figure 4.4B). As a result, myonuclear domain size was significantly lower in the 30 days training group ($1689 \pm 170.4\mu\text{m}^2$, vs. $1394 \pm 123\mu\text{m}^2$, $P > 0.05$), suggesting an addition of myonuclei prior to, or at a faster rate than an increase in fiber cross-sectional area. There were no significant changes between the control group and either the 120 days spillover group or detraining group respectively ($1522 \pm 132\mu\text{m}^2$ and $1636 \pm 109.7\mu\text{m}^2$), demonstrating that the detraining period was sufficient to return myonuclear domain size back to basal levels (Figure 4.4C).

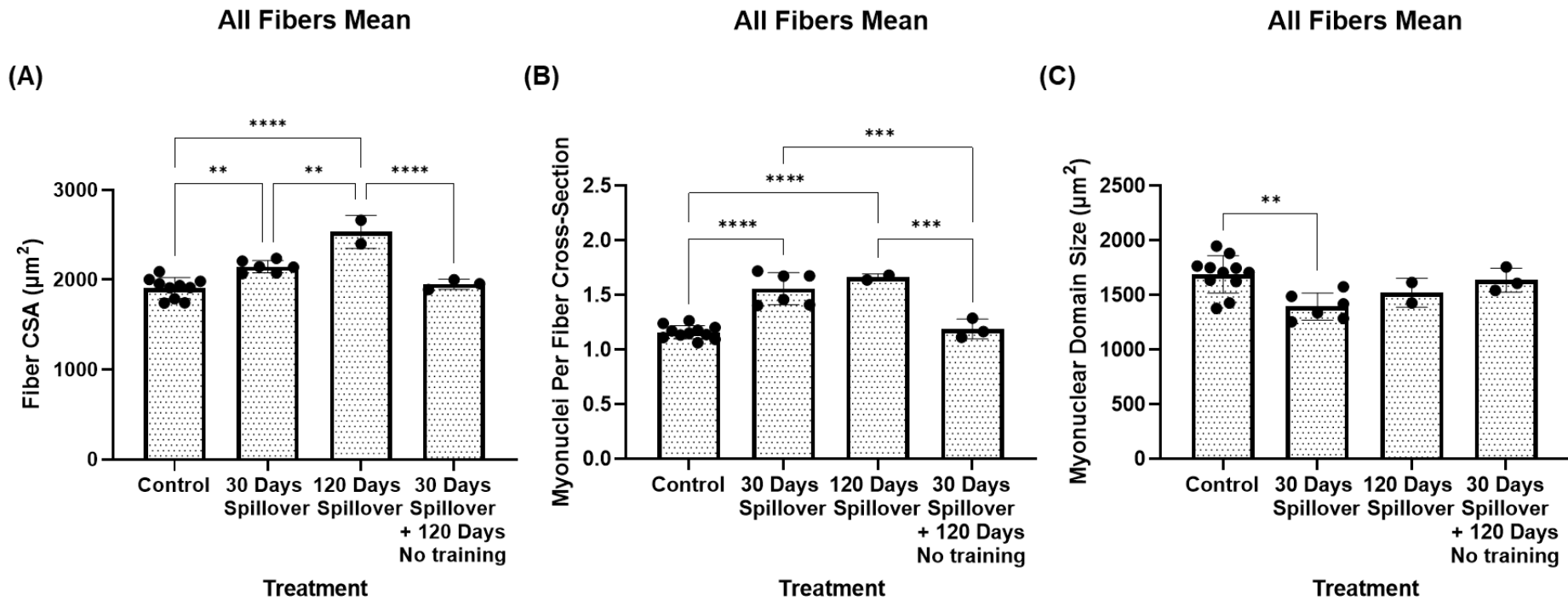


Figure 4.4: (A) Changes in tibialis anterior muscle fiber cross-sectional area following medium to long term spillover training with subsequent long-term detraining, across all muscle fibers. (B) Changes in tibialis anterior myonuclei per fiber cross-section following medium to long term spillover training with subsequent long-term detraining, across all muscle fibers. (C) Changes in tibialis anterior muscle fiber myonuclear domain size following medium to long term spillover training with subsequent long-term detraining. * $P \leq 0.05$. ** $P \leq 0.01$. *** $P \leq 0.001$. **** $P \leq 0.0001$. Mean \pm Standard Deviation.

Fiber type specific shifts, changes in size, myonuclei per fiber cross-section and myonuclear domain sizes.

Fiber type shifts were assessed and revealed no changes in type I fiber composition between control ($3.23 \pm 1.325\%$), 30 days ($3.92 \pm 1.36\%$), 120 days ($3.95 \pm 0.63\%$) and 30 days with 120 days detraining ($4.267 \pm 0.97\%$). Similarly, there was no change in type IIA fiber composition between control ($17.35 \pm 4.8\%$), 30 days ($17.17 \pm 3\%$), 120 days ($17.5 \pm 2.1\%$) and 30 days with 120 days detraining ($18.35 \pm 0.58\%$). More prominent effects of training and detraining were evident with IIX fibers. There was a significant increase between control ($20.09 \pm 6.3\%$) and 30 days training ($48 \pm 3.03\%$, $P < 0.0001$) and 120 days training ($47.5 \pm 2.12\%$, $P < 0.0001$). Following 120 days detraining, there was a partial shift back to control levels ($P = 0.0017$) but was significantly lower than the 30- and 120-day group ($35 \pm 3\%$, $P = 0.012$). Inversely, the shift to IIX after stimulation is attributed to a decrease in type IIB fibers from control levels ($34.2 \pm 3.16\%$) which are almost completely absent with 30 ($2.17 \pm 1.54\%$, $P < 0.0001$) and 120 days training ($1.15 \pm 1.63\%$, $P < 0.0001$). Hybrid fibers did not differ significantly between control ($25.36 \pm 4.94\%$), 30 days spillover ($29 \pm 3.89\%$), 120 days spillover ($30.5 \pm 6.36\%$) and 30 days spillover with detraining ($25.67 \pm 5.69\%$), $P > 0.05$, (Figure 4.5A-D). We note that our methods did not allow us to distinguish between the different hybrids on the cross-sections but that we observed type I/IIA hybrids, as well as type IIA/IIX, IIX/IIB and IIA/IIX/IIB hybrids. Whilst not quantified, from observations we believe there to be a shift from IIB/IIX hybrids to IIX/IIA hybrids, hence no change in the overall numbers of hybrid fibers, (Figure 4.5E).

Type I fiber CSA increased significantly from control ($981.8 \pm 116.9 \mu\text{m}^2$) after 30 days of spillover training ($1475 \pm 282.2 \mu\text{m}^2$, $P = 0.0002$), but did not reach significance after 120 days of spillover training ($1333 \pm 144.2 \mu\text{m}^2$, $P = 0.09$). Following the detraining period, type I fiber CSA had returned to that of control levels ($1019 \pm 132.1 \mu\text{m}^2$) and was significantly smaller than type I fiber CSA after 30 days of spillover training, ($P = 0.0109$). Type IIA control fiber CSA ($1318 \pm 190 \mu\text{m}^2$) was significantly smaller than type IIA fiber CSA after 30 ($1664 \pm 312.3 \mu\text{m}^2$, $P = 0.029$) and 120 days spillover training ($1962 \pm 57.98 \mu\text{m}^2$, $P = 0.0065$). There was no significant difference between the IIA fiber size between 30 and 120 days of spillover training, ($P = 0.3$). After detraining, type IIA fiber CSA returned to basal control levels ($1461 \pm 107.1 \mu\text{m}^2$, $P = > 0.05$). Type IIX fiber CSA showed a trend to increase from control ($1965 \pm 178.3 \mu\text{m}^2$), after 30 days training ($2189 \pm 204.8 \mu\text{m}^2$, $P = 0.1141$), later reaching significance after 120 days

spillover training ($2610 \pm 254.6\mu\text{m}^2$, $P = 0.0013$). The 120-day group was not significantly greater than the 30-day group, but showed a strong trend, ($P = 0.052$), which likely would have become significant with a larger sample size. 120 days of training was also significantly higher than the detraining group ($2058 \pm 91.69\mu\text{m}^2$, $P = 0.0195$). Type IIB fiber CSA increased significantly after 30 ($2793 \pm 209.9\mu\text{m}^2$, $P = 0.0008$), and 120 days of spillover training ($2901 \pm 71.42\mu\text{m}^2$, $P = 0.0027$), compared with control IIB CSA ($2300 \pm 224.4\mu\text{m}^2$) and returned to control levels after the 120-day detraining period ($2314 \pm 101\mu\text{m}^2$, $P = 0.1141$). Interestingly, hybrid fibers were the only fibers to show a progressive hypertrophic affect in fiber CSA, increasing significantly after 30 days of spillover training ($2009 \pm 184.3\mu\text{m}^2$ vs. $2793 \pm 209.9\mu\text{m}^2$, $P = 0.0008$) and furthermore after 120 days of spillover training ($2901 \pm 71.42\mu\text{m}^2$, vs. control ($P = 0.0027$)) and 30 days of spillover training ($P = 0.049$), Figure 4.5F-J).

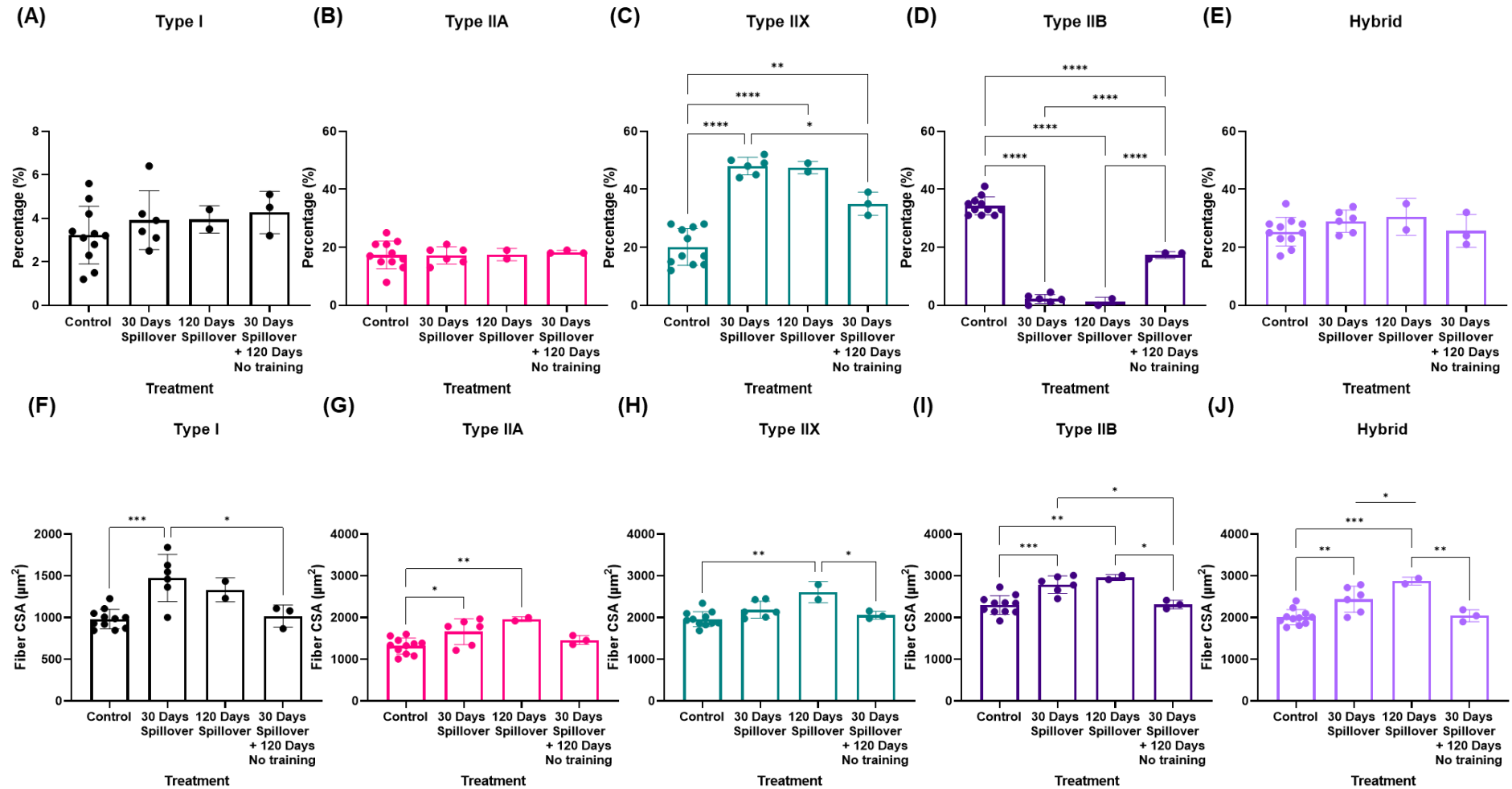


Figure 4.5: (A-E) Changes in fiber type composition across short- and long-term detraining and subsequent long-term detraining in type I, IIA, IIX, IIB and hybrid muscle fibers. (F-J) Changes in fiber cross-sectional area across short- and long-term detraining and subsequent long-term detraining in type I, IIA, IIX, IIB and hybrid muscle fibers. * $P \leq 0.05$. ** $P \leq 0.01$. *** $P \leq 0.001$. **** $P \leq 0.0001$. Mean \pm Standard Deviation.

Intriguingly, measurements of myonuclei per fiber cross-section increased significantly in all fiber types in response to training. In detail, myonuclei per fiber cross-section in type I fibers increased significantly from control (0.995 ± 0.116) and after both 30 (1.238 ± 0.18 , $P = 0.0158$) and 120 days of spillover training (1.48 ± 0.08 , $P = 0.0016$). Whilst there was a trend suggesting 120 days spillover training caused a greater increase in myonuclei per fiber cross-section compared with 30, this did not reach significance with our current sample size, ($P = 0.17$). Interestingly, detraining caused a significant reduction in myonuclei from the 120-day trained group (1.01 ± 0.16 , $P = 0.0091$), that did not differ significantly from the control type I myonuclei per fiber cross-section measurements. Similarly, type IIA measurements showed a significant increase in myonuclei per fiber cross-section from control (1.06 ± 0.17) and 30 days of training (1.457 ± 0.34 , $P = 0.0125$), and 120 days spillover training (1.59 ± 0.05 , $P = 0.0091$). Again, data suggested that myonuclei were lost following detraining, returning to control levels (1.057 ± 0.102 , $P > 0.05$). Myonuclei per fiber cross-section in IIX fibers did not differ between control (1.203 ± 0.129) and 30 days training with 120 days detraining (1.233 ± 0.15 , $P = 0.87$), but both were significantly lower than the 30 days (1.603 ± 0.11 , $P < 0.0001$) and 120 days spillover training groups (1.655 ± 0.09 , $P = 0.0008$). This was recapitulated in IIB fibers that showed a significant increase in myonuclei per fiber cross-section from control (1.236 ± 0.06), in response to 30 (1.747 ± 0.18 , $P < 0.0001$) and 120 days spillover training (1.75 ± 0.09 , $P < 0.0001$). This myonuclear addition was also reversed following the detraining period (1.303 ± 0.05), back to levels of the untreated controls. Hybrid fibers displayed a more progressive trend to myonuclear accretion with 30 days spillover training significantly increasing myonuclei per fiber cross-section compared with control (1.134 ± 0.112 , vs. 1.483 ± 0.19 $P = 0.0004$). Similarly, 120 days of spillover training caused an increase compared with control (1.72 ± 0.07 , $P = 0.0002$). There was a trend suggesting that further myonuclei were added to the hybrid fibers after 120 days vs. 30 days ($P = 0.17$), that may have reached significance with a larger sample size. Again, detraining returned myonuclei per fiber cross-section measurements back to control levels, (1.193 ± 0.09 , $P = 0.892$), (Figure 4.6A-E).

There was no significant difference between type I myonuclear domain sizes between control ($997.6 \pm 162.5\mu\text{m}^2$), 30 days ($1215 \pm 322.5\mu\text{m}^2$), 120 days spillover training ($899.4 \pm 45.91\mu\text{m}^2$), and 30 days training with 120 days detraining ($1012 \pm 49.36\mu\text{m}^2$). Similarly, no changes were found in myonuclear domain sizes in type IIA fibers ($1283 \pm 337.5\mu\text{m}^2$, $1177 \pm$

276.3 μm^2 , 1235 \pm 80.42 μm^2 and 1397 \pm 239.6 μm^2). Myonuclear domain size decreased in type IIX fibers from (1644 \pm 166.4 μm^2) to (1344 \pm 215 μm^2 , $P = 0.0228$) after 30 days training, but did not significantly differ from the 120 days training group (1584 \pm 241.8 μm^2) and the 30 days training with 120 detraining group (1694 \pm 141.4 μm^2), suggesting that myonuclei were added at a slightly faster rate than the increase in fiber CSA in this specific fiber type. There were no significant differences between type IIB myonuclear domain sizes between control (1865 \pm 197.5 μm^2), 30 days (1618 \pm 241.3 μm^2), 120 days spillover training (1693 \pm 54.97 μm^2), and 30 days training with 120 days detraining (1778 \pm 120.2 μm^2). Similarly, there were no significant differences between hybrid fiber myonuclear domain sizes between control (1791 \pm 255 μm^2), 30 days (1749 \pm 149 μm^2), 120 days spillover training (1672 \pm 148.6 μm^2), and 30 days training with 120 days detraining (1714 \pm 181.3 μm^2), (Figure 4.6F-J). This data suggests that apart from IIX fibers, all other fiber types increase fiber CSA in line with increases in myonuclei per fiber cross-section.

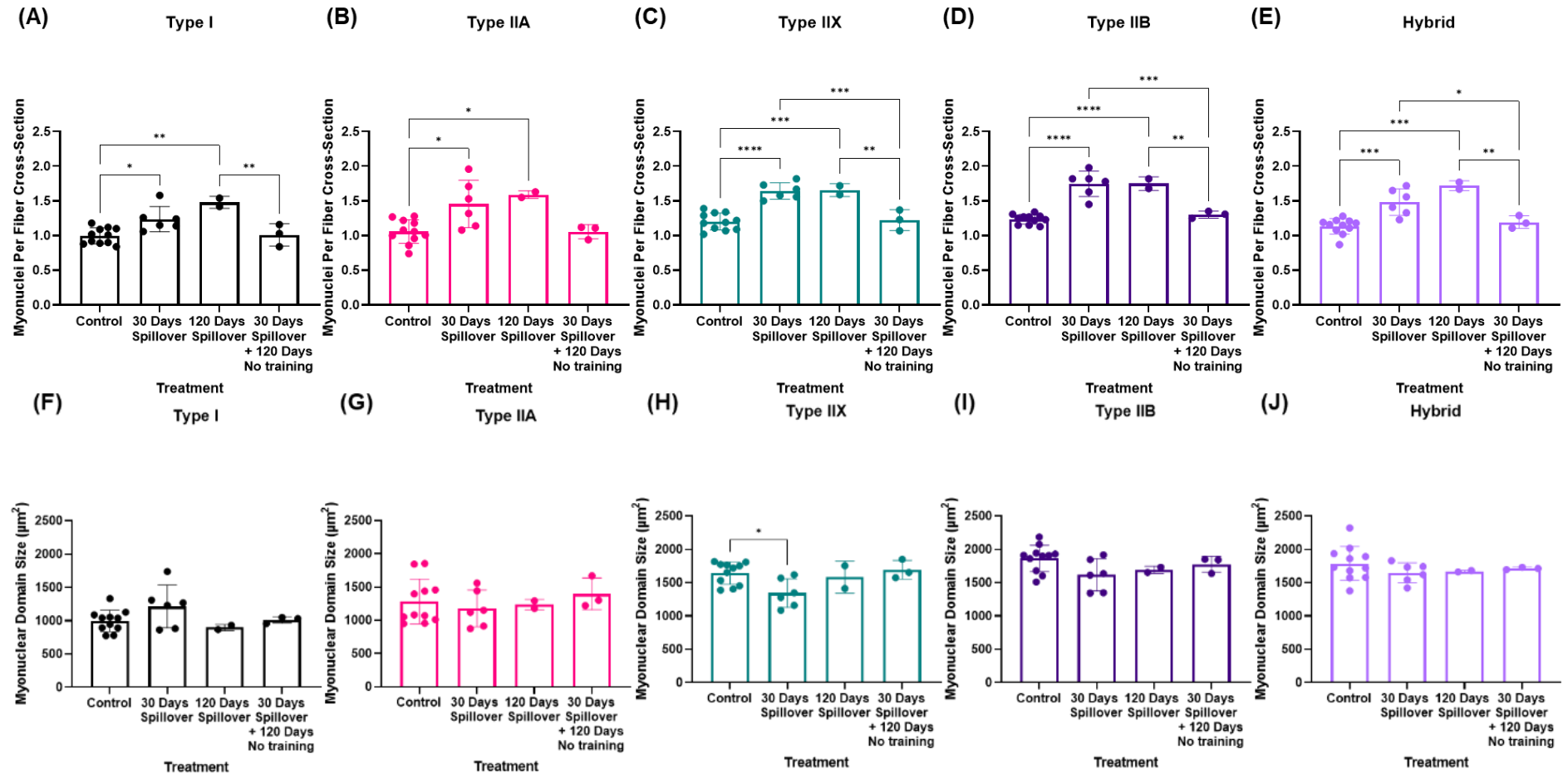


Figure 4.6: (A-E) Changes in myonuclei per fiber cross section across short- and long-term detraining and subsequent long-term detraining in type I, IIA, IIX, IIB and hybrid muscle fibers. (F-J) Changes in myonuclear domain size across short- and long-term detraining and subsequent long-term detraining in type I, IIA, IIX, IIB and hybrid muscle fibers. * $P \leq 0.05$. ** $P \leq 0.01$. *** $P \leq 0.001$. **** $P \leq 0.0001$. Mean \pm Standard Deviation.

Muscle mass, overall CSA, myonuclei per fiber cross-section and myonuclear domain sizes following severe atrophy and short- and long-term recovery.

Male wistar rats ($n=3$) in the 14 days TTX with 120 days recovery group had a mean body mass of $355 \pm 19\text{g}$ and were 18 weeks of age when implanted. When harvested, 120 days post cessation of TTX delivery, mean body mass was $495 \pm 29.4\text{g}$ and animals were 37 weeks of age. Body mass data for other groups in this timecourse can be found in chapter __. As previously highlighted, TTX-induced nerve silencing causes a significant decrease in muscle mass after 14 days ($-50.7 \pm 2.92\%$) versus sham surgery ($P < 0.00001$) which partially recovers after just 7 days recovery by ambulatory cage activity ($-24.46 \pm 9.49\%$). In our new pilot experiment, 120 days of recovery following 2 weeks of TTX-nerve silencing allows muscle mass to recover back to baseline values ($1.56 \pm 1.98\%$) of its contralateral control limb. In a new analysis of freshly cut $10\mu\text{m}$ cross-sections, MyoVision 2.0 analysis revealed a significant overall fiber cross-sectional area loss after 14 days from control ($1898 \pm 101.6\mu\text{m}^2$ vs. 979.7 ± 62.29 , $P < 0.0001$). Fiber CSA can partially recover after 7 days of recovery vs. 14 days of atrophy ($P < 0.0001$) yet is still significantly lower than control fiber CSA ($1480 \pm 67.06\mu\text{m}^2$, $P < 0.00001$). With 120 days recovery, fiber CSA is back in line with overall fiber CSA of control muscles ($1910 \pm 22.14\mu\text{m}^2$), (Figure 4.7A). Measurements of overall myonuclei per fiber cross-section revealed a loss of myonuclei per fiber cross-section after 14 days TTX treatment in comparison to the control group (1.14 ± 0.13 vs. 0.70 ± 0.09 , $P < 0.0001$), which unlike fiber CSA had already recovered in a super compensatory manner by day 7, so that there were more myonuclei than in the control muscles (1.423 ± 0.22 , $P = 0.002$). After 120 days recovery, myonuclei per fiber cross-section measurements were not significantly different from the 7-day recovery group (1.34 ± 0.04 $P = 0.76$), but a trend was present suggesting they had more than control muscles ($P = 0.15$), that may have reached significance with a larger sample size, (Figure 4.7B). As a result, myonuclear domain size did not differ between control and 14 days TTX treatment groups, ($1694 \pm 271\mu\text{m}^2$ vs. $1500 \pm 267\mu\text{m}^2$, $P = 0.3756$), suggesting that fiber cross-sectional area loss was in line with myonuclear losses. However, domain size did significantly reduce in the 14 days TTX treatment + 7 days recovery group to ($1089 \pm 186\mu\text{m}^2$, $P = 0.0001$ vs. control, $P = 0.0345$ vs. 14 days TTX treatment). After 120 days recovery, myonuclear domain size had returned to that of control levels ($1421 \pm 330\mu\text{m}^2$, $P = 0.31$), (Figure 4.7C).

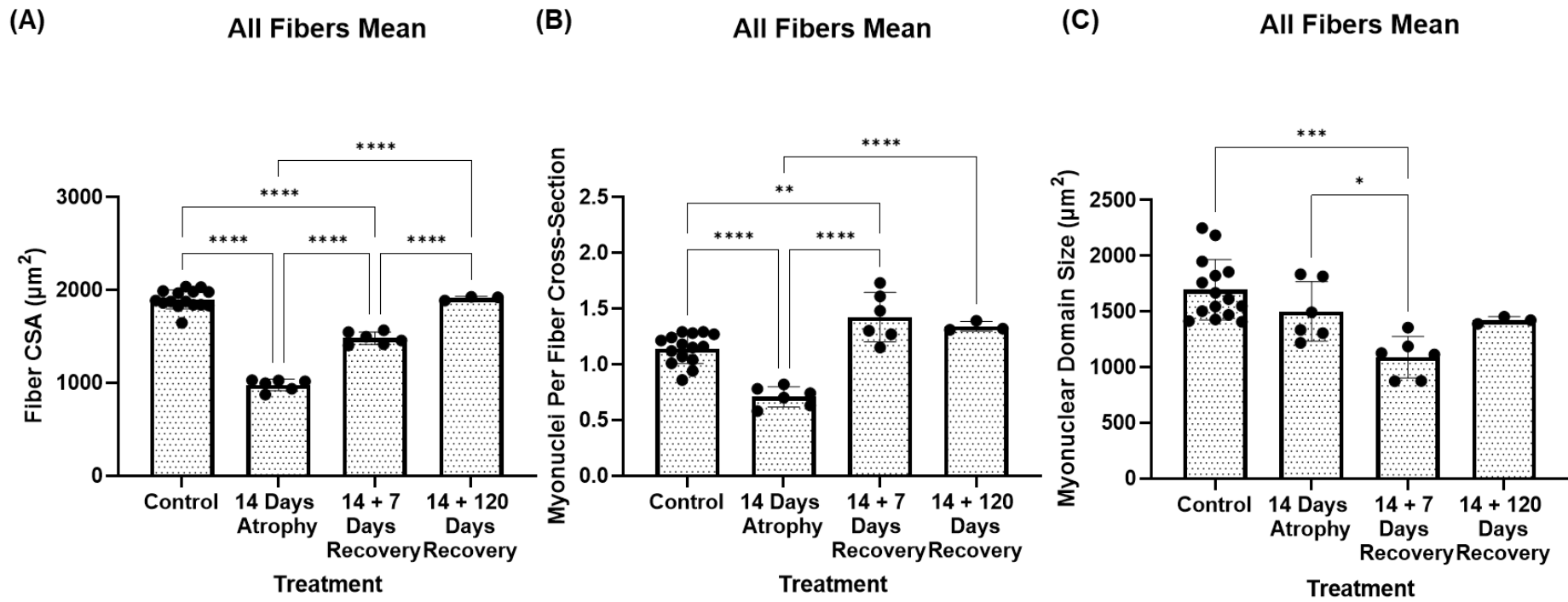


Figure 4.7: (A) Changes in tibialis anterior muscle fiber cross-sectional area following severe muscle atrophy and subsequent short- and long-term recovery by habitual cage activity, across all muscle fibers. (B) Changes in tibialis anterior myonuclei per fiber cross-section following severe muscle atrophy and subsequent short- and long-term recovery by habitual cage activity, across all muscle fibers. (C) Changes in tibialis anterior muscle fiber myonuclear domain size following severe muscle atrophy and subsequent short- and long-term recovery by habitual cage activity, across all muscle fibers. * $P \leq 0.05$. ** $P \leq 0.01$. *** $P \leq 0.001$. **** $P \leq 0.0001$. Mean \pm Standard Deviation.

Fiber type specific shifts, changes in size, myonuclei per fiber cross-section and myonuclear domain sizes.

Previous analyses in Chapter 4, revealed that there were no significant shifts in fiber type after atrophy and recovery. However, a fresh analysis of all fiber types revealed some shifts in response to these treatments. The new analyses found a decrease in the percentage of type I fibers after 14 days of atrophy from $(3.18 \pm 1.21\%$ vs. $1.13 \pm 0.78\%$, $P = 0.0029$), whereas only a trend was previously found in Chapter 4. This reduction in type I fibers from control levels was still prevalent after 7 days recovery ($1.75 \pm 0.69\%$, $P = 0.049$). However, 120 days of recovery allows for reversal of the percentage of type I fibers back to basal levels ($2.9 \pm 1.51\%$). Similarly, we previously only noted a trend suggesting an increase in IIA fibers, though our new analyses showed a significant increase after 14 days of atrophy ($32.17 \pm 8.28\%$, $P = 0.0008$) and after 7 days recovery ($34.5 \pm 11.95\%$, $P = 0.0001$) versus control muscles ($17.67 \pm 2.96\%$). 120 days recovery returned the percentage of type IIA fibers back to basal levels ($17.33 \pm 3.22\%$). Type IIX fibers did not differ significantly between control ($23.87 \pm 5.26\%$) and 14 days TTX treatment ($29.17 \pm 8.86\%$, $P = 0.33$). After 7 days recovery, the percentage of IIX fibers was reduced significantly to ($11.17 \pm 5.91\%$, $P = 0.0019$) from the control group and 14 days TTX treatment group ($P = 0.0003$). There was also a trend suggesting that after 120 days recovery, the percentage of type IIX fibers had not recovered fully to control levels ($17.33 \pm 7.57\%$, $P = 0.19$). The increase in type IIA's and IIX's after 14 days TTX treatment can be explained by the reduction in type IIB fibers from control levels ($33.07 \pm 6.84\%$ vs. $10.35 \pm 2.97\%$, $P < 0.0001$). 7 days recovery following atrophy partially increased the percentage of IIB fibers ($24 \pm 6.75\%$, $P = 0.0029$), but this was still significantly lower than control muscles ($P = 0.0209$). However, 120 days of recovery allowed for IIB fibers to return to their basal proportions ($36 \pm 2\%$). Furthermore, there were no alterations in the percentage of hybrid fibers between control, 14 days TTX treatment, atrophy with 7 days recovery and atrophy with 120 days recovery respectively ($22.33 \pm 4.92\%$, $27.17 \pm 7.89\%$, $28.83 \pm 12.73\%$, $26 \pm 6.24\%$), (Figure 4.8A-E).

Fiber type specific cross-sectional area measurements revealed a trend in type I fibers atrophying from control levels ($999.1 \pm 168.2\mu\text{m}^2$ vs. $796 \pm 169.5\mu\text{m}^2$, $P = 0.0764$) after 14 days of TTX nerve silencing. There was no significant difference between the control and 14 days TTX treatment with subsequent 7 days ($988.1 \pm 154.7\mu\text{m}^2$) and 120 days recovery group

($962.7 \pm 158\mu\text{m}^2$). In contrast, IIB fiber cross-sectional area did decrease during the 14-day treatment from the control group ($1253 \pm 128.7\mu\text{m}^2$ vs. $968 \pm 89.29\mu\text{m}^2$, $P < 0.0001$). With just 7 days recovery, IIA fiber cross-sectional area significantly increased back to control levels, ($1368 \pm 77.39\mu\text{m}^2$, $P < 0.0001$). As expected, control and 7 days recovery were not significantly different to the 120-day recovery group ($1262 \pm 58.8\mu\text{m}^2$, $P > 0.9$). Type IIX fiber CSA was significantly reduced after 14 days TTX treatment, ($1963 \pm 203.4\mu\text{m}^2$ vs. $939.3 \pm 101.2\mu\text{m}^2$, $P < 0.0001$), but significantly increased after 7 days recovery ($1451 \pm 142.3\mu\text{m}^2$, $P < 0.0001$), although this was still significantly less than control levels ($P < 0.0001$). Following 120 days recovery, type IIX fiber cross-sectional area had fully returned to control levels ($1916 \pm 142.3\mu\text{m}^2$). Type IIB fibers followed a similar pattern as IIX, significantly decreasing after 14 days TTX treatment ($2202 \pm 162.9\mu\text{m}^2$ vs. $1084 \pm 196.1\mu\text{m}^2$, $P < 0.0001$). Again, this significantly increased ($P < 0.0001$), after just 7 days recovery ($1708 \pm 151.6\mu\text{m}^2$) but was still significantly lower than control levels ($P < 0.0001$). There was no significant difference between control and the 120-day recovery group ($2255 \pm 111.8\mu\text{m}^2$, $P = 0.98$). Again, this pattern was observed in hybrid fibers that significantly decreased fiber cross-sectional area ($2000 \pm 968.8\mu\text{m}^2$ vs. $976 \pm 92.2\mu\text{m}^2$, $P < 0.0001$), after 14 days TTX treatment. 7 days recovery partially rescued fiber cross-sectional area ($1493 \pm 147.8\mu\text{m}^2$, $P < 0.0001$), which was fully restored to control levels after 120 days recovery ($1984 \pm 64.5\mu\text{m}^2$), (Figure 4.8F-J).

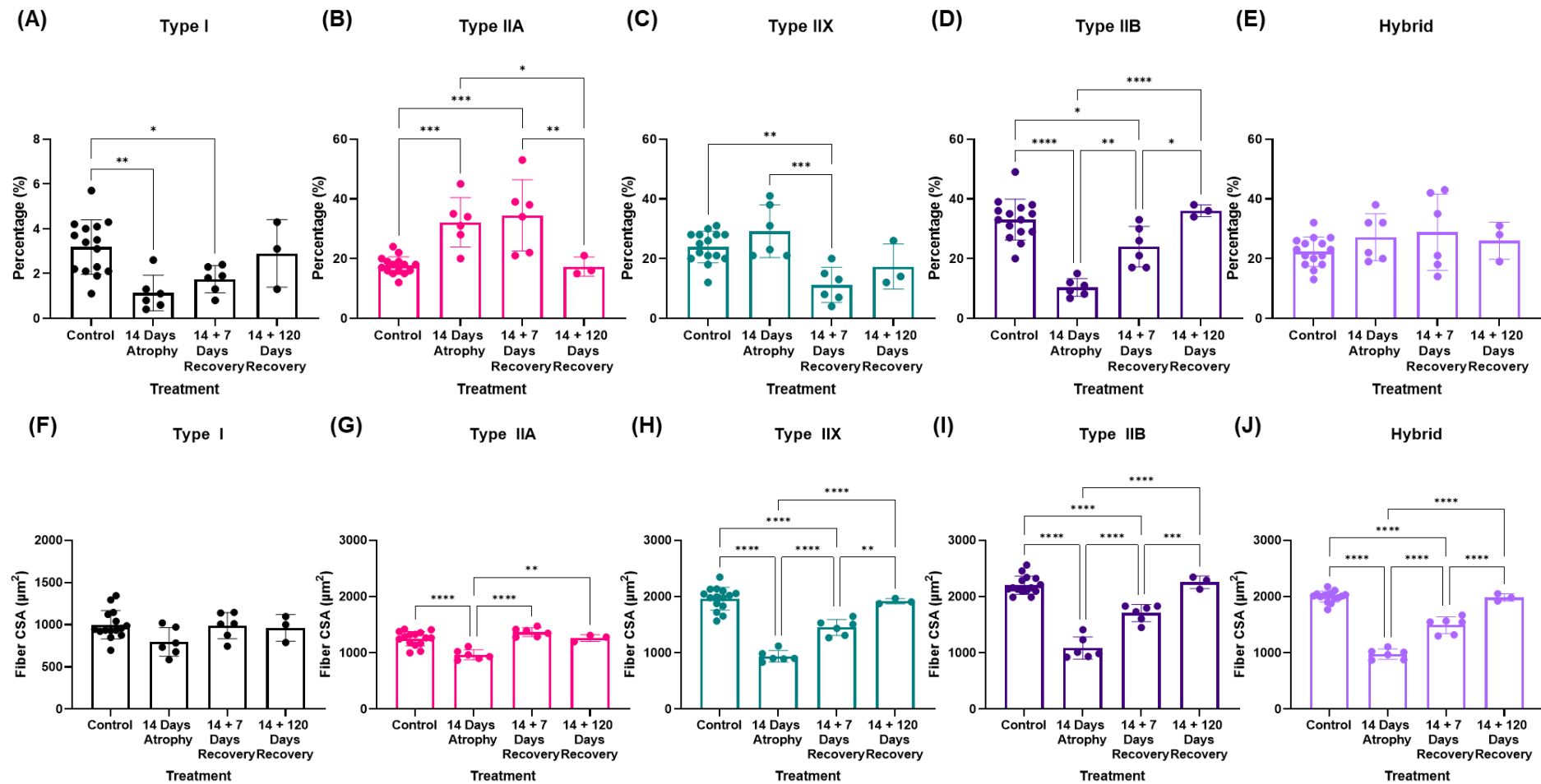


Figure 4.8: (A-E) Changes in tibialis anterior fiber type composition following severe muscle atrophy and subsequent short- and long-term recovery by habitual cage activity, in type I, IIA, IIX, IIB and hybrid muscle fibers. (F-J) Changes in tibialis anterior fiber cross-sectional area following severe muscle atrophy and subsequent short- and long-term recovery by habitual cage activity, in type I, IIA, IIX, IIB and hybrid muscle fibers. * $P \leq 0.05$. ** $P \leq 0.01$. *** $P \leq 0.001$. **** $P \leq 0.0001$. Mean \pm Standard Deviation.

Myonuclei per fiber cross-section measurements revealed no significant alterations between control (0.914 ± 0.23), 14 days TTX treatment (1.11 ± 0.22 , $P = 0.347$), 7 days recovery (0.85 ± 0.29 , $P = 0.96$) and 120 days recovery (0.96 ± 0.14 , $P = 0.99$) type I fibers. In type IIA fibers, myonuclei per fiber cross-section significantly reduced after 14 days TTX treatment (1.01 ± 0.17 vs. 0.69 ± 0.25 , $P = 0.0237$), which significantly increased back to basal levels after just 7 days recovery (1.17 ± 0.29 , $P = 0.0035$). As expected, there was no significant differences between the control, 7-day recovery group and 120-day recovery group (1.17 ± 0.07 , $P = 0.99$). Type IIX fiber myonuclei per fiber cross-section measurements were significantly reduced after 14 days TTX treatment (1.1 ± 0.22 vs. 0.68 ± 0.19 , $P = 0.0053$). After just 7 days recovery, myonuclei per fiber cross-section had significantly increased from both the 14-day period ($P = <0.0001$) and the control group (1.49 ± 0.3 , $P = 0.0075$). Interestingly, after 120 days recovery, myonuclei per fiber cross-section was still significantly elevated in comparison to the 14-day TTX treatment group (1.47 ± 0.17 , $P = 0.0003$), but did not reach significance compared with the control, although there was a strong trend ($P = 0.0691$). Again, type IIB fibers lost myonuclei during the 14 days of TTX treatment from control levels, (1.26 ± 0.12 vs. 0.87 ± 0.14 , $P = 0.0006$). As with type IIX fibers, type IIB gained significant amounts of myonuclei (1.63 ± 0.31), in comparison to both the control ($P = 0.0012$) and the 14-day atrophy group ($P < 0.0001$). It is unclear whether the super compensation of additional myonuclei fully remained after 120 days recovery (1.36 ± 0.05) as this did not significantly differ to either the control ($P = 0.61$) or the 7-day recovery group ($P = 0.16$). Hybrid fiber myonuclei per fiber cross section measurements followed a similar pattern, with loss after 14 days TTX treatment (1.14 ± 0.16 vs. 0.67 ± 0.13 , $P < 0.0001$), and significant recovery past control levels at 7 days (1.52 ± 0.25 , $P = 0.0007$). Once more, following 120 days recovery, myonuclei measurements did not differ between both control and 7-day recovery levels (1.35 ± 0.05), (Figure 4.9A-E).

Myonuclear domain calculations showed no significant differences between control ($1164 \pm 413.8\mu\text{m}^2$), 14 days TTX treatment ($767 \pm 318.1\mu\text{m}^2$, $P = 0.11$), 7 days recovery ($1216 \pm 251.6\mu\text{m}^2$, $P = 0.87$) and 120 days recovery ($1009 \pm 148.4\mu\text{m}^2$, $P = 0.65$) in type I fibers. Similarly, there were no significant effects in type IIA fibers from control levels ($1270 \pm 204.8\mu\text{m}^2$), 14 days TTX treatment ($1592 \pm 649\mu\text{m}^2$, $P = 0.3$), 7 days recovery ($1266 \pm 434.6\mu\text{m}^2$, $P = 0.98$), and 120 days recovery ($1081 \pm 108.4\mu\text{m}^2$, $P = 0.45$). In type IIX fibers, there was a trend

suggesting myonuclear domain size was reduced between control and 14 days of TTX induced atrophy, ($1893 \pm 583.5\mu\text{m}^2$ vs. $1437 \pm 286.8\mu\text{m}^2$, $P = 0.2$). This became significant after the expansive addition of myonuclei during the 7 days recovery period, ($1013 \pm 276\mu\text{m}^2$, $P = 0.003$). After 120 days recovery, there was a trend showing that myonuclear domain size was reduced in comparison with control ($1313 \pm 150.6\mu\text{m}^2$, $P = 0.227$), which suggests that myofibers are still slightly hypernucleated. Type IIB myonuclear domain size reduced after 14 days TTX treatment ($1755 \pm 212\mu\text{m}^2$ vs. $1278 \pm 374.5\mu\text{m}^2$, $P = 0.0029$) and remained significantly lower than control after 7 days recovery ($1079 \pm 231.4\mu\text{m}^2$, $P < 0.0001$). However, following 120 days recovery, myonuclear domain size had significantly increased ($P = 0.158$) back to basal levels ($1657 \pm 131\mu\text{m}^2$). In hybrid fibers, myonuclear domain size showed a trend suggesting a decrease in size ($1799 \pm 348.8\mu\text{m}^2$ vs. $1493 \pm 348\mu\text{m}^2$, $P = 0.18$) between the control and 14 days TTX treatment group. This reached significance during the 7-day recovery period ($993 \pm 115\mu\text{m}^2$, $P < 0.0001$ vs. control, $P = 0.03$ vs. 14 days TTX treatment). Following 120 days recovery, myonuclear domain size was not significantly different to control muscles, ($1476 \pm 90.1\mu\text{m}^2$, $P = 0.35$), (Figure 4.9F-J).

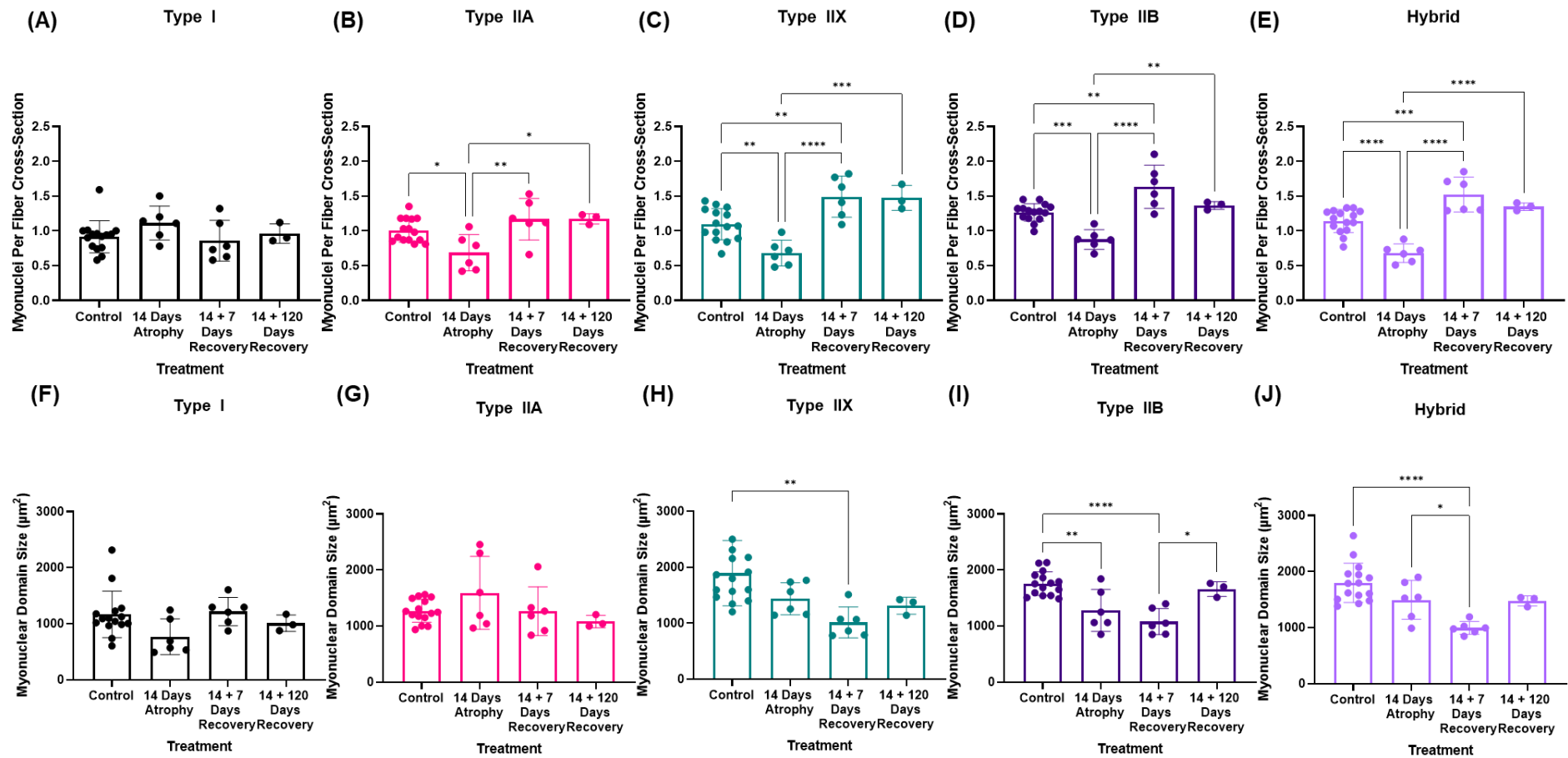


Figure 4.9: (A-E) Changes in tibialis anterior myonuclei per fiber cross-section measurements following severe muscle atrophy and subsequent short- and long-term recovery by habitual cage activity, in type I, IIA, IIX, IIB and hybrid muscle fibers. (F-J) Changes in tibialis anterior fiber myonuclear domain size following severe muscle atrophy and subsequent short- and long-term recovery by habitual cage activity, in type I, IIA, IIX, IIB and hybrid muscle fibers. * $P \leq 0.05$. ** $P \leq 0.01$. *** $P \leq 0.001$. **** $P \leq 0.0001$. Mean \pm Standard Deviation.

4.5 Discussion:

Long term spillover training and subsequent detraining after reaching a hypertrophic plateau.

For the first time we demonstrate the efficacy of being able to perform Spillover resistance training over long periods, that also probably represent close to the maximum predicted battery life of these miniature implants Bijak et al., (2020). The ability to successfully perform loading, unloading and reloading studies using this model is an exciting prospect for understanding myonuclear dynamics and transcriptional regulation of muscle mass after varying periods of training and untraining. We demonstrate that there is a complete absence of pure MyHCIIB fibers after just 30 days which probably transform into fibers containing the MyHCIIX isoform. Contrary to our hypothesis, 120 days of daily training did not result in further slowing of the tibialis anterior. The myosin heavy chain isoform profile was similar after both 30 and 120 days of training. Our lab has previously shown extreme slowing to almost pure type I myosins after 10 months of 'chronic' 10Hz stimulation in the rabbit tibialis anterior Sutherland et al., (1998). 2.5Hz and 5Hz stimulation for the same period resulted in the maintenance of a pool of MyHCIIA fibers. Clearly, the more infrequent and higher frequency stimulation used in this model maintains the need for the fast MyHCIIX fibers, without a complete slowing to type IIA or I.

Our model also supports the concept that satellite cell accretion is an early remodelling characteristic of resistance training and caused by the requirement to quickly increase DNA content and transcriptional output for the muscle to adapt. Myonuclear counts did not differ between any muscle fiber type at 30 or 120 days of training suggesting satellite cell fusion had ceased, or that there was consistent turnover of myonuclei resulting in numbers not increasing exponentially. We note that hybrid fibers were significantly larger after 120 days in comparison to hybrids after 30 days of training (Figure 4.5F), which may represent different myosin isoform fiber phenotypes between these two groups with differing metabolic properties and capabilities. Unfortunately, there are few comparisons to be made with published data from high frequency resisted contractions in rodents for this length of time, with the longest period studied being 6 weeks Baar and Esser, (1999a), Eftestøl et al., (2016), versus our ~17 weeks of stimulation.

Pilot investigations into 30 days of spillover training where muscle mass plateaus, followed by 120 days of detraining yielded interesting results, with mass remaining elevated despite fiber CSA returning to baseline in all fiber types. With no noticeable change in connective tissue present from H&E and immunohistochemical analysis, we suggest that this may be a result of architectural changes in the muscle in the previously trained limb, or changes in its shape towards its distal insertion, as fiber cross-sectional area was compared only at the mid-belly. We speculate that the fibers at the proximal or distal region may have retained some hypertrophic effect due to architectural adaptations earlier in training and may be a plausible explanation for the maintained increase in muscle mass. Interestingly, the substantial shift from IIB to IIX myosin heavy chain isoforms after 30 days of training had not yet returned to that of control levels. This agrees with previous suggestions that the recovery back to basal myosin heavy chain profiles occurs at a slower rate than the change in response to stimulation Brownson et al., (1992). This phenomenon may be explained by lasting epigenetic alterations or changes in accessibility to the myosin heavy chain isoform promoters caused by chromatin modifications, an area of research that is growing in interest Dos Santos et al., (2021).

In concurrently trained mice (PoWeR training) from the Peterson lab, 12 weeks of training followed by 8 weeks of wheel removal (detraining) resulted in myosin heavy chain isoform profiles in the plantaris to return to basal levels. Similar detraining was observed in the gastrocnemius. However, it could be argued that this model results in less extreme shifts in myosin phenotype, therefore allowing for a quicker return to control muscle levels. Interestingly, in the soleus muscle (which is considerably slower than the plantaris in the mouse) fiber type composition was maintained following detraining, with retention of more type I fibers and less type IIA fibers. This suggests that the slower, more oxidative soleus may be more resistant to detraining, although increases in body mass may have resulted in continued loading of the anti-gravity plantarflexors during the detraining period Dungan et al., (2019), Murach et al., (2020b), therefore maintaining activation and load even after wheel running had ceased.

Our detraining model challenges the concept that muscle fibers have a memory of previous hypertrophy Bruusgaard et al., (2010), Gundersen, (2016), Gundersen et al., (2018), by maintaining an elevated myonuclei number and smaller myonuclear domain. In our experiments myonuclei number returned to basal levels after 120 days detraining. Again, we

refer to concurrent training followed by detraining in mice as a comparison, where the plantaris lost myonuclei gained after a shorter period of 12 weeks of detraining. Interestingly, the previously suggested 'detraining resistant' soleus retained nuclei even after 6 months of detraining. The authors suggest that this may be related to natural increases in body mass with age which may have resulted in progressive loading of the muscle, resulting in enough transcriptional activity to maintain the hyper nucleation. Our data in the tibialis anterior potentially provides clearer evidence against muscle memory through myonuclear retention, as the dorsiflexor doesn't receive any additional body-weight load during detraining and added nuclei in type I and type IIA fibers were still lost, despite previous evidence suggesting oxidative muscles may be less prone to atrophy. However, further work is required to understand the molecular and physiological underpinnings of atrophy resistant and atrophy susceptible skeletal muscle Bass et al., (2021), Dungan et al., (2019), Murach et al., (2020b). We hope that further research will assess a timecourse of muscle detraining using this model and potential ways of mitigating losses of functional adaptation gained through resistance training.

Long-term recovery following severe atrophy-an interesting muscle growth paradigm?

In chapter 4, we demonstrated that TTX-induced nerve silencing disuse atrophy caused a progressive loss in myonuclei per fiber cross-section, and the subsequent short-term recovery caused significant super compensatory myonuclear addition in the type IIX and type IIB muscle fibers. We initially planned to follow a timecourse of muscle recovery through next-generation RNA-sequencing to aid us in understanding the transcriptional activity within muscle as it recovered its size back to basal levels, how transcriptional activity may act as a 'switch' to stop muscle continuing to grow as it returned to basal levels and whether transcriptionally the muscle retained any signature of previous severe atrophy, even after a long period of recovery. We hypothesised that muscle would have fully recovered back to that of contralateral control levels 120 days after cessation of 14 days-TTX treatment. However, this pilot experiment perhaps generated the most controversial data on myonuclear retention although low sample numbers make the data hard to fully interpret and require further attention.

While muscle mass, fiber type composition and fiber-type specific measurements of fiber area had returned to that of control levels, there was some evidence suggesting that the early

super compensatory addition of myonuclei remained even after 120 days of recovery, although with low group numbers we cannot confirm if this is or isn't the case. Speculatively if they did remain, this response would differ from the resistance training induced myonuclear addition which are lost through detraining. If the myonuclei added during the rapid recovery from atrophy did remain, it would provide evidence for a 'myonuclear memory' but only when the fusion occurs following a supraphysiological means of hypertrophy such as testosterone treatment or synergist ablation overload, Gundersen, (2016), Gundersen et al., (2018). This would perhaps be as a result of different signals acting on the muscles resident satellite cells leading to differential division (symmetric vs asymmetric) and fusion which may lead to newly added myonuclei having different epigenetic signatures and/or susceptibility to removal Sharples et al., (2016), Wen et al., (2021), Shinin et al., (2006), Cossu and Tajbakhsh, (2007), Dumont et al., (2015), Zammit, (2008), Fukada et al., (2020). This notion would also support the need for appropriate pre-clinical physiological models of resistance training and hypertrophy, such as spillover training in rodents that are more closely related to human resistance training.

4.6 Conclusion:

Within these pilot experiments we have highlighted that myonuclear addition is important for muscle growth, both in response to mechanical loading and in response to recovery from severe atrophy where myonuclei are lost in this model of disuse. However, the stability and permanence of newly added or existing myonuclei seems to differ depending on the model used to induce growth as previously suggested Bruusgaard et al., (2012), Bruusgaard et al., (2010). Following resistance training in healthy muscles, myonuclei added to support hypertrophy seem to be vulnerable to removal following a detraining period. However, myonuclei can be lost during severe atrophy and for muscle to recover, there is a supercompensation of added myonuclei to existing fibers which are potentially protected and do not undergo removal following long term recovery, despite muscle mass returning to basal levels. However, this requires further investigation and experimental repeats. The exact cause of myonuclear addition between these two models (resistance training vs. recovery from severe atrophy) may be reliant on different mechanisms and be caused by differences in

signalling and the requirements for satellite cell fusion (hypertrophy vs. damage) or symmetric vs asymmetric division of muscle progenitor progeny.

Chapter 5: Timecourse transcriptome analysis of programmed resistance exercise in rats.

5.1 Abstract:

The objective of this study was to perform a detailed transcriptomic analysis through RNA-sequencing on the acute response, that is one hour following a bout of resistance exercise, dependent on training status. We used a highly controllable resistance training model, termed Spillover training, that uses implantable pulse generators in free-living rats to induce hypertrophy in the tibialis anterior. We studied how the acute response to non-progressive training results in genome-wide transcriptional changes that are distinctly different dependent on training status. Studying the temporal clusters across our timecourse that spans 2, 10, 20 and 30 days of training revealed 5 unique clusters of genes, 4 of which contain genes that are upregulated in response to acute exercise and reach peak transcriptional expression at different periods of training. Further Venn diagram analysis of the significantly altered genes ($P=0.01$) was performed to establish upregulated and downregulated pathways associated with the early response to training, always responsive pathways, and adapted response pathways. The early response included genes related to the ribosome, proteasome, and protein processing in the endoplasmic reticulum as well as genes associated with inflammation/macrophages. These pathways were significantly downregulated in the adapted muscle, below control levels, whilst oxidative phosphorylation was upregulated. Always responsive upregulated pathways included focal adhesion, antigen processing and PI3k-Akt signalling whilst the downregulated, always responsive pathways included valine, leucine and isoleucine degradation suggesting a reduction in protein degradation. GeneMANIA network association analysis found that the genes associated with the early response to exercise, that we believe are most likely involved with hypertrophy are controlled by the transcription factor Myc, a well-known regulator of cell cycle, metabolism, growth, RNA polymerase activity and ribosomal biogenesis. Myc's expression peaks at 2-days of training and its expression reduces over time in response to training status, suggesting that this transcriptional regulator may be involved in the plateau of the growth response. The most significant differentially expressed genes in response to spillover training were overlapped with the most significant genes found to respond to synergist ablation in the mouse, squat-like exercises in the mouse and in two human meta-analyses containing data from both acute and chronic resistance exercise. There was surprisingly little overlap across models and species, with only 10 genes consistently upregulated across multiple models of resistance

training and across different species. These genes include ATF3, Amd1, Ankrd1, Bgn, Col1a1, Col3a1, Ehd4, Hmox1, Lox and Myc. These genes are largely understudied in skeletal muscle, and we propose that it is likely important to further elucidate the function of these genes/transcription factors and their involvement in muscle adaptation. The study of these genes may lead to important therapeutic findings for muscle plasticity.

We also show that this daily application of resistance exercise, while providing a potent hypertrophic stimulus, also causes changes, such as a reduction in the fastest myosin isoforms, that would be considered typical of endurance training. It may be that a reduction in the frequency of the exercise bouts would achieve hypertrophy without 'slowing' of the muscle phenotype.

Exercise is a potent trigger for the molecular muscle clock McCarthy et al., (2007). Our investigation of the contralateral control muscles, that serve as un-exercised internal controls revealed dynamic changes in genes related to circadian biology. This phenomenon requires further attention. In conclusion, we map out the behaviour of gene expression in response to an acute training bout dependent on training status in a physiological model in rats, showing that genes have very distinct time dependant patterns of expression during hypertrophic adaptation in a fast skeletal muscle. We identified several pathways that are upregulated or downregulated dependent on training status, as well as a cluster of genes whose expression seems to track with muscle growth and the plateau of mass, some of which are consistently expressed across multiple models of resistance training and across different species.

5.2 Introduction:

Resistance exercise training provides both a mechanical and metabolic stress within skeletal muscle to stimulate hypertrophy and increase force generating capacities van Ingen and Kirby, (2021), Wackerhage et al., (2019). It is well known that muscle mass, quality and strength are crucial factors in preventing metabolic diseases, premature mortality and maintaining independent living in older life Gabriel and Zierath, (2019), Neuffer et al., (2015), Liu et al., (2019), Baskin et al., (2015).

Decades of research have revealed that mechanical overload-induced hypertrophy occurs because of prolonged net increases in protein synthesis, to increase the amount of myofibrillar protein present in muscle fibers Glass, (2005), Bodine et al., (2001b), Chaillou et al., (2015), Chaillou et al., (2013). This is orchestrated through the reprogramming of the muscle transcriptome to positively regulate cell growth and translational capacity, whilst suppressing negative regulators of cell growth Schiaffino et al., (2020). The anabolic process is reported to be centrally controlled by the insulin-like growth factor (IGF1)/ protein kinase B (Akt)/ mechanistic target of rapamycin complex-1 (mTORC1) signalling pathway and its upstream regulators and downstream effectors Baar and Esser, (1999a), Sartori et al., (2021), Ogasawara et al., (2017), Ogasawara et al., (2016), Hornberger, (2011), You et al., (2019).

However, much of this knowledge has been gathered from supra-physiological models of overload such as surgical ablation of muscle synergists Chaillou et al., (2015), Chaillou et al., (2013), McCarthy et al., (2011), Goodman et al., (2011), which can cause both damage and inflammation, or models that require repeated anaesthesia/ handling to perform resistance training sessions Baar and Esser, (1999a), Eftestøl et al., (2016), Potts et al., (2017). Recently, a novel voluntary weightlifting model in mice, which required mice to perform squat-like activities in order to feed has been developed which presents great promise in developing a physiological animal model of mechanical-overload induced hypertrophy Cui et al., (2020). However, this differs greatly to the classical human resistance training through sessions of sets and repetitions due to the long working periods of activity Cui et al., (2020). The search for a physiological model of resistance exercise continues and this has recently been highlighted by the current NIH funded Molecular Transducers of Physical Activity Consortium (MoTrPAC) Sanford et al., (2020) who decided not to pursue a pre-clinical animal model of

resistance exercise training in their goal of mapping the molecular responses to exercise. We present here evidence that our model in rats is reliable and practical for close investigations of the response to resistance exercise.

While microarray and RNA-sequencing technologies have started to become widely used to characterise the most influential or differentially expressed gene transcripts across various modalities of acute and chronic training datasets, across sex, and different training histories Pillon et al., (2020), Damas et al., (2018b), Raue et al., (2012), Bonafiglia et al., (2019), Lundberg et al., (2016), Dickinson et al., (2018), Chapman et al., (2020), Turner et al., (2019), none assess *temporal* changes in the transcriptome as muscle becomes adapted to an ongoing hypertrophic stimulus. While recent studies have attempted to map the time trajectories of the acute transcriptomic response to resistance exercise in blood and muscle Amar et al., (2021), Amar et al., (2019) through meta-analyses of acute and long term responses, very few studies to our knowledge have characterised the precise time course of hypertrophic adaptation to repeated acute resistance exercise bout as muscle becomes more trained and accustomed (in the sense that the acute response is reduced), to the resistance exercise stimulus Chaillou et al., (2015), Chaillou et al., (2013).

We used our novel rodent model of resistance training in the rat tibialis anterior (TA) muscle Schmoll et al., (2018), to investigate the acute transcriptional response one hour after a 20 minute resistance training session delivered once per day over a period of 30 days. Such daily resistance training results in significant hypertrophy of the TA muscle, but with ongoing daily training this muscle growth plateaus at approximately 20 days. After that time even though daily resistance training is continued, there is no further muscle growth. We presume, then, that the stimulus for hypertrophy declines because of changes in the muscle that reduce the drive for a hypertrophic response despite ongoing daily training.

Through RNA-sequencing, we characterise the genes, pathways and networks associated with this timecourse of muscle hypertrophy which includes the exercise naïve response, an intermediate response, an adapted response as muscle mass plateaus in response to training and finally a set of genes that are commonly regulated in response to the exercise bout independent of training status. We hypothesise that genes or gene families whose response to an acute exercise session is up/downregulated in the early sessions of training, but then returns to near control levels over the 30-day timecourse will include important regulators

for inducing or suppressing muscle growth. We identify MYC Proto-Oncogene, BHLH Transcription Factor (Myc) as the master regulator of the transcriptional regulation of hypertrophy and identify that its expression in response to acute resistance exercise dissipates, as muscle becomes accustomed to an exercise bout and therefore may provide a basis of objectively designing progressive resistance exercise to continue to promote ribosomal biogenesis and hypertrophy. We also note that EH Domain Containing 4 (Ehd4) is consistently upregulated across species and models of resistance training and its function in the adaptation warrants further investigation.

5.3 Methods:

Experimental Design

The animal experiments were conducted under the provisions of the Animals (Scientific Procedures) Act 1986 and approved by the British Home Office (PA6930221). 17 Male Wistar rats were group-housed with 2-3 per cage maintaining an alternating 12 h light 12 h dark cycle. The mean age when euthanised was 23 ± 2 weeks.

Resistance Training Protocol & Pattern

Animals received 1 session per day of Spillover resistance training in the left hind-limb via stimulation from an implanted pulse generator (IPG) as previously described Schmoll et al., (2018), for 2, 10, 20 or 30 days or underwent sham surgery. Training was conducted within the first two hours of the relatively inactive light cycle of the rat. Briefly, for high load (Spillover) exercise to elicit slight stretch under load, the dorsiflexor muscles, tibialis anterior (TA) and extensor digitorum longus (EDL), received supramaximal activation via a cathode placed underneath the common peroneal nerve (CPN), while the anode was positioned underneath the tibial nerve and the stimulation current was adjusted if necessary by remote programming, to recruit enough of the gastrocnemius, plantaris and soleus (plantarflexor muscles) to provide resistance against the contraction of the dorsiflexors.

Daily training was delivered automatically by the IPG and consisted of an initial 10 seconds of preparatory stimulation at a low frequency ($F = 4\text{Hz}$, phase width $=258 \mu\text{s}$, current $=$ approximately 1 mA), followed by 5 sets of 10 tetanic contractions at 100 Hz. Each contraction lasted for 2s with 2s rest between contractions and 2.5 minutes of rest between sets. The

stimulation was delivered only in the left hind-limb, so muscles of the right hind-limb act as unstimulated contralateral controls. Stimulation with these settings and the amplitude chosen to balance dorsiflexion and plantarflexion described above was well-tolerated by all animals without further anaesthesia or sedation. Regular observations during daily training across the time course revealed no adverse behavioural signs.

Whilst dynamic proteomic profiling results are not discussed in this manuscript, deuterium oxide ($2\text{H}_2\text{O}$; Sigma-Aldrich, St. Louis, MO) administration was initiated on the first day of training by an intraperitoneal loading injection of $10\ \mu\text{l/g}$ 99% $2\text{H}_2\text{O}$ -saline, and then, maintained by administration of 5% (v/v) $2\text{H}_2\text{O}$ in the drinking water available to the rats, as described previously Hesketh et al., (2016), Hesketh et al., (2020b).

Electrical Stimulation Surgical Procedure

Animals were anaesthetised during implant procedures by inhalation of a gaseous mixture of isoflurane in oxygen at approximately 3% for induction and 1-2% for maintenance. Once anaesthetised, a subcutaneous injection of Enrofloxacin ($5\text{mg}/\text{kg}^{-1}$ body mass (Baytril®) and an intramuscular injection of Buprenorphine ($0.05\text{mg}/\text{kg}^{-1}$ body mass) (Temgesic, Indivior, Slough, UK) into the right quadriceps was administered with strict asepsis maintained throughout the procedure. Silicone encapsulated radio frequency controlled implanted pulse generators (IPGs) (MiniVStim 12B, Competence Team for Implanted Devices, Center for Medical Physics and Biomedical Engineering, Medical University Vienna, Austria) were used to deliver impulses. The devices were implanted into the abdominal cavity accessed by a lateral incision through the skin and peritoneum, between the rib cage and pelvis on the left side of the animal. A polyester mesh attached to the IPG was incorporated into the suture line closing the peritoneum, securing the device against the abdominal wall. Two PVC-insulated stainless-steel electrode leads (Cooner Sales Company, Chatsworth, California, USA) with terminal conductive loops, were fed through the peritoneal incision and tunnelled under the skin to the lateral side of the upper left hind-limb. A second incision was made through the skin and biceps femoris muscle to give access to the CPN under which the cathode was placed (to stimulate the dorsiflexors). The anode was placed in the muscular tissue deep to the tibial nerve about 5mm distal to its bifurcation from the sciatic nerve to allow Spillover stimulation to produce additional partial activation of the plantarflexors to resist the

contraction of the dorsiflexors. All incisions were closed in layers and 7 days were allowed for recovery from surgery before the start of the training protocol.

Rat muscle sampling & preservation

Animals were humanely killed using rising concentrations of carbon dioxide, followed by cervical dislocation 1 hour post their last exercise bout. TA muscles from both hind limbs were immediately harvested, cleaned of excess connective tissue and weighed. The mid-belly of the TA was cut out, placed on cork for transverse sectioning and frozen in melting isopentane above liquid nitrogen for histological analysis. The rest of the muscle was flash frozen in liquid nitrogen for subsequent RNA-extraction.

Muscle homogenisation

Part of the whole muscle samples (approx. 200mg) were added to 2ml MagNA Lyser Green Bead screw-capped tubes, prefilled with 1.4-mm (diameter) ceramic beads as supplied (PN:03358941001, Roche, Germany) and 1ml of Trizol (Thermo Fisher Scientific Inc, Waltham, USA). Samples were homogenised using a MagNA Lyser (Roche Diagnostics, Germany) for 40 secs at 6 m/s before being placed back on ice. This was repeated 5 times with 3 minutes on ice between each repeat to ensure complete disruption of the muscle sample. RNA was extracted using the standard Tri-Reagent procedure with chloroform/isopropanol for phase separation and precipitation of RNA, with further washing with 75% ethanol. RNA pellets were resuspended in 51µl of DEPC-treated water (Thermo Fisher Scientific Inc, Waltham, USA).

RNA-Sequencing

High quality mRNA libraries were constructed from 100ng of total RNA using NEBNext® Ultra™ II Directional RNA Library Prep with Sample Purification Beads kit, #E7765S (New England Biolabs, MA, USA) as per manufacturers guidelines, by Bart's and the London Genome Centre at Queen Mary, University of London. This kit enriches for mRNA whilst depleting rRNA's. The resultant barcoded libraries were sequenced on an Illumina NextSeq which runs on a single flow cell that has four lanes, ran using paired-end sequencing for a minimum of 12 million reads per sample. FastQ files were imported to Partek® Flow® Genomic Analysis Software Partek Inc. Missouri, USA) for pipeline processing. Pre-alignment QA/QC was performed on all reads prior to read trimming below a Phred quality score of 20. STAR alignment 4.4.1d was

used to align reads to the *Rattus Norvegicus*, Rnor_6.0 genome assembly Dobin et al., (2013). Aligned reads were then quantified to the Ensembl transcriptome annotation model associated with *Rattus Norvegicus* Rnor 6.0, release 99_v2. Transcript expression was normalised using DESeq2 median of ratios Love et al., (2014) and differentially expressed genes identified through Partek® Flow® Gene Set Analysis (GSA function, at $P < 0.01$). Data is presented as fold change \pm confidence intervals or Log^2 fold change \pm confidence intervals.

Pathway Analysis, Self-Organized Mapping, Venn Diagram Analyses & GeneMANIA multiple association network analysis

Biological interpretation was performed in Partek® Flow® Genomic Analysis Software to identify associated KEGG pathways and GO enrichment analysis Kanehisa and Goto, (2000). To visualise groups of genes with similar temporal changes in gene expression across the time-course studied, we implemented Self Organising Map (SOM) profiling of the change in mean gene expression within each condition using Partek Genomics Suite V.7.0 (Partek Inc. Missouri, USA). Venn Diagram Analysis was performed using Partek® Flow® and using the VIB/UGent Venn online tool, <http://bioinformatics.psb.ugent.be/webtools/Venn/>. Publicly available data was taken for comparison from the following studies Chaillou et al., (2013), Chaillou et al., (2015), Cui et al., (2020), Pillon et al., (2020), Turner et al., (2019). GeneMANIA multiple association network analysis Mostafavi et al., (2008), Warde-Farley et al., (2010) was performed in Cytoscape 3.8.2 Shannon et al., (2003) and interaction networks selected based from physical protein interactions, shared pathways and shared protein domains.

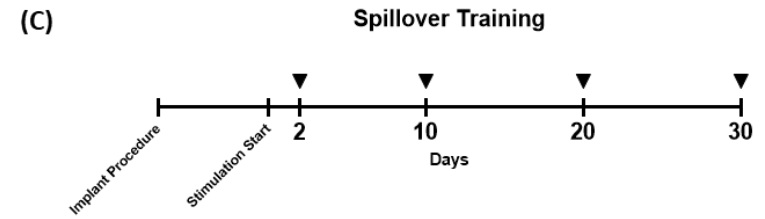
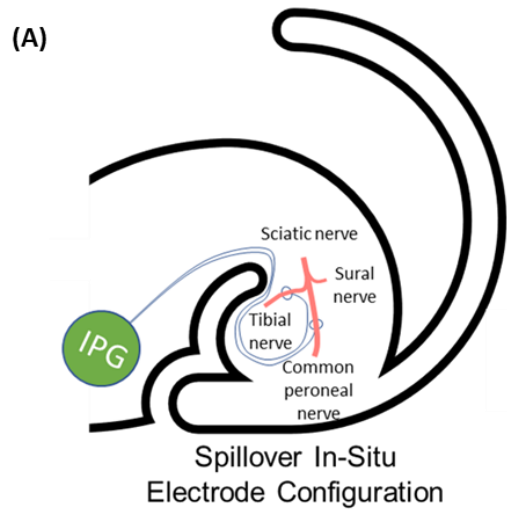
Imaging & MyoVision 2.0 Analysis

Once immunofluorescently labelled, whole muscle cross-sections were imaged using a widefield fluorescent microscope (Leica DMB 6000, Wetzlar, Germany) with a 20x objective. Nicotinamide adenine dinucleotide (NADH) stained muscle cross-sections were imaged using a transmitted light filter. Multiple images were automatically stitched together using the tilescan feature in the Leica Application Suite and transferred to the MyoVision 2.0 programme for myofiber detection and subsequent morphological and fiber-type characterisation as described previously Viggars et al., (2022).

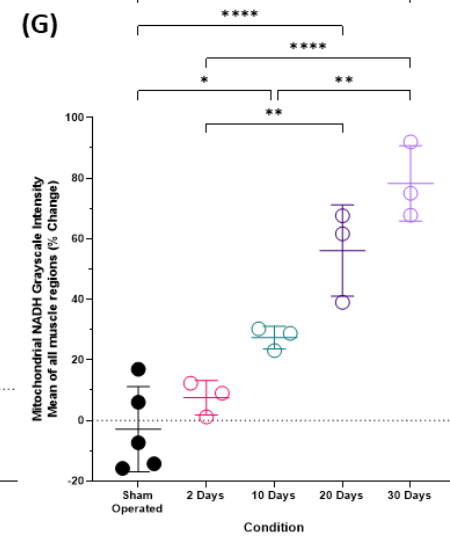
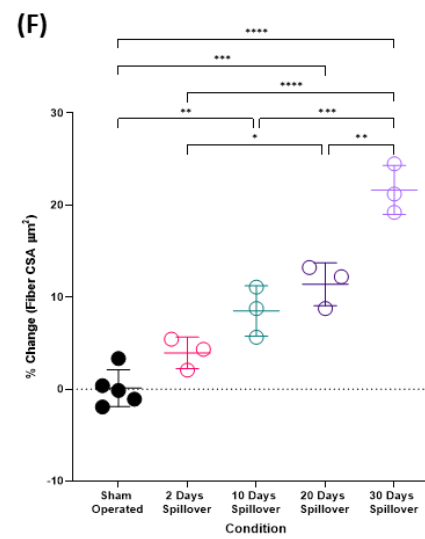
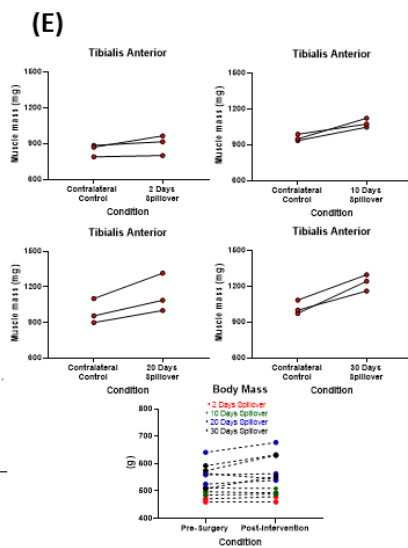
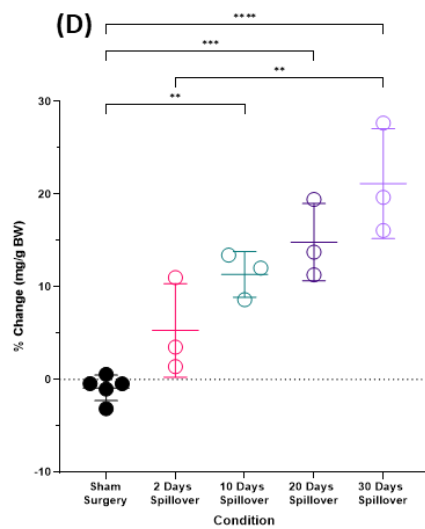
Statistics

Muscle mass data are presented as the % change between the left experimental hind-limb and right internal contralateral control hind-limb for overall muscle mass (mg/kg bodyweight), fiber CSA, that is, the absolute difference expressed as a percentage of the control limb value. The resultant percentage changes were then compared via one-way ANOVA, followed by Tukey's post-hoc analysis to confirm differences between groups. For body mass and fiber type-specific analysis, absolute values of fiber type proportion, fiber CSA, were compared between groups using one-way ANOVAs, followed by Tukey's post-hoc analysis to confirm differences between groups. Significance was set at $P < 0.05$ for all morphological statistical analyses, performed in GraphPad Prism 9.0 software. All data are presented as mean \pm standard deviation (SD).

5.4 Results:



- Stimulated daily during the early phase of the light period.
- Initial 10s of 4Hz contractions. Phase width = 258 μ s, current = ~1 mA, adjusted individually.
- 5 sets of 10 2s on 2s off, tetanic contractions at 100Hz. 2.5 minutes of rest between sets.
- Delivered to only left-hind limb allowing for the muscles of the right hind-limb to be used as unstimulated contralateral controls.



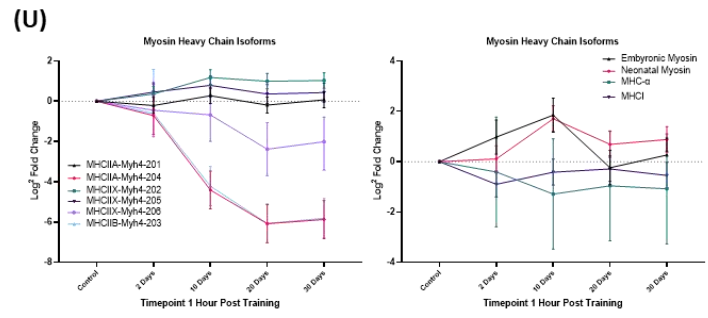
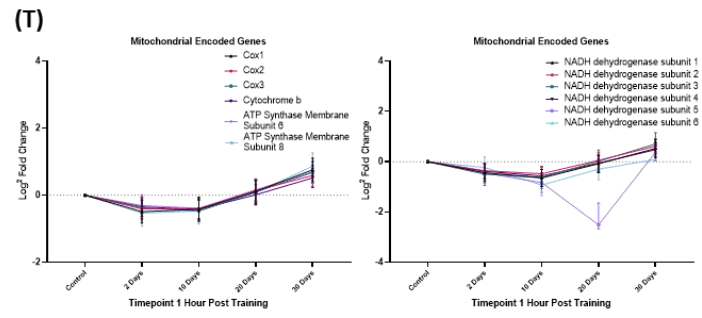
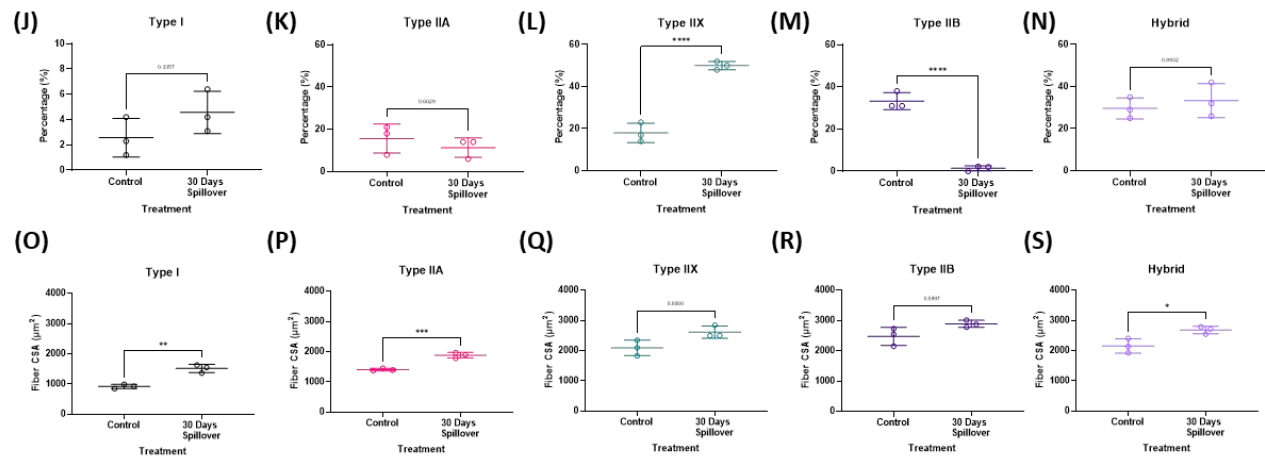
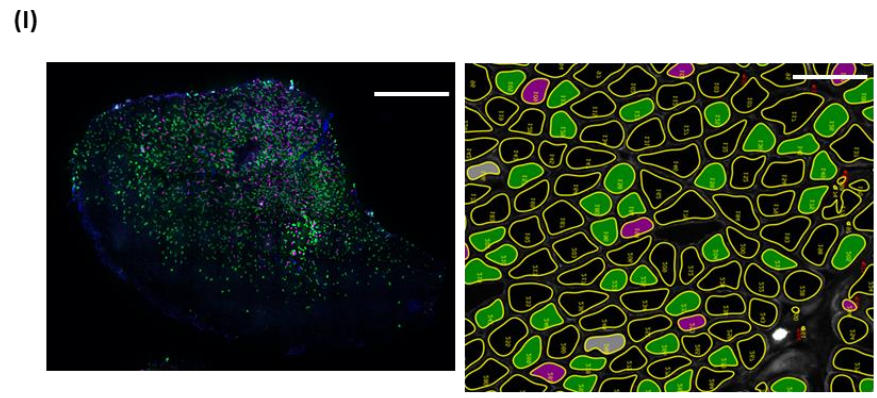
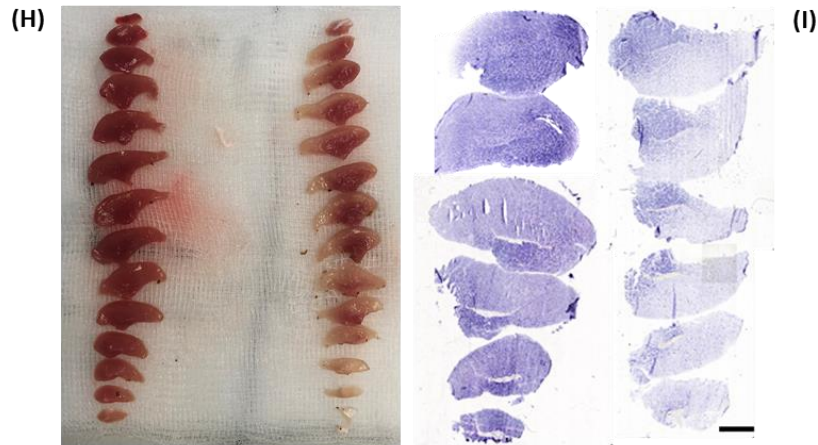


Figure 5.1: (A) Schematic representation of IPG and electrode placement for delivery of electrical stimulation to produce Spillover resistance training in free living rats. An IPG was placed within the abdomen with electrodes leading subcutaneously to the left hindlimb with the anode placed under the tibial nerve and the cathode under the CPN to produce Spillover resistance training. (B) Spillover stimulation fully activates the dorsiflexor tibialis anterior muscle (cyan-green) and 'spills over' to partially activate the larger antagonistic plantarflexors at the back of the leg (plantaris = pink, soleus = purple, gastrocnemius = green). This results in a loaded (resisted) contraction in the tibialis anterior. (C) Schematic representation of the timecourse of training studied and the daily training pattern. (D) Percentage changes in muscle mass between left stimulated and the right unstimulated contralateral control tibialis anterior muscles in mg/g/body weight across the timecourse of training. (E) Changes in wet muscle mass (mg) between trained and contralateral control tibialis anterior muscle. Body mass changes in each condition from pre-surgical weight to post-intervention and euthanasia. (F) Percentage changes in fiber cross-sectional area (μm^2) between left stimulated and the right unstimulated contralateral control tibialis anterior muscles across the timecourse of training. (G) Percentage changes in mitochondrial NADH-TR greyscale intensity across all muscle regions (12 cross-sections per muscle) between left stimulated and the right unstimulated contralateral control tibialis anterior muscles across the timecourse of training. * $P \leq 0.05$. ** $P \leq 0.01$. *** $P \leq 0.001$. **** $P \leq 0.0001$. Mean \pm Standard Deviation. (H) Representative image of muscle slices, left (stimulated), right (contralateral control), top (proximal), bottom (distal) from the tibialis anterior muscle displaying increased red coloration. Adjacent are representative images of nicotinamide adenine dinucleotide dehydrogenase-tetrazolium reductase stains of 30 day trained and the contralateral control muscle. Scale bar = 2000 μm . (I) Example immunofluorescent image of whole TA cross-section. (Blue = dystrophin, Green = Type IIA, Magenta = Type I), scale bar = 2000 μm . Subsequent automated MyoVision 2.0 analysis of fiber cross-sectional area and associated fiber types, scale bar = 40 μm . (J-N) Percentage fiber type distribution between control and 30 days spillover training. (O-S) Fiber type-specific changes in fiber cross-sectional area between control and 30 days spillover training. (T) The \log^2 fold changes \pm confidence intervals of mitochondrial encoded genes. (U) The \log^2 fold changes \pm confidence intervals for transcripts of myosin heavy chain isoforms.

Daily spillover training results in progressive hypertrophy, increases in mitochondrial content and a shift to a IIX phenotype.

As previously reported Viggars et al., (2022), daily spillover training results in a progressive increase in muscle mass after 2 (5.29 ± 5.05 %, $P = 0.223$), 10 (11.35 ± 2.47 %, $P = 0.006$), 20 (14.82 ± 4.17 %, $P = 0.0009$) and 30 days (21.14 ± 5.94 %, $P < 0.0001$), in comparison to sham surgery (-0.91 ± 1.38 %). The increase in muscle mass plateaus between 20 and 30 days of training ($P = 0.31$), (Figure 5.1D). Similarly, fiber CSA progressively increases after 2 (3.94 ± 1.71 %, $P = 0.207$), 10 (8.5 ± 2.73 %, $P = 0.002$), 20 (11.4 ± 2.33 %, $P = 0.0002$) and 30 days (21.65 ± 2.66 %, $P < 0.0001$), in comparison to sham surgery (0.1 ± 2.06 %), with fiber CSA being significantly higher after 30 days in comparison with 20 days training ($P = 0.001$, (Figure 5.1F). Body mass did not significantly differ between any pre-surgical or post intervention measure or between any condition ($P > 0.4$), (Figure 5.1E).

Mitochondrial NADH grayscale intensity across all muscle regions also progressively increased after 2 (7.5 ± 5.7 %, $P = 0.85$), 10 (27.37 ± 3.76 %, $P = 0.0382$), 20 (56.06 ± 15.08 %, $P < 0.0001$) and 30 days (78.24 ± 12.42 %, $P < 0.0001$), in comparison to sham surgery (-2.92 ± 14.04 %), with no significant difference between 20 and 30 days ($P = 0.2891$), (Figure 5.1G). Interestingly, the significant, near linear, increase in NADH staining was not concomitant with changes in mRNA values for key mitochondrial encoded enzymes Cyclooxygenase 1 (COX1), COX2, COX3, cytochrome b (Cyb), ATP Synthase Membrane Subunit 6, ATP Synthase Membrane Subunit 8 and NADH dehydrogenase subunits 1-6. COX1-3, Cyb and ATP Synthase Membrane subunit 8 were significantly downregulated ($P < 0.01$, $q < 0.1$) after 2 days of training by a \log^2 fold change between -0.31 and -0.7 . Following 10 days, COX1-3, Cyb and NADH dehydrogenase subunits 1-6 were all significantly downregulated versus control ($P < 0.01$, $q < 0.05$) with a \log^2 fold change between -0.39 and -0.93 . After 20 days, expression had returned to control levels in all mitochondrial encoded genes apart from NADH dehydrogenase subunit 5 which was significantly lower than all other timepoints ($-2.51 \log^2$ fold change, $P < 0.05$, $q = 0.11$). Significant upregulation of these mitochondrial genes 1 hour post exercise versus control only occurred after 30 days of training in all above genes ($P = < 0.0001$, $q < 0.01$), consisting of 0.5 - $0.75 \log^2$ fold changes, except for NADH dehydrogenase subunits 5 ($P = 0.0688$, $q = 0.38$) and 6 ($P = 0.68$, $q = 0.74$) that did not differ from control levels, (Figure 5.1T).

Fiber type changes after 30 days of training were assessed immunohistochemically to determine proportion and fiber-type specific size and changes in the mRNA abundance of the characteristic myosin heavy chain isoforms via RNA-sequencing across the timecourse. Type I ($2.57 \pm 1.5\%$ vs. $4.56 \pm 1.68\%$, $P = 0.3357$), type IIA ($15.63 \pm 6.8\%$ vs. $11.33 \pm 4.619\%$, $P = 0.6629$) and hybrid ($29.67 \pm 5.03\%$ vs. $33.33 \pm 8.08\%$, $P = 0.893$) muscle fiber percentages did not significantly differ between control and 30 days training respectively (Figure 5.1J-K). However, we note that visually, the type of hybrids shifted from predominately IIB/IIX hybrids to IIB/IIX/IIA hybrids. The main changes occurred between the proportion of IIX fibers, which significantly increased following 30 days of training ($18 \pm 4.59\%$ vs. $50 \pm 4.1\%$, $P < 0.0001$) and conversely there was a significant decline in the number of IIB fibers ($33.33 \pm 4.04\%$ vs. $1.4 \pm 1.22\%$, $P < 0.0001$) (Figure 5.1J-S). At the gene expression level, MyHCI mRNA content significantly decreased after 2 days of training ($-0.9 \log^2$ fold change, $P = 0.0005$, $q = 0.03$), before returning to control levels for the remainder of the training periods studied, opposing the increase in type I fibers observed in the immunohistochemical analysis. For MyHCIIA expression there are 2 transcript variants in the rat genome assembly used to align reads. MyHCIIA-Myh4-201 remained unchanged in response to training at all time points, but MyHCIIA-Myh4-204 decreased progressively in relation to control muscles after 2 ($-0.71 \log^2$ FC, $P = 0.14$, $q = 0.33$), 10 ($-4.41 \log^2$ FC, $P < 0.00001$, $q < 0.00001$), 20 ($-6.08 \log^2$ FC, $P < 0.00001$, $q < 0.00001$), and 30 days training ($-5.87 \log^2$ FC, $P < 0.00001$, $q < 0.00001$) respectively. For MyHCIIX, there are three transcript variants. Interestingly MyHCIIX-Myh4-206 was unchanged from control levels after 2 and 10 days of training but decreased in abundance after 20 ($-2.38 \log^2$ FC, $P = 0.0003$, $q = 0.01$) and 30 days of training ($-2.01 \log^2$ FC, $P = 0.0001$, $q = 0.008$). MyHCIIX-Myh4-202 ($0.35 \log^2$ FC, $P = 0.01$, $q = 0.05$) and MyHCIIX-Myh4-205 ($0.45 \log^2$ FC, $P = 0.05$, $q = 0.06$) increased after 2 days and remained elevated vs control samples at 10, 20 and 30 days, ($P < 0.0001$, $q < 0.002$). There was no significant difference in these specific transcripts between 2, 10, 20 and 30 days. In line with our immunohistochemical analysis, MyHCIIB-Myh4-203 transcript levels remained unaltered after 2 days of training ($-0.61 \log^2$ FC, $P = 0.21$) but then sharply declined after 10 ($-4.22 \log^2$ FC, $P < 0.00001$), 20 ($-6.07 \log^2$ FC, $P < 0.00001$) and 30 days of training ($-5.81 \log^2$ FC, $P < 0.00001$). There was no significant difference in this specific transcript level between 20 and 30 days of training suggesting that the downregulation of this gene transcript had plateaued at around ~ 5000 reads per million, (Figure 5.1U).

Embryonic and neonatal myosin expression remained low at all time points (with less than 10 reads per million) despite embryonic myosin significantly increasing after 2 ($P = 0.004$, $q = 0.03$) and 10 days of training ($P < 0.0001$, $q < 0.0001$), before returning to that of control levels. As expected of the myogenic programme, increases in neonatal myosin heavy chain occurred after embryonic expression, reaching significance after 10 ($P < 0.0001$, $q < 0.0001$), 20 ($P = 0.0009$, $q = 0.09$) and 30 days ($P = 0.0008$). However, despite significant fold changes occurring, mRNA reads for these gene transcripts were less than 10 per million which is likely insignificant to the physiology of the muscle. This also highlights the lack of regeneration/new fibers noted in this model, (Figure 5.1U).

Fiber type-specific measurements of fiber area revealed that all fiber types hypertrophied, type I ($918.8 \pm 69.7\mu\text{m}^2$ vs. $1514 \pm 134\mu\text{m}^2$, $P = 0.0022$), type IIA ($1405 \pm 44.9\mu\text{m}^2$ vs. $1883 \pm 92.6\mu\text{m}^2$, $P = 0.0008$), type IIX ($2023 \pm 171.6\mu\text{m}^2$ vs. $2611 \pm 201.3\mu\text{m}^2$, $P = 0.0199$), type IIB, ($2476 \pm 298\mu\text{m}^2$ vs. $2888 \pm 115.8\mu\text{m}^2$, $P = 0.018$) and hybrid fibers ($2154 \pm 237.6\mu\text{m}^2$ vs. $2684 \pm 124.9\mu\text{m}^2$, $P = 0.0237$) in response to the 30 days training. Interestingly the percentage change was highest in type I fibers that increased their area by 64% versus fast fibers that increased between 21-34% (Figure 5.1O-S). Another observation is that as there was almost a complete shift from IIB to IIX myosin heavy chain isoforms as assessed through immunohistochemistry so it could be argued that IIX fibers didn't hypertrophy to as great an extent as reported above. Briefly, untrained IIB fiber CSA ($2476 \pm 205.2\mu\text{m}^2$), was only slightly lower than trained IIX fibers ($2611 \pm 201.3\mu\text{m}^2$, $P = 0.006$), a 9.8% increase rather than a 29% increase in fiber CSA suggesting that despite all being activated, slower fibers increase their size to a greater extent.

Self-organising mapping reveals 5 distinct temporal clusters of gene expression during hypertrophy.

A principal components analysis (PCA) on all identified gene transcripts identified clear clustering of gene transcript responses dependent on training itself and the length of training (Figure 5.2A), with all contralateral control samples clustering together independent of length of training in the opposite limb. The acute responses after 2 and 10 days of training are similar, yet there is distinct separation between 2 and 10 days versus 20 and 30 days, and further division between 20 and 30 days across PC1 (66.43%), (Figure 5.2A). We then performed GSA on DeSeq2 normalised reads to identify differentially expressed genes with a cut off at ($P <$

0.01) across the timecourse of adaptation. For genes assessed in more detail, FDR q values are presented as the statistical analysis was performed with multiple comparisons. As shown in Figure 5.2B, from the 20,027 gene transcripts identified across all tibialis anterior samples, 2398 were differentially expressed at the 2-day timepoint, with the majority being upregulated (71.26%). A similar pattern was present after 10 days, with 71.28% of 2218 differentially expressed genes being upregulated. After 20 days, the number of differentially expressed genes decreased to 1755, and only 54.41% were upregulated. Interestingly, after 30 days of training, acute exercise upregulated only 484 genes (17.11%) and downregulated 2828 (82.89%) genes (Figure 5.2B). Across all timepoints, we identified 519 gene transcripts that were differentially expressed across all time points (or always responsive), 66.47% of which were upregulated, Figure 5.2C.

We then performed unsupervised hierarchical clustering of the top 500 statistically differentially regulated genes across the timecourse versus control samples and found good similarity between samples from the same condition and a temporal shift in differentially regulated genes between 2, 10, 20 and 30 days but not in control samples (Figure 5.2D). Further analyses by SOM temporal analysis of these 500 genes resulted in 5 distinct temporal clusters identified through the inflection point of the minimum centroid distance between clusters. The 5 clusters contained 74, 115, 97, 61, and 153 genes respectively.

In rank order of significance SOM1 (peak at two days with early decline) contained the following genes: *Ankrd1* (Ankyrin Repeat Domain 1), *Otud1* (OTU Deubiquitinase 1), *LOC498675*, *Egr1* (Early Growth Response-1), *Serpine1* (Serpin Family E Member 1), *Csrnp1* (Cysteine and Serine Rich Nuclear Protein 1), *Mustn1* (Musculoskeletal, Embryonic Nuclear Protein 1), *Hbegf* (Heparin Binding EGF Like Growth Factor), *Csrp3* (Cysteine-Rich Protein 3/Muscle LIM Protein), *Fos* (Fos Proto-Oncogene, AP-1 Transcription Factor Subunit), *Xirp1* (Xin Actin Binding Repeat Containing 1), *Hspb7* (Heat Shock Protein Family B (Small) Member 7), *Tnfrsf12a* (Tumor necrosis factor Receptor Superfamily Member 12A), *Dnajb1* (DnaJ Heat Shock Protein Family (Hsp40) Member B1), *MYC* Proto-Oncogene, BHLH Transcription Factor), *Klhl40* (Kelch Like Family Member 40), *Ier5* (Immediate Early Response 5), *Cryab* (Crystallin Alpha B), *Fhl1* (Four And A Half LIM Domains 1), *Enah* (ENAH Actin Regulator), *Thbs1* (Thrombospondin 1), *Tuba1c* (Tubulin Alpha 1c), *Asb5* (Ankyrin Repeat And SOCS Box Containing 5) and *Flnc* (Filamin C).

In rank order of significance SOM2 (Peak at 2 days and maintained at 10 before gradual decline) contained the following genes: *Atf3* (Activating transcription factor 3), *Csrnp1* (Cysteine and Serine Rich Nuclear Protein 1), *Hspa1b* (Heat shock 70kDa protein 1B), *Maff* (MAF BZIP Transcription Factor F), *LOC108348108* (heat shock 70 kDa protein 1A), *Phlda1* (Pleckstrin Homology Like Domain Family A Member 1), *Rtn4* (Reticulon 4), *Midn* (Midnolin), *Irs2* (Insulin Receptor Substrate 2), *Rcan1* (Regulator of Calcineurin 1), *Fhl1* (Four and a half LIM domains protein 1), *Bcl2l11* (Bcl-2-like protein 11/BIM), *Map1a-202* (Microtubule Associated Protein 1A), *LOC100909784* (leiomodim-2-like), *Btg2* (BTG Anti-Proliferation Factor 2), *Map1a-201* (Microtubule Associated Protein 1A), *Nr4a1* (Nuclear Receptor Subfamily 4 Group A Member 1), *Itga5* (Integrin Subunit Alpha 5), *Emp1* (Epithelial Membrane Protein 1), *Loxl1* (Lysyl Oxidase Like 1), *Lgals3* (Galectin 3), *Cd14* (cluster of differentiation 14), *Tyrobp* (TYRO protein tyrosine kinase-binding protein), *Gfpt2* (Glutamine-Fructose-6-Phosphate Transaminase 2) and *Mfap4* (Microfibril Associated Protein 4).

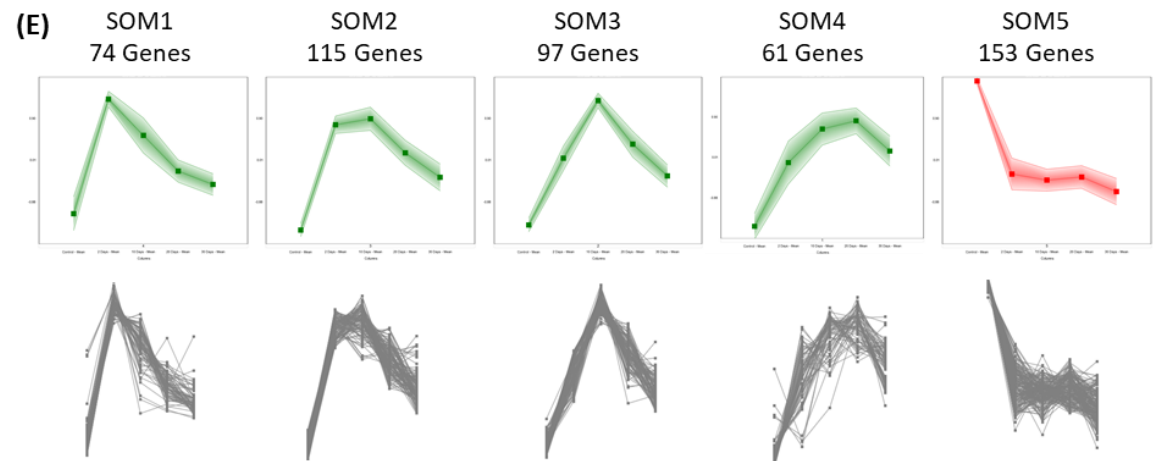
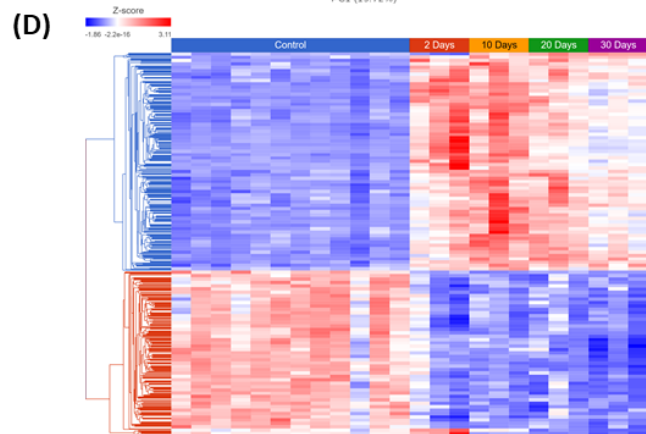
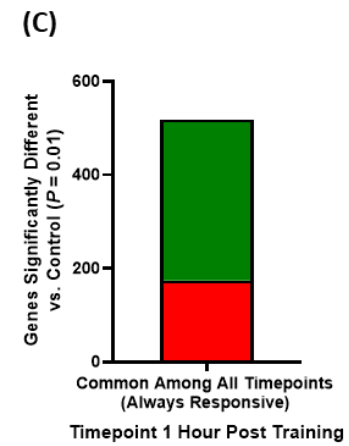
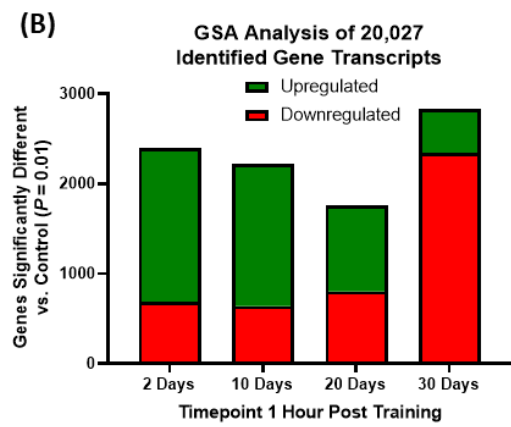
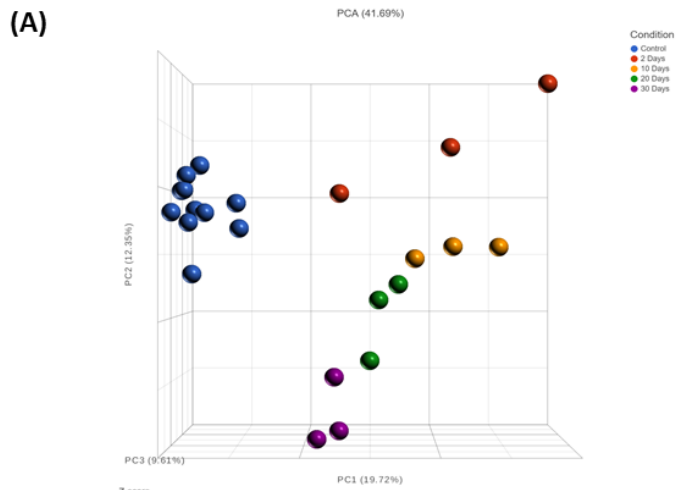
In rank order of significance SOM3 (Peak at 10 days with sharp subsequent decline) contained the following genes: *Bgn* (Biglycan), *Hspb6* (Heat Shock Protein Family B (Small) Member 6), *Hmox1* (Heme Oxygenase 1), *Vat1* (Vesicle Amine Transport 1), *Rab7b* (*RAB7B*, Member RAS Oncogene Family), *Gpx1* (Glutathione Peroxidase 1), *Actn2* (Actinin Alpha 2), *Habp4* (Hyaluronan Binding Protein 4), *Tsp* (Translocator Protein), *Col4a1* (Collagen type IV alpha 1), *LOC100364435* (thymosin, beta 10-like), *AABR07068316.1*, *Mgp* (Matrix Gla Protein), *Dnaja4* (DnaJ Heat Shock Protein Family (Hsp40) Member A4), *Efna1* (Ephrin A1), *F2r* (Coagulation Factor II Thrombin Receptor), *Vopp1* (Vesicular, Overexpressed In Cancer, Pro-survival Protein 1), *Thy1* (Thy-1 Membrane Glycoprotein/CD90), *Sel1l3* (Suppressor Of Lin-12-Like Protein 3), *Col18a1* (Collagen Type XVIII Alpha 1 Chain), *Lipg* (Lipase G, Endothelial Type), *Ecm1* (Extracellular matrix protein 1), *Col4a2* (Collagen Type IV Alpha 2 Chain), *Ppp1r27* (Protein Phosphatase 1 Regulatory Subunit 27) and *Klf5* (Kruppel Like Factor 5).

In rank order of significance SOM4 (Gradual increase with peak at 20 days before decline) contained the following genes: *Slc20a1* (Sodium-dependent phosphate transporter 1), *Olfml3*, (*Olfactomedin Like 3*), *Snai3* (Snail Family Transcriptional Repressor 3), *Sparc* (Secreted Protein Acidic And Cysteine Rich), *Id4* (Inhibitor Of DNA Binding 4, HLH Protein), *Hk2* (Hexokinase 2), *Nr4a3* (Nuclear Receptor Subfamily 4 Group A Member 3), *Nupr1* (Nuclear Protein 1, Transcriptional Regulator), *Zfp622* (Zinc finger protein 622), *Gpnmb*

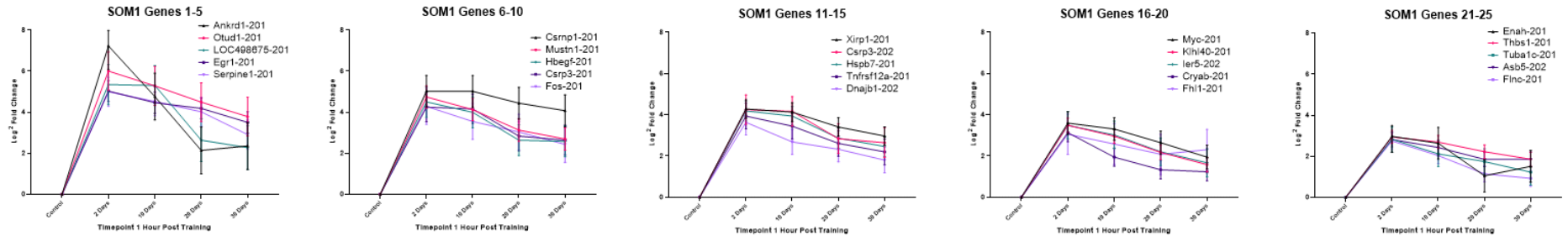
(Glycoprotein Nmb), Cox7a1 (Cytochrome C Oxidase Subunit 7A1), Apoe (Apolipoprotein E), Scd2 (Stearoyl-CoA desaturase-2), LOC100361457 (actin, gamma 1 propeptide-like), Coro1c (Coronin 1C), Gsn (Gelsolin), Tmem140 (Transmembrane Protein 140), Sorbs3 (Sorbin And SH3 Domain Containing 3), Dap (Death Associated Protein), Ppp1r36 ((Protein Phosphatase 1 Regulatory Subunit 36), Junb (JunB Proto-Oncogene, AP-1 Transcription Factor Subunit), Cnn2 (Calponin 2), Slfn2 (Schlafen 2), Uap1l1 (UDP-N-Acetylglucosamine Pyrophosphorylase 1 Like 1) and Vegfa (Vascular Endothelial Growth Factor A).

In rank order of significance SOM5 (Downregulated after 2 days and consistently over 10, 20 and 30 days) contained the following genes: Dhrs7c (Dehydrogenase/Reductase 7C), Srd1 (S1 RNA Binding Domain 1), Actn3 (Alpha-actinin-3), Myh4-203 (MyHC IIB), Myh4 (MyHC IIX), Pvalb (Parvalbumin), Fam78a (Family With Sequence Similarity 78 Member A), Dhrs4 (Dehydrogenase/ Reductase 4), Ampd1 (AMP deaminase 1), Tcea3 (Transcription Elongation Factor A3), R3hdm2 (R3H Domain Containing 2), Masp1 (MBL Associated Serine Protease 1), Mylk2 (Myosin Light Chain Kinase 2), Reep1 (receptor expression-enhancing protein 1), Dbt (Dihydrolipoamide Branched Chain Transacylase E2), Eif4e3 (Eukaryotic Translation Initiation Factor 4E Family Member 3), Tab2 (TGF-Beta Activated Kinase 1 (MAP3K7) Binding Protein 2), Bcat2 (Branched Chain Amino Acid Transaminase 2), Calm2 (Calmodulin 2), Slc9a2 (Solute Carrier Family 9 Member A2), Gstm7 (Glutathione S-transferase 7), Hjuv (hemojuvelin), Me1 (Malic Enzyme 1), *Sar1b* (Secretion Associated Ras Related GTPase 1B) and Lmod1 (Leiomodin 1).

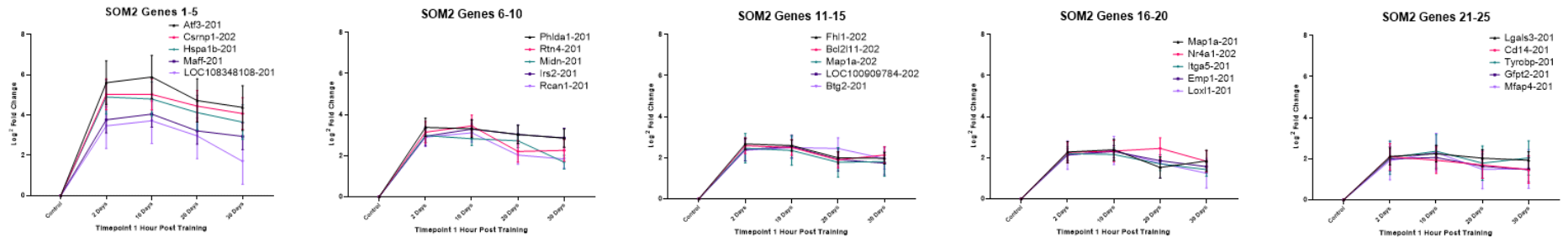
All genes presented in the SOM analysis reached an FDR cut off value of $q < 0.001$, at two or more timepoints compared to control levels.



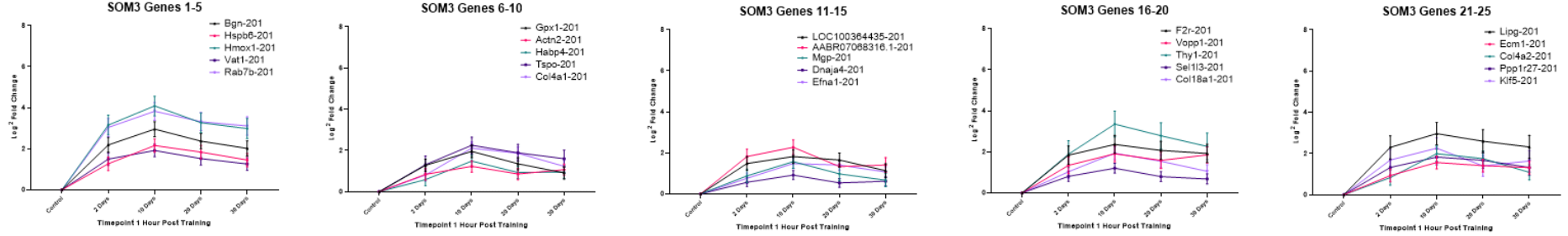
(F) Self Organizing Map (Cluster 1 Gene Transcripts)



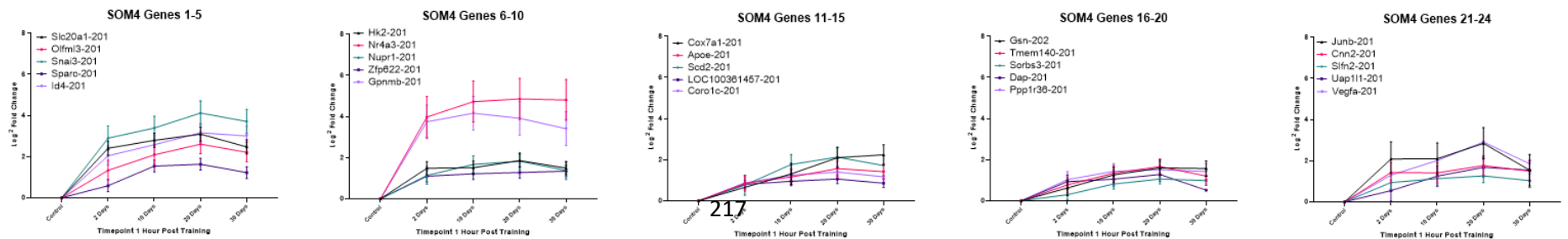
(G) Self Organizing Map (Cluster 2 Gene Transcripts)



(H) Self Organizing Map (Cluster 3 Gene Transcripts)



(I) Self Organizing Map (Cluster 4 Gene Transcripts)



(J) Self Organizing Map (Cluster 5 Gene Transcripts)

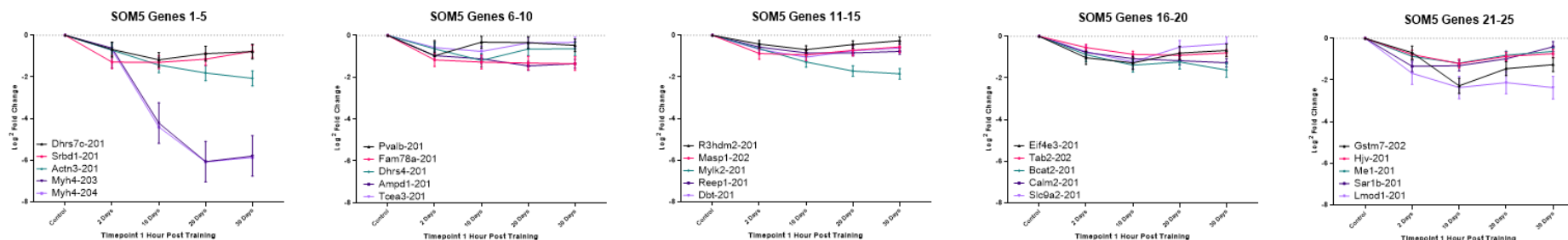


Figure 5.2: (A) Principal component analysis (PCA) of control (blue), 2 days spillover stimulation (red), 10 days spillover stimulation (yellow), 20 days spillover stimulation (green), 30 days spillover stimulation (purple). Principal component 1 accounted for 19.72% of the variance in the data, principal component 2 12.35% and principal component 3, 9.61% respectively. (B) A total of 20,027 different gene transcripts were identified across all samples and were further filtered following differential gene set analysis between the control group (n=12) and each spillover resistance training group (n=3) per training group. (C) Differentially expressed genes that are common (always responsive) at each time point of training. (D) Hierarchical heat map for analysis of all differentially expressed genes between 2-day, 10-day, 20-day, 30 day and the control group. (x-axis: Blue=control, red=2 days spillover training, orange=10 days spillover training, green=20 days spillover training, purple=30 days spillover training). (E) The top 500 differentially expressed genes from Figure 5.2D, were characterised into 5 distinct clusters following self-organising map (SOM) temporal analysis. 5 were selected based on the inflection point of the minimum centroid distance between clusters, meaning the point at which differences between additional clusters becomes negligible. SOM1= 74, SOM2=115, SOM3=97, SOM4=66, SOM5=174). (F) The timecourse of expression of the top 25 genes present in SOM1 ranked by order of significance. (G) The timecourse of expression of the top 25 genes present in SOM2 ranked by order of significance. (H) The timecourse of expression of the top 25 genes present in SOM3 ranked by order of significance. (I) The timecourse of expression of the top 25 genes present in SOM4 ranked by order of significance. (J) The timecourse of expression of the top 25 genes present in SOM5 ranked by order of significance. Data is presented as log₂ fold changes \pm confidence intervals.

Expression levels of electively chosen common regulators of muscle mass show little transcriptional changes and do not reflect the adjustment to training status.

In this section, we electively chose genes from our dataset that are commonly studied as regulators of muscle mass, protein synthesis or are responsive to exercise and the induction of multiple pathways related to regulation of growth. Often these genes (Figure 5.3A) have very low expression (mRNA abundance), and it is thought that their activity/phosphorylation is potentially more important than changes in their gene transcript abundance. However, we report here that myostatin gene expression was significantly increased after 2 days of training (1.7 FC, $P = 0.003$, $q = 0.02$) before returning to basal levels at 10 days of training (1.2 FC, $P = 0.22$, $q = 0.41$). While decreased myostatin expression is associated with increases in muscle mass, we report that after 20 and 30 days of training, myostatin becomes downregulated (-2.4 FC, $P < 0.00001$, $q < 0.0001$ and -2.6 FC, $P < 0.00001$, $q < 0.0001$) respectively, despite us reporting a plateau in muscle mass. Similarly, Myogenin is upregulated after 2 days of training (3.5 FC, $P < 0.00001$, $q < 0.0001$) before returning to levels similar to control muscles after 10 days (1.3 FC, $P = 0.39$, $q = 0.54$). Like myostatin, myogenin is then downregulated at 20 and 30 days compared with control levels but does not reach statistical significance (-1.5 FC, $P = 0.12$, $q = 0.49$ and -1.6 FC, $P = 0.09$, $q = 0.15$) respectively. Conversely, Fbxo32 (Mafbx) is significantly downregulated after 2 days of training (-2.1 FC, $P < 0.00001$, $q = 0.048$) and returned to baseline after 10 (-1.1 FC, $P = 0.78$, $q = 0.85$), 20 (1.38 FC, $P = 0.34$, $q = 0.45$) and 30 (1.31 FC, $P = 0.42$, $q = 0.56$) days of spillover training. Trim63 (MuRF1) was upregulated at all timepoints versus control (2.3 FC, 2.1 FC, 2.0 FC, 1.6 FC, $P < 0.00001$, $q < 0.001$). IGF1 remained unchanged after 2 days of training versus control levels, (1.3 FC, $P = 0.11$, $q = 0.16$), but was significantly upregulated after 10 (1.8 FC, $P = 0.001$, $q < 0.005$) and 20 days (2.08 FC, $P < 0.00001$, $q = 0.01$) before returning to that of control levels after 30 days of training (1.26 FC, $P = 0.71$, $q = 0.78$). Interestingly, the IGF1 receptor was only significantly upregulated after 2 days of training (2.1 FC, $P = 0.02$, $q = 0.06$). IRS1 gene expression remained unchanged in response to training at all time points ((-1.57 FC, $P = 0.15$, $q = 0.74$), (1.03 FC $P = 0.91$, $q = 0.75$), (-1.45 FC $P = 0.23$, $q = 0.46$), (-1.63 FC $P = 0.12$, $q = 0.31$)). Akt1 gene expression did not change after 2 days of training (1.1 FC, $P = 0.13$, $q = 0.28$) but was then significantly upregulated following 10 (1.4 FC, $P < 0.0001$, $q < 0.001$), 20 (1.4 FC, $P < 0.0001$, $q < 0.001$) and 30 days of training (1.3 FC, $P < 0.01$, $q < 0.1$). Similarly, Akt2 expression was significantly

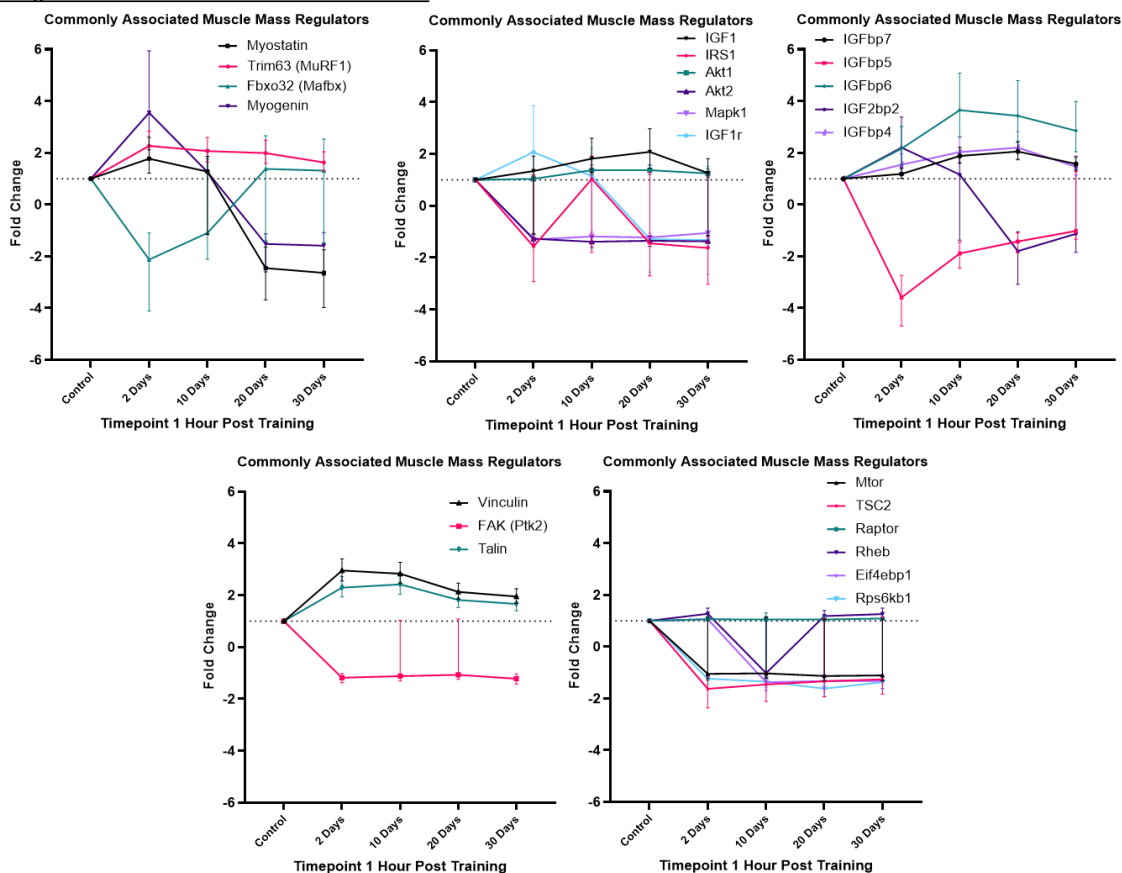
upregulated at all timepoints (1.4 FC, $P < 0.0009$, $q < 0.09$). Mapk1 was significantly downregulated after 2 (-1.3 FC, $P = 0.0004$, $q = 0.02$), 10 (-1.2 FC, $P = 0.02$) and 20 days of training (-1.2 FC, $P = 0.007$, $q < 0.1$), before returning to levels like control (-1.1 FC, $P = 0.16$, $q = 0.54$) after 30 days. Expression of the IGF1/2BP family was much more varied across the timecourse of training likely reflecting their different functions and binding properties. IGFbp4 was significantly increased versus control levels after 2 (1.5 FC, $P = 0.0007$, $q < 0.001$), 10 (2 FC, $P < 0.0001$, $q < 0.0001$), 20 (2.2 FC, $P < 0.0001$, $q < 0.0001$) and 30 days of spillover training (1.5 FC, $P = 0.0003$, $q = 0.19$). Similarly, IGFbp7 was significantly upregulated versus control muscles after 2 (1.2 FC, $P = 0.04$, $q = 0.08$), 10 (1.9 FC, $P < 0.0001$, $q < 0.0001$), 20 (2.1 FC, $P < 0.0001$) and 30 days of spillover training (1.6 FC, $P < 0.0001$). IGFbp6 showed the largest increases in gene expression of the family, increasing after 2 (2.2 FC, $P < 0.0006$, $q < 0.001$), 10 (3.7 FC, $P < 0.0001$, $q < 0.0001$), (3.4 FC, $P < 0.0001$, $q < 0.0001$) and 30 (2.9 FC, $P < 0.0001$, $q < 0.0001$) days. In contrast, IGFbp5 was significantly downregulated after 2 (-3.6 FC, $P < 0.0001$, $q < 0.0001$), 10 (-1.9 FC, $P < 0.0001$, $q = 0.02$) and 20 (-1.4 FC, $P = 0.008$, $q = 0.16$) days of training, but returned to control levels after 30 days of training (-1.02 FC, $P = 0.86$, $q = 0.49$). We also note that the IGF2bp2 showed an early upregulation after 2 days of training (2.2 FC, $P = 0.003$, $q = 0.041$), before being downregulated at 20 (-1.8 FC, $P = 0.03$, $q = 0.11$) and returning to levels like control by 30 days of training (-1.13 FC, $P = 0.62$, $q = 0.75$).

We next looked at genes whose protein products form or regulate mTORC1 activity. mTOR and RAPTOR did not differ from control at any timepoints ($P > 0.59$, $q < 0.87$). However, Rheb was significantly upregulated following 2 days (1.3 FC, $P = 0.004$, $q < 0.01$), 20 (1.2 FC, $P = 0.04$, $q = 0.08$), and 30 days of training (1.3 FC, $P = 0.0005$, $q = 0.39$). There was no significant difference between control and 10 days (-1.02 FC, $P = 0.84$, $q = 0.001$). TSC2 was consistently downregulated vs control TA muscles, reaching significance after 2 (-1.6 FC, $P = 0.009$, $q = 0.021$) and 10 days (-1.4 FC, $P = 0.04$, $q = 0.32$), but did not reach significance after 20 (1.3 FC, $P = 0.12$, $q = 0.45$), and 30 days of training (1.3 FC, $P = 0.06$, $q = 0.14$). Downstream of mTOR, we observed downregulation of Eif4ebp1 after 10 (-1.4 FC, $P = 0.002$, $q = 0.01$), 20 (-1.3 FC, $P = 0.006$, $q = 0.04$) and 30 days of daily spillover training (-1.3 FC, $P = 0.0009$, $q = 0.001$). 2 days of training did not change gene expression of Eif4ebp1 (1.1 FC, $P = 0.55$, $q = 0.66$) versus levels in control muscles. Rps6kb1 was also significantly downregulated after 2 (1.2 FC, $P = 0.009$, $q = 0.05$), 10 (-1.4 FC, $P = 0.004$, $q = 0.13$), 20 (-1.6 FC, $P < 0.0001$, $q = 0.003$) and 30 days of

training (1.4 FC, $P = 0.0002$, $q < 0.003$) in comparison to control muscles. The only genes that corresponded to our muscle mass changes that we electively chose were Vinculin and Talin which have fundamental roles in integrin-mediated cell adhesion and linking the actin cytoskeleton of muscle to the extracellular matrix. Vinculin and Talin increased significantly after just 2 days of training (3 FC, $P < 0.0001$, $q < 0.0001$, 2.3 FC, $P < 0.0001$, $q < 0.0001$) respectively. This significant upregulation was maintained in both genes after 10 days of training (2.8 FC, $P < 0.0001$, $q < 0.0001$, 2.4 FC, $P < 0.0001$, $q < 0.0001$). At this point Vinculin expression was significantly reduced versus 2 and 10 days, ($P = 0.001$, $q = 0.02$), but remained significantly higher than control (2.1 FC, $P < 0.0001$). Again, there was a significant reduction from 2, 10 and 20 days of training, ($P < 0.001$, $q < 0.01$), but remained significantly elevated vs control (2 FC, $P < 0.0001$, $q < 0.0001$). Talin followed the same trend, decreasing significantly from its peak at 10 days ($P < 0.001$, $q = 0.018$) after 20 (1.8 FC, $P < 0.0001$, $q < 0.001$ vs. control) and 30 (1.7 FC, $P < 0.0001$ vs. control) days of daily spillover training. Interestingly FAK/PTK2 was downregulated after 2 days of training (-1.2 FC, $P = 0.02$, $q = 0.16$) and 30 days of training (-1.2 FC, $P = 0.01$, $q = 0.02$) but did not differ from control after 10 and 20 days of training ($P > 0.12$, $q > 0.6$).

As the above gene transcripts overall failed to replicate the increase and plateau of muscle mass with our training model, we filtered the genes from the top 500 DEG at 2 days vs. control based on them having more than a +/- 3-fold change after 2 days of training (vs. control), and then returning most nearly back to baseline at 30 days as muscle mass plateaus (lowest fold change at 30 days vs. control). We aim with this analysis to identify transcripts whose gene expression does follow the hypertrophic response. We hypothesised that genes whose expression is changed in the early sessions of training but then returns near to control levels of the 30-day timecourse include genes representing a signal for muscle growth. The fact that their expression returns to near normal levels despite ongoing daily resistance training suggest that the muscle adapts to this daily training so that signal for growth is no longer triggered by the daily sessions. The top 20 genes identified that followed the growth and plateau/cessation of growth of the tibialis anterior muscle mass included P4htm, Rhoc, Pmepa1, Arfgap3, Zfand2a, Rnf115, LOC680491, Usp28, Flnc, Ckap4, Hsp90aa1, Emp3, Glmp, Ehd4, Anxa2, Asb5, Cotl1, Ddit3, Tuba1c and Cd44.

(A) Classical genes associated with control of muscle mass



(B) Genes acutely upregulated showing the greatest decline between 2 and 30 days.

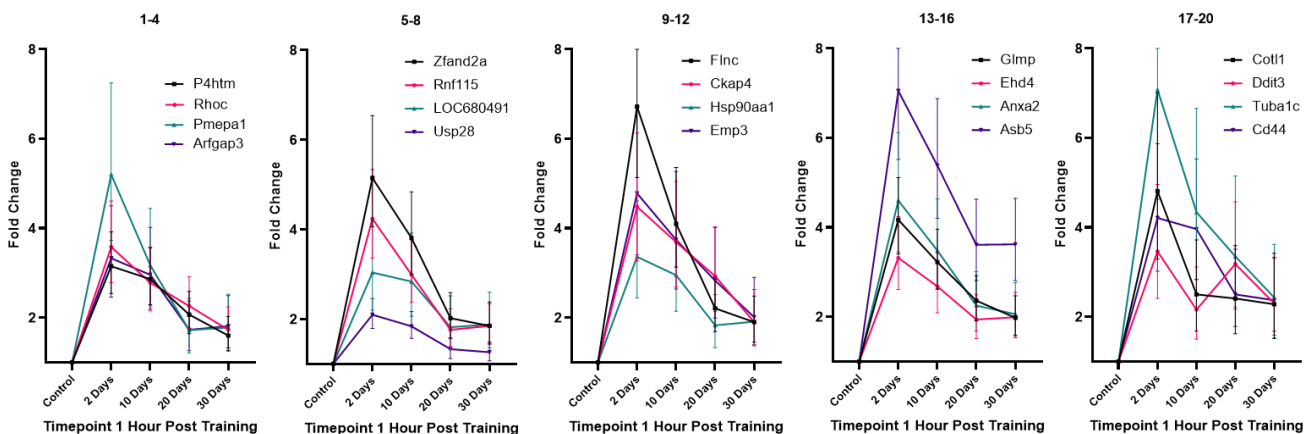


Figure 5.3: (A) Electively chosen genes previously reported to be involved in regulation of muscle mass; insulin sensitive, mTOR associated or proteasomal pathways. (B) Genes from the top 500 DEG at 2 days vs. control were filtered based on having more than a +/- 3-fold change after 2 days of training (vs. control), and then returning most nearly back to baseline at 30 days as muscle mass plateaus (lowest fold change at 30 days vs. control).

Pathway enrichment in response to acute resistance training reveals differential responses dependent on training status and pathways containing genes that are always responsive to exercise.

Venn diagram analysis of differentially expressed gene transcripts at each timepoint of training (vs. control) was used to categorise 3 unique phases of the hypertrophic process, and further split into up and downregulated genes for KEGG pathway analysis. The 'Early Response' consisted of genes differentially expressed at 2 days, 10 days and 2 and 10 days. 'Always Responsive' consisted of gene transcripts differentially expressed at all timepoints and an 'Adapted Response' consisting of genes differentially expressed at 20 days, 30 days and 20 and 30 days.

During the 'Upregulated-Early Response' (Figure 5.4A), genes associated with 'Ribosome' (Figure 5.5A), 'Proteasome' (Figure 5.6), 'Protein processing in endoplasmic reticulum' (Figure 5.7) were significantly enriched ($P < 0.0001$), which likely reflects the requirement for increased ribosomal content and protein synthesis Figueiredo et al., (2015), Figueiredo and McCarthy, (2019), Figueiredo et al., (2021), von Walden et al., (2020), Wen et al., (2016). There was also an upregulation of 'Epstein-Barr virus infection', 'Salmonella Infection' and 'Phagosome' ($P < 0.0001$) which is indicative of an immune/inflammatory response and an increase in macrophage content well reported after unaccustomed exercise Schlagheck et al., (2020), Chaillou et al., (2013), Jensen et al., (2020), Trollet et al., (2021). Coinciding with this, genes falling into the 'Downregulated-Early Response' group (Figure 5.5B), were significantly enriched in the KEGG pathway 'Metabolic pathways'. Closer inspection of this complex and broad KEGG pathway revealed downregulation of fatty acid biosynthesis, fatty acid degradation, fatty acid elongation in mitochondria and oxidative phosphorylation ($P < 0.0001$). Furthermore, 'Carbon Metabolism', 'Fatty Acid Degradation', 'Fatty Acid Metabolism' and 'Glyoxylate and dicarboxylate metabolism' which likely reflects the glycolytic use of energy production and downregulation of fatty acid metabolism, and in this sense, the opposite of what would be expected as an 'endurance' training response.

Pathways associated with 'Upregulated-Always Responsive' genes (Figure 5.5A), included 'AGE-RAGE signaling pathway in diabetic complications', 'Focal Adhesion', 'Amoebiasis', 'Antigen processing and presentation', 'Proteoglycans in cancer', 'PI3K-Akt-Signalling', 'ECM-receptor interaction' and 'Haematopoietic cell lineage', ($P < 0.0001$).

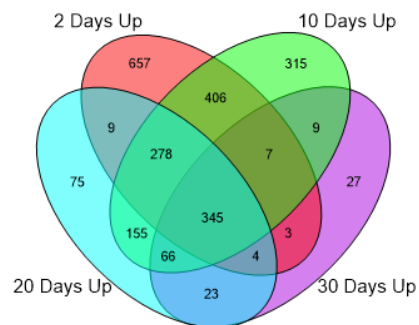
pathways in diabetic complications' incorporates TGF β -SMAD signalling, MAPK signalling, PI3k-Akt signalling, JAK-Stat signalling and pathways leading to angiogenesis and vascular function including the following genes Col1a1, Col3a1, Vinculin, Rab7b, Serpinb6a and Tgfb1. 'Focal Adhesion' is also well characterised in response to muscle adaptation including costamerogenesis, transmitting load activated phosphorylation cascades (integrin signalling), muscle stiffness and regulation of insulin sensitivity Graham et al., (2015), Wackerhage et al., (2019), Quach and Rando, (2006), Franchi et al., (2018), Flück et al., (1999), Klossner et al., (2009), Bisht et al., (2007), Boppart and Mahmassani, (2019). Pathways associated with 'Downregulated-Always Responsive' genes (Figure 5.5B), included 'Valine, leucine and isoleucine degradation' which has previously been identified as being significantly downregulated during synergist ablation-induced hypertrophy of the plantaris Chaillou et al., (2015), Chaillou et al., (2013). 'Propanoate Metabolism', 'Glucagon Signalling Pathway', 'Metabolic Pathways' and 'Carbon Metabolism' were also significantly enriched ($P < 0.0001$). When inspecting the glucagon signalling pathway, there was a consistent reduction (independent of training status) of the expression of genes relating to glycogen breakdown including glycogen phosphorylase (PYGM) and Phosphorylase b kinase (Phkg1), which is responsible for phosphorylating and activating glycogen phosphorylase and therefore promoting glycogenolysis.

This may be explained by studying the 'Adapted Response' to acute exercise gene sets. These gene sets revealed stark contrasts to the 'Early Response' to a single spillover bout. 'Upregulated-Adapted Response' genes were highly enriched in pathways including 'Oxidative Phosphorylation', Figure 5.9, 'Parkinson disease', 'Non-alcoholic fatty liver disease (NAFLD)', 'Huntington disease', 'Thermogenesis', 'Alzheimer disease', 'Retrograde endocannabinoid signalling' and 'Metabolic Pathways', ($P < 0.0001$) suggesting that despite the exercise stimulus being the same length and intensity, metabolic properties of the muscle had now been adapted and were no longer as reliant on glycolysis shortly after the exercise bout had ceased. Unfortunately, we did not measure glycogen content in the tibialis anterior muscle at any time point but further analyses of fuel availability, use and the metabolome may provide useful insights into the obvious shift in transcription of metabolic components. These pathways, mainly 'Oxidative Phosphorylation' (Figure 5.9), also seem to show the opposing response to 'Ribosome', 'Proteasome' and 'Protein processing in endoplasmic

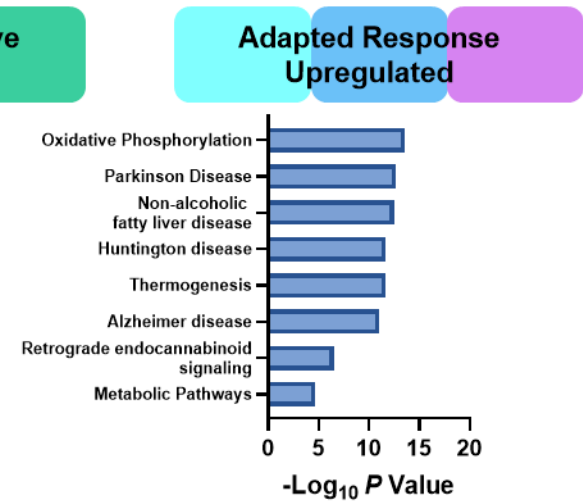
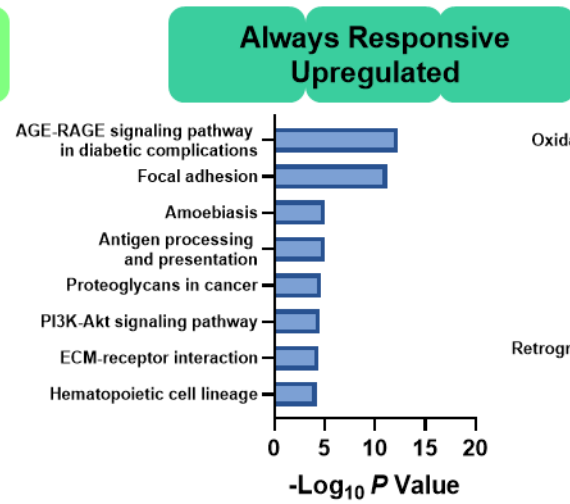
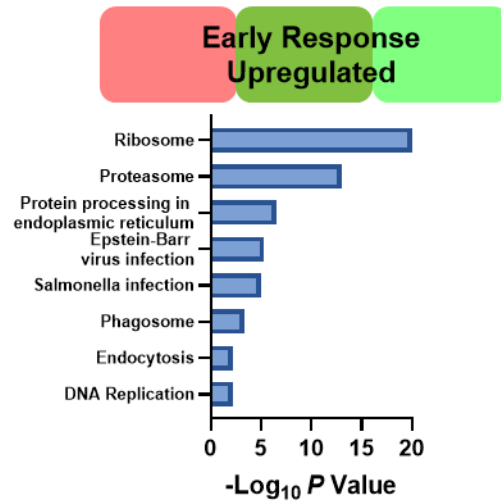
reticulum' which make a dramatic response after 2-10 days of exercise but rapid changes within the muscle mean that the same acute resistance exercise bout no longer stimulates enrichment of these transcripts and instead, downregulates to below control levels. Conversely, 'Oxidative Phosphorylation' is downregulated acutely in untrained muscle but its enrichment becomes paramount in the adapted/trained muscle between 20-30 days.

Curiously, pathway enrichment for 'Downregulated-Adapted Response' was very similar to the 'Upregulated- Early Response'. The 'Downregulated-Adapted Response' contained genes enriched in pathways including 'Spliceosome', 'Protein processing in endoplasmic reticulum', 'RNA transport', 'mRNA surveillance pathway', 'Proteasome', 'Ribosome biogenesis in eukaryotes', 'Ubiquitin mediated proteolysis' and 'mTOR signalling pathway'-Figure 5.8, ($P < 0.0001$), suggesting that the acute bout of exercise was no longer stimulating growth related pathways to the same extent. Furthermore, after 30 days of spillover training, these pathways were even downregulated versus control muscles. We emphasise this in Figure 5.5A/C, 5.6-5.8 which show an early upregulation, a gradual switching off and finally, a negative regulation of associated pathways at each timepoint. This may be suggestive of the daily stimulation providing a hypertrophic stimulus at the early stages but providing an endurance like stimulus later in the timecourse. We note that we performed training on a daily basis whereas a large majority of studies choose to resistance train animals every 3 days as per the current American College of Sports Medicine (ACSM) guidelines for use in human training Medicine, (2013). Further work from our lab hopes to elucidate required rest periods between training sessions to optimise resistance exercise prescription, to optimise hypertrophy itself and determine the 'switching point' where resistance training becomes overtraining or endurance like.

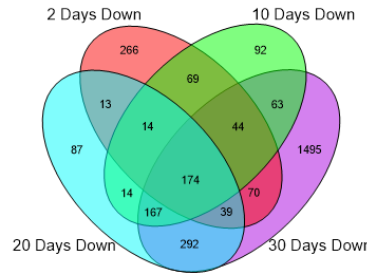
(A) Upregulated Gene Transcripts



Early Response			Always Responsive			Adapted Response		
KEGG Pathway	Enrichment Score	P-value	KEGG Pathway	Enrichment Score	P-value	KEGG Pathway	Enrichment Score	P-value
Ribosome	52	3E-23	AGE-RAGE signaling pathway in diabetic complications	12.2	5E-06	Oxidative phosphorylation	31.3	3E-14
Proteasome	29.9	1E-13	Focal adhesion	12.1	6E-06	Parkinson disease	29.5	2E-13
Protein processing in endoplasmic reticulum	15.1	3E-07	Amoebiasis	11.4	1E-05	Non-alcoholic fatty liver disease (NAFLD)	28.8	3E-13
Epstein-Barr virus infection	12.2	5E-06	Antigen processing and presentation	11.3	1E-05	Huntington disease	27.1	2E-12
Salmonella infection	11.5	1E-05	Proteoglycans in cancer	10.6	2E-05	Thermogenesis	27.1	2E-12
Phagosome	7.6	5E-04	PI3K-Akt signaling pathway	10.6	3E-05	Alzheimer disease	25.4	1E-11
Endocytosis	5.1	6E-03	ECM-receptor interaction	10.1	4E-05	Retrograde endocannabinoid signaling	15.0	3E-07
DNA Replication	5	7E-03	Hematopoietic cell lineage	9.7	6E-05	Metabolic pathways	10.8	2E-05



(B) **Downregulated Gene Transcripts**



Early Response			Always Responsive			Adapted Response		
KEGG Pathway	Enrichment Score	P-value	KEGG Pathway	Enrichment Score	P-value	KEGG Pathway	Enrichment Score	P-value
Metabolic pathways	33.8	2E-15	Valine, leucine and isoleucine degradation	12.7	3E-06	Spliceosome	19.7	3E-09
Carbon metabolism	22.1	2E-10	Propanoate metabolism	12.5	4E-06	Protein processing in endoplasmic reticulum	10.2	4E-05
Fatty acid degradation	21.4	5E-10	Glucagon signaling pathway	10.7	2E-05	RNA transport	7.7	4E-04
Fatty acid metabolism	18.0	2E-08	Metabolic pathways	8.0	3E-04	mRNA surveillance pathway	6.5	1E-03
Glyoxylate and dicarboxylate metabolism	16.4	7E-08	Carbon metabolism	7.7	5E-04	Proteasome	6.4	2E-03
Thermogenesis	15.0	3E-07	Starch and sucrose metabolism	5.9	3E-03	Ribosome biogenesis in eukaryotes	6.4	2E-03
Parkinson disease	13.8	1E-06	Calcium signaling pathway	5.5	4E-03	Ubiquitin mediated proteolysis	6.0	2E-03
Valine, leucine and isoleucine degradation	13.3	2E-06	beta-Alanine metabolism	5.4	5E-03	mTOR signaling pathway	5.9	3E-03

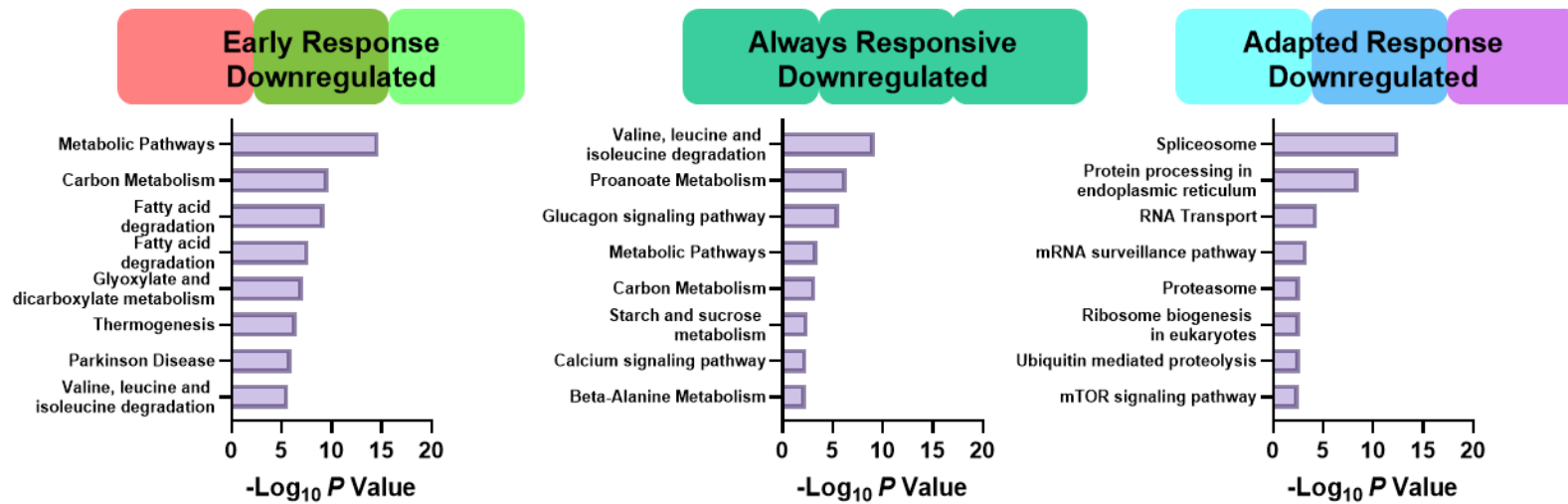


Figure 5.4: (A) Venn Diagram showing the overlap of upregulated genes between each of the stimulated groups. Subsequent KEGG pathway analysis reveals pathways involved in the ‘early response’ group (genes contained within the 2 days only, 10 days only and 2 and 10 days only samples), the ‘always responsive’ group and ‘adapted response’ group (20 days only, 30 days only and 20 and 30 days only samples). (B) Venn Diagram showing the overlap of downregulated genes between each of the stimulated groups. Subsequent KEGG pathway analysis reveals pathways involved in the ‘early response’ group (genes contained within the 2 days only, 10 days only and 2 and 10 days only samples), always responsive group and ‘adapted response’ group (20 days only, 30 days only and 20 and 30 days only samples).

Ribosomal gene expression following acute resistance exercise is highly responsive in untrained but is downregulated in trained rats orchestrated through Myc protein interactions.

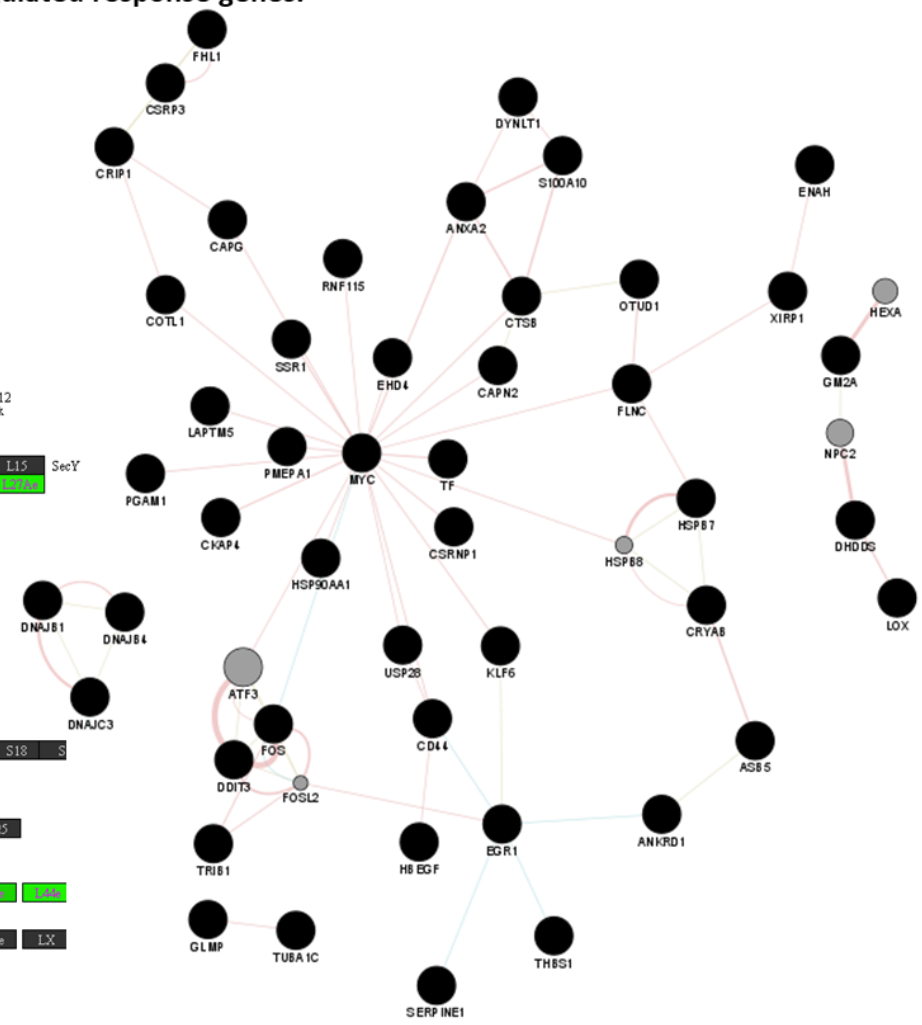
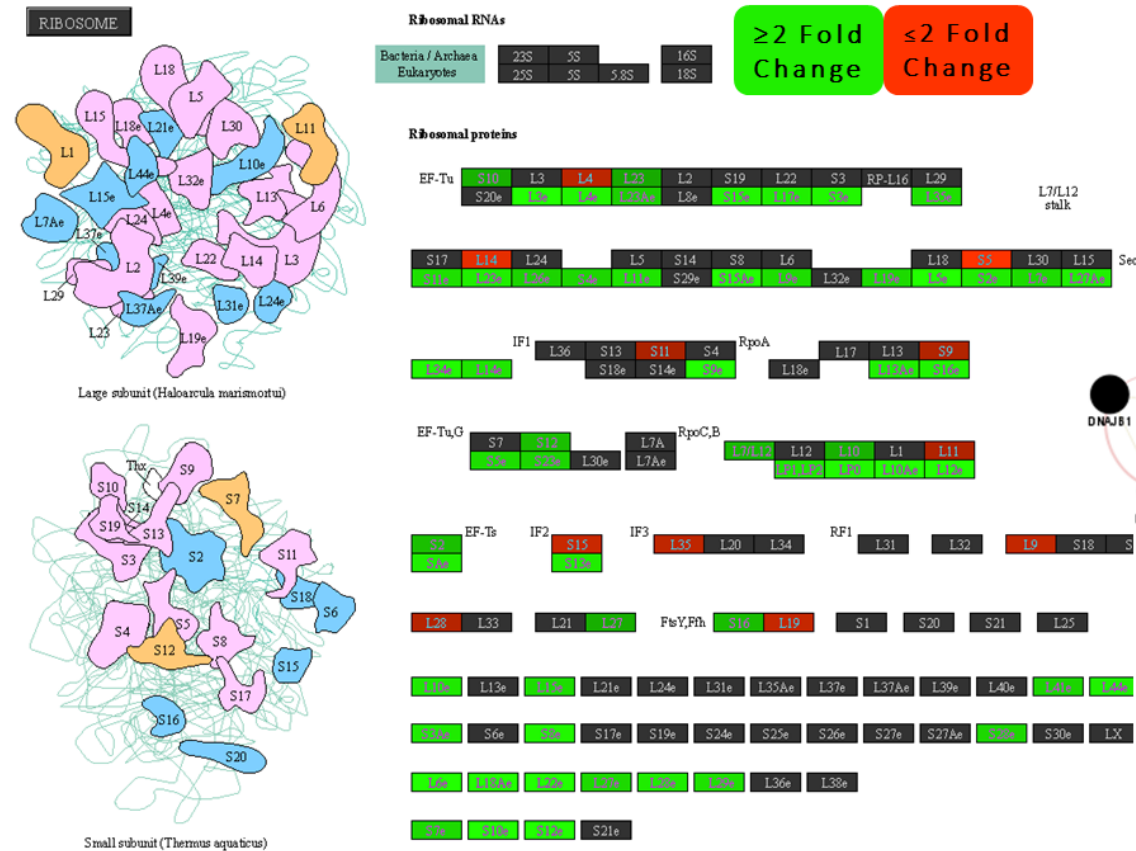
'Upregulated-Early Response' genes were highly enriched within the KEGG pathway 'Ribosome', Figure 5.5A whose upregulation 1 hour post spillover resistance training followed a similar pattern to the change in muscle mass. When compared with control, 54 genes associated with 'Ribosome' were upregulated and none were downregulated. This decreased after 10 days to 43 upregulated genes and 11 downregulated genes. As mentioned earlier, we believe that muscle mass using our model generally plateaus somewhere between 20 and 30 days of daily training. In line with these timepoints, we see a shift in the regulation of genes associated with 'Ribosome' with only 17 genes upregulated and 36 downregulated after 20 days vs. control. This shift in 'Ribosome' pathway gene regulation shifted further after 30 days of training, where only 8 genes were upregulated and 46 were downregulated vs control. This likely reflects the shift of the model being a hypertrophic stimulus (requiring ribosomal biogenesis and activity), to the muscle adjusting, muscle mass plateauing and reprogramming to a more oxidative phenotype.

Similarly to Amar et al. (2021), we performed network analysis of the genes in the 'Upregulated-Early Response' list with the GeneMANIA tool to reveal connected components identified through previously identified physical protein interactions, shared pathways and shared protein domains. This analysis showed that Myc (previously identified in our data as a SOM1 gene) was the central hub controlling these transcriptional networks in the 'Upregulated-Early Response'. Myc which is a downstream target of SMAD3, which was recently highlighted as an exercise modality-independent regulator of the transcriptional response to exercise through an extensive meta-analysis Amar et al., (2021). Proteins in the network analysis closely connected to Myc included Ehd4, Capn2, Tf, Csrnp1, Usp28, Cd44, Hsp90aa1, Ckap4, Pmepa1, Laptm5, Cotl1, Ssr1, Rnf115, Anxa2, CTSB, Fos, Klf6 and Atf3. Myc is an extensively studied oncoprotein and transcriptional activator that has an N-terminal transcription activation domain that interacts with various co-activators and a N-terminal basic-helix-loop-helix-leucine zipper domain required for enhancer box-specific DNA binding. Myc is reported to bind to E-boxes that regulate ribosomal proteins, translation factors, RNA polymerase subunits and genes within the TCA cycle, glycolysis, and biosynthesis.

(A) Early Upregulated Response

2 Day Acute Response vs. Control

(B) GeneMANIA Multiple Association Network Analysis of early upregulated response genes.



03010 46/17
(c) Kanehisa Laboratories

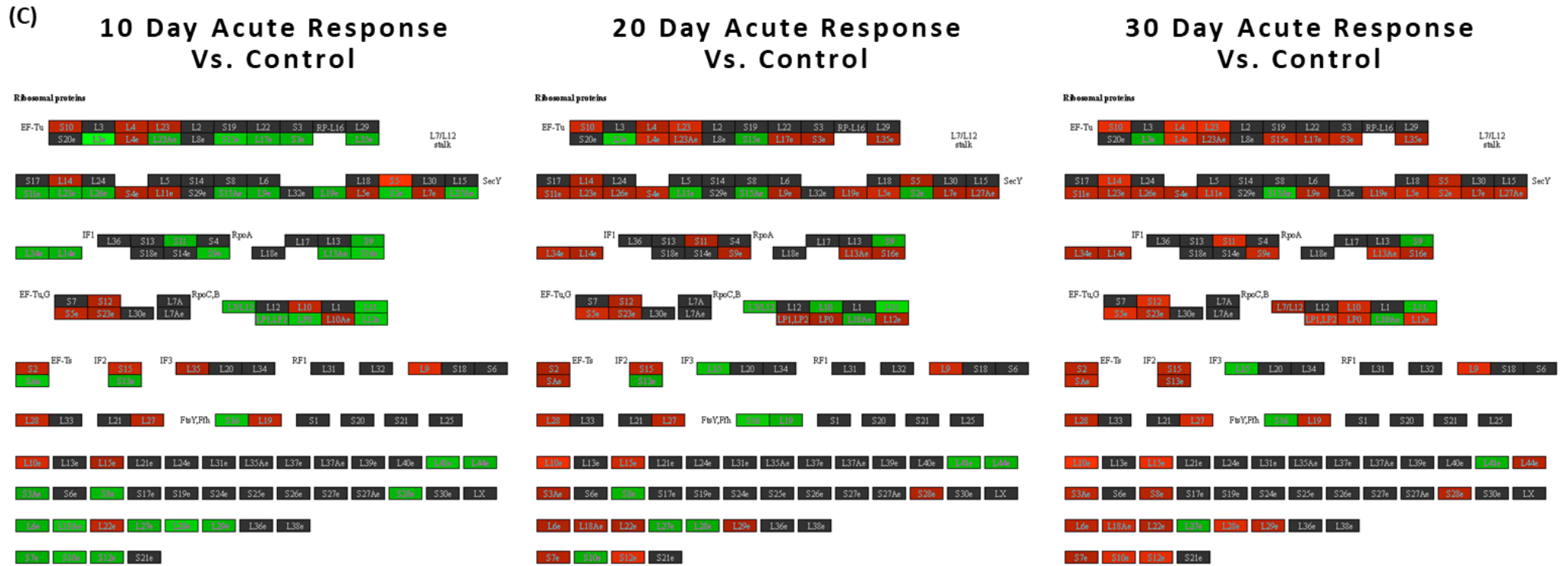
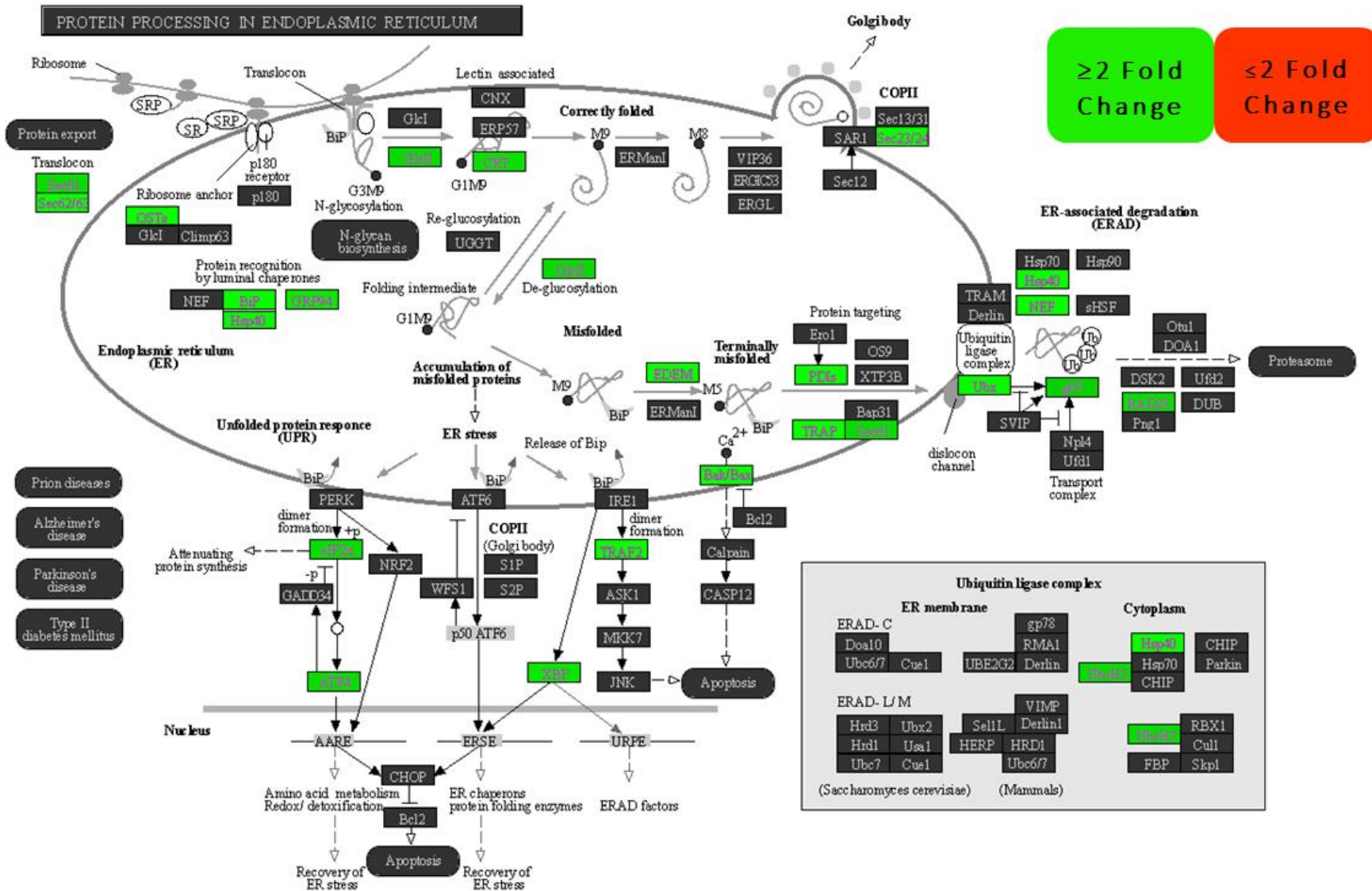
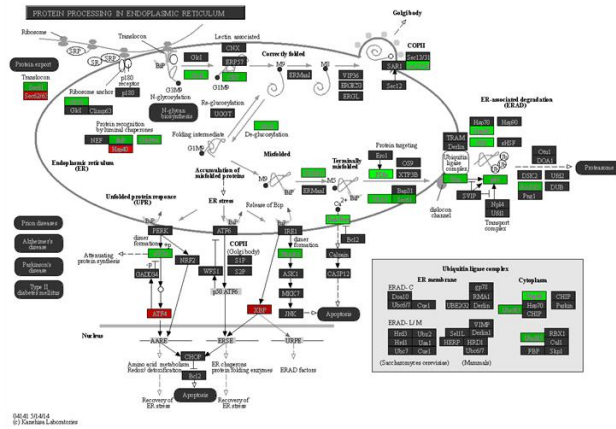


Figure 5.5: (A) Changes in expression of genes associated with the KEGG term, ‘Ribosome’ in response to acute exercise (1 hour post) after 2 days of training shows a large upregulation of genes versus control muscles. (B) GeneMANIA multiple association network analysis of the early upregulated response genes identifies MYC Proto-Oncogene, BHLH Transcription Factor as the master regulator of the response. Myc appears in SOM cluster 1 and its expression level is progressively less elevated in response to acute resistance exercise as muscle becomes more trained. (C) Temporal changes in expression in genes associated with the KEGG term, ‘Ribosome’ in response to acute exercise (1 hour post) reveal a gradual shift to downregulation over time in comparison to the unexercised, contralateral controls.

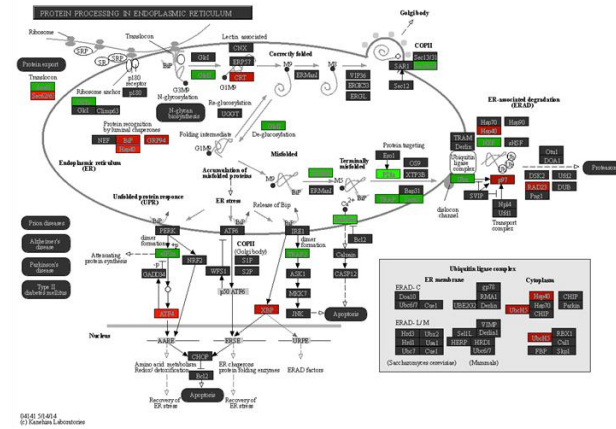
2 Day Acute Response vs. Control



10 Day Acute Response Vs. Control



20 Day Acute Response Vs. Control



30 Day Acute Response vs. Control

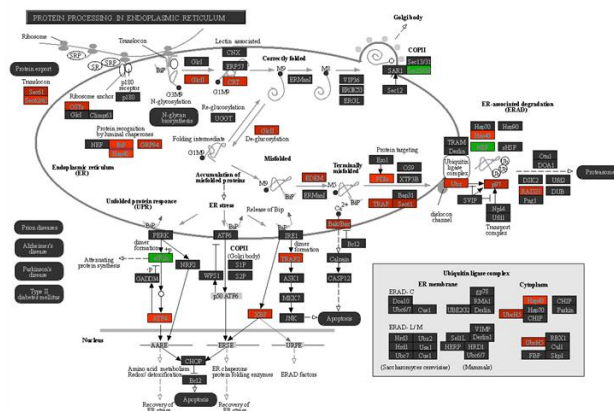


Figure 5.7: Changes in expression of genes associated with the KEGG term, 'Protein processing in endoplasmic reticulum' in response to acute exercise (1 hour post) after 2, 10, 20 and 30 days of training versus control muscles shows an early upregulation followed by a gradual decline in expression of genes in this KEGG pathway.

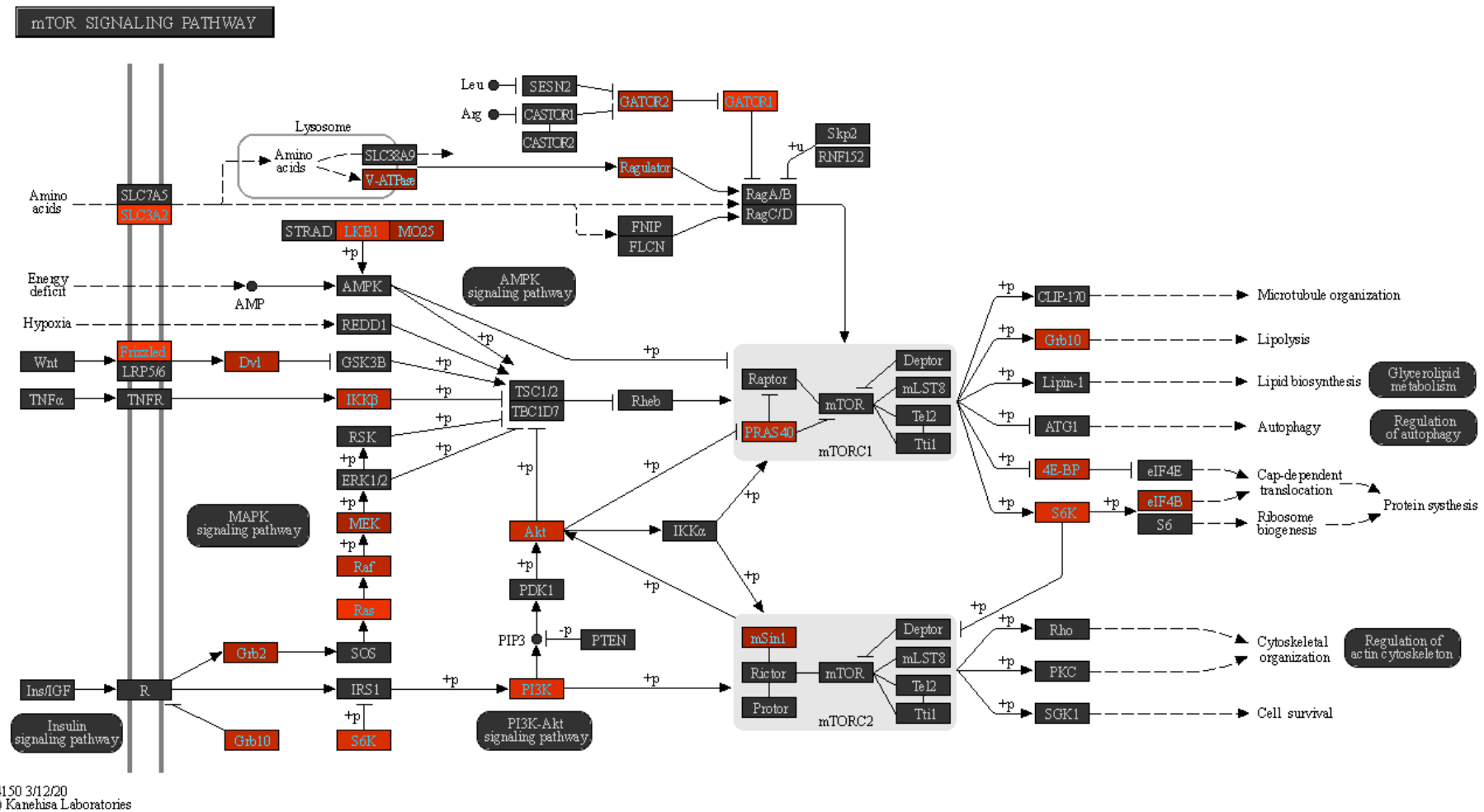
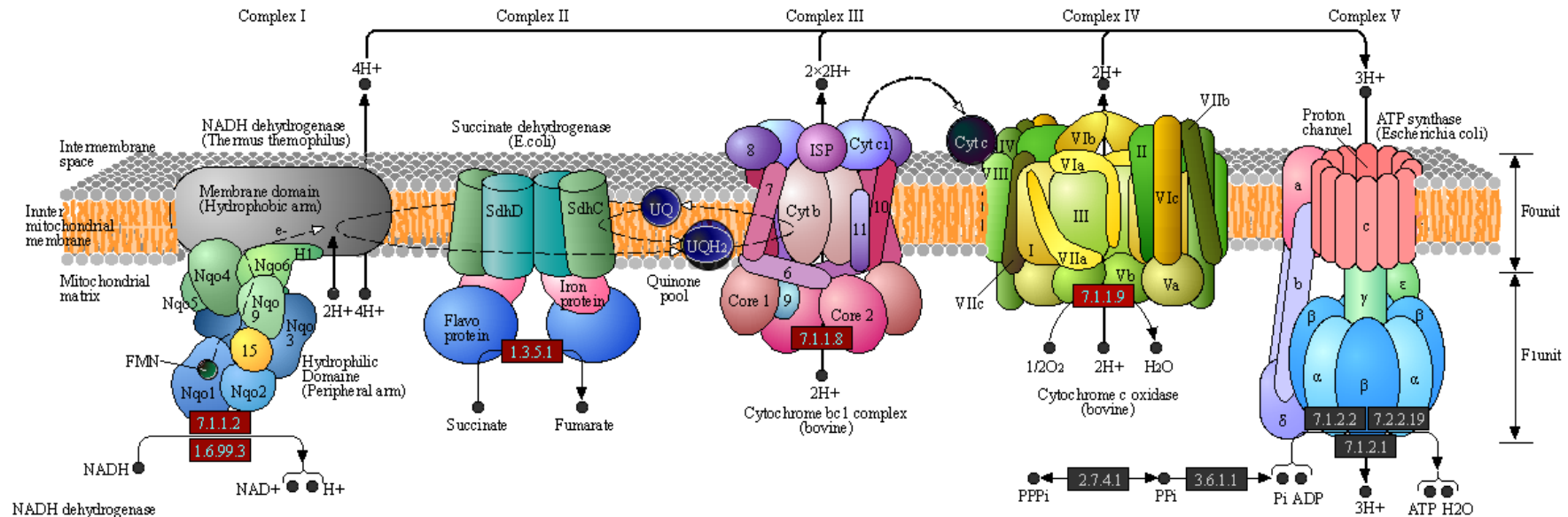


Figure 5.8: Changes in expression of genes associated with the KEGG term, 'mTOR signaling pathway' in response to acute exercise (1 hour post) after 30 days of training versus control muscles.

OXIDATIVE PHOSPHORYLATION



NADH dehydrogenase

E	ND1	ND2	ND3	ND4	ND4L	ND5	ND6										
E	Ndufs1	Ndufs2	Ndufs3	Ndufs4	Ndufs5	Ndufs6	Ndufs7	Ndufs8	Ndurf1	Ndurf2	Ndurf3						
B/A	NuoA	NuoB	NuoC	NuoD	NuoE	NuoF	NuoG	NuoH	NuoI	NuoJ	NuoK	NuoL	NuoM	NuoN			
B/A	NdhC	NdhK	NdhJ	NdhH	NdhA	NdhI	NdhG	NdhE	NdhF	NdhD	NdhB	NdhL	NdhM	NdhN	HoxE	HoxF	HoxU
E	Ndufa1	Ndufa2	Ndufa3	Ndufa4	Ndufa5	Ndufa6	Ndufa7	Ndufa8	Ndufa9	Ndufa10	Ndufab1	Ndufa11	Ndufa12	Ndufa13			
E	Ndubf1	Ndubf2	Ndubf3	Ndubf4	Ndubf5	Ndubf6	Ndubf7	Ndubf8	Ndubf9	Ndubf10	Ndubf11	Ndubf1	Ndubf2				

Succinate dehydrogenase / Fumarate reductase

E	SDHC	SDHD	SDHA	SDHB				
B/A	SdhC	SdhD	SdhA	SdhB	FrdA	FrdB	FrdC	FrdD

Cytochrome c reductase

E/B/A	ISP	Cyt b	Cyt 1				
E	COR1	QCR2	QCR6	QCR7	QCR8	QCR9	QCR10

Cytochrome c oxidase

E	COX10	COX3	COX1	COX2	COX4	COX5A	COX5B	COX6A	COX6B	COX6C	COX7A	COX7B	COX7C	COX8	E/B/A	COX11	COX15	COX17
B/A	CyoE	CyoD	CyoC	CyoB	CyoA	CoxD	CoxC	CoxA	CoxB	QoxD	QoxC	QoxB	QoxA	SoxD	SoxC	SoxB	SoxA	

Cytochrome c oxidase, ab2 type

B	I	II	IV	III
---	---	----	----	-----

Cytochrome bc1 complex

B/A	CydA	CydB	CydX
-----	------	------	------

F-type ATPase (Bacteria)

alpha	beta	gamma	delta	epsilon
a	b	c		

F-type ATPase (Eukaryotes)

alpha	beta	gamma	delta	epsilon	
OSCP	a	b	c	d	e
f	g	f6/h	j	k	8

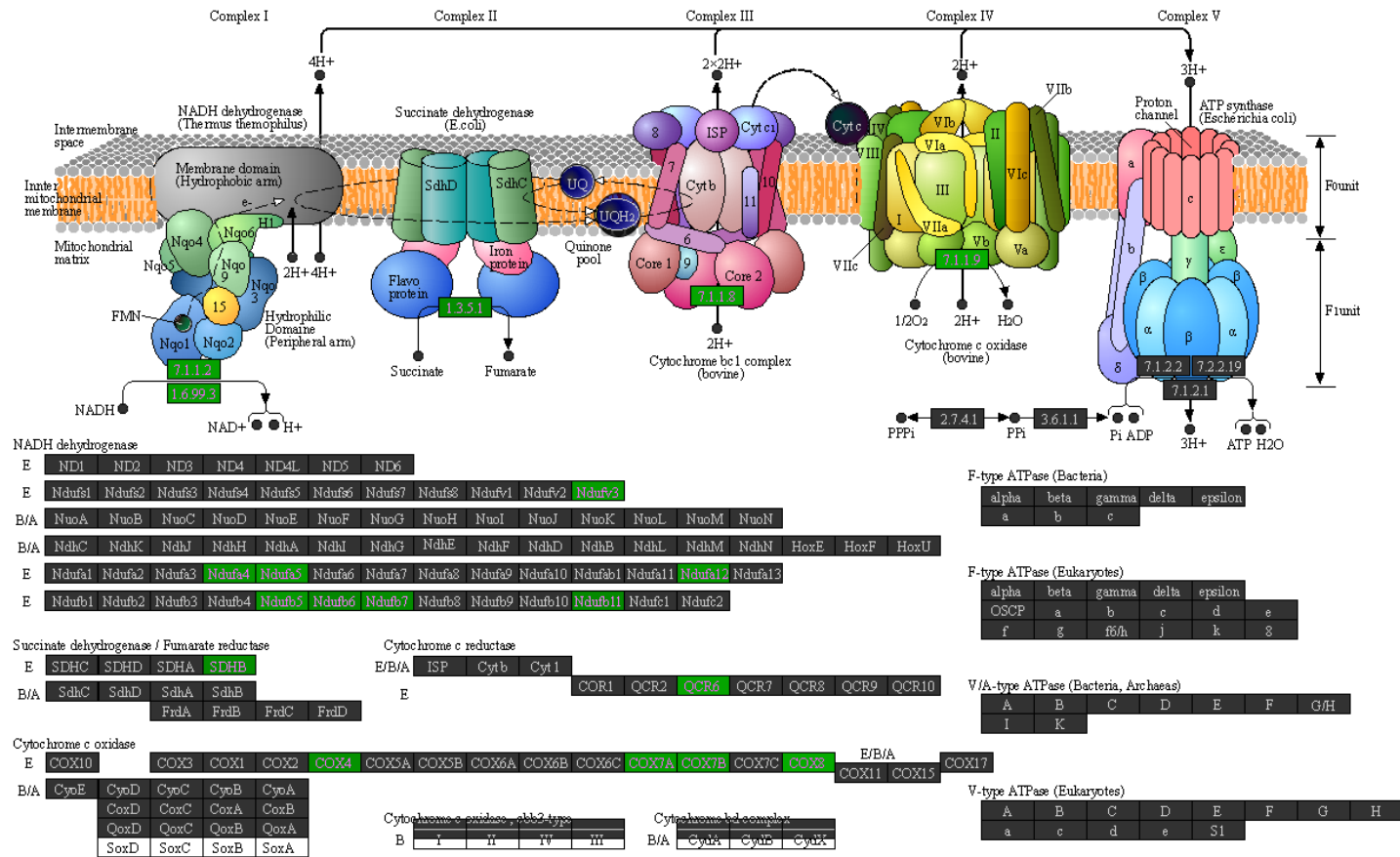
V/A-type ATPase (Bacteria, Archaea)

A	B	C	D	E	F	G/H
I	K					

V-type ATPase (Eukaryotes)

A	B	C	D	E	F	G	H
a	c	d	e	S1			

OXIDATIVE PHOSPHORYLATION



190 1/31/20
Kanehisa Laboratories

Figure 6.9: Changes in expression of genes associated with the KEGG term, 'Oxidative Phosphorylation' in response to acute exercise (1 hour post) after 2 and 30 days of training, versus control muscles reveals a downregulation acutely after exercise in 2-day trained muscles and an upregulation of oxidative phosphorylation related genes after 30 days.

Comparative transcriptome analysis between species and models reveals only 10 common regulators of resistance training induced hypertrophy.

Despite recent high-profile attempts Pillon et al., (2020), Amar et al., (2019), Amar et al., (2021), Contrepois et al., (2020), there is not a great deal of consensus surrounding the transcriptional underpinnings of adaptation to exercise and specifically resistance exercise. This is likely due to the huge variability in the origin and the activation history of the samples studied making it near on impossible to identify ‘master regulators or key gene interactions to target to improve exercise responsiveness and ultimately lead to more efficient adaptation through individualised, prescribed exercise. Samples themselves may differ in species, age, metabolic state, training history, timepoint post exercise, exercise variability (reps, sets, rest, contraction modality) and muscle group to name a few Amar et al., (2021). There will also be differences in the detail and versions of the genome assembly used which may further contribute to genes identified. In rodent studies, researchers often study the ‘anti-gravity’ ankle plantarflexors as they may have more physiological relevance to strength and mobility in humans than dorsiflexors, but individual muscles can vary considerably within these muscle groups. Additionally, there is no approved consensus on the appropriate normalization methods and filtering used in next-generation RNA-sequencing, with different labs adopting completely different approaches leading to differing conclusions.

There is no other previous dataset showing changes in gene expression over a similar well-controlled timecourse of muscle growth to what we have studied in our experiment. However, we made comparison with five existing datasets from human and rodent exercise experiments Chaillou et al., (2013), Cui et al., (2020), Turner et al., (2019), Pillon et al., (2020). By overlapping the top 400 genes from the above rodent studies Chaillou et al., (2013), Cui et al., (2020) and the top (by significance) 750 acute and 750 chronically differentially regulated genes with exercise from two meta-dataset analyses with our spillover dataset we hoped to identify commonly differentially expressed genes that were specific to individual rodent models of exercise, genes that were shared across rodent models and ultimately whether they overlapped with meta-analyses performed on differentially expressed genes identified following human resistance exercise both acutely and in resting, chronically trained muscle, Figure 5.10A.

We note disappointing correspondence with the systematic review from the Zierath Pillon et al., (2020) and Sharples lab Turner et al., (2019), even when their list of most significant genes is extended to include both acute and chronic resistance training responses and the stringency is lowered to include even more genes (750). When overlapped, only 528 of the 1500 genes (35%) were noted in both human resistance training meta-analyses, presumably due to differences in datasets studied and statistical approaches used. Furthermore, 419 genes (27.9%) of those 528 genes failed to be captured in the top 400 most significantly differentially regulated genes in the three rodent models of resistance exercise, perhaps highlighting a group of genes that are responsive to exercise in humans, but not in rodents, which requires further investigation. We speculate that some of these differences may arise from differences in genome coverage within and between databases. We then compared the most significant, differentially regulated genes after spillover training with both human datasets revealing that 134/400 genes (33.5%) were overlapping. 35 genes (8.75%) were specific to the overlap between spillover training and the Turner et al. (2019) human resistance training dataset and 46 genes (11.5%) were specific to the overlap between spillover training and the Pillon et al. (2020) human resistance training dataset. A further 53 (13.25%) were found to overlap between spillover training and both human resistance training meta-analyses.

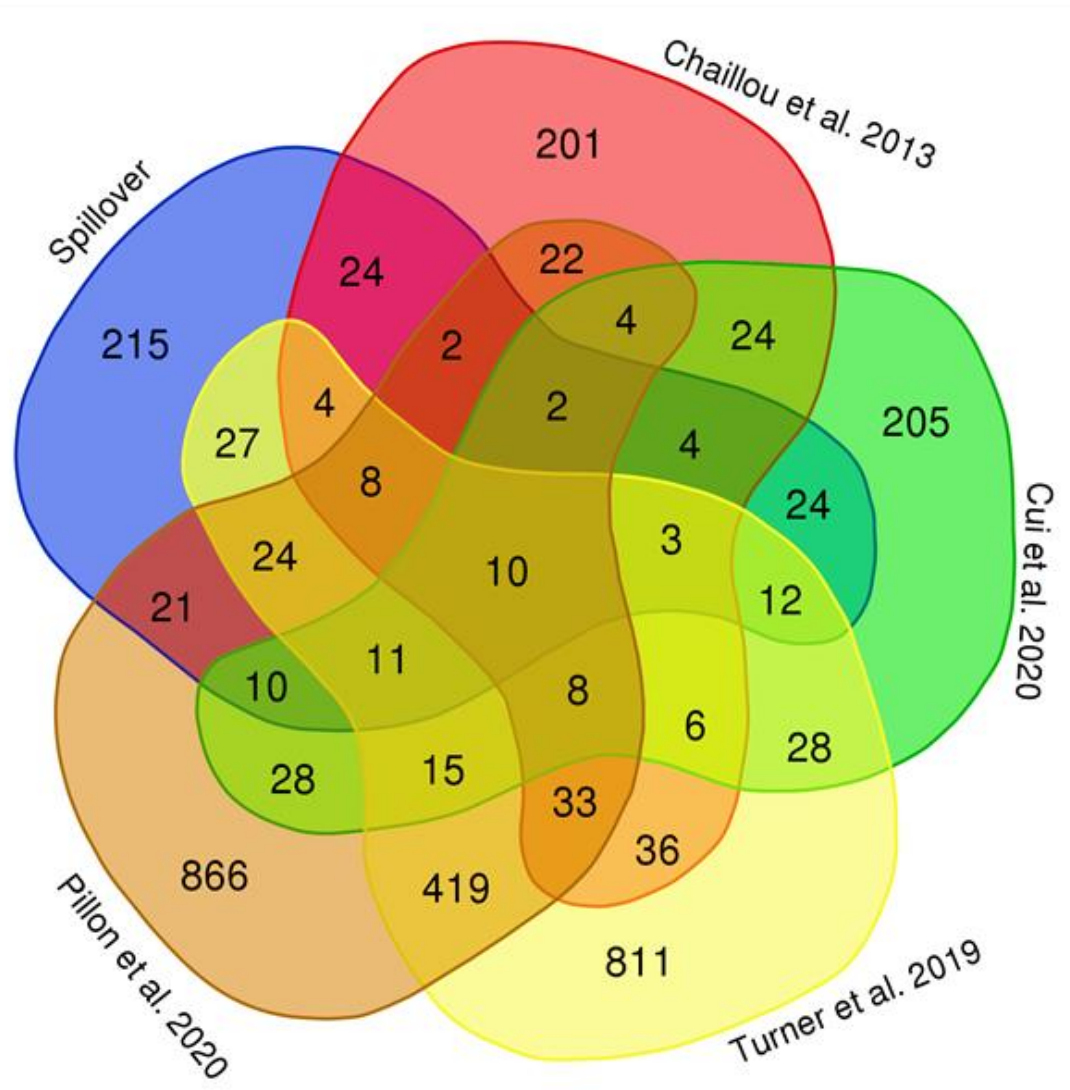
Furthermore, the changes in gene expression associated with hypertrophy induced by synergist ablation overload are distinct from the changes we have observed. Only 57 genes (14.25%) overlapped with spillover training, 24 of which were completely specific to synergist ablation in mice and spillover training in rats. There was slightly more overlap observed between spillover training and voluntary weightlifting in mice (66 genes, 16.5%), of which 24 were completely specific to spillover training and voluntary weightlifting. There was similar overlap observed between synergist ablation and voluntary weightlifting in mice (61 genes, 15.25%), of which 24 genes were unique between these models. This analysis emphasises that the synergist ablation model is a model of continuous overload to failure with extensive damage/regeneration, rather than a model of training-induced muscle growth. This is an important caveat because the changes in gene expression with synergist ablation are often considered as representative of muscle growth. We caution against this interpretation. The acute response that we capture with our timepoints may not also be comparable to the Zhen

Yan voluntary squat-like weightlifting model which comprises of one timepoint muscle transcriptome analysis of resting and 8-week trained gastrocnemius muscle. Furthermore, there were 19 genes (4.5%) from the top 400 spillover genes that appeared in all 3 rodent models, 4 of which (1% of the 400 spillover genes) were only found in rodent models and did not appear in any of the human datasets. These genes were *C1qb*, *Csf1r*, *Serpine1*, *Mfap4*, (Figure 5.10H), appearing in SOM2, 2, 1 and 2 respectively.

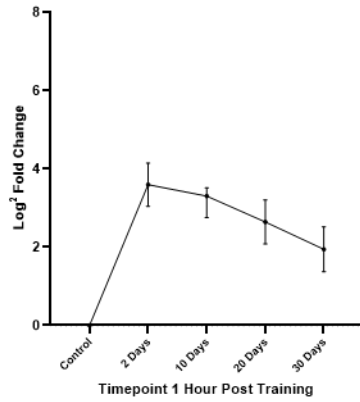
Of the top 400 genes significantly altered after spillover training, 215 (53.75%) of them were specific to spillover training. These responses may be specific to rats following exercise and require further investigation. To our surprise, only 10 genes were found to overlap across all models of resistance exercise and species (2.5% of the 400 differentially expressed spillover genes) including our main hub gene *Myc* (SOM1), identified through GeneMANIA analysis, Figure 5.5B. The remainder included, *ATF3* (SOM2), *adenosylmethionine Decarboxylase 1* (*Amd1*) (SOM5), *Bgn* (SOM3), *Hmox1* (SOM3), *Ankrd1* (SOM1), *Lysyl Oxidase* (*Lox*) (SOM2), *Collagen Type III Alpha 1 Chain* (*Col3a1*) (SOM3), *EH Domain Containing 4* (*Ehd4*) (SOM1) and *Collagen Type I Alpha 1 Chain* (*Col1a1*) (SOM3), Figure 5.10B.

We also highlight other genes that were missing from only one dataset that we compared in our Venn diagram analysis, as they are likely extremely important in the hypertrophic process/muscle adaptation as their change in gene expression seems to be conserved across all species and models. *Hk2* (SOM4), *Egr1* (SOM1), *Itga5* (SOM2) appeared in the overlap between all studies apart from the Pillon et al., (2020) dataset, Figure 5.10C. *Klhl40* (SOM1) and *Lum* (SOM2) appeared in the overlap between all studies but was missing from the Turner et al., (2019) dataset, Figure 5.10D. *Thy1* (SOM3), *Col6a2* (SOM3), *Maff* (SOM3), *F2r* (SOM3), *Col6a1* (SOM3), *Fabp5* (SOM2), *Sparc* (SOM4), *Msn* (SOM3) were absent from Cui et al., (2020), Figure 5.10E. *Tnfrsf12a* (SOM1), *Hbegf* (SOM2), *Ppp1r27* (SOM3), *Irs2* (SOM2), *Abra* (SOM2), *Nr4a3* (SOM2), *Mgp* (SOM3), *Dnajb4* (SOM2), *Xirp1* (SOM1) and *Dnaja4* (SOM3) overlapped in all datasets, but was absent from the synergist ablation dataset Chaillou et al., (2013), Figure 5.10G. Genes that were not included in the spillover dataset but were included in all other data sets included *Ifrd1* (SOM5), *Angptl2* (SOM4), *Strp2* (SOM4), *Col5a2* (SOM2), *Ky* (SOM5) and *Rrad* (SOM1), Figure 5.10F.

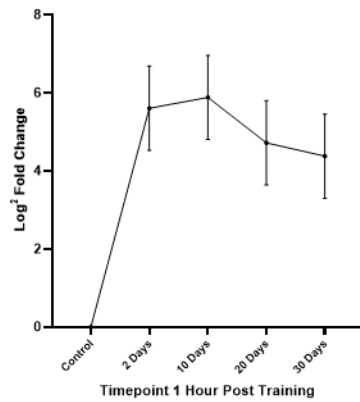
(A)



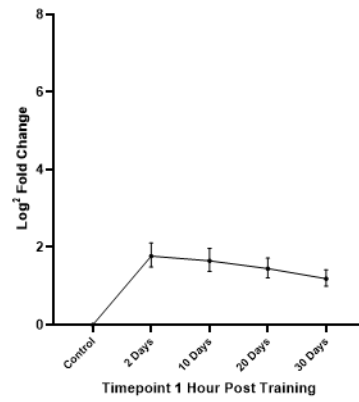
(B) MYC Proto-Oncogene,
BHLH Transcription Factor
(Myc)



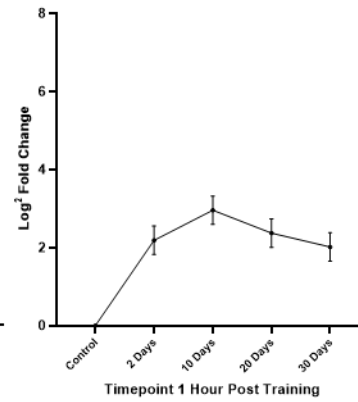
Activating Transcription Factor 3
(ATF3)



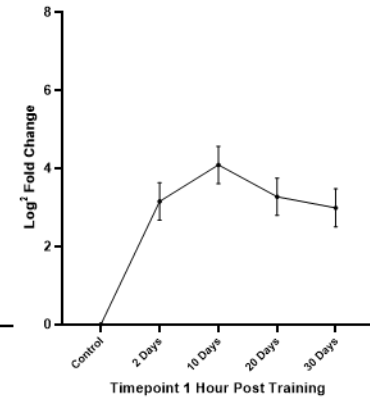
Adenosylmethionine Decarboxylase 1
(Amd1)



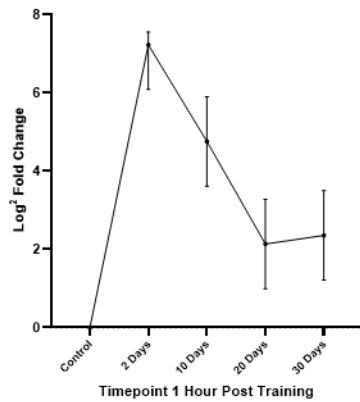
Biglycan
(Bgn)



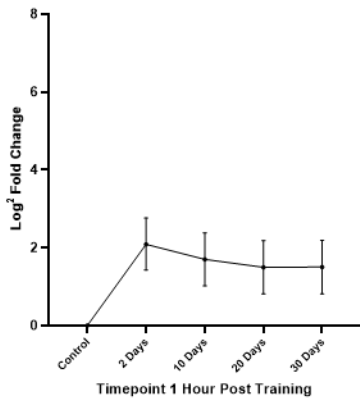
Heme Oxygenase 1
(Hmox1)



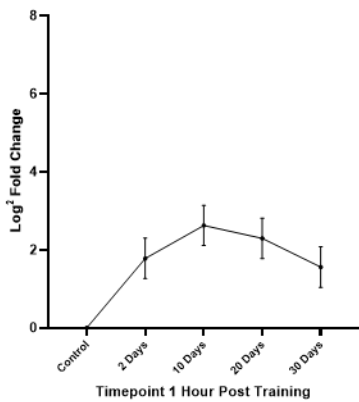
Ankyrin Repeat Domain 1
(Ankrd1)



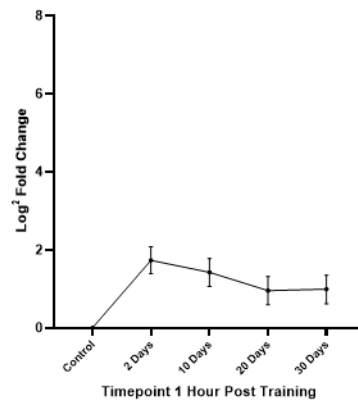
Lysyl Oxidase
(Lox)



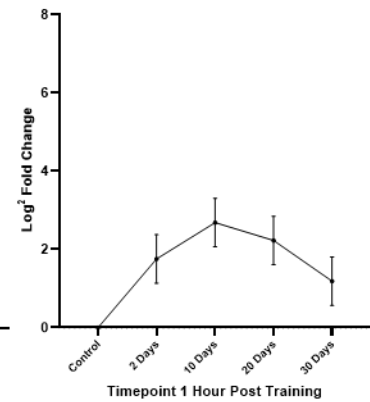
Collagen Type III Alpha 1 Chain
(Col3a1)



EH Domain Containing 4
(Ehd4)



Collagen Type I Alpha 1 Chain
(Col1a1)



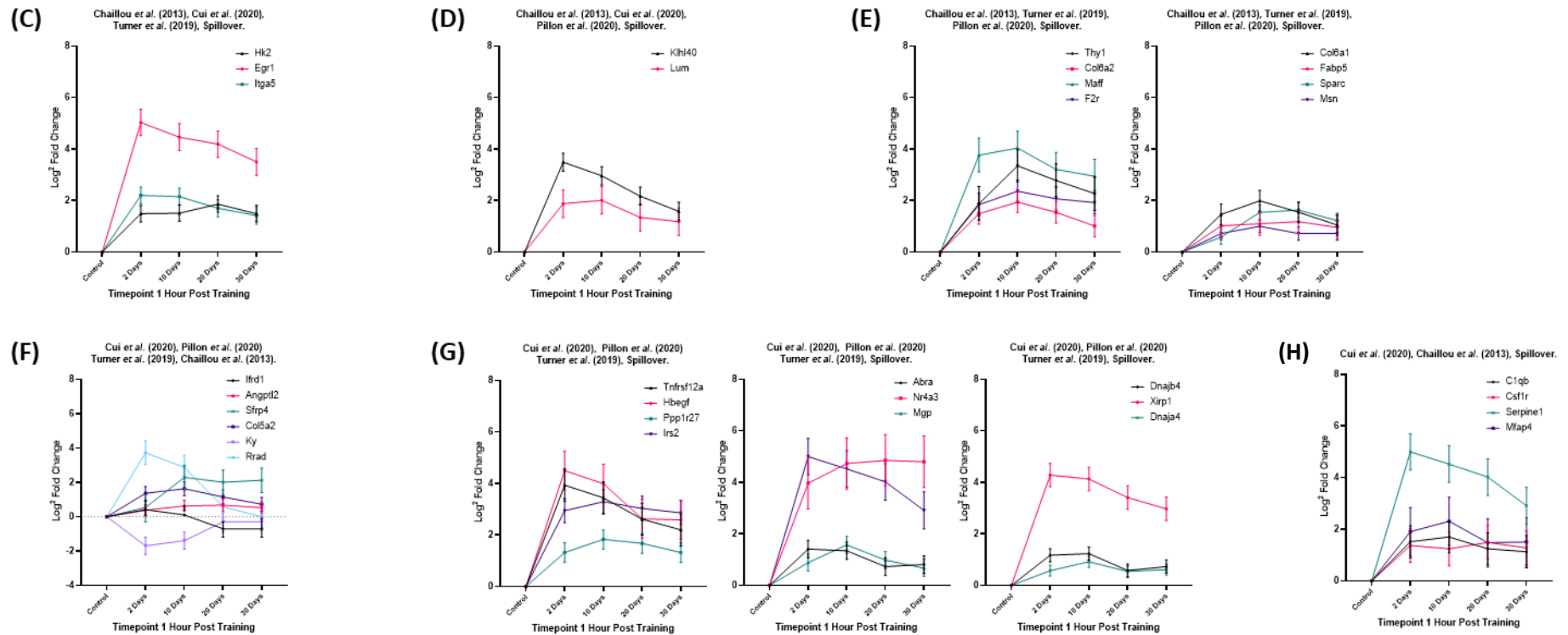


Figure 5.10: (A) Venn diagram analysis of the top 400 differentially expressed genes ordered by significance in 3 distinct rodent models of hypertrophy and two meta-analyses of data from studies of resistance exercise in humans. Human data sets contain both the top 750 genes following acute resistance exercise and top 750 genes associated with chronic resistance exercise in humans from each publication (Turner et al. 2019; Pillon et al. 2020). Time course changes in our dataset for (B) The \log^2 fold changes \pm confidence intervals for the 10 genes found to overlap between all transcriptomic data sets. (C) The \log^2 fold changes \pm confidence intervals for the 3 genes found to overlap between Chaillou et al. (2013), Cui et al. (2020), Turner et al. (2019) and Spillover datasets. (D) The \log^2 fold changes \pm confidence intervals for the 2 genes found to overlap between Chaillou et al. (2013), Cui et al. (2020), Pillon et al. (2020) and Spillover datasets. (E) The \log^2 fold changes \pm confidence intervals

*for the 8 genes found to overlap between Chaillou et al. (2013), Turner et al. (2019), Pillon et al. (2020) and Spillover datasets. (F) The log² fold changes ± confidence intervals for the 6 genes found to overlap between Cui et al. (2020), Pillon et al. (2020), Turner et al. (2019) and Chaillou et al. (2013) datasets. Genes *Srxn1* and *Col1a2* also overlapped in this group but did not appear in our RNA-sequencing analysis for comparison. (G) The log² fold changes ± confidence intervals for the 11 genes found to overlap between Cui et al. (2020), Pillon et al. (2020), Turner et al. (2019) and Spillover datasets. (H) The log² fold changes ± confidence intervals for the 4 genes found to overlap between Cui et al. (2020), Chaillou et al. (2013) and Spillover datasets (rodent only models).*

Small, yet notable temporal patterns in contralateral muscles dependent on training status of the trained limbs show effects on genes involved in circadian regulation.

One benefit of having a unilateral model of resistance exercise is that the contralateral leg can be used as an internal comparison more specific to the animal. On the other hand, numerous studies have reported contralateral effects of unilateral limb training including both biochemical and neurological/motor learning adaptations (cross-education of strength), some of which have suggested that training the contralateral limb during immobilisation or injury can help alleviate muscle mass loss Munn et al., (2005), Andrushko et al., (2018a), Andrushko et al., (2018b), Farthing et al., (2009), Hendy et al., (2012), Valdes et al., (2021). One mechanism behind this may be from muscle secreted factors (myokines/chemokines) that can regulate glucose homeostasis, enhance insulin sensitivity, alter metabolism and inflammation through systemic organ crosstalk which has been studied (and reviewed) extensively both in-vitro and in-vivo Sanford et al., (2020), Scisciola et al., (2021), Chen et al., (2021), Kim et al., (2021), Gupta et al., (2021), Rai and Demontis, (2016), Huh, (2018), Díaz et al., (2018), Raschke et al., (2013), Severinsen and Pedersen, (2020), Lee and Jun, (2019)

We performed gene set analysis (shown in Figure 5.11A through hierarchical cluster mapping) to identify gene significantly different between 2 days control and the control muscles after a further 10, 20 and 30 days of training. 77 genes were upregulated and 32 downregulated in the 10-day control muscles (109 total), versus the 2-day control muscles, despite the control muscles remaining the same weight throughout the timecourse of training. Most of the fold changes present in the control tissues were minimal, with the largest fold changes between 2 and 30 days appearing with genes *Aqp4* (-17.25FC), *Dbp* (-12.8 FC) and *Dgkz* (-6.3FC), all of which are circadian output genes. This difference increased as training duration increased with 158 upregulated and 51 downregulated after 20-days (209 total), compared with the 2-day control group. This peaked after 30 days with a total of 369 genes differentially regulated compared to 2 days, 82 of which were upregulated and 287 that were downregulated, Figure 5.11B. Interestingly, the 30-day timepoint in the trained TA's also demonstrated the largest number of differentially expressed genes. The number of changes was significantly lower between the untrained muscles compared with the trained muscles across the timecourse of training. Only 6 of the genes were differentially expressed consistently across 10, 20 and 30

days, all of which were downregulated. These included *Tubb4b*, *Tuba4a*, *Ufsp1* and *Dbp-201* and *Dbp-202*, Figure 5.11B.

SOM clustering was performed on the 369 differentially expressed genes between 2- and 30-day contralateral control muscles, from which 4 clusters were identified, Figure 5.11C. SOM1 contained 82 upregulated genes (Figure 5.11D), SOM2 108 downregulated genes (Figure 5.11E), SOM3 95 downregulated genes (Figure 5.11E) and SOM4 84 downregulated genes, (Figure 5.11G).

In rank order SOM1 contained the following genes: *Ubc1* (Ubiquitin-conjugating enzyme E2), *AABR07044759* (MFS domain-containing protein), *Arntl1/Bmal1* (Aryl Hydrocarbon Receptor Nuclear Translocator Like/Brain and muscle Arnt-like protein-1), *Lrrc30* (Leucine Rich Repeat Containing 30), *Pnrc1* (Proline Rich Nuclear Receptor Coactivator 1), *Fbxo32* (F-box only protein 32/MAFbx), *PDK4* (Pyruvate Dehydrogenase Kinase 4), *Gramd1b* (GRAM domain containing 1B), *Aradc3* (Arrestin Domain Containing 3), *CD4* (cluster of differentiation 4), *Mt-nd4l* (Mitochondrially Encoded NADH: Ubiquinone Oxidoreductase Core Subunit 4L) and *Myh4* (Myosin Heavy Chain IIX), Figure 5.11D.

In rank order SOM2 contained the following genes: *Dhrs7c* (Dehydrogenase/Reductase 7C), *Tinagl1* (Tubulointerstitial Nephritis Antigen Like 1), *RT1-T24-4* (RT1 class I, locus T24, gene 4), *Csrp1* (Cysteine And Glycine Rich Protein 1), *Arfp2* (ADP Ribosylation Factor Interacting Protein 2), *Kank2* (KN Motif And Ankyrin Repeat Domains 2), *Usp2* (Ubiquitin carboxyl-terminal hydrolase 2), *Per 1* (Period Circadian Regulator 1), *Atf3* (Activating transcription factor 3), *Timm10* (Translocase Of Inner Mitochondrial Membrane 10), *Hspb6* (Heat shock protein B6), *Vegfa* (Vascular Endothelial Growth Factor A), Figure 5.11E.

In rank order SOM3 contained the following genes: *Dbp* (D-Box Binding PAR BZIP Transcription Factor), *Hras* (*HRas* Proto-Oncogene, GTPase), *Cox6a1* (Cytochrome C Oxidase Subunit 6A1), *Tcap* (Telethonin/Titin-Cap Protein), *Tuba8* (Tubulin Alpha 8), *Tuba4b* (Tubulin Alpha 4b), *Rplp0* (Ribosomal Protein Lateral Stalk Subunit P0), *Tubb4b* (Tubulin Beta 4B Class IVb), *Rplp2* (Ribosomal Protein Lateral Stalk Subunit P2), *Per2* (Period Circadian Regulator 2) and *Rps2* (Ribosomal Protein S2), Figure 5.11F.

In rank order SOM4 contained the following genes: *Rbm3* (RNA Binding Motif Protein 3), *Csrp3* (Cysteine And Glycine Rich Protein 3), *Tmem233* (Transmembrane Protein 233), *Dgkz*

(Diacylglycerol Kinase Zeta), Taf9 (TATA-Box Binding Protein Associated Factor 9), Ppie (Peptidylprolyl Isomerase E), Becn1 (Beclin 1), Cox7a2l (Cytochrome C Oxidase Subunit 7A2 Like), Pmp22 (Peripheral Myelin Protein 22), Ankrd2 (Ankyrin Repeat Domain 2), Sh3gl1 (SH3 Domain Containing GRB2 Like 1, Endophilin A2) and Mcam (Melanoma Cell Adhesion Molecule) Figure 5.11G.

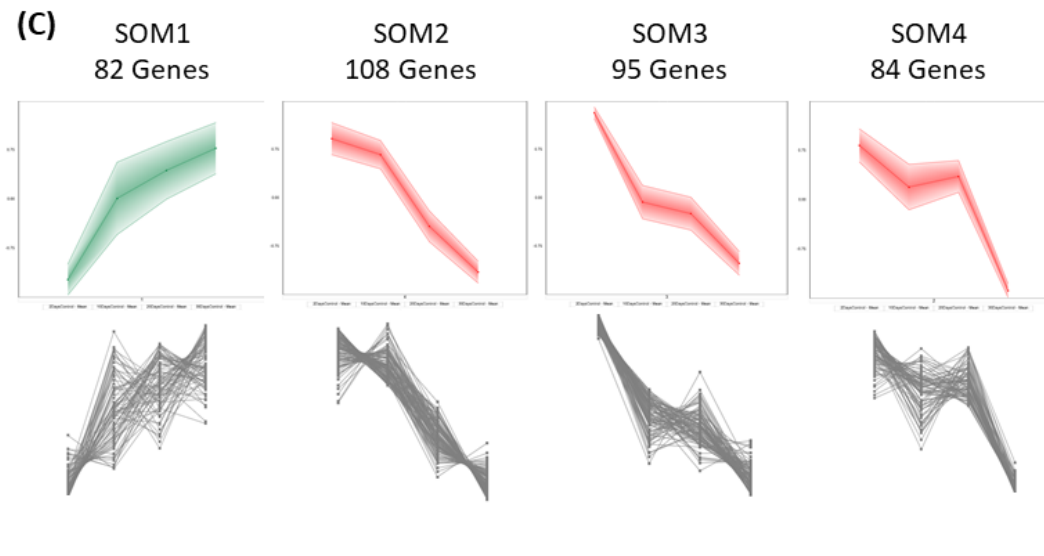
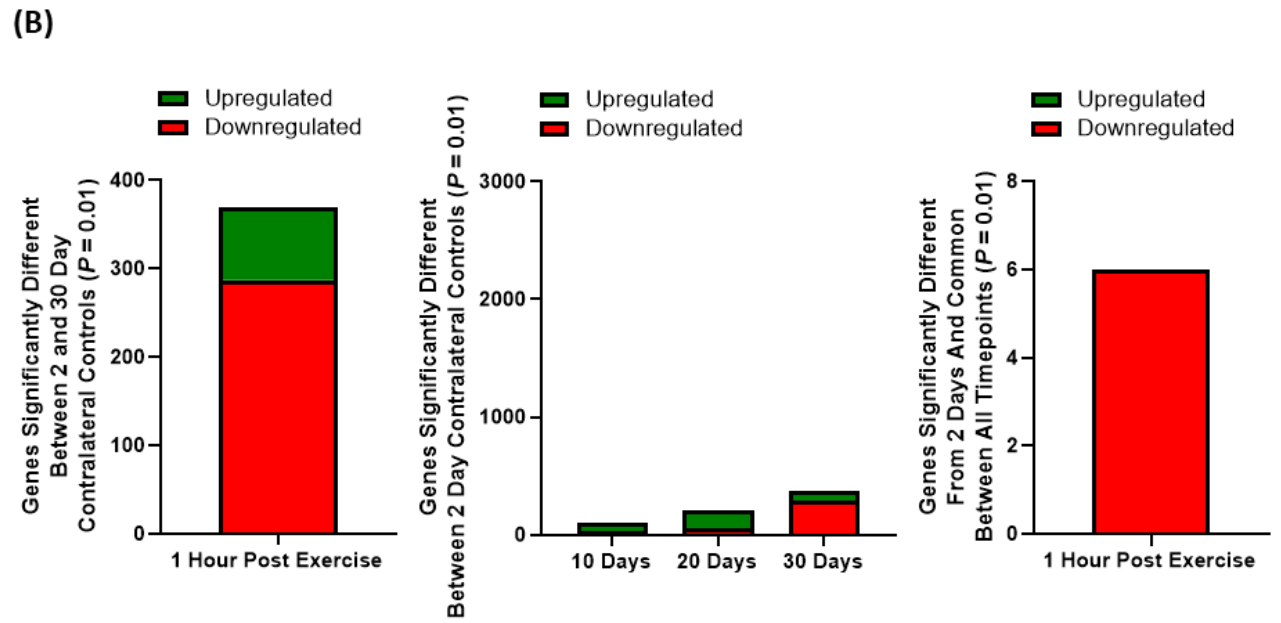
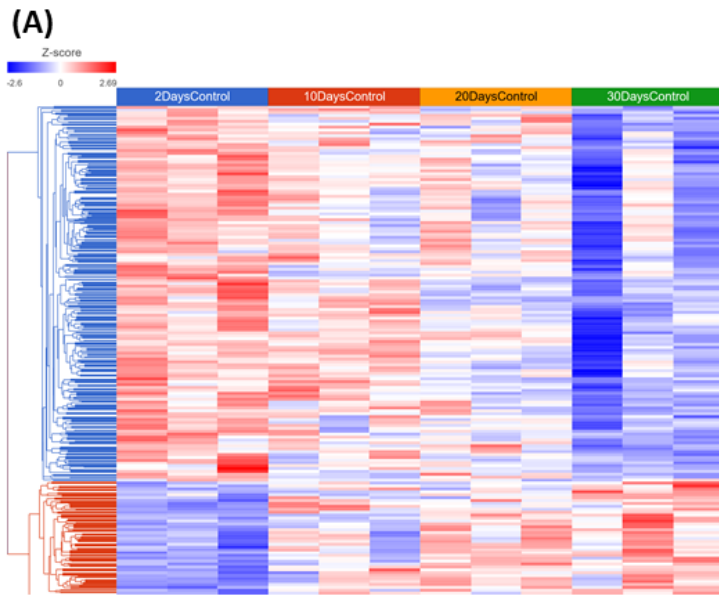
We plotted these genes as normalised mRNA counts in both the exercised limb and contralateral control limb to show whether the change in expression was happening in both limbs (potentially because of systemic factors) or in one limb alone (exercised or unexercised). Of the 48 plotted genes in Figure 5.11D-G, we note that 21 genes show similar responses in both the exercised and unexercised limb, characterised by the normalised mRNA reads being within 1.5 standard deviations of each other in at least 3 out of 4 of the timepoints studied. This suggests that they are likely under systemic or circadian control and their gene transcripts are being changed to the same extent in both exercised and unexercised muscles as training progresses. These include Fbxo32, Pdk4 and Mt-nd4l from SOM1 which are key for muscle mass regulation and mitochondrial activity. Other genes included Tinagl1, RT1-T24-4 and Arfp2 from SOM2, Dbp, Hras, Tcap, Tuba8, Tuba4b, Rplp0, Rplp2, Per2 and Rps2 from SOM3, some of which are important in sarcomere structure and stability and ribosomal function. Rbm3, Dgkz, Taf9, Ppie, Becn1 and Pmp22 from SOM4 also fell under this classification.

Pathway analysis on all 396 genes that were differentially expressed between 2 and 30 days revealed 'Circadian rhythm', 'Carbon Metabolism', 'Oxidative Phosphorylation', 'Thermogenesis' and 'Parkinson disease' to be significantly enriched, Figure 5.12. Furthermore, 26 out of the top 100 of the genes significantly altered between 2- and 30-day control tibialis anterior muscles appeared under the CircaDB (Circadian Expression Profiles Database for skeletal muscle when using a JTK circadian Q value of 0.05), (<http://circadb.hogeneschlab.org/>). Circadian rhythms are continuous ~24-hour cycles inherent in nearly all organisms and their cells that align to their behaviour, biochemical and physiological processes. The timing of these synchronous rhythms is dependent on external cues such as activity, light and feeding. Exercise is well known to help synchronise these clocks independent of other stimuli through regulation of the circadian clock which comprises transcriptional-translational feedback loops controlling key transcription factors imperative for muscle homeostasis and cell homeostasis in general Andrews et al., (2010), Hodge et al.,

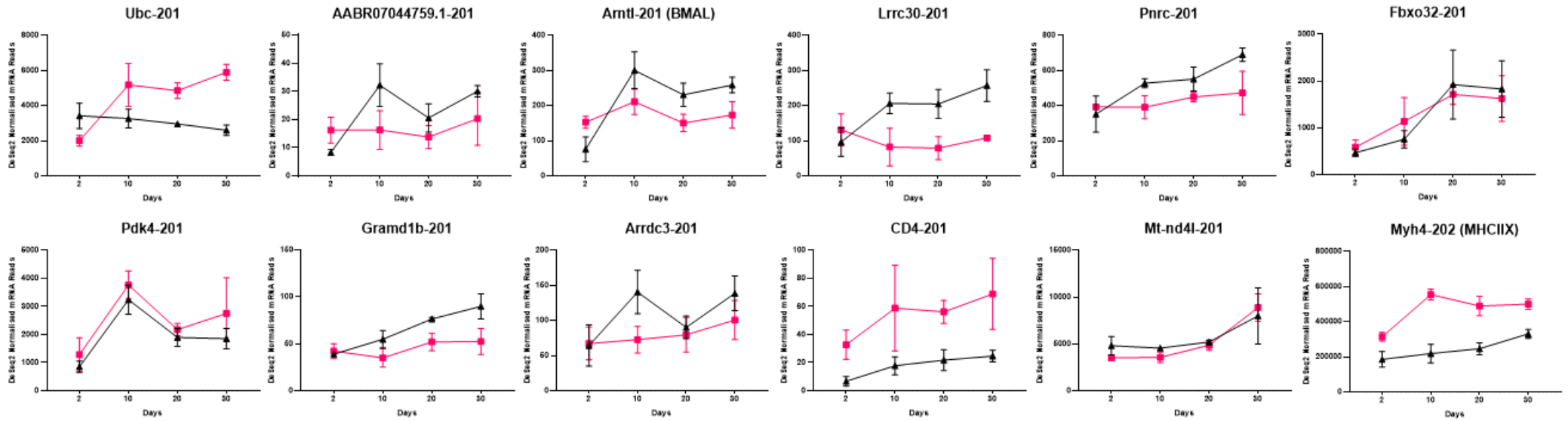
(2015), Schroder et al., (2015). This molecular circadian clock is well defined and consists of a positive limb comprising of PAS domain containing basic-Helix-Loop-Helix factors and core clock factors Arntl1/Bmal1 and circadian locomotor output cycles kaput (CLOCK). These factors heterodimerize and bind to segments of DNA at enhancer-box elements promoting transcription of Cryptochrome Circadian Regulator 1/2 (Cry1/2), as well as Per 1, 2 and 3. These two proteins can then be translated in the cytoplasm where they then dimerize, translocate back into the nucleus and interact with the Bmal1 dimer. This interaction inhibits CLOCK/Bmal1s ability to stimulate transcription of Per and Cry genes. As Per and Cry genes degrade in the nucleus, Clock and Bmal1 can start transcription of Per and Cry again and thus a ~24-hour negative feedback loop is formed. The Bmal1/Clock dimer can also start transcription of REV-ERB and RAR-related orphan receptor alpha (Ror). REV-ERB protein can inhibit transcription of Bmal1 thus directly regulating its own transcription. REV-ERB can also bind to D-box controlling the transcription of other genes where they generate circadian gene cascades through recruitment of histone acetylases and transcriptional protein complexes, many of which regulate expression of master transcriptional regulators and enzymes involved in key biochemical pathways Hodge et al., (2015), Hodge et al., (2019), Schroder et al., (2015), Andrews et al., (2010), Zhang et al., (2012). Ror protein meanwhile can promote Bmal1 transcription and therefore act as an auxiliary feedback loop helping to maintain circadian oscillations.

In our data, genes downregulated relating to circadian rhythm include Arntl/Bmal1, (CLOCK), RAR-related orphan receptor alpha (Ror) and Cryptochrome Circadian Regulator 1/2 (Cry1/2) which are part of the positive arm of the negative feedback loop, whilst Per1/2 genes were upregulated. We speculate that these large and obvious changes in the core circadian clock occurring in the unexercised limb may be because of several factors. Firstly, our training was performed during the rat's inactive light period (when they are normally resting or sleeping). Whilst we cannot confirm this because we did not measure cage activity, we predict that the disturbance of training, as well as the programmed exercised in one hind limb may have resulted in more activity during their usual inactive period, therefore stimulating components of the core clock and as a result their circadian gene expression was shifted. The exercised limb may not have had such drastic circadian phase shifts as the resistance exercise session may have helped to reset this locally. This may have either continued to shift from 2 days to 30 days, however we believe that the 30-day control group may be closer to a complete

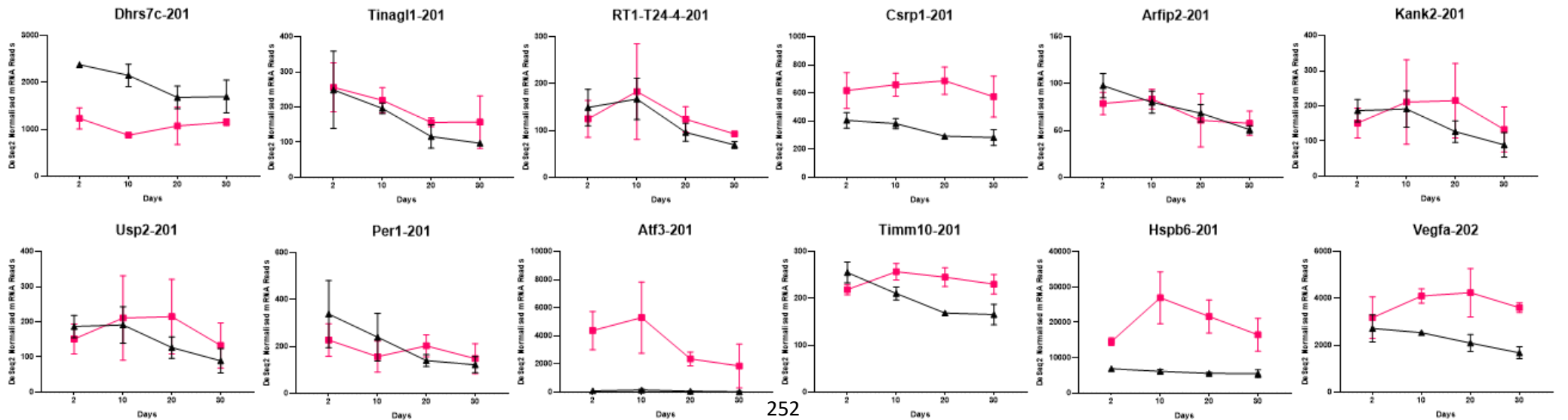
untrained control (a 0-day timepoints), which unfortunately we did not run for RNA-sequencing analysis. However, further experimental timepoints across the 24-hour period and with different exercise times are required to confirm the contralateral effects on circadian disruption and which way the muscle clock is shifting phases.



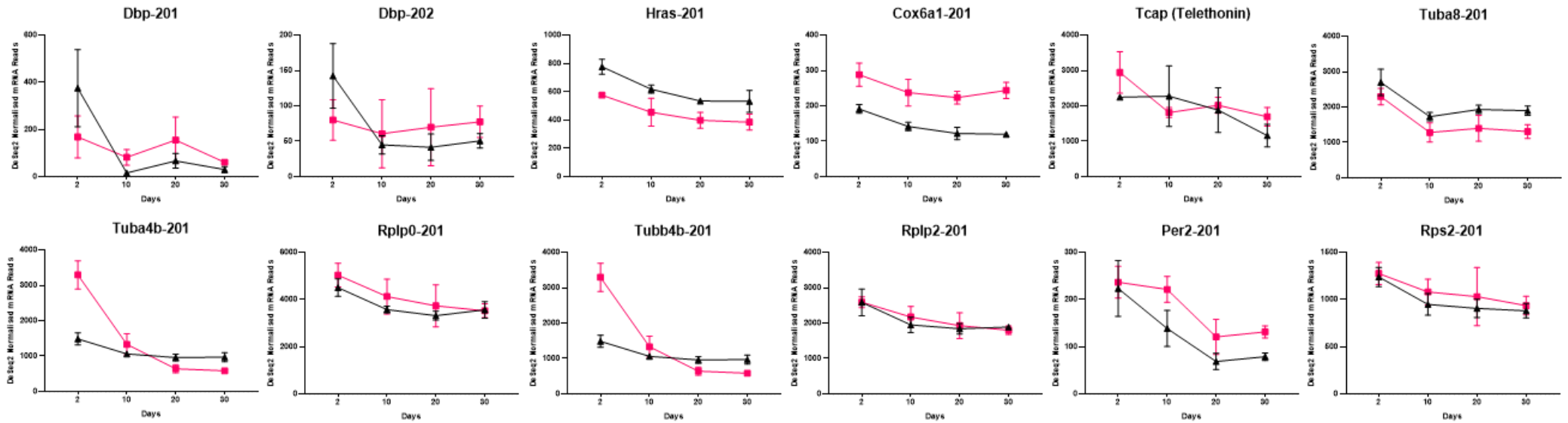
(D) Self Organizing Map (Cluster 1 Gene Transcripts)



(E) Self Organizing Map (Cluster 2 Gene Transcripts)



(F) Self Organizing Map (Cluster 3 Gene Transcripts)



(G) Self Organizing Map (Cluster 4 Gene Transcripts)

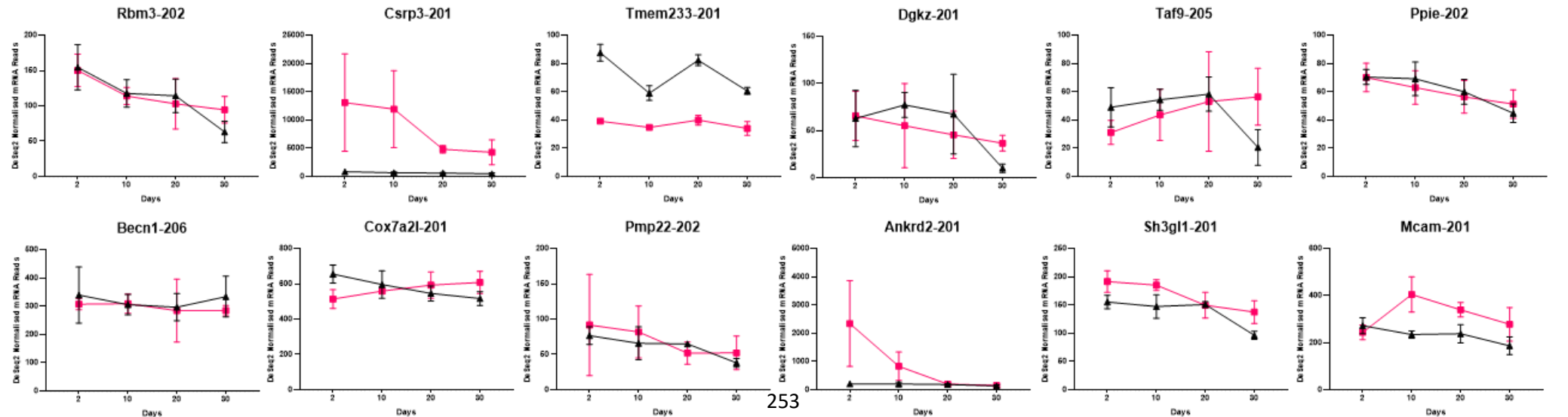


Figure 5.11: (A) Hierarchical heat map for analysis of differentially expressed genes between 2-day, 10-day, 20-day, and 30-day contralateral control muscles. (Blue=2-day control, red=10-day control, orange 20-day control, green=30-day control). (B) the number of differentially expressed genes between the 2-day control and 30-day control group. Timecourse of differentially upregulated and downregulated genes in comparison to 2-day controls. Commonly shared genes significantly different across all timepoints vs. control. (C) The top 369 differentially expressed genes from Figure 5.3a, were characterised into 4 distinct clusters following self-organising map (SOM) temporal analysis. (SOM1= 82, SOM2=108, SOM3=95, SOM4=84). For panels D to H, data for the exercised limb are presented in red and data from the unexercised limb are presented in black. (D) The top 12 genes present in SOM1 ranked by order of significance showing trained and untrained limbs at each timepoint. (E) The top 12 genes present in SOM2 ranked by order of significance showing trained and untrained limbs at each timepoint. (F) The top 12 genes present in SOM3 ranked by order of significance showing trained and untrained limbs at each timepoint. (G) The top 25 genes present in SOM4 ranked by order of significance showing trained and untrained limbs at each timepoint.

KEGG Pathway	Enrichment Score	P-value
Circadian rhythm	7.6	5.0E-04
Carbon Metabolism	6.7	1.3E-03
Oxidative phosphorylation	6.6	1.4E-03
Thermogenesis	6.1	2.2E-03
Parkinson disease	5.8	3.1E-03

CIRCADIAN RHYTHM

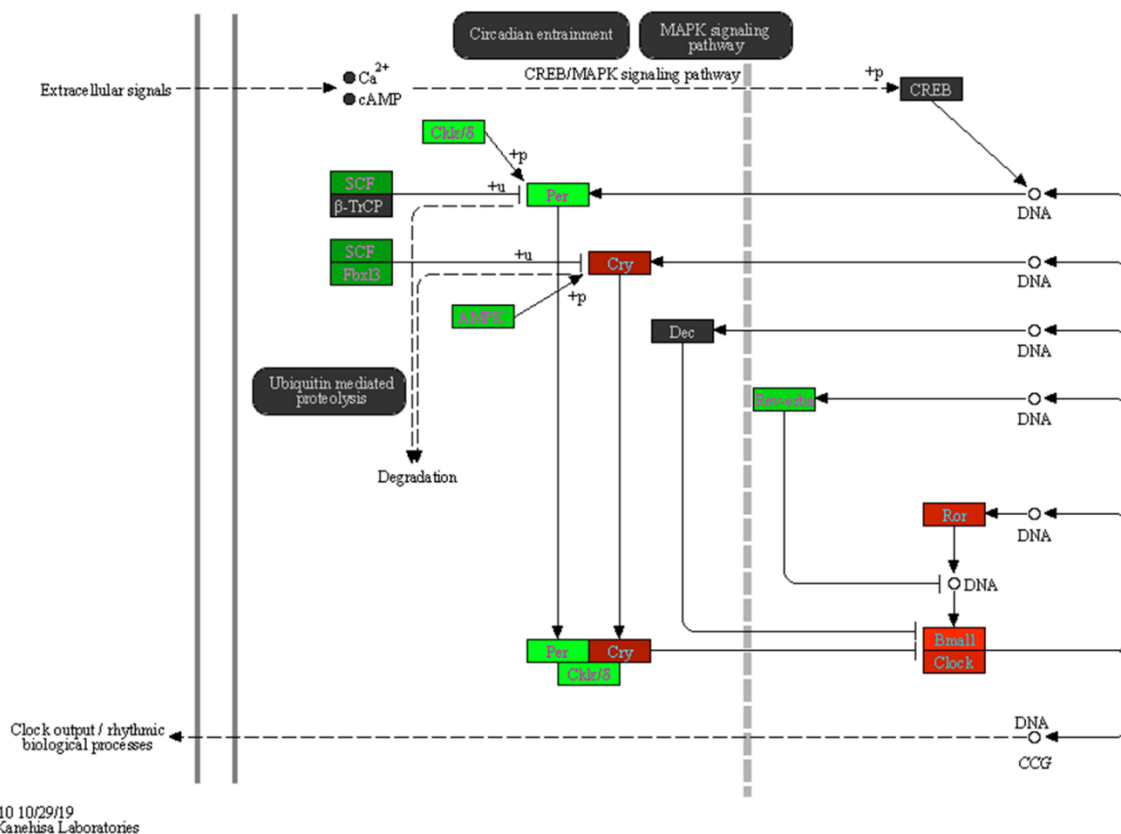


Figure 5.12: KEGG pathways enriched between control tissues at 2 days and 30 days include disruption of 'Circadian Rhythm'.

5.5 Discussion:

This study was designed to characterise the acute transcriptional response to resistance exercise dependent on training status, using a programmable resistance training model in free-living rats. With this characterisation, we hypothesised that the genes and associated pathways that were differentially expressed to the greatest extent in the early response to exercise, but whose expression decreased close to baseline levels likely represent an important composite transcriptional signal for muscle growth to identify candidates that could be delineated further.

In response to our spillover training timecourse, muscle mass plateaus between 20 and 30 days of daily training, with fiber cross-sectional area lagging slightly behind Viggars et al., (2022). This is concomitant with an increase in mitochondrial content (NADH staining) and a shift in the predominant myosin heavy chain isoform from IIB to IIX as measured through immunohistochemistry on whole tibialis anterior cross-sections. Mitochondrial encoded genes were not upregulated until 30 days of training, despite the gradual increase in NADH activity observed after just 10 days of daily training. This may indicate that this model becomes more endurance-like as opposed to a hypertrophic stimulus between 20 and 30 days. Longer rest periods between training (every 48/72 hours rather than every 24), may remove some of these endurance-like training effects and provide more of a pure hypertrophic stimulus.

Despite small group sizes, our PCA plot (Figure 5.2A) for RNA-sequencing shows that our groups are tightly clustered and there is minimal variation between all our control muscles independent of the contralateral muscles training status. The largest variation is evident during the acute response with 2 days of training, and as training progresses, the clusters become more alike. The acute transcriptional response to spillover training is strikingly different dependent on training status, with only 345 genes consistently upregulated and 174 genes consistently downregulated (Figure 5.2C). We believe these likely reflect genes whose expression is directly related to calcium signalling and muscle activity (Figure 5.2E). Temporal clustering of gene expression across the timecourse of training revealed 5 distinct patterns of gene expression, revealing potential important information about the adaptation of muscle growth and when the up/downregulation of a gene is most important. We highlight that

genes commonly associated with regulation of muscle mass do not follow these 5 clusters and some proteins are unchanged at the mRNA level despite likely changes in their protein activity, (Figure 5.3A). Transcriptionally, genes associated with IGF-1/MAPK/ERK are mostly unaltered 1 hour post exercise (IGF1, IRS1, Akt1, Akt2, Mapk1, IGF1r), as are genes further downstream of these pathways associated with mTOR complex activity and its downstream processes (Mtor, TSC2, Raptor, Rheb, Eif4ebp1, Rps6kb1). However, the different IGF binding proteins show a large degree of variability in expression acutely after exercise (Figure 5.3A), likely reflecting the complex networks involved in their regulation which include changes in metabolism, hormone levels and substrate availability, that occurs independently of IGF1 and 2 expression Clemmons, (2018). Interestingly, myostatin which is known to negatively regulate muscle mass is increased after 2 days of training but is significantly downregulated acutely after exercise after 20 and 30 days of training, despite muscle mass and fiber cross-sectional area beginning to plateau at this point. Myogenin also shows a similar trajectory and is known as a negative regulator of muscle mass. Fbxo32 (Mafbx) shows an opposite response, with significant downregulation after 2 and 20 days of training, before returning to baseline levels at 20 and 30 days. Trim63 (MurF1) is consistently upregulated in response to the acute training bout, independent of training status suggesting ongoing remodelling and control of the ubiquitin proteasome system during hypertrophy Baehr et al., (2021), Baehr et al., (2014). Whilst most of these genes do not follow an early change before returning to baseline, representative of a quick increase in muscle mass before plateauing, we provide a list of genes that warrant further investigation and may be important regulators of increasing muscle mass (Figure 5.3B).

We classified associated pathways involved with an early response (2 and 10 days), a group of genes that are always responsive (all timepoints), and an adapted response (20 and 30 days), further classified into genes that were upregulated and those that were downregulated. The early upregulated response contains pathways related to remodelling of the ribosome and protein synthetic machinery as well as some immune related pathways. During this time genes associated with metabolism, specifically fatty acid metabolism and carbon metabolism are part of an early downregulated response, as are degradation of valine, leucine. In contrast, the adapted upregulated response contains genes associated with pathways relating to oxidative metabolism and mitochondrial remodelling suggesting that

there is more emphasis to regulate oxidative metabolism when the muscle is trained, as opposed to adding protein synthetic machinery. Interestingly, spliceosome and several other ribosomal/ protein synthetic/ proteasome associated pathways are downregulated in response to acute resistance exercise in the adapted muscle, in comparison to control muscles. This suggests a reduction in the requirement for both transcription and translation, despite ongoing daily exercise and perhaps a limiting factor in preventing muscle from continually growing. Genes consistently upregulated (always responsive) were enriched in pathways associated with oxidative stress (AGE-RAGE), focal adhesion as well as ECM/plasma membrane associated signalling and downstream PI3K-Akt signalling pathways. These are presumably genes that respond most directly to the activation of the muscle but do not always represent a signal for growth. Network analysis in GENEMANIA revealed that the early upregulated gene list was centrally controlled by the protooncogene Myc which has previously been reported to transcriptionally regulate metabolism, RNA polymerase activity and ribosomal biogenesis. Mycs expression in response to acute exercise is reduced as training status increases and warrants further attention in promoting muscle growth in already trained muscles.

Furthermore, overlapping our dataset with previous acute resistance exercise like responses in mice, rats and humans shows extremely little overlap of differentially regulated genes. Only 10 genes were found to overlap in our analyses including *Ankrd1*, *Amd1*, *Atf3*, *Bgn*, *Col1a1*, *Col3a1*, *Ehd4*, *Hmox1*, *Lox* and *Myc* (Figure 5.6A-B). We also highlight several other genes that were commonly shared across all but one of our included datasets (Figure 5.6C-H). We illustrate that these genes have very different profiles of expression to acute resistance exercise dependent on training status and their exact roles in muscle adaptation should be further elucidated. Here we discuss the potential mechanisms of 3 of these genes some of which have not been linked before to skeletal muscle adaptation.

ATF3 is also a well-known, early response transcription factor that appeared in our transcriptomic venn diagram analysis. ATF3 is a member of the activating transcription factor – cyclic AMP responsive element binding protein (ATF/CREB) family of transcription factors which bind to the DNA sequence (TGACGTCA) and share a basic leucine zipper domain element, Ku and Cheng, (2020), Zhou et al., (2011). Genes within this transcription factor family can form homodimers or heterodimers with each other via the basic leucine zipper

domain element. Transcription of ATF3 occurs in response to several factors including growth factors, hormones, cytokines, and stress of the endoplasmic reticulum, appearing downstream of ERK and cAMP-PKA/p38-MAPK pathways Lu et al., (2007), and can lead to both promoter and suppressor activity at the genome level Thompson et al., (2009). Whilst it has not been studied to a great extent in skeletal muscle, ATF3 has been widely implicated in cardiac hypertrophy, and it is presumed that most of these cell growth pathways are conserved between tissues. Overexpression of ATF3 via AAV delivery and tetracycline inducible germline models have been shown to promote cardiac hypertrophy, heart dysfunction and fibrosis Koivisto et al., (2014), Koren et al., (2013). Conversely, ATF3 deficient hearts show reduced cardiac hypertrophy in response to 4 weeks of aortic banding to produce pressure overload, in comparison to wild type mice Ku and Cheng, (2020), Zhou et al., (2011). A recent training study in ATF3 knockout mice showed that ATF3 modulated genes relating to chemokine/cytokine activity and reduced the expression of inflammation-related genes after exercise to facilitate training adaptation Fernández-Verdejo et al., (2017). Therefore, when knocked out, the muscle did not adapt metabolically or shift to a more oxidative phenotype after training. In our dataset, ATF3 shows a large upregulation that is identical at 2 and 10 days before reducing its expression in response to exercise at 20 and 30 days, perhaps because of reduced upstream signalling factors such as endoplasmic reticulum stress and growth factors/cytokines and therefore its expression was attenuated. This finding has also been reported in humans, with untrained individuals having a much higher expression of ATF3, in comparison to those who had 6 weeks training, in response to an acute resistance exercise bout Nader et al., (2014).

Despite a large body of evidence that Ehd4 is implicated in muscle hypertrophy across models and species in large transcriptomic data sets, there is little to no understanding of the role Ehd4 may play in adapting skeletal muscle. Ehd4 was previously highlighted following synergist ablation and regrowth from hindlimb suspension in mice Chaillou et al., (2013), Chaillou et al., (2015) and was highlighted after acute resistance exercise in humans Bonafiglia et al., (2019). In all the above reports, Ehd4 is upregulated during skeletal muscle hypertrophy. Ehd4 has also been highlighted in proteomic datasets following denervation-induced atrophy between 3-5 days post nerve transection, whilst the muscle is atrophying. In this instance Ehd4 is again upregulated suggesting that the expression and increased protein

content is important in both hypertrophy and atrophy. Ehd4 is also upregulated following TTX-induced atrophy ~3.5 fold in both microarray data sets and recent pilot NG-RNA sequencing data, not included in this thesis. During this period Ehd1 is also upregulated, whilst Ehd2 and 3 are downregulated after 14-days of TTX treatment.

There is some evidence that Ehd4 is expressed at low levels in the skeletal muscle myoblasts and this increases as muscle develops Posey et al., (2011), Demonbreun et al., (2015). The other Eps15 homology domain containing proteins (EHDs) 1, 2, and 3, have been studied in more detail in skeletal muscle, including in muscle membrane fusion and membrane repair both developmentally and in context of dystrophic disease. Depletion of Ehd1 and Ehd2 or both together results in decreased fusion efficiency in C2C12 myoblast cells in comparison to controls Posey et al., (2011). This was also demonstrated in myoblasts isolated from Ehd1-null mice, and was concomitant with reduced fiber size in-vivo. Posey Jr et al., (2014). In these smaller fibers it was also reported that there was decreased vesicle trafficking required for muscle growth and overgrown transverse t-tubules Posey Jr et al., (2014). Both Ehd1 and Ehd2 are located at the periphery of the myoblast in a prime position for cell-to cell contact and fusion Posey et al., (2011). Ehd2 has also been reported to interact with Myoferlin through binding of the asparagine-proline-phenylalanine motif found in myoferlin's C2B domain Demonbreun et al., (2015). Loss of function dysferlin mutations cause muscular dystrophy and are characterized by defective membrane sealing Bansal et al., (2003). This results in increased muscle proteins and lipids leaking from the sarcolemma into the serum. Dysferlin and myoferlin also regulate endocytic recycling during fusion and repair Demonbreun et al., (2011), Doherty et al., (2008). Ehd3 and Ehd4 have been studied to a lesser extent in skeletal muscle and their function has not been elucidated. Ehd3 was reported to be upregulated in human and mouse heart tissue after injury, suggesting a role in the repair process Gudmundsson et al., (2012), potentially through endocytosis vesicle trafficking and t-tubule formation and maintenance. Ehd4 has also been implicated in the infarcted heart, aiding with the transport of protein from the early endosome to the endosome recycling centre Gudmundsson et al., (2010), George et al., (2007). To our best knowledge, Ehd3 and Ehd4 have not been studied in mammalian adult skeletal muscle. However, in the Torpedo Californica, Ehd1 was associated with perinuclear regions and primary synaptic clefts, similarly to Ehd4, although Ehd4 was less abundant. Ehd2 is associated with muscle

vasculature and Ehd3 localised to perisynaptic regions Mate et al., (2012). In our model, Ehd4 is upregulated, and its expression post-acute resistance exercise is highest after just 2 days of training, before gradually declining and plateauing at 20 and 30 days of training. Further investigation is required to elucidate the importance of Ehd4 in adult, mammalian skeletal muscle and particularly its potential role during muscle adaptation. The other members of the EH domain proteins are also differentially regulated across our timecourse with Ehd1 decreasing after 20 and 30 days versus control, 2, and 10 days of daily training. Ehd2 increases after 10 and 20 days but is unaltered after 2 and 30 days, whereas Ehd3 remains unaltered across all timepoints in response to training.

MYC Proto-Oncogene, BHLH Transcription Factor appeared as a potential master regulator of the transcriptional response to resistance exercise from three separate lines of our investigation. Firstly, it appeared in the top 20 differentially expressed genes in SOM1, the temporal cluster that shows genes most responsive in untrained muscle before slowly decreasing at each timepoint as training status increases. Similarly Din et al., (2019) reported an increase in Myc expression acutely after resistance exercise after 0, 2 and 4 weeks of training in humans. After 6 weeks Myc was no longer upregulated in response to acute exercise. Again, further work in humans shows that untrained individuals having a much higher expression of Myc, in comparison to those who had 6 weeks training, in response to an acute resistance exercise bout Nader et al., (2014). This suggests that either the human training protocol was no longer stimulating Myc expression or that our timecourse of training in rats is very similar to a 6-week training protocol in humans. Secondly, through GeneMANIA multiple association network analysis, it appeared as a central hub regulating the genes in the early upregulated response to exercise, which we predict closely follow the signals for muscle hypertrophy. Lastly, a comparison of 5 studies, which includes 3 species, 3 models of mechanical load induced hypertrophy and 2 large human meta-analyses of previously published resistance exercise transcriptomic datasets found that Myc was one of only 10 genes that were commonly differentially regulated. This suggests that Myc plays a pertinent role in the transcriptional regulation of mechanical loading induced hypertrophy.

Myc is a nuclear phosphoprotein that binds to DNA through a helix-loop-helix (HLH) motif. Following heterodimerization with its partner MAX (Myc associated factor X) to bind E-box sequences (5'-CACGTG-3') or non-canonical sites in target gene promoters or enhancers that

regulate transcription Nie et al., (2020), Allevato et al., (2017). MAX is consistently downregulated in the acute response to spillover training, to the point where it is nearly completely switched off at 20, 30 days with less than 10 mRNA reads per million. The N-terminus of the Myc protein has a conserved domain with strong transcriptional activity, controlling cellular genes relating to cell growth, glycolysis, oxidative metabolism, glutamine metabolism, mitochondrial and ribosomal biogenesis, and cell cycle regulation.

It was first reported to be involved in muscle growth, increasing at the mRNA level following synergist ablation (gastrocnemius tenotomy) in the plantaris and soleus of the rat Whitelaw and Hesketh, (1992). This was also shown to occur following B-adrenoreceptor agonist administration (clenbuterol), and in both instances Myc expression peaked within 12 hours Whitelaw and Hesketh, (1992). This was later repeated in chickens, with mechanical stretch of the wing muscles producing an upregulation of Myc peaking 1 hour post stretch injury Eppley et al., (1993). The belief that Myc expression may be confined to satellite cells only (not post-mitotic myonuclei) has recently been refuted as Myc is still upregulated after mechanical overload even when satellite cells are depleted (GSE153542 dataset). This has also been shown following stretch-induced hypertrophy of the anterior latissimus dorsi muscles of young and aged quail (6 vs 90 weeks). In this model Myc upregulation was significantly reduced in the old quail, but was still responsive to the mechanical load Alway, (1997).

Myc has previously being implicated in other tissues and oncogenesis as a major transcriptional regulator Yagi et al., (2002), Poole and Van Riggelen, (2017) and there has been considerable interest in developing small molecules to inhibit Myc Huang et al., (2006). Overexpression of Myc is a hallmark of many human cancers (60-70% estimated), deregulating the expression of many target genes and increasing cell proliferation and growth. Myc appears downstream of SMAD3 (part of the Myostatin-TGF- β pathway) which has recently been confirmed as a central regulator of exercise responsiveness via meta-analyses Amar et al., (2021), previously reported experimentally Lessard et al., (2018), Lessard et al., (2013), Dalbo et al., (2011). Myc downregulation is critical for growth and proliferation inhibition by TGF- β and is frequently impaired/mutated in cancer cells and tumours, leading to extensive cell growth and proliferation Yagi et al., (2002), Poole and Van Riggelen, (2017), Shostak et al., (2016). Conversely, downregulation of Myc and Myc downstream targets has also been linked to failing heart tissue through meta-analysis of heart failure gene expression

datasets Wang et al., (2020), Wang et al., (2019). Myc contains a Smad-responsive element in its promoter region, a complex of the TGF- β inhibitory element (TIE) Yagi et al., (2002), Chen et al., (2001), Chen et al., (2002) and an E2 factor family transcription factor (E2F) site for activation of the Myc promoter. Smad3 can directly bind to these elements, repressing the transcription of Myc 1 hour after treatment with TGF- β Yagi et al., (2002). Interestingly, Tgfb1 and 2 are found within SOM2 and SOM1 respectively within our dataset, whereas Smad3 is found in SOM5.

Myc also has a strong link to the biological circadian clock and therefore, the regulation of transcriptional homeostasis and cell metabolism. Myc can directly upregulate REV-ERBa, resulting in suppression of Bmal1 expression and the strength of its oscillations Altman et al., (2015). This expression can be rescued by knockdown of REV-ERBa Altman et al., (2015). As previously reported, Myc can bind to E-boxes, identical to the binding sites of the heterodimeric Clock-Bmal1 master circadian transcription factor complex Andrews et al., (2010), McCarthy et al., (2007), Ehlen et al., (2017), Harfmann et al., (2016), Hodge et al., (2015), therefore upregulating a large number of transcriptional processes related to growth. Myc can also suppress gene expression through interactions with other transcription factors and other transcription factor complexes. Whilst Myc can bind ubiquitously to E-boxes, the availability of E-boxes is reliant on chromatin accessibility and chromatin modifying co-factors in the vicinity of the enhancer box regions. Using comparative gene profiling and genomic location analysis, there is very little overlap between Myc regulated genes between tissues because of chromatin structuring Poole and Van Riggelen, (2017). To our knowledge, Chip-seq has never been performed on Myc and mature skeletal muscle, only during differentiation in-vitro Luo et al., (2019b). Further work should look to elucidate whether Myc transcriptional binding and chromatin accessibility is altered dependent on training status in this model as an explanation for the muscle having a hypertrophic versus oxidative transcriptional response to the acute bout of exercise.

More recently, Myc has been studied in relation to exercise adaptation and ribosome biogenesis. Overexpression of Myc through AAV transfected delivery for 2 weeks increased DNA polymerase subunit POL1 mRNA, 45S-pre-rRNA, total RNA, and muscle protein synthesis without altering mTORC1 signaling. Increase in Myc was also reported after high intensity muscle contractions even with the presence of rapamycin, a potent mTORC1 inhibitor Mori

et al., (2021), West et al., (2016), Ogasawara et al., (2016). Transcriptome analysis of the Myc transfected muscles showed that overexpression mainly regulated ribosome biogenesis. Overexpression of Myc produced the same increase in protein synthesis as high intensity muscle contractions, but there was no further effect found when overexpression and high intensity muscle contractions were combined, as measured through puromycin incorporation assay. The mechanism behind Myc increasing transcription, protein synthesis and ribosomal biogenesis has been studied by several groups and has been reviewed extensively Figueiredo and McCarthy, (2019), Van Riggelen et al., (2010). Myc levels are regulated by the ubiquitin proteasome degradation system Oster et al., (2002), Sun et al., (2015), Cole and Cowling, (2008), with the inhibition of this system leading to Myc accumulation in the nucleoli Arabi et al., (2003). Myc/Max heterodimer transcription factor complexes activate transcription by binding to enhancers boxes in regulatory regions and through recruitment of transcription domain associated protein with histone acetyltransferase KAT2A to preferentially acetylate histones H3 and H4. Histone acetylation reduces the electrostatic affinity between histone proteins and DNA, therefore allowing for chromatin to become more accessible and more permissive to gene transcription Arabi et al., (2005), Gräff and Tsai, (2013). A lot of the genes within this area of the genome encode for proteins associated with protein synthetic machinery Oster et al., (2002). Myc can also directly activate RNA polymerase I Grandori et al., (2005), II and III and is localised at tRNA and 5S rRNA genes, identified through chromatin immunoprecipitation Gomez-Roman et al., (2003). This has been further evidenced through transfection of Myc in neuroblastoma cells, which resulted in a large induction of proteins present in the ribosomes, ribosomal biogenesis and proteins necessary for synthesis, degradation and glycolysis Boon et al., (2001).

As previously alluded to Wen et al., (2016), the rodent and human ribosomal biogenesis response seems to be conserved across species. The decline of Myc expression acutely after resistance exercise as training status increases has been previously reported in humans after 6 and 12 weeks of training respectively Din et al., (2019), Nader et al., (2014). The latter also reported that 45s-pre-RNA followed a similar trend to Myc in response to training status. This consensus between species was also found with the rDNA methylation patterns in myonuclei following acute hypertrophy stimuli in mice and humans. Methylation patterns were modified in enhancer, intergenic, and non-canonical regions but did not change the methylation status

of the promoter region Figueiredo et al., (2021). Further research should investigate whether post translational modifications or chromatin accessibility can explain the reduced Myc and ribosomal associated gene response to acute resistance exercise.

We accept that there are several limitations to this current study. We were only able to study one timepoint post exercise (1-hour), which we selected based on early MoTrPAC data that suggested that in a 48-hour timecourse post-acute exercise, that the largest number of transcriptional changes occurred 1-hour post exercise. We highlight that in this limited approach, key transcriptional signals that happen earlier or later than 1-hour post exercise may also be important factors involved in resistance training induced hypertrophy. We also note that among the genes that show a diminishing response at 1-hour post exercise as training status increases may possibly respond at an earlier or later timepoint post exercise. It would also be interesting to consider the 'resting' transcriptome of these muscles, dependent on training status to identify whether the transcriptional network is altered because of training status but independent of acute exercise-induced transcription. The MoTrPAC consortium funded by the NIH has also noted large variability in males and females in response to both the acute whole-omics response to exercise as well as in the pattern of adaptation in response to training which we believe deserves further attention in our model. We also trained the muscles at the start of the inactive light phase of the rats which may affect the translatability of this study. Whilst we exercised the rats at the same time of day each day, and harvested tissues at roughly the same period, we did not specifically control for circadian factors such as light during harvesting, which may subsequently affect the expression of circadian controlled genes. We also do not have a 0-day training control to understand whether there are circadian phase shifts occurring in both control and exercised TA muscles.

5.6 Conclusion:

In conclusion, we map out the behaviour of gene expression in response to an acute training bout dependent on training status in a physiological model in rats, illustrating that genes have very distinct patterns during hypertrophic adaptation in a fast skeletal muscle. We identified several pathways that are upregulated/downregulated dependent on training status, as well as a cluster of genes whose expression seems to track with muscle growth and the plateau of

mass, some of which are consistently expressed across multiple models of resistance training and across different species.

Chapter 6: Investigating Pericentriolar Material-1 (PCM1) as a marker for skeletal muscle myonuclei: A cross-species and model's approach.

6.1 Abstract

Background and Aim: Myonuclei control protein synthesis within the muscle fibre and are key regulators of muscle plasticity. Determining the distribution and number of myonuclei per mm of fibre, or the percentage of nuclei in a transverse cross-section is an important measure in determining the phenotype of myopathies or the effect of treatment, as well as understanding the roles of satellite cells in muscle plasticity following loading and unloading. Given the potential of myonuclei as plasticity markers, their correct identification is key. The objective of this study was to determine whether Pericentriolar Material-1 (PCM1) is, as claimed, a reliable specific marker of myonuclei using transverse cross-sections of skeletal muscle, isolated myofibres, human primary muscle cells and C2C12 myoblast cultures.

Methods: Single isolated myofibres and bundles of myofibres from mouse, rat and human were studied from several models of overload hypertrophy and regeneration including Wild-type and Lamin A/C mutant (LMNA^{+/ Δ K32}) mice, after functional overload by synergist ablation, 'Spillover' resistance training in rats, and electrical stimulation invoked eccentric damage and recovery in humans. Nuclei were immuno-labelled with PCM1 and Pax7 and counterstained for DNA, (DAPI). C2C12 myoblasts and adult human primary muscle cells were also studied to investigate changes in PCM1 localisation during myogenesis.

Results: PCM1 labelled the nuclear envelope of myonuclei in mature myofibres and in newly formed myotubes but also labelled centrosomes in proliferating myogenic pre-cursors which may or may not fuse to join the myofibre syncytium. It also labelled some non-myogenic proliferating nuclei in close proximity to the sarcolemma especially in the regenerating areas of the LMNA^{+/ Δ K32} mouse following synergist ablation overload. Nuclear deformities also make determination of PCM1 localisation in LMNA^{+/ Δ K32} transverse muscle cross-sections difficult. The number of Pax7+ cells that were also PCM1+, reflects the previously reported proliferative state of the satellite cell pool across all these models.

Conclusion: While PCM1 is not specific to the myonucleus specifically, the impact of false positive identification of proliferating Pax7+ cells on total myonuclei counts would be minimal in most physiologically relevant models of overload hypertrophy but may be problematic in regenerative models or myo/laminopathies. We suggest the use of PCM1, Pax7 and a basement membrane marker to make completely sure the PCM1 labelling is associated with

the perinuclear labelling of the myonucleus. PCM1 may also prove useful as a marker of both *in-vitro* and *in-vivo* satellite cell dynamics due to the distinct change in localisation during differentiation which reveals satellite cells in their quiescent (PCM1-), proliferating (PCM1+ centrosome) and pre-fusion state (PCM1+ nuclear envelope).

6.2 Introduction

Skeletal muscle is a versatile tissue responsible for locomotion and energy metabolism and is the most abundant tissue in the mammalian body Karagounis and Hawley, (2010). Maintenance and adaptation of its structure and function are key throughout the mammalian lifespan. In both developing and adult skeletal muscle, mechanical loading and activity is transduced into signalling cascades through mTORC1 so that muscle will hypertrophy if net protein synthesis rates are greater than degradation rates Baar and Esser, (1999a), Hornberger, (2011), Olsen et al., (2019). In the absence of activity and mechanical signalling, muscle will atrophy (reduction in myofibrillar volume), driven by the ubiquitin-proteasome pathway and FoxO/MuRF1 gene regulation Fisher et al., (2017), Sandri et al., (2004). Intrinsic regulators of skeletal muscle size include DNA content, nuclear size and the consequent nuclear activity Windner et al., (2019).

Skeletal muscle myofibres are long, cylindrical cells formed following fusion of myoblasts into myotubes, which then differentiate into mature myofibres, capable of contracting and producing force. Myofibres have large volumes of cytoplasm with homeostasis being maintained through multiple post-mitotic myonuclei regularly distributed along the length of the sarcolemma Bruusgaard et al., (2006), except at specialised regions such as the myotendinous junction where they are centralised and responsive to stretch Jakobsen et al., (2018) and neuromuscular junctions where they appear in clusters Roman and Gomes, (2018).

Skeletal muscles are encased in fascia called the epimysium and are further subdivided into interconnected fascicles sheathed by the perimysium Rowe, (1981). Myofibres within these bundles are themselves encased in loose, areolar connective tissue called the endomysium which also contains fibroblasts, capillaries and nerves Sakamoto, (1996). This close interplay of myogenic and non-myogenic cells means that nuclei from different origins reside near to each other. Myonuclei are generally spindle shaped, with a long axis of 20-30 μ m and short axis of 6-10 μ m. On transverse cryosections, typically 5-12 μ m thick, it becomes a challenge to

differentiate between myonuclei and the nuclei of stromal, vascular and satellite cells. Typically, around 56% and 67% of the total nuclei are considered to be myonuclei in the 'Slow' soleus and 'Fast' Tibialis Anterior respectively, assessed through electron micrograph cross-sections Schmalbruch and Hellhammer, (1977). Labelling with dystrophin allows for determination of the geometrical position of a nucleus and whether it resides inside the sarcoplasm (myonuclei), between the basal lamina and sarcolemma (satellite cell) or outside of the basal lamina (stromal/vascular), yet identification is still sometimes uncertain and can vary between investigator, especially when identifying small changes in myonuclei number Gundersen, (2016).

As myogenic nuclei are predominately responsible for the transcriptional activity within a myofibre after loading (Kirby *et al.* 2016), they are mainly responsible for regulating the volume of muscle fibres, in response to changes in activity and load. Identifying their distribution and changes in their number is of key importance in understanding muscle adaptation to age Bruusgaard *et al.*, (2006) and loading Murach *et al.*, (2017). This is also important in myopathies and laminopathies that are characterised by the disruption or lack of satellite cell proliferation and fusion such as in Lamin A/C deficiency, in which faulty nuclear mechanics and impaired mechanically-activated gene transcription lead to severe muscle dystrophy and weakness Folker and Baylies, (2013).

Previously, the identification of myonuclei (judging and interpretation of DAPI positioning in relation to the myofibre border by eye) and the use of supra-physiological overload models has potentially caused confusion in determining whether new myonuclei have been added to the myofibre to support hypertrophy following overload or whether substantial functional hypertrophy could be achieved without the addition of new myonuclei Englund *et al.*, (2019a), Gundersen, (2016), Murach *et al.*, (2017). Similar measurements of nuclear position have been used to investigate whether and when myonuclei number per fibre increases during hypertrophy and whether an increased number of nuclei per fibre is maintained in the longer term to support a potentially beneficial increased rate of recovery of muscle mass when re-training Dungan *et al.*, (2019), Gundersen, (2016), Psilander *et al.*, (2019). The same techniques have also been used to assess whether following unloading/atrophy myonuclei are selectively removed through apoptosis Dungan *et al.*, (2019), Meneses *et al.*, (2015), Zhang *et al.*, (2010) or not. Whilst our lab has previously demonstrated that skeletal muscle

shows epigenetic adaptations that may allow for accelerated muscle growth after previous training episodes Seaborne et al., (2018b), Seaborne et al., (2019a), it is still disputed as to whether the maintenance of an increased number of myonuclei is a potential cellular adaptive mechanism enabling rapid re-growth in humans (so-called 'muscle memory'), Gundersen, (2016), Psilander et al., (2019), Murach et al., (2019a).

In an attempt to identify myonuclei reliably, Winje et al., (2018) reported that a pericentriolar protein, pericentriolar material-1 (PCM1), can be used "as a specific histological marker for myonuclei in skeletal muscle tissue without relying on counterstaining of other structures or cumbersome and subjective analysis of nuclear positioning". The protein is responsible for preparing a cell to divide and to support the stability of centrosomes during mitosis Dammermann et al., (2004), Espigat-Georger et al., (2016), Kubo et al., (1999). Counter-intuitively, it then marks the post mitotic nuclei by sustained expression in the nuclear envelope, so that the myonuclei are stained across their whole outline in thick sections and with a ring appearance in thin sections. A total of 1298 PCM1+/DAPI+ nuclei from 3 species and 13 mature muscles were analysed in that study. All were found to be within the inner dystrophin ring using 3D rendering of confocal Z-stacks. It was also reported that some PCM1+/DAPI+ nuclei appeared to be partly overlapping the myofibre membrane but on more detailed inspection were inside, suggesting that PCM1 labelling of myonuclei will prove advantageous to the field.

In order to make an independent assessment of PCM1 as a suitable marker of myonuclei in a more varied set of samples, we separated and observed single myofibres and myofibre bundles to assess the localisation and cell cycle stage of the nuclei within and in close proximity to the myofibre to better visualise nuclei in comparison to cross-sectional analyses. We analysed mouse, rat and human fibres from muscles after physiological and supra-physiological overload-induced hypertrophy and regeneration as follows: 1) Synergist ablation overload in WT and LMNA^{+/ Δ K32} mice, 2) 'Spillover resistance training in rat, 3) Eccentric damage and recovery after electrical activation during active muscle stretch in humans. We also investigated the change in PCM1 localisation during maturation in C2C12 myoblasts and myotubes as well as human primary myoblasts and myotubes. Our objective was to elucidate whether PCM1 antibody labelling can be used on skeletal muscle transverse cross-sections as a specific marker of myonuclei in any case, or whether its use may produce

false positives produced by its presence in proliferating myogenic, fibroblasts, endothelial or inflammatory cells. We hypothesised that models of overload and regeneration that greatly expand the satellite cell pool may be the most affected and vulnerable to misidentification.

6.3 Methods

Mouse and Human Cell Culture

Mouse C2C12 Cells

C2C12 murine skeletal myoblasts Blau et al., (1985), Yaffe and Saxel, (1977), purchased from ATCC®, (Virginia, United States), were incubated on gelatin (0.2%) coated plastic cover slips placed into 12 well-plates in a humidified 5% CO₂ atmosphere at 37°C in 1ml growth medium (GM) containing DMEM, 10 % foetal bovine serum, 10% newborn calf serum, 1% l-glutamine (2mM final) and 1% penicillin–streptomycin solution. Upon reaching confluence, cells were either fixed with 0.5% PBS/BSA containing 2% paraformaldehyde or, to produce multinucleated myotubes, myoblasts were differentiated by washing with PBS and transferring to low serum media (LSM; DMEM with 2% horse serum, 1% l-glutamine and 1% penicillin–streptomycin). C2C12 cells spontaneously differentiate under these conditions without the addition of additional growth factors Blau et al., (1985). Media was topped up every 2 days. Following 2 and 7 days in LSM, multinucleated myofibres were washed and fixed as above.

Human Muscle Derived Cells

Human muscle derived cells from a healthy, young male were donated by the Sharples lab, (originally obtained under ethical approval granted by NHS West Midlands Black Country, UK, Research Ethics Committee (NREC approval no. 16/WM/0103) and cultured in monolayer onto gelatin (0.2%) coated plastic six-well plates in 2ml of human GM containing Ham's F10 nutrient mix supplemented with 10% hi-NCS, 10% hi-FBS, 100U mL⁻¹ penicillin, 100µg mL⁻¹ streptomycin, 2.5µg mL⁻¹ amphotericin B and 5mM L-glutamine until confluent. GM was then removed, and cells washed 3 times in PBS before transference to 2ml of DM containing Ham's F10 nutrient mix supplemented with 2% hiFBS, 100 U mL⁻¹ penicillin, 100µg mL⁻¹ streptomycin, 2.5µg mL⁻¹ amphotericin B and 5 mM L-glutamine). Following 3 days and 7 days in LSM, myoblast/multinucleated myofibres were washed and fixed as above.

Animal Studies (Rat)

Experimental design

The animal experiments were conducted under the provisions of the Animals (Scientific Procedures) Act 1986 and approved by the British Home Office (PPL 40/3280). Samples were taken from 3 male adult Wistar rats (544-590g, 25 weeks). The rats were group-housed 2 per cage maintaining an alternating 12 h light 12 h dark cycle. Animals received 1 session per day of resistance training in the left hind limb via 'SpillOver stimulation' as previously described Schmolli et al., (2018), for 10 days. Briefly, to elicit slight stretch under load, the tibialis anterior and extensor digitorum longus (dorsiflexors) were stimulated via a cathode placed underneath the common peroneal nerve (CPN), while the anode was positioned underneath the tibial nerve to stimulate enough of the gastrocnemius, plantaris and soleus (plantarflexor muscles), to provide resistance against the contraction of the dorsiflexors.

Surgical Procedure

Silicone encapsulated radio frequency controlled implantable pulse generators (MiniVStim 12B, Competence Team for Implanted Devices, Center for Medical Physics and Biomedical Engineering, Medical University Vienna, Austria) were used to deliver impulses (See training pattern below). The devices were implanted into the abdominal cavity accessed by a lateral incision through the skin and peritoneum, directly below the rib cage on the left side of the animal.

Animals were anaesthetised during implant procedures by inhalation of a gaseous mixture of isoflurane in oxygen at approximately 3%. Once anaesthetised, a subcutaneous injection of Enrofloxacin (5mg/kg⁻¹ body mass (Baytril®)) and an intramuscular injection of Buprenorphine (0.05mg/kg⁻¹ body mass) (Temgesic, Indivior, Slough, UK) were administered into the right quadriceps with strict asepsis kept throughout the procedure. A polyester mesh attached to the implant was incorporated into the suture line closing the peritoneum, securing the position of the device. Two PVC-insulated stainless-steel electrode leads (Cooner Sales Company, Chatsworth, California, U.S.A.), with terminal conductive loops, were fed through the peritoneal incision and tunnelled under the skin to the lateral side of the upper left hind limb. A second incision was made laterally through the skin and biceps femoris muscle to give access to the CPN under which the cathode was placed (to stimulate the dorsiflexors). The

anode was placed in muscle deep to the tibial nerve about 5mm distal to its bifurcation from the sciatic nerve. All incisions were closed in layers and the animal given a minimum of 3 days without muscle stimulation to recover before the training protocol.

Training Pattern

Animals received 10 days of daily training which comprised an initial 10 seconds of stimulation at a low frequency ($F = 4\text{Hz}$, $\text{PhW} = 258\ \mu\text{s}$, $I = 1\ \text{mA}$). This was followed by 5 sets of 10 tetanic contractions at 100 Hz. Each contraction lasted for 2s with 2s rest between contractions and 2.5 minutes rest between sets. The stimulation was delivered only in the left hind-limb, providing the right hind-limb as an unstimulated contralateral control. Stimulation with these settings and the amplitude chosen to balance dorsiflexion and plantarflexion described above was tolerated very well by all animals without further anaesthesia or sedation. Regular observations during daily training across the time course revealed no adverse behavioural signs.

Rat Muscle sampling and preservation

Approximately 24 hours post their last training session, animals were euthanised with a rising concentration of carbon dioxide, followed by cervical dislocation. TA muscles from both lower limbs were harvested, excess connective tissue removed and immediately weighed. The TA was pinned at resting length and cut transversely to leave only the mid-belly which was cut into medial and lateral samples. One piece was placed on cork and frozen in isopentane, pre-cooled in liquid nitrogen for histological analysis and the other pinned at resting length and covered in Krebs-Henseleit bicarbonate buffer for 2 minutes. Krebs-Henseleit bicarbonate buffer was then removed, and the muscle samples submerged in 2% formaldehyde for 30 min. Samples were then transferred to a glass jar containing fresh 2% formaldehyde and placed at 4°C for approximately 4 h, after which the formaldehyde was replaced by 50% glycerol in PBS. On the following day, the jar was moved to a -20 °C freezer for storage.

Human Studies

Participants and experimental design

The Regional Scientific Ethical Committees of Copenhagen in Denmark approved this study (Ref: HD-2008-074) and all procedures conformed to the Declaration of Helsinki. Young, healthy males ($n=2$), age; 20.5 ± 0.5 years, height; 1.78 ± 0.02 cm, body mass; 76.5 ± 1.5 kg) gave informed consent on inclusion and underwent a muscle injury protocol which consisted of 200 forced lengthening contractions with the use of electrical stimulation to activate the target muscle during each contraction, as described in detail Mackey et al., (2016). The protocol was performed on the vastus lateralis muscles of one leg, leaving the other as an internal control. The muscle biopsies analysed in this study are a subset of samples from previous studies from participants in whom extensive muscle damage was observed Mackey et al., (2016), Mackey and Kjaer, (2017a).

Human Muscle sampling and preservation

Muscle biopsies were collected from the vastus lateralis muscle immediately before the damaging exercise from both legs and 2, 7 and 30 days from the damaged leg thereafter. Biopsies were taken under local anaesthetic (1% lidocaine: Amgros I/S, Copenhagen, Denmark), using the percutaneous needle biopsy technique of Bergström Bergström, (1975), with 5–6-mm-diameter biopsy needles and manual suction.

On extraction, biopsies were prepared for both histology and single fibre analysis. Parts of the biopsy suited for histology were aligned in parallel, embedded in Tissue-Tek (Sakura Finetek Europe, Zoeterwoude, The Netherlands), frozen in isopentane pre-cooled by liquid nitrogen and stored at -80°C until analysis. If the biopsy contained long intact bundles of fibres, those were prepared for single fibre analysis Bergström, (1975). Fibre bundles were pinned to maintain fibre length and covered in Krebs-Henseleit bicarbonate buffer (containing 0.1% procaine) for 2 minutes, followed by Zamboni fixative (2% formaldehyde, 0.15% picric acid) for 30 min. Fibres were then transferred into fresh Zamboni fixative and placed in the fridge for approximately 4 hours. Zamboni fixative was then replaced with 50% glycerol in PBS and moved to -20°C on the following day until extraction, staining and observation.

Animal Studies (Mouse)

Experimental Design and Surgical Procedure

8 Wildtype (WT) and 10 LMNA^{+/ Δ K32} used in previous analyses Owens et al., (2020b) were included in this study and underwent a sham operation or functional overload (FO) of the plantaris muscles, induced through the tenotomy of soleus and gastrocnemius muscles, in both hind limbs Serrano et al., (2008). The cut distal tendons were folded proximally and sutured to the proximal musculotendinous region leaving the plantaris intact with strict asepsis maintained throughout. Animals recovered within 1-2 hours following the end of the procedure and were then monitored daily following surgery for signs of discomfort and infection. For pain management, Buprenorphine was administered prior to and following surgery (Vetergesic© 0.3 mg/ml, SC: 0.10 mg/kg).

Mouse Muscle sampling and preservation

After 1 week of FO or sham surgery, animals were sacrificed by cervical dislocation, plantaris muscles were dissected, and visible fat and connective tissue removed. Isolated plantaris muscles were snap frozen in isopentane pre-cooled by liquid nitrogen for histological analysis or fixed in 4% paraformaldehyde at room temperature for one hour for analysis of single muscle fibres. After fixation, PLN muscles were placed on ice and sucrose solution was added in increasing molarity from 0.5mM, 1mM, 1.5mM and then frozen at -80°C in 2mM sucrose. When ready to isolate, sucrose frozen fibres were placed on ice and sequentially changed into decreasing molarity sucrose into immunobuffer (IB): PBS (10mM phosphate pH 7.4, 150mM NaCl), 50mM glycine (Merk 1.02401_1000), 0.25% BSA, 0.03% saponin (Sigma 100g S-7900), 0.05% sodium azide.

Immunostaining of single fibres, cross-sections, and cells

Myofibre Isolation

Single fibres were mechanically teased from fibre bundles from all species with the aid of a stereomicroscope in a petri dish containing IB. Due to the reduced size and sensitivity to handling of WT and LMNA^{+/ Δ K32} mouse fibres both with and without overload, they were instead extracted in small bundles of fibres to avoid breaking.

Myofibres

Primary antibodies were diluted as per table 2.1 in IB + plus 0.2% Triton-X100 (Sigma-Aldrich) overnight and then washed 3 x 10 minutes in IB. Secondary antibodies were diluted as per

table 2.1 in IB for 2 hours, followed by 3 x 10 minutes in IB. Following incubation with primary and secondary antibodies, single fibres were mounted in DAPI (Vectashield® Antifade Mounting Medium with DAPI (1.5µg/ml), Burlingame, CA, USA) onto glass slides and cover slips added and stored at -20°C until imaging.

Transverse Cross-sections

Isopentane snap-frozen muscle was sectioned at 10µm using an OTF5000 Cryostat (Bright Instruments, UK) onto Thermo Scientific™ SuperFrost Plus™ Adhesion slides (Thermo Fisher Scientific Inc, Waltham, USA). Immunostaining and cover slipping were completed as above on glass slides.

Cells

Fixed cells were stained as above in 12 well plates (C2C12s) or 6 well plates (Human). Following staining of C2C12 cells, the plastic coverslips were removed, blotted dry and placed on glass slides in mounting medium (Vectashield® Antifade Mounting Medium with DAPI (1.5µg/ml), Burlingame, CA, USA)) before cell imaging. Human cells were imaged directly in the 6 well plate in which they were cultured.

Imaging and PCM1 localisation

Myofibres were imaged under 20x magnification and 30µm Z-stacks produced with 3µm steps using a widefield fluorescent microscope (Leica DMB 6000, Wetzlar, Germany) to determine PCM1 presence and localisation. An A4 filter was used to image DAPI (EX: 340-380, EM: 450-490), L5 filter to image FITC and Alexa Fluor® 488 (EX: 460-500, EM: 512-542) and an RHO filter to image Alexa Fluor® 568 and 594 (EX: 541-551, EM: 565-605). Images were taken with a monochrome DFC365 FX camera (Leica, Wetzlar, Germany) and fluorescent channels overlaid to determine PCM1 and Pax7 localisation. The percentage of Pax7+ cells that also displayed PCM1 positivity were studied on single myofibres across all models.

Cells and muscle cross-sections were imaged under 20x magnification using a widefield fluorescent microscope (Leica DMB 6000, Wetzlar, Germany). For whole muscle cross-sections multiple images were taken and stitched together using the tilescan feature in Leica Application Suite X (Leica Microsystems GmbH, Wetzlar, Germany).

Automated estimated fibre cross-sectional area measurements (π *minimum feret diameter) were performed as previously reported previously Schmoll et al., (2018). Briefly, tile-scanned muscle cross-sections were converted to grayscale and filtered to outline edges in order to highlight muscle cell membranes using Adobe Photoshop (Adobe Systems, San Jose, California, USA) and fibres counted using pre-determined ranges of acceptance to identify individual cells; (Area 500-500,000 μm^2 , minimum feret diameter 0-500,000 μm , Perimeter 0-430 μm , Roundness 0-3) with Image-Pro Plus 5.1 software (Media Cybernetics, MD, USA).

Statistics

Data were analysed using GraphPad Prism 8 software (GraphPad Software, San Diego, CA, USA). Changes in rat muscle mass and mid-belly, estimated myofiber cross-sectional area and % of PCM1+ Pax7+ cells were compared using a paired t-test (Mean \pm SD). The % of PCM1+ Pax7+ cells from human isolated myofibers were compared by 1-way repeated measures ANOVA with Tukey's post hoc testing and by 1-way ANOVA with Tukey's post hoc testing for the % of PCM1+ Pax7+ cells from isolated WT and LMNA^{+/ Δ K32} mice.

6.3 Results

Results:

PCM1 localisation changes consistently during C2C12 and human primary myoblast proliferation and differentiation into myotubes in-vitro.

As previously reported Srsen et al., (2009), in-vitro PCM1 is present at the centrosome during proliferation in both C2C12 mouse muscle cells (Figure 6.1A, C) and human muscle-derived primary cells (Figure 6.2A). When myoblasts are transferred to low serum media, a differentiation programme is initiated where PCM1 re-localises to form a perinuclear matrix around the myoblast seen as nuclear envelope staining. This change in localisation precedes fusion of two myoblasts into a myotube as previously reported Srsen et al., (2009). The change in PCM1 localisation may be required for appropriate cytoskeletal reorganisation, as motor proteins pull two myoblasts together before fusion. Once fused, PCM1 remains present at the nuclear envelope in the myotube (Figure 6.1B, 6.1D and 6.2B).

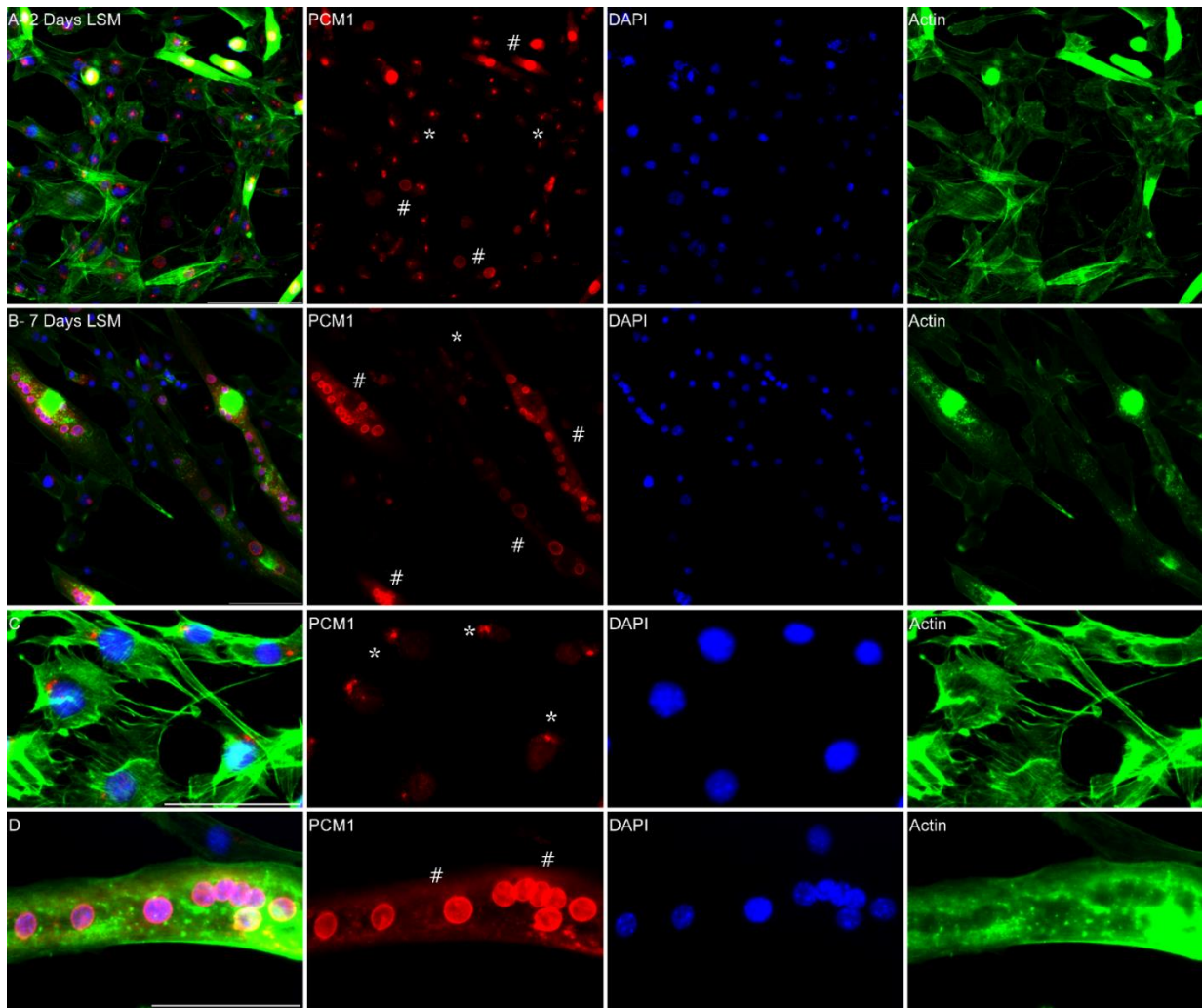


Figure 6.1 PCM1 localisation in C2C12 myoblast/myotube cultures. **A** Following 2 days in LSM, the culture contains both undifferentiated myoblasts (*) and differentiated myotubes (#). Higher intensity actin staining is present in multinucleated cells whose nuclei all have a PCM1+ nuclear envelope. **B** After 7 days in LSM, few undifferentiated myoblasts remain. Most nuclei are incorporated into multinucleated myotubes and show high PCM1 positivity. Scale bars indicate 50 μ m. **C** PCM1 is localised to the centrosome in the myoblast (*) and **D** at the nuclear envelope in the myotube (#). Scale bars indicate 25 μ m.

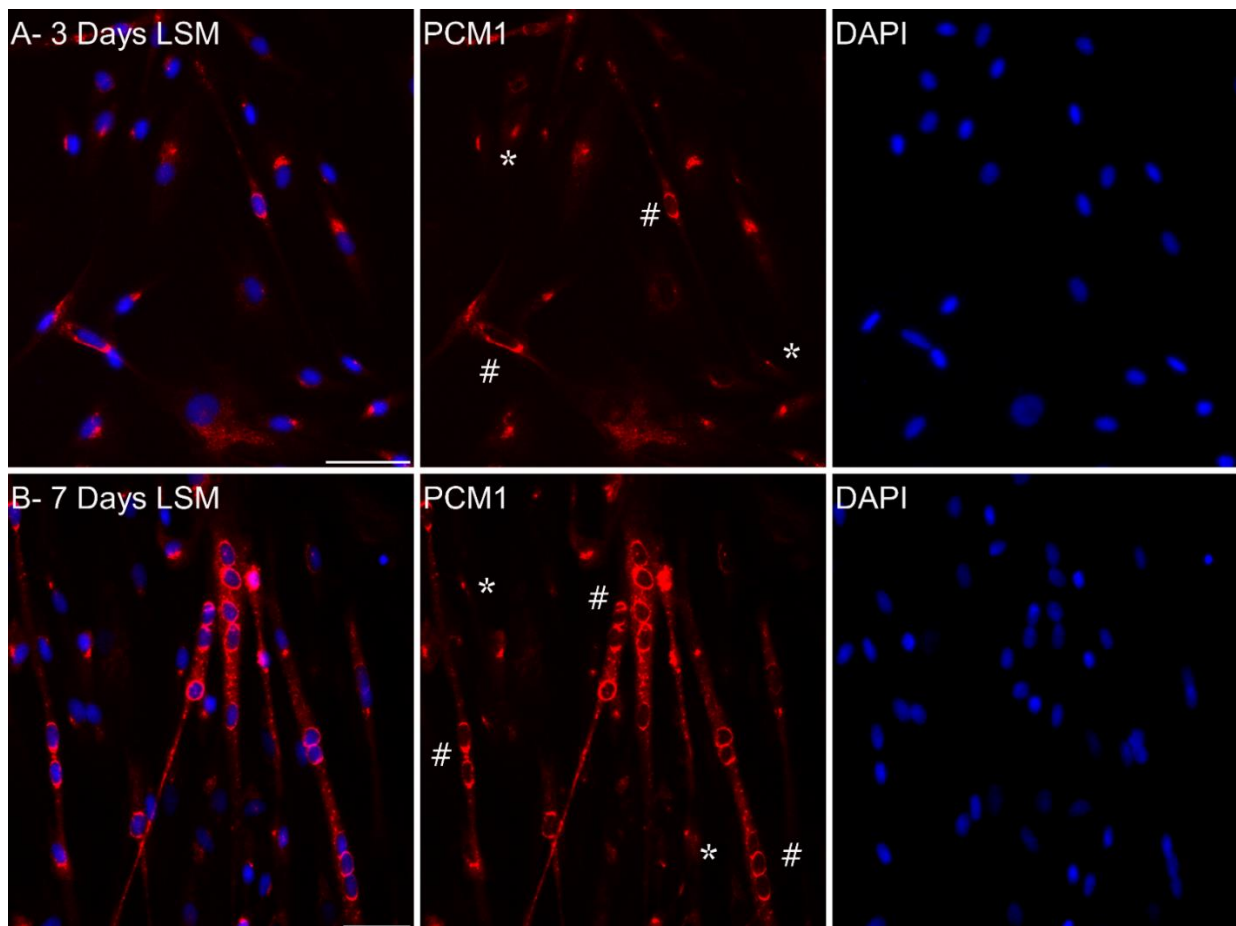


Figure 6.2 PCM1 localisation in human muscle-derived primary myoblasts/myotubes shows a very similar progression to the C2C12 cultures. **(A)** Following 3 days in LSM, the culture contains mainly undifferentiated myoblasts (*) with a few binucleated myotubes. **(B)** After 7 days in LSM, multinucleated myotubes (#) have formed. Many nuclei show perinuclear PCM1 staining (nuclear envelopes) but a few undifferentiated myoblasts (*) remain. Scale bars indicate 30 μ m.

Daily 'Spillover' resistance training in rats causes an increase in PCM1+ satellite cells which may be indicative of satellite cell proliferation to support hypertrophy.

Following 10 days of daily, unilateral 'Spillover' resistance training in rats, PCM1 is present at the nuclear envelope of post-mitotic myonuclei on isolated myofibres. Following this training period, we observe a 13.6% \pm 5.7 ($p < 0.0001$) increase in TA muscle mass and a 12.7% \pm 0.9 ($p < 0.001$) increase in estimated fibre cross-sectional area between the stimulated and contralateral unstimulated muscle (Figure 6.3C), similar to previous work from our lab Schmoll et al., (2018). In a subset of animals, we observe a \sim 3-fold increase which approached

significance ($17.6 \pm 3.2\%$ from 6.3 ± 1.7 , $p = 0.085$) in Pax7+ satellite cells that also have PCM1+ centrosomes, in the stimulated (Figure 6.3A) vs. unstimulated TA (Figure 6.3B). PCM1+ granules were also present on the stimulated myofibres surrounding myonuclei which were absent in the large majority of control myofibres (Figure 6.3B). Connective tissue nuclei that remain attached to the isolated myofiber consistently showed no PCM1 positivity.

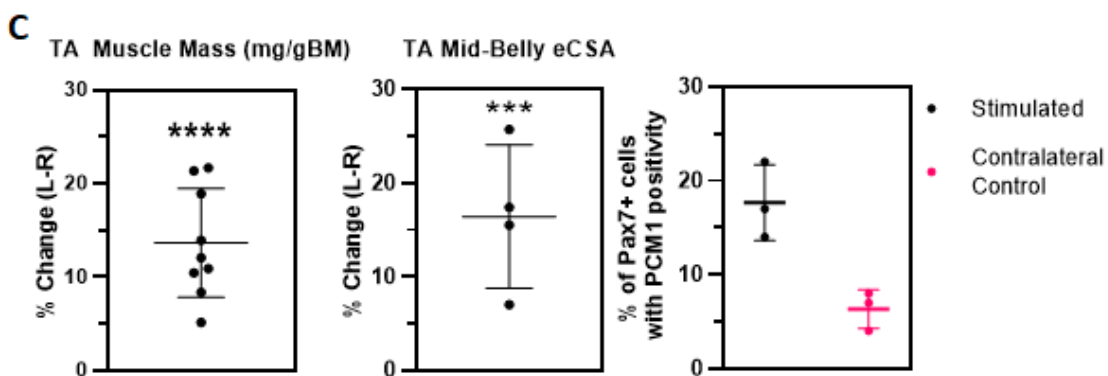
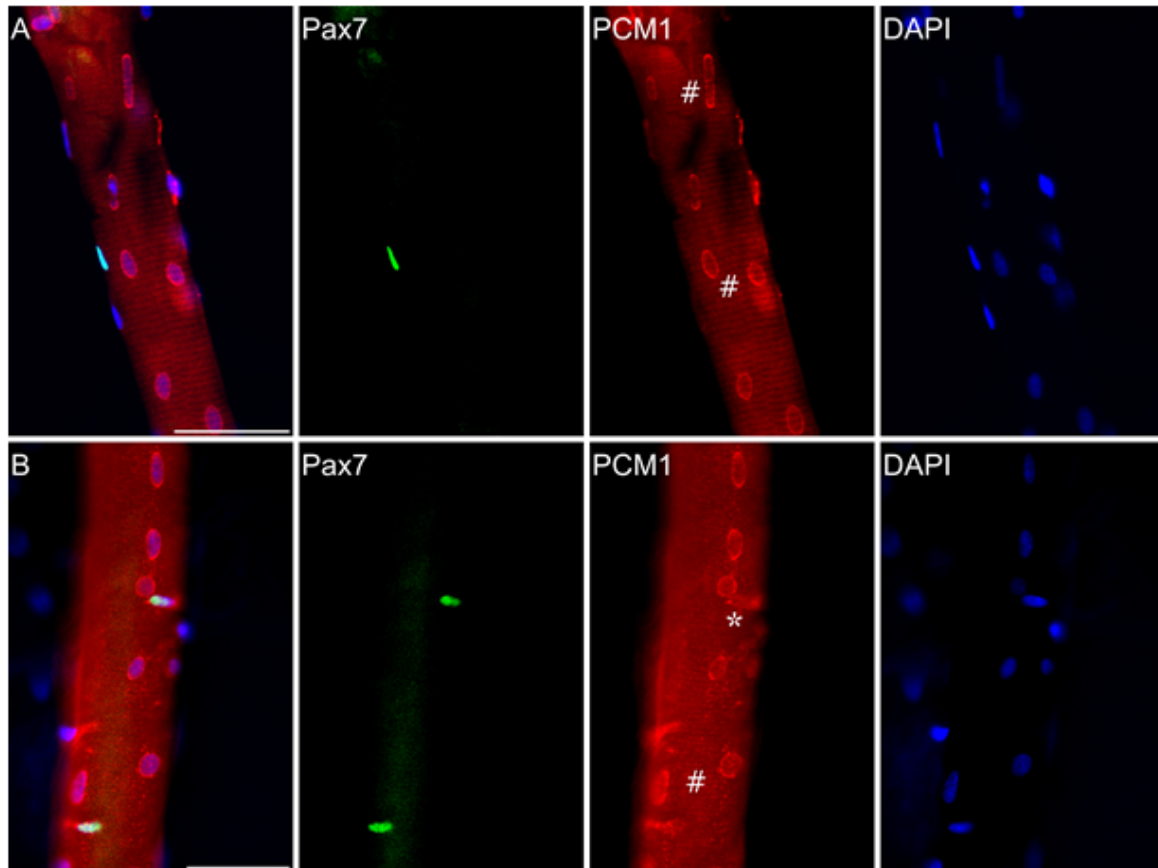


Figure 6.3 Pax7+ cells ($n = 80$) were assessed from each animal from the stimulated and contralateral control muscle. **(A)** Shows PCM1 being present in the nuclear envelope of myonuclei (#) but not the Pax7+ satellite cell. **(B)** After 10 days of 'Spillover' Stimulation, PCM1 labels a certain population of satellite cells (*) and centriolar satellite granules around certain

myonuclei (#). PCM1 is not found on the attached capillary/connective tissue nuclei on the mechanically separated fibre to the left of the myofiber. **(C)** In the stimulated limb after 10 days of daily 'Spillover' stimulation a $13.6\% \pm 5.7$ increase ($p < 0.0001$) in TA muscle mass and a $12.7\% \pm 0.9$ ($p < 0.001$) increase in estimated fibre cross-sectional area was concomitant with a ~3-fold increase in the number of Pax7+ satellite cells that also had PCM1+ centrosomes. Scale bars indicate $50\mu\text{m}$.

Human skeletal muscle degeneration and regeneration reveals multiple PCM1+ cell populations.

We next examined single muscle fibers isolated from vastus lateralis biopsies taken before and 2, 7 and 30 days post eccentric damage that has been shown to produce adult myogenesis in-vivo. We report that on transverse cross-sections, PCM1 labelling of myonuclei at the nuclear envelope can appear as both a hollow ring and as a single spot depending on where the nucleus is cut (Figure 6.4A). Interstitial connective tissue contains populations of cells with PCM1+ nuclear envelopes and cells with PCM1+ centrosomes in close proximity to the myofiber border in both control and damaged tissue (Figure 6.4A).

The percentage of Pax7+ cells that were also PCM1+ at their centrosome was $9.5\% \pm 1.5$ in the control state and increased at 2 days ($20\% \pm 3$, $p = 0.14$) and 7 days ($29.5\% \pm 3.5$, $p = 0.01$) post eccentric damage (Figure 6.5). Across the time course studied, the 7-day post eccentric damage is the time point that reveals the largest scale of regeneration of damaged or necrotic myofibres (Figure 6.6, 6.7). In both transverse cross-sections and isolated myofibres, there are large populations of PCM1+ proliferating cells in necrotic zones between intact fibres. These are immune cells (CD68+) that infiltrate and remove severely damaged myofibres. Some extensively damaged myofibres contain both myonuclei with a PCM1+ nuclear envelope that remain at the basement membrane and infiltrated macrophages with a PCM1+ centrosome that disperse the whole cytoplasm. PCM1+/Pax7+ cells remain slightly elevated at 30 days post damage compared to baseline ($19\% \pm 2$, $p = 0.18$), with some Pax7+ cells exhibiting PCM1+ nuclear envelopes which we believe are myocytes or pre-fusion cells. By 30 days post eccentric damage, multiple central myonuclei are present as well as populations of Pax7+ cells that express PCM1 at their centrosome (proliferating) and PCM1 at the nuclear envelope (pre-fusion cells) (Figure 6.8), which replicates our in-vitro observations of PCM1 relocalisation.

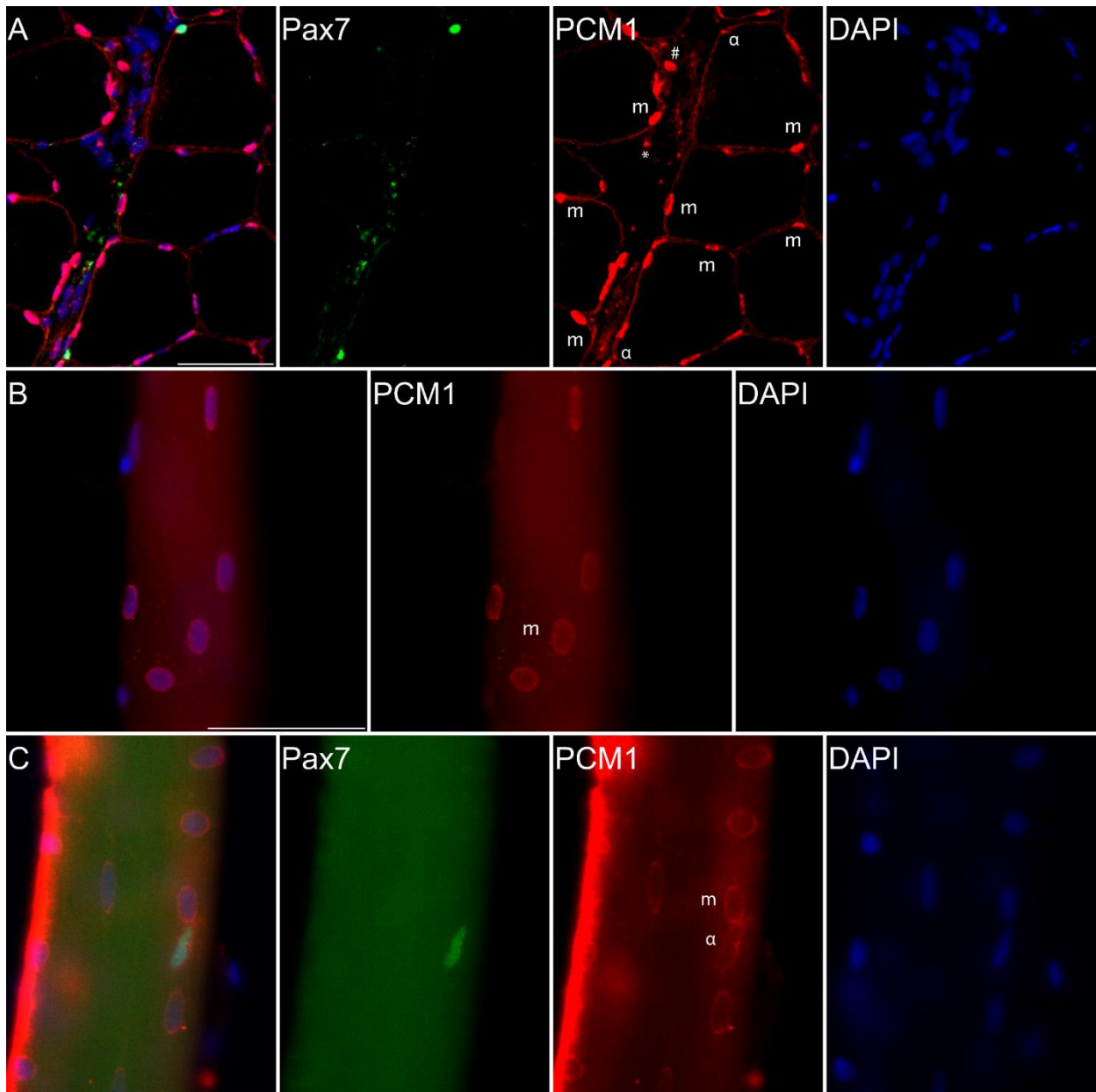


Figure 6.4 As shown *in-vitro*, localisation of PCM1 moves from the centrosome in proliferating myoblast cells. Upon differentiation and fusion into multinucleated myotubes, becomes more distinctive to highlight the nuclear envelope of myonuclei. Transverse cross sections from control human muscle (**A**) illustrate the PCM1+ nuclear envelope of transversely sectioned myonuclei associated with the myofibre border (m). The distribution of PCM1 staining on myonuclei reflects whether the nuclei has been cut through the middle revealing an envelope or the end where PCM1 staining does not have a hollow centre. Some nuclei within the interstitial space have PCM1 staining at the centrosome (*) and are 'presumably' proliferative. They are not Pax7+ and most are probably non-myogenic cells. There are also post-mitotic cells in the endomysium identified by PCM1+ nuclear envelopes (#). There is a risk of confusing

these nuclei with myonuclei especially if no specific basement membrane marker is used. Additionally, a few Pax7+ cells exhibit PCM1 positivity at the centrosome even in the control state (α). (B) Normal distribution of myonuclei in a control fibre with PCM1+ nuclear envelopes with centriolar satellites (granules) present in close proximity to the nuclear envelope. (C) A control human myofibre exhibiting a Pax7+ cell that is also PCM1+. Scale bars indicate 80µm.

Human ES Induced Eccentric Damage

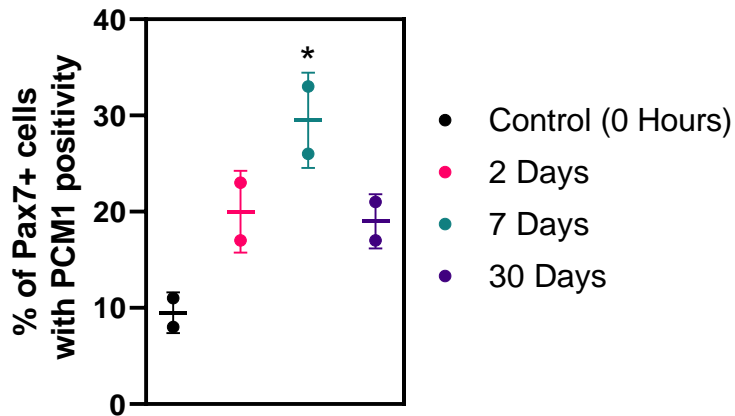


Figure 6.5 The number of proliferating Pax7+ cells during adult human skeletal muscle regeneration based on PCM1+ centrosomes. * Indicates a significant change from control.

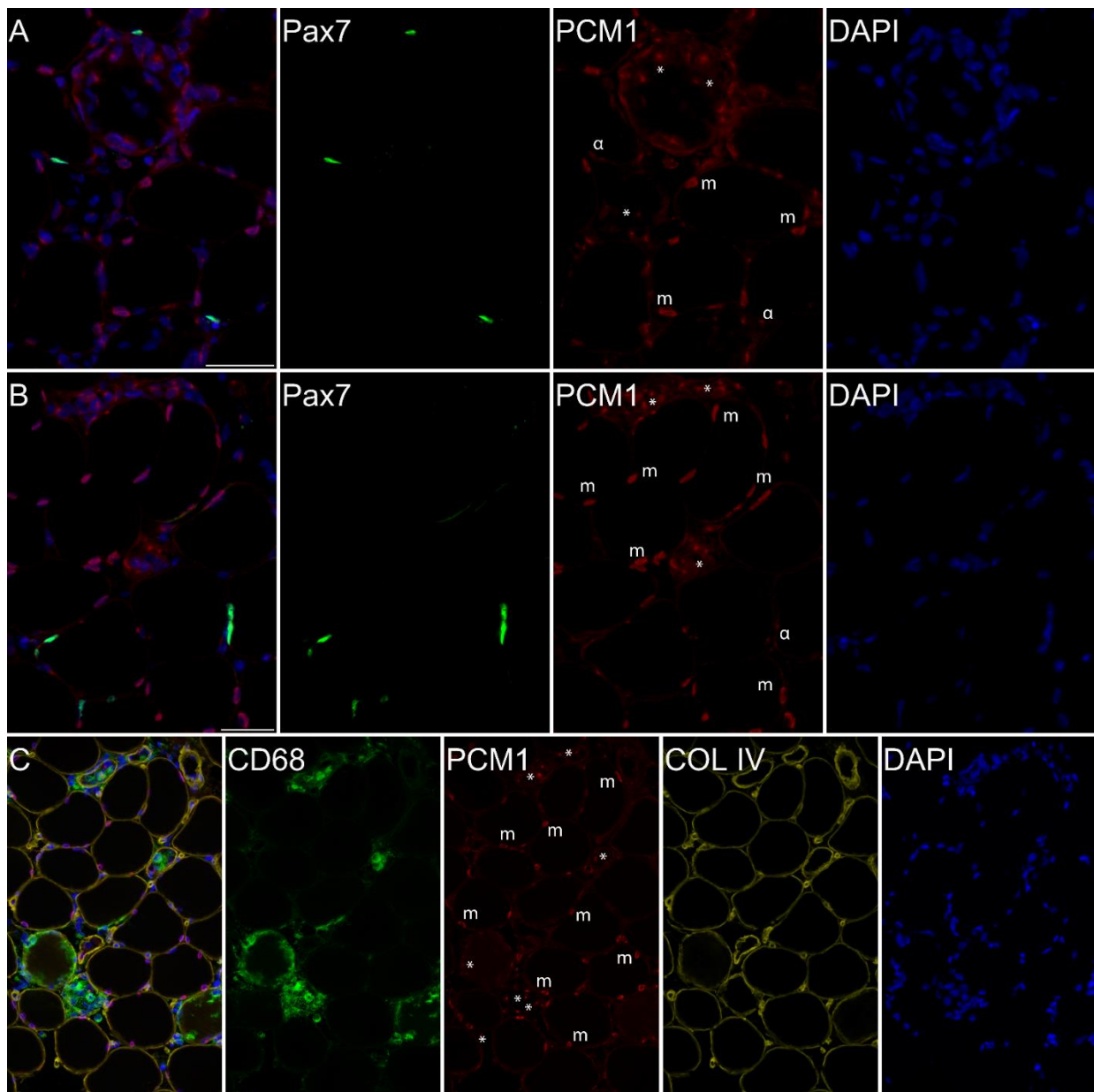


Figure 6.6 Transverse muscle cross-sections, 7 Days post eccentric damage from two separate participants (**A**, **B**). Large bodies of proliferating immune cells can be observed in necrotic zones and regenerating fibres identified through PCM1+ centrosomes (*), alongside myonuclei (m) and PCM1+ Pax7+ cells (α). (**C**) confirms that macrophages are PCM1+ inside and around myofibres through CD68 labelling. Scale bars indicate 80μm.

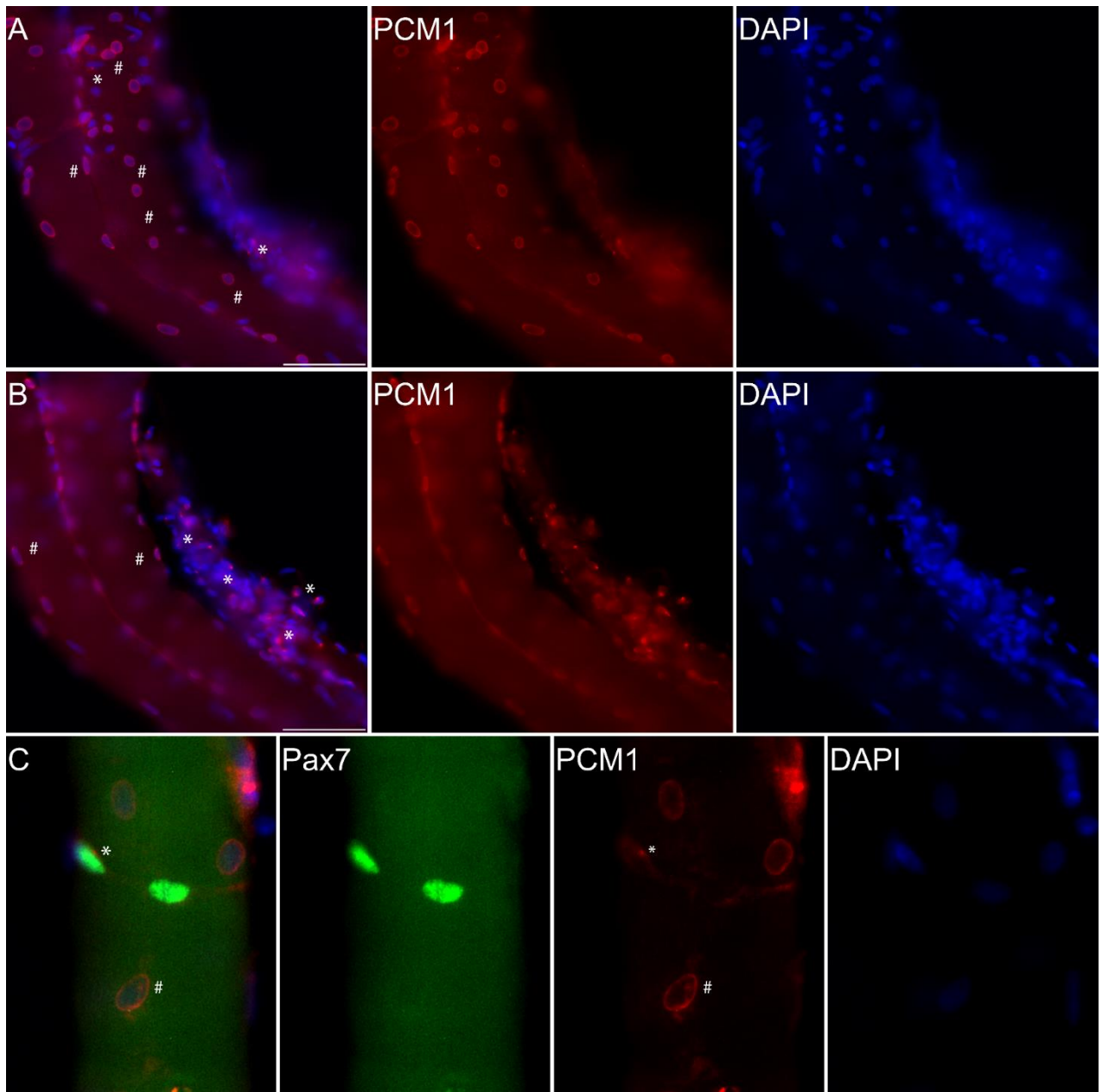


Figure 6.7 Single human myofibres extracted 7 days post eccentric damage. **(A, B)** shows 3 myofibres at different positions in the z-stacks. The right most fibre is necrotic, indicated by infiltration of a dense population of nuclei belonging to proliferating macrophages with PCM1+ centrosomes (*). Some myonuclei (PCM1+ nuclear envelope) remain within the regenerating myofibre, which may already be engulfed by macrophages but is not possible to be certain using fluorescent microscopy at this resolution. **(C)** Two Pax7+ cells in close proximity one of which displays PCM1 positivity (*) adjacent to PCM1+ myonuclei (#). Scale bars indicate 100 μ m.

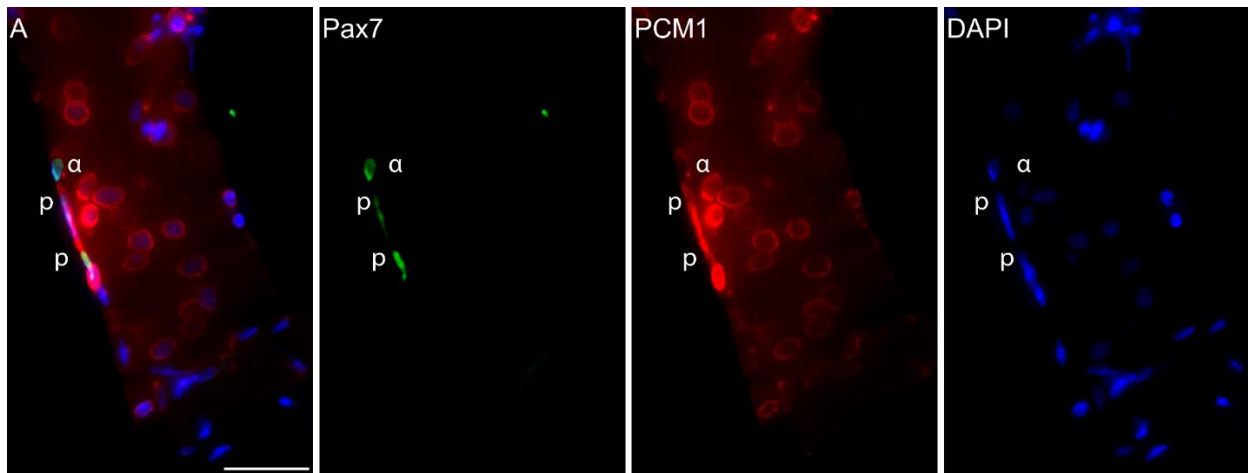
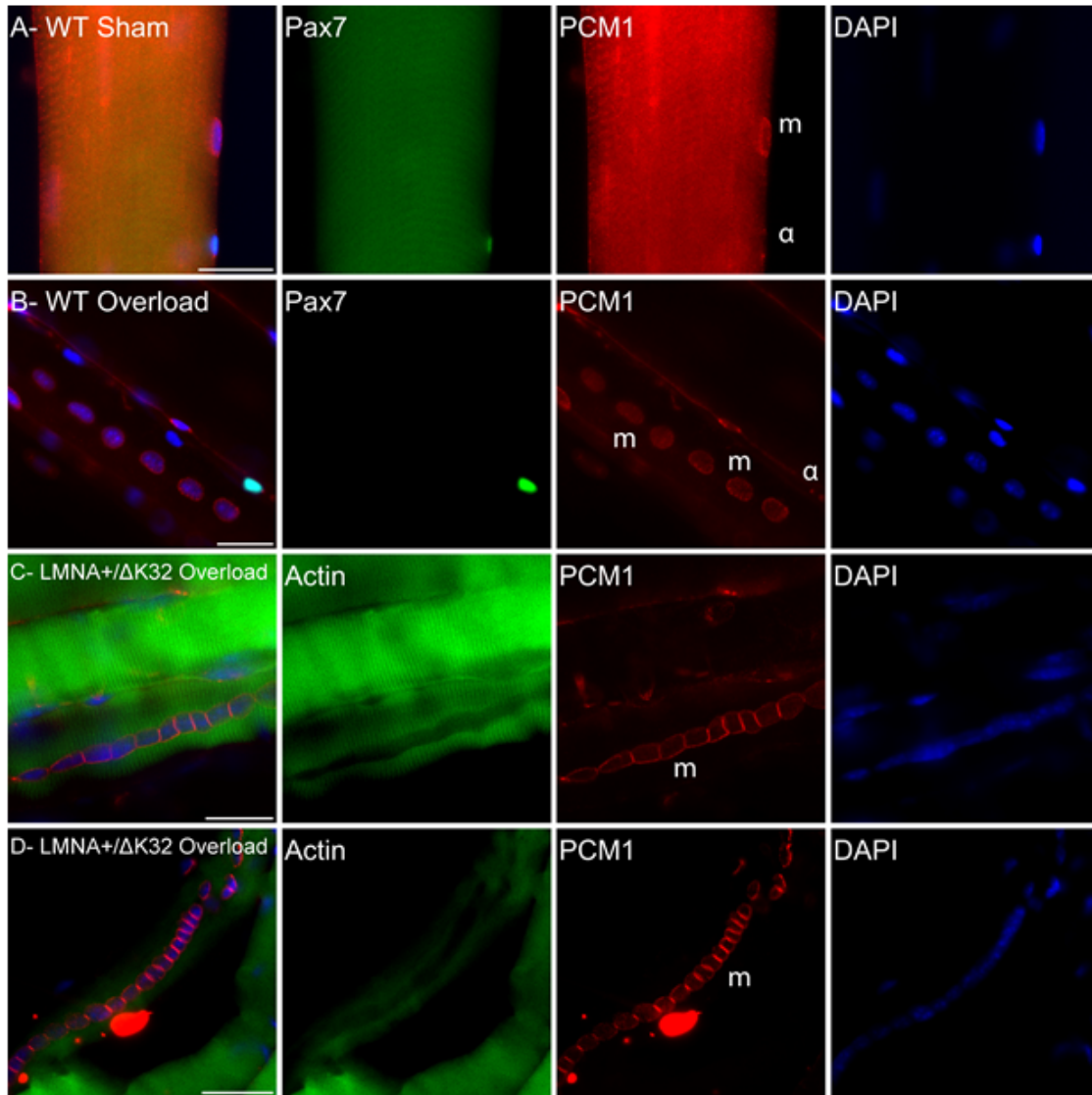


Figure 6.8 Single human myofibers 30 days post eccentric damage display large numbers of central myonuclei. (α) indicates a Pax7+ cell with a PCM1+ centrosome indicating a proliferative state. Nearby are a population of Pax7+ cells at the periphery of the myofiber which express both Pax7 and PCM1 at their nuclear envelopes, which we predict are pre-fusion cells (p) evidenced by our in-vitro observations and previous work by Srsen et al., (2009). Scale bar indicates 100 μ m.

Defective muscle plasticity in LMNA^{+/ Δ K32} mutant mice following mechanical overload is accompanied with higher numbers of PCM1+ Pax7+ cells and impaired nuclear spreading in-vivo.

We have recently reported Owens et al., (2020b) that under basal conditions WT and LMNA^{+/ Δ K32} mutant plantaris muscles are equivalent in mass (WT = 0.69 ± 0.02 mg. g⁻¹ vs. LMNA^{+/ Δ K32} 0.65 ± 0.02 mg. g⁻¹). Following one week of mechanical overload, WT muscles present a robust hypertrophic response (1.15 ± 0.07 mg. g⁻¹), whilst the mutant presents a defective hypertrophy (0.84 ± 0.05 mg. g⁻¹). This reduced hypertrophic response to mechanical overload is accompanied by defective myonuclear accretion, nuclear deformity, and an increase in both Pax7+ and EdU+ fibers both inside and outside of the dystrophin ring Owens et al., (2020b). From the single isolated myofibres assessed here, we find that at baseline the number of PCM1+ Pax7+ cells is comparable at baseline in both the WT (8 ± 3.55 %) and mutant (8.75 ± 5.9 %, $p = 0.99$), (Figure 6.9E). After overload, the number of PCM1+ Pax7+ cells are not significantly different from the sham control in the WT but shows a trend to increase (16 ± 6.65 %, $p = 0.337$). However, there is a significant increase in the mutant (22 ± 7.89 %, $p = 0.02$) in the vs the mutant sham control (Figure 6.9E). However, due to the

severity of the phenotype of the mutant following overload, which includes an increased number of cells throughout the connective tissue, it becomes challenging to delineate the positioning and localisation of PCM1 on nuclei and their relationship to the sarcolemma on transverse cross-sections (Figure 6.10 D, E). Additionally, we observe that myotubes that form in the LMNA^{+/ Δ K32} mutant after overload have closely chained myonuclei (Figure 6.9), characteristic of earlier development. Conversely myotubes present in the WT exhibit appropriate nuclear spreading and peripheral migration, which occurs at a later stage of myogenesis which may be an additional factor contributing to defective hypertrophy.



Synergist Ablation Mechanical Overload

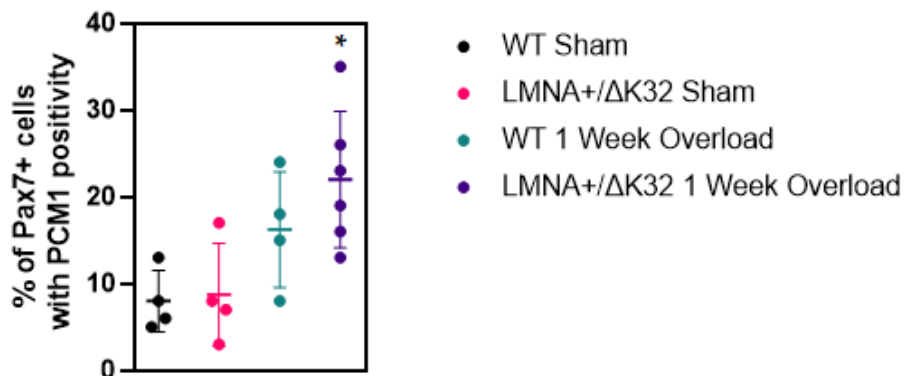


Figure 6.9 (A) Single extracted myofiber from WT sham operated mouse showing PCM1+ centrosome labelling around a single Pax7+ cell and mature myonuclei. **(B)** PCM1 labels the nuclear envelope of newly differentiated myonuclei during nuclear spreading following 1 week

of synergist ablation in the WT mouse (m). PCM1 also labels a single Pax7+ cell at its centrosome in an adjacent mature fibre (α). **(C, D)** LMNA^{+/ Δ K32} intact myofibres adjacent to early myocyte/myofibre following 1 week of synergist ablation. The nuclei appear to be in the alignment stage of myogenesis mediated by LINC, Nesprin 1 α and PCM1 itself by anchoring motor proteins to the nuclear envelope Roman and Gomes, (2018). This earlier stage of myogenesis was observed throughout our study of extracted myofibres/myotubes, presenting a delayed regenerative response in comparison to the WT synergist ablation where nuclei were consistently separated and move along the length of the fibre before peripheral migration and anchoring to the sarcolemma. Scale bars indicate 20 μ m. **(E)** WT and LMNA^{+/ Δ K32} have similar levels of Pax7+ cells with PCM1+ centrosomes which is elevated following 1-week of mechanical overload. * Indicates statistical significance vs sham control ($p < 0.05$)

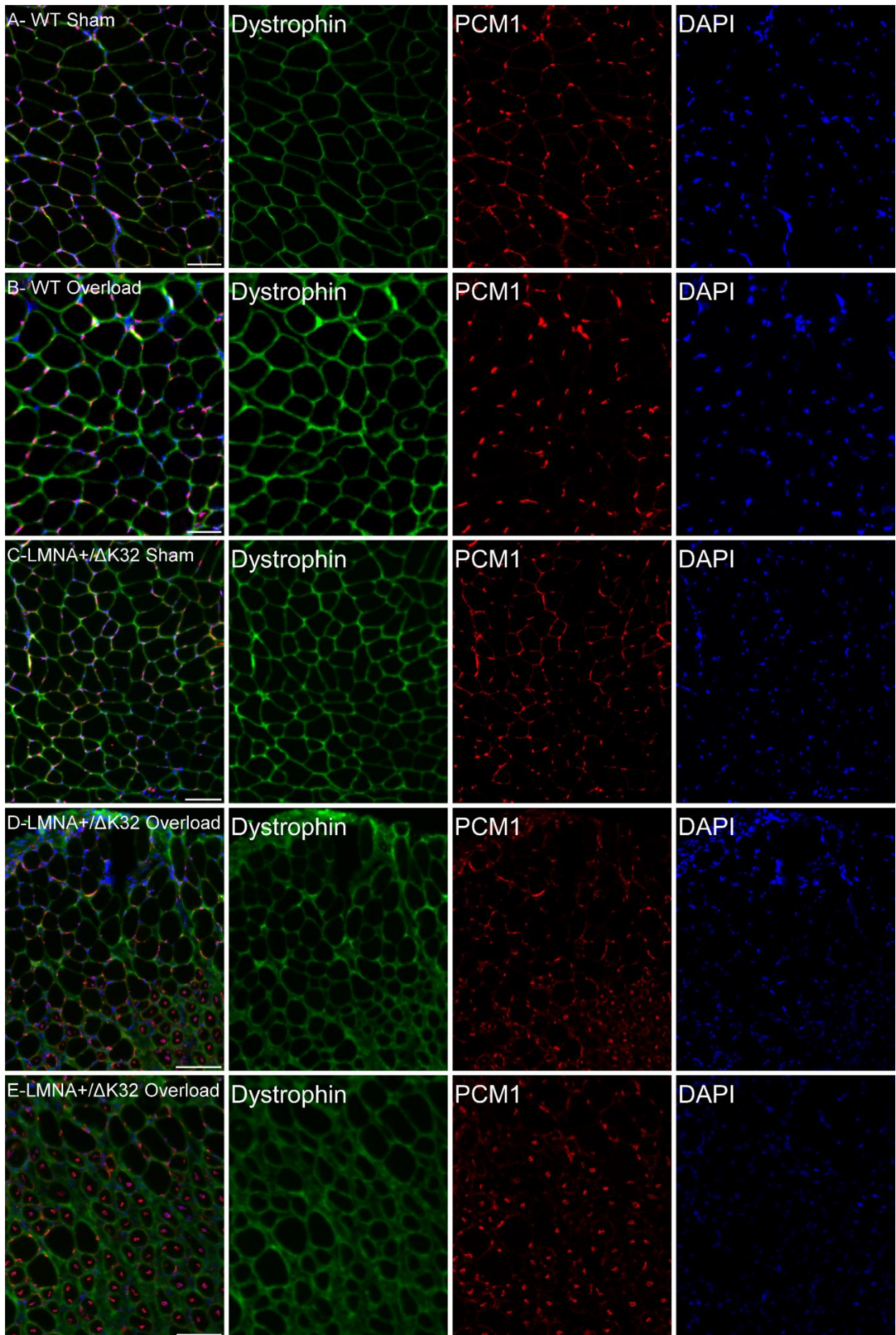


Figure 6.10 Morphology of WT and LMNA^{+/ Δ K32} mouse plantaris muscle, 1 week post sham surgery or synergist ablation overload. **(B)** shows an increase in fiber cross-sectional area in comparison to **(A)**. **(C)** shows that sham surgery alone sustains normal LMNA^{+/ Δ K32} muscle phenotype. **(D and E)** show excessive dystrophin protein in regenerating areas with myofibres containing centralised nuclei with a PCM1+ nuclear envelope. Scale bars indicate 50 μ m.

6.4 Discussion

We present novel data concerning the localisation of PCM1 across multiple models (WT mice, LMNA^{+/ Δ K32} mice, rats, and humans) of ‘physiological’ and supra-physiological overload induced hypertrophy and regeneration. Importantly, our main findings illustrate that anti-PCM1 does label certain Pax7 cells at the centrosome, contrasting previous reports suggesting it was specific to myonuclei Winje et al., (2018). The pattern of staining in satellite cells is distinctively different, with localisation at poles of the satellite cell centrosome. Furthermore, the percentage of satellite cells that were PCM1 positive was heavily dependent on the model of overload, regenerative state, and species/genetic mutation, leading to the proposal that this staining reflects the extent of proliferative expansion of the satellite cell seen most obviously in regenerating muscle.

Furthermore, we have confirmed distinct changes in PCM1 localisation both *in-vitro* and *in-vivo* that represent cell cycle stages of satellite cells; first at the centrosome during prophase or anaphase, and then at the nuclear envelope, when PCM1 forms an insoluble perinuclear matrix when the nucleus exits the cell cycle into G0 to prepare for fusion into differentiated myotubes Fant et al., (2009), Gimpel et al., (2017), Srsen et al., (2009). We also highlight that the change in PCM1 localisation from the centrosome to the nuclear envelope occurs in single muscle cell precursors and precedes fusion of two mononucleated cells into a myotube (Fig. 1) Single mononucleated Pax7+ cells with PCM1+ nuclear envelopes we believe are indicative of ‘pre-fusion’ cells. Srsen et al., (2009) have previously reported that these mononucleated cells with PCM1+ nuclear envelopes express both embryonic myosin and myogenin which are upregulated during differentiation. This suggests this change in localisation to the nuclear envelope is important for the migration and anchoring of two myocytes toward each other via dynein and microtubules. In this instance, PCM1 may prove useful as a marker of the *in-*

vitro cell cycle and fusion index of myotubes due to a distinct change in localisation during differentiation.

Bergmann et al., (2011), Bergmann and Jovinge, (2012) first took advantage of PCM1 localisation changes, to the nuclear envelope, during differentiation in heart tissue to identify mature cardiomyocytes. Winje et al., (2018) later investigated PCM1 as a potential gold standard marker of myonuclei in skeletal muscle and claimed that PCM1 can be used as a specific histological marker of myonuclei without counterstaining of the sarcolemma for nuclear positioning, across species and following synergist ablation overload in the rat in both existing and newly incorporated nuclei. Whilst Winje et al., (2018) should be commended for studying PCM1 across mice, rats and humans and after overload, their analyses screened only 24 Pax7+ cells from plantaris muscle after 2-weeks of overload in the rat for PCM1 localisation, we had concerns that due to the previously reported change in localisation of PCM1 that Pax7+ cells could in fact also be Pax7+ when proliferating. Srsen et al., (2009) previously reported that all Ki67+ proliferating myoblasts were also PCM1+ at the centrosome and upon PCM1 relocalisation the nuclear envelope Ki67 positivity was lost. Furthermore, we interpret Figure 5 of Winje et al., (2018) to potentially show a transversely cut Pax7+ nucleus that is also PCM1+, albeit less distinctive than the PCM1+ nuclear envelope staining of nearby myonuclei.

The corresponding editorial Brunn, (2018) discusses how PCM1 is an appropriate diagnostic tool for the identification of the myonucleus, yet also highlights how PCM1 is reportedly ubiquitously expressed independent of cell lineage during mitosis. Our study supports this caveat by identifying PCM1 in certain connective tissue nuclei and also inside regenerating and necrotic myofibres that belong to proliferating macrophages which adds concern in analysing myonuclear fusion on transverse cross-sections in complicated myopathies where the nuclear envelope is implicated. Supporting our claim of PCM1 expression across multiple cell types, a recent pre-print Petrany et al., (2020a) utilising single-cell RNA sequencing (scRNA-seq) displays PCM1 expression in a range of cells as well as myonuclei including schwann, immune, fibro-adipogenic, endothelial cells, smooth muscle, tenocytes, satellite cells and neurons across multiple muscles, developmental stages and adulthood which could add to false positive identification of myonuclei through PCM1 labelling.

With this in mind, in mature tissue the myonucleus is approximately 10µm wide and 20-30µm long and therefore when studied cross-sectionally may be cut through the centre, pole or obliquely. We therefore hypothesised that at certain phases of the cell cycle or in particular sectional planes, the presence of PCM1 may be misinterpreted between a PCM1+ nuclear envelope of a myonucleus and a PCM1+ centrosome of a proliferating myogenic or non-myogenic cell, if careful consideration wasn't taken for sub-sarcolemma positioning and the distinctive perinuclear patterning, which can be challenging at light microscopy level. Myonuclei in transverse cross sections are also reported to be positioned inside, on or outside the sub-sarcolemmal, dystrophin ring due to physiological changes in nuclei angle, as well as non-physiological changes in nuclei angle based on preparation of tissue Winje et al., (2018). Furthermore, as previously reported our LMNA^{+/ Δ K32} exhibit increased nuclear deformity following mechanical overload Owens et al., (2020b), also seen in Fig. 9 D, E. This further makes determination of PCM1 localisation in close proximity to the sarcolemma challenging for manual identification and development of automatic quantification.

We suggest that in addition to marking myonuclei in non-damaged muscle, PCM1 staining may have a novel role in enabling interpretation of degeneration and repair in skeletal muscle. In control tissue it is a useful discriminating tool between 50-60% of the nuclei in a cross section that are myonuclei and the interstitial nuclei that are still capable of mitosis.

The main concern with this marker would be the false-positive identification of a myonucleus, which is in fact a pre-fusion cell, or another proliferating cell in close proximity to the sarcolemma (vascular cells, immune cells and connective tissue/stromal cells) Giordani et al., (2019), which often occurs during remodelling of hypertrophic or regenerating muscle Hoier et al., (2012), Holloway et al., (2018), Mackey and Kjaer, (2017a). Additionally, satellite cells either undergo symmetric division (generating 2 stem cells), or asymmetric division in which a stem cell and muscle progenitor is produced Feige et al., (2018) and only certain populations will exit the cell cycle and fuse to an existing myofibre. Previous reports show that from the proliferative satellite cell pool, approximately 80% differentiate and fuse to join the myofibre syncytium, whereas 20% simply renew and expand the satellite cell pool Charge and Rudnicki, (2004), Schultz, (1996), at least in growing rats (30 days). While this may be significantly fewer in the adult rodent/human muscle, its influence on interpreting small changes in myonuclei

per fibre may be real, or whether it is an increase in satellite cells, inflammatory cells, or interstitial nuclei.

Hypothetical View:

Determining the extent to which inappropriate identification may affect myonuclear counts therefore important, especially if automated counting or subjective microanatomical analysis is performed. From our analyses, we found that in sham operated WT and LMNA^{+/ Δ K32} mice, the number of PCM1⁺/Pax7⁺ cells were 8% \pm 4.4 and 8.8% \pm 5.9 respectively after 1 week. Following 1 week of synergist ablation overload this increased to 15.7% \pm 8 and 22% \pm 7.9. Following 1 week of 'Spillover' stimulation in the rat, Pax7⁺ cells with PCM1 positivity was 19.5% \pm 3.5 in the stimulated TA and 5.5% \pm 1.5 in the contralateral control limb. In our human investigation, 9.5% \pm 2.1 of Pax7⁺ cells were PCM1⁺ in the control state. Following an eccentric damaging protocol, this increased to 20% \pm 4.2 after 2 days and to 29.5% \pm 5 at 7 days before returning back down to 19% \pm 2.8 after 30 days.

It has previously been reported that myonuclei make up only about 56% and 67% of the total nuclei and satellite cells account for around 4-8% within skeletal muscle Schmalbruch and Hellhammer, (1977). From previous analyses, the number of myonuclei per fibre cross-section in mature skeletal muscle ranges between around 1.5 and 4.5 and for every 100 myonuclei there are roughly 1-5 satellite cells, or in other terms 0.04-0.25 Pax7⁺ cells per fibre cross-section (dependent on species, age, predominant fibre type composition, tissue section thickness and geometrical inclusion criteria to define a myonucleus) Damas et al., (2018a), Gundersen, (2016), Karlsen et al., (2019), Karlsen et al., (2015), Snijders et al., (2019), Snijders et al., (2016), Snijders et al., (2014), Winje et al., (2018). In our study, across models and species we report a range between 5.5 and 29.5% of Pax7⁺ satellite cells expressing the protein PCM1. Whilst the impact on misrepresenting myonuclear behaviour by false-positive identification of satellite cells as myonuclei would most likely be of minimal concern in healthy control muscle, the effect in regenerating muscle could potentially be a 2.4% error (29.5% of 8% of Pax7 cells (total skeletal muscle), without further considering proliferating or post-mitotic PCM1⁺ cells within the interstitial space close to the myofibre border. Whilst this is minimal, the effects on developing an automated based PCM1 recognition plugin for myonuclear counting must be considered dependant on the investigated model and sample size.

Both Winje et al., (2018), Blocquiaux et al., (2020) have reported and noted higher myonuclei per fibre cross-section values (~11-16%) when labelling with PCM1 in comparison to conventional positional methods. This may be as a consequence of both counting a small number of false positives with PCM1 labelling and being over cautious in identifying myonuclei using a positional only method (false negative). PCM1 is also presumed not suitable for automated cell sorting and isolation of 'myonuclei' specific populations for transcriptomic or DNA methylome analysis.

Limitations

This investigation was performed across species and models on small sample sizes and also on a small number of single fibres from each animal/participant. Therefore, data presented may not be fully representative of the whole muscle yet highlights issues in potential false identification of the myonucleus.

As previously discussed by Mackey and Kjaer, (2017a), some single fibres had no Pax7+ cells whereas others showed large clustered populations across all samples. This may reflect the heterogeneity of muscle fibre damage across the whole muscle or the extent of the fixation of muscle fibres throughout the muscle presumably due to the depth of penetration of the fixative. In particular, we observed varying amounts of background staining in rat muscle fibres presumably due to their size, which may have affected the heterogeneity of Pax7 labelling and autofluorescence within fibres. We must note that the absence of staining may not necessarily indicate lack of protein.

We also did not quantify PCM1+ centrosomes on Pax7- cells which we note were present on single myofibres, presumably from connective tissue or vasculature that stays attached using the mechanical separation technique which may further alter the potential for false positive identification of the myonucleus.

6.5 Conclusion:

We conclude that whilst perinuclear PCM1 is not specific to the myonucleus specifically, the impact of false positive identification of Pax7+ cells on total myonuclei counts would be minimal in most physiologically relevant models of overload hypertrophy but may be problematic in regenerative models or myo/laminopathies. We suggest the use of PCM1, Pax7

and a basement membrane marker to make completely sure the PCM1 labelling is associated with the perinuclear labelling of the myonucleus. PCM1 may also prove useful as a marker of both *in-vitro* and *in-vivo* satellite cell dynamics due to the distinct change in localisation during differentiation which reveals satellite cells in their quiescent (PCM1-), proliferating (PCM1+ centrosome) and pre-fusion state (PCM1+ nuclear envelope).

Thesis Conclusion

We have used and characterised the temporal myonuclear dynamics and cellular adaptations in two *in-vivo* models which induce muscle hypertrophy through resistance exercise or atrophy through disuse. Using immunohistochemistry and automated, high-throughput computational analyses we demonstrated that changes in fiber size and myonuclear dynamics occur in a fiber type specific manner. We demonstrate that myonuclear accretion occurs both as a consequence of resistance training, but also following extensive endurance training in order to support transcriptional demands. It has previously been suggested that myonuclei are permanent, yet we show they can be lost during disuse, lost following detraining, but can be retained when added following recovery from atrophy. This suggests that some myonuclei but not all can be retained for long periods of time. Alongside the morphometric observations, we present a highly controlled time series of acute gene expression changes following resistance exercise, dependant on the training status of the muscle as well as conserved genes/transcription factors that warrant further investigation by the muscle biology field. These genes include ATF3, Amd1, Ankrd1, Bgn, Col1a1, Col3a1, Ehd4, Hmox1, Lox and Myc, the latter of which we identify as a central regulator of the early muscle growth response. These genes are largely understudied in skeletal muscle, and we propose that it is likely important to further elucidate the function of these genes/ transcription factors and their involvement in muscle adaptation. The study of these genes may lead to important therapeutic findings for muscle mass and quality preservation. These preliminary findings open further avenues of research and the potential for future studies that study the transcriptional regulation of muscle homeostasis and adaptation to different exercise modalities.

References

- AKIMOTO, T., LI, P. & YAN, Z. 2008. Functional interaction of regulatory factors with the Pgc-1 α promoter in response to exercise by in vivo imaging. *American Journal of Physiology-Cell Physiology*, 295, C288-C292.
- AKIMOTO, T., SORG, B. S. & YAN, Z. 2004. Real-time imaging of peroxisome proliferator-activated receptor- γ coactivator-1 α promoter activity in skeletal muscles of living mice. *American Journal of Physiology-Cell Physiology*, 287, C790-C796.
- ALESSI, D. R., JAMES, S. R., DOWNES, C. P., HOLMES, A. B., GAFFNEY, P. R., REESE, C. B. & COHEN, P. 1997. Characterization of a 3-phosphoinositide-dependent protein kinase which phosphorylates and activates protein kinase B α . *Current biology*, 7, 261-269.
- ALLBROOK, D., HAN, M. & HELLMUTH, A. 1971. Population of muscle satellite cells in relation to age and mitotic activity. *Pathology*, 3, 233-243.
- ALLEN, D. L., HARRISON, B. C., MAASS, A., BELL, M. L., BYRNES, W. C. & LEINWAND, L. A. 2001. Cardiac and skeletal muscle adaptations to voluntary wheel running in the mouse. *Journal of applied physiology*, 90, 1900-1908.
- ALLEVATO, M., BOLOTIN, E., GROSSMAN, M., MANE-PADROS, D., SLADEK, F. M. & MARTINEZ, E. 2017. Sequence-specific DNA binding by MYC/MAX to low-affinity non-E-box motifs. *PLoS one*, 12, e0180147.
- ALTMAN, B. J., HSIEH, A. L., SENGUPTA, A., KRISHNANAIAH, S. Y., STINE, Z. E., WALTON, Z. E., GOUW, A. M., VENKATARAMAN, A., LI, B. & GORAKSHA-HICKS, P. 2015. MYC disrupts the circadian clock and metabolism in cancer cells. *Cell metabolism*, 22, 1009-1019.
- ALVARADO, J. C., FUENTES-SANTAMARÍA, V., GABALDÓN-ULL, M. C., BLANCO, J. L. & JUIZ, J. M. 2014. Wistar rats: a forgotten model of age-related hearing loss. *Frontiers in aging neuroscience*, 6, 29.
- ALWAY, S., WINCHESTER, P., DAVIS, M. & GONYEA, W. 1989. Regionalized adaptations and muscle fiber proliferation in stretch-induced enlargement. *Journal of Applied Physiology*, 66, 771-781.
- ALWAY, S. E. 1997. Overload-induced C-Myc oncoprotein is reduced in aged skeletal muscle. *The Journals of Gerontology Series A: Biological Sciences and Medical Sciences*, 52, B203-B211.
- AMAR, D., LINDHOLM, M. E., NORRBOM, J., WHEELER, M. T., RIVAS, M. & ASHLEY, E. A. 2019. Differential response trajectories to acute exercise in blood and muscle. *Available at SSRN 3508810*.
- AMAR, D., LINDHOLM, M. E., NORRBOM, J., WHEELER, M. T., RIVAS, M. A. & ASHLEY, E. A. 2021. Time trajectories in the transcriptomic response to exercise-a meta-analysis. *Nature Communications*, 12, 1-12.
- AN, C.-I., DONG, Y. & HAGIWARA, N. 2011. Genome-wide mapping of Sox6 binding sites in skeletal muscle reveals both direct and indirect regulation of muscle terminal differentiation by Sox6. *BMC developmental biology*, 11, 59.
- ANDREWS, J. L., ZHANG, X., MCCARTHY, J. J., MCDEARMON, E. L., HORNBERGER, T. A., RUSSELL, B., CAMPBELL, K. S., ARBOGAST, S., REID, M. B. & WALKER, J. R. 2010. CLOCK and BMAL1 regulate MyoD and are necessary for maintenance of skeletal muscle phenotype and function. *Proceedings of the National Academy of Sciences*, 107, 19090-19095.
- ANDRUSHKO, J. W., GOULD, L. A. & FARTHING, J. P. 2018a. Contralateral effects of unilateral training: sparing of muscle strength and size after immobilization. *Applied Physiology, Nutrition, and Metabolism*, 43, 1131-1139.
- ANDRUSHKO, J. W., LANOVAZ, J. L., BJÖRKMAN, K. M., KONTULAINEN, S. A. & FARTHING, J. P. 2018b. Unilateral strength training leads to muscle-specific sparing effects during opposite homologous limb immobilization. *Journal of Applied Physiology*, 124, 866-876.
- ANTONIO, J. & GONYEA, W. J. 1993. Progressive stretch overload of skeletal muscle results in hypertrophy before hyperplasia. *Journal of applied physiology*, 75, 1263-1271.
- ANTONIO, J. & GONYEA, W. J. 1994. Muscle fiber splitting in stretch-enlarged avian muscle. *Medicine and science in sports and exercise*, 26, 973.

- ARABI, A., RUSTUM, C., HALLBERG, E. & WRIGHT, A. P. 2003. Accumulation of c-Myc and proteasomes at the nucleoli of cells containing elevated c-Myc protein levels. *Journal of cell science*, 116, 1707-1717.
- ARABI, A., WU, S., RIDDERSTRÅLE, K., BIERHOFF, H., SHIUE, C., FATYOL, K., FAHLÉN, S., HYDBRING, P., SÖDERBERG, O. & GRUMMT, I. 2005. c-Myc associates with ribosomal DNA and activates RNA polymerase I transcription. *Nature cell biology*, 7, 303-310.
- ARAKI, E., LIPES, M. A., PATTI, M.-E., BRÜNING, J. C., HAAG III, B., JOHNSON, R. S. & KAHN, C. R. 1994. Alternative pathway of insulin signalling in mice with targeted disruption of the IRS-1 gene. *Nature*, 372, 186-190.
- ASCENZI, F., BARBERI, L., DOBROWOLNY, G., VILLA NOVA BACURAU, A., NICOLETTI, C., RIZZUTO, E., ROSENTHAL, N., SCICCHITANO, B. M. & MUSARÒ, A. 2019. Effects of IGF-1 isoforms on muscle growth and sarcopenia. *Aging cell*, 18, e12954.
- ASHLEY, Z., SALMONS, S., BONCOMPAGNI, S., PROTASI, F., RUSSOLD, M., LANMULLER, H., MAYR, W., SUTHERLAND, H. & JARVIS, J. C. 2007a. Effects of chronic electrical stimulation on long-term denervated muscles of the rabbit hind limb. *Journal of Muscle Research and Cell Motility*, 28, 203-217.
- ASHLEY, Z., SUTHERLAND, H., LANMULLER, H., RUSSOLD, M., UNGER, E., BIJAK, M., MAYR, W., BONCOMPAGNI, S., PROTASI, F. & SALMONS, S. 2007b. Atrophy, but not necrosis, in rabbit skeletal muscle denervated for periods up to one year. *American Journal of Physiology-Cell Physiology*, 292, C440-C451.
- ASLANIDI, O. V., NIKOLAIDOU, T., ZHAO, J., SMAILL, B. H., GILBERT, S. H., HOLDEN, A. V., LOWE, T., WITHERS, P. J., STEPHENSON, R. S. & JARVIS, J. C. 2012. Application of micro-computed tomography with iodine staining to cardiac imaging, segmentation, and computational model development. *IEEE transactions on medical imaging*, 32, 8-17.
- ATHERTON, P. J., BABRAJ, J. A., SMITH, K., SINGH, J., RENNIE, M. J. & WACKERHAGE, H. 2005. Selective activation of AMPK-PGC-1 α or PKB-TSC2-mTOR signaling can explain specific adaptive responses to endurance or resistance training-like electrical muscle stimulation. *The FASEB journal*, 19, 1-23.
- AUBERT, M., O'DONOHUE, M.-F., LEBARON, S. & GLEIZES, P.-E. 2018. Pre-ribosomal RNA processing in human cells: from mechanisms to congenital diseases. *Biomolecules*, 8, 123.
- AUREILLE, J., BUFFIÈRE-RIBOT, V., HARVEY, B. E., BOYAULT, C., PERNET, L., ANDERSEN, T., BACOLA, G., BALLAND, M., FRABOULET, S. & VAN LANDEGHEM, L. 2019. Nuclear envelope deformation controls cell cycle progression in response to mechanical force. *EMBO reports*, 20, e48084.
- BAAR, K. 2010. Epigenetic control of skeletal muscle fibre type. *Acta physiologica*, 199, 477-487.
- BAAR, K. & ESSER, K. 1999a. Phosphorylation of p70(S6k) correlates with increased skeletal muscle mass following resistance exercise. *Am J Physiol*, 276, C120-7.
- BAAR, K. & ESSER, K. 1999b. Phosphorylation of p70S6k correlates with increased skeletal muscle mass following resistance exercise. *American Journal of Physiology-Cell Physiology*, 276, C120-C127.
- BAAR, K., WENDE, A. R., JONES, T. E., MARISON, M., NOLTE, L. A., CHEN, M., KELLY, D. P. & HOLLOSZY, J. O. 2002. Adaptations of skeletal muscle to exercise: rapid increase in the transcriptional coactivator PGC-1. *The FASEB journal*, 16, 1879-1886.
- BACHMAN, J. F., KLOSE, A., LIU, W., PARIS, N. D., BLANC, R. S., SCHMALZ, M., KNAPP, E. & CHAKKALAKAL, J. V. 2018. Prepubertal skeletal muscle growth requires Pax7-expressing satellite cell-derived myonuclear contribution. *Development*, 145.
- BAEHR, L. M., HUGHES, D. C., LYNCH, S. A., VAN HAVER, D., MAIA, T. M., MARSHALL, A. G., RADOSHEVICH, L., IMPENS, F., WADDELL, D. S. & BODINE, S. C. 2021. Identification of the MuRF1 skeletal muscle ubiquitylome through quantitative proteomics. *Function*, 2, zqab029.

- BAEHR, L. M., TUNZI, M. & BODINE, S. C. 2014. Muscle hypertrophy is associated with increases in proteasome activity that is independent of MuRF1 and MAFbx expression. *Frontiers in physiology*, 5, 69.
- BAEHR, L. M., WEST, D. W., MARCOTTE, G., MARSHALL, A. G., DE SOUSA, L. G., BAAR, K. & BODINE, S. C. 2016. Age-related deficits in skeletal muscle recovery following disuse are associated with neuromuscular junction instability and ER stress, not impaired protein synthesis. *Aging (Albany NY)*, 8, 127.
- BAEHR, L. M., WEST, D. W., MARSHALL, A. G., MARCOTTE, G. R., BAAR, K. & BODINE, S. C. 2017. Muscle-specific and age-related changes in protein synthesis and protein degradation in response to hindlimb unloading in rats. *Journal of applied physiology*, 122, 1336-1350.
- BALDWIN, K., KLINKERFUSS, G., TERJUNG, R., MOLE, P. & HOLLOSZY, J. 1972. Respiratory capacity of white, red, and intermediate muscle: adaptative response to exercise. *American Journal of Physiology-Legacy Content*, 222, 373-378.
- BANSAL, D., MIYAKE, K., VOGEL, S. S., GROH, S., CHEN, C.-C., WILLIAMSON, R., MCNEIL, P. L. & CAMPBELL, K. P. 2003. Defective membrane repair in dysferlin-deficient muscular dystrophy. *Nature*, 423, 168-172.
- BASKIN, K. K., WINDERS, B. R. & OLSON, E. N. 2015. Muscle as a “mediator” of systemic metabolism. *Cell metabolism*, 21, 237-248.
- BASS, J. J., HARDY, E. J., INNS, T. B., WILKINSON, D. J., PIASECKI, M., MORRIS, R. H., SPICER, A., SALE, C., SMITH, K. & AHERTON, P. J. 2021. Atrophy Resistant vs. Atrophy Susceptible skeletal muscles: “ARAS” as a novel experimental paradigm to study the mechanisms of human disuse atrophy. *Frontiers in Physiology*, 12, 545.
- BEITER, T., NIEß, A. M. & MOSER, D. 2020. Transcriptional memory in skeletal muscle. Don't forget (to) exercise. *Journal of cellular physiology*, 235, 5476-5489.
- BELOVA, S., MOCHALOVA, E. & NEMIROVSKAYA, T. 2020. The Role of Class IIa HDACs in the Expression of E3 Ligases ATROGIN-1/MAFbx and MuRF1 under Muscle Unloading. *Biochemistry (Moscow), Supplement Series A: Membrane and Cell Biology*, 14, 74-80.
- BENTZINGER, C. F., ROMANINO, K., CLOËTTA, D., LIN, S., MASCARENHAS, J. B., OLIVERI, F., XIA, J., CASANOVA, E., COSTA, C. F. & BRINK, M. 2008. Skeletal muscle-specific ablation of raptor, but not of rictor, causes metabolic changes and results in muscle dystrophy. *Cell metabolism*, 8, 411-424.
- BERGMANN, O. & JOVINGE, S. 2012. Isolation of cardiomyocyte nuclei from post-mortem tissue. *JoVE (Journal of Visualized Experiments)*, e4205.
- BERGMANN, O., ZDUNEK, S., ALKASS, K., DRUID, H., BERNARD, S. & FRISÉN, J. 2011. Identification of cardiomyocyte nuclei and assessment of ploidy for the analysis of cell turnover. *Experimental cell research*, 317, 188-194.
- BERGMEISTER, K. D., GRÖGER, M., AMAN, M., WILLENSDORFER, A., MANZANO-SZALAI, K., SALMINGER, S. & ASZMANN, O. C. 2016. Automated muscle fiber type population analysis with ImageJ of whole rat muscles using rapid myosin heavy chain immunohistochemistry. *Muscle & Nerve*, 54, 292-299.
- BERGSTRÖM, J. 1975. Percutaneous needle biopsy of skeletal muscle in physiological and clinical research. *Scandinavian journal of clinical and laboratory investigation*, 35, 609-616.
- BERMAN, A. J., THOREEN, C. C., DEDEIC, Z., CHETTLE, J., ROUX, P. P. & BLAGDEN, S. P. 2021. Controversies around the function of LARP1. *RNA biology*, 18, 207-217.
- BERTRAND, A. T., ZIAEI, S., EHRET, C., DUCHEMIN, H., MAMCHAOU, K., BIGOT, A., MAYER, M., QUIJANO-ROY, S., DESGUERRE, I. & LAINÉ, J. 2014. Cellular microenvironments reveal defective mechanosensing responses and elevated YAP signaling in LMNA-mutated muscle precursors. *Journal of cell science*, 127, 2873-2884.
- BIJAK, M., SCHMOLL, M., JARVIS, J. C., UNGER, E. & LANMÜLLER, H. 2020. MiniVStimA: A miniaturized easy to use implantable electrical stimulator for small laboratory animals. *Plos one*, 15, e0241638.

- BIRESSI, S., MOLINARO, M. & COSSU, G. 2007. Cellular heterogeneity during vertebrate skeletal muscle development. *Developmental biology*, 308, 281-293.
- BISHT, B., GOEL, H. & DEY, C. 2007. Focal adhesion kinase regulates insulin resistance in skeletal muscle. *Diabetologia*, 50, 1058-1069.
- BLAAUW, B., CANATO, M., AGATEA, L., TONIOLO, L., MAMMUCARI, C., MASIERO, E., ABRAHAM, R., SANDRI, M., SCHIAFFINO, S. & REGGIANI, C. 2009. Inducible activation of Akt increases skeletal muscle mass and force without satellite cell activation. *The FASEB journal*, 23, 3896-3905.
- BLADT, F., RIETHMACHER, D., ISENMANN, S., AGUZZI, A. & BIRCHMEIER, C. 1995. Essential role for the c-met receptor in the migration of myogenic precursor cells into the limb bud. *Nature*, 376, 768-771.
- BLAU, H. M., WEBSTER, C., PAVLATH, G. K. & CHIU, C.-P. 1985. Evidence for defective myoblasts in Duchenne muscular dystrophy. *Gene Expression in Muscle*. Springer.
- BLOCQUIAUX, S., GORSKI, T., VAN ROIE, E., RAMAEKERS, M., VAN THIENEN, R., NIELENS, H., DELECLUSE, C., DE BOCK, K. & THOMIS, M. 2020. The effect of resistance training, detraining and retraining on muscle strength and power, myofibre size, satellite cells and myonuclei in older men. *Experimental Gerontology*, 133, 110860.
- BOBER, E., FRANZ, T., ARNOLD, H.-H., GRUSS, P. & TREMBLAY, P. 1994. Pax-3 is required for the development of limb muscles: a possible role for the migration of dermomyotomal muscle progenitor cells. *Development*, 120, 603-612.
- BODINE, S. C. & BAEHR, L. M. 2014. Skeletal muscle atrophy and the E3 ubiquitin ligases MuRF1 and MAFbx/atrogen-1. *American Journal of Physiology-Endocrinology and Metabolism*, 307, E469-E484.
- BODINE, S. C., LATRES, E., BAUMHUETER, S., LAI, V. K.-M., NUNEZ, L., CLARKE, B. A., POUEYMIROU, W. T., PANARO, F. J., NA, E. & DHARMARAJAN, K. 2001a. Identification of ubiquitin ligases required for skeletal muscle atrophy. *Science*, 294, 1704-1708.
- BODINE, S. C. & PIEROTTI, D. J. 1996. Myosin heavy chain mRNA and protein expression in single fibers of the rat soleus following reinnervation. *Neuroscience letters*, 215, 13-16.
- BODINE, S. C., STITT, T. N., GONZALEZ, M., KLINE, W. O., STOVER, G. L., BAUERLEIN, R., ZLOTCHENKO, E., SCRIMGEOUR, A., LAWRENCE, J. C. & GLASS, D. J. 2001b. Akt/mTOR pathway is a crucial regulator of skeletal muscle hypertrophy and can prevent muscle atrophy in vivo. *Nature cell biology*, 3, 1014-1019.
- BONAFIGLIA, J. T., MENZIES, K. J. & GURD, B. J. 2019. Gene expression variability in human skeletal muscle transcriptome responses to acute resistance exercise. *Experimental physiology*, 104, 625-629.
- BONNE, G., DI BARLETTA, M. R., VARNOUS, S., BÉCANE, H.-M., HAMMOUDA, E.-H., MERLINI, L., MUNTONI, F., GREENBERG, C. R., GARY, F. & URTIZBEREA, J.-A. 1999. Mutations in the gene encoding lamin A/C cause autosomal dominant Emery-Dreifuss muscular dystrophy. *Nature genetics*, 21, 285-288.
- BOON, K., CARON, H. N., VAN ASPEREN, R., VALENTIJN, L., HERMUS, M. C., VAN SLUIS, P., ROOBEEK, I., WEIS, I., VOUTE, P. & SCHWAB, M. 2001. N-myc enhances the expression of a large set of genes functioning in ribosome biogenesis and protein synthesis. *The EMBO journal*, 20, 1383-1393.
- BOPPART, M. D. & MAHMASSANI, Z. S. 2019. Integrin signaling: linking mechanical stimulation to skeletal muscle hypertrophy. *American Journal of Physiology-Cell Physiology*, 317, C629-C641.
- BRAZIL, D. P., CHURCH, R. H., SURAE, S., GODSON, C. & MARTIN, F. 2015. BMP signalling: agony and antagonism in the family. *Trends in cell biology*, 25, 249-264.
- BRIGGS, M. M. & SCHACHAT, F. 2002. The superfast extraocular myosin (MYH13) is localized to the innervation zone in both the global and orbital layers of rabbit extraocular muscle. *Journal of experimental biology*, 205, 3133-3142.

- BROOK, M. S., WILKINSON, D. J., SMITH, K. & ATHERTON, P. J. 2019. It's not just about protein turnover: the role of ribosomal biogenesis and satellite cells in the regulation of skeletal muscle hypertrophy. *Eur J Sport Sci*, 19, 952-963.
- BROOKE, M. H. & KAISER, K. K. 1970. Muscle fiber types: how many and what kind? *Archives of neurology*, 23, 369-379.
- BROOKS, M. J., HAJIRA, A., MOHAMED, J. S. & ALWAY, S. E. 2018. Voluntary wheel running increases satellite cell abundance and improves recovery from disuse in gastrocnemius muscles from mice. *Journal of Applied Physiology*, 124, 1616-1628.
- BROWN, M. D., COTTER, M. A., HUDLICKÁ, O. & VRBOVÁ, G. 1976. The effects of different patterns of muscle activity on capillary density, mechanical properties and structure of slow and fast rabbit muscles. *Pflügers Archiv*, 361, 241-250.
- BROWNSON, C., LITTLE, P., JARVIS, J. C. & SALMONS, S. 1992. Reciprocal changes in myosin isoform mRNAs of rabbit skeletal muscle in response to the initiation and cessation of chronic electrical stimulation. *Muscle & Nerve: Official Journal of the American Association of Electrodiagnostic Medicine*, 15, 694-700.
- BRUNN, A. 2018. The complex pericentriolar material 1 protein allows differentiation between myonuclei and nuclei of satellite cells of the skeletal muscle. *Acta Physiologica*, 223, e13103.
- BRUUSGAARD, J., LIESTØL, K. & GUNDERSEN, K. 2006. Distribution of myonuclei and microtubules in live muscle fibers of young, middle-aged, and old mice. *Journal of applied physiology*, 100, 2024-2030.
- BRUUSGAARD, J. C., EGNER, I. M., LARSEN, T. K., DUPRE-AUCOUTURIER, S., DESPLANCHES, D. & GUNDERSEN, K. 2012. No change in myonuclear number during muscle unloading and reloading. *Journal of Applied Physiology*, 113, 290-296.
- BRUUSGAARD, J. C. & GUNDERSEN, K. 2008. In vivo time-lapse microscopy reveals no loss of murine myonuclei during weeks of muscle atrophy. *The Journal of clinical investigation*, 118, 1450-1457.
- BRUUSGAARD, J. C., JOHANSEN, I., EGNER, I., RANA, Z. & GUNDERSEN, K. 2010. Myonuclei acquired by overload exercise precede hypertrophy and are not lost on detraining. *Proceedings of the National Academy of Sciences*, 107, 15111-15116.
- BUCKINGHAM, M., BAJARD, L., CHANG, T., DAUBAS, P., HADCHOUEL, J., MEILHAC, S., MONTARRAS, D., ROCAN COURT, D. & RELAIX, F. 2003. The formation of skeletal muscle: from somite to limb. *Journal of anatomy*, 202, 59-68.
- BURDEN, S. J., HUIJBERS, M. G. & REMEDIO, L. 2018. Fundamental molecules and mechanisms for forming and maintaining neuromuscular synapses. *International journal of molecular sciences*, 19, 490.
- BURKE, S. K., FENTON, A. I., KONOKHOVA, Y. & HEPPLER, R. T. 2021. Variation in muscle and neuromuscular junction morphology between atrophy-resistant and atrophy-prone muscles supports failed re-innervation in aging muscle atrophy. *Experimental gerontology*, 156, 111613.
- CALL, J. A., MCKEEHEN, J. N., NOVOTNY, S. A. & LOWE, D. A. 2010. Progressive resistance voluntary wheel running in the mdx mouse. *Muscle & nerve*, 42, 871-880.
- CALL, J. A., WILSON, R. J., LAKER, R. C., ZHANG, M., KUNDU, M. & YAN, Z. 2017. Ulk1-mediated autophagy plays an essential role in mitochondrial remodeling and functional regeneration of skeletal muscle. *American Journal of Physiology-Cell Physiology*, 312, C724-C732.
- CAMPBELL, K. J. & WHITE, R. J. 2014. MYC regulation of cell growth through control of transcription by RNA polymerases I and III. *Cold Spring Harbor Perspectives in Medicine*, 4, a018408.
- CARDASIS, C. A. & COOPER, G. W. 1975. An analysis of nuclear numbers in individual muscle fibers during differentiation and growth: A satellite cell-muscle fiber growth unit. *Journal of Experimental Zoology*, 191, 347-357.

- CARLING, D. & HARDIE, D. G. 1989. The substrate and sequence specificity of the AMP-activated protein kinase. Phosphorylation of glycogen synthase and phosphorylase kinase. *Biochim Biophys Acta*, 1012, 81-6.
- CASTETS, P., LIN, S., RION, N., DI FULVIO, S., ROMANINO, K., GURIDI, M., FRANK, S., TINTIGNAC, L. A., SINNREICH, M. & RÜEGG, M. A. 2013. Sustained activation of mTORC1 in skeletal muscle inhibits constitutive and starvation-induced autophagy and causes a severe, late-onset myopathy. *Cell metabolism*, 17, 731-744.
- CASTRO, A. F., REBHUN, J. F., CLARK, G. J. & QUILLIAM, L. A. 2003. Rheb binds tuberous sclerosis complex 2 (TSC2) and promotes S6 kinase activation in a rapamycin-and farnesylation-dependent manner. *Journal of Biological Chemistry*, 278, 32493-32496.
- CHAILLOU, T., JACKSON, J. R., ENGLAND, J. H., KIRBY, T. J., RICHARDS-WHITE, J., ESSER, K. A., DUPONT-VERSTEEGDEN, E. E. & MCCARTHY, J. J. 2015. Identification of a conserved set of upregulated genes in mouse skeletal muscle hypertrophy and regrowth. *Journal of applied physiology*, 118, 86-97.
- CHAILLOU, T., LEE, J. D., ENGLAND, J. H., ESSER, K. A. & MCCARTHY, J. J. 2013. Time course of gene expression during mouse skeletal muscle hypertrophy. *Journal of applied physiology*.
- CHAL, J. & POURQUIÉ, O. 2017. Making muscle: skeletal myogenesis in vivo and in vitro. *Development*, 144, 2104-2122.
- CHAPMAN, M. A., ARIF, M., EMANUELSSON, E. B., REITZNER, S. M., LINDHOLM, M. E., MARDINOGLU, A. & SUNDBERG, C. J. 2020. Skeletal muscle transcriptomic comparison between long-term trained and untrained men and women. *Cell reports*, 31, 107808.
- CHARGE, S. B. & RUDNICKI, M. A. 2004. Cellular and molecular regulation of muscle regeneration. *Physiological reviews*, 84, 209-238.
- CHEN, C.-R., KANG, Y. & MASSAGUÉ, J. 2001. Defective repression of c-myc in breast cancer cells: a loss at the core of the transforming growth factor β growth arrest program. *Proceedings of the National Academy of Sciences*, 98, 992-999.
- CHEN, C.-R., KANG, Y., SIEGEL, P. M. & MASSAGUÉ, J. 2002. E2F4/5 and p107 as Smad cofactors linking the TGF β receptor to c-myc repression. *Cell*, 110, 19-32.
- CHEN, W., WANG, L., YOU, W. & SHAN, T. 2021. Myokines mediate the cross talk between skeletal muscle and other organs. *Journal of Cellular Physiology*, 236, 2393-2412.
- CHEN, X., LIU, M., TIAN, Y., LI, J., QI, Y., ZHAO, D., WU, Z., HUANG, M., WONG, C. C. & WANG, H.-W. 2018. Cryo-EM structure of human mTOR complex 2. *Cell research*, 28, 518-528.
- CHIN, E. R., OLSON, E. N., RICHARDSON, J. A., YANG, Q., HUMPHRIES, C., SHELTON, J. M., WU, H., ZHU, W., BASSEL-DUBY, R. & WILLIAMS, R. S. 1998. A calcineurin-dependent transcriptional pathway controls skeletal muscle fiber type. *Genes & development*, 12, 2499-2509.
- CHOLEWA, J., GUIMARÃES-FERREIRA, L., DA SILVA TEIXEIRA, T., NAIMO, M. A., ZHI, X., DE SÁ, R. B. D. P., LODETTI, A., CARDOZO, M. Q. & ZANCHI, N. E. 2014. Basic models modeling resistance training: an update for basic scientists interested in study skeletal muscle hypertrophy. *Journal of cellular physiology*, 229, 1148-1156.
- CLARKE, B. A., DRUJAN, D., WILLIS, M. S., MURPHY, L. O., CORPINA, R. A., BUROVA, E., RAKHILIN, S. V., STITT, T. N., PATTERSON, C. & LATRES, E. 2007. The E3 Ligase MuRF1 degrades myosin heavy chain protein in dexamethasone-treated skeletal muscle. *Cell metabolism*, 6, 376-385.
- CLEMMONS, D. R. 2018. 40 YEARS OF IGF1: Role of IGF-binding proteins in regulating IGF responses to changes in metabolism. *Journal of molecular endocrinology*, 61, T139-T169.
- COLE, M. D. & COWLING, V. H. 2008. Transcription-independent functions of MYC: regulation of translation and DNA replication. *Nature reviews Molecular cell biology*, 9, 810-815.
- CONCEICAO, M. S., VECHIN, F. C., LIXANDRAO, M., DAMAS, F., LIBARDI, C. A., TRICOLI, V., ROSCHEL, H., CAMERA, D. & UGRINOWITSCH, C. 2018. Muscle fiber hypertrophy and myonuclei addition: a systematic review and meta-analysis.

- CONTREPOIS, K., WU, S., MONEGHETTI, K. J., HORNBERG, D., AHADI, S., TSAI, M.-S., METWALLY, A. A., WEI, E., LEE-MCMULLEN, B. & QUIJADA, J. V. 2020. Molecular choreography of acute exercise. *Cell*, 181, 1112-1130. e16.
- CORMERY, B., PONS, F., MARINI, J.-F. & GARDINER, P. F. 2000. Myosin heavy chains in fibers of TTX-paralyzed rat soleus and medial gastrocnemius muscles. *Journal of Applied Physiology*, 88, 66-76.
- COSGROVE, B. D., LOEBEL, C., DRISCOLL, T. P., TSINMAN, T. K., DAI, E. N., HEO, S.-J., DYMENT, N. A., BURDICK, J. A. & MAUCK, R. L. 2021. Nuclear envelope wrinkling predicts mesenchymal progenitor cell mechano-response in 2D and 3D microenvironments. *Biomaterials*, 270, 120662.
- COSSU, G. & TAJBAKSH, S. 2007. Oriented cell divisions and muscle satellite cell heterogeneity. *Cell*, 129, 859-861.
- CRAMER, A. A., PRASAD, V., EFTESTØL, E., SONG, T., HANSSON, K.-A., DUGDALE, H. F., SADAYAPPAN, S., OCHALA, J., GUNDERSEN, K. & MILLAY, D. P. 2020. Nuclear numbers in syncytial muscle fibers promote size but limit the development of larger myonuclear domains. *Nature communications*, 11, 1-14.
- CRAMERI, R., AAGAARD, P., QVORTRUP, K., LANGBERG, H., OLESEN, J. & KJÆR, M. 2007. Myofibre damage in human skeletal muscle: effects of electrical stimulation versus voluntary contraction. *The Journal of physiology*, 583, 365-380.
- CUI, D., DRAKE, J. C., WILSON, R. J., SHUTE, R. J., LEWELLEN, B., ZHANG, M., ZHAO, H., SABIK, O. L., ONENGUT, S. & BERR, S. S. 2020. A novel voluntary weightlifting model in mice promotes muscle adaptation and insulin sensitivity with simultaneous enhancement of autophagy and mTOR pathway. *The FASEB Journal*, 34, 7330-7344.
- CUTLER, A. A., JACKSON, J. B., CORBETT, A. H. & PAVLATH, G. K. 2018. Non-equivalence of nuclear import among nuclei in multinucleated skeletal muscle cells. *Journal of cell science*, 131.
- D'HULST, G., MASSCHELEIN, E., PALMER, A., BAR-NUR, O. & DE BOCK, K. 2020. Exercise promotes satellite cell contribution to myofibers in a load-dependent manner. *The FASEB Journal*, 34, 1-1.
- DALBO, V. J., ROBERTS, M. D., SUNDERLAND, K. L., POOLE, C. N., STOUT, J. R., BECK, T. W., BEMBEN, M. & KERKSICK, C. M. 2011. Acute loading and aging effects on myostatin pathway biomarkers in human skeletal muscle after three sequential bouts of resistance exercise. *Journals of Gerontology Series A: Biomedical Sciences and Medical Sciences*, 66, 855-865.
- DAMAS, F., LIBARDI, C. A., UGRINOWITSCH, C., VECHIN, F. C., LIXANDRÃO, M. E., SNIJDERS, T., NEDERVEEN, J. P., BACURAU, A. V., BRUM, P. & TRICOLI, V. 2018a. Early-and later-phases satellite cell responses and myonuclear content with resistance training in young men. *PloS one*, 13, e0191039.
- DAMAS, F., UGRINOWITSCH, C., LIBARDI, C. A., JANNIG, P. R., HECTOR, A. J., MCGLORY, C., LIXANDRÃO, M. E., VECHIN, F. C., MONTENEGRO, H. & TRICOLI, V. 2018b. Resistance training in young men induces muscle transcriptome-wide changes associated with muscle structure and metabolism refining the response to exercise-induced stress. *European journal of applied physiology*, 118, 2607-2616.
- DAMMERMANN, A., MÜLLER-REICHERT, T., PELLETIER, L., HABERMANN, B., DESAI, A. & OEGEMA, K. 2004. Centriole assembly requires both centriolar and pericentriolar material proteins. *Developmental cell*, 7, 815-829.
- DAS NEVES, W., DE OLIVEIRA, L., DA SILVA, R., ALVES, C. & LANCHETA JR, A. 2018. Fasting: a major limitation for resistance exercise training effects in rodents. *Brazilian Journal of Medical and Biological Research*, 51.
- DAVEY, J. R., WATT, K. I., PARKER, B. L., CHAUDHURI, R., RYALL, J. G., CUNNINGHAM, L., QIAN, H., SARTORELLI, V., SANDRI, M. & CHAMBERLAIN, J. 2016. Integrated expression analysis of muscle hypertrophy identifies *Asb2* as a negative regulator of muscle mass. *JCI insight*, 1.

- DAVIS, R. J. 1993. The mitogen-activated protein kinase signal transduction pathway. *Journal of Biological Chemistry*, 268, 14553-14556.
- DEFREITAS, J. M., BECK, T. W., STOCK, M. S., DILLON, M. A. & KASISHKE, P. R. 2011. An examination of the time course of training-induced skeletal muscle hypertrophy. *European journal of applied physiology*, 111, 2785-2790.
- DEMONBREUN, A. R., BIERSMITH, B. H. & MCNALLY, E. M. Membrane fusion in muscle development and repair. *Seminars in cell & developmental biology*, 2015. Elsevier, 48-56.
- DEMONBREUN, A. R., FAHRENBACH, J. P., DEVEAUX, K., EARLEY, J. U., PYTEL, P. & MCNALLY, E. M. 2011. Impaired muscle growth and response to insulin-like growth factor 1 in dysferlin-mediated muscular dystrophy. *Human molecular genetics*, 20, 779-789.
- DESCHENES, M. R., ROBY, M. A. & GLASS, E. K. 2011. Aging influences adaptations of the neuromuscular junction to endurance training. *Neuroscience*, 190, 56-66.
- DESGEORGES, T., LIOT, S., LYON, S., BOUVIERE, J., KEMMEL, A., TRIGNOL, A., ROUSSEAU, D., CHAPUIS, B., GONDIN, J. & MOUNIER, R. 2019. Open-CSAM, a new tool for semi-automated analysis of myofiber cross-sectional area in regenerating adult skeletal muscle. *Skeletal muscle*, 9, 2.
- DESHAIES, R. J. & JOAZEIRO, C. A. 2009. RING domain E3 ubiquitin ligases. *Annual review of biochemistry*, 78.
- DESHMUKH, A., STEENBERG, D., HOSTRUP, M., BIRK, J., LARSEN, J., SANTOS, A., KJØBSTED, R., HINGST, J., SCHÉELE, C. & MURGIA, M. 2021. Deep muscle-proteomic analysis of freeze-dried human muscle biopsies reveals fiber type-specific adaptations to exercise training. *Nature communications*, 12, 1-15.
- DÍAZ, B. B., GONZÁLEZ, D. A., GANNAR, F., PÉREZ, M. C. R. & DE LEÓN, A. C. 2018. Myokines, physical activity, insulin resistance and autoimmune diseases. *Immunology letters*, 203, 1-5.
- DICKINSON, J. M., D'LUGOS, A. C., NAYMIK, M. A., SINIARD, A. L., WOLFE, A. J., CURTIS, D. R., HUENTELMAN, M. J. & CARROLL, C. C. 2018. Transcriptome response of human skeletal muscle to divergent exercise stimuli. *Journal of Applied Physiology*, 124, 1529-1540.
- DIN, U., BROOK, M., SELBY, A., QUINLAN, J., BOEREBOOM, C., ABDULLA, H., FRANCHI, M., NARICI, M. V., PHILLIPS, B. E. & WILLIAMS, J. 2019. A double-blind placebo controlled trial into the impacts of HMB supplementation and exercise on free-living muscle protein synthesis, muscle mass and function, in older adults. *Clinical Nutrition*, 38, 2071-2078.
- DOBIN, A., DAVIS, C. A., SCHLESINGER, F., DRENKOW, J., ZALESKI, C., JHA, S., BATUT, P., CHAISSON, M. & GINGERAS, T. R. 2013. STAR: ultrafast universal RNA-seq aligner. *Bioinformatics*, 29, 15-21.
- DOHERTY, K. R., DEMONBREUN, A. R., WALLACE, G. Q., CAVE, A., POSEY, A. D., HERETIS, K., PYTEL, P. & MCNALLY, E. M. 2008. The endocytic recycling protein EHD2 interacts with myoferlin to regulate myoblast fusion. *Journal of Biological Chemistry*, 283, 20252-20260.
- DOS SANTOS, M., BACKER, S., AURADÉ, F., WONG, M., WURMSER, M., PIERRE, R., LANGA, F., DO CRUZEIRO, M., SCHMITT, A. & CONCORDET, J.-P. 2021. A fast Myh super enhancer dictates adult muscle fiber phenotype through competitive interactions with the fast Myh genes. *bioRxiv*.
- DOS SANTOS, M., BACKER, S., SAINTPIERRE, B., IZAC, B., ANDRIEU, M., LETOURNEUR, F., RELAX, F., SOTIROPOULOS, A. & MAIRE, P. 2020. Single-nucleus RNA-seq and FISH identify coordinated transcriptional activity in mammalian myofibers. *Nature communications*, 11, 1-16.
- DREYER, H. C., FUJITA, S., CADENAS, J. G., CHINKES, D. L., VOLPI, E. & RASMUSSEN, B. B. 2006. Resistance exercise increases AMPK activity and reduces 4E-BP1 phosphorylation and protein synthesis in human skeletal muscle. *The Journal of physiology*, 576, 613-624.
- DUMONT, N. A., BENTZINGER, C. F., SINCENNES, M.-C. & RUDNICKI, M. A. 2015. Satellite cells and skeletal muscle regeneration. *Compr Physiol*, 5, 1027-1059.

- DUNCAN, N. D., WILLIAMS, D. A. & LYNCH, G. S. 1998. Adaptations in rat skeletal muscle following long-term resistance exercise training. *European journal of applied physiology and occupational physiology*, 77, 372-378.
- DUNGAN, C. M., MURACH, K. A., FRICK, K. K., JONES, S. R., CROW, S. E., ENGLUND, D. A., VECHETTI JR, I. J., FIGUEIREDO, V. C., LEVITAN, B. M. & SATIN, J. 2019. Elevated myonuclear density during skeletal muscle hypertrophy in response to training is reversed during detraining. *American Journal of Physiology-Cell Physiology*, 316, C649-C654.
- DUPONT-VERSTEEGDEN, E. E., STROTMAN, B. A., GURLEY, C. M., GADDY, D., KNOX, M., FLUCKEY, J. D. & PETERSON, C. A. 2006. Nuclear translocation of EndoG at the initiation of disuse muscle atrophy and apoptosis is specific to myonuclei. *Am J Physiol Regul Integr Comp Physiol*, 291, R1730-40.
- EDDINS, M. J., MARBLESTONE, J. G., KUMAR, K. S., LEACH, C. A., STERNER, D. E., MATTERN, M. R. & NICHOLSON, B. 2011. Targeting the ubiquitin E3 ligase MuRF1 to inhibit muscle atrophy. *Cell biochemistry and biophysics*, 60, 113-118.
- EFTESTØL, E., EGNER, I. M., LUNDE, I. G., ELLEFSEN, S., ANDERSEN, T., SJÅLAND, C., GUNDERSEN, K. & BRUUSGAARD, J. C. 2016. Increased hypertrophic response with increased mechanical load in skeletal muscles receiving identical activity patterns. *American Journal of Physiology-Cell Physiology*, 311, C616-C629.
- EGGERS, B., SCHORK, K., TUREWICZ, M., BARKOVITS, K., EISENACHER, M., SCHRÖDER, R., CLEMEN, C. S. & MARCUS, K. 2021. Advanced Fiber Type-Specific Protein Profiles Derived from Adult Murine Skeletal Muscle. *Proteomes*, 9, 28.
- EGGINTON, S. & HUDLICKA, O. 1999. Early changes in performance, blood flow and capillary fine structure in rat fast muscles induced by electrical stimulation. *The Journal of physiology*, 515, 265-275.
- EGNER, I. M., BRUUSGAARD, J. C. & GUNDERSEN, K. 2016. Satellite cell depletion prevents fiber hypertrophy in skeletal muscle. *Development*, 143, 2898-2906.
- EGNER, I. M., BRUUSGAARD, J. C. & GUNDERSEN, K. 2017. An apparent lack of effect of satellite cell depletion on hypertrophy could be due to methodological limitations. Response to 'Methodological issues limit interpretation of negative effects of satellite cell depletion on adult muscle hypertrophy'. *Development (Cambridge, England)*, 144, 1365.
- EHLEN, J. C., BRAGER, A. J., BAGGS, J., PINCKNEY, L., GRAY, C. L., DEBRUYNE, J. P., ESSER, K. A., TAKAHASHI, J. S. & PAUL, K. N. 2017. Bmal1 function in skeletal muscle regulates sleep. *Elife*, 6, e26557.
- EISENBERG, B. R. & SALMONS, S. 1981. The reorganization of subcellular structure in muscle undergoing fast-to-slow type transformation. *Cell and tissue research*, 220, 449-471.
- ELDRIDGE, A. & O'BRIEN, T. 2010. Therapeutic strategies within the ubiquitin proteasome system. *Cell Death & Differentiation*, 17, 4-13.
- ELOSEGUI-ARTOLA, A., ANDREU, I., BEEDLE, A. E., LEZAMIZ, A., UROZ, M., KOSMALSKA, A. J., ORIA, R., KECHAGIA, J. Z., RICO-LASTRES, P. & LE ROUX, A.-L. 2017. Force triggers YAP nuclear entry by regulating transport across nuclear pores. *Cell*, 171, 1397-1410. e14.
- ENCARNACION-RIVERA, L., FOLTZ, S., HARTZELL, H. C. & CHOO, H. 2020. Myosoft: an automated muscle histology analysis tool using machine learning algorithm utilizing FIJI/ImageJ software. *PloS one*, 15, e0229041.
- ENGLUND, D. A., FIGUEIREDO, V. C., DUNGAN, C. M., MURACH, K. A., PECK, B. D., PETROSINO, J. M., BRIGHTWELL, C. R., DUPONT, A. M., NEAL, A. C. & FRY, C. S. 2021. Satellite cell depletion disrupts transcriptional coordination and muscle adaptation to exercise. *Function*, 2, zqaa033.
- ENGLUND, D. A., MURACH, K. A., DUNGAN, C. M., FIGUEIREDO, V. C., VECHETTI, I. J., DUPONT-VERSTEEGDEN, E. E., MCCARTHY, J. J. & PETERSON, C. A. 2019a. Depletion of resident muscle stem cells inhibits muscle fiber hypertrophy induced by lifelong physical activity. *bioRxiv*, 588731.

- ENGLUND, D. A., MURACH, K. A., DUNGAN, C. M., FIGUEIREDO, V. C., VECHETTI JR, I. J., DUPONT-VERSTEEGDEN, E. E., MCCARTHY, J. J. & PETERSON, C. A. 2020. Depletion of resident muscle stem cells negatively impacts running volume, physical function and muscle hypertrophy in response to lifelong physical activity. *American Journal of Physiology-Cell Physiology*.
- ENGLUND, D. A., PECK, B. D., MURACH, K. A., NEAL, A. C., CALDWELL, H. A., MCCARTHY, J. J., PETERSON, C. A. & DUPONT-VERSTEEGDEN, E. E. 2019b. Resident muscle stem cells are not required for testosterone-induced skeletal muscle hypertrophy. *American Journal of Physiology-Cell Physiology*, 317, C719-C724.
- ENYEDI, B. & NIETHAMMER, P. 2016. A Case for the Nuclear Membrane as a Mechanotransducer. *Cellular and molecular bioengineering*, 9, 247-251.
- EPPLEY, Z., KIM, J. & RUSSELL, B. 1993. A myogenic regulatory gene, qmf1, is expressed by adult myonuclei after injury. *American Journal of Physiology-Cell Physiology*, 265, C397-C405.
- ESPIGAT-GEORGER, A., DYACHUK, V., CHEMIN, C., EMORINE, L. & MERDES, A. 2016. Nuclear alignment in myotubes requires centrosome proteins recruited by nesprin-1. *Journal of cell science*, 129, 4227-4237.
- EVANS, M. J. & SCARPULLA, R. 1989. Interaction of nuclear factors with multiple sites in the somatic cytochrome c promoter. Characterization of upstream NRF-1, ATF, and intron Sp1 recognition sequences. *Journal of Biological Chemistry*, 264, 14361-14368.
- EVANS, M. J. & SCARPULLA, R. C. 1990. NRF-1: a trans-activator of nuclear-encoded respiratory genes in animal cells. *Genes & development*, 4, 1023-1034.
- FAN, M., RHEE, J., ST-PIERRE, J., HANDSCHIN, C., PUIGSERVER, P., LIN, J., JÄEGER, S., ERDJUMENT-BROMAGE, H., TEMPST, P. & SPIEGELMAN, B. M. 2004. Suppression of mitochondrial respiration through recruitment of p160 myb binding protein to PGC-1 α : modulation by p38 MAPK. *Genes & development*, 18, 278-289.
- FANT, X., SRSEN, V., ESPIGAT-GEORGER, A. & MERDES, A. 2009. Nuclei of non-muscle cells bind centrosome proteins upon fusion with differentiating myoblasts. *PLoS One*, 4, e8303.
- FARTHING, J. P., KRENTZ, J. R. & MAGNUS, C. R. 2009. Strength training the free limb attenuates strength loss during unilateral immobilization. *Journal of Applied Physiology*, 106, 830-836.
- FAYH, A. P. T., DE SOUSA, I. M. & GONZALEZ, M. C. 2020. New insights on how and where to measure muscle mass. *Current Opinion in Supportive and Palliative Care*, 14, 316-323.
- FEIGE, P., BRUN, C. E., RITSO, M. & RUDNICKI, M. A. 2018. Orienting muscle stem cells for regeneration in homeostasis, aging, and disease. *Cell Stem Cell*, 23, 653-664.
- FERNÁNDEZ-VERDEJO, R., VANWYNSBERGHE, A. M., ESSAGHIR, A., DEMOULIN, J. B., HAI, T., DELDICQUE, L. & FRANCAUX, M. 2017. Activating transcription factor 3 attenuates chemokine and cytokine expression in mouse skeletal muscle after exercise and facilitates molecular adaptation to endurance training. *The FASEB Journal*, 31, 840-851.
- FIGUEIREDO, V. C., CALDOW, M. K., MASSIE, V., MARKWORTH, J. F., CAMERON-SMITH, D. & BLAZEVICH, A. J. 2015. Ribosome biogenesis adaptation in resistance training-induced human skeletal muscle hypertrophy. *American Journal of Physiology-Endocrinology And Metabolism*, 309, E72-E83.
- FIGUEIREDO, V. C. & MCCARTHY, J. J. 2019. Regulation of ribosome biogenesis in skeletal muscle hypertrophy. *Physiology*, 34, 30-42.
- FIGUEIREDO, V. C., ROBERTS, L. A., MARKWORTH, J. F., BARNETT, M. P., COOMBES, J. S., RAASTAD, T., PEAKE, J. M. & CAMERON-SMITH, D. 2016. Impact of resistance exercise on ribosome biogenesis is acutely regulated by post-exercise recovery strategies. *Physiological reports*, 4, e12670.
- FIGUEIREDO, V. C., WEN, Y., ALKNER, B., FERNANDEZ-GONZALO, R., NORRBOM, J., VECHETTI JR, I. J., VALENTINO, T., MOBLEY, C. B., ZENTNER, G. E. & PETERSON, C. A. 2021. Genetic and epigenetic regulation of skeletal muscle ribosome biogenesis with exercise. *The Journal of Physiology*.

- FISHER, A. 2012. *Transcriptional profiling to identify therapeutic targets influencing skeletal muscle atrophy*. University of Liverpool.
- FISHER, A. G., SEABORNE, R. A., HUGHES, T. M., GUTTERIDGE, A., STEWART, C., COULSON, J. M., SHARPLES, A. P. & JARVIS, J. C. 2017. Transcriptomic and epigenetic regulation of disuse atrophy and the return to activity in skeletal muscle. *The FASEB Journal*, 31, 5268-5282.
- FISHER, L. 2010. *Time-and activity-dependence of transcriptional changes in stimulated rat skeletal muscle*. University of Liverpool.
- FLÜCK, M., CARSON, J. A., GORDON, S. E., ZIEMIECKI, A. & BOOTH, F. W. 1999. Focal adhesion proteins FAK and paxillin increase in hypertrophied skeletal muscle. *American Journal of Physiology-Cell Physiology*, 277, C152-C162.
- FOLKER, E. & BAYLIES, M. 2013. Nuclear positioning in muscle development and disease. *Frontiers in physiology*, 4, 363.
- FONSECA, B. D., ZAKARIA, C., JIA, J.-J., GRABER, T. E., SVITKIN, Y., TAHMASEBI, S., HEALY, D., HOANG, H.-D., JENSEN, J. M. & DIAO, I. T. 2015. La-related protein 1 (LARP1) represses terminal oligopyrimidine (TOP) mRNA translation downstream of mTOR complex 1 (mTORC1). *Journal of Biological Chemistry*, 290, 15996-16020.
- FOUGEROUSSE, F., DURAND, M., LOPEZ, S., SUEL, L., DEMIGNON, J., THORNTON, C., OZAKI, H., KAWAKAMI, K., BARBET, P. & BECKMANN, J. S. 2002. Six and Eya expression during human somitogenesis and MyoD gene family activation. *Journal of Muscle Research & Cell Motility*, 23, 255-264.
- FRANCHI, M. V., RUOSS, S., VALDIVIESO, P., MITCHELL, K. W., SMITH, K., ATHERTON, P. J., NARICI, M. V. & FLÜCK, M. 2018. Regional regulation of focal adhesion kinase after concentric and eccentric loading is related to remodelling of human skeletal muscle. *Acta physiologica*, 223, e13056.
- FRY, C. S., KIRBY, T. J., KOSMAC, K., MCCARTHY, J. J. & PETERSON, C. A. 2017. Myogenic progenitor cells control extracellular matrix production by fibroblasts during skeletal muscle hypertrophy. *Cell stem cell*, 20, 56-69.
- FRY, C. S., LEE, J. D., JACKSON, J. R., KIRBY, T. J., STASKO, S. A., LIU, H., DUPONT-VERSTEEGDEN, E. E., MCCARTHY, J. J. & PETERSON, C. A. 2014a. Regulation of the muscle fiber micro environment by activated satellite cells during hypertrophy. *The FASEB Journal*, 28, 1654-1665.
- FRY, C. S., NOEHREN, B., MULA, J., UBELE, M. F., WESTGATE, P. M., KERN, P. A. & PETERSON, C. A. 2014b. Fibre type-specific satellite cell response to aerobic training in sedentary adults. *The Journal of physiology*, 592, 2625-2635.
- FUKADA, S.-I., AKIMOTO, T. & SOTIROPOULOS, A. 2020. Role of damage and management in muscle hypertrophy: different behaviors of muscle stem cells in regeneration and hypertrophy. *Biochimica et Biophysica Acta (BBA)-Molecular Cell Research*, 1867, 118742.
- FUQUA, J. D., HUGHES, J., KUENNEN, D., HARRIS, M., TURNER, K., KRONEMBERGER, A., EBERT, S., DIERDORFF, J., ZHU, Z. & ZINGMAN, L. 2020. Skeletal Muscle ULK1 and ULK2 Jointly Couple Muscle Mass with Force and Are Required for Survival Under Low Nutrient Availability. *The FASEB Journal*, 34, 1-1.
- GABRIEL, B. M. & ZIERATH, J. R. 2019. Circadian rhythms and exercise—re-setting the clock in metabolic disease. *Nature Reviews Endocrinology*, 15, 197-206.
- GARAMI, A., ZWARTKRUIS, F. J., NOBUKUNI, T., JOAQUIN, M., ROCCIO, M., STOCKER, H., KOZMA, S. C., HAFEN, E., BOS, J. L. & THOMAS, G. 2003. Insulin activation of Rheb, a mediator of mTOR/S6K/4E-BP signaling, is inhibited by TSC1 and 2. *Molecular cell*, 11, 1457-1466.
- GEISS, G. K., RADEBAUGH, C. A. & PAULE, M. R. 1997. The fundamental ribosomal RNA transcription initiation factor-IB (TIF-IB, SL1, factor D) binds to the rRNA core promoter primarily by minor groove contacts. *Journal of Biological Chemistry*, 272, 29243-29254.
- GEORGE, M., YING, G., RAINEY, M. A., SOLOMON, A., PARIKH, P. T., GAO, Q., BAND, V. & BAND, H. 2007. Shared as well as distinct roles of EHD proteins revealed by biochemical and functional comparisons in mammalian cells and *C. elegans*. *BMC cell biology*, 8, 1-22.

- GIMPEL, P., LEE, Y. L., SOBOTA, R. M., CALVI, A., KOULLOUROU, V., PATEL, R., MAMCHAOU, K., NÉDÉLEC, F., SHACKLETON, S. & SCHMORANZER, J. 2017. Nesprin-1 α -dependent microtubule nucleation from the nuclear envelope via Akap450 is necessary for nuclear positioning in muscle cells. *Current Biology*, 27, 2999-3009. e9.
- GIORDANI, L., HE, G. J., NEGRONI, E., SAKAI, H., LAW, J. Y. C., SIU, M. M., WAN, R., CORNEAU, A., TAJBAKHS, S., CHEUNG, T. H. & LE GRAND, F. 2019. High-Dimensional Single-Cell Cartography Reveals Novel Skeletal Muscle-Resident Cell Populations. *Molecular Cell*, 74, 609-621.e6.
- GLASS, D. J. 2005. Skeletal muscle hypertrophy and atrophy signaling pathways. *The international journal of biochemistry & cell biology*, 37, 1974-1984.
- GOH, Q., SONG, T., PETRANY, M. J., CRAMER, A. A., SUN, C., SADAYAPPAN, S., LEE, S.-J. & MILLAY, D. P. 2019. Myonuclear accretion is a determinant of exercise-induced remodeling in skeletal muscle. *Elife*, 8, e44876.
- GOLDSPINK, D. F., COX, V. M., SMITH, S. K., EAVES, L. A., OSBALDESTON, N. J., LEE, D. M. & MANTLE, D. 1995. Muscle growth in response to mechanical stimuli. *American Journal of Physiology-Endocrinology And Metabolism*, 268, E288-E297.
- GOLLNICK, P., ARMSTRONG, R., SAUBERT 4TH, C., PIEHL, K. & SALTIN, B. 1972. Enzyme activity and fiber composition in skeletal muscle of untrained and trained men. *Journal of applied physiology*, 33, 312-319.
- GOLLNICK, P., TIMSON, B., MOORE, R. & RIEDY, M. 1981. Muscular enlargement and number of fibers in skeletal muscles of rats. *Journal of Applied Physiology*, 50, 936-943.
- GOLLNICK, P. D., ARMSTRONG, R., SALTIN, B., SAUBERT 4TH, C., SEMBROWICH, W. L. & SHEPHERD, R. E. 1973. Effect of training on enzyme activity and fiber composition of human skeletal muscle. *Journal of applied physiology*, 34, 107-111.
- GOMEZ-ROMAN, N., GRANDORI, C., EISENMAN, R. N. & WHITE, R. J. 2003. Direct activation of RNA polymerase III transcription by c-Myc. *Nature*, 421, 290-294.
- GOODMAN, C. A., FREY, J. W., MABREY, D. M., JACOBS, B. L., LINCOLN, H. C., YOU, J. S. & HORNBERGER, T. A. 2011. The role of skeletal muscle mTOR in the regulation of mechanical load-induced growth. *The Journal of physiology*, 589, 5485-5501.
- GOODMAN, C. A. & HORNBERGER, T. A. 2014. New roles for Smad signaling and phosphatidic acid in the regulation of skeletal muscle mass. *F1000prime reports*, 6.
- GORZA, L., GUNDERSEN, K., LØMO, T., SCHIAFFINO, S. & WESTGAARD, R. 1988. Slow-to-fast transformation of denervated soleus muscles by chronic high-frequency stimulation in the rat. *The Journal of physiology*, 402, 627-649.
- GOTO, M., TERADA, S., KATO, M., KATO, M., YOKOZEKI, T., TABATA, I. & SHIMOKAWA, T. 2000. cDNA cloning and mRNA analysis of PGC-1 in epitrochlearis muscle in swimming-exercised rats. *Biochemical and biophysical research communications*, 274, 350-354.
- GRABER, T. G., FANDREY, K. R. & THOMPSON, L. V. 2019. Novel individualized power training protocol preserves physical function in adult and older mice. *GeroScience*, 41, 165-183.
- GRÄFF, J. & TSAI, L.-H. 2013. Histone acetylation: molecular mnemonics on the chromatin. *Nature Reviews Neuroscience*, 14, 97-111.
- GRAHAM, Z. A., GALLAGHER, P. M. & CARDOZO, C. P. 2015. Focal adhesion kinase and its role in skeletal muscle. *Journal of muscle research and cell motility*, 36, 305-315.
- GRANDORI, C., GOMEZ-ROMAN, N., FELTON-EDKINS, Z. A., NGOUENET, C., GALLOWAY, D. A., EISENMAN, R. N. & WHITE, R. J. 2005. c-Myc binds to human ribosomal DNA and stimulates transcription of rRNA genes by RNA polymerase I. *Nature cell biology*, 7, 311-318.
- GRIFONE, R., LACLEF, C., SPITZ, F., LOPEZ, S., DEMIGNON, J., GUIDOTTI, J.-E., KAWAKAMI, K., XU, P.-X., KELLY, R. & PETROF, B. J. 2004. Six1 and Eya1 expression can reprogram adult muscle from the slow-twitch phenotype into the fast-twitch phenotype. *Molecular and cellular biology*, 24, 6253-6267.

- GROBET, L., MARTIN, L. J. R., PONCELET, D., PIROTTIN, D., BROUWERS, B., RIQUET, J., SCHOEBERLEIN, A., DUNNER, S., MÉNISSIER, F. & MASSABANDA, J. 1997. A deletion in the bovine myostatin gene causes the double-muscling phenotype in cattle. *Nature genetics*, 17, 71-74.
- GROBET, L., PONCELET, D., ROYO, L. J., BROUWERS, B., PIROTTIN, D., MICHAUX, C., MÉNISSIER, F., ZANOTTI, M., DUNNER, S. & GEORGES, M. 1998. Molecular definition of an allelic series of mutations disrupting the myostatin function and causing double-muscling in cattle. *Mammalian genome*, 9, 210-213.
- GRUMATI, P., COLETTI, L., SCHIAVINATO, A., CASTAGNARO, S., BERTAGGIA, E., SANDRI, M. & BONALDO, P. 2011. Physical exercise stimulates autophagy in normal skeletal muscles but is detrimental for collagen VI-deficient muscles. *Autophagy*, 7, 1415-1423.
- GUAN, K.-L. 1994. The mitogen activated protein kinase signal transduction pathway: from the cell surface to the nucleus. *Cellular signalling*, 6, 581-589.
- GUDMUNDSSON, H., CURRAN, J., KASHEF, F., SNYDER, J. S., SMITH, S. A., VARGAS-PINTO, P., BONILLA, I. M., WEISS, R. M., ANDERSON, M. E. & BINKLEY, P. 2012. Differential regulation of EHD3 in human and mammalian heart failure. *Journal of molecular and cellular cardiology*, 52, 1183-1190.
- GUDMUNDSSON, H., HUND, T. J., WRIGHT, P. J., KLINE, C. F., SNYDER, J. S., QIAN, L., KOVAL, O. M., CUNHA, S. R., GEORGE, M. & RAINEY, M. A. 2010. EH domain proteins regulate cardiac membrane protein targeting. *Circulation research*, 107, 84-95.
- GUILLUY, C. & BURRIDGE, K. 2015. Nuclear mechanotransduction: forcing the nucleus to respond. *Nucleus*, 6, 19-22.
- GUILLUY, C., OSBORNE, L. D., VAN LANDEGHEM, L., SHAREK, L., SUPERFINE, R., GARCIA-MATA, R. & BURRIDGE, K. 2014. Isolated nuclei adapt to force and reveal a mechanotransduction pathway in the nucleus. *Nature cell biology*, 16, 376-381.
- GUMUCIO, J. P., PHAN, A. C., RUEHLMANN, D. G., NOAH, A. C. & MENDIAS, C. L. 2014. Synergist ablation induces rapid tendon growth through the synthesis of a neotendon matrix. *Journal of applied physiology*, 117, 1287-1291.
- GUNDERSEN, K. 2016. Muscle memory and a new cellular model for muscle atrophy and hypertrophy. *Journal of Experimental Biology*, 219, 235-242.
- GUNDERSEN, K., BRUUSGAARD, J. C., EGNER, I., EFTESTØL, E. & BENGTSSEN, M. 2018. Muscle memory: virtues of your youth? *The Journal of physiology*, 596, 4289.
- GUPTA, R., KHAN, R. & CORTES, C. J. 2021. Forgot to Exercise? Exercise Derived Circulating Myokines in Alzheimer's Disease: A Perspective. *Frontiers in Neurology*, 12.
- HAGIWARA, N., YEH, M. & LIU, A. 2007. Sox6 is required for normal fiber type differentiation of fetal skeletal muscle in mice. *Developmental dynamics: an official publication of the American Association of Anatomists*, 236, 2062-2076.
- HÄKKINEN, K., ALEN, M. & KOMI, P. 1985. Changes in isometric force-and relaxation-time, electromyographic and muscle fibre characteristics of human skeletal muscle during strength training and detraining. *Acta physiologica scandinavica*, 125, 573-585.
- HÄKKINEN, K., KRAEMER, W., NEWTON, R. & ALEN, M. 2001. Changes in electromyographic activity, muscle fibre and force production characteristics during heavy resistance/power strength training in middle-aged and older men and women. *Acta Physiologica Scandinavica*, 171, 51-62.
- HANSSON, K.-A., EFTESTØL, E., BRUUSGAARD, J. C., JUVKAM, I., CRAMER, A. W., MALTHE-SØRENSEN, A., MILLAY, D. P. & GUNDERSEN, K. 2020. Myonuclear content regulates cell size with similar scaling properties in mice and humans. *Nature communications*, 11, 1-14.
- HARA, K., MARUKI, Y., LONG, X., YOSHINO, K.-I., OSHIRO, N., HIDAYAT, S., TOKUNAGA, C., AVRUCH, J. & YONEZAWA, K. 2002. Raptor, a binding partner of target of rapamycin (TOR), mediates TOR action. *Cell*, 110, 177-189.

- HARFMANN, B. D., SCHRODER, E. A., KACHMAN, M. T., HODGE, B. A., ZHANG, X. & ESSER, K. A. 2016. Muscle-specific loss of Bmal1 leads to disrupted tissue glucose metabolism and systemic glucose homeostasis. *Skeletal muscle*, 6, 1-13.
- HASTINGS, R. L., MASSOPUST, R. T., HADDIX, S. G., LEE, Y. I. & THOMPSON, W. J. 2020. Exclusive vital labeling of myonuclei for studying myonuclear arrangement in mouse skeletal muscle tissue. *Skeletal Muscle*, 10, 1-13.
- HASTY, P., BRADLEY, A., MORRIS, J. H., EDMONDSON, D. G., VENUTI, J. M., OLSON, E. N. & KLEIN, W. H. 1993. Muscle deficiency and neonatal death in mice with a targeted mutation in the myogenin gene. *Nature*, 364, 501-506.
- HAWLEY, S. A., BOUDEAU, J., REID, J. L., MUSTARD, K. J., UDD, L., MÄKELÄ, T. P., ALESSI, D. R. & HARDIE, D. G. 2003. Complexes between the LKB1 tumor suppressor, STRAD α/β and MO25 α/β are upstream kinases in the AMP-activated protein kinase cascade. *Journal of biology*, 2, 28.
- HAWLEY, S. A., DAVISON, M., WOODS, A., DAVIES, S. P., BERI, R. K., CARLING, D. & HARDIE, D. G. 1996. Characterization of the AMP-activated protein kinase kinase from rat liver and identification of threonine 172 as the major site at which it phosphorylates AMP-activated protein kinase. *Journal of Biological Chemistry*, 271, 27879-27887.
- HELLMUTH, A. & ALLBROOK, D. 1971. Muscle satellite cell numbers during the postnatal period. *Journal of anatomy*, 110, 503-503.
- HENDY, A. M., SPITTLE, M. & KIDGELL, D. J. 2012. Cross education and immobilisation: mechanisms and implications for injury rehabilitation. *Journal of science and medicine in sport*, 15, 94-101.
- HERSHKO, A. & CIECHANOVER, A. 1998. The ubiquitin system. *Annual review of biochemistry*, 67, 425-479.
- HESKETH, S., SRISAWAT, K., SUTHERLAND, H., JARVIS, J. & BURNISTON, J. 2016. On the rate of synthesis of individual proteins within and between different striated muscles of the rat. *Proteomes*, 4, 12.
- HESKETH, S. J., STANSFIELD, B. N., STEAD, C. A. & BURNISTON, J. G. 2020a. The application of proteomics in muscle exercise physiology. *Expert Review of Proteomics*, 17, 813-825.
- HESKETH, S. J., SUTHERLAND, H., LISBOA, P. J., JARVIS, J. C. & BURNISTON, J. G. 2020b. Adaptation of rat fast-twitch muscle to endurance activity is underpinned by changes to protein degradation as well as protein synthesis. *The FASEB Journal*, 34, 10398-10417.
- HETTINGER, Z. R., HAMAGATA, K., CONFIDES, A. L., LAWRENCE, M. M., MILLER, B. F., BUTTERFIELD, T. A. & DUPONT-VERSTEEGDEN, E. E. 2021. Age-Related Susceptibility to Muscle Damage Following Mechanotherapy in Rats Recovering From Disuse Atrophy. *The Journals of Gerontology: Series A*, 76, 2132-2140.
- HIPPENMEYER, S., HUBER, R. M., LADLE, D. R., MURPHY, K. & ARBER, S. 2007. ETS transcription factor Erm controls subsynaptic gene expression in skeletal muscles. *Neuron*, 55, 726-740.
- HO, K. W., ROY, R., TWEEDLE, C., HEUSNER, W., VAN HUSS, W. & CARROW, R. 1980. Skeletal muscle fiber splitting with weight-lifting exercise in rats. *American Journal of Anatomy*, 157, 433-440.
- HOCK, M. B. & KRALLI, A. 2009. Transcriptional control of mitochondrial biogenesis and function. *Annual review of physiology*, 71, 177-203.
- HODGE, B. A., WEN, Y., RILEY, L. A., ZHANG, X., ENGLAND, J. H., HARFMANN, B. D., SCHRODER, E. A. & ESSER, K. A. 2015. The endogenous molecular clock orchestrates the temporal separation of substrate metabolism in skeletal muscle. *Skeletal muscle*, 5, 1-16.
- HODGE, B. A., ZHANG, X., GUTIERREZ-MONREAL, M. A., CAO, Y., HAMMERS, D. W., YAO, Z., WOLFF, C. A., DU, P., KEMLER, D. & JUDGE, A. R. 2019. MYOD1 functions as a clock amplifier as well as a critical co-factor for downstream circadian gene expression in muscle. *Elife*, 8, e43017.

- HOIER, B., NORDSBORG, N., ANDERSEN, S., JENSEN, L., NYBO, L., BANGSBO, J. & HELLSTEN, Y. 2012. Pro-and anti-angiogenic factors in human skeletal muscle in response to acute exercise and training. *The Journal of physiology*, 590, 595-606.
- HOLLOSZY, J. O. 1967. Biochemical adaptations in muscle effects of exercise on mitochondrial oxygen uptake and respiratory enzyme activity in skeletal muscle. *Journal of biological chemistry*, 242, 2278-2282.
- HOLLOSZY, J. O. 2011. Regulation of mitochondrial biogenesis and GLUT4 expression by exercise. *Comprehensive Physiology*, 1, 921-940.
- HOLLOWAY, T. M., SNIJDERS, T., VAN, J. K., VAN, L. L. & VERDIJK, L. B. 2018. Temporal response of angiogenesis and hypertrophy to resistance training in young men. *Medicine and science in sports and exercise*, 50, 36-45.
- HOLM, H., GUDBJARTSSON, D. F., SULEM, P., MASSON, G., HELGADOTTIR, H. T., ZANON, C., MAGNUSSON, O. T., HELGASON, A., SAEMUNDSDOTTIR, J. & GYLFASSON, A. 2011. A rare variant in MYH6 is associated with high risk of sick sinus syndrome. *Nature genetics*, 43, 316.
- HORNBERGER JR, T. A. & FARRAR, R. P. 2004. Physiological hypertrophy of the FHL muscle following 8 weeks of progressive resistance exercise in the rat. *Canadian journal of applied physiology*, 29, 16-31.
- HORNBERGER, T., CHU, W., MAK, Y., HSIUNG, J., HUANG, S. & CHIEN, S. 2006. The role of phospholipase D and phosphatidic acid in the mechanical activation of mTOR signaling in skeletal muscle. *Proceedings of the National Academy of Sciences*, 103, 4741-4746.
- HORNBERGER, T. A. 2011. Mechanotransduction and the regulation of mTORC1 signaling in skeletal muscle. *The international journal of biochemistry & cell biology*, 43, 1267-1276.
- HUANG, M.-J., CHENG, Y.-C., LIU, C.-R., LIN, S. & LIU, H. E. 2006. A small-molecule c-Myc inhibitor, 10058-F4, induces cell-cycle arrest, apoptosis, and myeloid differentiation of human acute myeloid leukemia. *Experimental hematology*, 34, 1480-1489.
- HUDLICKA, O., BROWN, M., COTTER, M., SMITH, M. & VRBOVA, G. 1977. The effect of long-term stimulation of fast muscles on their blood flow, metabolism and ability to withstand fatigue. *Pflügers Archiv*, 369, 141-149.
- HUDLICKA, O., DODD, L., RENKIN, E. & GRAY, S. 1982. Early changes in fiber profile and capillary density in long-term stimulated muscles. *American Journal of Physiology-Heart and Circulatory Physiology*, 243, H528-H535.
- HUDLICKÁ, O., EGGINTON, S. & BROWN, M. 1988. Capillary diffusion distances-their importance for cardiac and skeletal muscle performance. *Physiology*, 3, 134-138.
- HUGHES, D. C., TURNER, D. C., BAEHR, L. M., SEABORNE, R. A., VIGGARS, M., JARVIS, J. C., GORSKI, P. P., STEWART, C. E., OWENS, D. J. & BODINE, S. C. 2020. Knockdown of the E3 Ubiquitin ligase UBR5 and its role in skeletal muscle anabolism. *American Journal of Physiology-Cell Physiology*.
- HUH, J. Y. 2018. The role of exercise-induced myokines in regulating metabolism. *Archives of pharmacal research*, 41, 14-29.
- HUIJING, P., BAAN, G. C. & REBEL, G. T. 1998. Non-myotendinous force transmission in rat extensor digitorum longus muscle. *Journal of Experimental Biology*, 201, 683-691.
- INOKI, K., ZHU, T. & GUAN, K.-L. 2003. TSC2 mediates cellular energy response to control cell growth and survival. *Cell*, 115, 577-590.
- ISHIHARA, A., ROY, R. R., OHIRA, Y., IBATA, Y. & EDGERTON, V. R. 1998. Hypertrophy of rat plantaris muscle fibers after voluntary running with increasing loads. *Journal of Applied Physiology*, 84, 2183-2189.
- IVEY, F., TRACY, B., LEMMER, J., NESSAIVER, M., METTER, E., FOZARD, J. & HURLEY, B. F. 2000. Effects of strength training and detraining on muscle quality: age and gender comparisons. *The Journals of Gerontology Series A: Biological Sciences and Medical Sciences*, 55, B152-B157.
- JACKSON, J. R., MULA, J., KIRBY, T. J., FRY, C. S., LEE, J. D., UBELE, M. F., CAMPBELL, K. S., MCCARTHY, J. J., PETERSON, C. A. & DUPONT-VERSTEEGDEN, E. E. 2012. Satellite cell depletion does not

- inhibit adult skeletal muscle regrowth following unloading-induced atrophy. *American Journal of Physiology-Cell Physiology*.
- JACOBS, B. L., GOODMAN, C. A. & HORNBERGER, T. A. 2014. The mechanical activation of mTOR signaling: an emerging role for late endosome/lysosomal targeting. *Journal of muscle research and cell motility*, 35, 11-21.
- JAKOBSEN, J. R., JAKOBSEN, N., MACKEY, A. L., KOCH, M., KJAER, M. & KROGSGAARD, M. R. 2018. Remodeling of muscle fibers approaching the human myotendinous junction. *Scandinavian journal of medicine & science in sports*, 28, 1859-1865.
- JAKOBSEN, J. R., JAKOBSEN, N. R., MACKEY, A. L., KNUDSEN, A. B., HANNIBAL, J., KOCH, M., KJAER, M. & KROGSGAARD, M. R. 2021a. Adipocytes are present at human and murine myotendinous junctions. *Translational Sports Medicine*, 4, 223-230.
- JAKOBSEN, J. R., SCHJERLING, P., SVENSSON, R. B., BUHL, R., CARSTENSEN, H., KOCH, M., KROGSGAARD, M. R. R., KJAER, M. & MACKEY, A. L. 2021b. RNA-sequencing and immunofluorescence of the myotendinous junction of mature horses and humans. *American Journal of Physiology-Cell Physiology*, 0, null.
- JÄNKÄLÄ, H., HARJOLA, V.-P., PETERSEN, N. E. & HÄRKÖNEN, M. 1997. Myosin heavy chain mRNA transform to faster isoforms in immobilized skeletal muscle: a quantitative PCR study. *Journal of Applied Physiology*, 82, 977-982.
- JARVIS, J. & SALMONS, S. 1991. A family of neuromuscular stimulators with optical transcutaneous control. *Journal of medical engineering & technology*, 15, 53-57.
- JARVIS, J. C. 1993. Power production and working capacity of rabbit tibialis anterior muscles after chronic electrical stimulation at 10 Hz. *The Journal of Physiology*, 470, 157-169.
- JARVIS, J. C., MOKRUSCH, T., KWENDE, M. M., SUTHERLAND, H. & SALMONS, S. 1996a. Fast-to-slow transformation in stimulated rat muscle. *Muscle & Nerve: Official Journal of the American Association of Electrodiagnostic Medicine*, 19, 1469-1475.
- JARVIS, J. C., MOKRUSCH, T., KWENDE, M. M. N., SUTHERLAND, H. & SALMONS, S. 1996b. Fast-to-slow transformation in stimulated rat muscle. *Muscle & Nerve*, 19, 1469-1475.
- JEFFERY, N. S., STEPHENSON, R. S., GALLAGHER, J. A., JARVIS, J. C. & COX, P. G. 2011. Micro-computed tomography with iodine staining resolves the arrangement of muscle fibres. *Journal of biomechanics*, 44, 189-192.
- JENSEN, S. M., BECHSHØFT, C. J., HEISTERBERG, M. F., SCHJERLING, P., ANDERSEN, J. L., KJAER, M. & MACKEY, A. L. 2020. Macrophage subpopulations and the acute inflammatory response of elderly human skeletal muscle to physiological resistance exercise. *Frontiers in Physiology*, 11, 811.
- JIN, R. & ZHOU, W. 2016. TIF-1A: An oncogenic target of pre-ribosomal RNA synthesis. *Biochimica et Biophysica Acta (BBA)-Reviews on Cancer*, 1866, 189-196.
- JOPLIN, R., FRANCHI, L. & SALMONS, S. 1987. Changes in the size and synthetic activity of nuclear populations in chronically stimulated rabbit skeletal muscle. *Journal of anatomy*, 155, 39.
- JORGENSEN, K. W. & HORNBERGER, T. A. 2019. The overlooked role of fiber length in mechanical load-induced growth of skeletal muscle. *Exercise and sport sciences reviews*, 47, 258-259.
- JOY, J. M., GUNDERMANN, D. M., LOWERY, R. P., JÄGER, R., MCCLEARY, S. A., PURPURA, M., ROBERTS, M. D., WILSON, S. M., HORNBERGER, T. A. & WILSON, J. M. 2014. Phosphatidic acid enhances mTOR signaling and resistance exercise induced hypertrophy. *Nutrition & metabolism*, 11, 1-10.
- KADOWAKI, T., TOBE, K., HONDA-YAMAMOTO, R., TAMEMOTO, H., KABURAGI, Y., MOMOMURA, K., UEKI, K., TAKAHASHI, Y., YAMAUCHI, T. & AKANUMA, Y. 1996. Signal transduction mechanism of insulin and insulin-like growth factor-1. *Endocrine journal*, 43, S33-S41.
- KAMBADUR, R., SHARMA, M., SMITH, T. P. & BASS, J. J. 1997. Mutations in myostatin (GDF8) in double-musled Belgian Blue and Piedmontese cattle. *Genome research*, 7, 910-915.

- KAMEI, Y., MIZUKAMI, J., MIURA, S., SUZUKI, M., TAKAHASHI, N., KAWADA, T., TANIGUCHI, T. & EZAKI, O. 2003. A forkhead transcription factor FKHR up-regulates lipoprotein lipase expression in skeletal muscle. *FEBS letters*, 536, 232-236.
- KANEHISA, M. & GOTO, S. 2000. KEGG: kyoto encyclopedia of genes and genomes. *Nucleic acids research*, 28, 27-30.
- KANN, A. P. & KRAUSS, R. S. 2019. Multiplexed RNAscope and immunofluorescence on whole-mount skeletal myofibers and their associated stem cells. *Development*, 146, dev179259.
- KARAGOUNIS, L. G. & HAWLEY, J. A. 2010. Skeletal muscle: increasing the size of the locomotor cell. *The international journal of biochemistry & cell biology*, 42, 1376-1379.
- KARLSEN, A., BECHSHØFT, R. L., MALMGAARD-CLAUSEN, N. M., ANDERSEN, J. L., SCHJERLING, P., KJAER, M. & MACKEY, A. L. 2019. Lack of muscle fibre hypertrophy, myonuclear addition, and satellite cell pool expansion with resistance training in 83-94-year-old men and women. *Acta Physiologica*, 227, e13271.
- KARLSEN, A., COUPPÉ, C., ANDERSEN, J. L., MIKKELSEN, U. R., NIELSEN, R. H., MAGNUSSON, S. P., KJAER, M. & MACKEY, A. L. 2015. Matters of fiber size and myonuclear domain: does size matter more than age? *Muscle & nerve*, 52, 1040-1046.
- KARLSEN, A., SOENDENBROE, C., MALMGAARD-CLAUSEN, N. M., WAGENER, F., MOELLER, C. E., SENHAJI, Z., DAMBERG, K., ANDERSEN, J. L., SCHJERLING, P. & KJAER, M. 2020. Preserved capacity for satellite cell proliferation, regeneration, and hypertrophy in the skeletal muscle of healthy elderly men. *The FASEB Journal*, 34, 6418-6436.
- KASTENSCHMIDT, J. M., ELLEFSEN, K. L., MANNAA, A. H., GIEBEL, J. J., YAHIA, R., AYER, R. E., PHAM, P., RIOS, R., VETRONE, S. A. & MOZAFFAR, T. 2019. QuantiMus: a machine learning-based approach for high precision analysis of skeletal muscle morphology. *Frontiers in physiology*, 10, 1416.
- KELLER, A., OTT, M.-O., LAMANDÉ, N., LUCAS, M., GROS, F., BUCKINGHAM, M. & LAZAR, M. 1992. Activation of the gene encoding the glycolytic enzyme β -enolase during early myogenesis precedes an increased expression during fetal muscle development. *Mechanisms of development*, 38, 41-54.
- KELLY, R. G., ZAMMIT, P. S., SCHNEIDER, A., ALONSO, S., BIBEN, C. & BUCKINGHAM, M. E. 1997. Embryonic and fetal myogenic programs act through separate enhancers at the MLC1F/3F locus. *Developmental biology*, 187, 183-199.
- KENNEDY, J., EISENBERG, B., REID, S., SWEENEY, L. & ZAK, R. 1988. Nascent muscle fiber appearance in overloaded chicken slow-tonic muscle. *American journal of anatomy*, 181, 203-215.
- KIM, D.-H., SARBASSOV, D. D., ALI, S. M., KING, J. E., LATEK, R. R., ERDJUMENT-BROMAGE, H., TEMPST, P. & SABATINI, D. M. 2002. mTOR interacts with raptor to form a nutrient-sensitive complex that signals to the cell growth machinery. *Cell*, 110, 163-175.
- KIM, D.-H., SARBASSOV, D. D., ALI, S. M., LATEK, R. R., GUNTUR, K. V., ERDJUMENT-BROMAGE, H., TEMPST, P. & SABATINI, D. M. 2003. G β L, a positive regulator of the rapamycin-sensitive pathway required for the nutrient-sensitive interaction between raptor and mTOR. *Molecular cell*, 11, 895-904.
- KIM, J.-S., GALVÃO, D. A., NEWTON, R. U., GREY, E. & TAAFFE, D. R. 2021. Exercise-induced myokines and their effect on prostate cancer. *Nature Reviews Urology*, 1-24.
- KIM, M., FRANKE, V., BRANDT, B., LOWENSTEIN, E. D., SCHÖWEL, V., SPULER, S., AKALIN, A. & BIRCHMEIER, C. 2020. Single-nucleus transcriptomics reveals functional compartmentalization in syncytial skeletal muscle cells. *Nature communications*, 11, 1-14.
- KIRBY, T. J. & LAMMERDING, J. 2018. Emerging views of the nucleus as a cellular mechanosensor. *Nature cell biology*, 20, 373-381.
- KIRBY, T. J., MCCARTHY, J. J., PETERSON, C. A. & FRY, C. S. 2016a. Synergist ablation as a rodent model to study satellite cell dynamics in adult skeletal muscle. *Skeletal Muscle Regeneration in the Mouse*. Springer.

- KIRBY, T. J., PATEL, R. M., MCCLINTOCK, T. S., DUPONT-VERSTEEGDEN, E. E., PETERSON, C. A. & MCCARTHY, J. J. 2016b. Myonuclear transcription is responsive to mechanical load and DNA content but uncoupled from cell size during hypertrophy. *Molecular biology of the cell*, 27, 788-798.
- KLITGAARD, H. 1988. A model for quantitative strength training of hindlimb muscles of the rat. *Journal of applied physiology*, 64, 1740-1745.
- KLOSSNER, S., DURIEUX, A.-C., FREYSSENET, D. & FLUECK, M. 2009. Mechano-transduction to muscle protein synthesis is modulated by FAK. *European journal of applied physiology*, 106, 389-398.
- KNUTTI, D., KRESSLER, D. & KRALLI, A. 2001. Regulation of the transcriptional coactivator PGC-1 via MAPK-sensitive interaction with a repressor. *Proceedings of the National Academy of Sciences*, 98, 9713-9718.
- KOCH, M., SCHULZE, J., HANSEN, U., ASHWODT, T., KEENE, D. R., BRUNKEN, W. J., BURGESSON, R. E., BRUCKNER, P. & BRUCKNER-TUDERMAN, L. 2004. A novel marker of tissue junctions, collagen XXII. *Journal of Biological Chemistry*, 279, 22514-22521.
- KOIVISTO, E., JURADO ACOSTA, A., MOILANEN, A.-M., TOKOLA, H., ARO, J., PENNANEN, H., SÄKKINEN, H., KAIKKONEN, L., RUSKOAHO, H. & RYSÄ, J. 2014. Characterization of the regulatory mechanisms of activating transcription factor 3 by hypertrophic stimuli in rat cardiomyocytes. *PLoS One*, 9, e105168.
- KONG, X., MANCHESTER, J., SALMONS, S. & LAWRENCE JR, J. C. 1994. Glucose transporters in single skeletal muscle fibers. Relationship to hexokinase and regulation by contractile activity. *Journal of Biological Chemistry*, 269, 12963-12967.
- KONHILAS, J. P., WIDEGREN, U., ALLEN, D. L., PAUL, A. C., CLEARY, A. & LEINWAND, L. A. 2005. Loaded wheel running and muscle adaptation in the mouse. *American Journal of Physiology-Heart and Circulatory Physiology*, 289, H455-H465.
- KOREN, L., ELHANANI, O., KEHAT, I., HAI, T. & ARONHEIM, A. 2013. Adult cardiac expression of the activating transcription factor 3, ATF3, promotes ventricular hypertrophy. *PLoS One*, 8, e68396.
- KRIVICKAS, L. S., DORER, D. J., OCHALA, J. & FRONTERA, W. R. 2011. Relationship between force and size in human single muscle fibres. *Experimental physiology*, 96, 539-547.
- KU, H.-C. & CHENG, C.-F. 2020. Master regulator activating transcription factor 3 (ATF3) in metabolic homeostasis and cancer. *Frontiers in Endocrinology*, 11.
- KUANG, J., MCGINLEY, C., LEE, M. J., SANER, N. J., GARNHAM, A. & BISHOP, D. J. 2020. Interpretation of exercise-induced changes in human skeletal muscle mRNA expression depends on the timing of the post-exercise biopsies. *bioRxiv*.
- KUBO, A., SASAKI, H., YUBA-KUBO, A., TSUKITA, S. & SHIINA, N. 1999. Centriolar satellites: molecular characterization, ATP-dependent movement toward centrioles and possible involvement in ciliogenesis. *The Journal of cell biology*, 147, 969-980.
- LASH, J. W., HOLTZER, H. & SWIFT, H. 1957. Regeneration of mature skeletal muscle. *The Anatomical Record*, 128, 679-697.
- LAU, Y. S., XU, L., GAO, Y. & HAN, R. 2018. Automated muscle histopathology analysis using CellProfiler. *Skeletal muscle*, 8, 1-9.
- LE, H. Q., GHATAK, S., YEUNG, C.-Y. C., TELLKAMP, F., GÜNSCHMANN, C., DIETERICH, C., YEROSLAVIZ, A., HABERMANN, B., POMBO, A. & NIESSEN, C. M. 2016. Mechanical regulation of transcription controls Polycomb-mediated gene silencing during lineage commitment. *Nature cell biology*, 18, 864-875.
- LEE, J. H. & JUN, H.-S. 2019. Role of myokines in regulating skeletal muscle mass and function. *Frontiers in physiology*, 10, 42.
- LEHMAN, J. J., BARGER, P. M., KOVACS, A., SAFFITZ, J. E., MEDEIROS, D. M. & KELLY, D. P. 2000. Peroxisome proliferator-activated receptor γ coactivator-1 promotes cardiac mitochondrial biogenesis. *The Journal of clinical investigation*, 106, 847-856.

- LEONE, T. C., LEHMAN, J. J., FINCK, B. N., SCHAEFFER, P. J., WENDE, A. R., BOUDINA, S., COURTOIS, M., WOZNIAK, D. F., SAMBANDAM, N. & BERNAL-MIZRACHI, C. 2005. PGC-1 α deficiency causes multi-system energy metabolic derangements: muscle dysfunction, abnormal weight control and hepatic steatosis. *PLoS Biol*, 3, e101.
- LEPPER, C., PARTRIDGE, T. A. & FAN, C.-M. 2011. An absolute requirement for Pax7-positive satellite cells in acute injury-induced skeletal muscle regeneration. *Development*, 138, 3639-3646.
- LESSARD, S. J., MACDONALD, T. L., PATHAK, P., HAN, M. S., COFFEY, V. G., EDGE, J., RIVAS, D. A., HIRSHMAN, M. F., DAVIS, R. J. & GOODYEAR, L. J. 2018. JNK regulates muscle remodeling via myostatin/SMAD inhibition. *Nature communications*, 9, 1-14.
- LESSARD, S. J., RIVAS, D. A., ALVES-WAGNER, A. B., HIRSHMAN, M. F., GALLAGHER, I. J., CONSTANTIN-TEODOSIU, D., ATKINS, R., GREENHAFF, P. L., QI, N. R. & GUSTAFSSON, T. 2013. Resistance to aerobic exercise training causes metabolic dysfunction and reveals novel exercise-regulated signaling networks. *Diabetes*, 62, 2717-2727.
- LEWIS, W. H. & LEWIS, M. R. 1917. Behavior of cross striated muscle in tissue cultures. *American Journal of Anatomy*, 22, 169-194.
- LEXELL, J., JARVIS, J., DOWNHAM, D. & SALMONS, S. 1993. Stimulation-induced damage in rabbit fast-twitch skeletal muscles: a quantitative morphological study of the influence of pattern and frequency. *Cell and Tissue Research*, 273, 357-362.
- LI, J., ITO, M., OHKAWARA, B., MASUDA, A. & OHNO, K. 2018a. Differential effects of spinal motor neuron-derived and skeletal muscle-derived Rspo2 on acetylcholine receptor clustering at the neuromuscular junction. *Scientific reports*, 8, 1-14.
- LI, L., XIONG, W.-C. & MEI, L. 2018b. Neuromuscular junction formation, aging, and disorders. *Annual review of physiology*, 80, 159-188.
- LI, P., AKIMOTO, T., ZHANG, M., WILLIAMS, R. S. & YAN, Z. 2006. Resident stem cells are not required for exercise-induced fiber-type switching and angiogenesis but are necessary for activity-dependent muscle growth. *American Journal of Physiology-Cell Physiology*, 290, C1461-C1468.
- LIN, J., HANDSCHIN, C. & SPIEGELMAN, B. M. 2005. Metabolic control through the PGC-1 family of transcription coactivators. *Cell metabolism*, 1, 361-370.
- LIN, J., WU, H., TARR, P. T., ZHANG, C.-Y., WU, Z., BOSS, O., MICHAEL, L. F., PUIGSERVER, P., ISOTANI, E. & OLSON, E. N. 2002. Transcriptional co-activator PGC-1 α drives the formation of slow-twitch muscle fibres. *Nature*, 418, 797-801.
- LIU, G. Y. & SABATINI, D. M. 2020. mTOR at the nexus of nutrition, growth, ageing and disease. *Nature Reviews Molecular Cell Biology*, 21, 183-203.
- LIU, Y., LEE, D.-C., LI, Y., ZHU, W., ZHANG, R., SUI, X., LAVIE, C. J. & BLAIR, S. N. 2019. Associations of resistance exercise with cardiovascular disease morbidity and mortality. *Medicine and science in sports and exercise*, 51, 499.
- LODISH, H. & ZIPURSKY, S. L. 2001. Molecular cell biology. *Biochem Mol Biol Educ*, 29, 126-133.
- LOENNEKE, J. P., ROSSOW, L. M., FAHS, C. A., THIEBAUD, R. S., GRANT MOUSER, J. & BEMBEN, M. G. 2017. Time-course of muscle growth, and its relationship with muscle strength in both young and older women. *Geriatrics & gerontology international*, 17, 2000-2007.
- LOEWITH, R., JACINTO, E., WULLSCHLEGER, S., LORBERG, A., CRESPO, J. L., BONENFANT, D., OPPLIGER, W., JENOE, P. & HALL, M. N. 2002. Two TOR complexes, only one of which is rapamycin sensitive, have distinct roles in cell growth control. *Molecular cell*, 10, 457-468.
- LOMAKIN, A., CATTIN, C., CUVELIER, D., ALRAIES, Z., MOLINA, M., NADER, G., SRIVASTAVA, N., SÁEZ, P., GARCIA-ARCOS, J. & ZHITNYAK, I. 2020. The nucleus acts as a ruler tailoring cell responses to spatial constraints. *Science*, 370.
- LOVE, M. I., HUBER, W. & ANDERS, S. 2014. Moderated estimation of fold change and dispersion for RNA-seq data with DESeq2. *Genome biology*, 15, 1-21.

- LOWE, D. A. & ALWAY, S. E. 2002. Animal models for inducing muscle hypertrophy: are they relevant for clinical applications in humans? *Journal of Orthopaedic & Sports Physical Therapy*, 32, 36-43.
- LU, D., CHEN, J. & HAI, T. 2007. The regulation of ATF3 gene expression by mitogen-activated protein kinases. *Biochemical Journal*, 401, 559-567.
- LUCAS, C. A., KANG, L. H. & HOH, J. F. 2000. Monospecific antibodies against the three mammalian fast limb myosin heavy chains. *Biochemical and biophysical research communications*, 272, 303-308.
- LUNDBERG, T. R., FERNANDEZ-GONZALO, R., TESCH, P. A., RULLMAN, E. & GUSTAFSSON, T. 2016. Aerobic exercise augments muscle transcriptome profile of resistance exercise. *American Journal of Physiology-Regulatory, Integrative and Comparative Physiology*, 310, R1279-R1287.
- LUNDBERG, T. R., GARCÍA-GUTIÉRREZ, M. T., MANDIĆ, M., LILJA, M. & FERNANDEZ-GONZALO, R. 2019. Regional and muscle-specific adaptations in knee extensor hypertrophy using flywheel versus conventional weight-stack resistance exercise. *Applied Physiology, Nutrition, and Metabolism*, 44, 827-833.
- LUNDBERG, T. R., MARTÍNEZ-ARANDA, L. M., SANZ, G., HANSSON, B., VON WALDEN, F., TESCH, P. A. & FERNANDEZ-GONZALO, R. 2020. Early accentuated muscle hypertrophy is strongly associated with myonuclear accretion. *American Journal of Physiology-Regulatory, Integrative and Comparative Physiology*.
- LUO, L., MARTIN, S. C., PARKINGTON, J., CADENA, S. M., ZHU, J., IBEBUNJO, C., SUMMERMATTER, S., LONDRAVILLE, N., PATORA-KOMISARSKA, K. & WIDLER, L. 2019a. HDAC4 Controls Muscle Homeostasis through Deacetylation of Myosin Heavy Chain, PGC-1 α , and Hsc70. *Cell Reports*, 29, 749-763. e12.
- LUO, W., CHEN, J., LI, L., REN, X., CHENG, T., LU, S., LAWAL, R. A., NIE, Q., ZHANG, X. & HANOTTE, O. 2019b. c-Myc inhibits myoblast differentiation and promotes myoblast proliferation and muscle fibre hypertrophy by regulating the expression of its target genes, miRNAs and lincRNAs. *Cell Death & Differentiation*, 26, 426-442.
- MACKEY, A. L., KARLSEN, A., COUPPÉ, C., MIKKELSEN, U. R., NIELSEN, R. H., MAGNUSSON, S. & KJAER, M. 2014. Differential satellite cell density of type I and II fibres with lifelong endurance running in old men. *Acta physiologica*, 210, 612-627.
- MACKEY, A. L. & KJAER, M. 2017a. The breaking and making of healthy adult human skeletal muscle in vivo. *Skeletal muscle*, 7, 24.
- MACKEY, A. L. & KJAER, M. 2017b. The breaking and making of healthy adult human skeletal muscle in vivo. *Skeletal muscle*, 7, 1-18.
- MACKEY, A. L., MAGNAN, M., CHAZAUD, B. & KJAER, M. 2017. Human skeletal muscle fibroblasts stimulate in vitro myogenesis and in vivo muscle regeneration. *The Journal of physiology*, 595, 5115-5127.
- MACKEY, A. L., RASMUSSEN, L. K., KADI, F., SCHJERLING, P., HELMARK, I. C., PONSOT, E., AAGAARD, P., DURIGAN, J. L. Q. & KJAER, M. 2016. Activation of satellite cells and the regeneration of human skeletal muscle are expedited by ingestion of nonsteroidal anti-inflammatory medication. *The FASEB Journal*, 30, 2266-2281.
- MADARO, L., MOZZETTA, C., BIFERALI, B. & PROIETTI, D. 2019. Fibro-Adipogenic Progenitors (FAPs) cross-talk in skeletal muscle: the social network. *Frontiers in physiology*, 10, 1074.
- MANDIĆ, M., RULLMAN, E., WIDHOLM, P., LILJA, M., LEINHARD, O. D., GUSTAFSSON, T. & LUNDBERG, T. R. 2020. Automated assessment of regional muscle volume and hypertrophy using MRI. *Scientific reports*, 10, 1-8.
- MARTINOV, V. N. & NJÅ, A. 2005. A microcapsule technique for long-term conduction block of the sciatic nerve by tetrodotoxin. *Journal of neuroscience methods*, 141, 199-205.

- MASSCHELEIN, E., D'HULST, G., ZVICK, J., HINTE, L., SORO-ARNAIZ, I., GORSKI, T., VON MEYENN, F., BAR-NUR, O. & DE BOCK, K. 2020. Exercise promotes satellite cell contribution to myofibers in a load-dependent manner. *Skeletal Muscle*, 10, 21.
- MATE, S. E., VAN DER MEULEN, J. H., ARYA, P., BHATTACHARYYA, S., BAND, H. & HOFFMAN, E. P. 2012. Eps homology domain endosomal transport proteins differentially localize to the neuromuscular junction. *Skeletal muscle*, 2, 1-13.
- MATHENY JR, R. W., NINDL, B. C. & ADAMO, M. L. 2010. Minireview: Mechano-growth factor: a putative product of IGF-I gene expression involved in tissue repair and regeneration. *Endocrinology*, 151, 865-875.
- MAURO, A. 1961. Satellite cell of skeletal muscle fibers. *The Journal of biophysical and biochemical cytology*, 9, 493.
- MAYEUF-LOUCHART, A., HARDY, D., THOREL, Q., ROUX, P., GUENIOT, L., BRIAND, D., MAZERAUD, A., BOUGLÉ, A., SHORTE, S. L. & STAELS, B. 2018. MuscleJ: a high-content analysis method to study skeletal muscle with a new Fiji tool. *Skeletal muscle*, 8, 1-11.
- MCCARTHY, J. J., ANDREWS, J. L., MCDEARMON, E. L., CAMPBELL, K. S., BARBER, B. K., MILLER, B. H., WALKER, J. R., HOGENESCH, J. B., TAKAHASHI, J. S. & ESSER, K. A. 2007. Identification of the circadian transcriptome in adult mouse skeletal muscle. *Physiological genomics*, 31, 86-95.
- MCCARTHY, J. J., DUPONT-VERSTEEGDEN, E. E., FRY, C. S., MURACH, K. A. & PETERSON, C. A. 2017. Methodological issues limit interpretation of negative effects of satellite cell depletion on adult muscle hypertrophy. *Development*, 144, 1363-1365.
- MCCARTHY, J. J., MULA, J., MIYAZAKI, M., ERFANI, R., GARRISON, K., FAROOQUI, A. B., SRIKUEA, R., LAWSON, B. A., GRIMES, B. & KELLER, C. 2011. Effective fiber hypertrophy in satellite cell-depleted skeletal muscle. *Development*, 138, 3657-3666.
- MCCORMICK, K. & SCHULTZ, E. 1992. Mechanisms of nascent fiber formation during avian skeletal muscle hypertrophy. *Developmental biology*, 150, 319-334.
- MCCROSKERY, S., THOMAS, M., MAXWELL, L., SHARMA, M. & KAMBADUR, R. 2003. Myostatin negatively regulates satellite cell activation and self-renewal. *Journal of Cell Biology*, 162, 1135-1147.
- MCPHERRON, A. C., LAWLER, A. M. & LEE, S.-J. 1997. Regulation of skeletal muscle mass in mice by a new TGF- β superfamily member. *Nature*, 387, 83-90.
- MEDICINE, A. C. O. S. 2013. *ACSM's guidelines for exercise testing and prescription*, Lippincott Williams & Wilkins.
- MENESES, C., MORALES, M. G., ABRIGO, J., SIMON, F., BRANDAN, E. & CABELLO-VERRUGIO, C. 2015. The angiotensin-(1-7)/Mas axis reduces myonuclear apoptosis during recovery from angiotensin II-induced skeletal muscle atrophy in mice. *Pflügers Archiv-European Journal of Physiology*, 467, 1975-1984.
- MESSINA, G., BIRESSI, S., MONTEVERDE, S., MAGLI, A., CASSANO, M., PERANI, L., RONCAGLIA, E., TAGLIAFICO, E., STARNES, L. & CAMPBELL, C. E. 2010. Nfix regulates fetal-specific transcription in developing skeletal muscle. *Cell*, 140, 554-566.
- MICHAEL, L. F., WU, Z., CHEATHAM, R. B., PUIGSERVER, P., ADELMANT, G., LEHMAN, J. J., KELLY, D. P. & SPIEGELMAN, B. M. 2001. Restoration of insulin-sensitive glucose transporter (GLUT4) gene expression in muscle cells by the transcriptional coactivator PGC-1. *Proceedings of the National Academy of Sciences*, 98, 3820-3825.
- MICHEL, R. N. & GARDINER, P. F. 1990. To what extent is hindlimb suspension a model of disuse? *Muscle & Nerve: Official Journal of the American Association of Electrodiagnostic Medicine*, 13, 646-653.
- MICHELS, A. A., ROBITAILLE, A. M., BUCZYNSKI-RUCHONNET, D., HODROJ, W., REINA, J. H., HALL, M. N. & HERNANDEZ, N. 2010. mTORC1 directly phosphorylates and regulates human MAF1. *Molecular and cellular biology*, 30, 3749-3757.

- MIYAZAKI, M., MCCARTHY, J. J., FEDELE, M. J. & ESSER, K. A. 2011. Early activation of mTORC1 signalling in response to mechanical overload is independent of phosphoinositide 3-kinase/Akt signalling. *The Journal of physiology*, 589, 1831-1846.
- MOBLEY, C. B., HAUN, C. T., ROBERSON, P. A., MUMFORD, P. W., KEPHART, W. C., ROMERO, M. A., OSBURN, S. C., VANN, C. G., YOUNG, K. C. & BECK, D. T. 2018. Biomarkers associated with low, moderate, and high vastus lateralis muscle hypertrophy following 12 weeks of resistance training. *PLoS One*, 13, e0195203.
- MOBLEY, C. B., HORNBERGER, T. A., FOX, C. D., HEALY, J. C., FERGUSON, B. S., LOWERY, R. P., MCNALLY, R. M., LOCKWOOD, C. M., STOUT, J. R. & KAVAZIS, A. N. 2015. Effects of oral phosphatidic acid feeding with or without whey protein on muscle protein synthesis and anabolic signaling in rodent skeletal muscle. *Journal of the International Society of Sports Nutrition*, 12, 1-11.
- MONSALVE, M., WU, Z., ADELMANT, G., PUIGSERVER, P., FAN, M. & SPIEGELMAN, B. M. 2000. Direct coupling of transcription and mRNA processing through the thermogenic coactivator PGC-1. *Molecular cell*, 6, 307-316.
- MORESI, V., WILLIAMS, A. H., MEADOWS, E., FLYNN, J. M., POTTHOFF, M. J., MCANALLY, J., SHELTON, J. M., BACKS, J., KLEIN, W. H. & RICHARDSON, J. A. 2010. Myogenin and class II HDACs control neurogenic muscle atrophy by inducing E3 ubiquitin ligases. *Cell*, 143, 35-45.
- MORGAN, J. & PARTRIDGE, T. 2020. Skeletal muscle in health and disease. *Disease Models & Mechanisms*, 13.
- MORI, T., ATO, S., KNUDSEN, J., HENRIQUEZ-OLGUIN, C., LI, Z., WAKABAYASHI, K., SUGINOHARA, T., HIGASHIDA, K., TAMURA, Y. & NAKAZATO, K. 2020. C-Myc Overexpression Increases Ribosome Biogenesis and Protein Synthesis Independent of mTORC1 Activation in Mouse Skeletal Muscle.
- MORI, T., ATO, S., KNUDSEN, J. R., HENRIQUEZ-OLGUIN, C., LI, Z., WAKABAYASHI, K., SUGINOHARA, T., HIGASHIDA, K., TAMURA, Y. & NAKAZATO, K. 2021. c-Myc overexpression increases ribosome biogenesis and protein synthesis independent of mTORC1 activation in mouse skeletal muscle. *American Journal of Physiology-Endocrinology and Metabolism*, 321, E551-E559.
- MORO, T., BRIGHTWELL, C. R., VOLPI, E., RASMUSSEN, B. B. & FRY, C. S. 2020. Resistance exercise training promotes fiber type-specific myonuclear adaptations in older adults. *Journal of Applied Physiology*, 128, 795-804.
- MORTREUX, M., ROSA-CALDWELL, M. E., STIEHL, I. D., SUNG, D. M., THOMAS, N. T., FRY, C. S. & RUTKOVE, S. B. 2021. Hindlimb suspension in Wistar rats: Sex-based differences in muscle response. *Physiological Reports*, 9, e15042.
- MOSS, T. & STEFANOVSKY, V. Y. 1995. Promotion and regulation of ribosomal transcription in eukaryotes by RNA polymerase. *Progress in nucleic acid research and molecular biology*, 50, 25-66.
- MOSTAFAVI, S., RAY, D., WARDE-FARLEY, D., GROUIOS, C. & MORRIS, Q. 2008. GeneMANIA: a real-time multiple association network integration algorithm for predicting gene function. *Genome biology*, 9, 1-15.
- MUJIKI, I. & PADILLA, S. 2001. Muscular characteristics of detraining in humans. *Medicine & Science in Sports & Exercise*, 33, 1297-1303.
- MUNN, J., HERBERT, R. D., HANCOCK, M. J. & GANDEVIA, S. C. 2005. Training with unilateral resistance exercise increases contralateral strength. *Journal of Applied Physiology*, 99, 1880-1884.
- MURACH, K. A. & BAGLEY, J. R. 2016. Skeletal muscle hypertrophy with concurrent exercise training: contrary evidence for an interference effect. *Sports Medicine*, 46, 1029-1039.
- MURACH, K. A., DUNGAN, C. M., DUPONT-VERSTEEGDEN, E. E., MCCARTHY, J. J. & PETERSON, C. A. 2019a. "Muscle memory" not mediated by myonuclear number? Secondary analysis of human detraining data. *Journal of Applied Physiology*, 127, 1814-1816.

- MURACH, K. A., DUNGAN, C. M., KOSMAC, K., VOIGT, T. B., TOURVILLE, T. W., MILLER, M. S., BAMMAN, M. M., PETERSON, C. A. & TOTH, M. J. 2019b. Fiber typing human skeletal muscle with fluorescent immunohistochemistry. *Journal of Applied Physiology*, 127, 1632-1639.
- MURACH, K. A., DUNGAN, C. M., PETERSON, C. A. & MCCARTHY, J. J. 2019c. Muscle fiber splitting is a physiological response to extreme loading in animals. *Exercise and sport sciences reviews*, 47, 108.
- MURACH, K. A., ENGLUND, D. A., DUPONT-VERSTEEGDEN, E. E., MCCARTHY, J. J. & PETERSON, C. A. 2018a. Myonuclear domain flexibility challenges rigid assumptions on satellite cell contribution to skeletal muscle fiber hypertrophy. *Frontiers in physiology*, 9, 635.
- MURACH, K. A., FRY, C. S., KIRBY, T. J., JACKSON, J. R., LEE, J. D., WHITE, S. H., DUPONT-VERSTEEGDEN, E. E., MCCARTHY, J. J. & PETERSON, C. A. 2018b. Starring or supporting role? Satellite cells and skeletal muscle fiber size regulation. *Physiology*, 33, 26-38.
- MURACH, K. A., MCCARTHY, J. J., PETERSON, C. A. & DUNGAN, C. M. 2020a. Making mice mighty: recent advances in translational models of load-induced muscle hypertrophy. *Journal of Applied Physiology*, 129, 516-521.
- MURACH, K. A., MOBLEY, C. B., ZDUNEK, C. J., FRICK, K. K., JONES, S. R., MCCARTHY, J. J., PETERSON, C. A. & DUNGAN, C. M. 2020b. Muscle memory: myonuclear accretion, maintenance, morphology, and miRNA levels with training and detraining in adult mice. *Journal of cachexia, sarcopenia and muscle*.
- MURACH, K. A., PECK, B. D., POLICASTRO, R. A., VECHETTI, I. J., VAN PELT, D. W., DUNGAN, C. M., DENES, L. T., FU, X., BRIGHTWELL, C. R. & ZENTNER, G. E. 2021. Early satellite cell communication creates a permissive environment for long-term muscle growth. *Iscience*, 24, 102372.
- MURACH, K. A., VECHETTI JR, I. J., VAN PELT, D. W., CROW, S. E., DUNGAN, C. M., FIGUEIREDO, V. C., KOSMAC, K., FU, X., RICHARDS, C. I. & FRY, C. S. 2020c. Fusion-independent satellite cell communication to muscle fibers during load-induced hypertrophy. *Function*, 1, zqaa009.
- MURACH, K. A., WALTON, R. G., FRY, C. S., MICHAELIS, S. L., GROSHONG, J. S., FINLIN, B. S., KERN, P. A. & PETERSON, C. A. 2016. Cycle training modulates satellite cell and transcriptional responses to a bout of resistance exercise. *Physiological reports*, 4, e12973.
- MURACH, K. A., WHITE, S. H., WEN, Y., HO, A., DUPONT-VERSTEEGDEN, E. E., MCCARTHY, J. J. & PETERSON, C. A. 2017. Differential requirement for satellite cells during overload-induced muscle hypertrophy in growing versus mature mice. *Skeletal muscle*, 7, 1-13.
- MURPHY, M. M., LAWSON, J. A., MATHEW, S. J., HUTCHESON, D. A. & KARDON, G. 2011. Satellite cells, connective tissue fibroblasts and their interactions are crucial for muscle regeneration. *Development*, 138, 3625-3637.
- MUSARÒ, A., MCCULLAGH, K., PAUL, A., HOUGHTON, L., DOBROWOLNY, G., MOLINARO, M., BARTON, E. R., SWEENEY, H. L. & ROSENTHAL, N. 2001. Localized Igf-1 transgene expression sustains hypertrophy and regeneration in senescent skeletal muscle. *Nature genetics*, 27, 195-200.
- MYERS, M., GRAMMER, T. C., WANG, L.-M., SUN, X. J., PIERCE, J. H., BLENIS, J. & WHITE, M. F. 1994. Insulin receptor substrate-1 mediates phosphatidylinositol 3'-kinase and p70S6k signaling during insulin, insulin-like growth factor-1, and interleukin-4 stimulation. *Journal of Biological Chemistry*, 269, 28783-28789.
- NABESHIMA, Y., HANAOKA, K., HAYASAKA, M., ESUML, E., LI, S., NONAKA, I. & NABESHIMA, Y.-I. 1993. Myogenin gene disruption results in perinatal lethality because of severe muscle defect. *Nature*, 364, 532-535.
- NADER, G. A., MCLOUGHLIN, T. J. & ESSER, K. A. 2005. mTOR function in skeletal muscle hypertrophy: increased ribosomal RNA via cell cycle regulators. *American Journal of Physiology-Cell Physiology*.

- NADER, G. A., VON WALDEN, F., LIU, C., LINDVALL, J., GUTMANN, L., PISTILLI, E. E. & GORDON, P. M. 2014. Resistance exercise training modulates acute gene expression during human skeletal muscle hypertrophy. *Journal of applied physiology*, 116, 693-702.
- NARICI, M. V., ROI, G., LANDONI, L., MINETTI, A. & CERRETELLI, P. 1989. Changes in force, cross-sectional area and neural activation during strength training and detraining of the human quadriceps. *European journal of applied physiology and occupational physiology*, 59, 310-319.
- NAVA, M. M., MIROSHNIKOVA, Y. A., BIGGS, L. C., WHITEFIELD, D. B., METGE, F., BOUCAS, J., VIHINEN, H., JOKITALO, E., LI, X. & ARCOS, J. M. G. 2020. Heterochromatin-driven nuclear softening protects the genome against mechanical stress-induced damage. *Cell*, 181, 800-817. e22.
- NAYA, F. J., MERCER, B., SHELTON, J., RICHARDSON, J. A., WILLIAMS, R. S. & OLSON, E. N. 2000. Stimulation of slow skeletal muscle fiber gene expression by calcineurin in vivo. *Journal of Biological Chemistry*, 275, 4545-4548.
- NEUFER, P. D., BAMMAN, M. M., MUOIO, D. M., BOUCHARD, C., COOPER, D. M., GOODPASTER, B. H., BOOTH, F. W., KOHRT, W. M., GERSZTEN, R. E. & MATTSON, M. P. 2015. Understanding the cellular and molecular mechanisms of physical activity-induced health benefits. *Cell metabolism*, 22, 4-11.
- NEWLANDS, S., LEVITT, L. K., ROBINSON, C. S., KARPF, A. C., HODGSON, V. R., WADE, R. P. & HARDEMAN, E. C. 1998. Transcription occurs in pulses in muscle fibers. *Genes & development*, 12, 2748-2758.
- NI, H., CASTRO, S. J., STEPHENSON, R. S., JARVIS, J. C., LOWE, T., HART, G., BOYETT, M. R. & ZHANG, H. Extracting myofibre orientation from micro-CT images: An optimisation study. *Computing in Cardiology 2013*, 2013. IEEE, 823-826.
- NIE, Z., GUO, C., DAS, S. K., CHOW, C. C., BATCHELOR, E., JNR, S. S. S. & LEVENS, D. 2020. Dissecting transcriptional amplification by MYC. *Elife*, 9, e52483.
- NIELSEN, J. N. & WOJTASZEWSKI, J. F. 2004. Regulation of glycogen synthase activity and phosphorylation by exercise. *Proceedings of the Nutrition Society*, 63, 233-237.
- NORRBOM, J., SUNDBERG, C. J., AMELN, H., KRAUS, W. E., JANSSON, E. & GUSTAFSSON, T. 2004. PGC-1 α mRNA expression is influenced by metabolic perturbation in exercising human skeletal muscle. *Journal of applied physiology*, 96, 189-194.
- OGASAWARA, R., ARIHARA, Y., TAKEGAKI, J., NAKAZATO, K. & ISHII, N. 2017. Relationship between exercise volume and muscle protein synthesis in a rat model of resistance exercise. *Journal of Applied Physiology*, 123, 710-716.
- OGASAWARA, R., FUJITA, S., HORNBERGER, T. A., KITAOKA, Y., MAKANAE, Y., NAKAZATO, K. & NAKOKATA, I. 2016. The role of mTOR signalling in the regulation of skeletal muscle mass in a rodent model of resistance exercise. *Scientific Reports*, 6, 1-12.
- OLSEN, L. A., NICOLL, J. X. & FRY, A. C. 2019. The skeletal muscle fiber: a mechanically sensitive cell. *Eur J Appl Physiol*, 119, 333-349.
- ORDAHL, C. 1993. Myogenic lineages within the developing somites. *Molecular basis of morphogenesis*, 165.
- ORDAHL, C. & LE DOUARIN, N. 1992. Two myogenic lineages within the developing somite. *Development*, 114, 339-353.
- OSTER, S. K., HO, C. S., SOUCIE, E. L. & PENN, L. Z. 2002. The myc oncogene: marvelously complex.
- OWENS, D. J., FISCHER, M., JABRE, S., MOOG, S., MAMCHAOU, K., BUTLER-BROWNE, G. & COIRAULT, C. 2020a. Lamin mutations cause increased YAP nuclear entry in muscle stem cells. *Cells*, 9, 816.
- OWENS, D. J., MESSEANT, J., MOOG, S., VIGGARS, M., FERRY, A., MAMCHAOU, K., LACENE, E., ROMERO, N., BRULL, A. & BONNE, G. 2020b. Lamin-related congenital muscular dystrophy alters mechanical signaling and skeletal muscle growth. *bioRxiv*.

- OWENS, D. J., MESSÉANT, J., MOOG, S., VIGGARS, M., FERRY, A., MAMCHAOU, K., LACÈNE, E., ROMÉRO, N., BRULL, A. & BONNE, G. 2021. Lamin-Related Congenital Muscular Dystrophy Alters Mechanical Signaling and Skeletal Muscle Growth. *International Journal of Molecular Sciences*, 22, 306.
- PALLAFACCHINA, G., CALABRIA, E., SERRANO, A. L., KALHOVDE, J. M. & SCHIAFFINO, S. 2002. A protein kinase B-dependent and rapamycin-sensitive pathway controls skeletal muscle growth but not fiber type specification. *Proceedings of the National Academy of Sciences*, 99, 9213-9218.
- PATSALOS, A., PAP, A., VARGA, T., TRENCSENYI, G., CONTRERAS, G. A., GARAI, I., PAPP, Z., DEZSO, B., PINTYE, E. & NAGY, L. 2017. In situ macrophage phenotypic transition is affected by altered cellular composition prior to acute sterile muscle injury. *The Journal of physiology*, 595, 5815-5842.
- PATTENGAL, P. K. & HOLLOSZY, J. O. 1967. Augmentation of skeletal muscle myoglobin by a program of treadmill running. *American Journal of Physiology-Legacy Content*, 213, 783-785.
- PETERSON, T. R., LAPLANTE, M., THOREEN, C. C., SANCAK, Y., KANG, S. A., KUEHL, W. M., GRAY, N. S. & SABATINI, D. M. 2009. DEPTOR is an mTOR inhibitor frequently overexpressed in multiple myeloma cells and required for their survival. *Cell*, 137, 873-886.
- PETRANY, M., SWOBODA, C., SUN, C., CHETAL, K., CHEN, X., WEIRAUCH, M., SALOMONIS, N. & MILLAY, D. 2020a. Single-nucleus RNA-seq identifies transcriptional heterogeneity in multinucleated skeletal myofibers. *bioRxiv*.
- PETRANY, M. J., SWOBODA, C. O., SUN, C., CHETAL, K., CHEN, X., WEIRAUCH, M. T., SALOMONIS, N. & MILLAY, D. P. 2020b. Single-nucleus RNA-seq identifies transcriptional heterogeneity in multinucleated skeletal myofibers. *Nature communications*, 11, 1-12.
- PETRELLA, J. K., KIM, J.-S., CROSS, J. M., KOSEK, D. J. & BAMMAN, M. M. 2006. Efficacy of myonuclear addition may explain differential myofiber growth among resistance-trained young and older men and women. *American Journal of Physiology-Endocrinology and Metabolism*, 291, E937-E946.
- PETRELLA, J. K., KIM, J.-S., MAYHEW, D. L., CROSS, J. M. & BAMMAN, M. M. 2008. Potent myofiber hypertrophy during resistance training in humans is associated with satellite cell-mediated myonuclear addition: a cluster analysis. *Journal of applied physiology*, 104, 1736-1742.
- PHILIPPOU, A., MARIDAKI, M., PNEUMATICOS, S. & KOUTSILIERIS, M. 2014. The complexity of the IGF1 gene splicing, posttranslational modification and bioactivity. *Molecular Medicine*, 20, 202-214.
- PIAZZESI, G., RECONDITI, M., LINARI, M., LUCII, L., BIANCO, P., BRUNELLO, E., DECOSTRE, V., STEWART, A., GORE, D. B. & IRVING, T. C. 2007. Skeletal muscle performance determined by modulation of number of myosin motors rather than motor force or stroke size. *Cell*, 131, 784-795.
- PIEKAROWICZ, K., MACHOWSKA, M., DZIANISAVA, V. & RZEPECKI, R. 2019. Hutchinson-Gilford progeria syndrome—current status and prospects for gene therapy treatment. *Cells*, 8, 88.
- PIEROTTI, D. J., ROY, R. R., FLORES, V. & EDGERTON, V. 1990. Influence of 7 days of hindlimb suspension and intermittent weight support on rat muscle mechanical properties. *Aviation, space, and environmental medicine*, 61, 205-210.
- PILEGAARD, H., SALTIN, B. & NEUFER, P. D. 2003. Exercise induces transient transcriptional activation of the PGC-1 α gene in human skeletal muscle. *The Journal of physiology*, 546, 851-858.
- PILLON, N. J., GABRIEL, B. M., DOLLET, L., SMITH, J. A., PUIG, L. S., BOTELLA, J., BISHOP, D. J., KROOK, A. & ZIERATH, J. R. 2020. Transcriptomic profiling of skeletal muscle adaptations to exercise and inactivity. *Nature communications*, 11, 1-15.
- POOLE, C. J. & VAN RIGGELEN, J. 2017. MYC—master regulator of the cancer epigenome and transcriptome. *Genes*, 8, 142.

- POSEY, A. D., PYTEL, P., GARDIKIOTES, K., DEMONBREUN, A. R., RAINEY, M., GEORGE, M., BAND, H. & MCNALLY, E. M. 2011. Endocytic recycling proteins EHD1 and EHD2 interact with fer-1-like-5 (Fer1L5) and mediate myoblast fusion. *Journal of Biological Chemistry*, 286, 7379-7388.
- POSEY JR, A. D., SWANSON, K. E., ALVAREZ, M. G., KRISHNAN, S., EARLEY, J. U., BAND, H., PYTEL, P., MCNALLY, E. M. & DEMONBREUN, A. R. 2014. EHD1 mediates vesicle trafficking required for normal muscle growth and transverse tubule development. *Developmental biology*, 387, 179-190.
- POTTHOFF, M. J., WU, H., ARNOLD, M. A., SHELTON, J. M., BACKS, J., MCANALLY, J., RICHARDSON, J. A., BASSEL-DUBY, R. & OLSON, E. N. 2007. Histone deacetylase degradation and MEF2 activation promote the formation of slow-twitch myofibers. *The Journal of clinical investigation*, 117, 2459-2467.
- POTTS, G. K., MCNALLY, R. M., BLANCO, R., YOU, J. S., HEBERT, A. S., WESTPHALL, M. S., COON, J. J. & HORNBERGER, T. A. 2017. A map of the phosphoproteomic alterations that occur after a bout of maximal-intensity contractions. *The Journal of physiology*, 595, 5209-5226.
- PSILANDER, N., EFTESTØL, E., CUMMING, K. T., JUVKAM, I., EKBLUM, M. M., SUNDING, K., WERNBOM, M., HOLMBERG, H. C., EKBLUM, B., BRUUSGAARD, J. C., RAASTAD, T. & GUNDERSEN, K. 2019. Effects of training, detraining, and retraining on strength, hypertrophy, and myonuclear number in human skeletal muscle. *J Appl Physiol (1985)*, 126, 1636-1645.
- PUCKELWARTZ, M. J., KESSLER, E. J., KIM, G., DEWITT, M. M., ZHANG, Y., EARLEY, J. U., DEPREUX, F. F., HOLASKA, J., MEWBORN, S. K. & PYTEL, P. 2010. Nesprin-1 mutations in human and murine cardiomyopathy. *Journal of molecular and cellular cardiology*, 48, 600-608.
- PUIGSERVER, P. 2005. Tissue-specific regulation of metabolic pathways through the transcriptional coactivator PGC1- α . *International journal of obesity*, 29, S5-S9.
- PUIGSERVER, P., RHEE, J., LIN, J., WU, Z., YOON, J. C., ZHANG, C.-Y., KRAUSS, S., MOOTHA, V. K., LOWELL, B. B. & SPIEGELMAN, B. M. 2001. Cytokine stimulation of energy expenditure through p38 MAP kinase activation of PPAR γ coactivator-1. *Molecular cell*, 8, 971-982.
- PUIGSERVER, P., WU, Z., PARK, C. W., GRAVES, R., WRIGHT, M. & SPIEGELMAN, B. M. 1998. A cold-inducible coactivator of nuclear receptors linked to adaptive thermogenesis. *Cell*, 92, 829-839.
- QUACH, N. L. & RANDO, T. A. 2006. Focal adhesion kinase is essential for costamereogenesis in cultured skeletal muscle cells. *Developmental biology*, 293, 38-52.
- QUIAT, D., VOELKER, K. A., PEI, J., GRISHIN, N. V., GRANGE, R. W., BASSEL-DUBY, R. & OLSON, E. N. 2011. Concerted regulation of myofiber-specific gene expression and muscle performance by the transcriptional repressor Sox6. *Proceedings of the National Academy of Sciences*, 108, 10196-10201.
- R DESCHENES, M. 2011. Motor unit and neuromuscular junction remodeling with aging. *Current aging science*, 4, 209-220.
- RAI, M. & DEMONTIS, F. 2016. Systemic nutrient and stress signaling via myokines and myometabolites. *Annual review of physiology*, 78, 85-107.
- RAO, A., LUO, C. & HOGAN, P. G. 1997. Transcription factors of the NFAT family: regulation and function. *Annual review of immunology*, 15, 707-747.
- RASCHKE, S., ECKARDT, K., BJØRKLUND HOLVEN, K., JENSEN, J. & ECKEL, J. 2013. Identification and validation of novel contraction-regulated myokines released from primary human skeletal muscle cells. *PLoS one*, 8, e62008.
- RAUE, U., TRAPPE, T. A., ESTREM, S. T., QIAN, H.-R., HELVERING, L. M., SMITH, R. C. & TRAPPE, S. 2012. Transcriptome signature of resistance exercise adaptations: mixed muscle and fiber type specific profiles in young and old adults. *Journal of applied physiology*, 112, 1625-1636.
- REID, B., MARTINOV, V. N., NJÅ, A., LØMO, T. & BEWICK, G. S. 2003. Activity-dependent plasticity of transmitter release from nerve terminals in rat fast and slow muscles. *Journal of Neuroscience*, 23, 9340-9348.

- RELAIX, F. & ZAMMIT, P. S. 2012. Satellite cells are essential for skeletal muscle regeneration: the cell on the edge returns centre stage. *Development*, 139, 2845-2856.
- RISSEON, V., MAZELIN, L., ROCERI, M., SANCHEZ, H., MONCOLLIN, V., CORNELOUP, C., RICHARD-BULTEAU, H., VIGNAUD, A., BAAS, D. & DEFOUR, A. 2009. Muscle inactivation of mTOR causes metabolic and dystrophin defects leading to severe myopathy. *Journal of Cell Biology*, 187, 859-874.
- ROBERTS, M. D., MOBLEY, C. B., VANN, C. G., HAUN, C. T., SCHOENFELD, B. J., YOUNG, K. C. & KAVAZIS, A. N. 2020. Synergist ablation-induced hypertrophy occurs more rapidly in the plantaris than soleus muscle in rats due to different molecular mechanisms. *American Journal of Physiology-Regulatory, Integrative and Comparative Physiology*, 318, R360-R368.
- ROEMERS, P., MAZZOLA, P., DE DEYN, P., BOSSERS, W., VAN HEUVELEN, M. & VAN DER ZEE, E. 2018. Burrowing as a novel voluntary strength training method for mice: a comparison of various voluntary strength or resistance exercise methods. *Journal of neuroscience methods*, 300, 112-126.
- ROMAN, W. & GOMES, E. R. 2018. Nuclear positioning in skeletal muscle. *Seminars in Cell & Developmental Biology*, 82, 51-56.
- ROMMEL, C., BODINE, S. C., CLARKE, B. A., ROSSMAN, R., NUNEZ, L., STITT, T. N., YANCOPOULOS, G. D. & GLASS, D. J. 2001. Mediation of IGF-1-induced skeletal myotube hypertrophy by PI (3) K/Akt/mTOR and PI (3) K/Akt/GSK3 pathways. *Nature cell biology*, 3, 1009-1013.
- RONNEBERGER, O., FISCHER, P. & BROX, T. U-net: Convolutional networks for biomedical image segmentation. International Conference on Medical image computing and computer-assisted intervention, 2015. Springer, 234-241.
- ROWE, G. C., PATTEN, I. S., ZSENGELLER, Z. K., EL-KHOURY, R., OKUTSU, M., BAMPOH, S., KOULISIS, N., FARRELL, C., HIRSHMAN, M. F. & YAN, Z. 2013. Disconnecting mitochondrial content from respiratory chain capacity in PGC-1-deficient skeletal muscle. *Cell reports*, 3, 1449-1456.
- ROWE, R. W. D. 1981. Morphology of perimysial and endomysial connective tissue in skeletal muscle. *Tissue and Cell*, 13, 681-690.
- ROY, R. R. & EDGERTON, V. 1995. Response of mouse plantaris muscle to functional overload: comparison with rat and cat. *Comparative Biochemistry and Physiology Part A: Physiology*, 111, 569-575.
- RUAS, J. L., WHITE, J. P., RAO, R. R., KLEINER, S., BRANNAN, K. T., HARRISON, B. C., GREENE, N. P., WU, J., ESTALL, J. L. & IRVING, B. A. 2012. A PGC-1 α isoform induced by resistance training regulates skeletal muscle hypertrophy. *Cell*, 151, 1319-1331.
- RUSSELL, A. P., FEILCHENFELDT, J., SCHREIBER, S., PRAZ, M., CRETENAND, A., GOBELET, C., MEIER, C. A., BELL, D. R., KRALLI, A. & GIACOBINO, J.-P. 2003. Endurance training in humans leads to fiber type-specific increases in levels of peroxisome proliferator-activated receptor- γ coactivator-1 and peroxisome proliferator-activated receptor- α in skeletal muscle. *Diabetes*, 52, 2874-2881.
- RUSSELL, A. P., HESSELINK, M. K., LO, S. K. & SCHRAUWEN, P. 2005. Regulation of metabolic transcriptional co-activators and transcription factors with acute exercise. *The FASEB journal*, 19, 986-988.
- RUSSELL, R. C., TIAN, Y., YUAN, H., PARK, H. W., CHANG, Y.-Y., KIM, J., KIM, H., NEUFELD, T. P., DILLIN, A. & GUAN, K.-L. 2013. ULK1 induces autophagy by phosphorylating Beclin-1 and activating VPS34 lipid kinase. *Nature cell biology*, 15, 741-750.
- RYBALKA, E., TIMPANI, C. A., DEBRUIN, D. A., BAGARIC, R. M., CAMPELJ, D. G. & HAYES, A. 2020. The failed clinical story of myostatin inhibitors against Duchenne muscular dystrophy: exploring the biology behind the battle. *Cells*, 9, 2657.
- SABERS, C. J., MARTIN, M. M., BRUNN, G. J., WILLIAMS, J. M., DUMONT, F. J., WIEDERRECHT, G. & ABRAHAM, R. T. 1995. Isolation of a Protein Target of the FKBP12-Rapamycin Complex in Mammalian Cells (*). *Journal of Biological Chemistry*, 270, 815-822.

- SAHA, A. K., SCHWARSIN, A. J., RODUIT, R., MASSE, F., KAUSHIK, V., TORNHEIM, K., PRENTKI, M. & RUDERMAN, N. B. 2000. Activation of malonyl-CoA decarboxylase in rat skeletal muscle by contraction and the AMP-activated protein kinase activator 5-aminoimidazole-4-carboxamide-1- β -D-ribofuranoside. *Journal of Biological Chemistry*, 275, 24279-24283.
- SAKAKIBARA, I., SANTOLINI, M., FERRY, A., HAKIM, V. & MAIRE, P. 2014. Six homeoproteins and a linc-RNA at the fast MYH locus lock fast myofiber terminal phenotype. *PLoS Genet*, 10, e1004386.
- SAKAKIBARA, I., WURMSER, M., DOS SANTOS, M., SANTOLINI, M., DUCOMMUN, S., DAVAZE, R., GUERNEC, A., SAKAMOTO, K. & MAIRE, P. 2016. Six1 homeoprotein drives myofiber type IIA specialization in soleus muscle. *Skeletal muscle*, 6, 1-20.
- SAKAMOTO, Y. 1996. Histological features of endomysium, perimysium and epimysium in rat lateral pterygoid muscle. *Journal of morphology*, 227, 113-119.
- SALAZAR, V. S., GAMER, L. W. & ROSEN, V. 2016. BMP signalling in skeletal development, disease and repair. *Nature Reviews Endocrinology*, 12, 203-221.
- SALMONS, S. & SRETER, F. 1976. Significance of impulse activity in the transformation of skeletal muscle type. *Nature*, 263, 30-34.
- SALTER, A.-C. D., RICHMOND, F. J. & LOEB, G. E. 2003. Effects of muscle immobilization at different lengths on tetrodotoxin-induced disuse atrophy. *IEEE Transactions on neural systems and rehabilitation engineering*, 11, 209-217.
- SAMBASIVAN, R., YAO, R., KISSENFENNIG, A., VAN WITTENBERGHE, L., PALDI, A., GAYRAUD-MOREL, B., GUENOU, H., MALISSEN, B., TAJBAKHSI, S. & GALY, A. 2011. Pax7-expressing satellite cells are indispensable for adult skeletal muscle regeneration. *Development*, 138, 3647-3656.
- SANCAK, Y., THOREEN, C. C., PETERSON, T. R., LINDQUIST, R. A., KANG, S. A., SPOONER, E., CARR, S. A. & SABATINI, D. M. 2007. PRAS40 is an insulin-regulated inhibitor of the mTORC1 protein kinase. *Molecular cell*, 25, 903-915.
- SANDRI, M., SANDRI, C., GILBERT, A., SKURK, C., CALABRIA, E., PICARD, A., WALSH, K., SCHIAFFINO, S., LECKER, S. H. & GOLDBERG, A. L. 2004. Foxo transcription factors induce the atrophy-related ubiquitin ligase atrogin-1 and cause skeletal muscle atrophy. *Cell*, 117, 399-412.
- SANES, J. R. & LICHTMAN, J. W. 2001. Induction, assembly, maturation and maintenance of a postsynaptic apparatus. *Nature Reviews Neuroscience*, 2, 791-805.
- SANFORD, J. A., NOGIEC, C. D., LINDHOLM, M. E., ADKINS, J. N., AMAR, D., DASARI, S., DRUGAN, J. K., FERNÁNDEZ, F. M., RADOM-AIZIK, S., SCHENK, S., SNYDER, M. P., TRACY, R. P., VANDERBOOM, P., TRAPPE, S. & WALSH, M. J. 2020. Molecular Transducers of Physical Activity Consortium (MoTrPAC): Mapping the Dynamic Responses to Exercise. *Cell*, 181, 1464-1474.
- SARAH ECKSTEIN, S., WEIGERT, C. & LEHMANN, R. 2017. Divergent roles of IRS (insulin receptor substrate) 1 and 2 in liver and skeletal muscle. *Current medicinal chemistry*, 24, 1827-1852.
- SARBASSOV, D. D., GUERTIN, D. A., ALI, S. M. & SABATINI, D. M. 2005. Phosphorylation and regulation of Akt/PKB by the rictor-mTOR complex. *Science*, 307, 1098-1101.
- SARTORI, R., MILAN, G., PATRON, M., MAMMUCARI, C., BLAAUW, B., ABRAHAM, R. & SANDRI, M. 2009. Smad2 and 3 transcription factors control muscle mass in adulthood. *American journal of physiology-cell physiology*, 296, C1248-C1257.
- SARTORI, R., ROMANELLO, V. & SANDRI, M. 2021. Mechanisms of muscle atrophy and hypertrophy: Implications in health and disease. *Nature Communications*, 12, 1-12.
- SARTORI, R., SCHIRWIS, E., BLAAUW, B., BORTOLANZA, S., ZHAO, J., ENZO, E., STANTZOU, A., MOUISEL, E., TONIOLO, L. & FERRY, A. 2013. BMP signaling controls muscle mass. *Nature genetics*, 45, 1309-1318.
- SCARPULLA, R. C. 2008. Transcriptional paradigms in mammalian mitochondrial biogenesis and function. *Physiological reviews*, 88, 611-638.
- SCHARNER, J. & ZAMMIT, P. S. 2011. The muscle satellite cell at 50: the formative years. *Skeletal Muscle*, 1, 28.

- SCHIAFFINO, S. 2018. Muscle fiber type diversity revealed by anti-myosin heavy chain antibodies. *The FEBS Journal*, 285, 3688-3694.
- SCHIAFFINO, S., DYAR, K. A., CICILIOT, S., BLAAUW, B. & SANDRI, M. 2013. Mechanisms regulating skeletal muscle growth and atrophy. *The FEBS journal*, 280, 4294-4314.
- SCHIAFFINO, S., GORZA, L., SARTORE, S., SAGGIN, L., AUSONI, S., VIANELLO, M., GUNDERSEN, K. & LØMO, T. 1989. Three myosin heavy chain isoforms in type 2 skeletal muscle fibres. *Journal of Muscle Research & Cell Motility*, 10, 197-205.
- SCHIAFFINO, S. & REGGIANI, C. 1994. Myosin isoforms in mammalian skeletal muscle. *Journal of applied physiology*, 77, 493-501.
- SCHIAFFINO, S. & REGGIANI, C. 1996. Molecular diversity of myofibrillar proteins: gene regulation and functional significance. *Physiological reviews*, 76, 371-423.
- SCHIAFFINO, S., REGGIANI, C., AKIMOTO, T. & BLAAUW, B. 2020. Molecular mechanisms of skeletal muscle hypertrophy. *Journal of Neuromuscular Diseases*, 1-15.
- SCHLAGHECK, M. L., WALZIK, D., JOISTEN, N., KOLIAMITRA, C., HARDT, L., METCALFE, A. J., WAHL, P., BLOCH, W., SCHENK, A. & ZIMMER, P. 2020. Cellular immune response to acute exercise: Comparison of endurance and resistance exercise. *European journal of haematology*, 105, 75-84.
- SCHMALBRUCH, H. & HELLHAMMER, U. 1977. The number of nuclei in adult rat muscles with special reference to satellite cells. *Anat Rec*, 189, 169-75.
- SCHMITTGEN, T. D. & LIVAK, K. J. 2008. Analyzing real-time PCR data by the comparative CT method. *Nature protocols*, 3, 1101-1108.
- SCHMOLL, M., UNGER, E., SUTHERLAND, H., HALLER, M., BIJAK, M., LANMÜLLER, H. & JARVIS, J. C. 2018. Spillover stimulation: A novel hypertrophy model using co-contraction of the plantar-flexors to load the tibial anterior muscle in rats. *PLOS ONE*, 13, e0207886.
- SCHRODER, E. A., HARFMANN, B. D., ZHANG, X., SRIKUEA, R., ENGLAND, J. H., HODGE, B. A., WEN, Y., RILEY, L. A., YU, Q. & CHRISTIE, A. 2015. Intrinsic muscle clock is necessary for musculoskeletal health. *The Journal of physiology*, 593, 5387-5404.
- SCHUELKE, M., WAGNER, K. R., STOLZ, L. E., HÜBNER, C., RIEBEL, T., KÖMEN, W., BRAUN, T., TOBIN, J. F. & LEE, S.-J. 2004. Myostatin mutation associated with gross muscle hypertrophy in a child. *New England Journal of Medicine*, 350, 2682-2688.
- SCHULER, M., ALI, F., CHAMBON, C., DUTEIL, D., BORNERT, J.-M., TARDIVEL, A., DESVERGNE, B., WAHLI, W., CHAMBON, P. & METZGER, D. 2006. PGC1 α expression is controlled in skeletal muscles by PPAR β , whose ablation results in fiber-type switching, obesity, and type 2 diabetes. *Cell metabolism*, 4, 407-414.
- SCHULTZ, E. 1996. Satellite Cell Proliferative Compartments in Growing Skeletal Muscles. *Developmental Biology*, 175, 84-94.
- SCHWANN, T. 1839. *Mikroskopische Untersuchungen über die Uebereinstimmung in der Struktur und dem Wachsthum der Thiere und Pflanzen*, Verlag der Sander'schen Buchhandlung (GE Reimer).
- SCISCIOLA, L., FONTANELLA, R. A., CATALDO, V., PAOLISSO, G. & BARBIERI, M. 2021. Sarcopenia and cognitive function: Role of myokines in muscle brain cross-talk. *Life*, 11, 173.
- SEABORNE, R., STRAUSS, J., COCKS, M., SHEPHERD, S., O'BRIEN, T., VAN SOMEREN, K., BELL, P., MURGATROYD, C., MORTON, J. & STEWART, C. 2018a. Methylome of human skeletal muscle after acute & chronic resistance exercise training, detraining & retraining. *Scientific data*, 5, 1-9.
- SEABORNE, R. A., HUGHES, D. C., TURNER, D. C., OWENS, D. J., BAEHR, L. M., GORSKI, P., SEMENOVA, E. A., BORISOV, O. V., LARIN, A. K. & POPOV, D. V. 2019a. UBR5 is a novel E3 ubiquitin ligase involved in skeletal muscle hypertrophy and recovery from atrophy. *The Journal of physiology*, 597, 3727-3749.
- SEABORNE, R. A., HUGHES, D. C., TURNER, D. C., OWENS, D. J., BAEHR, L. M., GORSKI, P., SEMENOVA, E. A., BORISOV, O. V., LARIN, A. K., POPOV, D. V., GENEROZOV, E. V., SUTHERLAND, H.,

- AHMETOV, II, JARVIS, J. C., BODINE, S. C. & SHARPLES, A. P. 2019b. UBR5 is a novel E3 ubiquitin ligase involved in skeletal muscle hypertrophy and recovery from atrophy. *J Physiol*, 597, 3727-3749.
- SEABORNE, R. A., STRAUSS, J., COCKS, M., SHEPHERD, S., O'BRIEN, T. D., VAN SOMEREN, K. A., BELL, P. G., MURGATROYD, C., MORTON, J. P. & STEWART, C. E. 2018b. Human skeletal muscle possesses an epigenetic memory of hypertrophy. *Scientific reports*, 8, 1-17.
- SEABORNE, R. A., VIGGARS, M. & SHARPLES, A. P. 2019c. How Long Does Muscle Memory Last?: The Role Of Epigenetics. *Journal Of Applied Physiology*, 127, 1819-1819.
- SEALE, P. & RUDNICKI, M. A. 2000. A new look at the origin, function, and "stem-cell" status of muscle satellite cells. *Developmental biology*, 218, 115-124.
- SEALE, P., SABOURIN, L. A., GIRGIS-GABARDO, A., MANSOURI, A., GRUSS, P. & RUDNICKI, M. A. 2000. Pax7 is required for the specification of myogenic satellite cells. *Cell*, 102, 777-786.
- SELDEEN, K. L., LASKY, G., LEIKER, M. M., PANG, M., PERSONIUS, K. E. & TROEN, B. R. 2018. High intensity interval training improves physical performance and frailty in aged mice. *The Journals of Gerontology: Series A*, 73, 429-437.
- SELDEEN, K. L., REDAE, Y. Z., THIYAGARAJAN, R., BERMAN, R. N., LEIKER, M. M. & TROEN, B. R. 2019. High intensity interval training improves physical performance in aged female mice: A comparison of mouse frailty assessment tools. *Mechanisms of Ageing and Development*, 180, 49-62.
- SENF, S. M., DODD, S. L. & JUDGE, A. R. 2010. FOXO signaling is required for disuse muscle atrophy and is directly regulated by Hsp70. *American Journal of Physiology-Cell Physiology*, 298, C38-C45.
- SERRANO, A. L., BAEZA-RAJA, B., PERDIGUERO, E., JARDÍ, M. & MUÑOZ-CÁNOVES, P. 2008. Interleukin-6 is an essential regulator of satellite cell-mediated skeletal muscle hypertrophy. *Cell metabolism*, 7, 33-44.
- SERTEL, O., DOGDAS, B., CHIU, C. S. & GURCAN, M. N. 2011. Microscopic image analysis for quantitative characterization of muscle fiber type composition. *Computerized Medical Imaging and Graphics*, 35, 616-628.
- SEVERINSEN, M. C. K. & PEDERSEN, B. K. 2020. Muscle–organ crosstalk: the emerging roles of myokines. *Endocrine reviews*, 41, 594-609.
- SEYNNES, O. R., DE BOER, M. & NARICI, M. V. 2007. Early skeletal muscle hypertrophy and architectural changes in response to high-intensity resistance training. *Journal of applied physiology*, 102, 368-373.
- SHANNON, P., MARKIEL, A., OZIER, O., BALIGA, N. S., WANG, J. T., RAMAGE, D., AMIN, N., SCHWIKOWSKI, B. & IDEKER, T. 2003. Cytoscape: a software environment for integrated models of biomolecular interaction networks. *Genome research*, 13, 2498-2504.
- SHARLO, K., PARAMONOVA, I., TURTIKOVA, O., TYGANOV, S. & SHENKMAN, B. 2019. Plantar mechanical stimulation prevents calcineurin-NFATc1 inactivation and slow-to-fast fiber type shift in rat soleus muscle under hindlimb unloading. *Journal of Applied Physiology*, 126, 1769-1781.
- SHARPLES, A. P., POLYDOROU, I., HUGHES, D. C., OWENS, D. J., HUGHES, T. M. & STEWART, C. E. 2016. Skeletal muscle cells possess a 'memory' of acute early life TNF- α exposure: role of epigenetic adaptation. *Biogerontology*, 17, 603-617.
- SHININ, V., GAYRAUD-MOREL, B., GOMÈS, D. & TAJBAKSHI, S. 2006. Asymmetric division and cosegregation of template DNA strands in adult muscle satellite cells. *Nature cell biology*, 8, 677-682.
- SHOR, B., WU, J., SHAKEY, Q., TORAL-BARZA, L., SHI, C., FOLLETTIE, M. & YU, K. 2010. Requirement of the mTOR kinase for the regulation of Maf1 phosphorylation and control of RNA polymerase III-dependent transcription in cancer cells. *Journal of Biological Chemistry*, 285, 15380-15392.

- SHORT, K. R., VITTONI, J. L., BIGELOW, M. L., PROCTOR, D. N., RIZZA, R. A., COENEN-SCHIMKE, J. M. & NAIR, K. S. 2003. Impact of aerobic exercise training on age-related changes in insulin sensitivity and muscle oxidative capacity. *Diabetes*, 52, 1888-1896.
- SHOSTAK, A., RUPPERT, B., HA, N., BRUNS, P., TOPRAK, U. H., EILS, R., SCHLESNER, M., DIERNFELLNER, A. & BRUNNER, M. 2016. MYC/MIZ1-dependent gene repression inversely coordinates the circadian clock with cell cycle and proliferation. *Nature communications*, 7, 1-11.
- SMITH, H. K., MAXWELL, L., RODGERS, C. D., MCKEE, N. H. & PLYLEY, M. J. 2001. Exercise-enhanced satellite cell proliferation and new myonuclear accretion in rat skeletal muscle. *Journal of Applied Physiology*, 90, 1407-1414.
- SMITH, L. R. & BARTON, E. R. 2014. SMASH—semi-automatic muscle analysis using segmentation of histology: a MATLAB application. *Skeletal muscle*, 4, 1-16.
- SNIJDERS, T., AUSSIEKER, T., HOLWERDA, A., PARISE, G., VAN LOON, L. J. & VERDIJK, L. B. 2020a. The concept of skeletal muscle memory: Evidence from animal and human studies. *Acta Physiologica*, e13465.
- SNIJDERS, T., HOLWERDA, A. M., VAN LOON, L. J. & VERDIJK, L. B. 2020b. Myonuclear content and domain size in small versus larger muscle fibres in response to 12 weeks of resistance exercise training in older adults. *Acta Physiologica*, e13599.
- SNIJDERS, T., NEDERVEEN, J. P., BELL, K. E., LAU, S. W., MAZARA, N., KUMBHARE, D. A., PHILLIPS, S. M. & PARISE, G. 2019. Prolonged exercise training improves the acute type II muscle fibre satellite cell response in healthy older men. *The Journal of physiology*, 597, 105-119.
- SNIJDERS, T., SMEETS, J. S., VAN KRANENBURG, J., KIES, A., VAN LOON, L. & VERDIJK, L. B. 2016. Changes in myonuclear domain size do not precede muscle hypertrophy during prolonged resistance-type exercise training. *Acta physiologica*, 216, 231-239.
- SNIJDERS, T., WALL, B. T., DIRKS, M. L., SENDEN, J. M., HARTGENS, F., DOLMANS, J., LOSEN, M., VERDIJK, L. B. & VAN LOON, L. J. 2014. Muscle disuse atrophy is not accompanied by changes in skeletal muscle satellite cell content. *Clinical science*, 126, 557-566.
- SOFFE, Z., RADLEY-CRABB, H., MCMAHON, C., GROUNDS, M. & SHAVLAKADZE, T. 2016. Effects of loaded voluntary wheel exercise on performance and muscle hypertrophy in young and old male C57BL/6J mice. *Scandinavian journal of medicine & science in sports*, 26, 172-188.
- SOLSONA, R., PAVLIN, L., BERNARDI, H. & SANCHEZ, A. M. 2021. Molecular Regulation of Skeletal Muscle Growth and Organelle Biosynthesis: Practical Recommendations for Exercise Training. *International Journal of Molecular Sciences*, 22, 2741.
- SPANGENBURG, E. & BOOTH, F. 2003. Molecular regulation of individual skeletal muscle fibre types. *Acta physiologica scandinavica*, 178, 413-424.
- SRSEN, V., FANT, X., HEALD, R., RABOUILLE, C. & MERDES, A. 2009. Centrosome proteins form an insoluble perinuclear matrix during muscle cell differentiation. *BMC cell biology*, 10, 28.
- STANLEY, E. F. 1981. Sensory and motor nerve conduction velocities and the latency of the H reflex during growth of the rat. *Experimental neurology*, 71, 497-506.
- STEC, M. J., KELLY, N. A., MANY, G. M., WINDHAM, S. T., TUGGLE, S. C. & BAMMAN, M. M. 2016. Ribosome biogenesis may augment resistance training-induced myofiber hypertrophy and is required for myotube growth in vitro. *American Journal of Physiology-Endocrinology and Metabolism*, 310, E652-E661.
- STEPHENS, A. D., BANIGAN, E. J. & MARKO, J. F. 2019a. Chromatin's physical properties shape the nucleus and its functions. *Current opinion in cell biology*, 58, 76-84.
- STEPHENS, A. D., LIU, P. Z., KANDULA, V., CHEN, H., ALMASSALHA, L. M., HERMAN, C., BACKMAN, V., O'HALLORAN, T., ADAM, S. A. & GOLDMAN, R. D. 2019b. Physicochemical mechanotransduction alters nuclear shape and mechanics via heterochromatin formation. *Molecular biology of the cell*, 30, 2320-2330.
- STEWART, M. D., JANG, C. W., HONG, N. W., AUSTIN, A. P. & BEHRINGER, R. R. 2009. Dual fluorescent protein reporters for studying cell behaviors in vivo. *genesis*, 47, 708-717.

- STOCK, M. S., MOTA, J. A., DEFRANCO, R. N., GRUE, K. A., JACOBO, A., CHUNG, E., MOON, J. R., DEFREITAS, J. M. & BECK, T. W. 2017. The time course of short-term hypertrophy in the absence of eccentric muscle damage. *European journal of applied physiology*, 117, 989-1004.
- STOCKDALE, F. E. 1992. Myogenic cell lineages. *Developmental biology*, 154, 284-298.
- STOKOE, D., STEPHENS, L. R., COPELAND, T., GAFFNEY, P. R., REESE, C. B., PAINTER, G. F., HOLMES, A. B., MCCORMICK, F. & HAWKINS, P. T. 1997. Dual role of phosphatidylinositol-3, 4, 5-trisphosphate in the activation of protein kinase B. *Science*, 277, 567-570.
- SUN, L. & CHEN, Z. J. 2004. The novel functions of ubiquitination in signaling. *Current opinion in cell biology*, 16, 119-126.
- SUN, X.-X., HE, X., YIN, L., KOMADA, M., SEARS, R. C. & DAI, M.-S. 2015. The nucleolar ubiquitin-specific protease USP36 deubiquitinates and stabilizes c-Myc. *Proceedings of the National Academy of Sciences*, 112, 3734-3739.
- SUTHERLAND, H., JARVIS, J. C., KWENDE, M. M., GILROY, S. J. & SALMONS, S. 1998. The dose-related response of rabbit fast muscle to long-term low-frequency stimulation. *Muscle & Nerve: Official Journal of the American Association of Electrodiagnostic Medicine*, 21, 1632-1646.
- SUWA, M., EGASHIRA, T., NAKANO, H., SASAKI, H. & KUMAGAI, S. 2006. Metformin increases the PGC-1 α protein and oxidative enzyme activities possibly via AMPK phosphorylation in skeletal muscle in vivo. *Journal of Applied Physiology*, 101, 1685-1692.
- TAJBAKSH, S., ROCANCOURT, D., COSSU, G. & BUCKINGHAM, M. 1997. Redefining the genetic hierarchies controlling skeletal myogenesis: Pax-3 and Myf-5 act upstream of MyoD. *Cell*, 89, 127-138.
- TAKAHASHI, M. & HOOD, D. A. 1993. Chronic stimulation-induced changes in mitochondria and performance in rat skeletal muscle. *Journal of Applied Physiology*, 74, 934-941.
- TAMAKI, T., UCHIYAMA, S. & NAKANO, S. 1992. A weight-lifting exercise model for inducing hypertrophy in the hindlimb muscles of rats. *Medicine and science in sports and exercise*, 24, 881.
- TAYLOR, N. A. & WILKINSON, J. G. 1986. Exercise-Induced Skeletal Muscle Growth Hypertrophy or Hyperplasia? *Sports medicine*, 3, 190-200.
- TERADA, S., GOTO, M., KATO, M., KAWANAKA, K., SHIMOKAWA, T. & TABATA, I. 2002. Effects of low-intensity prolonged exercise on PGC-1 mRNA expression in rat epitrochlearis muscle. *Biochemical and biophysical research communications*, 296, 350-354.
- TERADA, S., KAWANAKA, K., GOTO, M., SHIMOKAWA, T. & TABATA, I. 2005. Effects of high-intensity intermittent swimming on PGC-1 α protein expression in rat skeletal muscle. *Acta physiologica scandinavica*, 184, 59-65.
- TERMIN, A., STARON, R. & PETTE, D. 1989a. Myosin heavy chain isoforms in histochemically defined fiber types of rat muscle. *Histochemistry*, 92, 453-457.
- TERMIN, A., STARON, R. S. & PETTE, D. 1989b. Changes in myosin heavy chain isoforms during chronic low-frequency stimulation of rat fast hindlimb muscles: A single-fiber study. *European Journal of Biochemistry*, 186, 749-754.
- THOMPSON, M. R., XU, D. & WILLIAMS, B. R. 2009. ATF3 transcription factor and its emerging roles in immunity and cancer. *Journal of molecular medicine*, 87, 1053.
- TIERNEY, M. T., STEC, M. J., RULANDS, S., SIMONS, B. D. & SACCO, A. 2018. Muscle stem cells exhibit distinct clonal dynamics in response to tissue repair and homeostatic aging. *Cell Stem Cell*, 22, 119-127. e3.
- TIMSON, B. F., BOWLIN, B. K., DUDENHOEFFER, G. A. & GEORGE, J. B. 1985. Fiber number, area, and composition of mouse soleus muscle following enlargement. *Journal of applied physiology*, 58, 619-624.
- TOKER, A. & DIBBLE, C. C. 2018. PI 3-Kinase Signaling: AKTing up inside the Cell. *Molecular cell*, 71, 875-876.
- TOMASONI, R. & MONDINO, A. 2011. The tuberous sclerosis complex: balancing proliferation and survival. *Biochemical Society transactions*, 39, 466-471.

- TRAORE, M., GENTIL, C., BENEDETTO, C., HOGREL, J.-Y., DE LA GRANGE, P., CADOT, B., BENKHELIFA-ZIYYAT, S., JULIEN, L., LEMAITRE, M. & FERRY, A. 2019. An embryonic CaV β 1 isoform promotes muscle mass maintenance via GDF5 signaling in adult mouse. *Science translational medicine*, 11.
- TROLLET, C., CHENG, A. J., SYLOW, L., BATISTA JR, M. L. & PILLON, N. J. 2021. Skeletal Muscle Immunometabolism. *Frontiers in Physiology*, 12, 530.
- TUNELL, G. L. & HART, M. N. 1977. Simultaneous determination of skeletal muscle fiber, types I, IIA, and IIB by histochemistry. *Archives of Neurology*, 34, 171-173.
- TURNER, D. C., SEABORNE, R. A. & SHARPLES, A. P. 2019. Comparative transcriptome and methylome analysis in human skeletal muscle anabolism, hypertrophy and epigenetic memory. *Scientific reports*, 9, 1-12.
- TZIVION, G., DOBSON, M. & RAMAKRISHNAN, G. 2011. FoxO transcription factors; Regulation by AKT and 14-3-3 proteins. *Biochimica et Biophysica Acta (BBA)-Molecular Cell Research*, 1813, 1938-1945.
- VAFAI, S. B. & MOOTHA, V. K. 2012. Mitochondrial disorders as windows into an ancient organelle. *Nature*, 491, 374-383.
- VALDES, O., RAMIREZ, C., PEREZ, F., GARCIA-VICENCIO, S., NOSAKA, K. & PENAILILLO, L. 2021. Contralateral effects of eccentric resistance training on immobilized arm. *Scandinavian Journal of Medicine & Science in Sports*, 31, 76-90.
- VAN HORN, R. & CROW, M. T. 1989. Fast myosin heavy chain expression during the early and late embryonic stages of chicken skeletal muscle development. *Developmental biology*, 134, 279-288.
- VAN INGEN, M. J. & KIRBY, T. J. 2021. LINCing Nuclear Mechanobiology With Skeletal Muscle Mass and Function. *Frontiers in Cell and Developmental Biology*, 12, 6924.
- VAN RIGGELEN, J., YETIL, A. & FELSHER, D. W. 2010. MYC as a regulator of ribosome biogenesis and protein synthesis. *Nature Reviews Cancer*, 10, 301-309.
- VANDER HAAR, E., LEE, S.-I., BANDHAKAVI, S., GRIFFIN, T. J. & KIM, D.-H. 2007. Insulin signalling to mTOR mediated by the Akt/PKB substrate PRAS40. *Nature cell biology*, 9, 316-323.
- VENTURINI, V., PEZZANO, F., CASTRO, F. C., HÄKKINEN, H.-M., JIMÉNEZ-DELGADO, S., COLOMER-ROSELL, M., MARRO, M., TOLOSA-RAMON, Q., PAZ-LÓPEZ, S. & VALVERDE, M. A. 2020. The nucleus measures shape changes for cellular proprioception to control dynamic cell behavior. *Science*, 370.
- VENUTI, J. M., MORRIS, J. H., VIVIAN, J. L., OLSON, E. N. & KLEIN, W. H. 1995. Myogenin is required for late but not early aspects of myogenesis during mouse development. *The Journal of cell biology*, 128, 563-576.
- VERMA, M., ASAKURA, Y., MURAKONDA, B. S. R., PENGU, T., LATROCHE, C., CHAZAUD, B., MCLOON, L. K. & ASAKURA, A. 2018. Muscle satellite cell cross-talk with a vascular niche maintains quiescence via VEGF and notch signaling. *Cell stem cell*, 23, 530-543. e9.
- VICKERTON, P., JARVIS, J. & JEFFERY, N. 2013. Concentration-dependent specimen shrinkage in iodine-enhanced micro CT. *Journal of anatomy*, 223, 185-193.
- VICKERTON, P., JARVIS, J. C., GALLAGHER, J. A., AKHTAR, R., SUTHERLAND, H. & JEFFERY, N. 2014. Morphological and histological adaptation of muscle and bone to loading induced by repetitive activation of muscle. *Proceedings of the Royal Society B: Biological Sciences*, 281, 20140786.
- VIDAL-PUIG, A. J., GRUJIC, D., ZHANG, C.-Y., HAGEN, T., BOSS, O., IDO, Y., SZCZEPANIK, A., WADE, J., MOOTHA, V. & CORTRIGHT, R. 2000. Energy metabolism in uncoupling protein 3 gene knockout mice. *Journal of Biological Chemistry*, 275, 16258-16266.
- VIGGARS, M. R., WEN, Y., PETERSON, C. A. & JARVIS, J. C. 2022. Automated cross-sectional analysis of trained, severely atrophied, and recovering rat skeletal muscles using MyoVision 2.0. *Journal of Applied Physiology*, 132, 593-610.

- VIJAYAN, K., THOMPSON, J. L., NOREMBERG, K. M., FITTS, R. & RILEY, D. A. 2001. Fiber-type susceptibility to eccentric contraction-induced damage of hindlimb-unloaded rat AL muscles. *Journal of Applied Physiology*, 90, 770-776.
- VIJAYAN, K., THOMPSON, J. L. & RILEY, D. A. 1998. Sarcomere lesion damage occurs mainly in slow fibers of reloaded rat adductor longus muscles. *Journal of Applied Physiology*, 85, 1017-1023.
- VIRBASIUS, J. V. & SCARPULLA, R. C. 1994. Activation of the human mitochondrial transcription factor A gene by nuclear respiratory factors: a potential regulatory link between nuclear and mitochondrial gene expression in organelle biogenesis. *Proceedings of the National Academy of Sciences*, 91, 1309-1313.
- VIRBASIUS, J. V., VIRBASIUS, C.-M. A. & SCARPULLA, R. C. 1993. Identity of GABP with NRF-2, a multisubunit activator of cytochrome oxidase expression, reveals a cellular role for an ETS domain activator of viral promoters. *Genes & development*, 7, 380-392.
- VOIT, R. & GRUMMT, I. 2001. Phosphorylation of UBF at serine 388 is required for interaction with RNA polymerase I and activation of rDNA transcription. *Proceedings of the National Academy of Sciences*, 98, 13631-13636.
- VON WALDEN, F., CASAGRANDE, V., ÖSTLUND FARRANTS, A.-K. & NADER, G. A. 2012. Mechanical loading induces the expression of a Pol I regulon at the onset of skeletal muscle hypertrophy. *American Journal of Physiology-Cell Physiology*, 302, C1523-C1530.
- VON WALDEN, F., FIGUEIREDO, V., FERNANDEZ-GONZALO, R., MURACH, K., MOBLEY, B., NORRBOM, J., MCCARTHY, J. & ALKNER, B. 2020. Ribosomal DNA Transcription Induced by Acute Resistance Exercise is Dependent on rDNA Gene Dosage but not Promoter Methylation. *The FASEB Journal*, 34, 1-1.
- WACKERHAGE, H., SCHOENFELD, B. J., HAMILTON, D. L., LEHTI, M. & HULMI, J. J. 2019. Stimuli and sensors that initiate skeletal muscle hypertrophy following resistance exercise. *Journal of applied physiology*, 126, 30-43.
- WAGH, K., ISHIKAWA, M., GARCIA, D. A., STAVREVA, D. A., UPADHYAYA, A. & HAGER, G. L. 2021. Mechanical regulation of transcription: Recent Advances. *Trends in Cell Biology*.
- WAGNER, K. R., MCPHERRON, A. C., WINIK, N. & LEE, S. J. 2002. Loss of myostatin attenuates severity of muscular dystrophy in mdx mice. *Annals of Neurology: Official Journal of the American Neurological Association and the Child Neurology Society*, 52, 832-836.
- WAISMAN, A., NORRIS, A. M., COSTA, M. E. & KOPINKE, D. 2021. Automatic and unbiased segmentation and quantification of myofibers in skeletal muscle. *Scientific Reports*, 11, 1-14.
- WANG, H., WANG, X., XU, L. & CAO, H. 2019. Identification of transcription factors MYC and C/EBP β mediated regulatory networks in heart failure.
- WANG, H., WANG, X., XU, L. & CAO, H. 2020. Identification of transcription factors MYC and C/EBP β mediated regulatory networks in heart failure based on gene expression omnibus datasets. *BMC Cardiovascular Disorders*, 20, 1-11.
- WARDE-FARLEY, D., DONALDSON, S. L., COMES, O., ZUBERI, K., BADRAWI, R., CHAO, P., FRANZ, M., GROUIOS, C., KAZI, F. & LOPES, C. T. 2010. The GeneMANIA prediction server: biological network integration for gene prioritization and predicting gene function. *Nucleic acids research*, 38, W214-W220.
- WEN, Y., ALIMOV, A. P. & MCCARTHY, J. J. 2016. Ribosome biogenesis is necessary for skeletal muscle hypertrophy. *Exercise and sport sciences reviews*, 44, 110.
- WEN, Y., DUNGAN, C. M., MOBLEY, C. B., VALENTINO, T., VON WALDEN, F. & MURACH, K. A. 2021. Nucleus Type-Specific DNA Methyloomics Reveals Epigenetic “Memory” of Prior Adaptation in Skeletal Muscle. *Function*, 2, zqab038.
- WEN, Y., MURACH, K. A., JR., I. J. V., FRY, C. S., VICKERY, C., PETERSON, C. A., MCCARTHY, J. J. & CAMPBELL, K. S. 2018a. MyoVision: software for automated high-content analysis of skeletal muscle immunohistochemistry. *Journal of Applied Physiology*, 124, 40-51.

- WEN, Y., MURACH, K. A., VECHETTI JR, I. J., FRY, C. S., VICKERY, C., PETERSON, C. A., MCCARTHY, J. J. & CAMPBELL, K. S. 2018b. MyoVision: software for automated high-content analysis of skeletal muscle immunohistochemistry. *Journal of Applied Physiology*, 124, 40-51.
- WENDE, A. R., SCHAEFFER, P. J., PARKER, G. J., ZECHNER, C., HAN, D.-H., CHEN, M. M., HANCOCK, C. R., LEHMAN, J. J., HUSS, J. M. & MCCLAIN, D. A. 2007. A role for the transcriptional coactivator PGC-1 α in muscle refueling. *Journal of Biological Chemistry*, 282, 36642-36651.
- WEST, D. W., BAEHR, L. M., MARCOTTE, G. R., CHASON, C. M., TOLENTO, L., GOMES, A. V., BODINE, S. C. & BAAR, K. 2016. Acute resistance exercise activates rapamycin-sensitive and-insensitive mechanisms that control translational activity and capacity in skeletal muscle. *The Journal of physiology*, 594, 453-468.
- WESTMAN, A. M., DYER, S. E., REMER, J. D., HU, X., CHRIST, G. J. & BLEMKER, S. S. 2019. A coupled framework of in situ and in silico analysis reveals the role of lateral force transmission in force production in volumetric muscle loss injuries. *Journal of biomechanics*, 85, 118-125.
- WHITE, R. B., BIÉRINX, A.-S., GNOCCHI, V. F. & ZAMMIT, P. S. 2010. Dynamics of muscle fibre growth during postnatal mouse development. *BMC developmental biology*, 10, 21.
- WHITELAW, P. F. & HESKETH, J. E. 1992. Expression of c-myc and c-fos in rat skeletal muscle. Evidence for increased levels of c-myc mRNA during hypertrophy. *Biochemical Journal*, 281, 143-147.
- WILLINGHAM, T. B., KIM, Y., LINDBERG, E., BLECK, C. K. & GLANCY, B. 2020. The unified myofibrillar matrix for force generation in muscle. *Nature communications*, 11, 1-10.
- WINBANKS, C. E., CHEN, J. L., QIAN, H., LIU, Y., BERNARDO, B. C., BEYER, C., WATT, K. I., THOMSON, R. E., CONNOR, T. & TURNER, B. J. 2013. The bone morphogenetic protein axis is a positive regulator of skeletal muscle mass. *Journal of Cell Biology*, 203, 345-357.
- WINBANKS, C. E., WEEKS, K. L., THOMSON, R. E., SEPULVEDA, P. V., BEYER, C., QIAN, H., CHEN, J. L., ALLEN, J. M., LANCASTER, G. I. & FEBBRAIO, M. A. 2012. Follistatin-mediated skeletal muscle hypertrophy is regulated by Smad3 and mTOR independently of myostatin. *Journal of Cell Biology*, 197, 997-1008.
- WINCHESTER, P. & GONYEA, W. 1992. Regional injury and the terminal differentiation of satellite cells in stretched avian slow tonic muscle. *Developmental biology*, 151, 459-472.
- WINDER, W. A. & HARDIE, D. 1999. AMP-activated protein kinase, a metabolic master switch: possible roles in type 2 diabetes. *American Journal of Physiology-Endocrinology And Metabolism*, 277, E1-E10.
- WINDNER, S. E., MANHART, A., BROWN, A., MOGILNER, A. & BAYLIES, M. K. 2019. Nuclear scaling is coordinated among individual nuclei in multinucleated muscle fibers. *Developmental Cell*, 49, 48-62. e3.
- WINJE, I., BENGTSÉN, M., EFTESTØL, E., JUVKAM, I., BRUUSGAARD, J. C. & GUNDERSEN, K. 2018. Specific labelling of myonuclei by an antibody against pericentriolar material 1 on skeletal muscle tissue sections. *Acta Physiologica*, 223, e13034.
- WIRTH, O., GREGORY, E. W., CUTLIP, R. G. & MILLER, G. R. 2003. Control and quantitation of voluntary weight-lifting performance of rats. *Journal of applied physiology*, 95, 402-412.
- WONG, T. & BOOTH, F. W. 1988. Skeletal muscle enlargement with weight-lifting exercise by rats. *Journal of applied physiology*, 65, 950-954.
- WRIGHT, D. C., HAN, D.-H., GARCIA-ROVES, P. M., GEIGER, P. C., JONES, T. E. & HOLLOSZY, J. O. 2007. Exercise-induced mitochondrial biogenesis begins before the increase in muscle PGC-1 α expression. *Journal of Biological Chemistry*, 282, 194-199.
- WU, H., NAYA, F. J., MCKINSEY, T. A., MERCER, B., SHELTON, J. M., CHIN, E. R., SIMARD, A. R., MICHEL, R. N., BASSEL-DUBY, R. & OLSON, E. N. 2000. MEF2 responds to multiple calcium-regulated signals in the control of skeletal muscle fiber type. *The EMBO journal*, 19, 1963-1973.

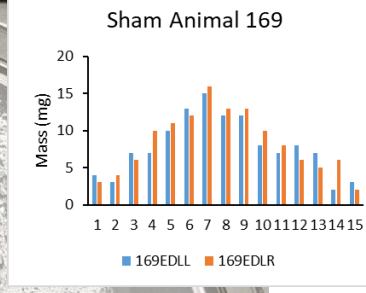
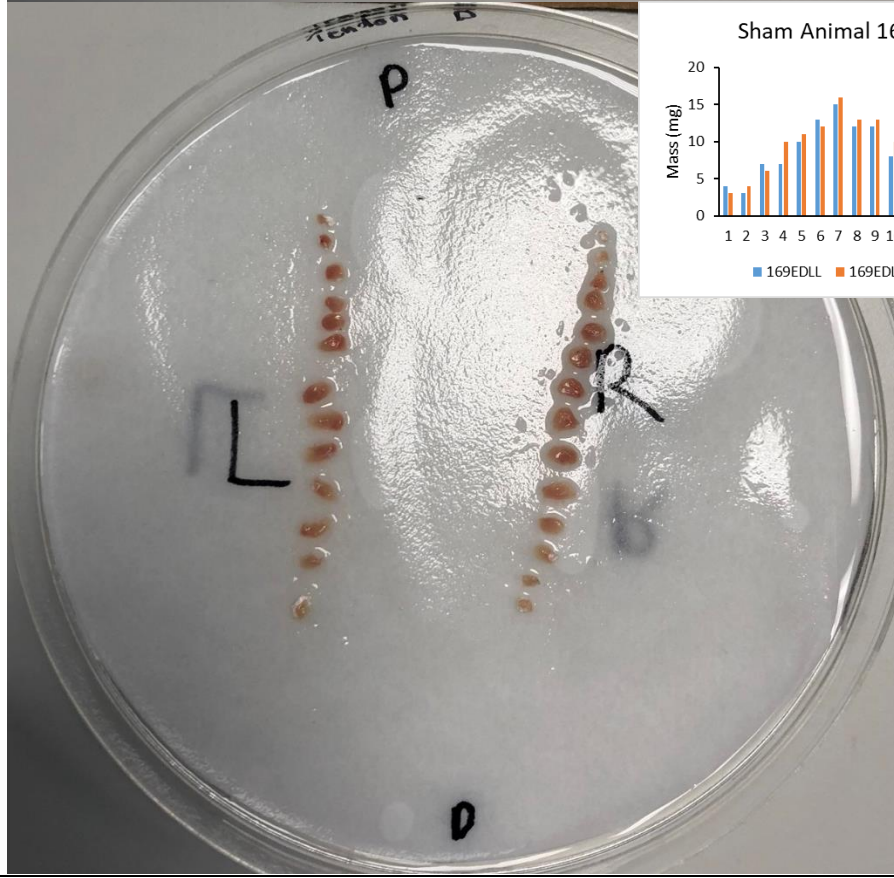
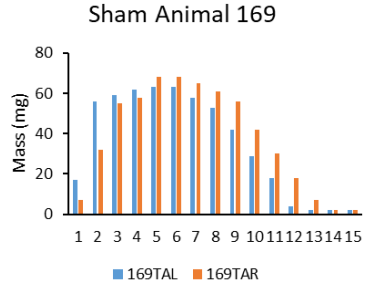
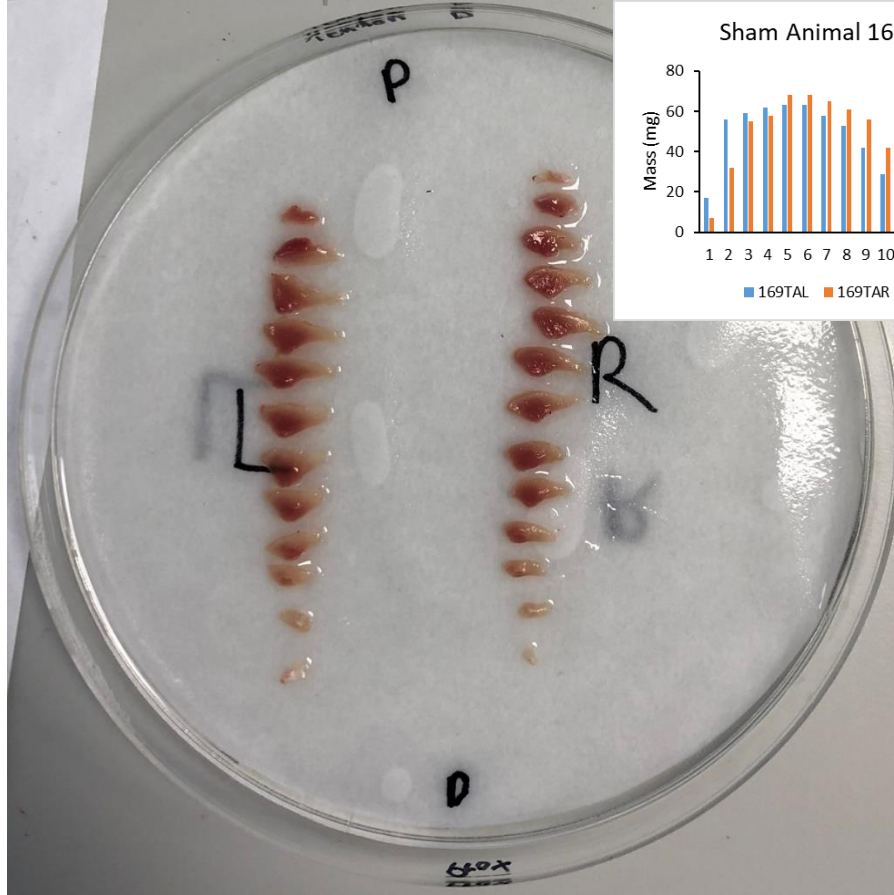
- WU, Z., PUIGSERVER, P., ANDERSSON, U., ZHANG, C., ADELMANT, G., MOOTHA, V., TROY, A., CINTI, S., LOWELL, B. & SCARPULLA, R. C. 1999. Mechanisms controlling mitochondrial biogenesis and respiration through the thermogenic coactivator PGC-1. *Cell*, 98, 115-124.
- YABLONKA-REUVENI, Z. & LEPPER, C. 2020. New Insight into a Classic Stem Cell: the Satellite Cell may Communicate with the Muscle Fiber via Extracellular Vesicles—A Perspective on “Fusion-Independent Satellite Cell Communication to Muscle Fibers During Load-Induced Hypertrophy”. *Function*, 1, zqaa015.
- YAFFE, D. & SAXEL, O. 1977. Serial passaging and differentiation of myogenic cells isolated from dystrophic mouse muscle. *Nature*, 270, 725-727.
- YAGI, K., FURUHASHI, M., AOKI, H., GOTO, D., KUWANO, H., SUGAMURA, K., MIYAZONO, K. & KATO, M. 2002. c-myc Is a Downstream Target of the Smad Pathway* 210. *Journal of Biological Chemistry*, 277, 854-861.
- YARASHESKI, K., LEMON, P. & GILLOTEAUX, J. 1990. Effect of heavy-resistance exercise training on muscle fiber composition in young rats. *Journal of applied physiology*, 69, 434-437.
- YOU, J.-S., DOOLEY, M. S., KIM, C.-R., KIM, E.-J., XU, W., GOODMAN, C. A. & HORNBERGER, T. A. 2018. A DGK ζ -FoxO-ubiquitin proteolytic axis controls fiber size during skeletal muscle remodeling. *Science signaling*, 11.
- YOU, J.-S., LINCOLN, H. C., KIM, C.-R., FREY, J. W., GOODMAN, C. A., ZHONG, X.-P. & HORNBERGER, T. A. 2014. The role of diacylglycerol kinase ζ and phosphatidic acid in the mechanical activation of mammalian target of rapamycin (mTOR) signaling and skeletal muscle hypertrophy. *Journal of Biological Chemistry*, 289, 1551-1563.
- YOU, J.-S., MCNALLY, R. M., JACOBS, B. L., PRIVETT, R. E., GUNDERMANN, D. M., LIN, K.-H., STEINERT, N. D., GOODMAN, C. A. & HORNBERGER, T. A. 2019. The role of raptor in the mechanical load-induced regulation of mTOR signaling, protein synthesis, and skeletal muscle hypertrophy. *The FASEB Journal*, 33, 4021-4034.
- ZABALETA-KORTA, A., FERNÁNDEZ-PEÑA, E. & SANTOS-CONCEJERO, J. 2020. Regional hypertrophy, the inhomogeneous muscle growth: A systematic review. *Strength & Conditioning Journal*, 42, 94-101.
- ZAID, A., LI, R., LUCIAKOVA, K., BARATH, P., NERY, S. & NELSON, B. D. 1999. On the role of the general transcription factor Sp1 in the activation and repression of diverse mammalian oxidative phosphorylation genes. *Journal of bioenergetics and biomembranes*, 31, 129-135.
- ZAMMIT, P. S. 2008. All muscle satellite cells are equal, but are some more equal than others? *Journal of cell science*, 121, 2975-2982.
- ZHANG, B.-T., YEUNG, S. S., LIU, Y., WANG, H.-H., WAN, Y.-M., LING, S.-K., ZHANG, H.-Y., LI, Y.-H. & YEUNG, E. W. 2010. The effects of low frequency electrical stimulation on satellite cell activity in rat skeletal muscle during hindlimb suspension. *BMC cell biology*, 11, 87.
- ZHANG, Q., DUPLANY, A., MONCOLLIN, V., MOURADIAN, S., GOILLOT, E., MAZELIN, L., GAUTHIER, K., STREICHENBERGER, N., ANGLERAUX, C. & CHEN, J. 2019. Lack of muscle mTOR kinase activity causes early onset myopathy and compromises whole-body homeostasis. *Journal of cachexia, sarcopenia and muscle*, 10, 35-53.
- ZHANG, X., PATEL, S. P., MCCARTHY, J. J., RABCHEVSKY, A. G., GOLDHAMER, D. J. & ESSER, K. A. 2012. A non-canonical E-box within the MyoD core enhancer is necessary for circadian expression in skeletal muscle. *Nucleic acids research*, 40, 3419-3430.
- ZHOU, C., LI, C., ZHOU, B., SUN, H., KOULLOUROU, V., HOLT, I., PUCKELWARTZ, M. J., WARREN, D. T., HAYWARD, R. & LIN, Z. 2017. Novel nesprin-1 mutations associated with dilated cardiomyopathy cause nuclear envelope disruption and defects in myogenesis. *Human molecular genetics*, 26, 2258-2276.
- ZHOU, H., SHEN, D.-F., BIAN, Z.-Y., ZONG, J., DENG, W., ZHANG, Y., GUO, Y.-Y., LI, H. & TANG, Q.-Z. 2011. Activating transcription factor 3 deficiency promotes cardiac hypertrophy, dysfunction, and fibrosis induced by pressure overload. *PLoS One*, 6, e26744.

ZIMMERS, T. A., DAVIES, M. V., KONIARIS, L. G., HAYNES, P., ESQUELA, A. F., TOMKINSON, K. N., MCPHERRON, A. C., WOLFMAN, N. M. & LEE, S.-J. 2002. Induction of cachexia in mice by systemically administered myostatin. *Science*, 296, 1486-1488.

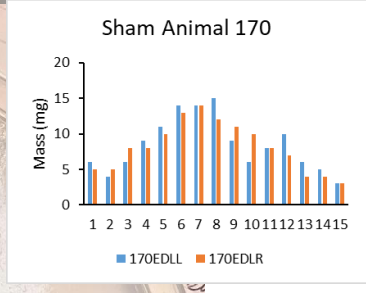
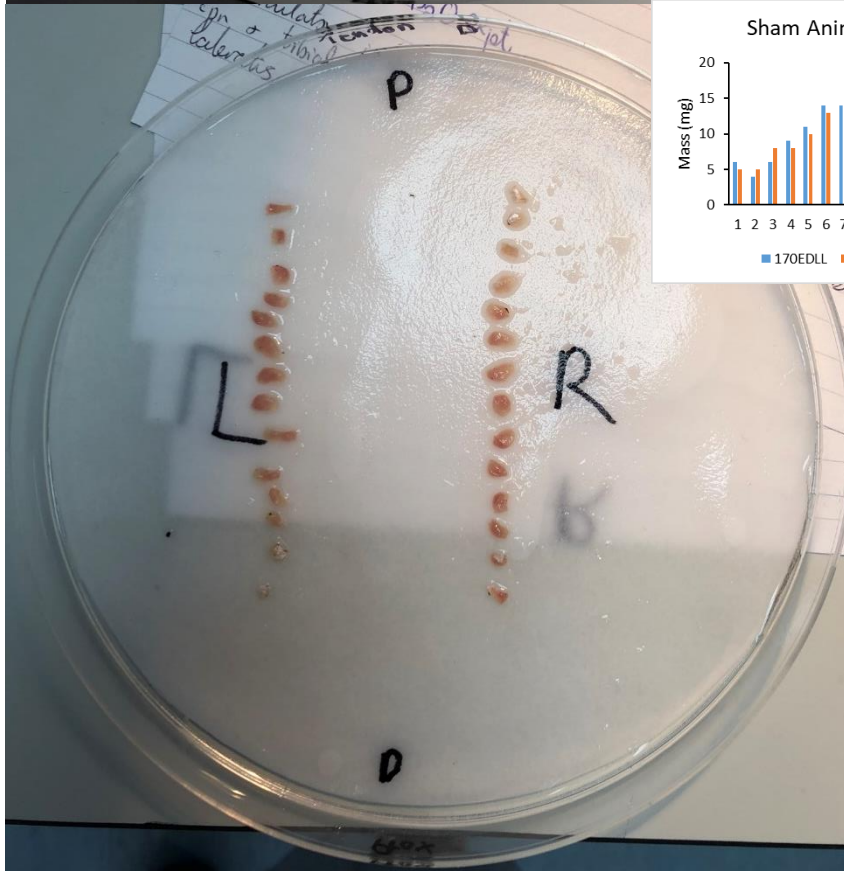
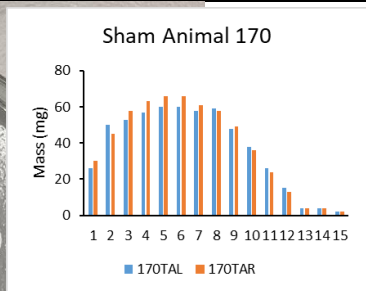
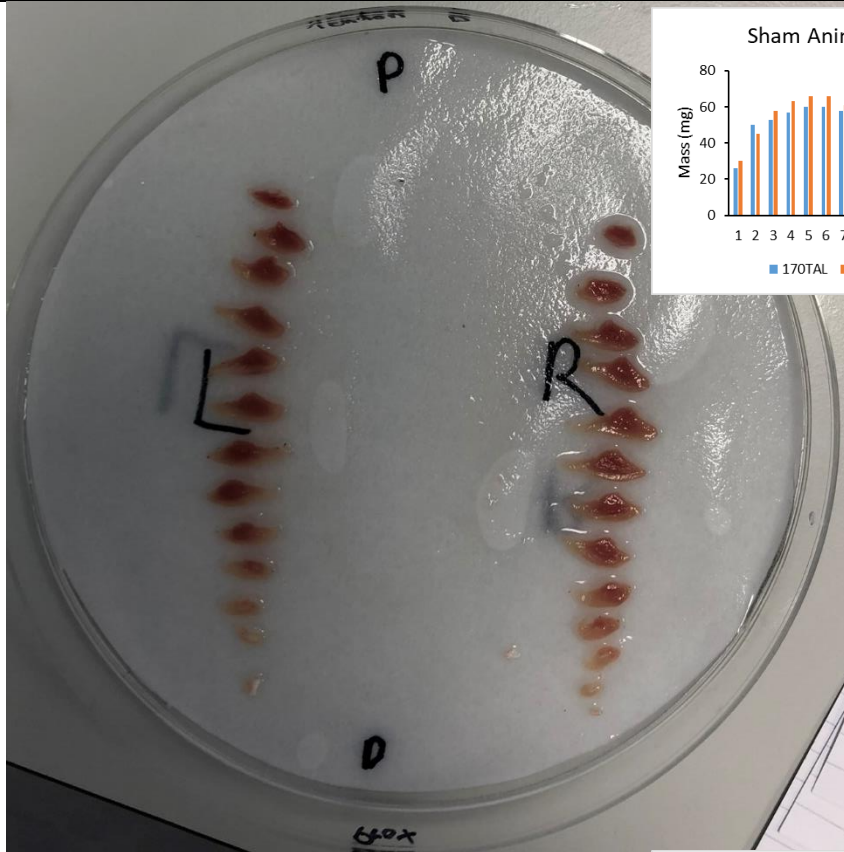
Appendices

Appendix 1: Muscle Regional Slice Images Showing Regional Changes in Shape/Mass with Spillover resistance training.

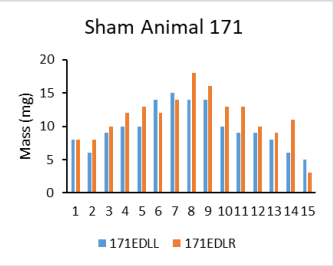
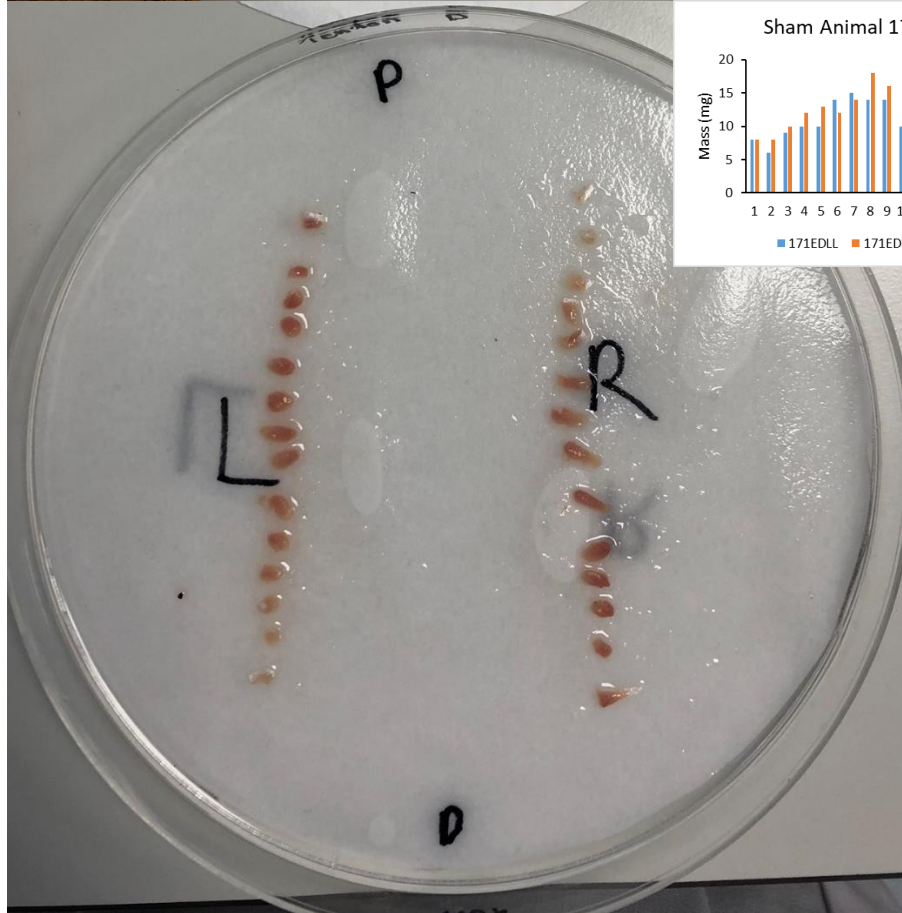
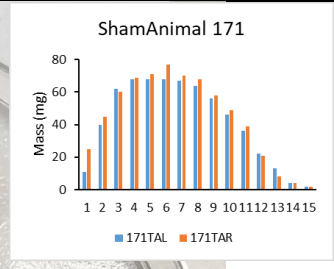
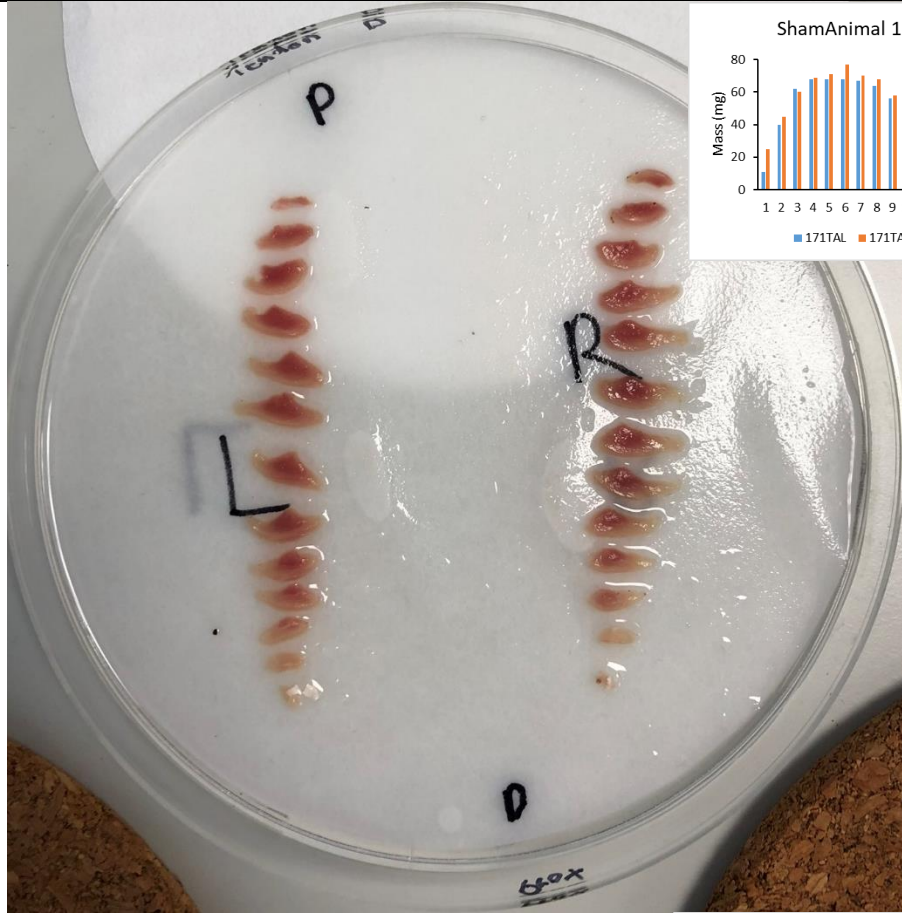
Sham
 Operated
 169
 (4 Days
 post-
 surgery)
 TA: -6.02%
 EDL: -4.61%



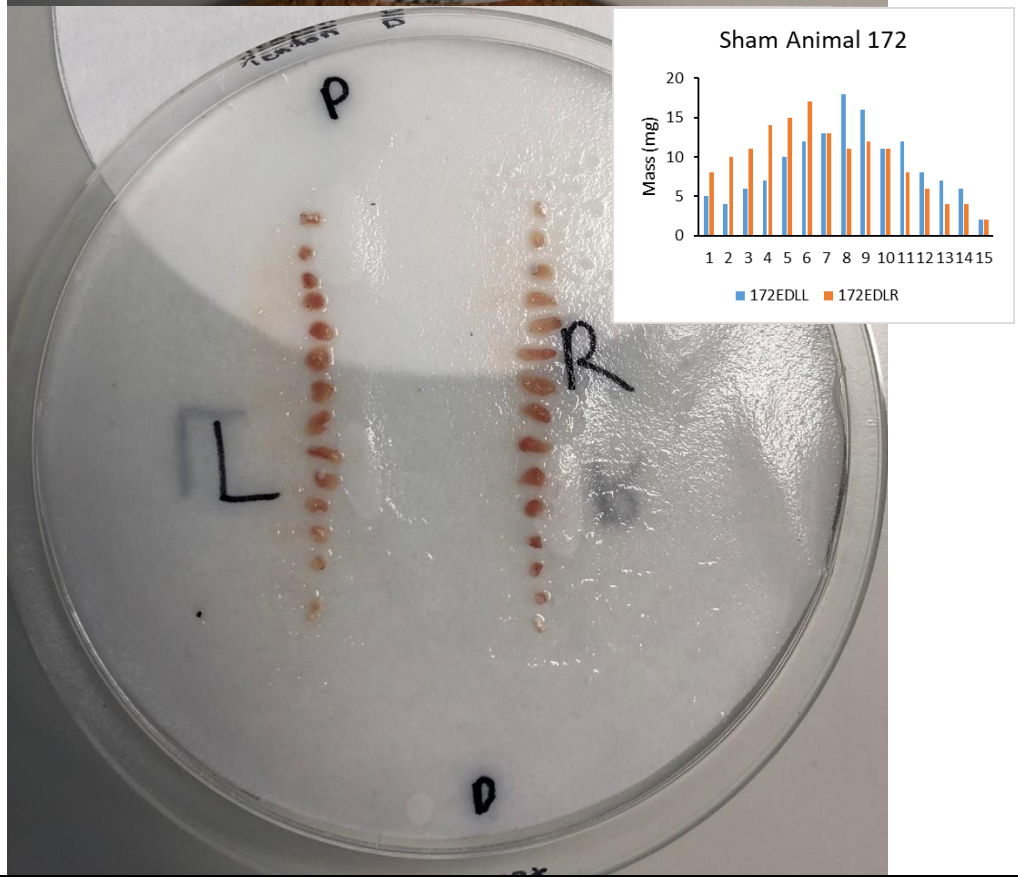
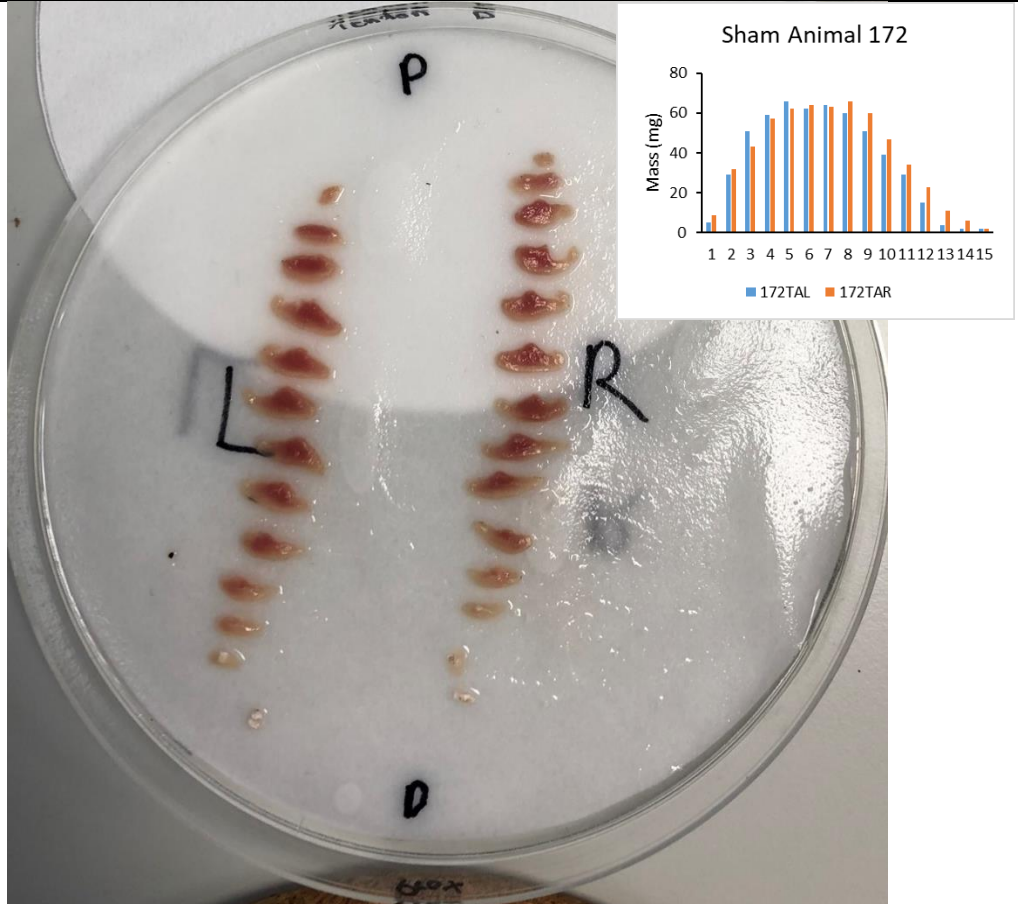
Sham
 Operated
 170
 (4 Days
 post-
 surgery)
 TA: -6.57%
 EDL: +2.27



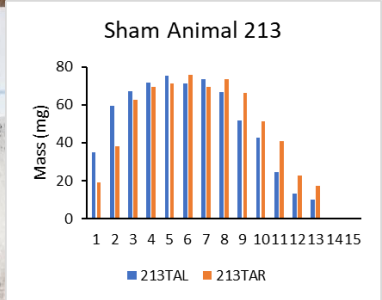
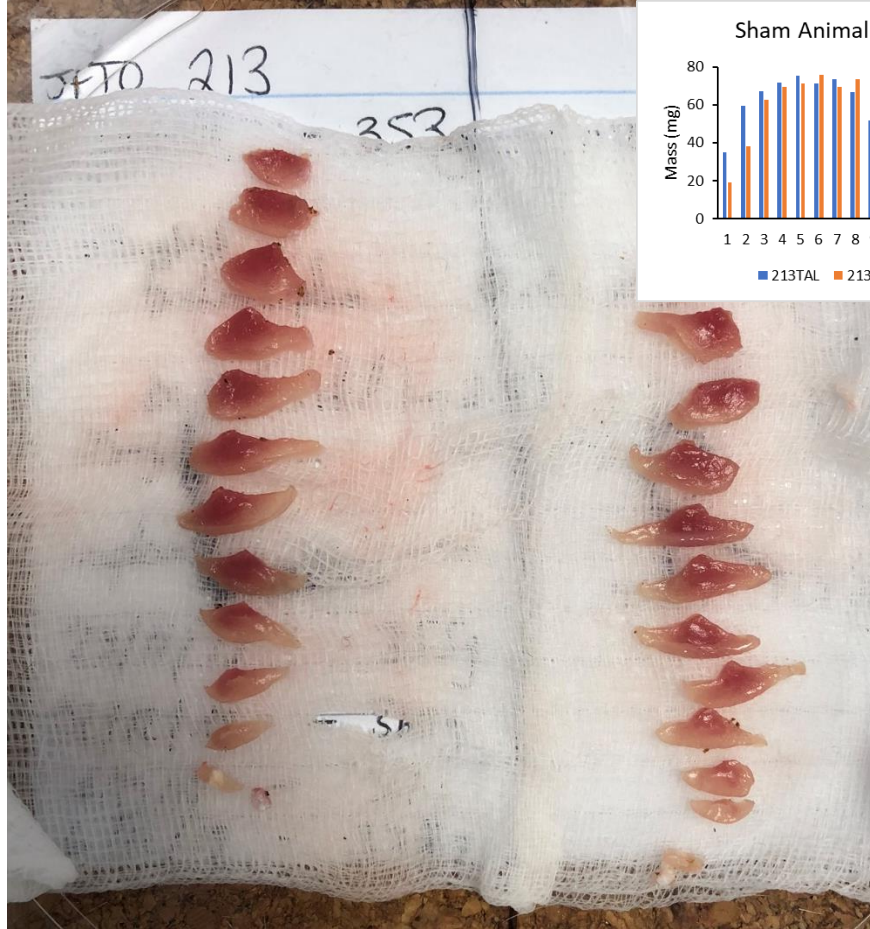
**Sham
 Operated
 171
 (4 Days
 post-
 surgery)
 TA: -5.81%
 EDL: -8.07%**



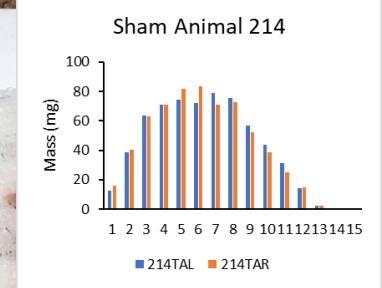
Sham
 Operated
 172
 (4 Days
 post-
 surgery)
 TA: -6.08%
 EDL: -6.25%



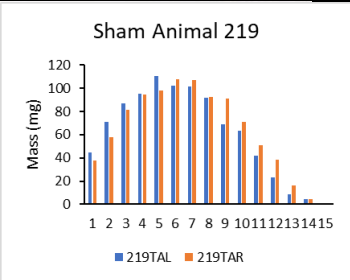
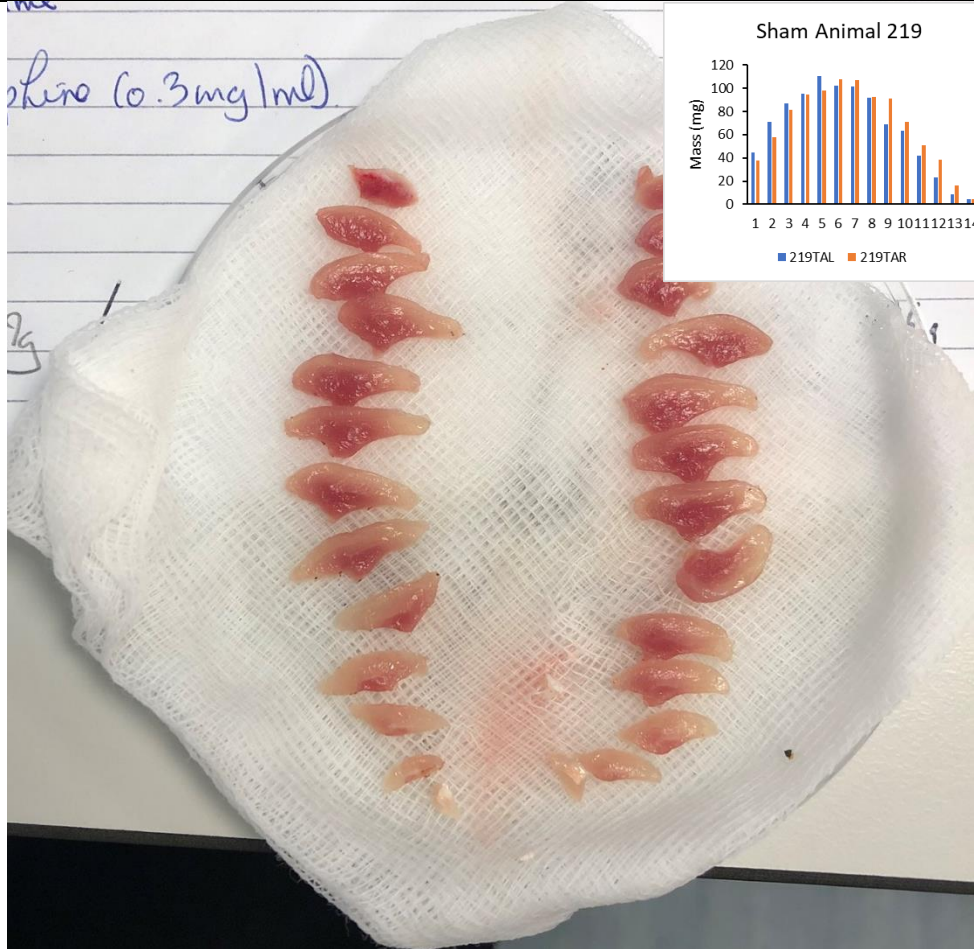
Sham
 Operated
 213
 (17 Days
 post-
 surgery)
 TA: -3.36%
 EDL: -2.35%



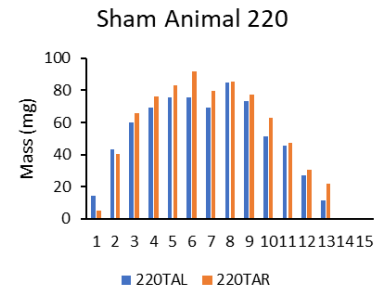
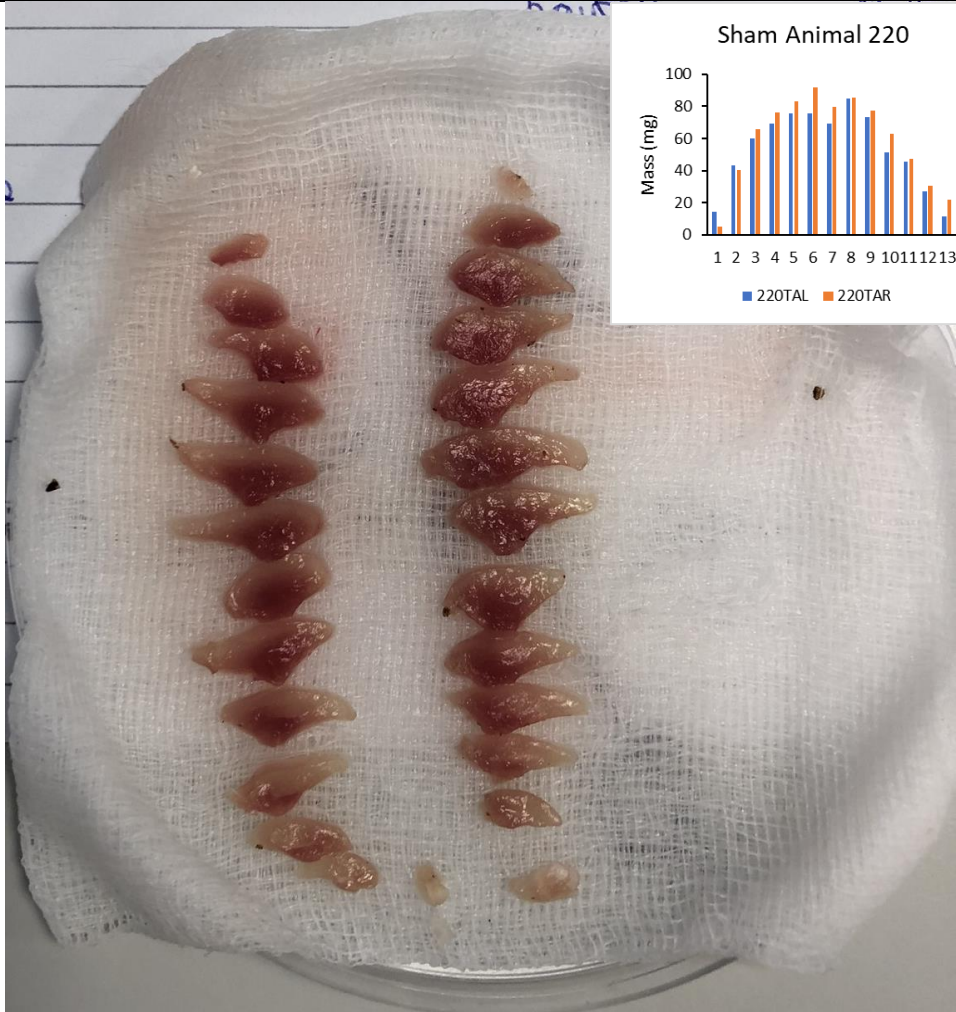
Sham
 Operated
 214
 (17 Days
 post-
 surgery)
 TA: +2.88%
 EDL: -1.34%



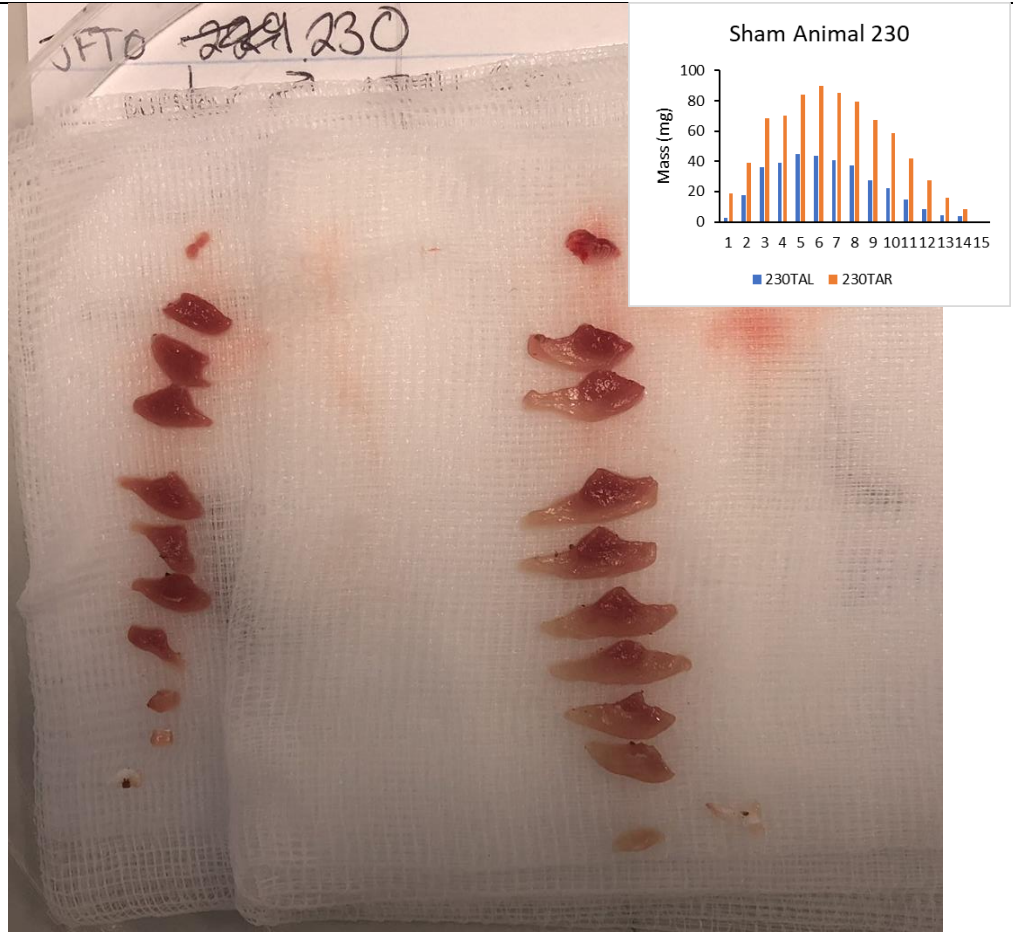
Sham
Operated
219
(27 Days
post-
surgery)
TA: -2.92%
EDL: -4.63%



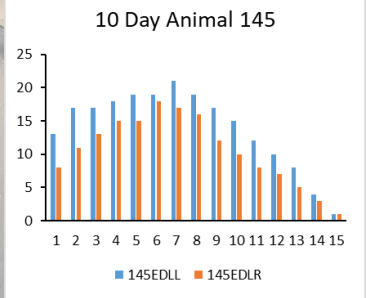
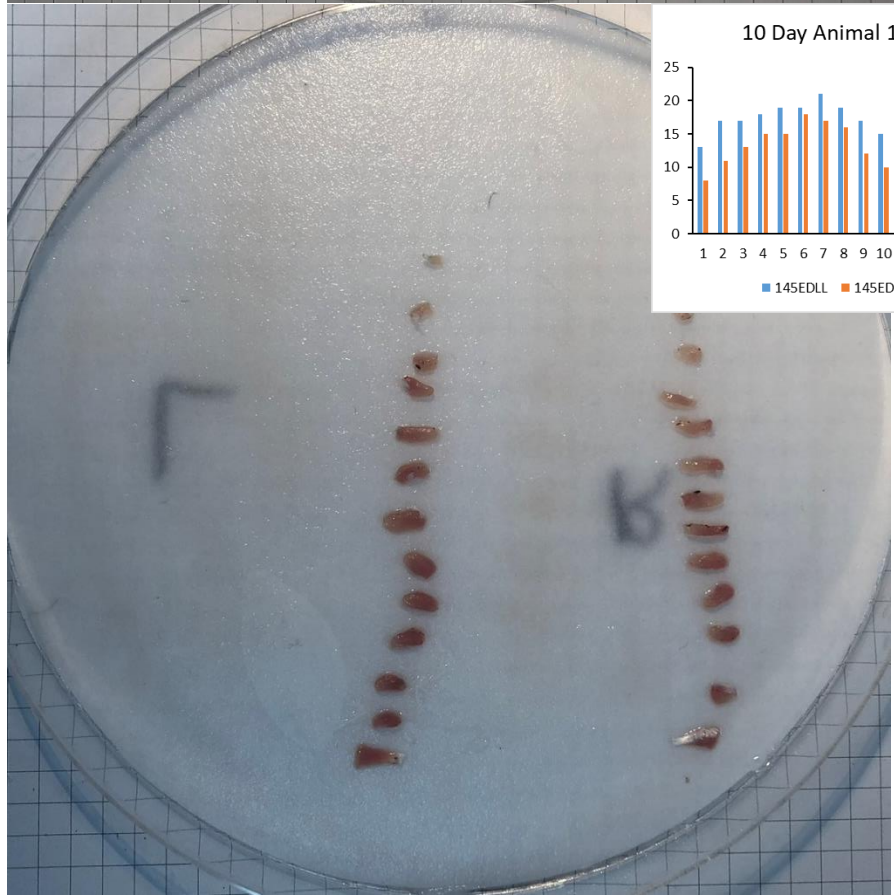
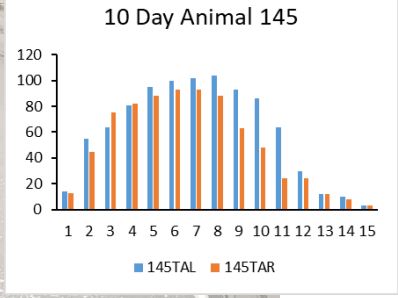
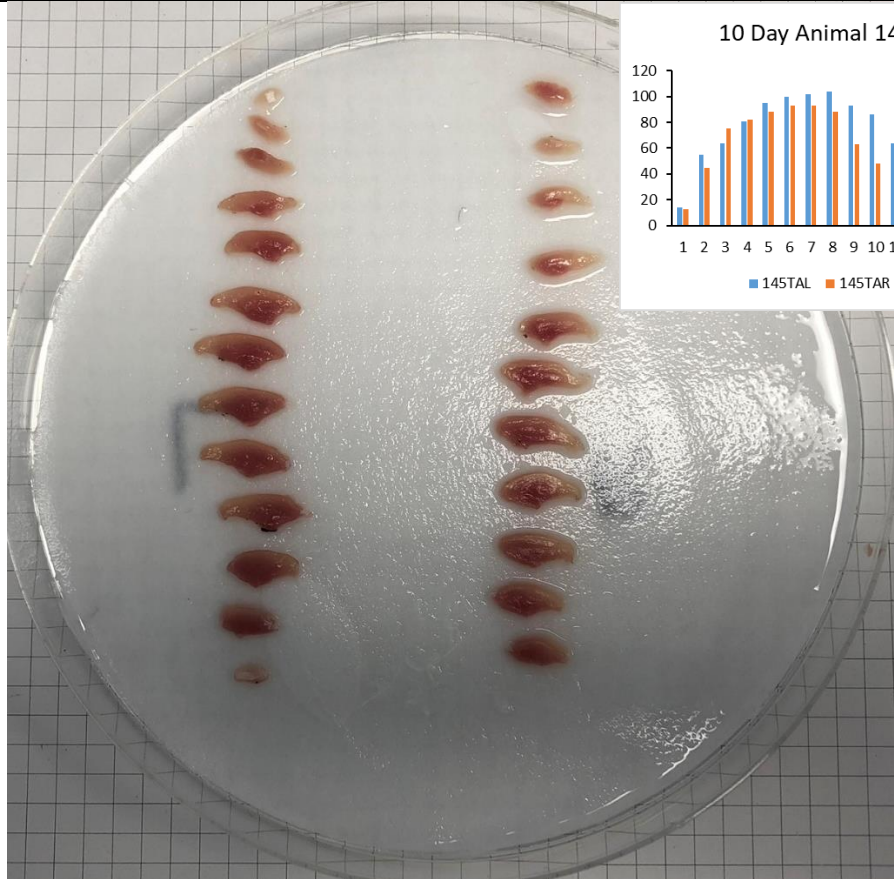
Sham
Operated
220
(27 Days
post-
surgery)
TA: -7.06%
EDL: -5.50%



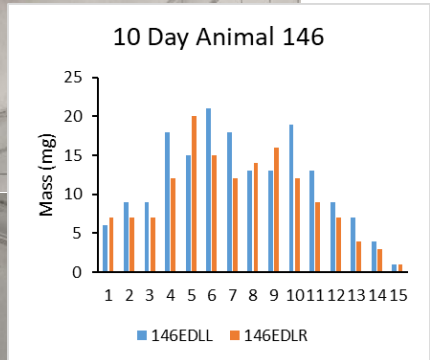
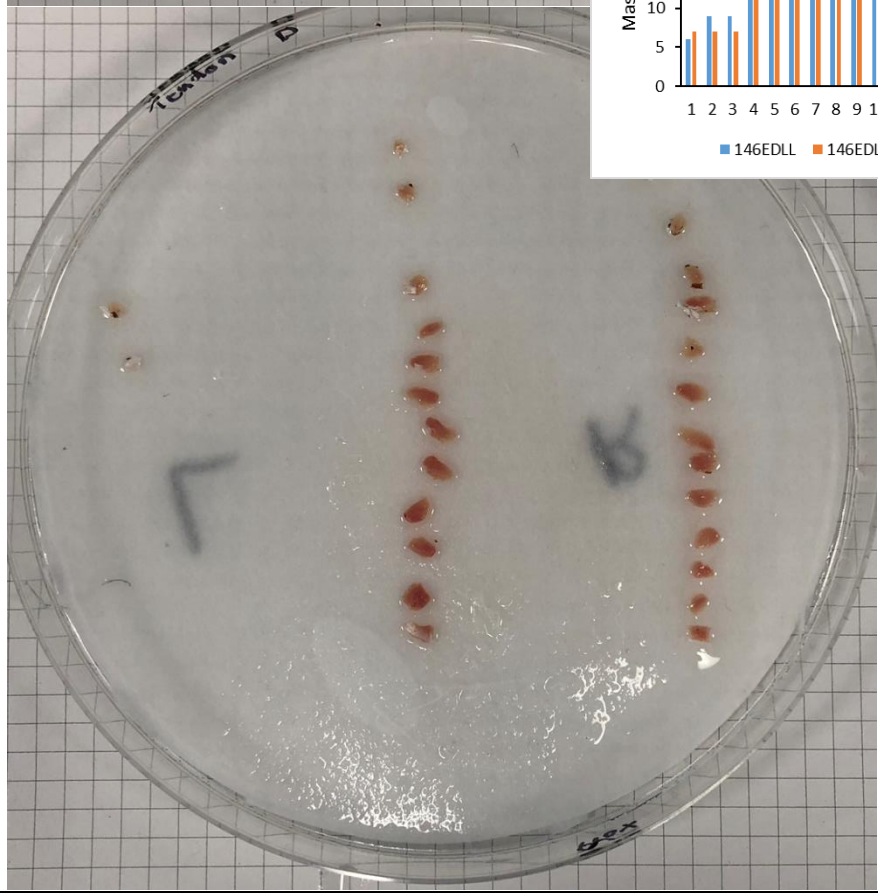
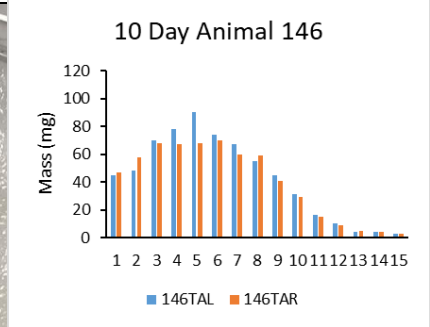
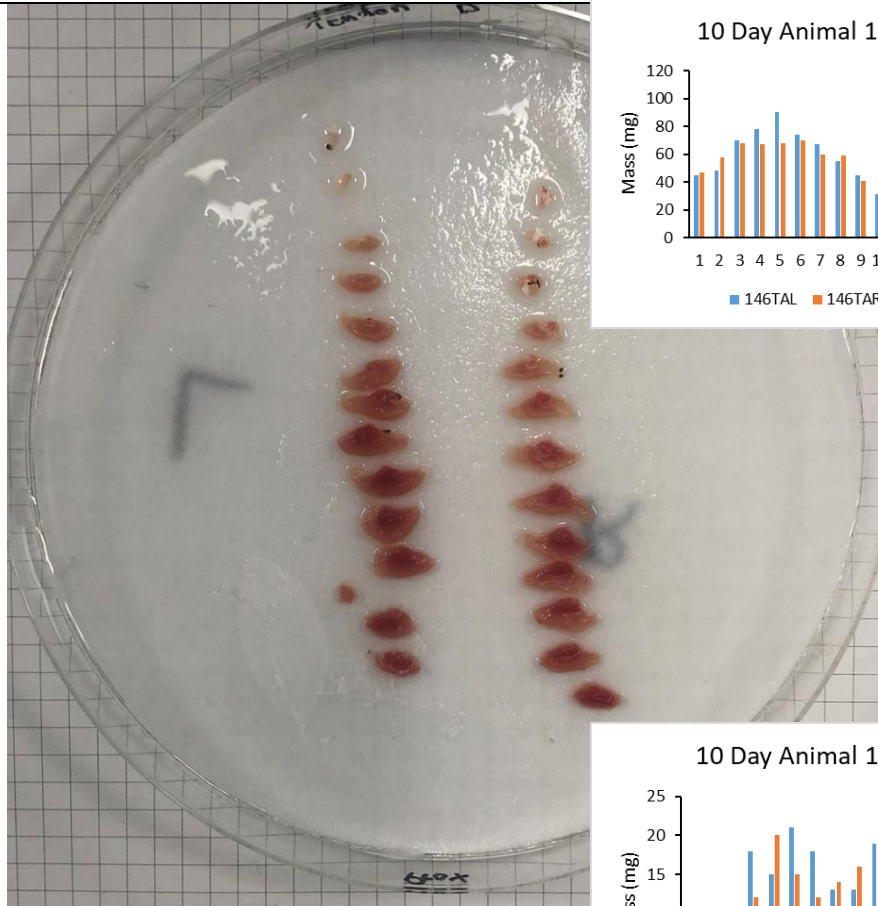
Sham
Operated
230
(27 Days
post-
surgery)
TA: -54.48%
EDL:
-42.15%



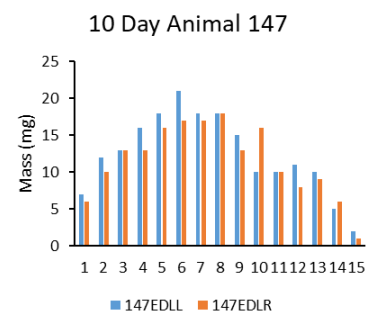
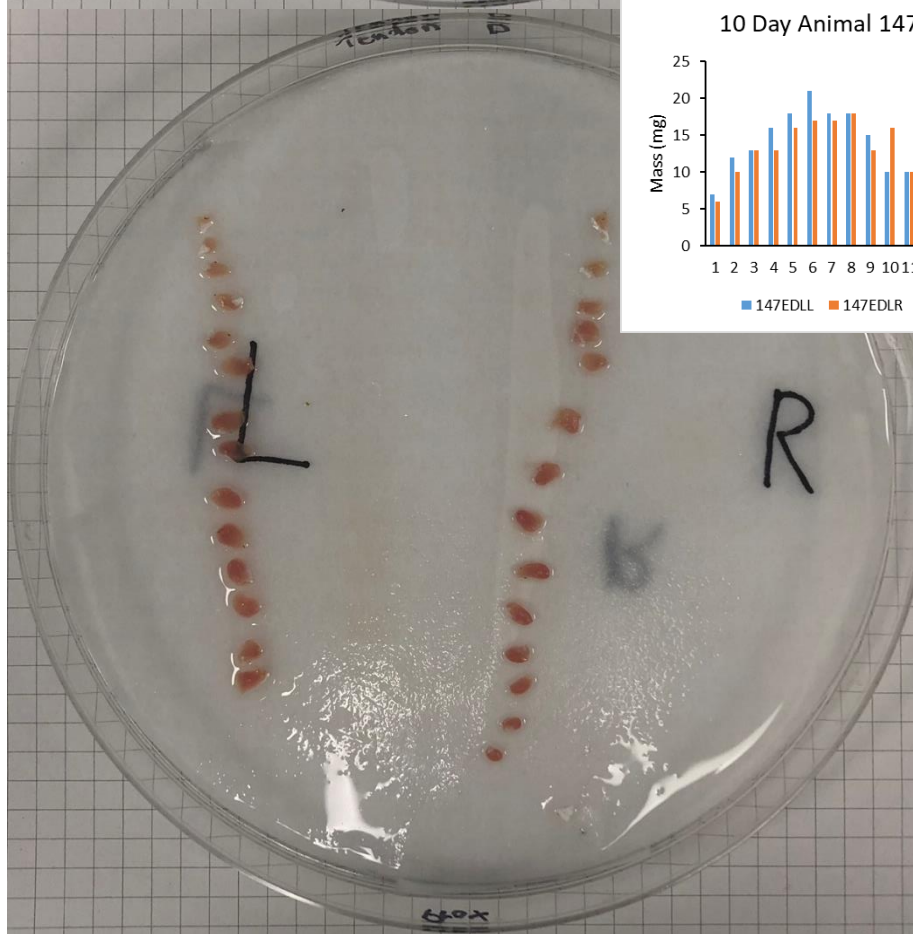
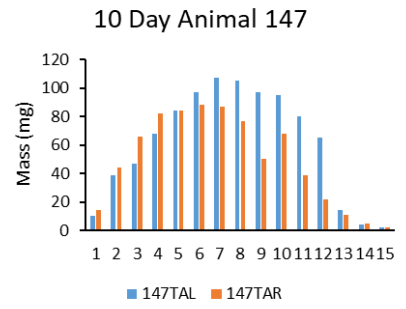
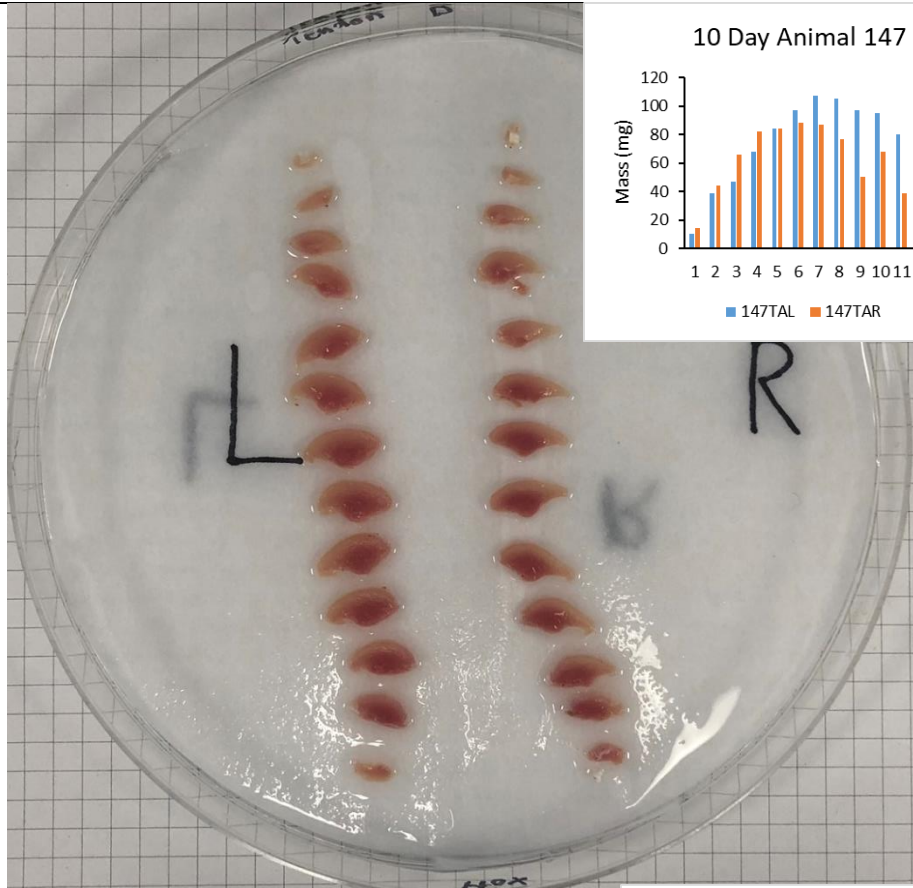
**10 Days
 'Spillover'
 Stimulation
 145
 TA:
 +21.67%
 EDL:
 +21.14%**



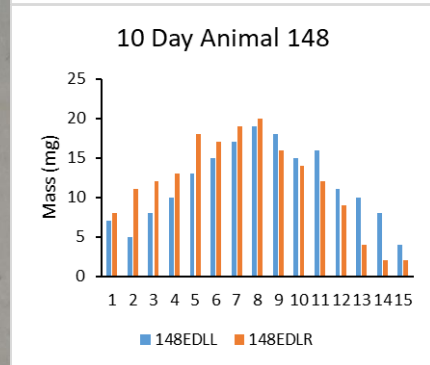
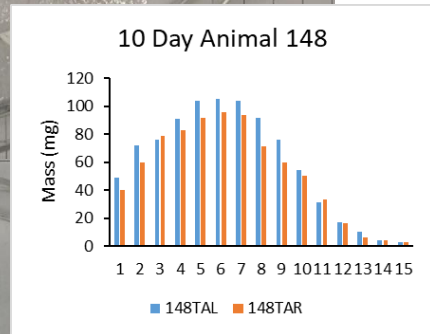
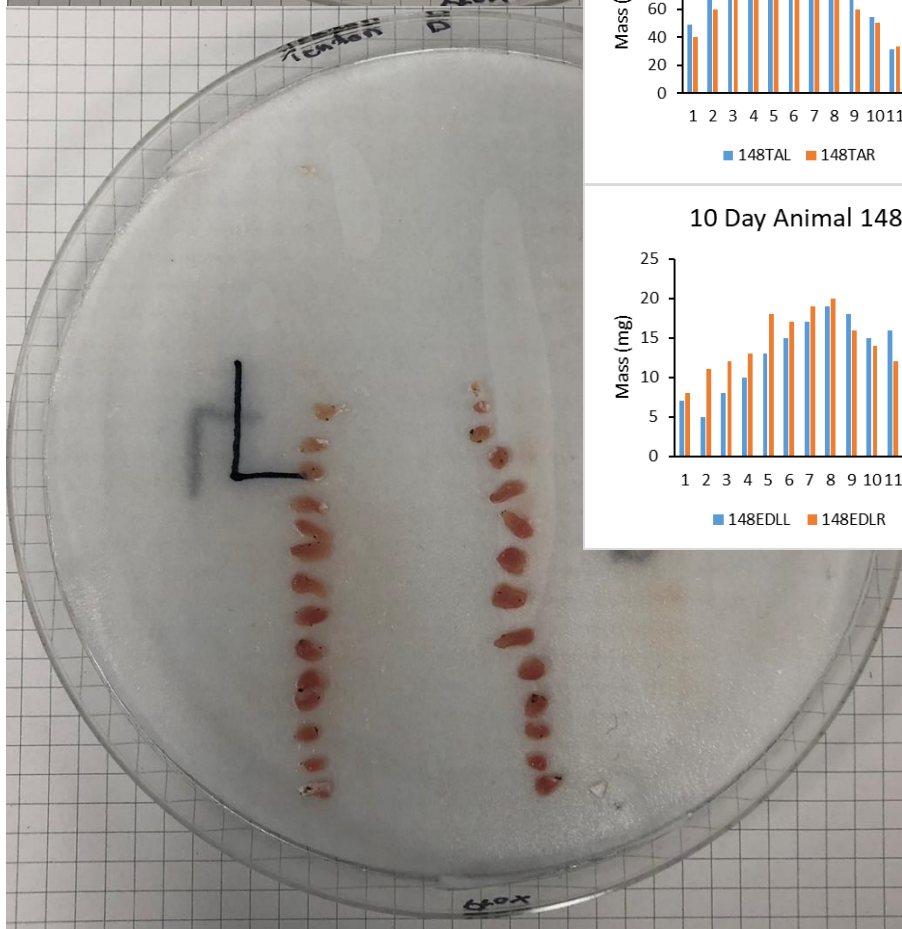
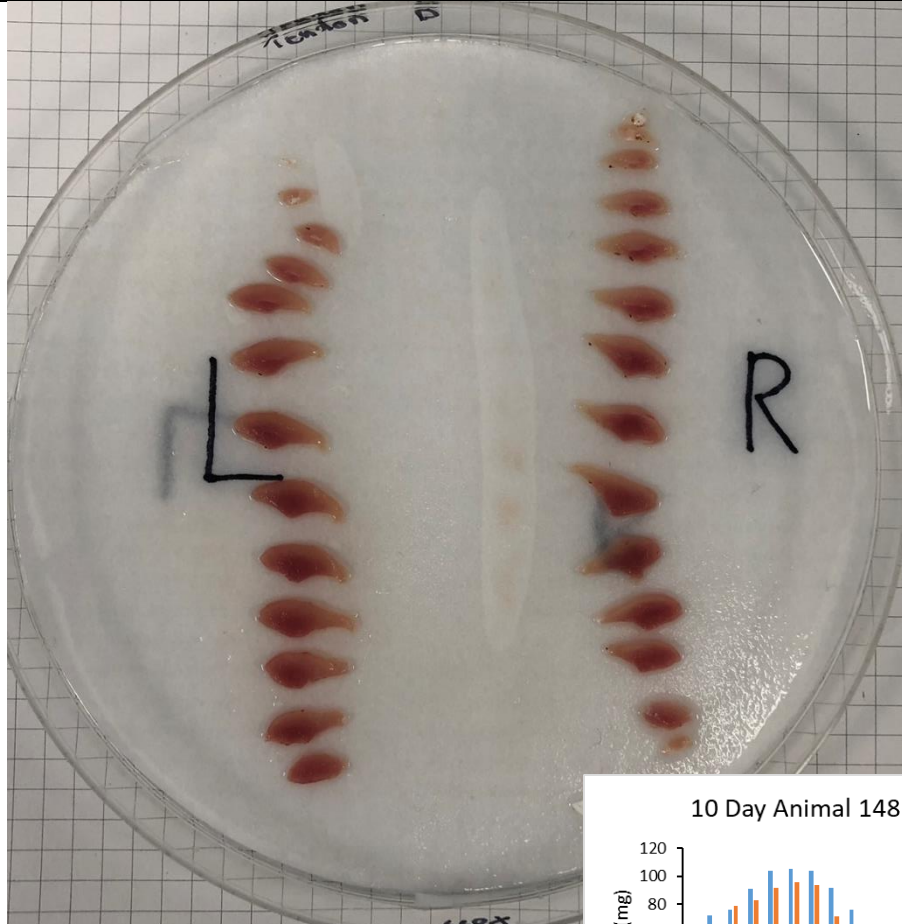
**10 Days
 'Spillover'
 Stimulation
 146
 TA: +5.14%
 EDL:
 +5.18%**



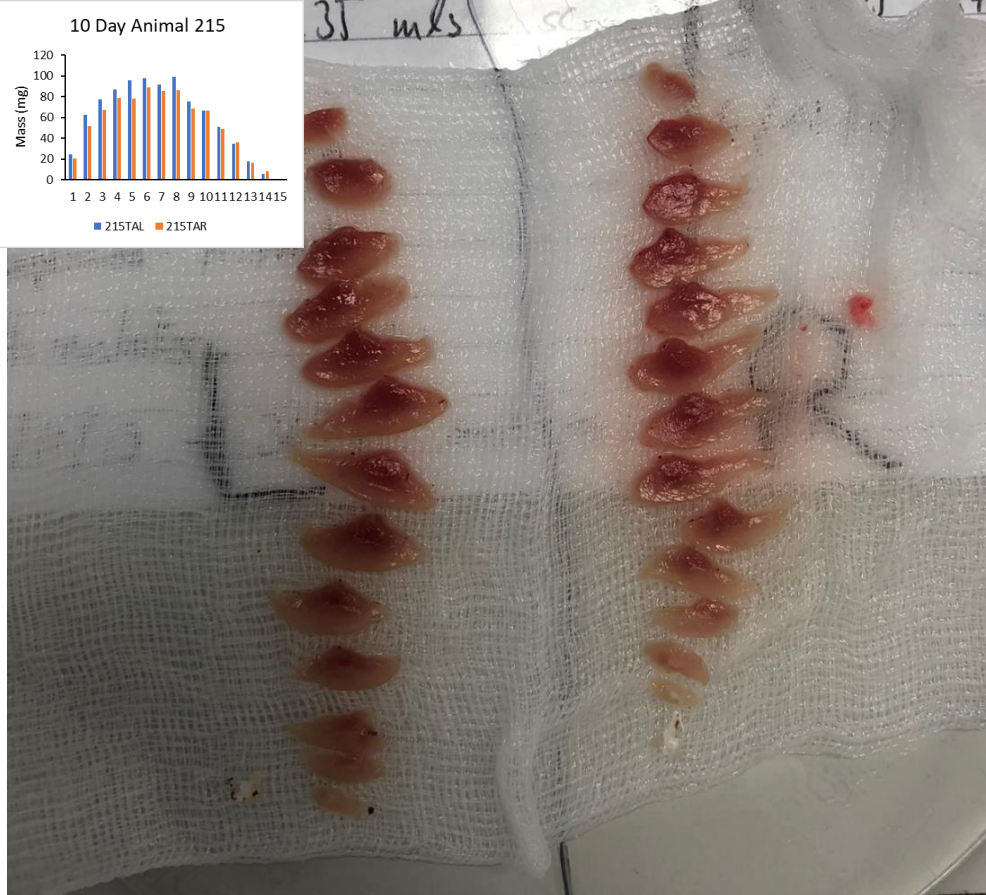
10 Days
'Spillover'
Stimulation
147
TA:
+21.35%
EDL:
+6.89%



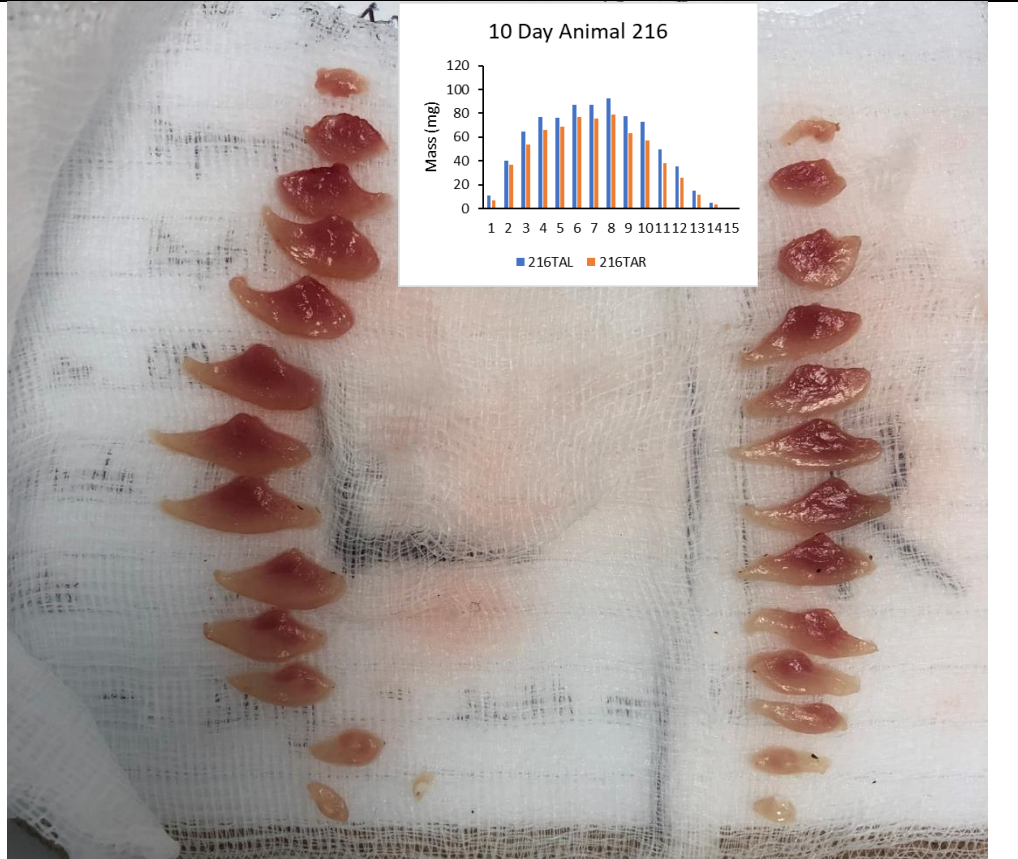
10 Days
'Spillover'
Stimulation
148
TA: +13.9%
EDL: +2.73%



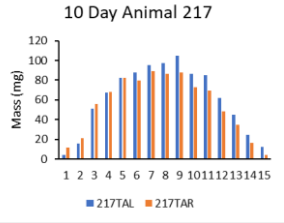
**10 Days
'Spillover'
Stimulation
215
TA:
+12.06%
EDL:
+9.26%**



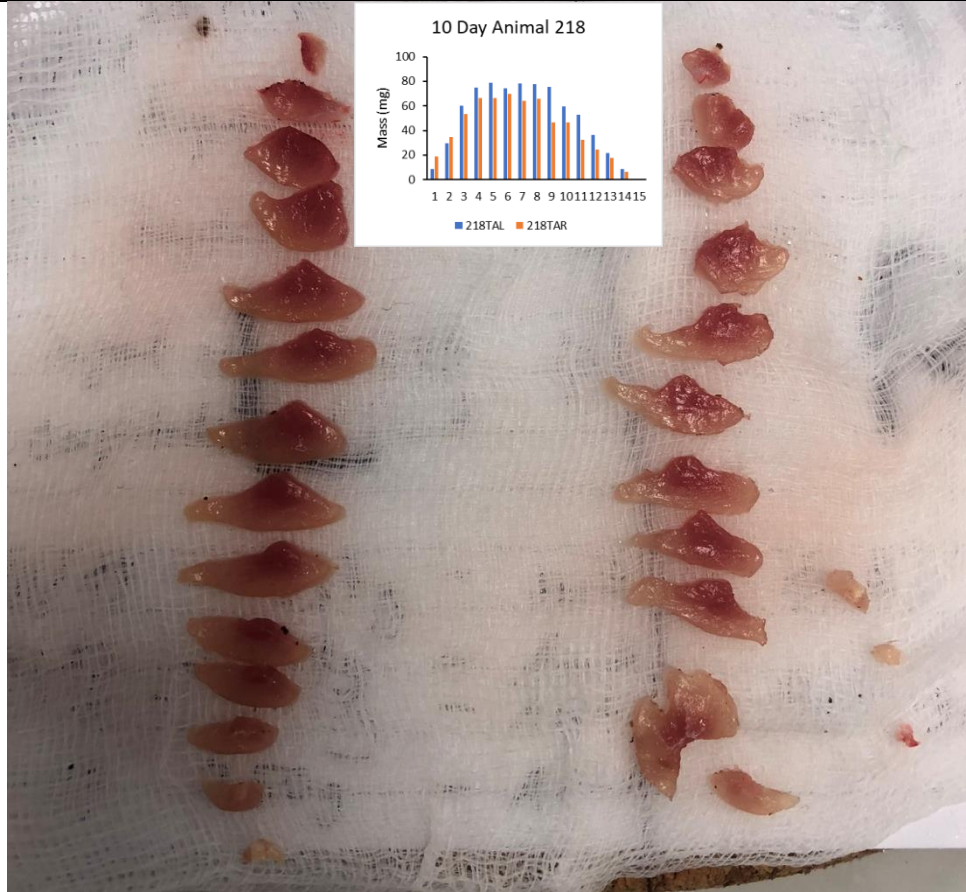
**10 Days
'Spillover'
Stimulation
216
TA:
+18.90%
EDL:
+6.15%**



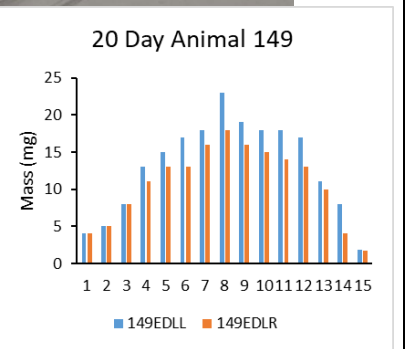
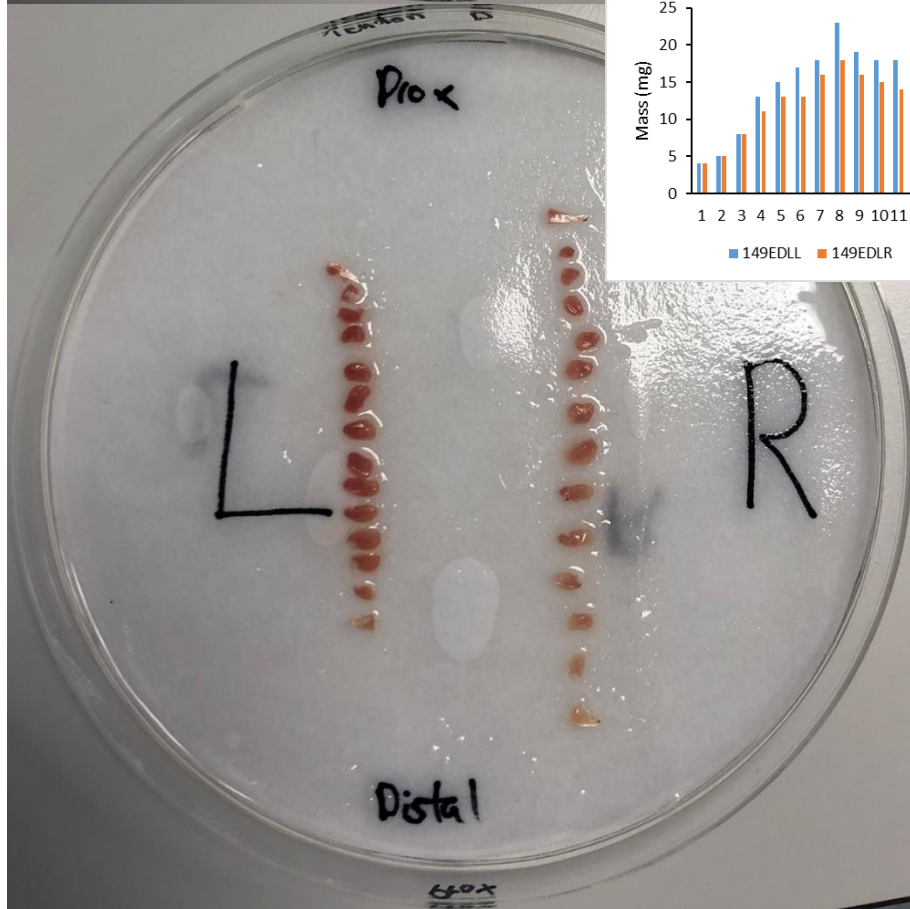
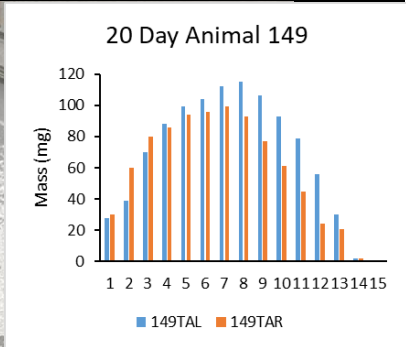
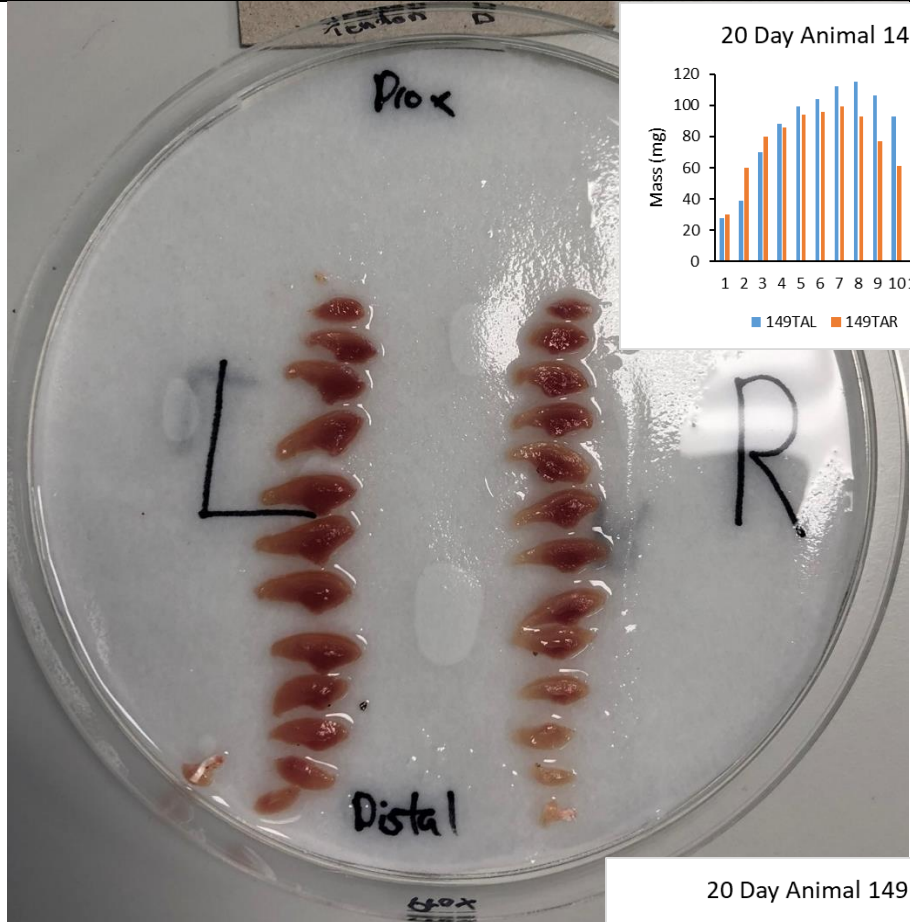
**10 Days
'Spillover'
Stimulation
217
TA:
+10.89%
EDL:
+2.35%**



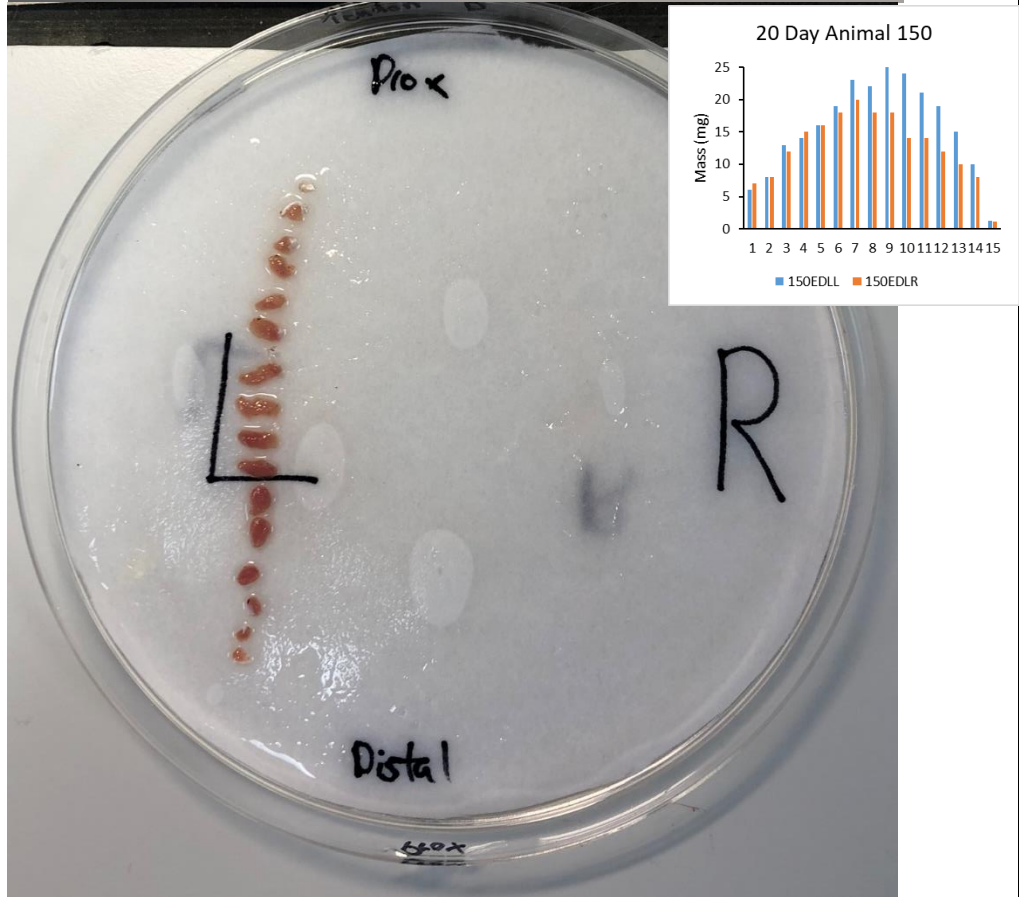
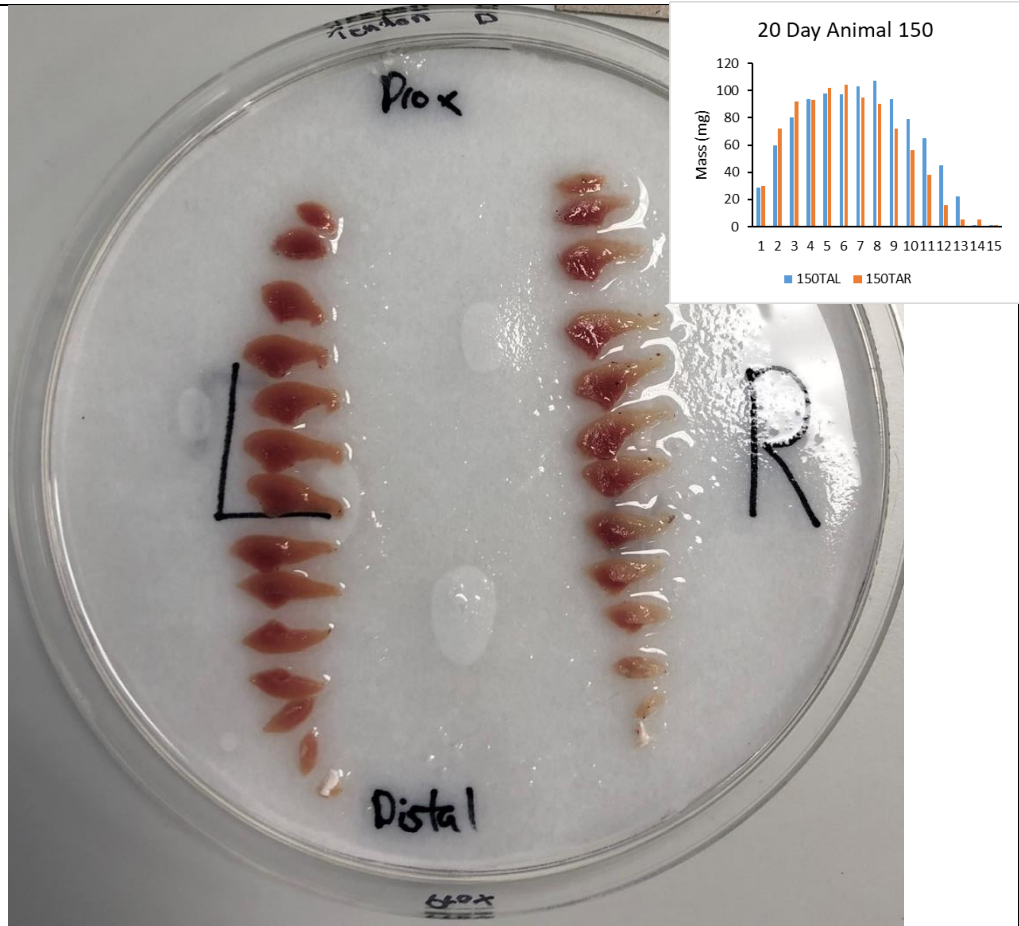
**10 Days
'Spillover'
Stimulation
218
TA:
+10.44%
EDL:
+5.98%**



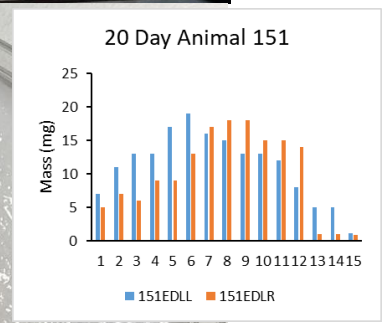
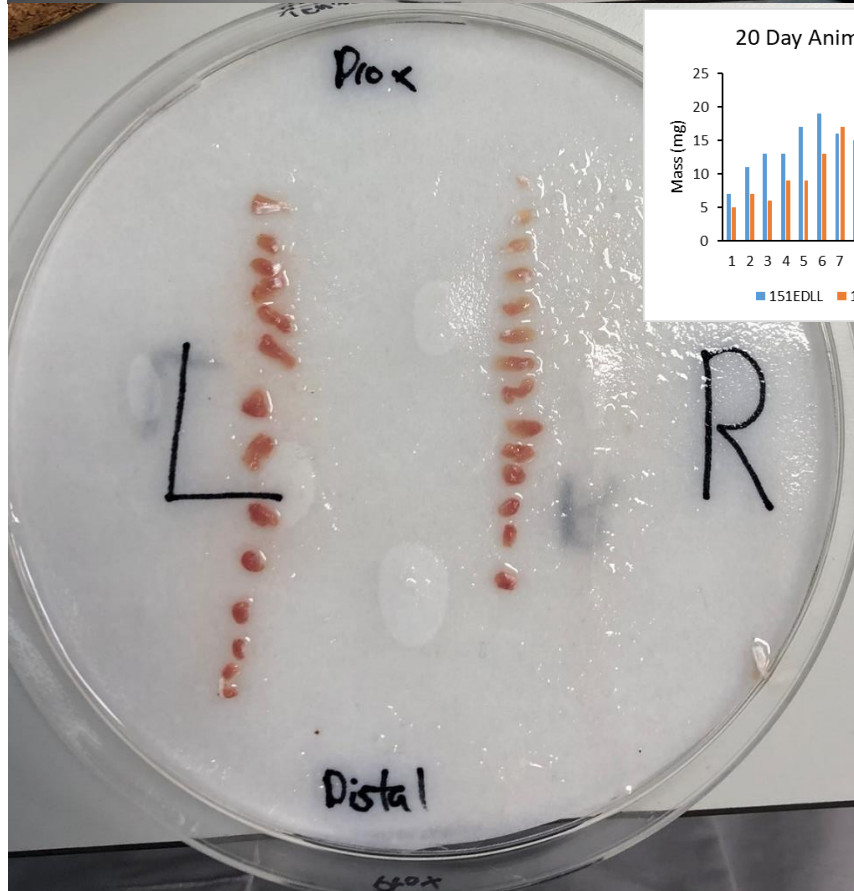
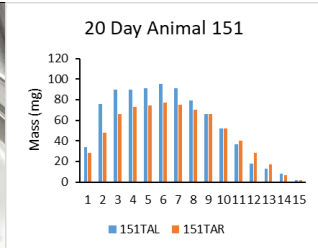
20 Days
'Spillover'
Stimulation
149
TA:
+18.64%
EDL:
+6.96%



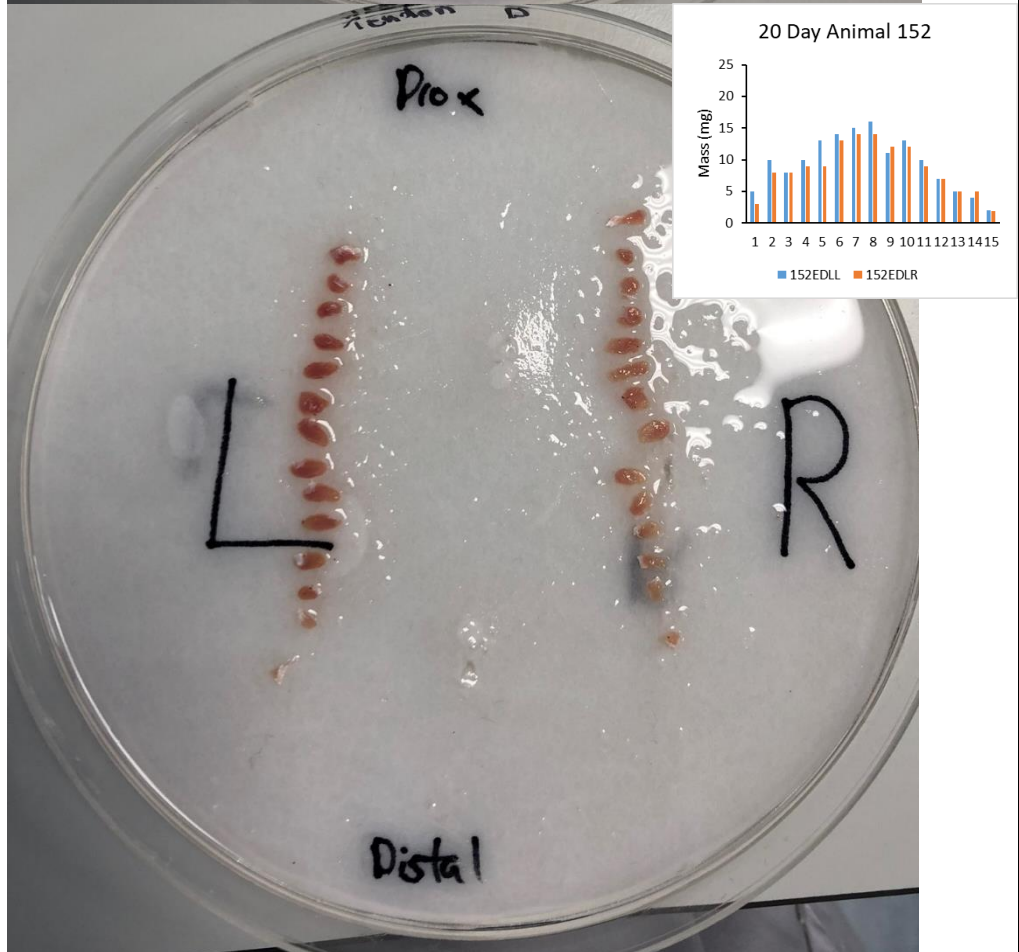
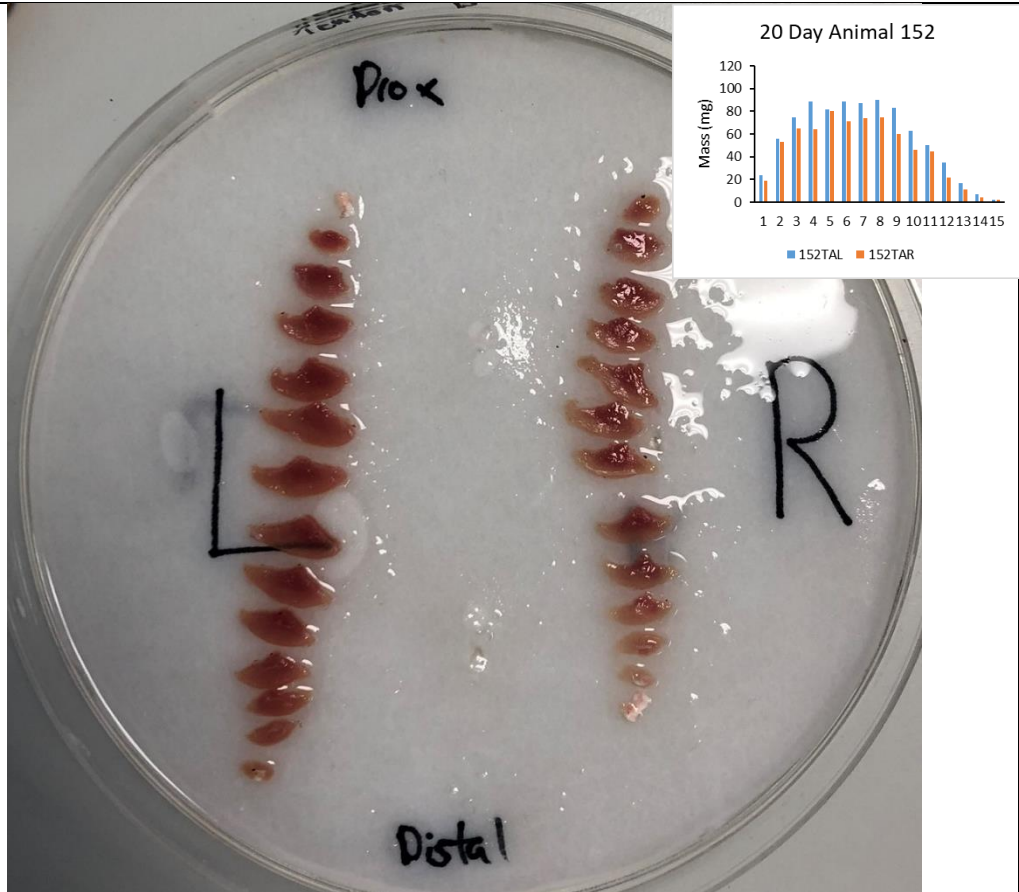
20 Days
'Spillover'
Stimulation
150
TA:
+15.87%
EDL:
+0.947%



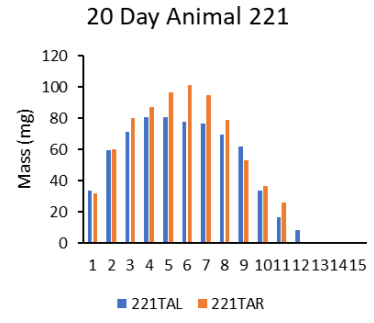
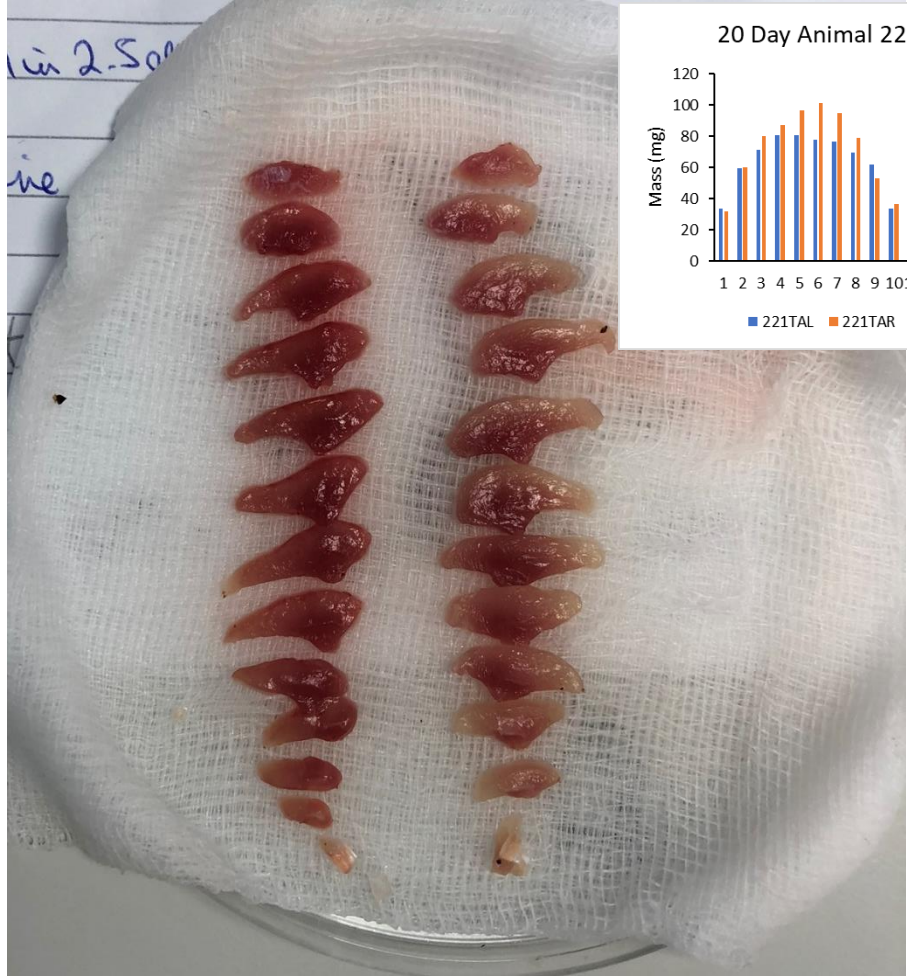
20 Days
'Spillover'
Stimulation
151
TA:
+19.72%
EDL:
+10.17%



20 Days
'Spillover'
Stimulation
152
TA:
+23.64%
EDL:
+1.32%

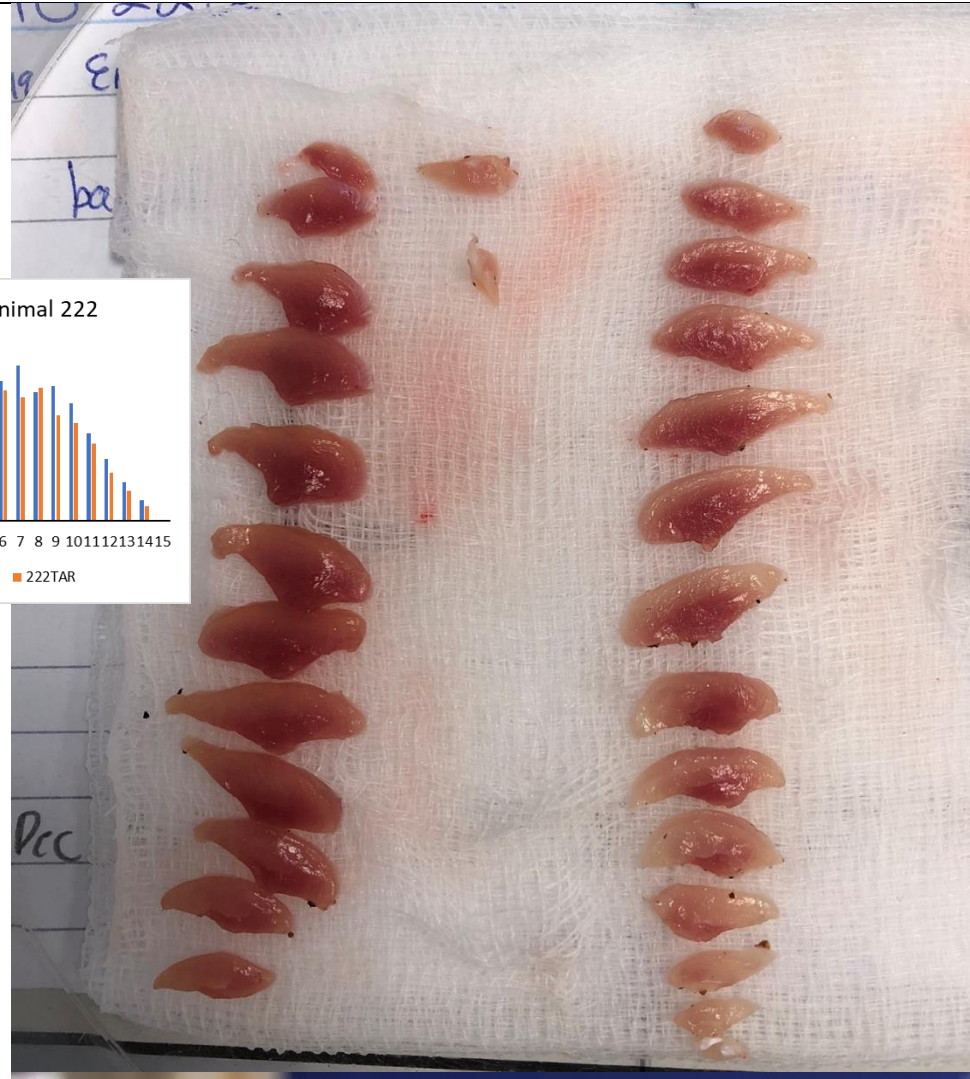
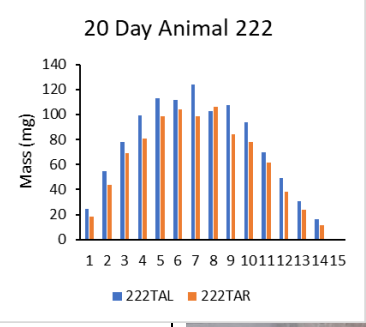


**20 Days
'Spillover'
Stimulation
221
TA: -12.93%
EDL:
+6.29%**



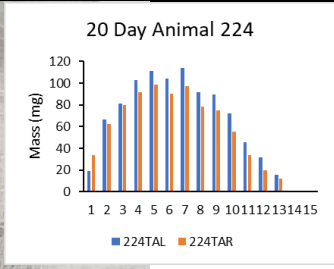


**20 Days
'Spillover'
Stimulation
222
TA:
+14.92%
EDL: +3.3%**

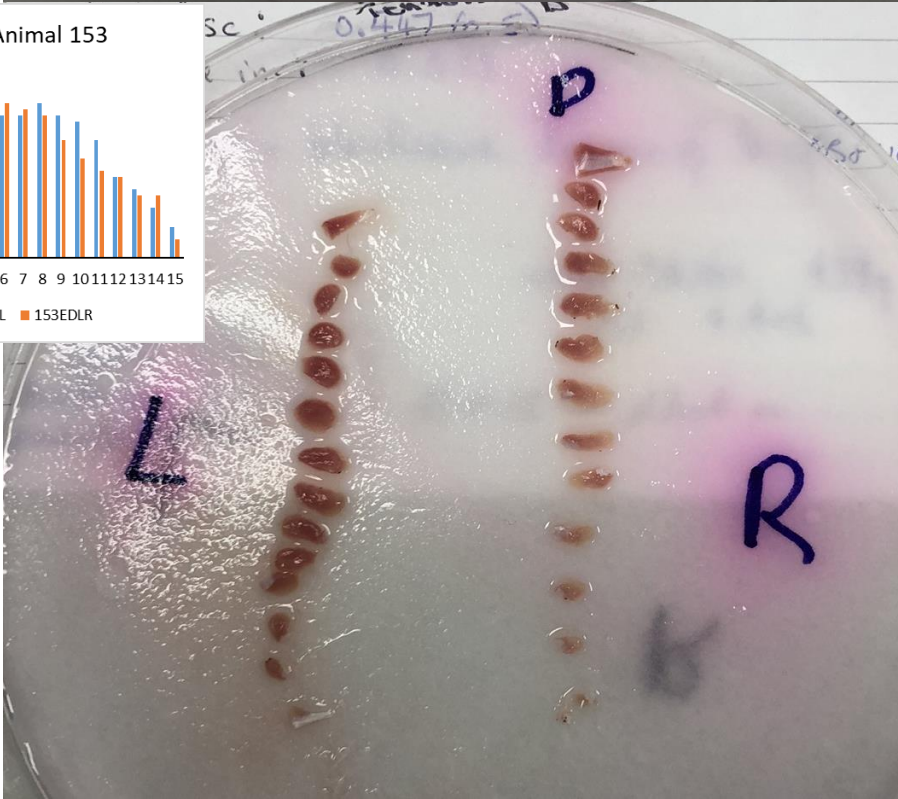
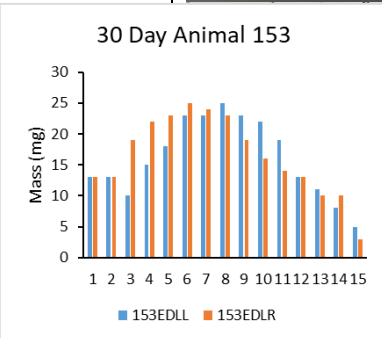
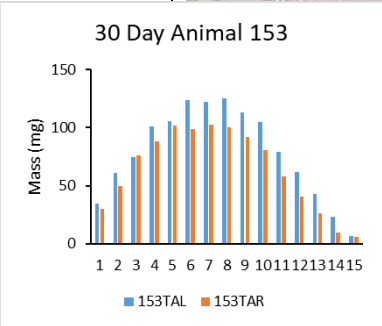
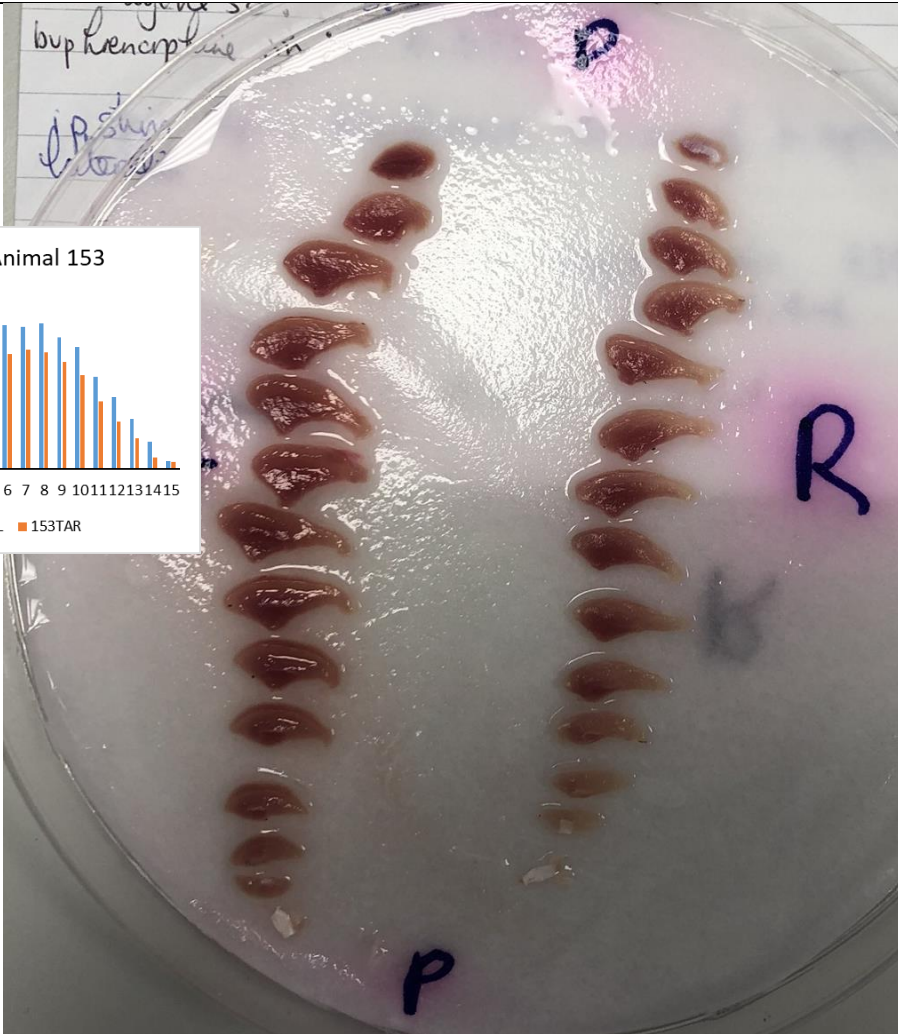




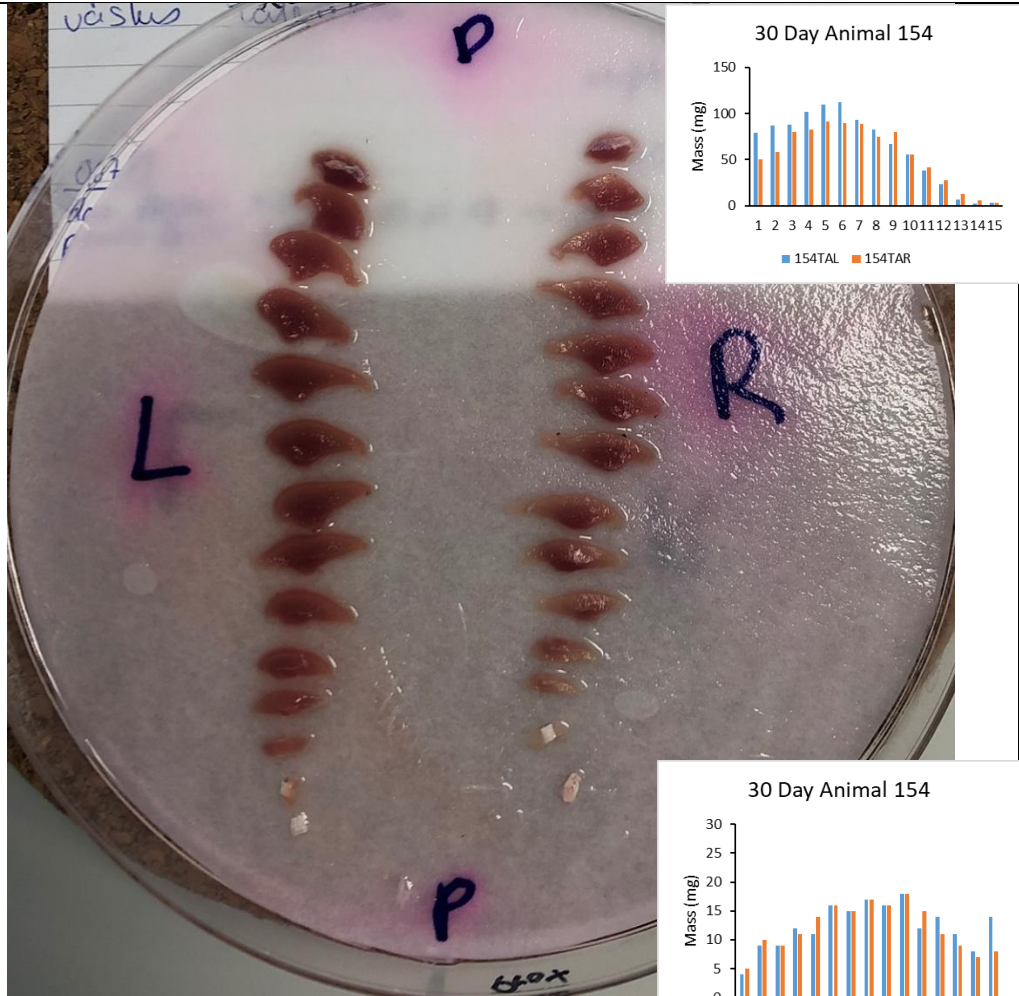
**20 Days
'Spillover'
Stimulation
224
TA: +10.5%
EDL:
+2.05%**



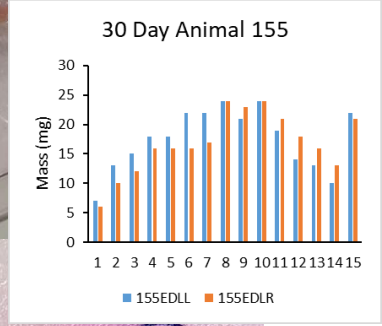
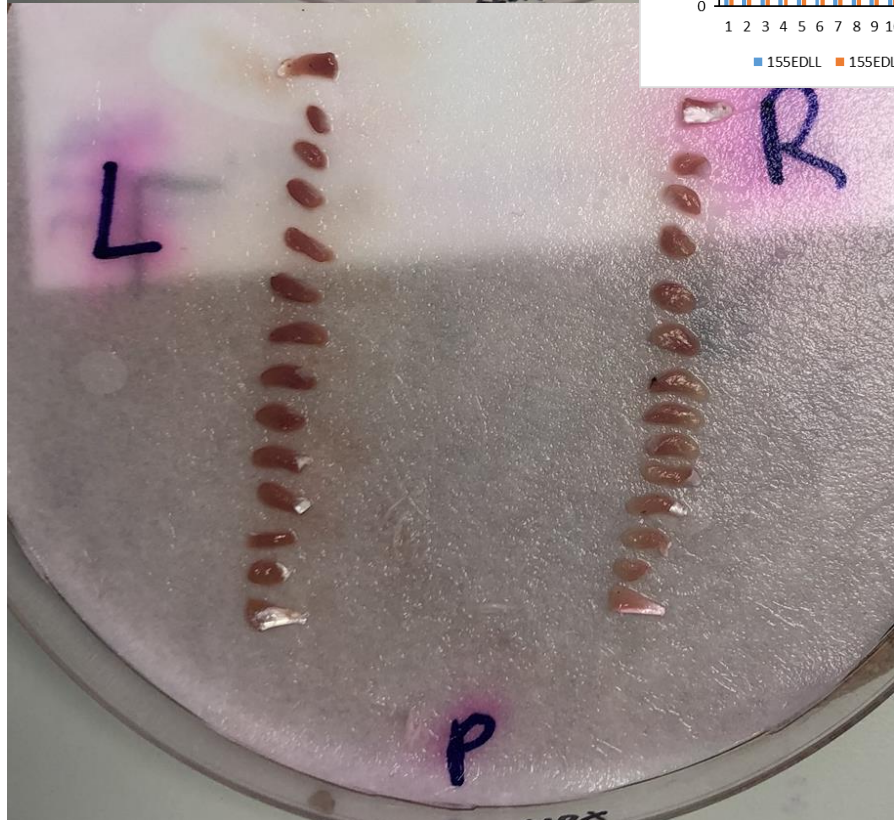
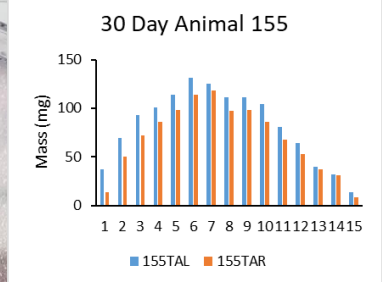
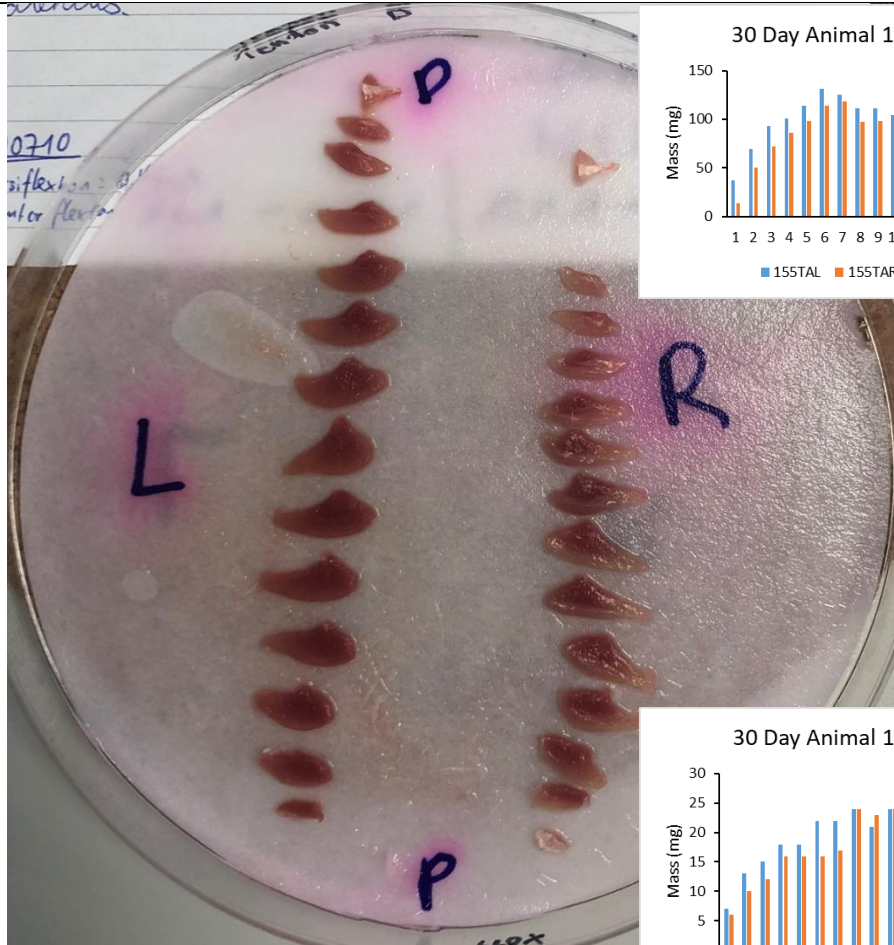
30 Days
 'Spillover'
 Stimulation
 153
 TA: +13.4%
 EDL: +7.3%



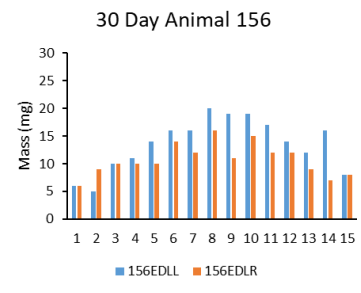
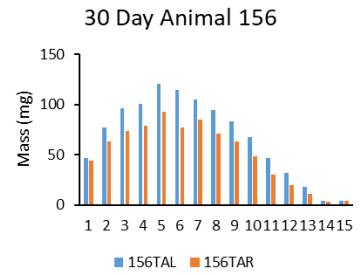
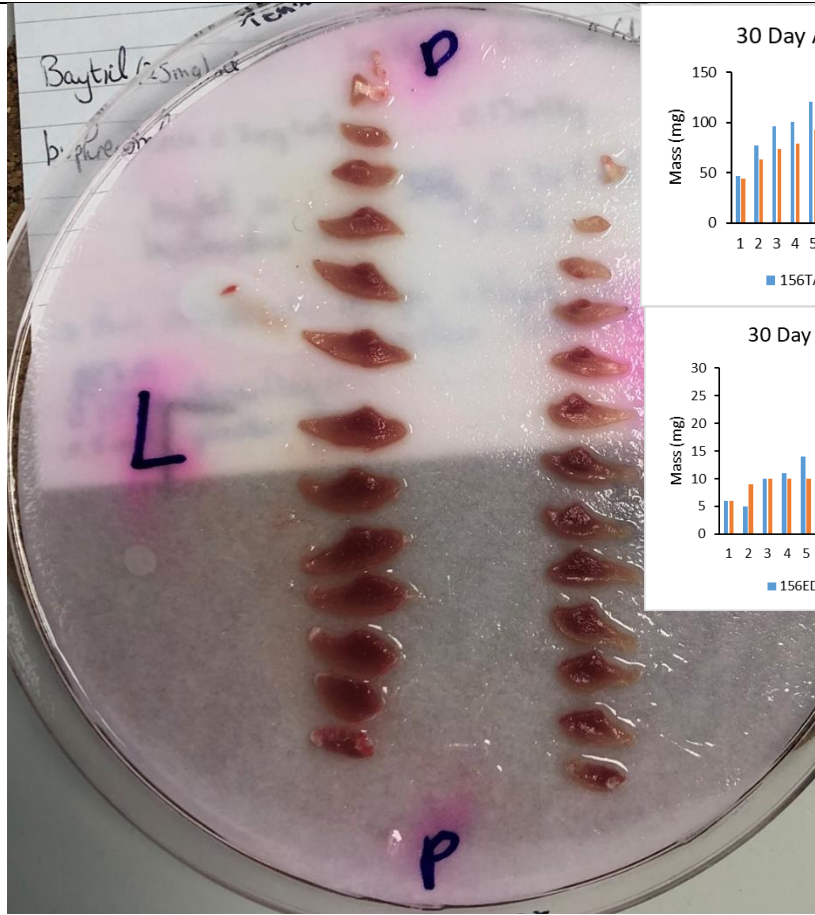
30 Days
 'Spillover'
 Stimulation
 154
 TA: +7.54%
 EDL:
 +6.95%



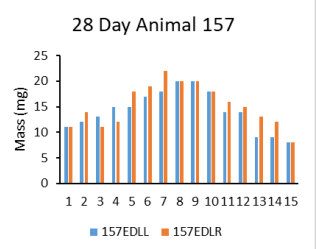
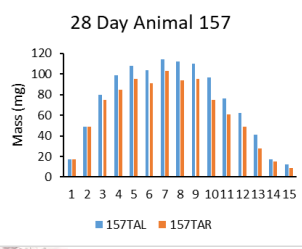
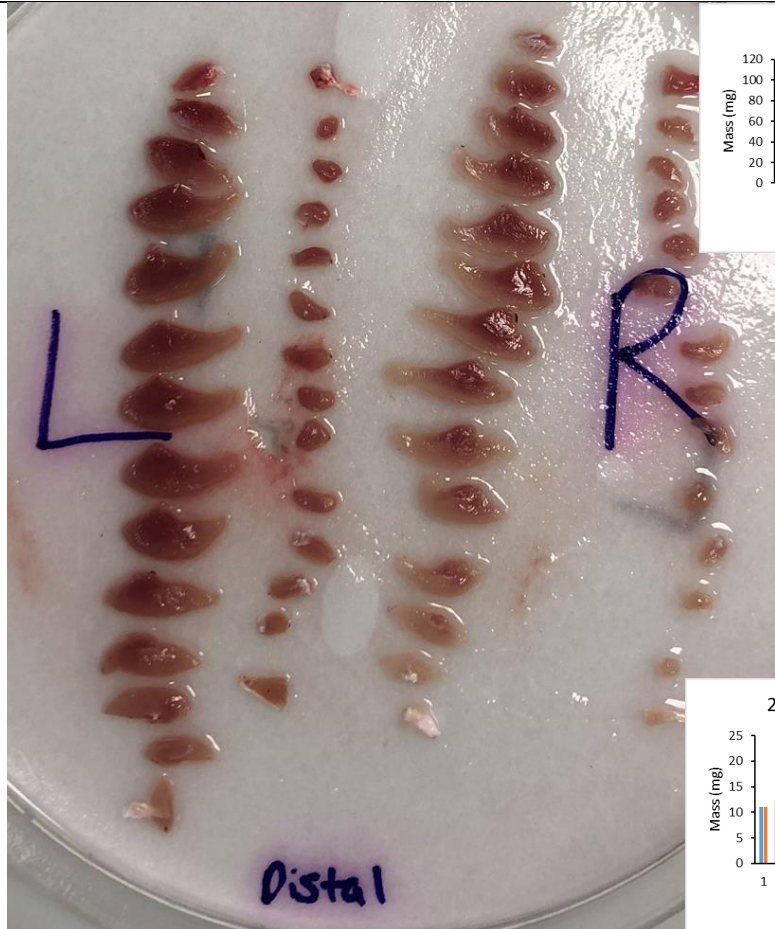
30 Days
'Spillover'
Stimulation
155
TA:
+21.11%
EDL:
+10.35%



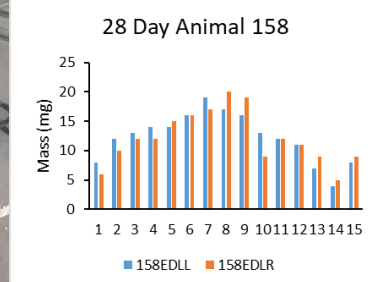
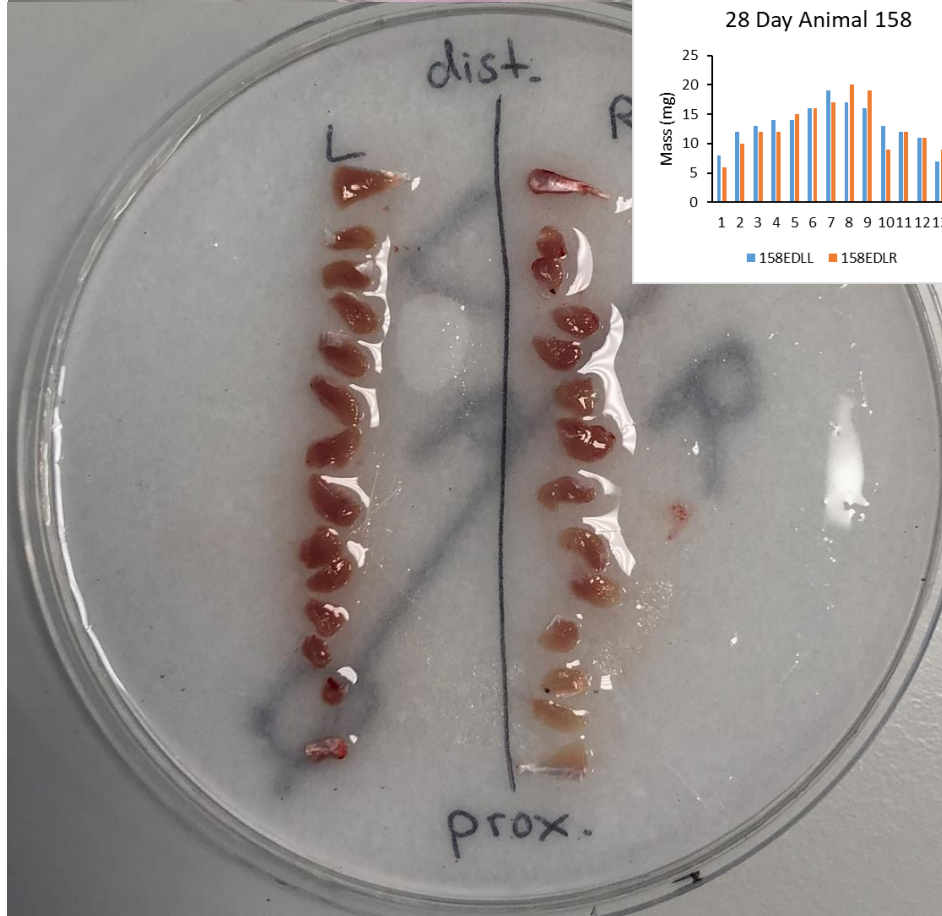
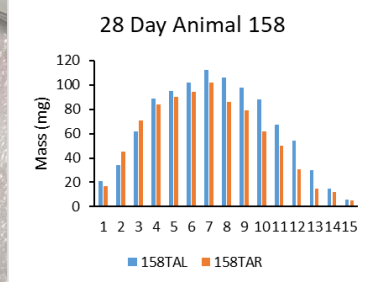
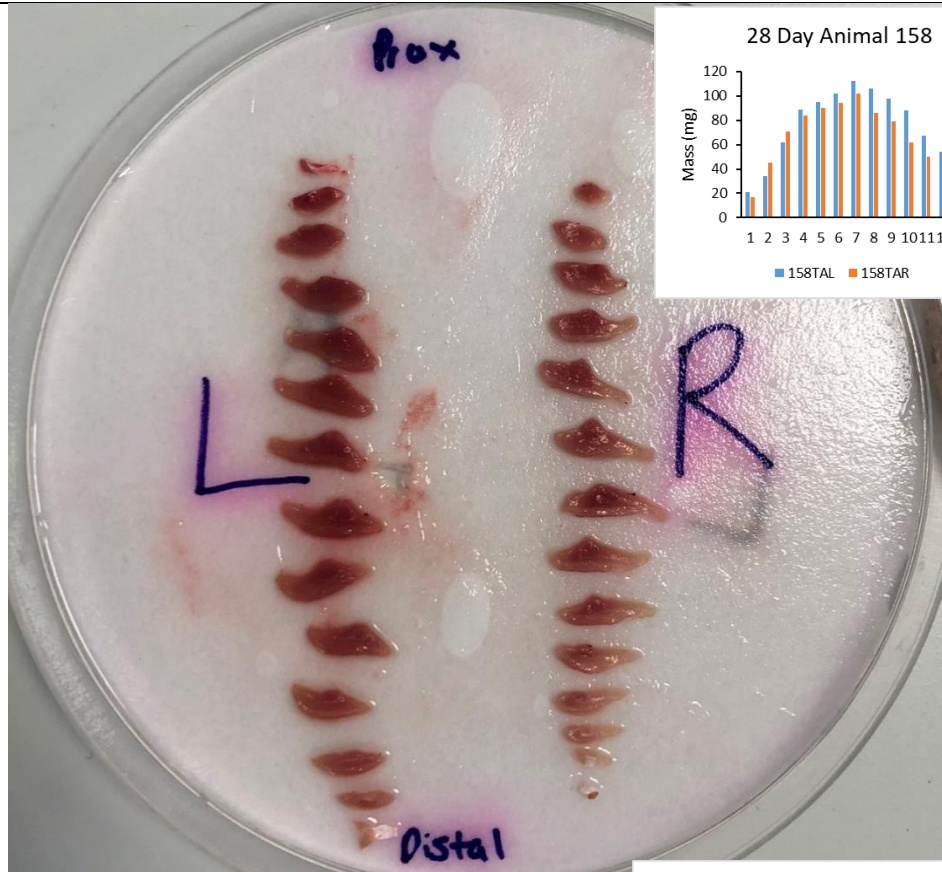
30 Days
'Spillover'
Stimulation
156
TA:
+26.32%
EDL:
+6.14%



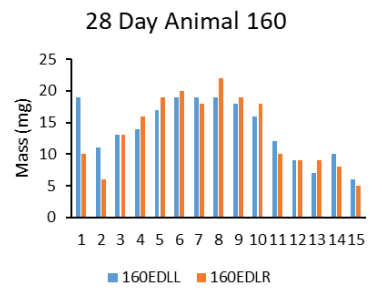
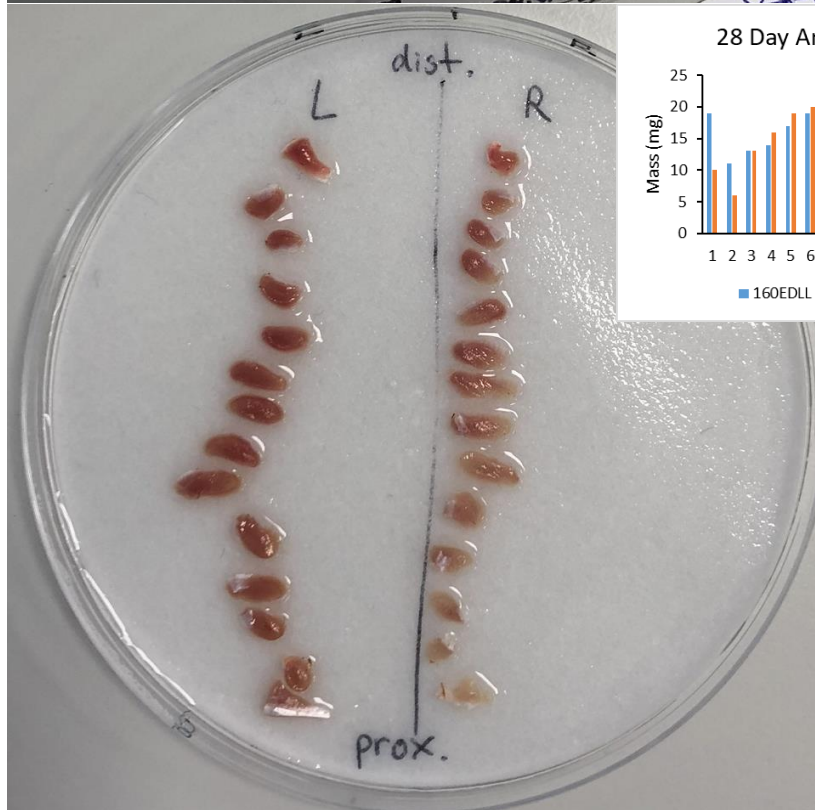
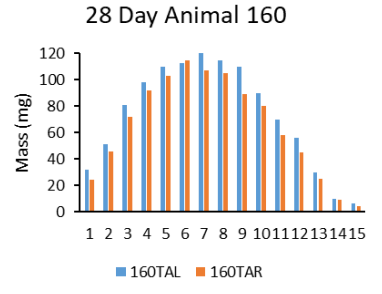
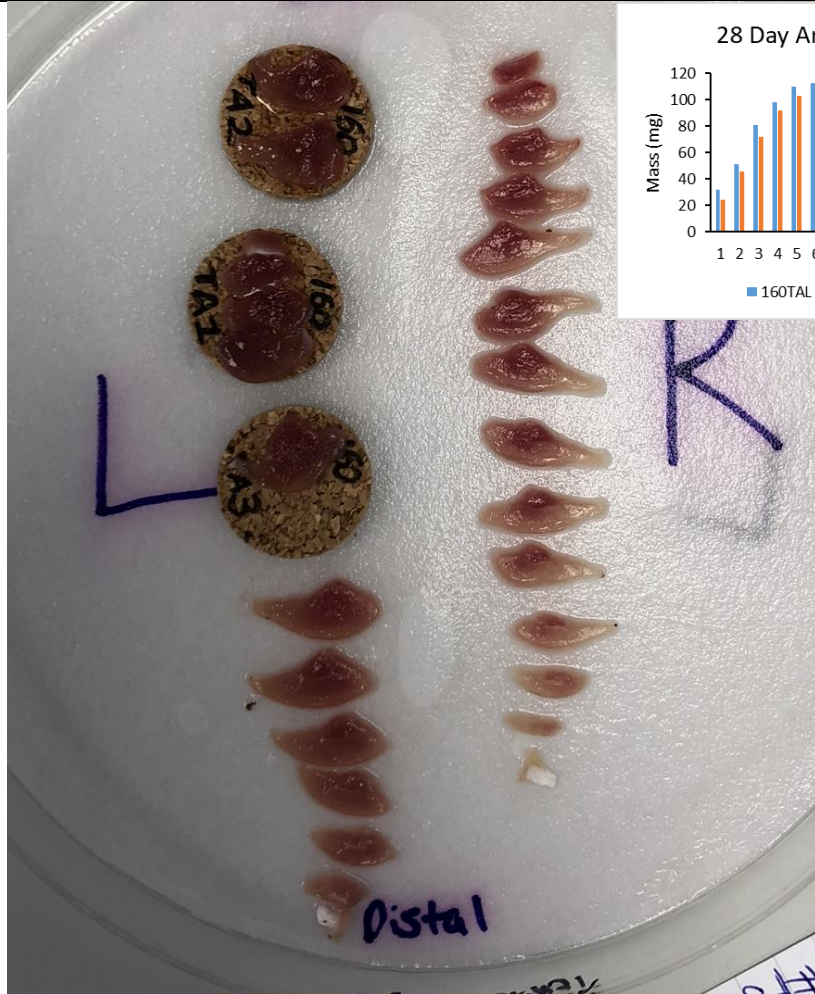
28 Days
'Spillover'
Stimulation
157
TA:
+20.33%
EDL: +5.82



28 Days
 'Spillover'
 Stimulation
 158
 TA: +9.78%
 EDL:
 +3.84%



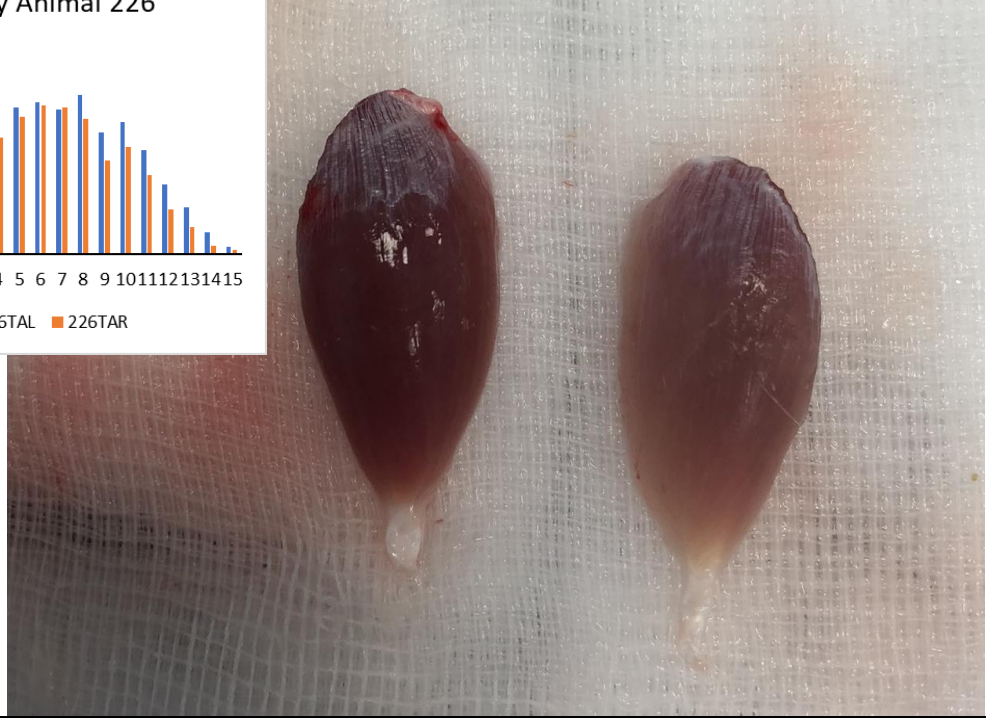
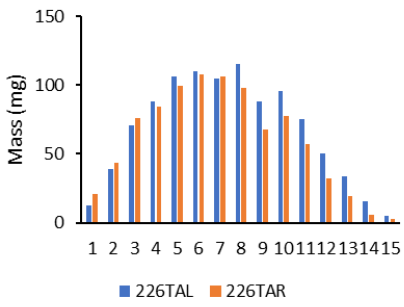
28 Days
 'Spillover'
 Stimulation
 160
 TA:
 +12.12%
 EDL:
 +3.00%



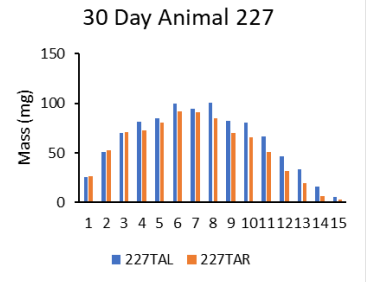
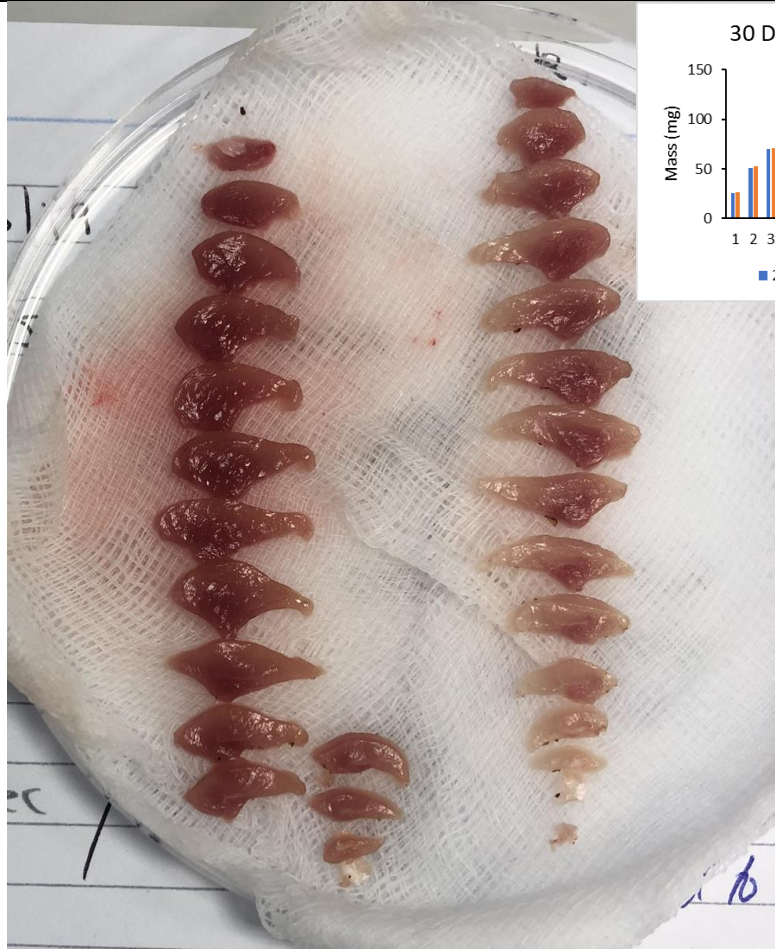
28 Days
'Spillover'
Stimulation
226
TA:
+13.37%
EDL:
+1.74%



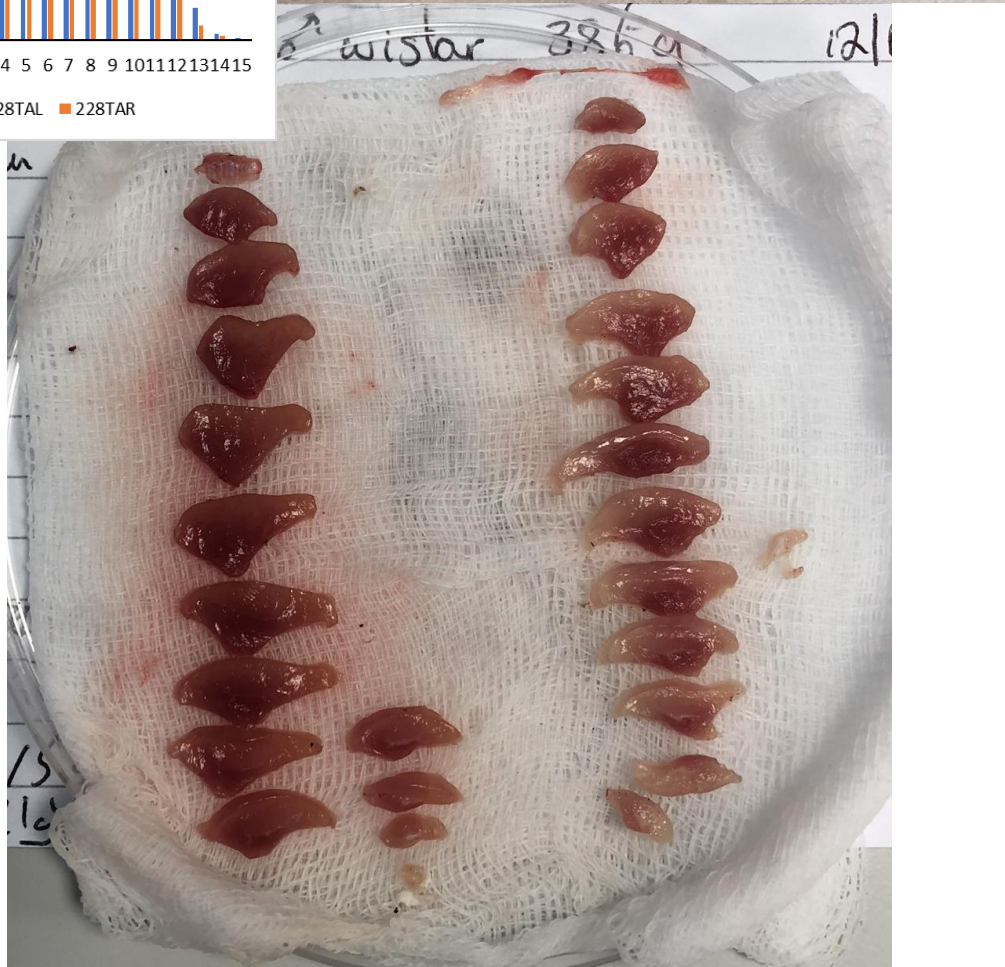
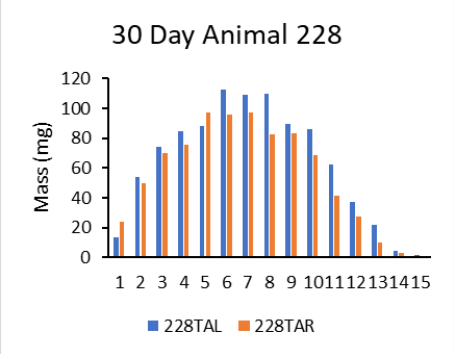
30 Day Animal 226



**28 Days
'Spillover'
Stimulation
227
TA:
+15.34%
EDL:
+10.75%**



28 Days
'Spillover'
Stimulation
228
TA:
+15.45%
EDL:
+14.42%



Appendix 2: QMUL Genome Centre Library Preparation & NG-RNA Sequencing Workflow

GC-JJ-9173

26 January 2021 11:26



Project Methods

Step	Date	Method	Scientist	Objective
1	26/01/2021	Samples receipted	Eva Wozniak	Sample receipt
2	26/01/2021	GC-JJ-9173 Sample QC	Eva Wozniak	Sample quantification & qualification
3	27/01/2021	GC-JJ-9173 Library Preparation	Eva Wozniak	mRNA Library preparation
4	28/01/2021	GC-JJ-9173 Library QC	Eva Wozniak	mRNA Library QC
5	29/01/2021	GC-JJ-9173 Library Dilution & Pooling	Eva Wozniak	Library dilutions and pooling for sequencing
6	02/02/2021	GC-JJ-9173 NextSeq Loading	Eva Wozniak	Library denaturation and NextSeq sequencing

GC-JJ-9173 Sample QC

26 January 2021 11:27



DRAFT Nanodrop SOP 240320 DX

User	Eva Wozniak
Date	26/01/2021
File path	Z:\shares\Projects\NGS_Projects\RNA_Sequencing\Jarvis_Jonathan\GC-JJ-9173\Process
File name	GC-JJ-9173_SampleQC_260121
Objective	Quantify RNA samples
Outcome	

Deviations from any step in the protocol should be noted in italicised green text under that step

Things to do before starting

- Ensure Nanodrop PC is on and log into the Nanodrop user account.

Protocol

- 1. Open ND-8000 V2 2.0 Software from the desktop.
- 2. Create a Sample ID file for batches of over 16 samples. Open the template below (which has 4 fields: Row, Column Sample ID, and Number Replicates) and save in the correct project folder on Apocrita as a Tab Delimited (.txt) file, naming it with the iLab project ID



Nanodrop_1
n_Template

- 3. Wipe the upper and lower pedestals with a kimwipe dampened with Milli-Q water, followed by a dry kimwipe.
- 4. Select the appropriate mode: Single Sample or 8 Sample.
- 5. Click on the Nucleic Acid option.
- 6. The software will prompt you to load clean water in order to initialise the instrument.
- 7. Pipette 1-2µL of MilliQ water to the lower pedestals only, lower the arm and click "Continue".
- 8. Open the arm and remove the water from both the upper and lower pedestals with a dry kimwipe.
- 9. The software will then prompt you to blank the instrument.
- 10. Load 1-2µl of suspension buffer onto the lower pedestals, lower the arm and click "Continue". Record the blanking buffer and lot number in the table below:

Blanking reagent name	Blanking reagent lot number

Note: It is important to use the same buffer type that your samples have been suspended in, failure to do this will result in inaccurate measurement.

- 11. Open the arm and remove the blanking reagent from both the upper and lower pedestals with a dry kimwipe.

12. The instrument will then prompt you to "Select Sample Loading Mode", select either "Load

- Sample ID file" or "Manual Sample Entry".
- ✓13. Select the file created in step2, if using "Load Sample ID file".
Note: It may be necessary to click "Define Sample ID File Format" and edit the Data Series Type. It is important that this is done correctly at the time.
 - ✓14. Select the sample type - DNA or RNA - from the drop-down menu on the top left hand side of the window.
Note: For Bisulphite Converted DNA sample type ssDNA-33 should be selected.
 - ✓15. Check the appropriate pedestals are selected as active, if using the single sample mode. Clicking "All Active On/Off" will select an entire 8-sample column.
Note: If using the 8-Sample mode, some additional settings can be chosen using the "Configuration" menu from the task bar:

***Auto Advance Columns** - this will show results for 5 seconds before automatically moving to the next active plate column.*

***Measurement Limits** - the user can define measurement limits. Once all active samples have been measured, a plate summary is shown with samples outside of these limits highlighted in red. These samples can be selected to be re-measured. Selecting the samples to repeat and clicking "Repeat selected" will allow the user to re-measure those specific samples.*
 - ✓16. Load 1-2µl of sample onto each corresponding pedestal, lower the arm and click "Measure".
 - ✓17. Once results are shown, open the arm and wipe the upper and lower pedestals with a kimwipe dampened with MilliQ water.
 - ✓18. Follow steps 16 and 17 to continue measuring all samples.
Note: If any samples need to be re-measured, toggle to those samples using the arrows above the plate graphic and select the Active checkbox for those samples, as per step 15. These repeated measurements will appear at the bottom of the final report. Only samples belonging to the same column can be measured simultaneously.
 - ✓19. When all samples have been measured click the "Show Report" button.
 - ✓20. In the new window, from the taskbar, select Reports and from the drop-down, select Save Report.
 - ✓21. Save the "Full Report" to the current project folder on Apocrita.
 - ✓22. Repeat step 20 and "Export Report Table Only" to save a text file of the data to the current project folder on Apocrita.
 - ✓23. Clean both upper and lower pedestals with a kimwipe dampened with Milli-Q water, followed by with a dry kimwipe.
 - ✓24. Exit the measurement module.
 - ✓25. Exit the software.

POSTSCRIPT

Expected Results

Quantified nucleic acid samples, including obtaining sample purity metrics.

Sources of error/ limitations

Inappropriate blanking solution used. Inadequate volume of sample loaded. Bubbles present in the loaded sample.

Responsibilities

The protocol operator is responsible.

Internal Quality Assessment Control

Calf thymus DNA of known concentration can be measured to determine the accuracy of the instrument.

Calibration

Equipment calibration conducted by engineer during preventative maintenance visits. Re-conditioning of the pedestals can be conducted as per the [NanoDrop 8000 Spectrophotometer V2.2 User Manual](#)

If required, more thorough cleaning can be performed by loading 2µL aliquots of water to the lower

pedestals, left for 5 minutes and then removed with a dry kimwipe.



PROTOCOL Agilent 2100 Bioanalyser 250320 ES

User	Eva Wozniak
Date	26/01/2021
File path	Z:\shares\Projects\NGS_Projects\RNA_Sequencing\Jarvis_Jonathan\GC-JJ-9173\Process
File name	
Objective	
Outcome	

Deviations from any step in the protocol should be noted in italicised green text under that step

Things to do before starting:

- Remove the Bioanalyzer reagents from the fridge to equilibrate to room temperature for at least 30 minutes.

Note: If a new box of Bioanalyzer chips is being used, replace the syringe on the priming station as detailed in section 2, and prepare new ladder as in section 1.

- Pre-heat the Thermomixer to 70°C.
- Thaw the RNA Nano/Pico/Small RNA ladder stock or aliquots on ice (one per chip).
- Thaw the Ambion Human Brain RNA Control aliquots on ice (one per chip).

Thaw RNA samples on ice, then heat denature at 70°C for 2 minutes and return immediately to ice.

Note: Denaturation only needs to be performed once.

Protocol

1. Prepare the RNA Ladder

Note: This section should be performed when a new box of Bioanalyser chips is opened.

1. Nano/Small RNA Ladder

Nano Ladder Lot Number	
Small RNA Ladder Lot Number	

- a. Thaw the stock ladder on ice.
- b. Centrifuge the tube briefly.
- c. Heat denature the ladder at 70°C for 2 minutes on the heat block.
- d. Immediately cool down on ice.
- e. Label 0.5mL RNase-free tubes with the ladder LOT number and expiry date.
- f. Aliquot 1.2µL of ladder per tube.
- g. Store aliquots at -20°C.

Note: If a ladder batch appears to be faulty, the entire batch of aliquots should be discarded.

2. Pico Ladder

Pico Ladder Lot Number

- a. Thaw the stock ladder on ice.
- b. Centrifuge the tube briefly.
- c. Heat denature the ladder at 70°C for 2 minutes on the heat block

- d. Immediately cool down on ice.
- e. Add 90 µl of RNase-Free water, vortex and centrifuge briefly.
- f. Label 0.5mL RNase-free tubes with the ladder LOT number and expiry date.
- g. Aliquot 4µl ladder per 0.5mL tube.
- h. Store aliquots at -20°C.

2. Prepare the Chip Priming Station

1. Replace the syringe with each new reagent kit.
 - a. Unscrew the old syringe from the lid of the chip priming station.
 - b. Release the old syringe from the clip. Discard the old syringe.
 - c. Open a new syringe and screw it on to the chip priming station.
2. Check the syringe is correctly installed:
 - a. Pull the plunger of the syringe to the 1.0 ml position.
 - b. Place an unused chip in the chip priming station.
 - c. Close the chip priming station and make sure to lock it by pressing the cover. The lock of the latch will audibly click when it closes.
 - d. Press the plunger down until it is locked by the clip.
 - e. Wait for 5 seconds and press the side of the clip to release the plunger.
 - f. Appropriate sealing is verified, if the plunger moves back up to the 0.3 ml mark within less than 1 second.

3. Prepare the filtered gel matrix

1. Pipette the volume of gel matrix (red) into a spin filter column, according to the table below. Label the tube and include the date of preparation:

Chip type	Volume of gel Matrix (µl)	Gel Matrix Lot No.
Pico	550	
Nano	550	2023
Small RNA	650	

2. Centrifuge the gel matrix using the conditions in the table below:

Chip type	Speed ± 20%	Time (minutes)
Pico	1,500 g	10
Nano	1,500 g	10
Small RNA	10,000g	15

3. Keep the filtered gel matrix and discard the spin filter column.
Note: Use filtered gel within 4 weeks of date of filtration.

4. Prepare the Gel-Dye Mix

1. Combine the filtered gel and dye concentrate in a labelled 1.7 ml tube, according to the table below:

Chip type	Volume of filtered gel (µl)	Volume of dye concentrate (µl)	No. chips /	Gel dye concentrate Lot
Pico	65	1	2	
Nano	65	1	2	2023
Small RNA	40	2	1	

2. Mix by vortexing for 5 seconds, and centrifuge for 10 minutes at room temperature at 13,000 g.
Note: Use prepared gel-dye mix within 24 hours.

5. Load the RNA Bioanalyser Chip

1. Adjust the syringe clip; Release the lever of the clip and slide it up to the top position

Nano RNA Chip Lot Number YE12BK20

(*Pico/Nano chip*) or Bottom position (*Small RNA chip*).

Pico RNA Chip Lot Number	
Small RNA Chip Lot Number	

- 2. Take the RNA chip out of its sealed bag, avoiding touching the underside.
- 3. Place the chip on the chip priming station.
- 4. Pipette 9.0 μ l of the gel-dye mix into the well marked with a 'G' in a black circle.
- 5. Make sure the syringe plunger is positioned at 1 ml and then close the chip priming station. The lock of the latch will click when the Priming Station is closed correctly.
- 6. Press the plunger of the syringe down until it is held by the clip.
- 7. Wait for 30 seconds (*Pico/Nano*) or 1 minute (*Small RNA*) and release plunger with clip release mechanism.
- 8. Visually inspect that the plunger moves back at least to the 0.3 ml mark.
- 9. Wait for 5 seconds, then slowly pull back the plunger to the 1 ml position.
- 10. Open the chip priming station. Pipette 9.0 μ l of the gel-dye mix in the remaining 2 wells marked 'G'. Proceed immediately to *step 12* for *Nano chips*.
- 11. *Pico & Small RNA Chip only*: Pipette 9 μ l of conditioning solution into well marked with 'CS'.

Conditioning solution Lot Number	
----------------------------------	--

- 12. Pipette 5 μ l of the RNA marker (green) into well marked with ladder symbol and all sample wells.

RNA Marker Lot Number	2023
-----------------------	------

Caution: Do not leave any wells empty or the chip will not run properly. Unused wells must be filled with 6 μ l of the marker (green)

6. Load the Ladder and Samples

- 1. Pipette 1 μ l of the RNA ladder into the well marked with ladder symbol.
- 2. Pipette 1 μ l of the Ambion Human Brain RNA Control (100ng/ μ L for Nano chip, or 5ng/ μ L for Pico chip) to sample well 1.

Agilent Human Reference RNA Lot Number	6507558
--	---------

- 3. Pipette 1 μ l of each sample into each of the remaining sample wells.
- 4. Place the chip in the IKA vortex mixer, and vortex for 60 seconds at 2400 rpm.

Caution: If the vortexing speed is too high, liquid spill may occur.

Note: The chip must be loaded within 5 minutes of vortexing.

7. Decontaminate electrodes

- 1. Fill one well of an electrode cleaner (Labelled RNaseZAP) with 350 μ l RNaseZAP.

RNaseZAP Lot Number	SLBX9295
---------------------	----------

- 2. Open the bioanalyser lid, place electrode cleaner inside the Agilent 2100 Bioanalyzer, close the lid and leave for 1 minute (*Nano*) or 5 minutes (*Pico*).
- 3. Remove the RNase ZAP electrode cleaner.
- 4. Repeat steps 1 – 3 with an electrode cleaner (labelled ddH₂O) filled with 350 μ l RNase-free water for 10 seconds.

Note: Use the same electrode cleaners for 25 chips, then discard and replace with fresh Electrode cleaners.

- 5. Leave the bioanalyser lid open for 10 seconds to allow the water to evaporate.

8. Start the chip run

- 1. Open the lid of Bioanalyzer, place chip carefully (*chip fits only one direction*), and close the lid.
- 2. Click Assay.
- 3. Click the Start button in the upper right of the window to start the chip run.

Caution: Bioanalyzer should not be moved once running, as this can potentially affect results.

- 4. After the chip run is complete, remove and dispose of the chip to clinical waste.
- 5. Clean the electrodes using the same electrode cleaners from Section 7, and follow the steps below.

Note: Empty RNase ZAP and RNase-free water out of the electrode cleaner once all runs are

complete.

1. Place the ddH₂O electrode cleaner in to the Bioanalyzer and leave for 5 minutes.
2. Remove the electrode cleaner and air dry the pins for 30 seconds before loading the next sample chip.
6. Save the raw chip run by going to 'file', then 'save as' and save the raw .xad file to the relevant project folder.
7. Create a PDF of the results:
 - a. Select 'File', then 'Print'.
 - b. Make sure 'All wells' is selected.
 - c. Change the file path to the relevant project folder by clicking "..." next to the PDF file path.
 - d. Click 'OK', then Click 'save'.

POSTSCRIPT

Expected Results

Samples assigned RNA integrity (RIN) scores, between 1 (low quality) to 10 (high quality).

Sources of error/ limitations

Using Starting RNA concentration outside of recommended quantitative range for Chip can cause the chip to be either overloaded or underloaded and ruin the run

Incorrect orientation of the Chip Priming Station i.e. Clip in wrong position for chip used, can adversely affect loading the gel matrix and ruin the run

Movement of the Bioanalyzer whilst running, can affect the run by producing extra peaks in the traces, which can adversely effect the results

Responsibilities

Responsibility lies with the operator

Internal Quality Assessment Control

Ambion Human brain RNA Control Sample is run at a known concentration on every chip: 5ng/μl for Pico and Small RNA Chips, and 100ng/μl for Nano Chip, with RIN of >7.

Note: if Controls start to produce RINs below 7, discard the batch and prepare fresh aliquots from the stock RNA.

Calibration

Instrument undergoes annual preventive maintenance as part of its service contract

GC-JJ-9173 Library Preparation

27 January 2021 08:50



PROTOCOL NEBNext Ultra II mRNA Library Preparation

User	Eva Wozniak
Date	27/01/2021
File path	Z:\shares\Projects\NGS_Projects\RNA_Sequencing\Jarvis_Jonathan\GC-JJ-9173\Process
File name	BLGCSEQ0191_GC-SVG-9169_GC-JJ-9173_LibraryPreparation_260121.xlsx
Objective	Prepare high-quality mRNA libraries
Outcome	

Deviations from any step in the protocol should be noted in italicised green text under that step

Things to do before starting:

- Clean down all benches, centrifuge and pipettes with RNaseZAP.
- Remove Ampure XP Beads from fridge, and bring up to room temperature (30 minutes minimum)
- Prepare the required volume of 80% Ethanol
- Calculate the volumes needed for each master mix throughout the protocol - record the volumes used in the appropriate places in this SOP.
- Pre-assign sample indexes, making sure that no overlapping indexes are used where samples will be multiplexed on a single sequencing run. Record these in the experiment template linked below.
- Prepare an experiment record using the template below, making sure all fields are filled in and save to the project process folder.

Template	Completed file saved as
 GenomeCentre_NGS...	

- Record library preparation batch details in: \data\WHRI-GenomeCentre\shares\Projects\NGS_Projects\NGS_Templates_Logs\GenomeCentre_NGS_LibraryPrep_Batch_Log.xlsx

Protocol

1. Prepare RNA samples and 1st strand synthesis Buffer mix

- 1. RNA samples should be diluted to 20-25ng/ μ L using RNase-free water, in a clean semi-skirted PCR plate.

- ✓ 2. Aliquot 100ng of sample, and Ambion Human Brain Total RNA control to a clean semi-skirted

Agilent Human Reference RNA Lot Number

PCR plate, and make them up to a final volume of 50 μ L with RNase-Free water. Keep on ice.

Note: Human Brain Total RNA control should be run in triplicate

Note: Diluted sample plate can be prepared and stored at -20°C in advance of library preparation

3. Make the 1st Strand Synthesis Buffer mastermix by combining following components at room temperature:

Component	1X Volume (μL)	Volume prepared (μL) [46.2]	Component added to mix?	Component Lot No.
1st Strand Synthesis Reaction Buffer	8	369.6	<input checked="" type="checkbox"/>	10071456
Random Primers	2	92.4	<input checked="" type="checkbox"/>	10071457
Nuclease-Free Water	10	462	<input checked="" type="checkbox"/>	10071468

4. Vortex, Centrifuge briefly and leave on ice.

2. mRNA Isolation, Fragmentation and Priming Starting with Total RNA

1. Aliquot 20μl of NEBNext Oligo d(T) beads per sample into a clean semi-skirted PCR plate.

NEBNext Oligo d(T) beads Lot Number 10071741

2. Wash the beads by adding 100μl of RNA Binding Buffer (2X). Pipette the entire volume up and down 6 times to mix thoroughly.

RNA Binding Buffer (2X) Lot Number 10071737

3. Place the plate on the magnetic rack at room temperature for 2 minutes.
 4. Remove and discard all of the supernatant from the plate. Take care not to disturb the beads.
 5. Remove the plate from the magnetic rack.
 6. Repeat steps 2–5 once, for a total of two washes.
 7. Resuspend the beads in 50μl of RNA Binding Buffer (2X).
 8. Add the 50μl of total RNA sample from Step 1.2.
 9. Seal the plate and place in a thermal cycler. Close the lid and incubate samples using following conditions, with the lid set at 75°C:

Program name:	65FOR5MI	
Temperature (°C)	Time	Cycles
65°C	5 mins	1
4°C	Hold	∞

Note: This step denatures the RNA and facilitates binding of the poly-A mRNA to the beads.

Tetrad thermal cycler used Tetrad 1

Block number Block 1

10. Remove the plate from the thermal cycler when the temperature reaches 4°C. Centrifuge briefly.
11. Resuspend the beads. Pipette up and down slowly 6 times to mix thoroughly.
 12. Incubate at room temperature for 5 minutes to allow the mRNA to bind to the beads.
 13. Place the plate on the magnetic rack at room temperature for 2 minutes to separate the poly-A mRNA bound to the beads from the solution.
 14. Remove and discard all of the supernatant. Take care not to disturb the beads.
 15. Remove the plate from the magnetic rack.
 16. Add 200μl of Wash Buffer to each well and pipette the entire volume up and down 6 times to mix thoroughly.

Wash Buffer Lot Number 10071738

17. Place the plate on the magnetic rack until the solution is clear (~2 minutes).



18. Remove and discard all of the supernatant from the plate. Take care not to disturb the beads.

- ✓ 19. Remove the plate from the magnetic rack.
- ✓ 20. Add 200µl of Wash Buffer to each well and pipette the entire volume up and down 6 times to mix thoroughly.
- ✓ 21. Place the plate on the magnetic rack until the solution is clear (~2 minutes).
- ✓ 22. Remove and discard all of the supernatant from the plate. Take care not to disturb the beads.
- ✓ 23. Remove the plate from the magnetic rack and add 50µl of Tris Buffer (supplied), into each well. Gently pipette the entire volume up and down 6 times .

Tris Buffer Lot Number 10071740

- ✓ 24. Seal the plate and place in a thermal cycler. Close the lid and incubate samples using following conditions, with the heated lid set at 90°C:

Program name:	MRNAELU	
Temperature (°C)	Time	Cycles
80°C	2 mins	1
25°C	Hold	∞
Block number	Tetrad 1	
Tetrad thermal cycler used	Block 1	

- ✓ 25. Remove the plate from the thermal cycler when the temperature reaches 25°C. Centrifuge briefly.
- ✓ 26. Add 50µl of RNA Binding Buffer (2X) to the sample to allow the mRNA to re-bind to the beads. Gently pipette the entire volume up and down 6 times to mix thoroughly.
- ✓ 27. Incubate the plate at room temperature for 5 minutes.
- ✓ 28. Place the plate on the magnetic rack at room temperature for 2 minutes.
- ✓ 29. Remove and discard all of the supernatant from the plate. Take care not to disturb the beads.
- ✓ 30. Remove the plate from the magnetic rack.
- ✓ 31. Adding 200µl of Wash Buffer. Gently pipette the entire volume up and down 6 times to mix thoroughly.
- ✓ 32. Place the plate on the magnetic rack at room temperature for 2 minutes.
- ✓ 33. Remove and discard all of the supernatant from the plate. Take care not to disturb the beads.
Note: It is important to remove all of the supernatant to successfully fragment the mRNA in the subsequent steps. Spin down the plate. Place the plate on the magnetic rack and with a 10µl tip remove the entire wash buffer.
Caution: Do not disturb beads that contain the mRNA.
- ✓ 34. Remove the plate from the magnetic rack.
- ✓ 35. Elute mRNA from the beads by adding 11.5µl of the First Strand Synthesis Buffer mastermix from Section 1.3 [Prepare RNA samples and 1st strand synthesis Buffer mix](#)
- ✓ 36. Seal the plate and place in a thermal cycler. Close the lid and incubate samples using following conditions, with the heated lid set at 105°C:

Program name:	94-4-10	
Temperature (°C)	Time	Cycles
94°C	10 mins	1
Tetrad thermal cycler used	Tetrad 1	
Block number	Block 1	

- ✓ 37. Once Incubation is complete, remove plate from thermal cycler and centrifuge briefly.
- ✓ 38. Place the plate immediately on the magnetic rack.
- ✓ 39. Collect the purified mRNA by transferring 10µl of the supernatant to a clean nuclease-free PCR plate.
Note: If the supernatant volume recovered is less than 10µl for any reason, bring the volume up to 10µl by adding the First Strand Synthesis Reaction Buffer and Random Primer Mix (2X) and continue with the protocol. Avoid transferring the magnetic beads.

40. Place the plate on ice and proceed directly to first strand cDNA synthesis.

3. First Strand cDNA Synthesis

1. Make the First Strand Enzyme Mastermix by combining following components, scale up with 10% excess as necessary:

Component	1X Volume (μL)	Volume prepared (μL) [46.2]	Component added to mix?	Component Lot No.
NEBNext Strand Specificity Reagent	8	369.6	<input checked="" type="checkbox"/>	10071469
NEBNext First Strand Synthesis Enzyme Mix	2	92.4	<input checked="" type="checkbox"/>	10071465

2. Mix by gently pipetting up and down 6 times. Spin briefly.
 3. Add 10μl of the First Strand Enzyme Mastermix to the fragmented and primed mRNA.
 4. Mix by gently pipetting up and down 6 times.
 5. Seal the plate and place in a thermal cycler. Close the lid and incubate samples (with the heated lid set at 80°C) using following conditions:

Program name:	1STRANDE	
Temperature (°C)	Time	Cycles
25°C	10 mins	1
42°C	50 mins	1
70°C	15 mins	1
4°C	Hold	∞

Tetrad thermal cycler used	Tetrad 1
Block number	Block 1

6. Once Incubation is complete, remove plate from thermal cycler and centrifuge briefly.
 7. Immediately, perform second strand cDNA synthesis reaction.

4. Second Strand cDNA Synthesis

1. Make the Second Strand Mastermix by combining following components, scale up with 10% excess as necessary:

Component	1X Volume (μL)	Volume prepared (μL) [46.2]	Component added to mix?	Component Lot No.
Nuclease free water	48	2217.6	<input checked="" type="checkbox"/>	10071739
NEBNext Second Strand Synthesis Buffer	8	369.6	<input checked="" type="checkbox"/>	10071459
NEBNext Second Strand Synthesis Enzyme Mix	4	184.8	<input checked="" type="checkbox"/>	10071458

2. Mix thoroughly by gently pipetting up and down 6 times
 3. Add 60μl of Second Strand Mastermix to First Strand Synthesis reaction.
 4. Mix thoroughly by gently pipetting up and down 6 times.
 5. Seal the plate and place in a thermal cycler. Close the lid and incubate samples using following conditions:

Program name:	16FOR1HR	
Temperature (°C)	Time	Cycles

16°C	60 mins	1
------	---------	---

Tetrad thermal cycler used	Tetrad 1
Block number	Block 1

6. Once Incubation is complete, remove plate from thermal cycler and centrifuge briefly.

5. Purify the Double-stranded cDNA Using 1.8X Agencourt AMPure XP Beads

1. Vortex AMPure XP Beads to resuspend.

AMPureXP Beads Lot Number	18222700
---------------------------	----------

2. Add 144µl (1.8X) of resuspended AMPure XP Beads to the second strand synthesis reaction (~80µl). Mix well on a vortex mixer or by pipetting up and down at least 10 times.

3. Incubate for 5 minutes at room temperature.

4. Place the plate on the magnetic rack and allow the solution to clear (about 5 minutes).

5. Carefully remove and discard the supernatant. Be careful not to disturb the beads that contain DNA targets.

6. Add 200µl of freshly prepared 80% ethanol to the wells while in the magnetic rack.

80% Ethanol Preparation Date	27/01/2021
------------------------------	------------

7. Incubate at room temperature for 30 seconds, and then carefully remove and discard the supernatant.

8. Add 200µl of freshly prepared 80% ethanol to the wells while in the magnetic rack.

9. Incubate at room temperature for 30 seconds, and then carefully remove and discard the supernatant.

10. Air dry the beads for 5 minutes while the plate is on the magnetic rack.

Caution: Do not over dry the beads. This may result in lower recovery of DNA target.

11. Remove the plate from the magnet.

12. Elute the DNA target from the beads by adding 53µl 0.1X TE Buffer (provided) to the beads. Mix well on a vortex mixer or by pipetting up and down.

0.1X TE Buffer Lot Number	10071467
---------------------------	----------

13. Quickly spin the plate and incubate for 2 minutes at room temperature. Place the plate in the magnetic rack until the solution is clear.

14. Transfer 50µl of the supernatant to a clean nuclease-free PCR plate.

SAFE STOPPING POINT: Samples can be stored at -20°C

Stop Date	27/01/2021	Continuation Date	28/01/2021
Stop Time	15:50	Continuation Time	09:55

6. Perform End Prep of cDNA Library

1. Make the End Prep mastermix by combining following components, scale up with 10% excess as necessary:

Component	1X Volume (µL)	Volume prepared (µL) [46.2X]	Component added to mix?	Component Lot No.
NEBNext Ultra II End Prep Reaction Buffer	7	323.4	<input type="checkbox"/>	10071462
NEBNext Ultra II End Prep Enzyme Mix	3	138.6	<input type="checkbox"/>	10071461

- ✓ 2. Mix thoroughly by gently pipetting up and down 6 times. Centrifuge briefly.
- ✓ 3. Add 10µl of End Prep Mastermix to the purified cDNA. Mix thoroughly by gently pipetting up and down six times. Centrifuge briefly.

Caution: It is important to mix well. The presence of a small amount of bubbles will not interfere with performance.

4. Seal the plate and place in a thermal cycler. Close the lid and incubate samples using following conditions, with the heated lid set at 75°C:

Program name:	NEBEREP	
Temperature (°C)	Time	Cycles
20°C	30 mins	1
65°C	30 mins	1
4°C	Hold	∞
Tetrad thermal cycler used	Tetrad 1	
Block number	Block 1	

5. Once the incubation reaches 4°C, remove the plate from thermal cycler and centrifuge briefly.

7. Adaptor Ligation

1. Make Diluted NEBNext Adaptor by combining following components, scale up with 10% excess as necessary:

Component	1X Volume (µL)	Volume prepared (µL) [X]	Component added to mix?	Component Lot No.
NEBNext Adaptor	1	5	<input checked="" type="checkbox"/>	10071758
Adaptor dilution buffer	24	120	<input checked="" type="checkbox"/>	10071466

2. Slowly and gently pipette up and down ten times. Centrifuge briefly and keep on ice.
 3. Make the *Ligation Mastermix* by combining following components, scale up with 10% excess as necessary:

Component	1X Volume (µL)	Volume prepared (µL) [X]	Component added to mix?	Component Lot No.
NEBNext Ligation Enhancer	1	46.2	<input checked="" type="checkbox"/>	10071455
NEBNext Ultra II Ligation Master Mix	30	1386.0	<input checked="" type="checkbox"/>	10071463

Caution: Do not pre-mix the Ligation Mastermix and Diluted Adaptor in order to prevent adaptor-dimer formation.

4. Add 31µL of Ligation Mastermix to each well.
 5. Add 2.5µL of diluted NEBNext Adaptor from step section 7.1 to each sample well
 6. Set a 100µL or 200µL pipette to 80µL. Slowly and gently pipette up and down ten times. Centrifuge briefly.
 7. Seal the plate and place in a thermal cycler. Close the lid and incubate samples using following conditions:

Program name:	20-4-15	
Temperature (°C)	Time	Cycles
20°C	15 mins	1
Tetrad thermal cycler used	Tetrad 1	
Block number	Block 1	

8. Once Incubation is complete, remove plate from thermal cycler and centrifuge briefly.
 9. Add 3µL USER Enzyme to each sample well, and mix by pipetting.

USER Enzyme Lot Number 10071460

10. Seal the plate, spin briefly and place in a thermal cycler. Close the lid and incubate samples (with the heated lid set to ≥45°C) using following conditions:

Program name:	37-4-15	
Temperature (°C)	Time	Cycles
37°C	15 mins	1
Tetrad thermal cycler used		Tetrad 1
Block number		Block 1

12. Proceed immediately to Purification of the Ligation Reaction.

8. Purify the Ligation Reaction Using AMPure XP Beads

Note: Size selection to enrich for libraries between 300 - 450bp

1. Vortex AMPure XP Beads to resuspend.

AMPureXP Beads Lot Number 18222700

2. Add 25µl (3.86X) of beads to the 96.5µl ligation reaction. Mix well by pipetting up and down at least 10 times.
3. Incubate for 5 minutes at room temperature.
4. Quickly spin the plate and place on the magnetic rack to separate the beads from the supernatant.
5. After the solution is clear (about 5 minutes), carefully transfer the supernatant containing your DNA to a new plate.

Caution: Do not discard the supernatant.

6. Discard the beads that contain the unwanted large fragments.
7. Add 10µl (12.15X) resuspended AMPure XP Beads to the supernatant and mix well.
8. Incubate for 5 minutes at room temperature.
9. Quickly spin the plate and place it on the magnetic rack to separate the beads from the supernatant.
10. After the solution is clear (about 5 minutes), carefully remove and discard the supernatant that contains unwanted DNA. Be careful not to disturb the beads that contain the desired DNA targets.

Caution: Do not discard beads.

11. Add 200µl of 80% freshly prepared ethanol to the plate while in the magnetic stand.

12. 80% Ethanol preparation date 28/01/2021

13. Incubate at room temperature for 30 seconds.
14. Carefully remove and discard the supernatant.
15. Add 200µl of 80% freshly prepared ethanol to the plate while in the magnetic stand.
16. Incubate at room temperature for 30 seconds.
17. Carefully remove and discard the supernatant.
18. Air the dry beads for 5 minutes while the plate is on the magnetic stand with the lid open.

Caution: Do not over dry the beads. This may result in lower recovery of DNA target.

19. Elute the DNA target from the beads by adding 17µl of 0.1 X TE (provided) to the beads. Mix well on a vortex mixer or by pipetting up and down. Quickly spin the plate and place it on a magnetic stand.

0.1X TE Buffer Lot Number 10071467

20. After the solution is clear (about 5 minutes), transfer 15µl to a new PCR plate for amplification.

SAFE STOPPING POINT: Samples can be stored at -20°C for up to 1 week.

Stop Date		Continuation Date	
Stop Time		Continuation Time	

9. PCR Library Enrichment

1. Add 25 μ L of NEBNext Q5 Hot Start HiFi PCR Master Mix to each well.

NEBNext Q5 Hot Start HiFi PCR Master Mix Lot No.	10071464
--	----------

- 2. Mix well by pipetting
- 3. Add 10µL of pre-assigned Index Primer to each well
NEBNext® Multiplex Oligos for Illumina® (96 Index Primers)

NEBNext® Multiplex Oligos for Illumina® (96 Index Primers) Lot No. 10071757

- 4. Mix thoroughly by gently pipetting up and down 10 times. Seal and briefly centrifuge.
- 5. Place the plate in a thermal cycler, close the lid and incubate samples (with the heated lid set at 105°C) using following conditions:

Program name:	NEB13	
Temperature (°C)	Time	Cycles
98°C	30 secs	1
98°C	10 secs	
65°C	75 secs	X 13
65°C	5 mins	1
4°C	Hold	∞

Note: The number of PCR cycles should be adjusted based on RNA input. If 100 ng total RNA is the starting input, it is recommended to perform 13 cycles of PCR.

Tetrad thermal cycler used	Tetrad 1
Block number	Block 1

10. Purify the PCR Reaction using Agencourt AMPure XP Beads

- 1. Vortex Agencourt AMPure XP Beads to resuspend.
AMPureXP Beads Lot Number 18222700
- 2. Add 45µl (0.9X) of resuspended Agencourt AMPure XP Beads to the PCR reaction (~ 50µl). Mix well on a vortex mixer or by pipetting up and down at least 10 times.
- 3. Incubate for 5 minutes at room temperature.
- 4. Quickly spin the plate in a microcentrifuge and place the plate on an appropriate magnetic rack to separate beads from the supernatant.
- 5. After the solution is clear (about 5 minutes), carefully remove and discard the supernatant. Be careful not to disturb the beads that contain DNA targets.
- 6. Add 200µl of freshly prepared 80% ethanol to the plate while in the magnetic rack.
80% Ethanol preparation date 28/01/2021
- 7. Incubate at room temperature for 30 seconds.
- 8. Carefully remove and discard the supernatant.
- 9. Repeat Steps 6-8 once for 2 washing steps.
- 10. Air dry the beads for 5 minutes while the plate is on the magnetic rack with the lid open.
Caution: Do not over dry the beads. This may result in lower recovery of DNA target.
- 11. Remove the plate from the magnetic rack.
- 12. Elute the DNA target from the beads into 23µl 0.1X TE.
0.1X TE Buffer Lot Number 10071467
- 13. Mix well on a vortex mixer or by pipetting up and down.
- 14. Quickly spin the plate in a microcentrifuge and incubate for 2 minutes at room temperature.
- 15. Place the plate in the magnetic rack until the solution is clear.
- 16. Transfer 20µl of the supernatant to a clean PCR plate, and store at -20°C.

11. Library Quality Control

- 1. All resulting libraries should be quantified using the Qubit HS dsDNA kit, and should be qualified on the appropriate 1000bp ScreenTape according to concentration.

- ✓ 2. A pooling strategy should be followed as per the users' requirements, and all control RNA samples should be pooled together in a separate tube to be spiked in to the sequencing run at 1%.

POSTSCRIPT

Expected Results

High-quality mRNA libraries with a peak around 300-450bp. Low PCR duplicate rate (<10%), and good alignment percentage (>90%) to the correct species genome.

Sources of error/ limitations

Over-drying of bead pellets can lead to a reduced yield due to difficulty in resuspending beads.

Using the incorrect number of PCR cycles can also either reduce library yield where the cycle number is too low, or produce a larger than expected percentage of PCR duplicates where the cycle number is too high.

Responsibilities

Responsibility lies with the operator

Internal Quality Assessment Control

Ambion Human Brain Total RNA control to be prepared in triplicate for each batch of library preparations. The control libraries should be pooled in an equimolar fashion, and denatured alongside the client library to be spiked in to the NGS sequence run at 1%.

Calibration

N/A

GC-JJ-9173 Library QC

28 January 2021 15:33



PROTOCOL Qubit 2.0 Fluorometer 250320EW

User	Eva Wozniak
Date	28/01/2021
File path	
File name	BLGCSEQ0191_GC-SVG-9169_GC-JJ-9173_LibraryPreparation_260121.xlsx BLGCSEQ0191_Library_Raw_QUBIT_2021-01-28_4-17-PM.csv
Objective	Quantify mRNA libraries
Outcome	

Deviations from any step in the protocol should be noted in italicised green text under that step

Things to do before starting

- If a new assay kit is being opened, make sure to label the standards with the same date as the reagent box.
- Remove the reagents from the fridge and allow to equilibrate to room temperature for 30 minutes
- If a new kit is opened, only the standards should be returned to the fridge at the end of the procedure.
- Prepare Calf-thymus DNA control if necessary:
 - Dissolve lyophilised CT-DNA (5mg) in 5mL 1xTE buffer to prepare 1mg/mL stock.
 - Dilute 100 μ L of 1mg/mL stock with 900 μ L 1xTE buffer to prepare 100ng/ μ L working stock.
 - Measure by Qubit and adjust with more 1xTE buffer/DNA as necessary.
 - Dilute 150 μ L of 100ng/ μ L working stock with 450 μ L 1xTE buffer to prepare 25ng/ μ L reference sample.
 - Measure by Qubit to ensure accurate dilution, and adjust with more DNA/1xTE buffer as necessary.
 - Aliquot 100 μ L of 25ng/ μ L to labelled 1.5mL tubes. Store one aliquot with Qubit standards, and remaining aliquots at -20°C until needed.

Protocol

Each Qubit kit contains fluorescent assay reagent, dilution buffer, and two pre-diluted standards.

Note: Always use the standards with the corresponding kit. When a new kit is opened dispose of the previous standards immediately, and label the standards with the same date as the kit they were taken from.

Each kit follows the same protocol below:

1. Preparing Qubit standards

- 1. Dilute the fluorescent assay reagent 1:200 using the dilution buffer provided. Prepare 200ul of this working solution per sample, plus three standards, with 10% excess.

Record the volume prepared in the table below (editing the number of samples):

Reagent	1 X Volume	Volume prepared for N samples + 3	Reagent Lot
Qubit Fluorescent	1.0	46	2200356
Qubit Dilution Buffer	199.0	9154	2200356

- 2. Pipette 190ul of working solution to each of two 0.5ml tubes labelled "S1" and "S2".
- 3. Pipette 199uL of working solution to another 0.5mL tube labelled "CT".
- 4. Pipette 10uL of Standard 1 to the tube labelled "S1"
- 5. Pipette 10uL of Standard 2 to the tube labelled "S2"
- 6. Pipette 1uL of 25ng/uL pre-prepared calf thymus DNA to the tube labelled "CT".

Date of CT DNA preparation 23/06/2020

- 7. Vortex the tubes for 5 seconds and spin briefly.

2. Measuring the Qubit Standards

- 1. On the Qubit home screen, select the sample type being measured: DNA, RNA or Protein
- 2. Next, Select the reagent kit being used: dsDNA HS, dsDNA BR etc
- 3. When prompted to measure new standards, choose "Yes".
- 4. Follow the on-screen prompts to measure the two kit standards
- 5. Remove S2 from the Qubit and insert the "CT" tube.
- 6. Measure the "CT" control DNA by selecting the "Sample" tab at the bottom of the screen, and pressing "Read".

Caution: The concentration shown on the screen is the raw reading and does not take in to account the dilution factor.

- 7. Select "Calculate stock conc." and use the wheel to choose the volume of DNA sample measured to determine the actual sample concentration and record this in the report.
Note: Units can also be changed by selecting the unit displayed and choosing an alternative, but it is recommended to record ng/ μ L.

- 8. Check the raw fluorescent readings by selecting "Check Stds." on the screen and record the values in the Qubit quantification report.
Note: For the BR Kit, standard 1 should be 100 times less than standard 2 and for the HS kit standard 1 should be 1000 times less than standard 2.

The calf thymus (CT) control sample should be 25ng/uL +/- 10%.

- 9. Record the values of the standards and control sample in the Qubit quantification report sheet (linked below), renaming with the iLab project ID and saving to the project Process folder:



Qubit_Quantification...

- 10. If the standards do not conform to the above conditions, discard the working solution and prepare a fresh batch. Repeat Section 2.

3. Measuring samples

- 1. Aliquot 199 μ L of the Qubit working solution (prepared in section 1.1) to a 0.5mL tube per sample.
- 2. Add 1 μ L sample to each 0.5mL tube.
- 3. Vortex for 5 seconds and spin briefly.
- 4. Remove the CT sample from the qubit and insert the first project sample



5. Press "Read next sample" to take the measurement
6. Select "Calculate stock conc.", changing the volume used if necessary and record the result.
7. Remove the sample tube
8. Repeat steps 2 to 4 until all samples have been quantified.

Note: Prepared samples may be kept at room temperature for up to 2 hours prior to measurement. It is advisable to re-measure the standards prior to the samples.

POSTSCRIPT

Expected Results

Concentration of each sample in the required units.

Sources of error/ limitations

Ensure that samples are measured at room temperature, and that the exterior of the tubes are clean and dry.

Small bubbles in the samples may alter results. Centrifuge the tubes briefly prior to measuring to minimize this.

Responsibilities

Responsibility for the protocol and equipment lies with the operator.

Internal Quality Assessment Control

Samples of known concentration can be used as a measure of quality control.

Calibration

Calibration of the equipment is performed using the pre-diluted standards provided in the assay kits. The standards from each kit can be measured as samples to ensure correct performance of the machine. The concentration of the standards for each kit are listed below:

Assay Kit	Standard 1 Concentration (ng/ul)	Standard 2 Concentration (ng/ul)
dsDNA HS	0	10
dsDNA BR	0	100
RNA HS	0	100
RNA BR	0	10
RNA HR	0	10
ssDNA	0	20



PROTOCOL TapeStation QC GC200212EW

User	Eva Wozniak
Date	28/01/2021
File path	
File name	
Objective	Qualify mRNA libraries
Outcome	

Deviations from any step in the protocol should be noted in italicised green text under that step

Things to do before starting:

- Remove ScreenTape and Reagents from the fridge and allow to equilibrate at room temperature for 30 minutes
- Once equilibrated, briefly vortex and spin down the TapeStation reagent and ladder tubes
- Ensure that the samples being run meet the requirements of the ScreenTape being used - see table below:

ScreenTape	Sizing range	Sample Concentration	Wells per
Genomic DNA	200 - >60,000	5 - 300 ng/uL	16

D1000	35 - 1,000 bp	0.1 - 50 ng/uL	16
HS D1000	35 - 1,000 bp	0.01 - 1 ng/uL	16
HS D5000	100 - 5,000 bp	0.01 - 1 ng/uL	16

Preparing Samples

- ✓ 1. Aliquot the appropriate volume of sample buffer per sample to each well of a strip tube (if <16 samples) or skirted 96-well PCR plate according to the table below. Indicate the kit used and record the tube lot number in the table.

Note: Only one HSD5000 screentape can be run at one time - only use a max. of 15 samples + ladder. All other tapes can be run in multiple with one ladder aliquot.

Reagent Kit	Buffer volume (uL)	Kit selected	Buffer Lot Number
Genomic DNA	10	<input type="checkbox"/>	
D1000	3	<input checked="" type="checkbox"/>	0006511134
HS D1000	2	<input type="checkbox"/>	
HS D5000	2	<input type="checkbox"/>	

- ✓ 2. Aliquot the kit ladder to the first well, using the volume in the table below. Record the ladder lot number:

Reagent Kit	Ladder volume (uL)	Kit selected	Ladder Lot Number
Genomic DNA	1	<input type="checkbox"/>	
D1000	1	<input checked="" type="checkbox"/>	2019
HS D1000	2	<input type="checkbox"/>	
HS D5000	2	<input type="checkbox"/>	

- ✓ 3. Aliquot each sample to a new well containing sample buffer, using the volume in the table below:

Reagent Kit	Sample volume (uL)	Kit selected
Genomic DNA	1	<input type="checkbox"/>
D1000	1	<input checked="" type="checkbox"/>
HS D1000	2	<input checked="" type="checkbox"/>
HS D5000	2	<input type="checkbox"/>

- ✓ 4. Seal the strip tube with caps, or seal the 96-well plate with adhesive foil.
 ✓ 5. Insert the strip tubes/plate in to the IKA MS3 vortex mixer and press start. The vortex mixer will automatically stop after 1 minute.
 ✓ 6. Remove the tubes/plate from the vortex mixer and pulse centrifuge.
 ✓ 7. On the TapeStation 2200, open the instrument lid and empty used tips from the tip bucket into a sharps bin. Load new tips into the tip holder.

Note: A full tip holder should be used each time the tapestation is run, whether the whole tape is being run or not.

- ✓ 8. Open the screentape foil packaging. Check that there is no damage to the screentape and gently flick to help remove any bubbles which may have formed during storage. Record the screentape lot number below (add additional columns for multiple tapes):

ScreenTape	Type Selected	ScreenTape Lot Number
Genomic DNA	<input type="checkbox"/>	
D1000	<input checked="" type="checkbox"/>	0201913-613
HS D1000	<input type="checkbox"/>	
HS D5000	<input type="checkbox"/>	

- ✓ 9. Insert the tape into the instrument. Tapes should be loaded with the top of the tape facing

towards the user with the barcode facing to the right.

Note: If the tape is inserted incorrectly the control software will notify you to correct the tape position.

Store partially used screen-tapes at 4 °C for a maximum of 2 weeks. Store the tape in the foil packaging it came in noting the date it was opened and how many lanes remain after its use.

- ✓10. Load the sample plate/strip tube(s) into the Agilent 2200 TapeStation instrument using the correct insert for either 96-well plate or strip tubes.
- ✓11. If you are using strip tubes carefully remove the caps. If you are using a 96 well plate with a foil seal please do not remove this seal.
- ✓12. Select the required sample positions on the TapeStation Controller Software plate or strip tube layout, by clicking and dragging over the sample locations, making sure the ladder is assigned to the correct well. Name all well positions with sample IDs.
Note: Sample IDs can be manually entered, or copied and pasted from an excel sheet, before the instrument is started and whilst the instrument is running, before TapeStation Analysis Software is launched.
- ✓13. Click **Start**. This will open the 'save as' page. Name the TapeStation file using the iLab project ID with a brief description of what is running and save to a known location on the local laptop.
- ✓14. Click **Save** and then **Start**.
- ✓15. The software will prompt you to check that samples and tips have been loaded. Click "**OK**" to begin the run.
- ✓16. If you are running the 96-well plate option and running a sample number which requires multiple tapes, the instrument will prompt you to insert a new tape/tips:
 - ✓1. Open the instrument and remove and dispose of the used tape.
 - ✓2. Empty the used tips in to a sharps bin and load fresh tips to the tip-holder.
 - ✓3. Open the foil packaging of a new tape and flick the screentape gently.
 - ✓4. Insert the new tape in to the instrument.
 - ✓5. Close the lid and click "Continue". The software will check that a new tape, and fresh tips have been loaded. Click "**OK**" to proceed with the run.
 - ✓6. If applicable, repeat steps 16.1 to 16.5 until all samples have been run.
- ✓17. The Agilent TapeStation Analysis Software will automatically open after the run has complete to display results.
- ✓18. Copy the file which has been locally saved to a USB stick and transfer over to the project folder on Apocrita.

POSTSCRIPT

Expected Results

A tapestation file which contains all analysed samples saved in the project folder on Apocrita.

Sources of error/ limitations

Incorrect buffer volumes may lead to failure.

Running tapes not equilibrated to room temperature may lead to failure.

Bubbles present in the screentape will inhibit proper running of samples/ladder.

If the ladder is omitted, an electronic ladder may be added. Electronic ladder functionality is not available for D5000, High Sensitivity D5000, or Genomic DNA assays.

Responsibilities

The protocol operator is responsible.

Internal Quality Assessment Control

Ensure each lane shows an upper and lower marker (dependent on tape) and no lanes have been skipped. If errors occur samples can be re-run or markers re-assigned manually.

Calibration

The TapeStation 2200 is serviced annually and further calibration should not be required.

GC-JJ-9173 Library Dilution & Pooling

29 January 2021 10:31



DRAFT SOP NGS Library Dilutions and Pooling for Sequencing

User	Eva Wozniak
Date	29/01/2021
File path	Z:\shares\Projects\NGS_Projects\RNA_Sequencing\Jarvis_Jonathan\GC-JJ-9173\Process
File name	GC-JJ-9173_Library_QC_Dilution_Pooling_290121.xlsx
Objective	Dilute and pool libraries for sequencing
Outcome	

Deviations from any step in the protocol should be noted in italicised green text under that step

Things to do before starting

- Save the following template in the project process folder on apocrita:

Template	Aprocrita Path of saved document
 Library_QC_Dilution...	Z:\shares\Projects\NGS_Projects\RNA_Sequencing\Jarvis_Jonathan\GC-JJ-9173\Process

- Remove the libraries from -20°C storage and let thaw to room temperature. Vortex and briefly centrifuge. Place on ice until needed.
- Remove from 4°C storage:
 - Qubit standards. Leave to equilibrate to room temperature for 30 minutes. Vortex before use.
 - High sensitivity D1000 and D1000 screentapes. Leave to equilibrate to room temperature for 30 minutes. Flick the screentapes to remove any bubbles before use.
 - High sensitivity D1000 and D1000 reagents. Leave to equilibrate to room temperature for 30 minutes. Vortex and briefly centrifuge.

Protocol

1. Quality Control

1. As per [DRAFT SOP Qubit 2.0 Fluorometer 250320EW](#) measure the concentration of each library/pool.

Qubit Lot Number

- 2. Record concentrations (ng/μl) in the 'Library QC' sheet of template Library_Dilution_Pooling_QC_Draft_150520.
- 3. Based on library concentration, run each library/pool on the tapestation as per [DRAFT SOP Tapestation QC 240320EB](#).

Screen tape Lot Number	
Ladder Lot Number	
Loading Buffer Lot Number	

- 4. Find the average sizes for each library/pool:
 - 1. On the Tapestation software, select 'Region'.
 - 2. Right click the main peak.
 - 3. Using the mouse, drag a region around the peak on the electropherogram. Average size (in base pairs, bp) will appear automatically in the data table below the electropherogram.
Note: For multiple libraries/pools, select "region setting", set the upper and lower limits for the region and click "apply" and "OK". This will place regions in each electropherogram. These can be altered manually if inaccurate.

Caution: only include the library peak in the region and no unspecific products. This will skew the molarity leading to incorrect concentration calculations.

- 5. Record average size (bp) in the 'Library QC' sheet of template Library_Dilution_Pooling_QC_Draft_150520. Molarities will be calculated automatically.
- 6. Options:
 - 1. If you are processing libraries with molarities > 4-5nM, proceed to [Library Dilution](#).
 - 2. If you are processing multiple libraries with molarities between 0.5nM-5nM, proceed to [Pooling individual libraries](#).
 - 3. If you are processing previously combined pools of libraries which require diluting to 4nM, proceed to [Combining Pools](#).
 - 4. If you are processing previously combined pools of libraries with concentration between 4-5nM, proceed to [Combining Pools](#), step 2.
 - 5. If you are processing a single library with molarity 4-5nM, proceed to library denaturation as per [DRAFT SOP Illumina NextSeq library denaturation and loading](#) or [DRAFT SOP Illumina MiSeq library denaturation and loading](#).

2. Library Dilution to 4nM

- 1. Into the 'Dilution' sheet of template Library_Dilution_Pooling_QC_Draft_150520, add the desired final volume (μl) of each 4nM library dilution. Dilution calculations will be calculated automatically.
Note: You may have a specific dilution volume in mind which may allow for repeated pooling in the future without the need for diluting libraries again.
- 2. Options:
 - 1. If processing <8 libraries, prepare each dilution in a fresh labelled 1.5mL LOBIND tube.
 - 2. If processing >8 libraries, prepare each dilution into wells of a 96-well plate.
- 3. Add calculated volumes of diluent to corresponding plate wells or LOBIND tubes.
Caution: This step must be witnessed and signed off by another member of staff.
- 4. Add calculated volumes of libraries to corresponding plate wells or LOBIND tubes.
Caution: This step must be witnessed and signed off by another member of staff.
- 5. Close tube caps or seal the plate with an adhesive seal. Vortex and briefly centrifuge the dilutions.
- 6. Label dilutions with Brady printer labels as per [SOP Brady Printer labels GC170216EW](#)
- 7. Measure each diluted library using the HS Qubit as per [DRAFT SOP Qubit 2.0 Fluorometer 250320EW](#).

Qubit Lot Number	
------------------	--

- 8. Record the results in column I of sheet 'Dilution'.
 - 9. Proceed to [Pooling individual libraries](#).
-

3. Pooling individual libraries

1. Using sheet 'Pooling - Libraries' in template Library_Dilution_Pooling_QC_Draft_150520, include information for final volume of pool, final concentration of pool and number of libraries to be pooled. Volumes of each library to combine will automatically be calculated.

Note: The typical desired final pool concentration is 4nM. This may be changed if dilutions to 4nM measure lower than expected. Make sure to dilute to the library with the lowest concentration.

2. Into a fresh 1.5mL LOBIND tube, add the calculated volumes of each library.
Caution: This step must be witnessed and signed off by another member of staff.
3. Calculate the volume of diluent to add for the desired final volume of the pool.
4. Add diluent to the 1.5 mL LOBIND tube containing combined libraries.
5. Vortex and briefly centrifuge the pool.
6. Label the pool with a Brady printed label as per [SOP Brady Printer labels GC170216EW](#)
7. Using the High Sensitivity Qubit kit, measure the concentration of the pool as per [DRAFT SOP Qubit 2.0 Fluorometer 250320EW](#).

Qubit Lot Number

8. Record the concentration in the appropriate 'Denaturation' sheet for the Illumina NGS platform being used.
9. Run the pool on a HSD1000 screentape as per [DRAFT SOP Tapestation QC 240320EB](#).

ScreenTape Lot Number	<input type="text"/>
Ladder Lot Number	<input type="text"/>
Loading Buffer Lot Number	<input type="text"/>

10. Record the average size in the appropriate 'Denaturation' sheet for the Illumina NGS platform being used.
11. Options:

1. If you have prepared multiple pools in this section, proceed to [Combining Pools](#), step 2.
2. If you now have your final pool prepared for sequencing, proceed to 'Library Denaturation' as per [DRAFT SOP Illumina NextSeq library denaturation and loading](#) or [DRAFT SOP Illumina MiSeq library denaturation and loading](#).
Note: The pool does not have to be sequenced straight away. It can be stored at -20°C for several months.

4. Combining Pools

1. For pools which required diluting to 4nM:
1. Into sheet 'Pooling - Pools' of template Library_Dilution_Pooling_QC_Draft_150520, add information for pool ID, volume of dilution required for each pool, current concentration (nM) and the desired concentration (nM) for each pool into table 1.
Note: The typical desired pool concentration is 4nM. This may need to be changed if dilutions to 4nM are measuring lower for example. Make sure to dilute to the library with the lowest concentration.
2. Into a 1.5mL LOBIND tube for each pool, add calculated volumes of diluent.
Caution: This step must be witnessed and signed off by another member of staff.
3. Into the corresponding 1.5mL LOBIND tube, add calculated volume of each pool.
Caution: This step must be witnessed and signed off by another member of staff.
4. Vortex and briefly centrifuge each dilution.
5. Label the pools with Brady printer labels as per [SOP Brady Printer labels GC170216EW](#)

- 2. Into table 2 of sheet 'Pooling - Pools' add information for the number of indexes included in each pool and the desired volume (μl) of the combined pool. A volume for each pool to be combined will automatically be calculated.

3. Combine the calculated volumes of each pool into a fresh 1.5mL LOBIND tube.
Caution: This step must be witnessed and signed off by another member of staff.
4. Add the calculated volume of diluent to the combined pool, for the desired final volume.
5. Vortex and briefly centrifuge.
6. Label the final pool with a Brady printer label as per [SOP Brady Printer labels GC170216EW](#)
7. Using the High Sensitivity Qubit kit, measure the concentration of the pool as per [DRAFT SOP Qubit 2.0 Fluorometer 250320EW](#).
- | | |
|------------------|--|
| Qubit Lot Number | |
|------------------|--|
8. Record the concentration in the appropriate 'Denaturation' sheet for the Illumina NGS platform being used.
9. Run the pool on a HSD1000 screentape as per [DRAFT SOP TapeStation QC 240320EB](#).
- | | |
|---------------------------|--|
| Screentape Lot Number | |
| Ladder Lot Number | |
| Loading Buffer Lot Number | |
10. Record the average size in the appropriate 'Denaturation' sheet for the Illumina NGS platform being used.
11. Proceed to 'Library Denaturation' as per [DRAFT SOP Illumina NextSeq library denaturation and loading](#) or [DRAFT SOP Illumina MiSeq library denaturation and loading](#).
Note: The pool does not have to be sequenced straight away. It can be stored at -20°C for several months.

POSTSCRIPT

Expected Results

A single pool of combined libraries at 4nM concentration ready for denaturation and loading onto an Illumina sequencer.

Sources of error/ limitations

Incorrect volumes are used for dilutions.

Libraries or pools are measured on the qubit incorrectly leading to false measurements being used to prepare the pool for loading.

Molarities for libraries or pools are calculated using incorrect average sizes from the tapestation.

The incorrect diluent is used.

Responsibilities

The protocol operator is responsible.

Internal Quality Assessment Control

N/A

Calibration

The qubit and tapestation require annual servicing to maintain performance.

GC-JJ-9173 NextSeq Loading

03 February 2021 19:07



DRAFT SOP Illumina NextSeq library denaturation and loading

User	Eva Wozniak
Date	01/02/2021
File path	Z:\shares\Projects\NGS_Projects\RNA_Sequencing\Jarvis_Jonathan\GC-JJ-9173\Process
File name	
Objective	
Outcome	

Deviations from any step in the protocol should be noted in italicised green text under that step

Things to do before starting:

Thaw on ice:

- Library. Vortex and centrifuge briefly.
- PhiX control (10nM stock or 20pM dilution). Vortex and centrifuge briefly.
- Custom primers. Vortex and centrifuge briefly.

HT1 Buffer. Invert 10 times to mix once thawed and return to ice.

Equilibrate to room temperature:

- Flow cell - keep in the foil packet until just before loading to the NextSeq.
- Sequencing cartridge - this may be thawed in a water bath for 30mins to 1 hour if necessary.

Prepare/Obtain:

- Fresh 0.2N NaOH from 1N NaOH aliquots.
 - 1N NaOH aliquots of 1mL should be prepared from 10N NaOH stock and can be kept at room temperature for 1 month.
- 200mM Tris-HCl.
 - 200mM Tris-HCl aliquots of 1mL should be prepared from 1M Tris-HCl stock, and can be stored at room temperature. Vortex and centrifuge briefly.
- 1 mL aliquot of EB Buffer. Vortex and centrifuge briefly.

- Make sure a Library QC sheet has been prepared as per SOP [DRAFT SOP NGS Library dilutions and pooling for sequencing](#)*
- Make sure you have valid Illumina Basespace credentials.*
- Record which number kit was used and the details of the run in the following document -*
/data/WHRI-
GenomeCentre/shares/Projects/NGS_Projects/NGS_Templates_Logs/GC_MiSeq_NextSeq_
RunLog_051119.xlsx

1. Local Run Manager - Run Setup

1. Prepare a NextSeq sample sheet:
1. Select a sample sheet template from the options below and open in Microsoft Excel:

Sample Sheet	Single Index	Dual Index
Output files	fastq	fastq
.csv Document	NextSeq_LR M_Gener...	NextSeq_LR M_Gener...

2. Edit the [Header] section as follows:
- i. Experiment Name - the iLab request ID
 - ii. Date - the date that the sequencing run will be started.
- Note: Leave the "Library Prep Kit" as "Custom". This allows indexes from multiple index kits to be run together.*
3. Edit the [Reads] for the number of sequencing cycles to be performed for Read 1 and Read 2.
4. Edit the [Data] section, entering all details as appropriate.

Caution: Only hyphens "-" may be used as ID delimiters - no characters other than alphanumeric are permitted.

Note: A list of common index sequences can be found in the following document: /data/WHRI-

GenomeCentre/shares/Projects/NGS_Projects/NGS_Templates_LogsNGS_IndexKit_Master Sheet_EW_120219.xlsx

5. Save the sample sheet to the project Process folder, including the iLab ID in the name.
2. On your PC open a web browser and enter the following URL: <https://138.37.142.216/#/home>
Note: you may be prompted to accept a new security certificate before you reach this page, follow the instructions on the screen.
3. From the LRM Run Dashboard click on "Create Run" and "GenerateFASTQ". This will open a new Create Run page.
4. Click on "Import Sample Sheet" and navigate to the saved sample sheet created in step 1. This will populate the fields with the information from the sample sheet.
5. Check all sample information is correct, in particular the read lengths, and click "Save Run". The run will now appear in the run dashboard as "Ready for sequencing".

2. Preparing 20pM PhiX

1. Pipette 2µl of 10nM PhiX into a clean 1.5ml LoBind microcentrifuge tube.
2. Add 3µl of EB Buffer. Vortex and briefly centrifuge.
3. Add 5µl of fresh 0.2N NaOH. Vortex and briefly centrifuge.
4. Incubate at room temperature for 5 minutes.
5. Add 5µl of 200mM Tris-HCl. Vortex and briefly centrifuge.
6. Add 985µl of chilled HT1 buffer. Vortex and briefly centrifuge.
7. Label appropriately with the dilution and date.

Note: This 20pM dilution can be stored at -20°C for up to 4 weeks.

3. Denature and dilute the library

1. Combine an equal volume of library and 0.2N NaOH in a 1.5mL LoBind microcentrifuge tube. Record the starting library molarity and volumes used in the table below (additional rows can be added for multiple libraries):
- Note: The starting library molarity should be no more than 4-5nM, and no less than 0.5nM. Dilute the stock further if necessary.*

0.2N NaOH preparation date 22/01/2021

2. Vortex and centrifuge briefly, then incubate at room temperature for 5 minutes.
3. Add the same volume of 200mM Tris-HCl as used for the library to the tube to neutralise the NaOH. Vortex and centrifuge briefly. Add an appropriate volume of HT1 Buffer to bring the total volume to 1mL.

HT1 Lot Number 20494411

4. Vortex and centrifuge briefly, and keep on ice.

Some example standard starting molarities are shown in the table below which can be used for guidance:

Starting Library Concentration	Library volume (µL)	0.2N NaOH (µL)	200mM Tris-HCl (µL)	Volume HT1 Buffer (µL)	Denatured Library molarity (pM)
4nM	5	5	5	985	20
2nM	10	10	10	970	20
1nM	20	20	20	940	20
0.5nM	40	40	40	880	20

5. Using the volumes calculated in the Library QC sheet (prepared as per SOP [DRAFT SOP NGS Library dilutions and pooling for sequencing](#)), dilute the denatured library using HT1 buffer to the molarity required for loading for a total volume of 1,300µL.
6. Following guidelines in the table below, select the %PhiX control to load
- Note: Including PhiX in the run allows for quality control of the sequencing run that is independent of the library. It is also required to provide base diversity for low-complexity libraries. Where mixed libraries are run, choose the library type that will use the highest % of the sequencing output.*

Library type	% PhiX required	Volume of 20pM PhiX (µL)	Selected option
Whole genome	1	1.2	<input type="checkbox"/>
Whole exome	1	1.2	<input type="checkbox"/>
mRNA	1	1.2	<input checked="" type="checkbox"/>
Total RNA	1	1.2	<input type="checkbox"/>
miRNA	1	1.2	<input type="checkbox"/>
scRNA	1	1.2	<input type="checkbox"/>
RRBS	20	24	<input type="checkbox"/>
ATAC-Seq	20	24	<input type="checkbox"/>
Amplicon (≤24 targets)	20	24	<input type="checkbox"/>
Amplicon (≥25 targets)	10	12	<input type="checkbox"/>
Bisulphite Amplicon (≤48 targets)	20	24	<input type="checkbox"/>
Bisulphite Amplicon (≥49 targets)	10	12	<input type="checkbox"/>

7. Remove and discard the chosen volume from the denatured library tube, and replace with PhiX control.
- Note: This is to maintain the 1,300µL loading volume.*
8. Vortex and centrifuge briefly and store on ice.

4. Load the sequencing cartridge

- 1. Invert the thawed cartridge 10 times to mix the reagents, then gently tap the cartridge on the lab bench to move the liquid to the bottom of the wells.
- 2. Using a P1000 pipette tip, pierce the foil at position 10 - labelled as "Load Sample".
- 3. Dispense the full 1,300 μ L of denatured library in to position 10.
- 4. Where custom sequencing primers are required, follow the steps below:
 - 1. Using a new P1000 pipette tip for each position, pierce the foil seals for each of positions 20, 21 and 22.
 - 2. Using a 1ml pasteur pipette, carefully remove 1mL of volume from each position and dispense to a new 2mL LoBind tube labelled with the well position number:
 - i. Position 20
 - ii. Position 21
 - iii. Position 22
 - 3. Add the appropriate volume of the appropriate custom primer to each of the LoBind tubes to a final concentration of 0.3 μ M. Complete the detail in the table below:

Primer	Reservoir Position	Custom primer name	Stock primer concentration (μ M)	Volume added (μ L)
Read 1	20			
Index read	22			
Read 2	21			
- 4. Vortex and centrifuge briefly.
- 5. Dispense the ~1mL of primer back in to the original reservoir position:
 - 1. Position 20
 - 2. Position 21
 - 3. Position 22

5. Starting a Run

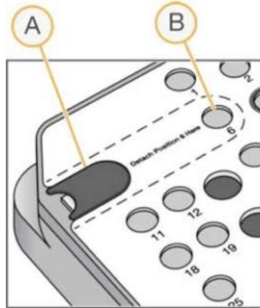
- 1. On the NextSeq, select "Sequence" from the welcome screen.
- 2. From the Run Setup screen, select the following and click next:
 - 1. Local Run Manger
 - 2. Use Basespace Sequencing Hub
 - 3. Run Monitoring and Storage
- 3. Log in to Basespace using your own Basespace account details.
Note: This ensures the audit trail correctly records the operator.
- 4. Select the "BLGC workgroup" for run monitoring and storage, then click Next.
- 5. A run list populated with all available runs for sequencing from the LRM will appear. Select the appropriate run and check that the sequencing parameters are correct. Click the Edit button under the output folder.
- 6. Edit the run parameters if necessary, and browse to the following location for run storage /data/WHRI-GenomeCentre/shares/Projects/NGS_Projects/NextSeq_LRM_runs. Click "Save". Click Next.
- 7. Load the Flow Cell:
 - 1. Remove the flow cell from the foil and plastic packaging.

Flow Cell Lot Number	20492914
----------------------	----------
 - 2. Wipe the glass surface of the flow cell with a kimwipe moistened with 70% ethanol.
 - 3. Clean the glass surface of the flow cell with a lens tissue removing any dust and debris.
 - 4. Inspect the flow cell making sure that the gaskets are intact and clear of blockages.
 - 5. Place the flow cell on the stage. Discard of the old flow cell in the clinical waste.
 - 6. Select Load. The door will close automatically.
 - 7. Select Next.
- 8. Empty the Spent Reagents container:
 - 1. Open the right side compartment door and carefully remove the waste cartridge from the

lower section.

- 2. Discard the contents into a clearly labelled Formamide waste container (under the centrifuge bench, LG150). Use the funnel to pour, and clear up any spillages which may occur.
- 3. Wipe away any drips from the outside of the container.
- 4. Load the empty waste container back into position. An audible click indicates that the container is in position.
- 5. Select Next.
- 9. Load the Buffer Cartridge:
 - 1. Carefully remove the used buffer cartridge from the right side upper compartment.
 - 2. Using a P1000 tip, widen the foil sealed wells on the top of the used cartridge.
 - 3. Invert the cartridge over the sink and leave to empty leftover buffers.
Note: Dispose of the cartridge in the clinical waste bin once drained.
 - 4. Load the new buffer cartridge into the buffer compartment. An audible click indicates that the cartridge is in position.
- 10. Load the Reagent Cartridge:
 - 1. Open the left side compartment and remove the used reagent cartridge from the NextSeq.
 - 2. Remove the rubber cover from position 6 and push down to remove the reservoir.

Buffer Cartridge Lot Number 20488125



- A Protective rubber cover
- B Position #6

- 3. Discard the formamide waste from position 6 into the Formamide waste bottle (under the centrifuge bench, LG150).
 - 4. Dispose of both reagent cartridge and reservoir into the clinical waste bin.
 - 5. Insert the new reagent cartridge into the compartment until the cartridge stops.
- Reagent Cartridge Number 20491807
- 6. Close the reagent compartment door.
 - 7. Select "Load". The software moves the cartridge into position automatically (~30 seconds), the reagent cartridge ID appears on the screen, and the sensors are checked.
 - 8. Select Next.
- 11. Pre-run checks will start automatically. Once all checks are complete and have passed, the run will start. Check the instrument after starting to ensure no errors have been flagged.
 - 12. Once the run has finished add the run metrics from Basespace run summary into the following document - /data/WHRI-GenomeCentre/shares/Projects/NGS_Projects/NGS_Templates_Logs/GC_MiSeq_NextSeq_RunLog_051119.xlsx.
Note: A post run wash will begin automatically.

POSTSCRIPT

Expected Results

A successfully completed NextSeq sequence run, producing results as outlined in the table below:

	NextSeq 550 System High-Output Kit	NextSeq 550 System Mid-Output Kit
--	------------------------------------	-----------------------------------

Single Reads	Up to 400 Million	Up to 130 Million
Paired-End Reads	Up to 800 Million	Up to 260 Million

NextSeq 550 System High-Output Kit	NextSeq 550 System Mid-Output Kit
> 75% bases higher than Q30 at 2 × 150 bp	> 75% bases higher than Q30 at 2 × 150 bp
> 80% bases higher than Q30 at 2 × 75 bp	> 80% bases higher than Q30 at 2 × 75 bp
> 80% bases higher than Q30 at 1 × 75 bp	

Sources of error/ limitations

Pipetting and QC errors will result in incorrect loading concentrations which may result on too few reads, a high number of reads which do not pass filter or failure of the run altogether.

Always prepare freshly diluted NaOH for denaturing libraries for cluster generation. This step is essential to the denaturation process.

It is important that not more than 1 mM NaOH is in the final solution after diluting with HT1. However, introducing 200 mM Tris-HCl ensures that the NaOH is fully hydrolyzed in the final solution.

Make sure each component of the kit is used from the same order and has the same number. This will ensure that there is no mix between high and mid output kits being run together.

Make sure that the run has the correct number of cycles.

Responsibilities

The protocol operator is usually responsible.

Internal Quality Assessment Control

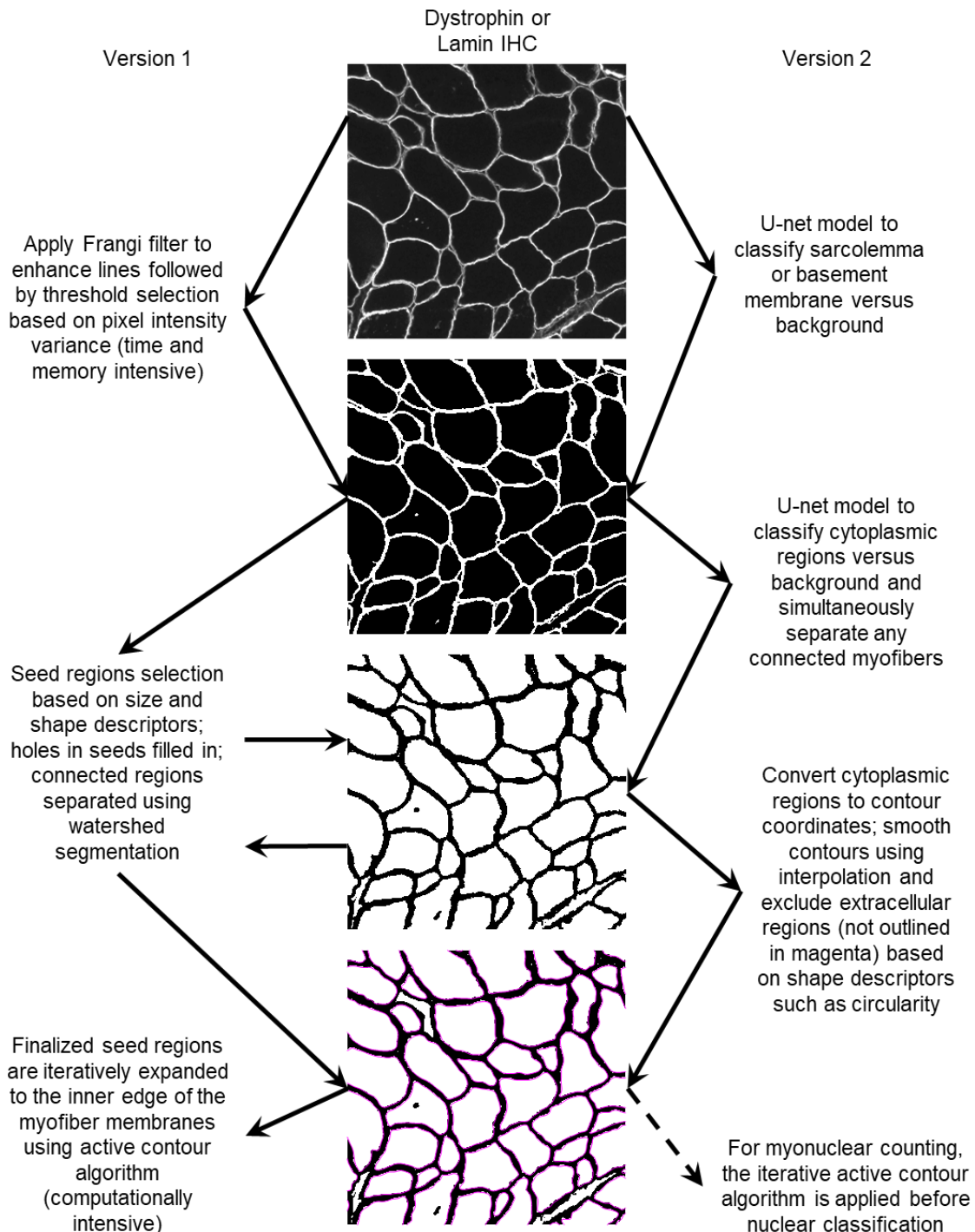
PhiX is spiked in to each cartridge to act as a measure of run performance. This is independent of library quality.

Calibration

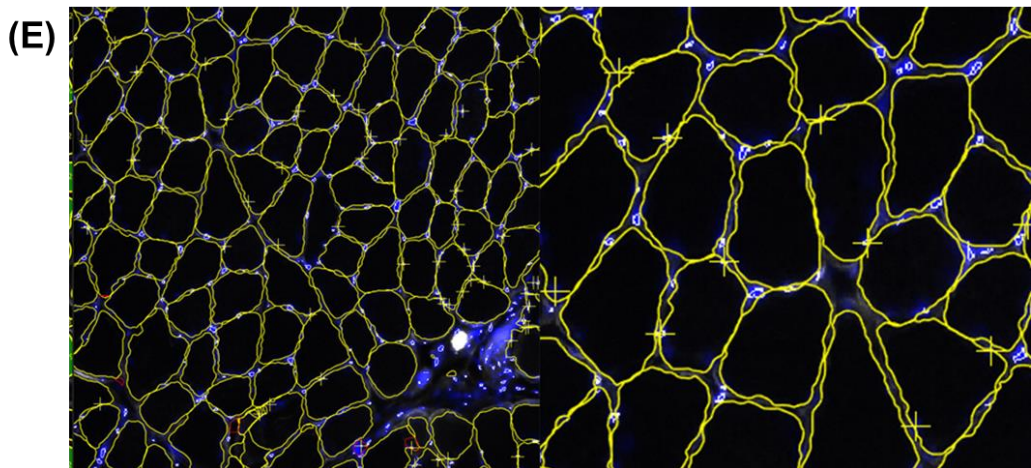
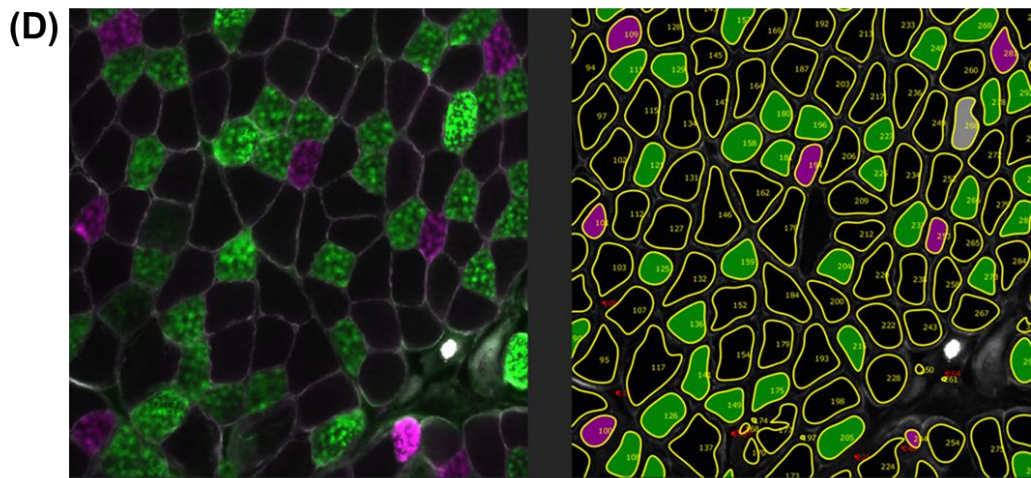
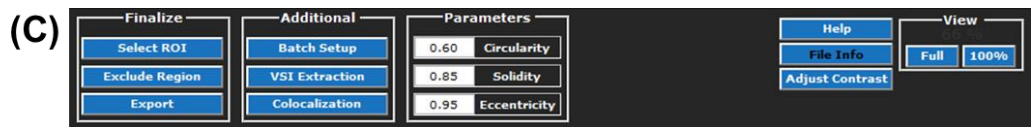
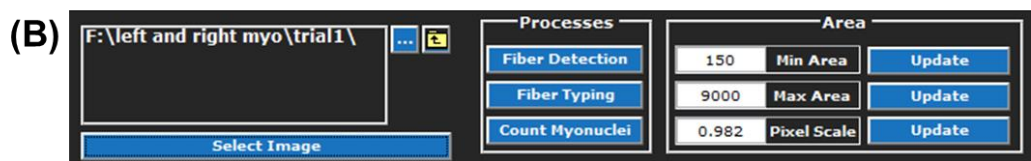
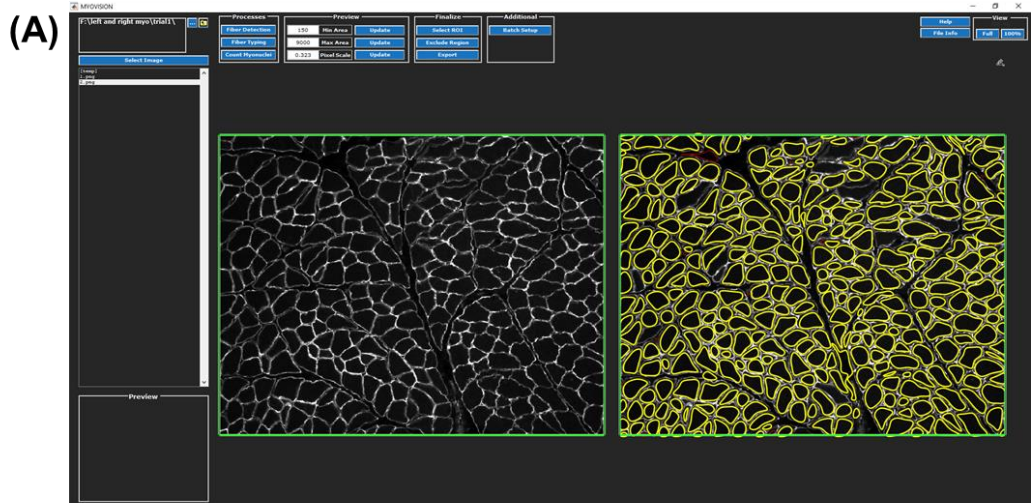
Use PhiX as a measure of how well the instrument is performing.

Appendix 3:

Overview of MyoVision 2.0 algorithm.



Appendix 3: Overview of MyoVision 2.0 algorithm. (Created by Dr. Yuan Wen).



Appendix 4: Overview of MyoVision 2.0 software and overview of new added features. (A) MyoVision 2.0 Programme. (B) MyoVision 1.0 features still included allow for selection of an image, automated fiber detection, automated fiber typing (3 channels) and automated myonuclear identification. User controlled parameters for minimum and maximum fiber area limits and pixel scale of input image. (C) Post analysis finalize tools allow the user to select a ROI or exclude regions, as well as the ability to export both a simple or more detailed report for each measured fiber. New features include the ability to batch set up a folder of images for large throughput or projects. VSI file extraction for use with Olympus microscopes. Co-localisation, allowing for pixel intensity of an additional channel to be measured within identified myonuclei. In addition, users now can alter measurement criteria for muscle fibers to give users flexibility with their muscle images and muscle phenotypes. These include, (1), Circularity (area to perimeter ratio excluding local irregularities. $(Circularity = 4\pi \cdot area / (convex\ perimeter)^2$. 1.0 indicating perfect circularity). (2), Solidity (measures the density of an object $(Solidity = Area/ Convex\ Area)$. 1.0 indicating perfect solidity). (3), Eccentricity (ratio of the length of the minor axis to the length of the major axis of an object $(Eccentricity = axis\ length\ short/axis\ length\ long$. More pennate fibers have higher eccentricity. Round fibers have low eccentricity). (D) Overview of MyoVision 2.0 analysis of a raw input myofiber membrane channel and two fiber types. Following automated analysis MyoVision 2.0 creates a computer-generated outline of the myofibers and associated fiber type. (E) MyoVision 2.0 then assesses whether nuclei are present within or outside of the myofiber border as previously described. Nuclei that meet the criteria are marked with a crosshair and can be subsequently checked by the user.

Analysis type selection. Channels can be selected for fiber detection and subsequent channels for analysis of fiber type and myonuclear counting.

Parameter selection for the minimum and maximum area for detected fibers. Pixel per micron selector.

Postanalysis finalize features. Select a region of interest or exclude part of an image. Region of interest is highlighted in green and can be altered. Export data from analyses.

Batch setup for multiple images (see Batch SetUp Section for more information). VSI Extraction for Olympus Microscopes. Co-localization tool for identification of an additional biomarker (separate channel) within identified myonuclei.

Parameter selection for circularity, solidity and eccentricity is now user controlled for more pennate muscle fibers and different phenotypes.

Contrast adjustment for lower quality images with too high/weak signal.

Image directory for single image selection.

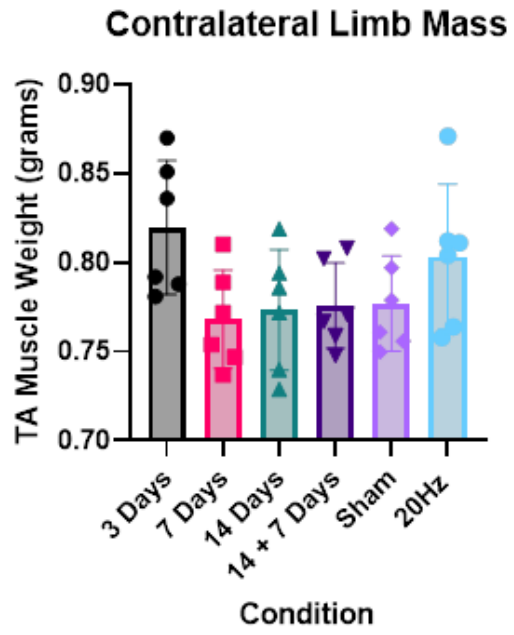
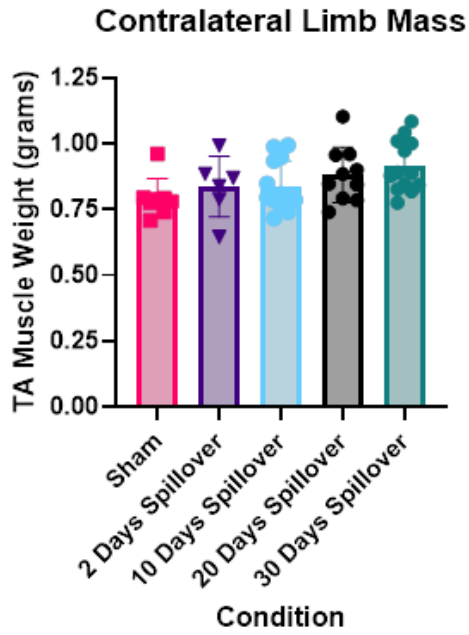
Help File Info Adjust Contrast View File LDRAR

Zoom control for postanalyses visual confirmation of fiber detection and myonuclear counting.

Identified fiber are highlighted in yellow. For fiber type analysis, fiber types are artificially colored. Myonuclei can be identified with crosshairs.

Status display for analysis progress.

Appendix 5: MyoVision 2.0 Help Sheet.



Appendix 7: One-way ANOVA with Tukey's post hoc analysis on contralateral muscle weights between resistance training group TA muscles and TTX-induced muscle atrophy TA muscles.